RELATIVE OPERATIONAL PERFORMANCE OF GEOSYNTHETICS USED AS SUBGRADE STABILIZATION

FHWA/MT-14-002/7712-251

Final Report

prepared for
THE STATE DEPARTMENTS OF TRANSPORTATION

Idaho	Ohio	South Dakota
Montana	Oklahoma	Texas
New York	Oregon	Wyoming

in cooperation with
THE U.S. DEPARTMENT OF TRANSPORTATION
FEDERAL HIGHWAY ADMINISTRATION

May 2014

prepared by
Eli Cuelho
Steve Perkins
Zachary Morris

Western Transportation Institute
Montana State University - Bozeman

RESEARCH PROGRAMS
MDT★

RELATIVE OPERATIONAL PERFORMANCE OF GEOSYNTHETICS USED AS SUBGRADE STABILIZATION

Final Project Report

by

Eli Cuelho, Steve Perkins and Zachary Morris

of the

Western Transportation Institute, College of Engineering
Montana State University – Bozeman

prepared for the

State of Montana, Department of Transportation
Research Programs

May 2014

TECHNICAL REPORT DOCUMENTATION PAGE

1. Report No. FHWA/MT-14-002/7712-251	2. Government Access No. TPF-5(251)	3. Recipient's Catalog No.	
4. Title and Subtitle Relative Operational Performance of Geosynthetics Used As Subgrade Stabilization		5. Report Date May 2014	
		6. Performing Organization Code	
7. Author(s) Eli Cuelho, Steve Perkins and Zachary Morris		8. Performing Organization Report Code	
9. Performing Organization Name and Address Western Transportation Institute PO Box 174250 Montana State University – Bozeman Bozeman, Montana 59717-4250		10. Work Unit No. (TRAIS)	
		11. Contract or Grant No. MSU G&C #4W3850 MDT Project #7712	
12. Sponsoring Agency Names and Addresses Project Administered by: Research Programs Montana Department of Transportation 2701 Prospect Ave. Helena, MT 59620-1001 Contributing DOTs: Idaho, Montana, New York, Ohio, Oklahoma, Oregon, South Dakota, Texas, Wyoming, USDOT		13. Type of Report and Period Covered Final Report December 2011 – May 2014	
		14. Sponsoring Agency Code 5401	
15. Supplementary Notes Research performed in cooperation with the Montana Department of Transportation, the U.S. Department of Transportation and the Federal Highway Administration. This report can be found at http://www.mdt.gov/research/projects/geotech/subgrade.shtml.			

16. Abstract

Full-scale test sections were constructed, trafficked and monitored to compare the relative operational performance of geosynthetics used as subgrade stabilization as well as determine which material properties are most related to performance. Seventeen, 50-ft. long test sections were constructed – fourteen containing geosynthetic reinforcement and three without. A subgrade material was prepared and constructed to an average strength of 1.79 CBR with the exception of two reinforced test sections which were constructed to greater and lesser strengths in order to determine the effect subgrade strength had on the performance of the test sections. The test sections were constructed with an average base course thickness of 10.9 in. with the exception of two controls where the base thickness was intentionally increased to evaluate the effect of base thickness on test section performance. Information from the test sections that were purposely constructed with different subgrade strength and base course thickness were used to correct any variability in the remaining reinforced test sections. Test sections were trafficked using a 45-kip, 3-axle dump truck. Rut, displacement, strain, and pore-water pressure were monitored during trafficking. Post-trafficking excavations were conducted to evaluate damage to the geosynthetic, base contamination from the subgrade, and strength and deformation of the layers. Longitudinal rut was the primary indicator of performance. Geosynthetic material properties were used in a linear regression analysis to determine which properties best related to performance of the test sections in this study as well as test sections from Phase I. It was determined that the strength and stiffness of the junctions and tensile strength properties in the cross-machine direction correlated well with performance. The woven and non-woven geotextiles also performed well, but further research is needed to determine which material properties correspond to performance. Additional work is needed to more confidently specify minimum values for geosynthetic material properties associated with good performance in subgrade stabilization applications.

| 17. Key Words
Geosynthetics, subgrade stabilization, reinforcement, separation, field test, junction stiffness, tensile strength, heave, geotextiles, geogrids, performance tests, subgrade (pavements), material tests, rutting, stability analysis, | | 18. Distribution Statement
No restrictions. This document is available through NTIS, Springfield, VA 22161. | |
| 19. Security Classif. (of this report)
Unclassified | 20. Security Classif. (of this page)
Unclassified | 21. No. of Pages
328 | 22. Price |

DISCLAIMER STATEMENT

This document is disseminated under the sponsorship of the Idaho Transportation Department, Montana Department of Transportation, New York Department of Transportation, Ohio Department of Transportation, Oklahoma Department of Transportation, Oregon Department of Transportation, South Dakota Department of Transportation, Texas Department of Transportation, Wyoming Department of Transportation, and the United States Department of Transportation in the interest of information exchange. The States of Idaho, Montana, New York, Ohio, Oklahoma, Ohio, Oregon, South Dakota, Texas, Wyoming, and the United States Government assume no liability of its contents or use thereof.

The contents of this report reflect the views of the authors, who are responsible for the facts and accuracy of the data presented herein. The contents do not necessarily reflect the official policies of the Idaho Transportation Department, Montana Department of Transportation, New York Department of Transportation, Ohio Department of Transportation, Oklahoma Department of Transportation, Oregon Department of Transportation, South Dakota Department of Transportation, Texas Department of Transportation, Wyoming Department of Transportation, and the United States Department of Transportation.

The States of Idaho, Montana, New York, Ohio, Oklahoma, Ohio, Oregon, South Dakota, Texas, Wyoming, and the United States Government do not endorse products of manufacturers. Trademarks or manufacturers' names appear herein only because they are considered essential to the object of this document.

This report does not constitute a standard, specification, or regulation.

ALTERNATIVE FORMAT STATEMENT

MDT attempts to provide accommodations for any known disability that may interfere with a person participating in any service, program, or activity of the Department. Alternative accessible formats of this information will be provided upon request. For further information, call (406) 444-7693, TTY (800) 335-7592, or Montana Relay at 711.

ACKNOWLEDGMENTS

EXECUTIVE SUMMARY

This research project was initiated as a follow-on study to the study completed by Cuelho and Perkins in 2009 (Phase I). In that study, it was found that test sections constructed on a weak subgrade and topped with a relatively thin layer of base aggregate carried very few passes of a fully-loaded three-axle dump truck. Results from that study indicated that, under those conditions, the tensile strength of the geosynthetic reinforcement in the cross-machine direction was primarily linked to performance and that current design methodologies for subgrade stabilization applications had inadequately predicted the depth of base course needed to stabilize the roadway. To further investigate the performance of geosynthetics under less severe conditions, new test sections were constructed with thicker base course. In addition, a broader set of material tests were conducted to more thoroughly evaluate the potential relationship between geosynthetic material properties and the relative performance of the test sections.

Full-scale test sections were constructed, trafficked and monitored at TRANSCEND, a full-scale transportation research facility managed by the Western Transportation Institute, to compare the relative operational performance of geosynthetics used as subgrade stabilization. In all, 17 test sections were constructed – 14 containing geosynthetic reinforcement and three without. Each test section was 50 ft. long. The average constructed strength of the subgrade was 1.79 CBR with the exception of two test sections reinforced with BX Type 2 geogrid, one of which was intentionally constructed to 2.17 CBR and the other at 1.64 CBR. These test sections were constructed to determine the effect that subgrade strength had on the performance of the test sections. Reinforced test sections were constructed with an average base course thickness of 10.9 in. Two control test sections were purposely constructed with thicker base course (16.3 in. and 24.9 in., respectively) to evaluate the effect of base thickness on test section performance. Information from the test sections that were purposely constructed with different subgrade strength and base course thickness were used to correct any variability in the remaining reinforced test sections.

Strength and consistency of the subgrade during construction was monitored using a variety of methods including vane shear, light-weight deflectometer (LWD), dynamic cone penetrometer (DCP), moisture content, in-field California Bearing Ratio (CBR), and density. The subgrade was built in 6 layers each approximately 6 in. deep. The geosynthetics and instrumentation were installed once the subgrade was built to the top of the trench. The base course aggregate was prepared to the proper moisture content and carefully placed on top of the geosynthetics in two lifts using a skid steer tractor. A large screed was used to create a uniform thickness of gravel over the test sections and a smooth-drum vibratory roller was used to compact the base aggregate.

A fully-loaded, three-axle dump truck was driven at 5 mph to traffic the test sections. Measurements of longitudinal rut, transverse rut, geosynthetic displacement, geosynthetic strain, and subgrade pore-water pressure were taken during trafficking. Trafficking of the test sections

was in one direction only and ran from mid-September to early November 2012to permit 740 passes of the truck prior to winter. Trafficking continued until rut levels reached approximately 3 in. (defined as failure in this project), at which time the ruts were filled in. This allowed the remaining un-failed portions of the test sections to be trafficked until failure.

Longitudinal rut measurements were periodically made at 40-inch intervals along the two rut paths formed by the truck. In addition, transverse rut measurements were made in two locations within each test section coincident with the instrumentation. Rut measurements were based on changes in elevation of the measurement points over time as compared to a baseline measurement made before trafficking. The accumulation of rut as a function of truck passes revealed that the woven geotextile (Mirafi RS580i) performed the best, followed by BX Type 2 geogrid, Secugrid 30-30 Q1 geogrid and the non-woven geotextile (Geotex 801). The poorest performance was observed in the Fornit 30, SF12 and TX160 geogrids.

An analysis of the longitudinal rut data was conducted to determine which geosynthetic material properties were most related to the performance of a particular test section. This analysis was conducted at various rut depths (1.0, 2.0 and 2.5 inches) to determine whether different material properties affected performance at various levels of rut. A linear regression analysis was performed using wide-width tensile strengths, cyclic tensile stiffness, resilient interface shear stiffness, junction strength and stiffness, and aperture stability modulus. Overall, this analysis revealed that wide-width tensile strength, junction strength and junction stiffness in the cross-machine direction were chiefly related to the performance of the reinforced test sections.

A similar regression analysis was conducted using data from Phase I (Cuelho and Perkins, 2009). The results indicated that under more severe conditions (primarily due to thinner base course) tensile strength properties of the geogrid were related to performance at higher rut levels. The benefit from junction strength and stiffness, however, peaked at around 3 in. of rut, and its contribution was less for higher rut levels.

The two geotextiles used in this research (TenCate Mirafi RS580i woven geotextile and Propex Geotex 801 non-woven geotextile) both performed well. The structure of these products and the way they interact and reinforce the weak subgrade is different than geogrids. Although surface friction and tensile strength are anticipated to be related to performance, additional research is needed to determine properties of geotextiles that relate to their performance in subgrade stabilization applications.

The transverse behavior of the test sections was characterized using transverse rut measurements (taken perpendicular to traffic), displacement measurements, and strain measurements. Bearing capacity failure was evident based on the heaving of the road surface adjacent to the wheel path. Heave occurred at different traffic levels within each test section, but most began around 100 to 300 truck passes, and test sections that began to heave earlier generally rutted more rapidly.

Long-term and dynamic displacement and strain data were collected during trafficking to further characterize the transverse behavior of the test sections through the movement and strain in the

material at two locations along the west edge of the wheel path. Information from these sensors seemed to indicate a transition of geosynthetic support from lateral confinement of the base course to membrane support involving deeper rutting and the tensioned-membrane effect. Changes in displacement revealed similar results to the heave and longitudinal rut response, namely, those test sections where the direction of the displacements transitioned earlier also reached higher levels of longitudinal rut earlier. This transition generally occurred at or before about 2 in. of longitudinal rut. Considering all of the test sections, maximum strains from the strain gages ranged from about 0.3 to 3.0 percent.

Two forensic investigations were conducted as part of this project: one immediately after trafficking had terminated and a second eight months later. During each of these visits, construction equipment was used to remove the base and subgrade layers so that large samples of the geosynthetic could be removed to assess damage and evaluate tensile properties, and to facilitate strength, stiffness and moisture measurements of the base and subgrade. The excavation of the base course, geosynthetic and subgrade provided a good opportunity to evaluate the shape of the rut in the two wheel paths, distortion of the geosynthetic from trafficking and rut accumulation, pullout, and other qualitative assessments. Damage to the geosynthetics was minimal. Products that failed earlier sustained the highest junction damage. Rib damage was greatest in the woven geogrid products, and these products also showed the greatest loss in tensile strength.

The results of a base course reduction (BCR) analysis indicated that the greatest reduction in base thickness was approximately 26.9 percent (TenCate Mirafi RS580i) corresponding to a difference of 4.0 in. of gravel; the least was 10.2 percent (Huesker Fornit 30) corresponding to 1.2 in. of gravel. These comparisons are valid for situations where additional gravel would be sufficient to allow heavy construction equipment to operate on the weak subgrade without excessive rutting or other damage. The results of the traffic benefit ratio (TBR) analysis indicated that the greatest benefit was achieved by using the TenCate Mirafi RS580i geotextile, resulting in an improvement of almost 11 times the traffic level when compared to the unreinforced test section (Control 1). The smallest TBR was in the Huesker Fornit 30 test section (TBR = 2.3).

The results of this study indicate that strength and stiffness of the junctions and tensile members mainly contribute to the performance of geosynthetics when used as subgrade stabilization, and the relative contribution of these material properties depends on the thickness of the base course aggregate layer and the anticipated rut depth. Practitioners who wish to use geosynthetics as subgrade stabilization should consider specifying minimum values for material properties that correlated with good performance of the test sections. These minimum values can be categorized by the severity of the site conditions, ranging from moderate to severe, as demonstrated in the two phases of this project. Further work is necessary to more confidently specify minimum values for geosynthetic material properties associated with good rut

performance. The specified properties are mutually important, and products having only one of the specified properties may not perform well. Further research is necessary to determine the combined effect of these properties as they relate to subgrade stabilization of a greater variety of base thicknesses and subgrade strengths. Information from that research could be used to augment or determine specific design parameters for a wider range of subgrade stabilization applications. Despite the fact that the woven and non-woven geotextiles performed well in the field study, it is unknown which material properties are directly responsible for their performance. Intuitively, surface friction properties and tensile strength of the materials play an important role; however, additional work is needed to evaluate the effect individual geotextile properties have on their performance in subgrade stabilization applications.

TABLE OF CONTENTS

LIST OF TABLES

LIST OF FIGURES

INTRODUCTION AND BACKGROUND

State departments of transportation (DOTs) routinely use geogrids and geotextiles for subgrade stabilization applications. This construction practice involves placing a geosynthetic on top of a weak subgrade to help stabilize the ground in order to construct the remaining gravel platform. The geosynthetic generally provides stabilization of the subgrade by increasing the load-carrying capacity of the system and maintaining separation between the soft subgrade and subbase materials. Subgrade stabilization allows for a firm construction platform to be built with less aggregate and less construction time as compared to construction without the stabilization geosynthetic. Typical applications are temporary haul roads or unpaved low-volume roads. There is a general consensus concerning the effectiveness of geosynthetics in this application; however, there is a lack of understanding and agreement on the geosynthetic's material properties needed for performance. Those properties should be specified in order to ensure its beneficial use and to allow a broad range of products to be considered.

Geogrids and geotextiles used in stabilization applications provide benefit through three possible reinforcement mechanisms: 1) lateral restraint of the base and subgrade through friction and interlock between the aggregate, soil, and geosynthetic; 2) increase in system bearing capacity by reducing the stress on the subgrade; and 3) membrane support of wheel loads, as illustrated in Figure 1. Further benefit is also provided through separation of the subgrade and base layers from one another which decreases intermixing of particles between the two layers. Understanding which material properties help provide this support is important and was the main thrust of the research conducted as part of this endeavor.

Multiple full-scale field studies have been conducted in the past to help understand the behavior and performance of geosynthetics in subgrade stabilization applications (Fannin and Sigurdsson, 1996; Tingle and Webster, 2003; Hufenus et al., 2006; and Cuelho and Perkins, 2009). The study conducted by Cuelho and Perkins (2009), which was the first phase of this current study, provided correlations between a limited number of material properties and performance for high rut and low traffic conditions and determined that the ultimate tensile strength and tensile strength at 2 percent axial strain were relatively important material properties in determining how well the geosynthetics performed under conditions of rapid rut development. These properties were most important because of the large loads the geosynthetic was required to support, which approached, and in some cases exceeded, the ultimate tensile strength of the materials. The results of this previous study were limited to situations where a relatively thin base course is placed over soft ground. The rapid rate of damage sustained by the test sections under low traffic levels (4 inches of elevation rut in less than 40 truck passes) was mainly thought to be a product of the shallow depth of gravel and the high percentage of rounded particles within the aggregate mix which were unable to carry the heavy loads imparted by the test vehicle. The mode of failure of most test sections was a clear bearing capacity (shear)

failure in the subgrade and involved tensile rupture of several geogrid products and pullout of one geotextile product.
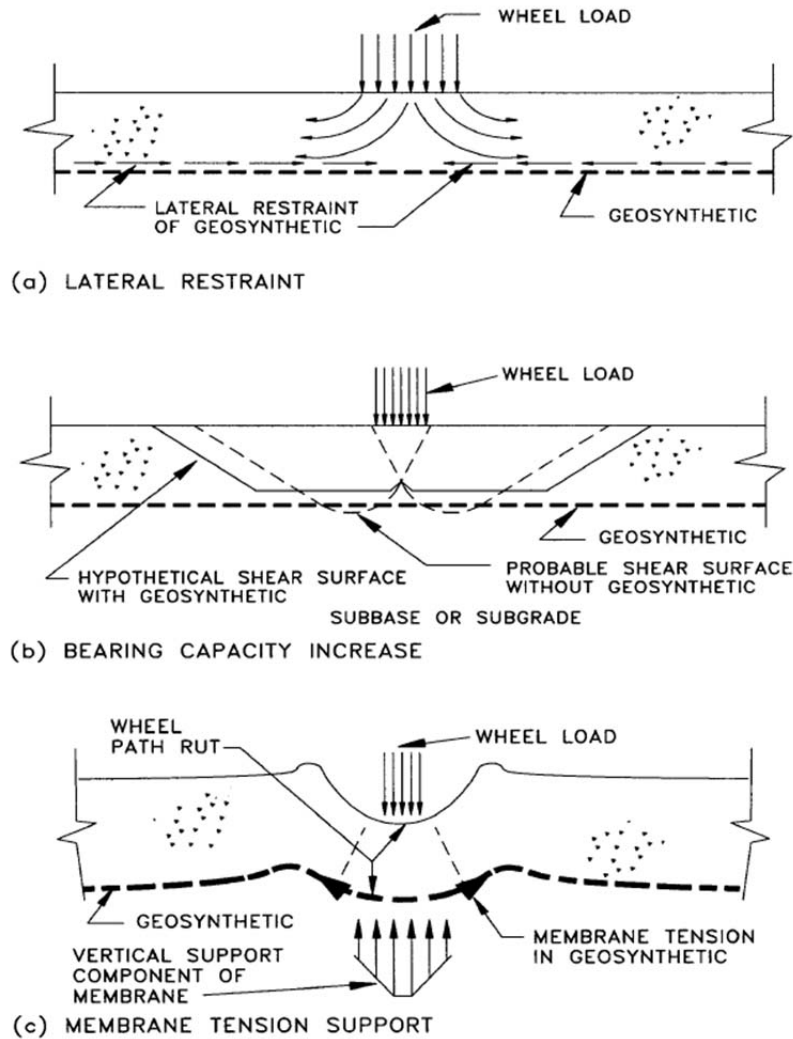
Figure 1: Possible reinforcement functions provided by geosynthetics in subgrade stabilization applications (from Haliburton et al., 1981).

Subgrade stabilization for roadway construction generally requires that the subgrade-geosynthetic-base layer system reaches a stable condition. This condition is typically assessed by observing the deformation of the system under the single pass of a loaded vehicle and seeing that this deformation is minimal. Under stable conditions, bearing capacity failure of the subgrade has not occurred. In this operational condition, it is anticipated that other geosynthetic properties might be more significant. The intention of this research project was to construct the test sections with thicker base course resulting in slower rut development to determine which material properties are most responsible for showing good performance in subgrade stabilization applications.

The main objective of this project was to determine material properties of geosynthetics most related to the in-field performance of geosynthetics used for subgrade stabilization, so that DOT personnel can objectively and confidently specify appropriate geosynthetics based on material properties and cost for a specific situation, while also allowing competition from different manufacturers. To accomplish this, test sections were constructed at a controlled test site to investigate the relative benefit to an unpaved road of various geosynthetics available on the market. An artificial subgrade was constructed to provide equivalent conditions for each test section; likewise the gravel surfacing along the entire test bed was uniformly constructed to be able to make direct comparisons between geosynthetic products. Transverse and longitudinal rut measurements were the primary indicators of performance benefits of each geosynthetic. Additionally, post-traffic examination provided information regarding the performance and installation survivability of the geosynthetics. The final analysis illustrated cost savings by optimizing material properties that most influence the design and performance of these materials, thereby increasing the Department's knowledge base, confidence and efficiency as it seeks to update its specifications.

Insight into the mechanisms of support that geosynthetics provide was determined based on strain gage and LVDT measurements, and transverse rut profiles. Mechanical properties of geosynthetics were compared to truck passes at the transition from lateral confinement to membrane support as well as at failure to evaluate which properties best predicted field performance. The properties evaluated included wide-width tensile strength, cyclic tensile modulus, resilient interface shear stiffness, junction strength, and aperture stability modulus.

EXPERIMENTAL DESIGN

The objectives of this research were accomplished through a comprehensive program that included constructing, monitoring and analyzing full-scale field test sections as well as extensive laboratory tests on geosynthetics. Seventeen test sections were constructed, trafficked and monitored during summer 2012 at the TRANSCEND test facility in Lewistown, Montana to evaluate geosynthetics when used as subgrade stabilization. Design of this experiment was based on previous work completed in 2009 (Cuelho and Perkins, 2009) and centered on providing a uniform platform to evaluate the performance of multiple geosynthetics and other unpaved road design characteristics. The first major subsection below documents the basic design attributes of the research test site, material properties and characterization of the various construction materials, how the test site was constructed, an overview of the instrumentation and data acquisition systems, and a description of the trafficking and monitoring efforts. The second major subsection provides an overview of the geosynthetic characteristics as provided in manufacturer's data sheets and material tests conducted by the Western Transportation Institute (WTI) and an outside testing lab.

Design and Layout of Field Experiment

The design and layout of the test area focused on creating a uniform roadway to study the effects of geosynthetic stabilization, subgrade strength, and base course gravel depth. This required removing the existing roadway and replacing it with a new road that was carefully constructed to minimize or control differences in site characteristics along its length. The TRANSCEND test facility in Lewistown, Montana was used for this research effort.

This research project was specifically planned to quantify differences in performance of various geosynthetic products under the same conditions (i.e., same subgrade strength and base course thickness). In addition, several additional test sections were constructed to study the effect that variations in subgrade strength and base course thickness had on the performance. Specifically, three control sections (i.e., no geosynthetic) were constructed, each having different thickness of base course aggregate, and three test sections were built using Tensar BX Type 2 geosynthetic, each having different subgrade strengths. The final arrangement of the test sections is shown in Figure 2, which includes the target subgrade strength and base thickness properties for construction.
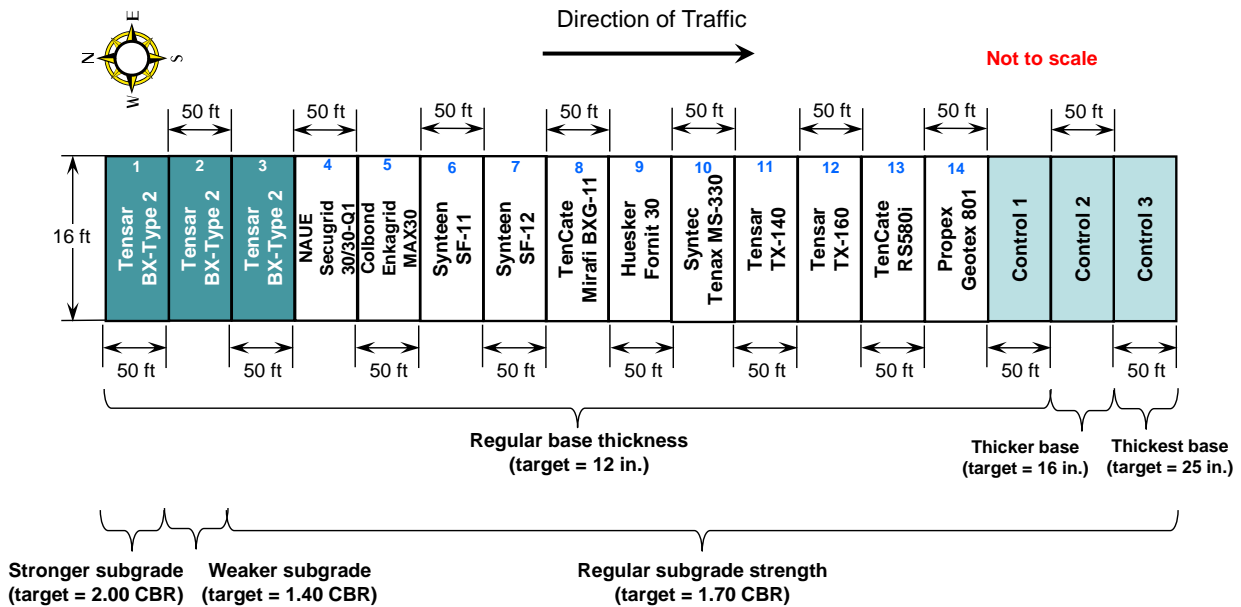
Figure 2: General layout of test sections with target construction parameters.

Design of this project is based on a single-lane, gravel road that is built on 3 ft. of soft subgrade above a strong, stable substrate. A trench was excavated so the final grade of the test site was similar to the surrounding grade (i.e., the existing taxiway). The size of the excavation was 16 ft. wide by 3 ft. deep to sufficiently minimize boundary affects from the trench walls and foundation. A length of 860 ft. was necessary to evaluate 14 geosynthetic test sections and three control sections. The bottom of the test pit was tapered at the ends to facilitate movement of the construction equipment into and out of the pit. The tapered area was in addition to the 860 ft and was not included in the experiment.

The surface of the subgrade was sloped at approximately 1 percent to match the existing east to west slope of the taxiway so that water from precipitation would not pool on the surface. The base course (which formed the driving surface) was also sloped in the same manner to maintain uniform gravel thickness across the test sections. The base aggregate extended past the outside edge of the subgrade and tapered down to the existing paved taxiway. Because the final level of the base aggregate was higher than the original level of the taxiway, a gradual ramp was built at each end using the base aggregate to allow the test vehicle to easily enter and exit the test sections during trafficking. A cross-sectional view of a typical test section is shown in Figure 3 with the test vehicle. Dimensions and loads on the wheels of the vehicle are presented in the Trafficking and Data Collections subsection below.
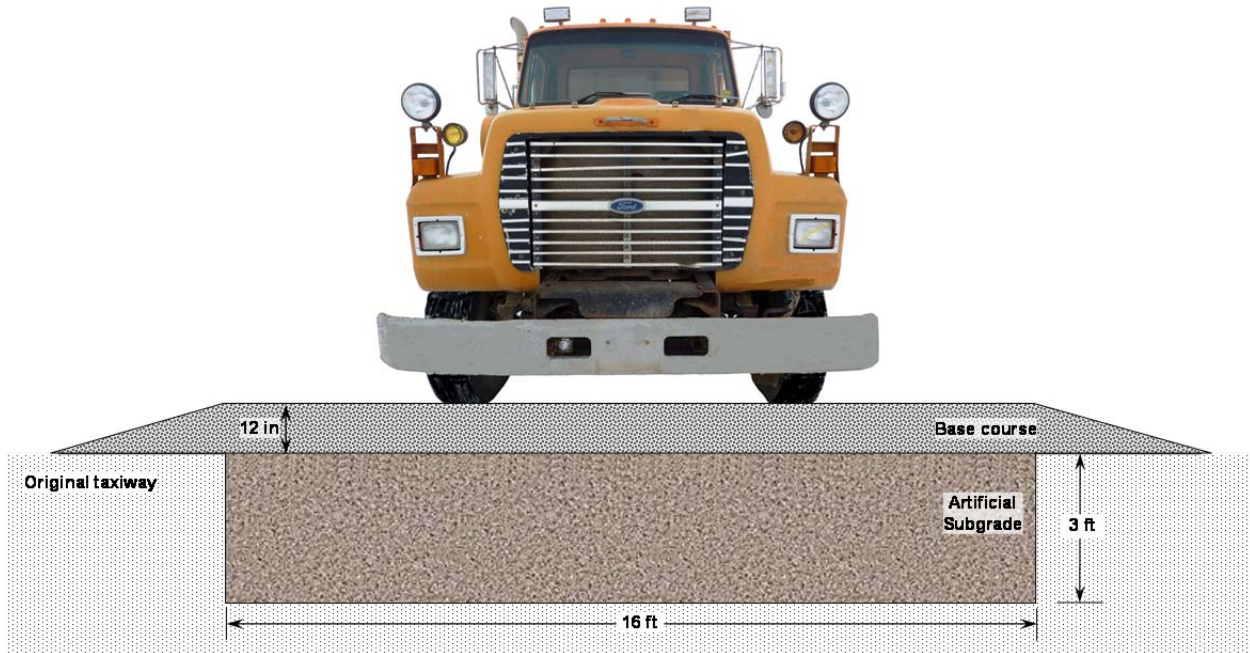
Figure 3: Cross-section of field test section with truck (truck scaled to approximate size).

Artificial Subgrade

The subgrade soil was obtained from a nearby gravel pit, and consisted of natural overburden material that was cleared and stockpiled to provide access to gravel sources below. The material was dried and screened to remove particles greater than 1 inch in diameter, and help blend the stockpile together to ensure uniformity. The subgrade was delivered to the test site and stockpiled adjacent to the trench along the test sections. This soil classified as A-6 according to the AASHTO classification system (AASHTO M-145) or CL (sandy lean clay) according to the USCS classification system (ASTM D 2487). Other relevant properties of the artificial subgrade are listed in Table 1. The gradation for the subgrade material is shown in Figure 4.

Table 1: General Properties of the Artificial Subgrade

Property	
Liquid Limit	34
Plastic Limit	17
Plasticity Index	17
% passing #200 sieve	55%
Max. dry unit weight[†]	112 lb/ft^3
Optimum moisture content[†]	16%

[†] using standard Proctor procedure (ASTM D698)
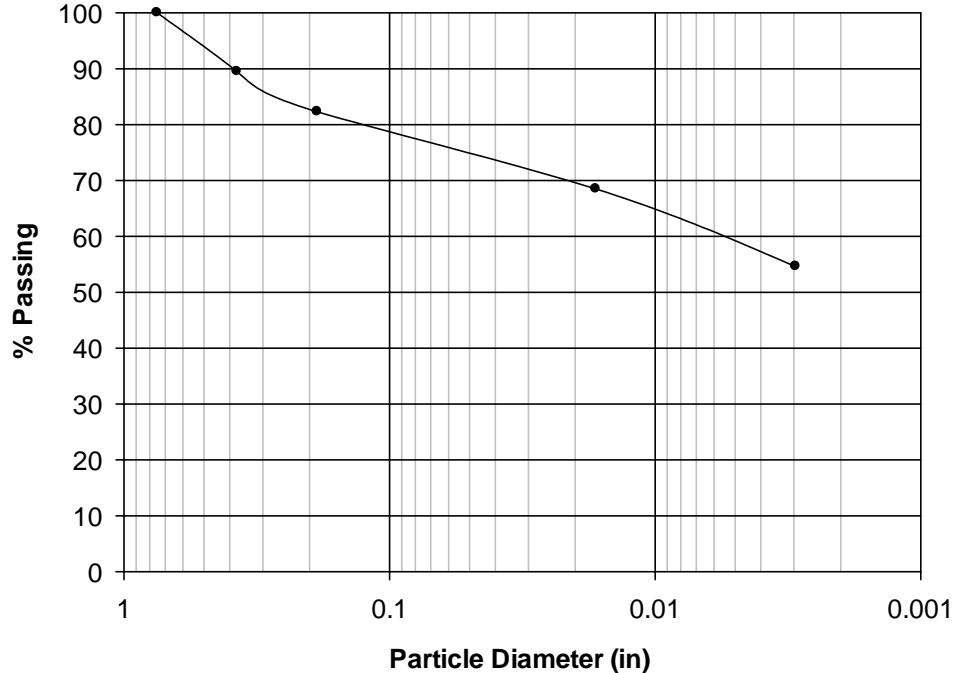
Figure 4: Grain-size distribution of the artificial subgrade soil.

For construction purposes, the subgrade was first characterized in the lab by evaluating the relationship between vane shear strength and California Bearing Ratio (CBR) as the water content was varied. Vane shear tests were conducted on unsaturated, laboratory CBR samples screened to 3/8 in. to relate CBR to vane shear strength. The linear relationship that was developed in the lab using both of these tests resulted in a linear regression R^2 factor of 0.843, as shown in Figure 5. According to this data, the shear strength as determined using the vane shear device must be between roughly 1,340 and 1,460 lb/ft^2 to achieve a CBR strength of 2.0 ±0.1 (Test Section 1), between roughly 960 and 1,090 lb/ft^2 to achieve a CBR strength of 1.4 ±0.1 (Test Section 2), and between roughly 1,150 and 1,270 lb/ft^2 to achieve a CBR strength of 1.7 ±0.1 (Test Sections 3–C3). Field measurements of shear strength using the hand-held vane-shear device were used as the primary means to characterize the subgrade as it was placed in the open trench because: 1) the device is simple to operate, 2) it provides an immediate assessment of strength, and 3) it was more precise than other devices. A dynamic cone penetrometer (DCP) and lightweight deflectometer were also used as a comparison to monitor subgrade material properties.
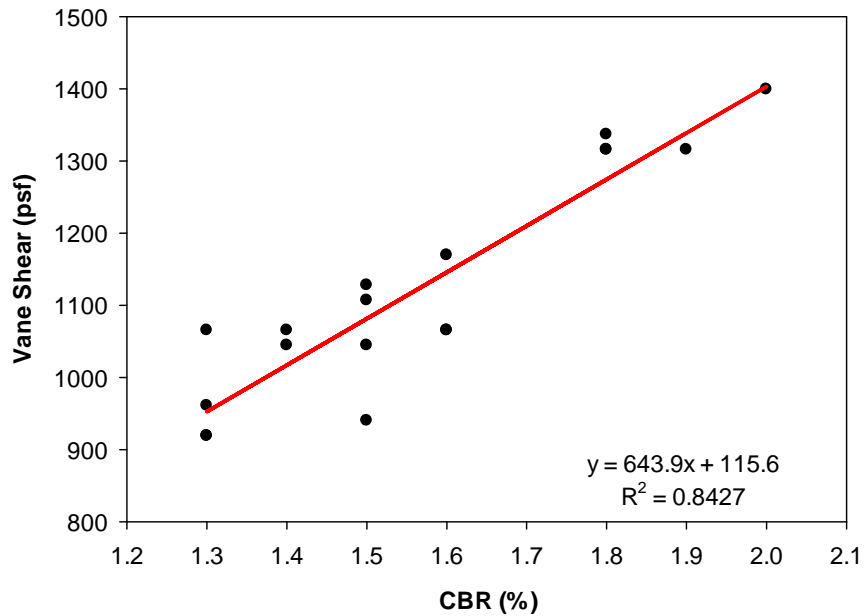
Figure 5: Relationship between California Bearing Ratio and the hand-held vane shear device.

Base Course Aggregate

Base course aggregate specifications were collected from Idaho, Montana, New York, Ohio, Oklahoma, Oregon, South Dakota, Texas and Wyoming (participating states to this pooled-fund research project) to help determine the specifications for the base course aggregate to be used in this research project. Gradation, percent fractured faces, minimum number of fractured faces, sieve size delineating fractured face content, liquid limit and plasticity index were considered as part of this analysis. The percent passing and range of values was averaged for all specifications. In some cases, more than one gradation in a given state was appropriate, so both were included in the analysis. Overall, the combined base course gradation specification is very similar to Montana's 5A Base Course. The Montana 5A specification and the average range of gradations from the various states are summarized in Figure 6 and Table 2.

Figure 6: Range of base course aggregate gradations for participating states.

Table 2: Comparison of Montana 5A and Participating States' Average Base Course Gradations

Sieve (US)	Sieve (in)	Montana 5A (% pass.)	Average range (% pass.)
2-inch	2	100	98-100
1 1/2-inch	1.5	94-100	89-100
3/4-inch	0.75	70-88	62-90
3/8-inch	0.375	50-70	46-74
#4	0.187	34-58	33-62
#40	0.0167	6-30	9-33
#200	0.00295	0-8	2-11

In general, fractured faces ranged from no requirement to 100 percent, with the average being between 40 and 50 percent. Most specifications specified a maximum liquid limit of 25 percent and maximum PI of around 6. Considering all of this information, the Montana 5A specification was used as the specification for the base course aggregate for this project with one exception, that the fractured face requirement for material larger than the #4 sieve be increased from 35 percent to 50 percent on at least two faces.

The final base course aggregate for this project was obtained from a gravel pit approximately 20 miles away from the test site. The gradation is provided in Figure 7. It classified as A-2-4 according to the AASHTO classification system (AASHTO M-145) or GP-GC (poorly graded gravel with clay with sand) according to the USCS classification system (ASTM D 2487). This

material would have classified as A-1-a if the plasticity index had been less than 6 percent, but because the PI was 8 percent it classified as an A-2-4 material. Other relevant properties of the base course aggregate are listed in Table 3. CBR tests run on the base course aggregate (ASTM D1883) resulted in bearing ratios that were higher at 0.2 inches displacement than at 0.1 inches displacement, meaning that the CBR at 0.2 inches should be used. Corrections were also necessary to account for the concave upward shape of the load-displacement curve from the CBR tests. These corrections resulted in CBR values greater than 100 for the base course material.
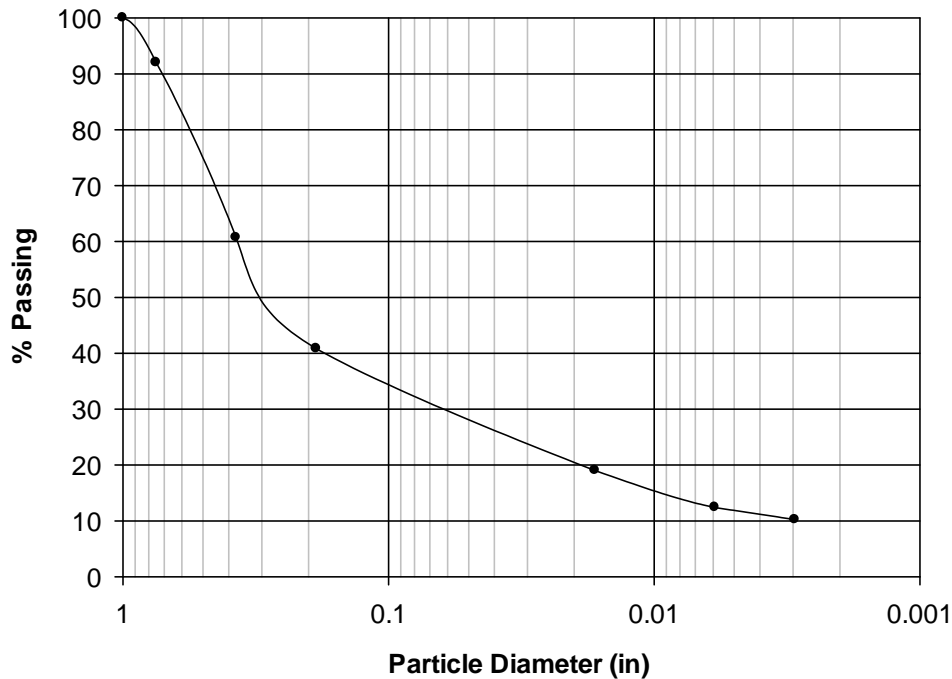
Figure 7: Base course aggregate grain-size distribution.

Table 3: General Properties of the Base Course Aggregate

Property	
Liquid Limit of fines	23
Plastic Limit of fines	15
Plasticity Index of fines	8
% passing #200 sieve	10%
Max. dry unit weight[†]	139 lb/ft^3
Optimum moisture content[†]	6.0%
% fractured faces	55%
CBR[†] (at ρ_{dry} = 140 lb/ft^3)	>100

[†] using modified Proctor procedure (ASTM D1557)

Separation and filtration criteria were checked using the gradation information from the subgrade and the base course. According to the specifications listed in Holtz et al. (2008), a separation geotextile between the base and subgrade is recommended when D_{85} of the base aggregate (D_{85agg} = 0.67 in.) is greater than $5 \cdot D_{85}$ of the subgrade ($5 \cdot D_{85sub} = 5 \cdot 0.3 = 1.5$ in.). In this case, no separation geotextile is required (0.67 in < 1.5 in.). Filter requirements were evaluated by considering the following two criteria: whether the quotient of D_{15} of the aggregate over the D_{85} of the subgrade is less than or equal to 5, and whether the quotient of D_{50} of the aggregate over the D_{50} of the subgrade is less than or equal to 25. For the subgrade and base course materials used in this research project, the first relationship was satisfied, but the second was not. As discussed below, contamination of the base course from the subgrade during trafficking was minimal for the small traffic levels and short duration of the project – increasing on average approximately 5 percent in the base directly above the geosynthetic.

Reinforced test sections 1 – 14 and control test section C1 were constructed with a target base course thickness of 12 inches. Control test sections C2 and C3 had a target base course thickness of 16 and 24 in., respectively. The base thickness of 12 in. was based primarily on results of box test sections performed at GeoTesting Express (GTX – Alpharetta, GA). Results from other test sections constructed at GTX over the past several years were also used.

The test section constructed at GTX for this project used the same subgrade and base aggregate as that used in the full-scale test sections. The GTX test section used 10 in. of aggregate, a peak plate pressure of 90 psi, and Tensar BX Type 2 as the reinforcement. The test section sustained 1,800 load cycles to reach 3 in. of rut depth. The AASHTO equation for equivalent axle load factor was used to compute the equivalent number of ESALs corresponding to the loading conditions used in the GTX facility. A factor of 1.75 was computed, resulting in 3,140 ESALs to reach 3 in. of rut depth.

A load factor of 1.25 was computed using the AASHTO equation for the truck used to traffic the test sections. It was anticipated that no more than 2,000 truck passes would be applied and the expectation was that all sections would reach about 3 in. of rut within 2,000 truck passes. Using a load factor of 1.25, this corresponds to 2,500 ESALs. Comparison of this goal to the results of the GTX test section suggested that the TRANSCEND test sections could be constructed with less than 10 in. of aggregate base. Based on the rapid rutting that occurred in the Phase I project when 8 in. of aggregate was used (Cuelho and Perkins, 2009), by examining other test section results from GTX, and by expecting that truck traffic would be more damaging than cyclic plate loading, the research team did not feel comfortable reducing the aggregate thickness to below 10 in. and felt that a thickness of greater than 10 in. was needed. This was especially true to avoid excessive rutting in the control section. These considerations led to the design thickness of 12 in. of aggregate base. For control sections C2 and C3, aggregate thickness of 16 and 24 in., respectively, were selected to allow base course reduction (BCR) ratios potentially as great as 60 percent to be calculated by comparison of results from reinforced test sections to the three

control sections. BCR is defined in Equation 1, and is calculated for each reinforced test section in the analysis section of this report.

$$BCR = \frac{D_\Delta}{D_{unreinforced}} * 100\% \qquad \textbf{Equation 1}$$

where,

D_Δ is the difference in gravel thickness between reinforced and unreinforced test sections that perform the same, and

$D_{unreinforced}$ is the gravel thickness for the unreinforced test section.

Geosynthetics

Twelve geosynthetic products were used in this research project to evaluate their relative performance under the conditions presented herein. A summary of the basic material characteristics of these products is listed in Table 4. Five laboratory tests were used to characterize the geosynthetics used in this research, and include wide-width tensile strength (ASTM D 4595 and ASTM D 6637), cyclic tensile modulus (ASTM D 7556), resilient interface shear stiffness (ASTM D 7499), junction strength (ASTM D7737), and aperture stability modulus (Kinney, 2000). The first three tests were performed by WTI and the last two tests were conducted by SGI Testing Services (Norcross, GA), an independent geosynthetic testing lab. All of the testing by WTI and SGI was performed in general accordance with the test's respective testing standard, and any deviations from the standard are noted in the subsections below.

Geosynthetic properties were checked against the survivability and aperture size specifications as outlined in Holtz et al. (2008) for stabilization applications. All of the geosynthetics met the Class 1 survivability requirements (ultimate strength > 1,230 lb/ft for geogrids, and grab strength > 900 lb for geotextiles), but not all geosynthetics met the aperture size criteria. According to the specifications, geogrid apertures must be between 0.5 and 3.0 inches, AND $\geq D_{50}$ of the aggregate above the geogrid, AND $\leq 2 \cdot D_{85}$ of aggregate above the geogrid. The D_{50} and D_{85} of the base aggregate are 0.3 in. and 0.67 in., respectively. All of the geogrids met the D_{50} requirement. All geogrids meet the $2 \cdot D_{85}$ requirement except Colbond – Enkagrid MAX 30. Even though the aperture size of the SynTec – Tenax MS 330 material is large, tripling the material reduces the apparent opening size and helps this material meet this requirement.

Table 4: Summary of Geosynthetic Characteristics

Geosynthetic Test Section	Product Manufacturer - Name	Structure	Polymer[a]	Roll Width (in)	Mass per unit area (oz/yd^2)	Aperture Size[b] (in) MD x XMD
1, 2 and 3	Tensar - BX Type2	integrally-formed, biaxial geogrid	PP	160	8.9	1.0 x 1.3
4	NAUE - Secugrid 30/30 Q1	vibratory-welded, biaxial geogrid	PP	186	5.9	1.3 x 1.3
5	Colbond - Enkagrid MAX 30	biaxial, welded geogrid	PP	197	6.0	1.7 x 1.6
6	Synteen - SF 11	PVC-coated, woven, biaxial geogrid	PMY	186	9.5	1.0 x 1.0
7	Synteen - SF 12	PVC-coated, woven, biaxial geogrid	PMY	183	12.3	1.0 x 1.0
8	TenCate - Mirafi BXG11	PVC-coated, woven, biaxial geogrid	PMY	158	9.1	1.0 x 1.0
9	Huesker - Fornit 30	polymer-coated, knitted, biaxial geogrid	PP	206	6.5	0.6 x 0.6
10	SynTec - Tenax MS 330	extruded, triple-layer, biaxial geogrid	PP	156	9.7	1.7 x 2.0[c]
11	Tensar - TX140	integrally-formed, triaxial geogrid	PP	160	5.3	1.6 x 1.6[d]
12	Tensar - TX160	integrally-formed, triaxial geogrid	PP	160	6.4	1.6 x 1.6[d]
13	TenCate - Mirafi RS580i	woven geotextile	PPF	204	12.3	40[e]
14	Propex - Geotex 801	non-woven, needle-punched geotextile	PP	186	8.0	80[e]

[a] PP = polypropylene, PMY = polyester multifilament yarn, PPF = polypropylene fiber
[b] MD = machine direction, XMD = cross-machine direction
[c] for a single layer; apparent opening size is reduced when three layers are stacked on top of one another
[d] reported as "rib pitch" in manufacturer's specification sheet
[e] Apparent Opening Size (AOS) in U.S. Standard sieve size, ASTM D 4751

Wide-Width Tensile Strength

The wide-width tensile strength test is used to determine the force-elongation curve of the geosynthetic in its two principal directions. A MTS servo-hydraulic load frame was used to conduct the wide-width tensile testing. The geosynthetics were held on both ends by Curtis Sure-Grip Geosynthetic Grips which apply pressure to the geosynthetics using a pneumatically driven hydraulic system. The grips can accommodate a sample up to 8 inches wide and have a capacity of 10,000 lbs. The setup for a typical wide-width tensile test is shown in Figure 8.
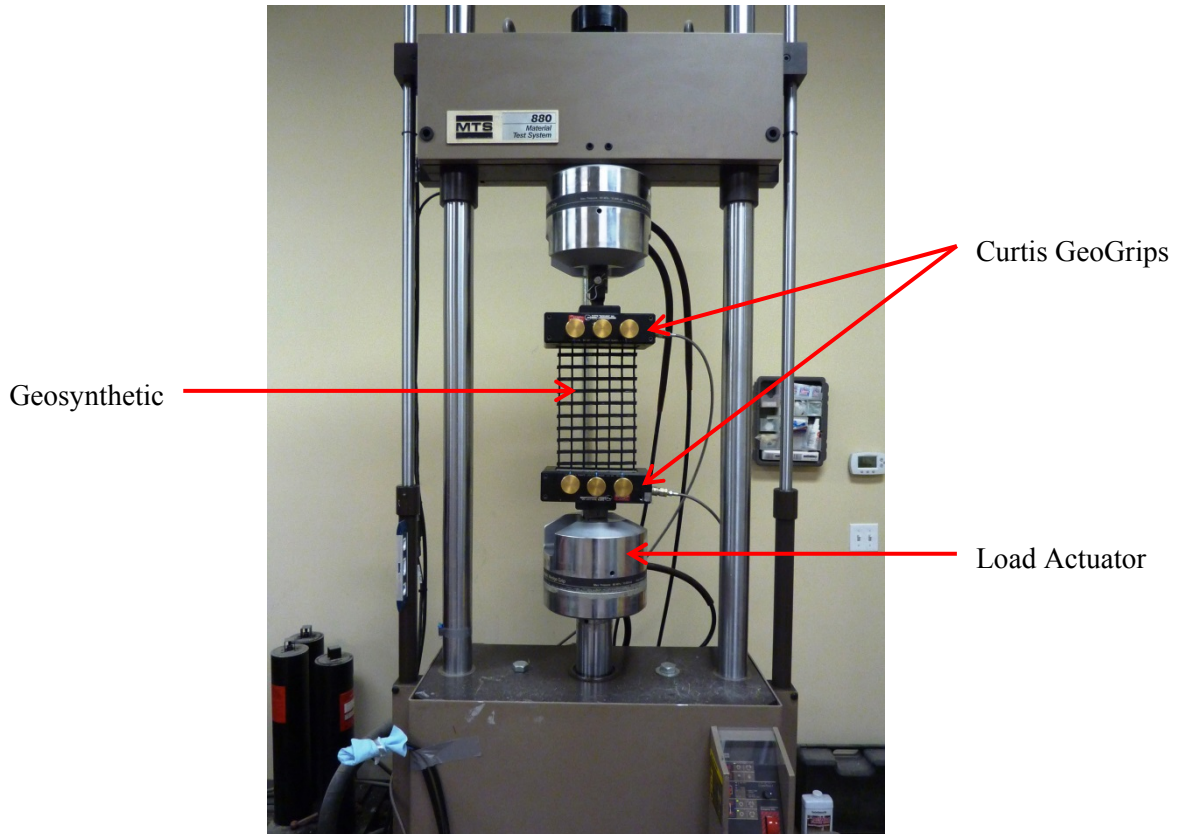
Figure 8: Wide-width tensile strength test setup.

The geogrid test samples were approximately 8 in. wide and had a gage length of approximately 12 in. long, while the geotextile test samples had a width of 8 in. and gage length of 4 in. Tension was applied at a constant rate of strain of 10 percent per minute based off of the initial gage length of the geosynthetic At least three samples, but no more than six, were tested in both the machine direction (MD) and cross-machine direction (XMD). The number of samples tested was based upon a statistical formula within the standard test methods to ensure uniformity of results.

A summary of the test results from WTI and the wide-width tensile results published by the manufacturer are listed in Table 5 and Table 6, respectively. For the most part, strength values exceeded MARV (minimum average roll value) results published by the manufacturer; however, some materials exhibited lower values.   Individual load-displacement plots are provided in Appendix A.

Table 5: Summary of Wide-Width Tensile Strength Test Results from WTI

Geosynthetic Test Section	Strength @ 2%[a] (lb/ft)		Strength @ 5%[a] (lb/ft)		Ultimate Strength[a] (lb/ft)		Strain at Ultimate Strength (%)	
	MD	XMD	MD	XMD	MD	XMD	MD	XMD
Tensar BX Type 2	582	822	1,076	1,494	1,480	1,946	11.3	9.3
NAUE Secugrid 30/30 Q1	966	946	1,809	1,830	2,083	2,713	6.2	8.9
Colbond Enkagrid Max 30	1,000	857	2,028	1,775	2,645	2,378	8.1	7.8
Synteen SF 11	397	617	685	925	2,042[b]	3,782[b]	11.9	16.0
Synteen SF 12	397	987	713	1,446	2,145[c]	5,818[c]	11.4	16.0
TenCate Mirafi BXG 11	644	740	1,377	1,281	2,631	3,221	10.5	11.9
Huesker Fornit 30	665	946	1,425	1,939	1,864	2,618	7.6	8.0
SynTec Tenax MS 330[c]	569	692	1,048	1,343	1,412	2,248	9.3	11.9
Tensar TX 140	34[d]	322	178[d]	665	624[d]	843	10.7	7.5
Tensar TX 160	69[d]	391	260[d]	747	754[d]	884	9.4	6.7
TenCate Mirafi RS580i	500	1,501	1,288	3,440	5,619	6,112	25.4	11.0
Propex Geotex 801[e,f]	44	25	122	73	1,195	1,519	78.5	141.7

[a] ASTM D4595 or ASTM D6637
[b] Synteen SF 11 and Synteen SF 12 materials experienced some grip slippage at their ultimate strength values
[c] Tested by WTI as a composite, i.e., not separately
[d] When the TX140 and TX160 geogrids are tested in the machine direction, tensile members are offset by 30 degrees from the direction of the applied load, resulting in large distortions of the material and lower and/or inaccurate strength values
[e] Results of wide-width tests on the Propex Geotex 801 geotextile having a 1 in. gage length
[f] Grab tensile strength of the Propex Geotex 80,1 as tested by SGI Testing Services, LLC (ASTM D-4632) was 231 lb in the machine direction and 255 lb in the cross-machine direction

Table 6: Summary of Wide-Width Tensile Strength Properties Published by Manufacturers

Geosynthetic Test Section	Strength @ 2%[a,b] (lb/ft)		Strength @ 5%[a,b] (lb/ft)		Ultimate Strength[a,b] (lb/ft)		Strain at Ultimate Strength (%)	
	MD	XMD	MD	XMD	MD	XMD	MD	XMD
Tensar BX Type 2	410	620	810	1,340	1,310	1,970	NP	NP
NAUE Secugrid 30/30 Q1	686	686	1,475	1,475	2,055	2,055	8.0	8.0
Colbond Enkagrid Max 30	754	754	1,576	1,576	2,056	2,056	8.0	8.0
Synteen SF 11	526	578	792	1,042	2,388	3,870	NP	NP
Synteen SF 12	526	797	1,042	1,367	2,388	5,268	NP	NP
TenCate Mirafi BXG 11	625	625	1,000	1,000	2,500	2,500	NP	NP
Huesker Fornit 30	548	890	1,370	1,850	1,850	2,398	6.0	6.0
SynTec Tenax MS 330	418	620	925	1,343	1,370	2,100	NP	NP
Tensar TX 140	NP	NP	NP	NP	NP	NP	NP	NP
Tensar TX 160	NP	NP	NP	NP	NP	NP	NP	NP
TenCate Mirafi RS580i	NP	NP	NP	NP	NP	NP	NP	NP
Propex Geotex 801	NP	NP	NP	NP	NP	205[c]	NP	NP

[a] ASTM D4595 or ASTM D6637
[b] Manufacturers' minimum average roll values (MARV)
[c] Grab tensile strength in lb. in the weaker principal direction (ASTM D-4632)
NP = Information was not provided by the manufacturer

Cyclic Tensile Modulus

The cyclic tensile modulus test used the same setup as the wide-width tensile strength test (i.e., grips, testing frame, and sample sizes). These tests were performed to evaluate the tensile modulus of geosynthetics for applications involving small-strain cyclic loading (representative of traffic loads) according to ASTM D7556. The test is used to determine the cyclic tensile modulus at various levels of permanent strain. The test procedure applies 1000 cycles at 1 Hz between axial strain limits of ±0.1 percent at six permanent strain values: 0.5, 1.0, 1.5, 2.0, 3.0, and 4.0 percent. The total number of tests is determined using the same statistical equation as the wide-width tensile strength test to ensure uniformity of results.

The cyclic tensile modulus (J_{cyclic}) is calculated using the following equations:

$$J_{cyclic} = \frac{(\alpha_f * 100)}{(\varepsilon_2 - \varepsilon_1)}$$ **Equation 2**

where α_f = the equivalent force per unit width (lb/ft), as determined using the following equation,

$$\alpha_f = \frac{(P_2 - P_1)}{W_s}$$ **Equation 3**

ε_2 = percent strain corresponding to the cycle's highest strain value,

ε_1 = percent strain corresponding to the cycle's lowest strain value,

P_2 = observed maximum force for the cycle (lb),

P_1 = minimum tensile load at the end of the cycle (lb), and

W_s = specimen width (ft).

The equivalent force per unit width is calculated for the last 10 cycles of each cyclic load step and averaged together to determine a single cyclic tensile modulus for each load step. The Propex Geotex 801 material was not tested because it has low strength at small stains and would not yield a representative cyclic tensile modulus. The results from the cyclic tensile modulus tests conducted by WTI are summarized in Figure 9 and Figure 10. Representative load-displacement results in the machine and cross-machine directions are shown for each geosynthetic in Appendix B.
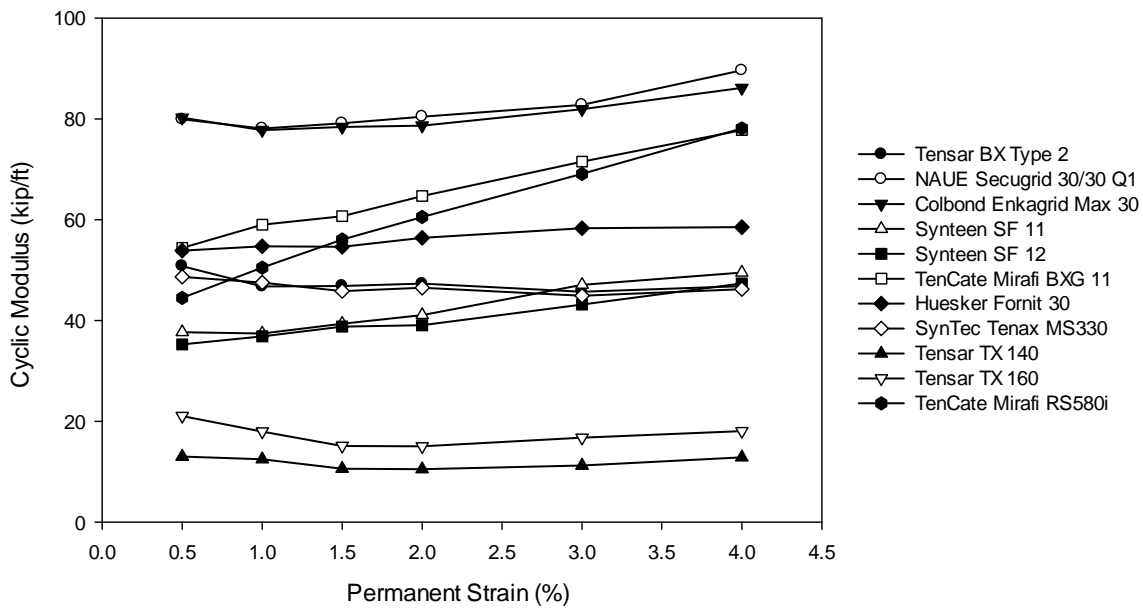
Figure 9: Cyclic tensile modulus summary - machine direction.
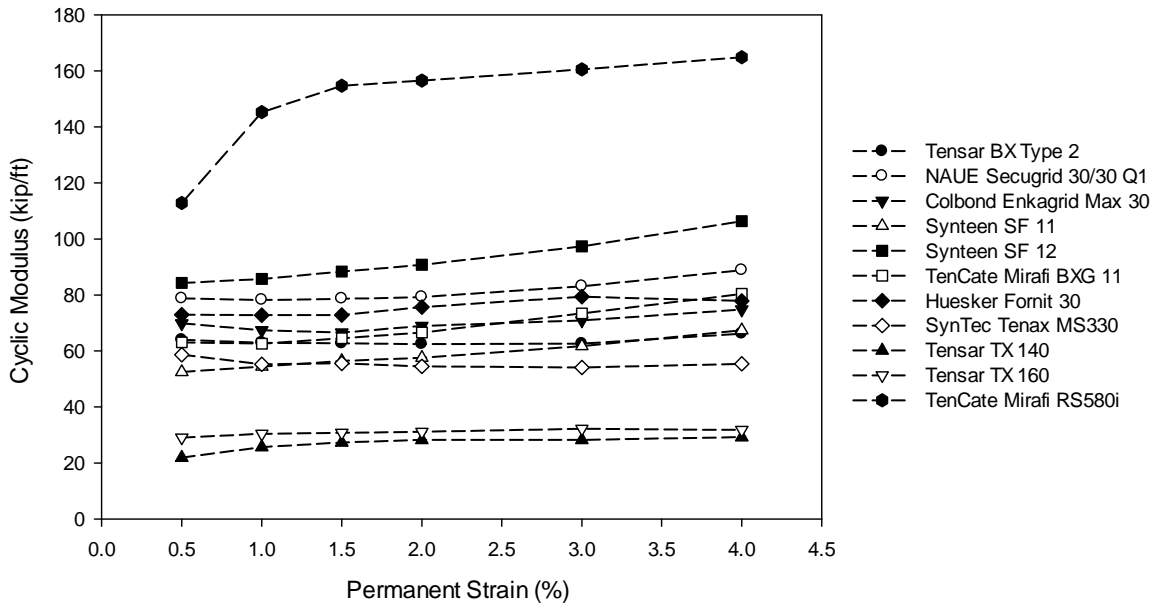
Figure 10: Cyclic tensile modulus summary - cross-machine direction.

Resilient Interface Shear Stiffness

The resilient interface shear stiffness test (ASTM D 7499) is used to measure the stiffness of the interface between the geosynthetic and the surrounding soil under small cyclic loads. The test is conducted by embedding a short sample of geosynthetic in soil and applying cyclic loads at various levels of confinement and load. Applied load and displacement along the front and rear of the embedded sample are recorded. An annotated illustration of the testing device is shown in Figure 11.
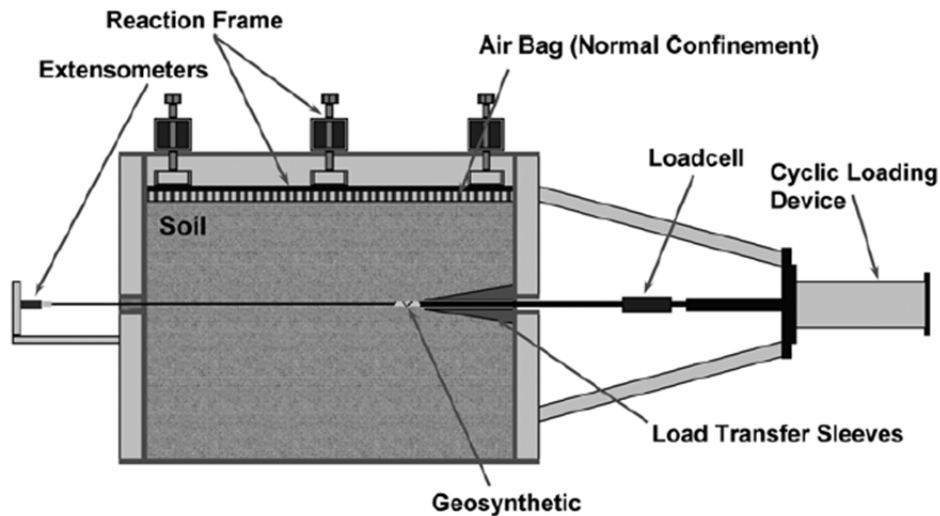
Figure 11: Resilient interface shear stiffness apparatus (from ASTM D 7499).

The length of the embedded geosynthetic is specified to be 2–4 inches long and contain at least two full grid apertures; the width should be at least 12 inches. The sample length is relatively short when compared to traditional pullout tests to ensure that strain and shear stress along the length of the geosynthetic are generally uniform when loaded.

A total of six prescribed levels of horizontal cyclic force are applied to the geosynthetic at five specified levels of normal stress confinement. Resilient interface shear stiffness (G_I) is calculated from the last 10 cycles and averaged to yield a value for each step using the illustration in Figure 12, which relates the shear along the geosynthetic as it is displaced. Up to 30 values of G_I can be obtained from each test using this method (corresponding to the various levels of applied load and confinement). A regression equation based on the general equation that describes the resilient modulus of unbound granular soils (Equation 4), can be used to predict G_I. A single value for the interface normal stress (σ_I = 5.076 psi) and the interface shear stress (τ_I = 0.725 psi) were used in this analysis, based on the work conducted by Perkins and Christopher (2010). Using these estimates will facilitate relative comparisons between products. A summary of the k_1, k_2, and k_3 material parameters and G_I is provided in Table 7. Individual plots of the measured versus predicted shear modulus plots are provided in Appendix C for each of the materials.
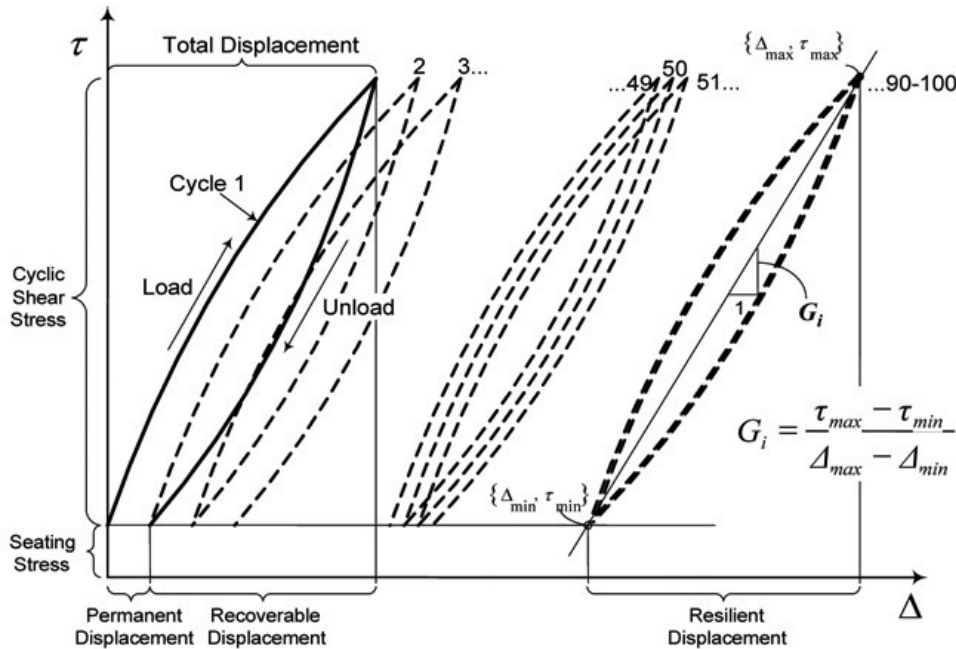
Figure 12: Illustrated calculation of resilient interface shear stiffness (from ASTM D 7499).

$$G_I = k_1 P_a \left(\frac{\sigma_I}{p_a}\right)^{k_2} \left(\frac{\tau_I}{p_a} + 1\right)^{k_3}$$

Equation 4

where,

G_I = resilient interface shear stiffness (psi/in),

p_a = atmospheric pressure (14.69 psi),

P_a = atmospheric pressure divided by a unit length of 1 in (14.69 lb/in^3),

σ_I = interface normal stress (psi),

τ_I = interface shear stress (psi), and

k_1, k_2, and k_3 are material parameters determined from the test results.

Table 7: Summary of Resilient Interface Shear Stiffness Test Results

Geosynthetic Test Section	k_1	k_2	k_3	G_I (ksi)[a]
Tensar BX Type 2	84,611	0.92	-8.9	305
NAUE Secugrid 30/30 Q1	62,815	0.82	-15.2	186
Colbond Enkagrid Max 30	156,570	1.18	-41.0	91
Synteen SF 11	173,469	1.52	-21.7	178
Synteen SF 12	104,984	1.14	-9.4	292
TenCate Mirafi BXG 11	108,376	1.21	-12.6	240
Huesker Fornit 30	44,194	0.94	-12.9	129
SynTec Tenax MS 330[b]	100,343	1.17	-16.8	190
Tensar TX 140	44,176	0.62	-27.8	88
Tensar TX 160	103,015	1.12	-13.4	242
TenCate Mirafi RS580i	59,303	0.81	-2.3	329
Propex Geotex 801	46,413	0.88	-12.4	147

[a] Interface normal stress σ_I = 5.076 psi, and interface shear stress τ_I = 0.725 psi used for all calculations

[b] Tested as a composite (i.e., all three layers of geosynthetic together)

Junction Strength

Junction strength tests (ASTM D 7737) on the geogrids were conducted by SGI Testing Services (Norcross, GA) in the cross-machine direction only. These tests are used to verify that the junctions of a particular geogrid have sufficient strength to undergo construction stresses, but may also potentially provide a way to quantify how well the grid structure transfers loads from members orthogonal to the direction of the applied load. The junction strength tests generally involve specimens to be cut in the shape of a "T" with at least one transverse member protruding from either side of the junction being tested. The specimen is gripped on both sides of the "T" and the orthogonal rib is pulled until failure of the junction occurs. A typical junction strength test setup is shown in Figure 13. The configuration of the clamps was modified to accommodate the unique material construction of the Tensar TX140 and TX160 geogrids, as illustrated in Figure 14, because they do not have machine direction ribs that are orthogonal to the cross-machine direction ribs like the remaining geogrids. Test data for these tests is summarized in Table 8 for the tests conducted by SGI as well as values published by the manufacturers. The

junction strength data (expressed in lb/junction) was normalized based on the number of ribs (or junctions) in the cross-machine direction per lineal inch of material (final units are expressed in lb/in). Plots of the junction strength with respect to displacement are shown for each material in Appendix D.
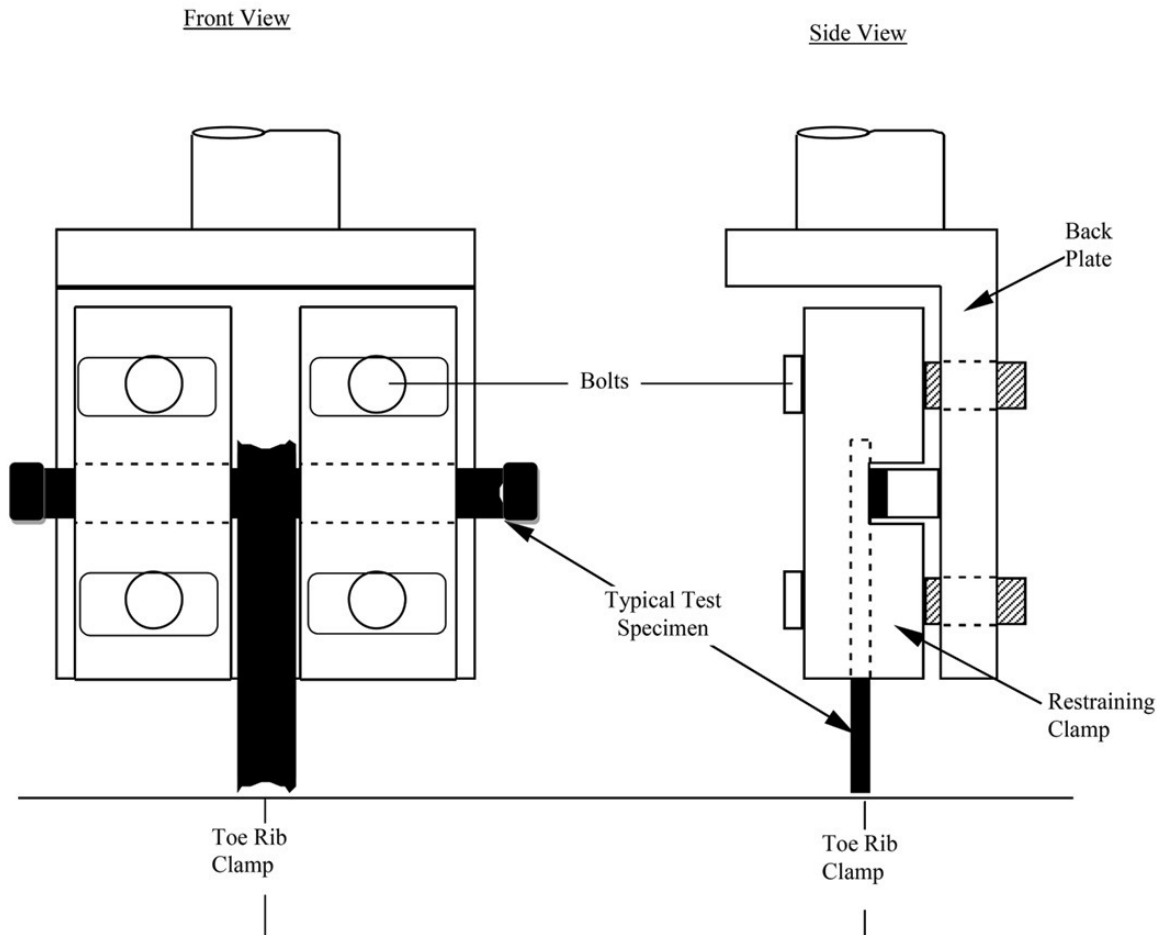
Figure 13: Typical junction strength test specimen setup (from ASTM D 7737).

Force

Gage length

θ = 60°

Two machine direction ribs clamped between steel plates
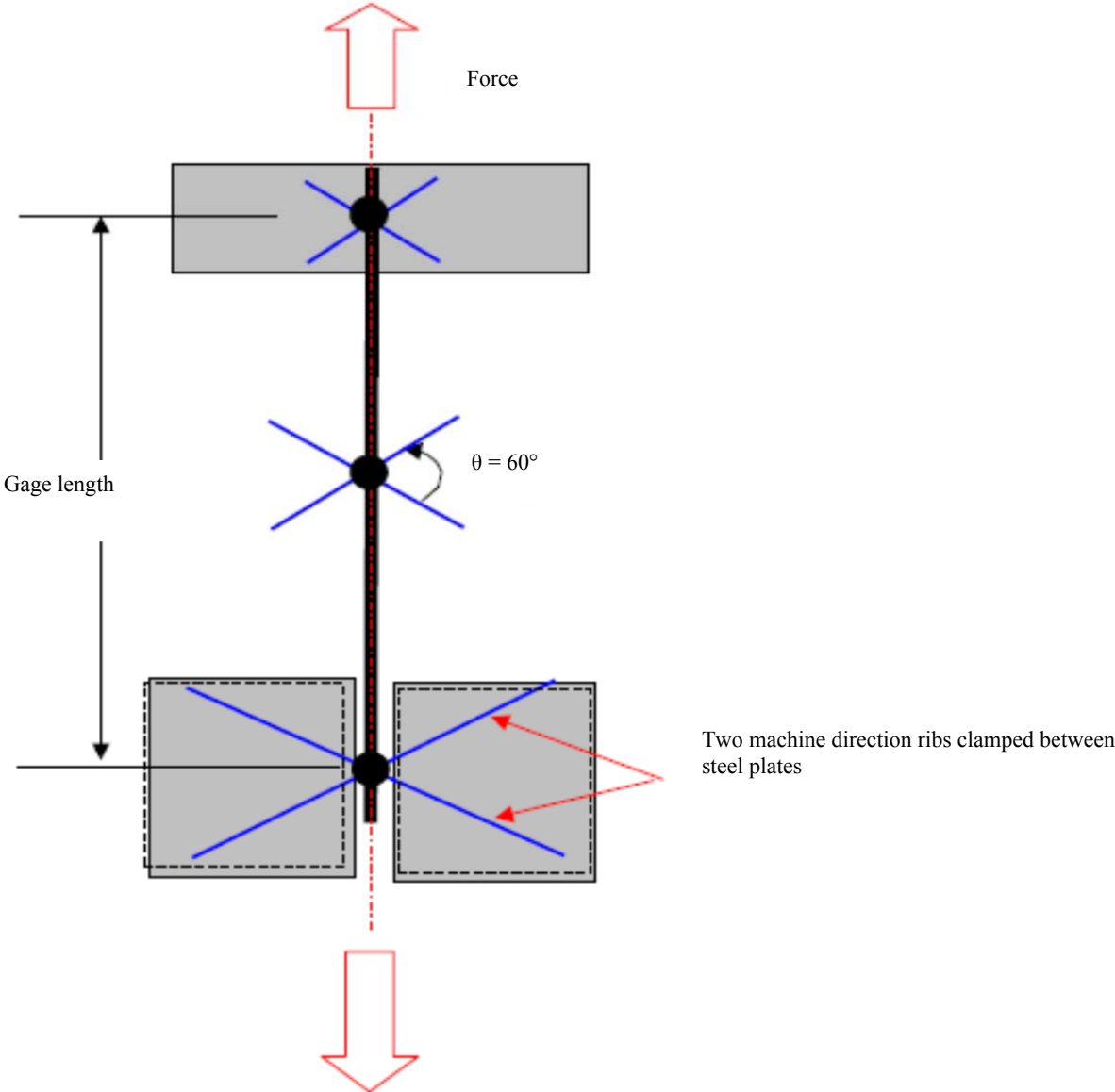
Figure 14: Modified junction strength specimen setup for Tensar TX140 and TX160 geogrids.

Table 8: Summary of Junction Strength Test Results

Geosynthetic Test Section	Tested by SGI				Published by Manufacturer			
	Strength (lb/junction)		Strength (lb/in)		Strength (lb/junction)		Strength (lb/in)	
	MD	XMD	MD	XMD	MD	XMD	MD	XMD
Tensar BX Type 2	NT	206.7	NT	171.6	NP	NP	NP	NP
NAUE Secugrid 30/30 Q1	NT	90.6	NT	57.6	80.4[a]	80.9[a]	51.4	51.4
Colbond Enkagrid Max 30	NT	106.6	NT	49.5	NP	NP	NP	NP
Synteen SF 11	NT	46.1	NT	37.1	59.4	47.6	47.9[b]	38.3[b]
Synteen SF 12	NT	34.4	NT	28.6	59.4	64.8	48.4[b]	53.8[b]
TenCate Mirafi BXG 11	NT	42.5	NT	35.8	NP	NP	NP	NP
Huesker Fornit 30	NT	8.9	NT	10.5	NP	NP	NP	NP
SynTec Tenax MS 330	NT	103.6[c]	NT	65.5[c]	206.1[a,d]	259.6[a,d]	106.2[d]	164.2[d]
Tensar TX 140	NT	111.8	NT	72.4	NP		NP	
Tensar TX 160	NT	123.4	NT	75.1	NP		NP	
TenCate Mirafi RS580i	NA		NA		NA		NA	
Propex Geotex 801	NA		NA		NA		NA	

[a] Values published by the manufacturer were in lb/ft. WTI adjusted these values to determine lb/junction
[b] Values published by the manufacturer were in lb/junction. WTI adjusted these values to determine junction strength in lb/in.
[c] Values are for a single layer (three layer material)
[d] Values are presumably for all three layers, based on the results from tests conducted by SGI on individual junctions
NA = Not Applicable
NP = Information was not provided by the manufacturer
NT = Not Tested

Aperture Stability Modulus

Aperture stability modulus tests were performed by SGI based on the method developed by Kinney (2000). The test is used to quantify the dimensional stiffness of a geogrid under a torsional load. Similar to the junction strength tests, the aperture stability tests can only be performed on geosynthetics that have open apertures (i.e., geogrids). The test is conducted by confining a square sample of geogrid in a stiff stationary square clamp, where the interior 9" x 9" portion of the material is not clamped, as shown in Figure 15. A moment is then applied to the center of the geogrid at five load increments and the degree of rotation is measured. The aperture stability modulus (*ASM*) is defined as the torque (17.70 in-lb), divided by the rotation at that torque (see Equation 5 below). According to the draft standard, the test is stopped if the rotation reaches 20 degrees. In this case the highest torque should be used in the equation, and the report should state that the aperture stability modulus is less than the calculated value (Kinney, 2000). The results for the aperture stability modulus tests performed by SGI and published by the manufacturers are shown in Table 9. Individual plots for each material are provided in Appendix E.

$$ASM = \frac{Torque\ (17.70\ in-lb)}{Rotation\ (deg.)}$$

Equation 5
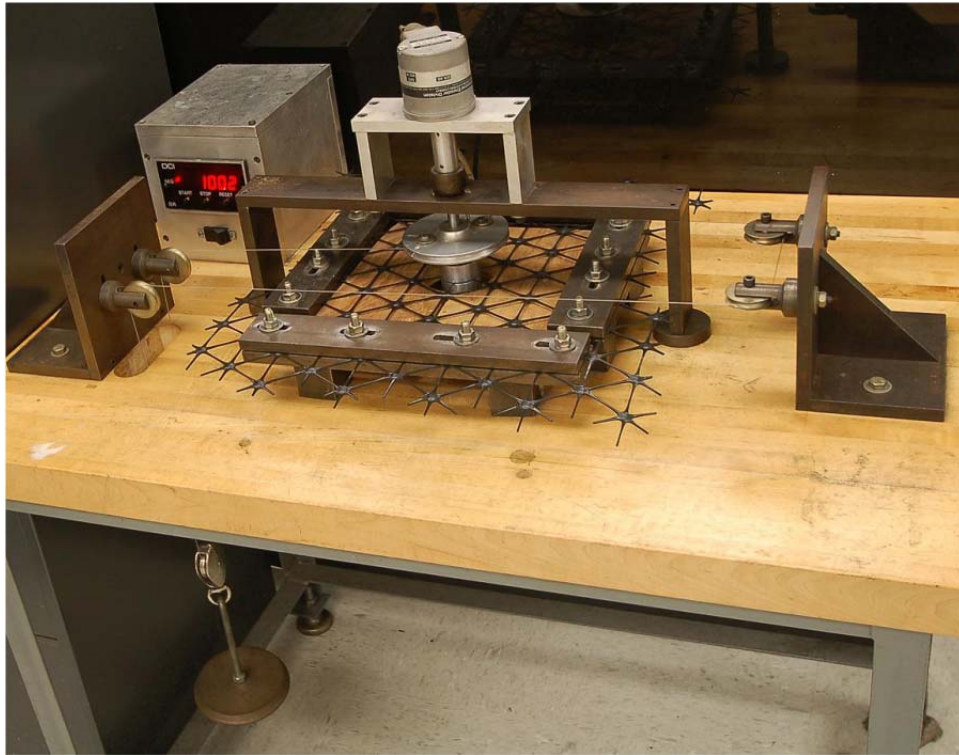
Figure 15: Aperture stability modulus testing device (photo courtesy of Tensar International, Inc.).

Table 9: Summary of Aperture Stability Modulus Test Results

Geosynthetic Test Section	Tested by SGI Aperture Stability Modulus (in-lb/deg)	Published by Manufacturer Aperture Stability Modulus (in-lb/deg)
Tensar BX Type 2	6.9	5.75
NAUE Secugrid 30/30 Q1	10.2	9.90
Colbond Enkagrid Max 30	13.9	NP
Synteen SF 11	2.2	NP
Synteen SF 12	2.4	NP
TenCate Mirafi BXG 11	3.1	NP
Huesker Fornit 30	9.6	6.55
SynTec Tenax MS 330	3.2[a]	NP
Tensar TX 140	2.5	2.60[b]
Tensar TX 160	4.9	3.13[b]
TenCate Mirafi RS580i	NA	NA
Propex Geotex 801	NA	NA

[a] Tested a single layer, and multiplied by 3 (three layer material)
[b] Test was performed using a torque of 4.34 in-lb. (the standard is 17.70 lb-in), which may imply that the aperture stability modulus is less than the value published by the manufacturer, according to the procedure outlined by Kinney (2000).
NA = Not applicable
NP = Information was not provided by the manufacturer

Construction of Field Experiment

Construction of the test sections included the following major consecutive steps: excavating and widening the trench, lining the trench with plastic, preparing and placing the artificial subgrade, installing the sensors and geosynthetics, and preparing and placing the base course aggregate. Preparation and construction of the subgrade and base course was monitored extensively to ensure that these materials were placed in a consistent and uniform manner. Each 50-foot long test section was delineated into 14 subsections (seven in each wheel path, labeled *A* through *G*), as shown in Figure 16. A 1.6 ft-long buffer zone at each end of a test section was avoided because the overlap of the geosynthetics coincident with the transitions between adjacent test sections.
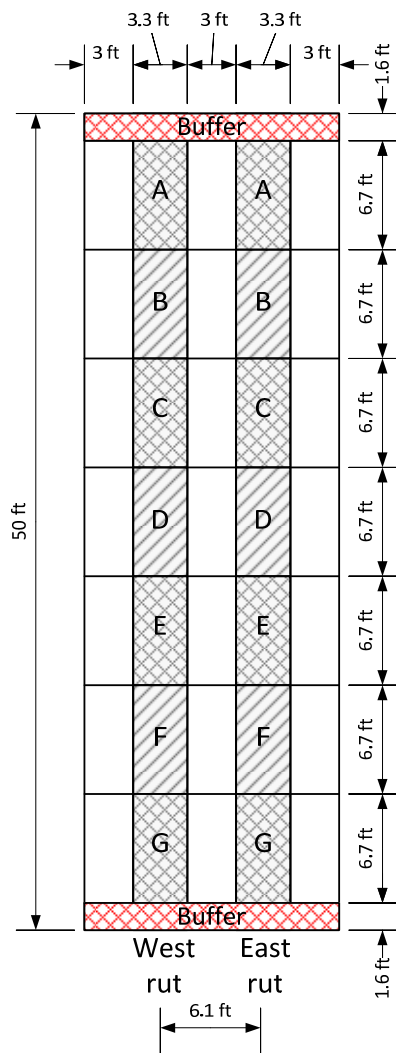
Figure 16: Measurement areas for field soil tests within a single test section.

For quality assurance/quality control during subgrade construction, four measurements of vane shear were made in each subsection for a total of 56 vane shear measurements in each layer in

each test section. Note that half of all measurements were made in the east wheel path and half in the west wheel path. Six lightweight deflectometer (LWD) measurements were also taken immediately after the layer was compacted. On the final lift of the subgrade, within each test section, 8 dynamic cone penetrometer (DCP) tests, 1 in-field CBR test, and 2 nuclear densometer tests were also conducted. During base course construction, 6 LWD measurements were conducted after the first and final passes of the compactor on the first lift. After the last compactor pass of the final lift, an additional 6 LWD, 6 DCP, 1 in-field CBR, and 2 nuclear densometer tests were conducted. A summary of the measurements to be made on the subgrade and base course during construction is provided in Table 10. Photos of each of these measurement devices are shown in Figure 17.

Table 10: Summary of Soil Monitoring Tests Conducted during Construction

Subgrade			
Measurement Device	**Layers**	**Measurements per Layer**	**Location of Measurement**
Vane Shear	all	56	A,B,C,D,E,F,G
Light-Weight Deflectometer	all	6	B,D,F
Dynamic Cone Penetrometer	final	6	A,D,G
In-Field CBR	final	2	D
Nuclear Density Gage	final	2	D

Base Course Aggregate			
Measurement Device	**Layers**	**Measurements per Layer**	**Location of Measurement**
Light-Weight Deflectometer	first	12	B,D,F
Light-Weight Deflectometer	final	6	B,D,F
Dynamic Cone Penetrometer	final	6	A,D,G
In-Field CBR	final	2	D
Nuclear Density Gage	final	2	D

Figure 17: Construction quality measuring devices: a) vane shear, b) LWD, c) DCP, d) in-field CBR, and e) nuclear density.

Trench

Construction work for this research project began in late June, 2012 by excavating the materials from an existing trench, and widening and lengthening the trench to its final dimensions of 16 ft wide by 860 ft long. A view of the trench before it was filled with the artificial subgrade is shown in Figure 18. The floor of the test pit was tapered at the ends to facilitate movement of the construction equipment into and out of the pit; the tapered area was not included in the experiment and is in addition to the 860 feet of length. The trench bottom was compacted with a vibratory roller to provide a stable platform for the remaining construction activities, and was lined with a 6-mil plastic liner to help maintain constructed moisture content of the subgrade throughout the duration of the project (Figure 19).

Figure 18: Completed trench.

Figure 19: Filling lined trench with subgrade.

Subgrade

The subgrade was built in 6 lifts that were approximately 6 inches deep for a total depth of about 3 feet. The subgrade was delivered adjacent to the test pit (refer to Figure 19) and was processed to reach the target strength by adding water from a water truck and fire hose (Figure 20). Water was added until the portion of the pile being prepared reached the target moisture content (e.g., 23 percent for test Sections 3 through C3). Processing was accomplished using a large excavator (Caterpillar 345B). The operator used the bucket to move and mix the material as water was being added (Figure 20). Sufficient material was processed to construct a single 6-inch deep layer over two test sections at a time (about 30 yd^3). The subgrade was then placed in the trench using the excavator and a track-mounted skid-steer tractor was used to level and initially compact the subgrade (Figure 21). A smooth, single-drum, vibratory roller (66-inch wide, 15,500 lb) was used to compact the subgrade by making two passes of the roller in three longitudinal paths of the freshly placed subgrade (Figure 22). The moisture in the top surface of the subgrade was maintained during construction by periodically wetting the surface and keeping it covered with plastic until the next layer of subgrade or the base course could be placed. Prior to placement of the base course, the top surface of the subgrade was smoothed and screeded to the height of the adjacent pavement surface. This was accomplished by tilling the top of the subgrade and pushing a large metal trench box along the surface to remove excess material (Figure 23). The top surface was then re-compacted using a smaller single-drum, vibratory roller. This was done from the side to minimize ruts in the subgrade surface during final

compaction. A topographic survey of the final level of the subgrade was made and the pore pressure sensors were installed prior to placing the geosynthetics.

Figure 20: Watering and mixing subgrade with excavator.

Figure 21: Tracking freshly placed subgrade with track-mounted skid-steer.

Figure 22: Smooth-drum roller used to compact subgrade.

Figure 23: Screeding final subgrade layer.

The upper layers of subgrade are responsible for supporting the majority of the load applied during trafficking. Consequently, the strength of the subgrade at the lower depths was less

important than the strength nearer the surface. In order to characterize the subgrade and assign an average value of strength to each test section, a strategy for weighting the strength of the subgrade layers was developed based on Boussinesq elastic stress distribution theory. Influence values can be determined using Boussinesq's theory based on the area of the load applied at the surface and the depth to the point of interest. Knowing that upper layers have more influence on behavior, the percent of the total influence was determined for each layer and was applied to vane shear measurements in those layers.

The influence value based on Boussinesq's theory (Equation 6) provides the percent of the total influence of each layer, where I_i is the influence value for a particular layer of subgrade. Values for the weighting factor (n_i) for the six subgrade layers were calculated based on the depth of measurement below the finished subgrade surface and actual base course thickness. The approximate weighting factors for individual layers are tabulated in Table 11. The upper three layers of subgrade have the greatest influence (cumulative weight is over 70 percent for these layers).

$$n_i = \frac{I_i}{\sum\limits_{i=1}^{6} I_i}$$

Equation 6

Table 11: Weighting Factors for the Artificial Subgrade

Subgrade layer	Depth to Center of Layer (in)	I_i	n_i
6 (top)	3	0.987	0.317
5	9	0.793	0.255
4	15	0.525	0.169
3	21	0.358	0.115
2	27	0.257	0.083
1	33	0.194	0.062

Composite shear strength ($\tau_{composite}$) was calculated using shear strength from the vane shear device and weighting factors for each layer, according to Equation 7, where τ_i is the shear strength for a particular layer of subgrade, and n_i is the weighting factor for a particular layer of subgrade. Composite shear strength values were calculated at regions *A* through *G* within each test section (Figure 24). Most test sections were constructed within ±0.1 CBR of the target. Both the stronger and weaker test sections (target CBR = 2.0 for test section 1 and 1.4 for test section 2) were constructed slightly stronger than targeted.

$$\tau_{composite} = \frac{\sum\limits_{i=1}^{6} n_i \tau_i}{\sum\limits_{i=1}^{6} n_i}$$

Equation 7
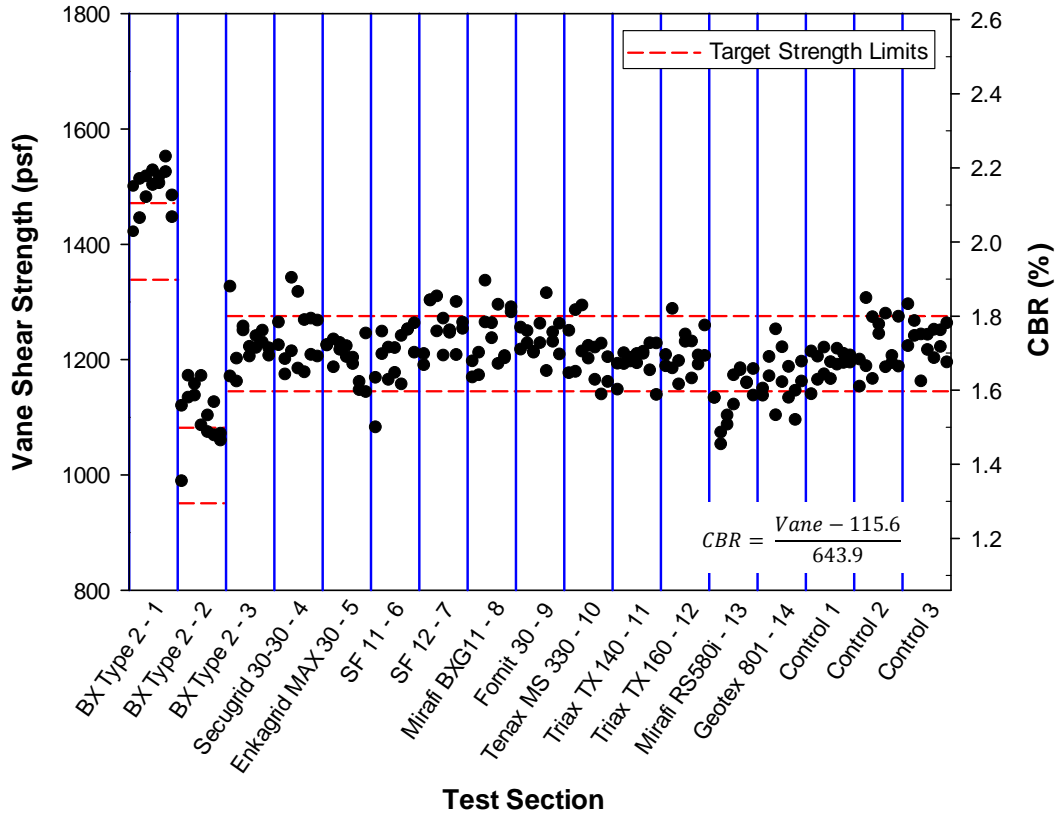
Figure 24: Composite vane shear strength of the constructed subgrade in regions *A–G* (west and east rut paths).

A Zorn ZFG 3000 Light Weight Deflectometer (LWD) was used to measure stiffness within regions *B, D,* and *F* of each layer of each test section during subgrade construction. The LWD has a 1 ft diameter plate, 22 lb drop weight, and provides the dynamic deflection modulus (E_{vd}). The depth of influence for the LWD is about 1 ft, thus measurements on the bottom two layers were neglected due to the presence of the densely compacted fill under the artificial subgrade. Similar to the analysis of vane shear data, a composite E_{vd} was calculated by assigning weights to individual layers using Boussinesq's theory and taking into consideration the measurement depths and base course thickness at individual measurement points. The composite E_{vd} for points within each test section are shown in Figure 25 in comparison to the composite CBR from the vane shear. (A correlation between E_{vd} and CBR was not developed, and the two ordinate axes in Figure 25 are not related.) About half of the test sections show similar behavior regarding E_{vd} and CBR, although there are notable differences for test sections 3–6 where the LWD indicated stiffer subgrade than what was measured by the vane shear.
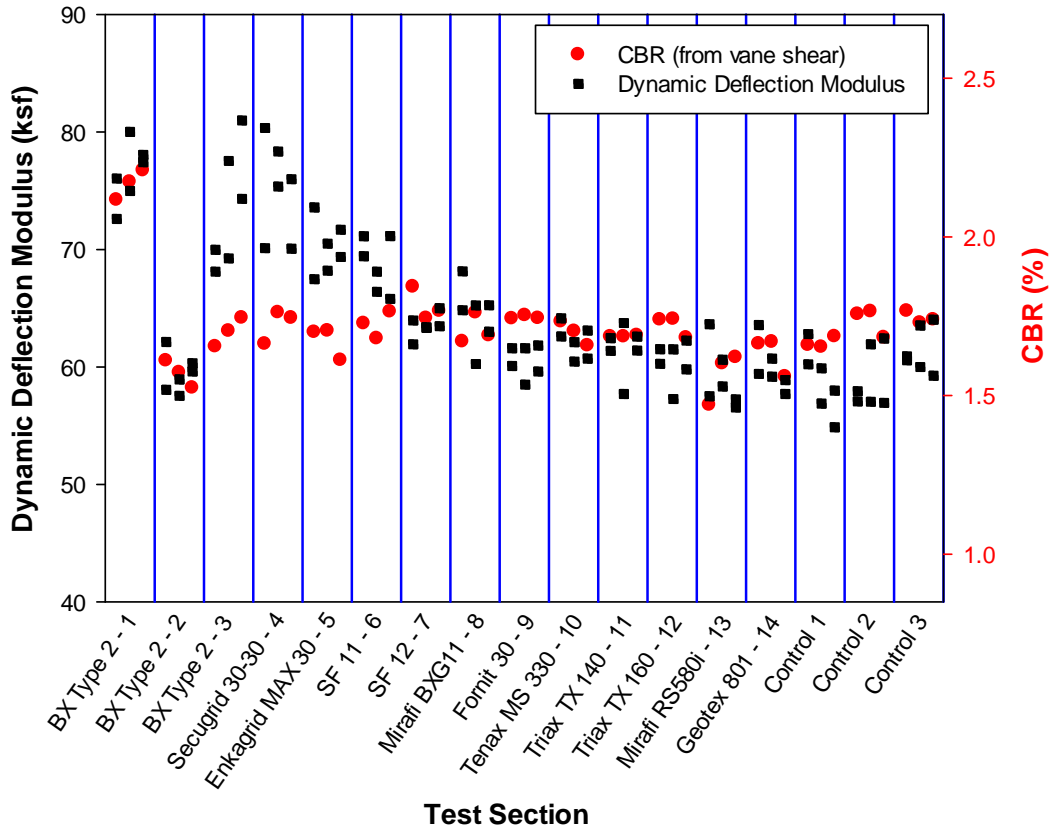
Figure 25: Composite dynamic deflection modulus in regions *B, D,* and *F* (west and east rut paths) of the constructed subgrade and composite CBR from vane shear in regions *B, D,* and *F* (average of west and east rut paths).

A Kessler Dual Mass Dynamic Cone Penetrometer (DCP) with magnetic ruler and a 10.1 lb. hammer was also used to evaluate the strength of the subgrade after it had been fully constructed (i.e., after placement of all six layers), despite the fact that the DCP device was not necessarily well suited to evaluate very small differences in soil strength. The DCP was used in regions *B*, *D*, and *F*, with duplicate measurements in region *D* (for a total of eight measurements in each test section) prior to construction of the base course. Numerous correlation equations exist for converting DCP data to CBR. A number of these relationships were used to compare DCP and vane shear results to identify the most appropriate correlation equation between the two. The original equation (Equation 8, where *DCP* is penetration rate in mm/blow) is one recommended by the US Army Corps of Engineers for CH (fat clay) soils (Kessler, 2010). A modified equation for the artificial subgrade used in this project is shown in Equation 9.

$$CBR = \frac{1}{0.002871\,(DCP)}$$
Equation 8

$$CBR = \frac{1}{0.008439\,(DCP)}$$
Equation 9

Using this optimized equation and the methodology suggested by Kessler (2010), CBR was calculated as a function of depth. Even with the optimized correlation equation, many of the CBR values were much higher than those estimated from the vane shear data and consistently showed a clear trend of increasing CBR at lower depths due to overburden pressures. Thus a technique commonly applied to Standard Penetration Test (SPT) data for overburden correction was adapted for the DCP analysis. In this case, a correction equation from Peck et al. (1974) was used as the basis for a DCP and CBR depth correction. Data from the vane shear tests conducted on the artificial subgrade were used to modify this equation. The final equation is shown below (Equation 10, where σ_o' is the overburden stress expressed in units of psf). An example of the uncorrected and corrected CBR values (for Test Section 2, region F, west rut) is shown in Figure 26.

$$CBR_{corrected} = 1.06 \, CBR \log\left[\frac{0.26}{(\sigma_o'/2000 \, \text{psf})}\right] \qquad \textbf{Equation 10}$$
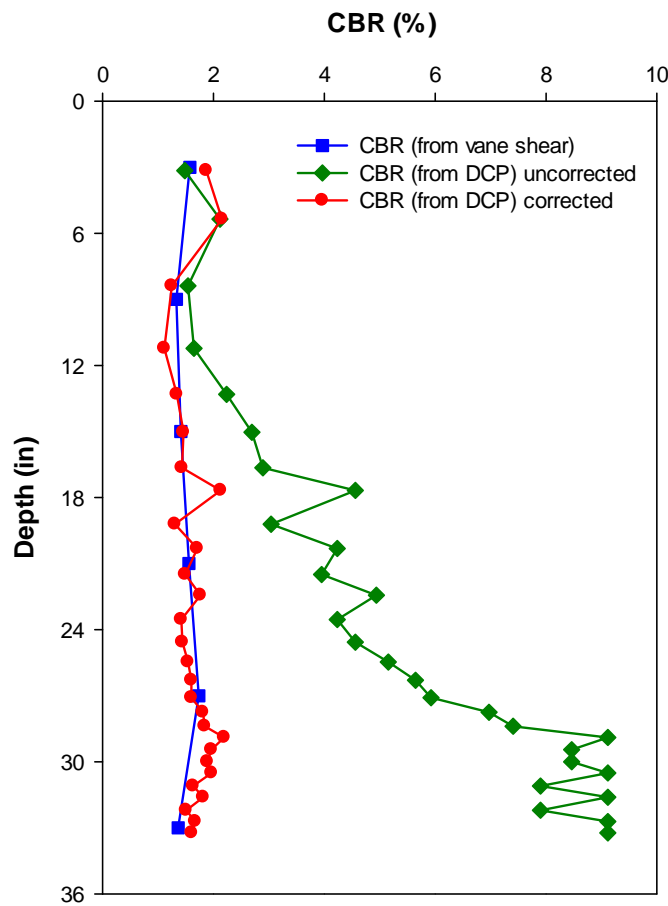
Figure 26: Comparison of corrected and uncorrected CBR results from a typical DCP test on the subgrade (data from Test Section 2, region _F_, west rut path).

As in the previous analysis of the vane shear and LWD data, a weighted average approach was employed to estimate a single composite CBR value for each test section using the DCP data. As before, the influence of the load in the subgrade as a function of depth was calculated using Boussinesq's theory, with adjustments for base course thickness at each measurement point. Weighting factors for the subgrade were calculated as the percent of the total influence at each point using Equation 11, where n_z is the weighting factor at depth z beneath the surface of the subgrade, I_z is the influence factor at depth z, and d_{tot} is the total number of drops to reach depth z. The composite CBR was calculated using Equation 12. Using this methodology, a composite CBR value was calculated for each test section, as shown in Figure 27 along with the composite CBR from the vane shear results. In general, the DCP indicated greater variability in the subgrade than the vane shear.

$$n_z = \frac{\frac{I_z}{d_{tot}}}{\sum_{z=1} I_z}$$

Equation 11

$$CBR_{composite} = \frac{\sum_{z=1}^{d_{tot}} n_z CBR_z}{\sum_{z=1}^{d_{tot}} n_z}$$

Equation 12
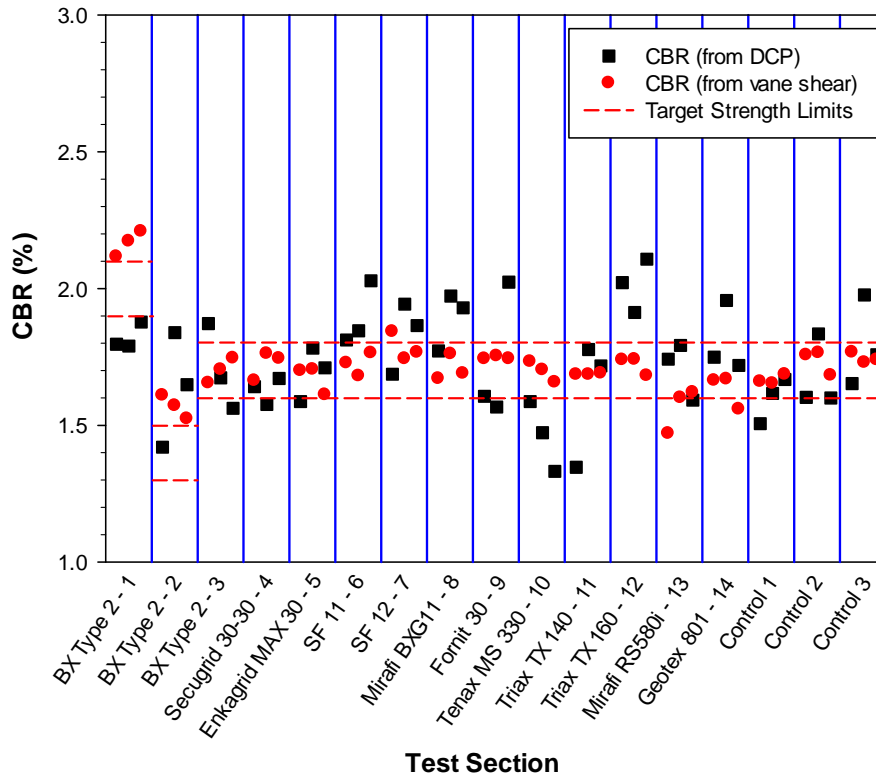
Figure 27: Composite CBR strength of the artificial subgrade from the DCP and vane shear.

In-field CBR tests were conducted on the final layer of the subgrade in substantial accordance to ASTM D 4429 with 60 lbs. of surcharge, representative of approximately 10 in. of gravel at 135 pcf. One test was conducted in each test section, located in region *D* in the west rut. The in-field CBR and the composite CBR determined from vane shear measurements located in region *D* (west rut) are shown in Figure 28. The in-field CBR data is limited and variable, but generally shows that the artificial subgrade is weak (ranging from about 1.3 to about 2.7).
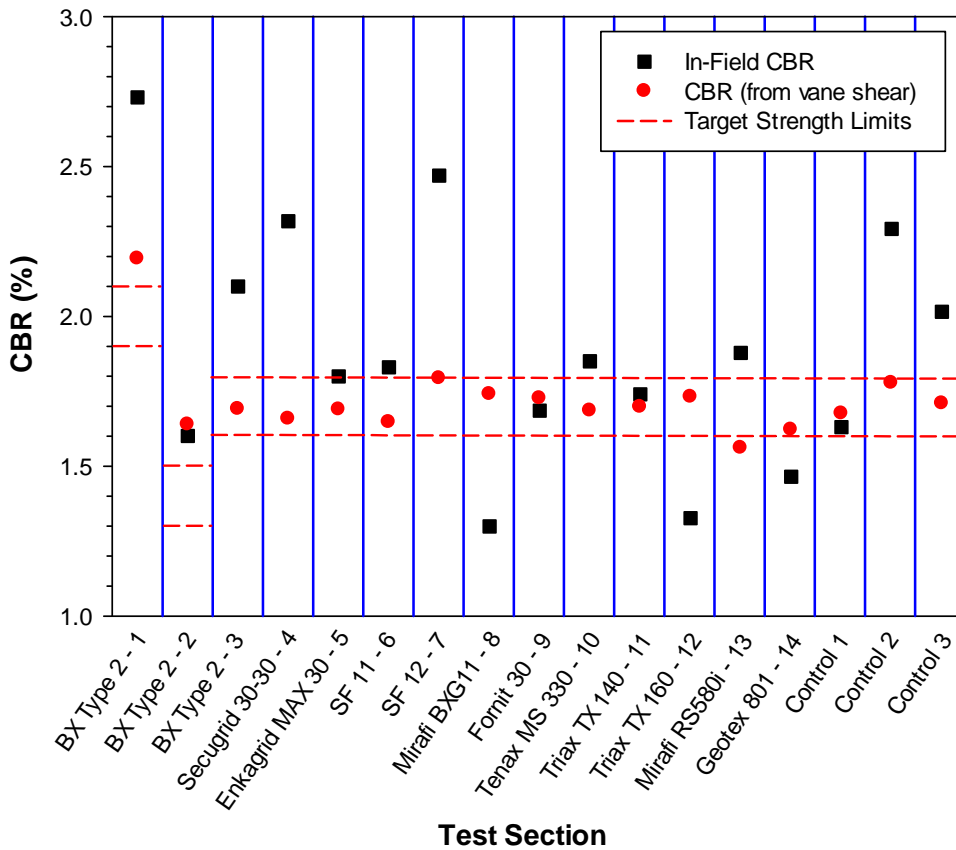
Figure 28: Comparison of subgrade strength from in-field CBR tests and composite CBR from vane shear in region *D* west rut path.

Density of the subgrade was measured with a nuclear densometer in region *D* after the subgrade was constructed. Moisture samples were collected near the density measurements and microwave-dried to determine water content. Test Section 2 had the lowest dry unit weight and the highest water content. Moisture contents at the surface ranged from about 21 to 28 percent, and the dry unit weight ranged from about 100 to 106 pcf (Figure 29). The maximum dry density of the subgrade was 112 lb/ft^3 and optimum moisture content was 16 percent, as determined using the Standard Proctor test. The in-place density and moisture content of the subgrade is plotted with respect to the Standard Proctor curve in Figure 30.
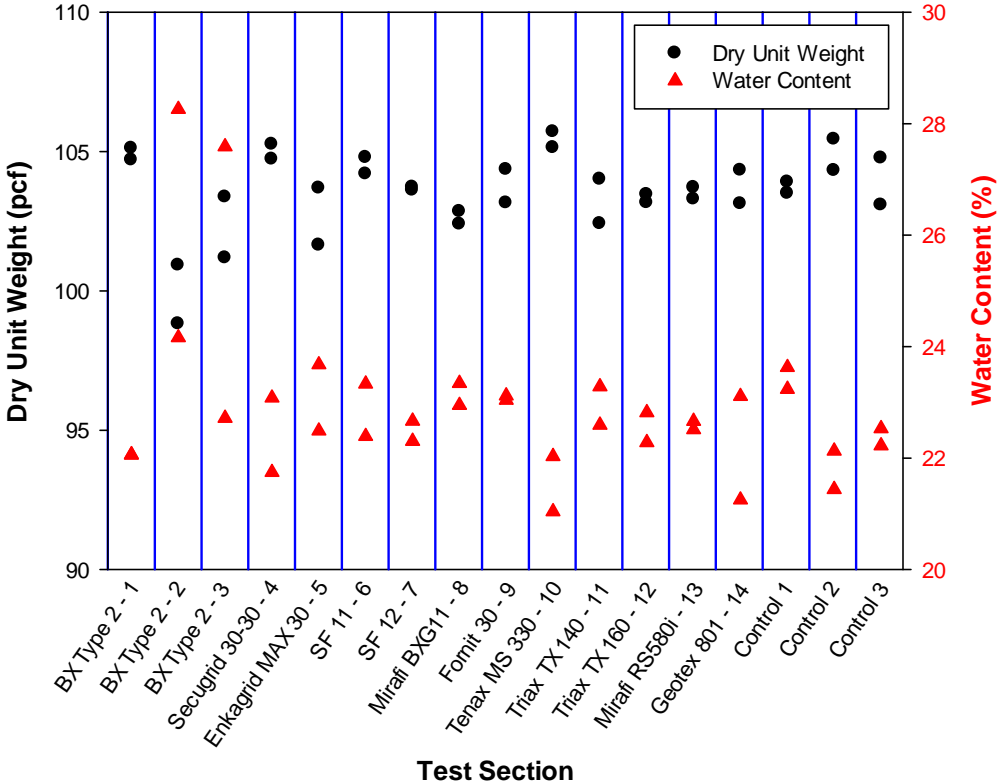
Figure 29: In-place density and water content of the subgrade in region *D* (west and east rut paths).
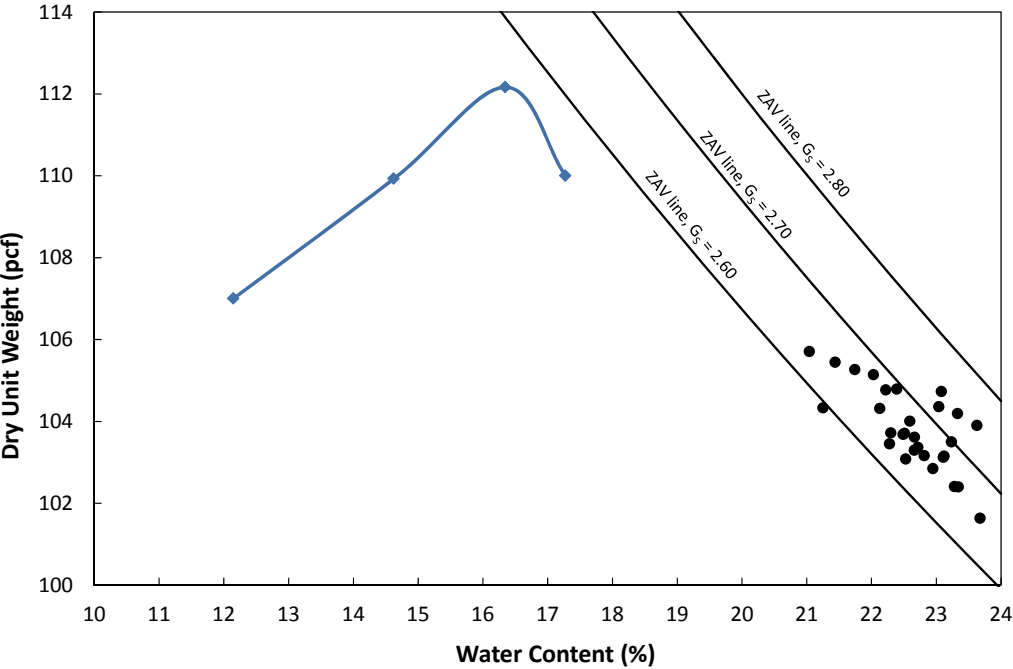
Figure 30: In-place density and moisture of the subgrade plotted with respect to Standard Proctor curve.

Installation of Geosynthetics

Geosynthetics were delivered to the test site and stored indoors to keep them from exposure to direct sunlight. A single piece of geosynthetic was cut from the roll and strain gages were bonded to the material in two locations prior to installation in the test sections. Geosynthetics were installed on the surface of the subgrade in each test section by carefully rolling them out in the direction of traffic (Figure 31). Any wrinkles were removed by gently pulling on the end of the material. The edges of the geosynthetic were not tensioned or staked in place. Because the widths of the geosynthetics varied between products (as indicated in Table 4), they were centered on the subgrade from side-to-side so that the test vehicle would be centered on the material during trafficking and properly positioned in relation to the displacement, strain and pore-water pressure measurements.

Figure 31: Installed geosynthetic.

Base Course Aggregate

The base course was delivered and stored adjacent to the test sections. Preparation of the base course aggregate began by adding water and mixing with an end loader until it reached optimum water content. A large screed that rested on the paved surface on both sides of the subgrade trench was used to level the surface of the gravel layer (Figure 32). The base course was placed in two layers. The final thickness of the first layer of base course was about 8 inches when compacted and the second was about 3 inches deep for a total of about 11 inches of gravel, on average. The two control test sections contained thicker base material. The Control 2 test section was constructed of two layers of about 8 inches thick, for a total of about 16 inches of gravel when compacted, and the Control 3 test section was constructed of three layers of about 8

inches thick, and had a final average thickness of 25 inches of gravel when compacted. Twenty-eight measurements of the thickness of the base course were made within each test section, corresponding to the locations that the longitudinal rut measurements were made during trafficking. The final average thickness of the base course in each test section is shown in Figure 33. Compaction was achieved using a smooth, single-drum, vibratory roller (54-inch wide, 12,000 lb). In total, eight passes of the roller were made per lift at three transverse positions. In addition to a topographic survey, the final gravel surface was measured using DCP, LWD, CBR, and nuclear densometer.

Figure 32: Screeding gravel surface.
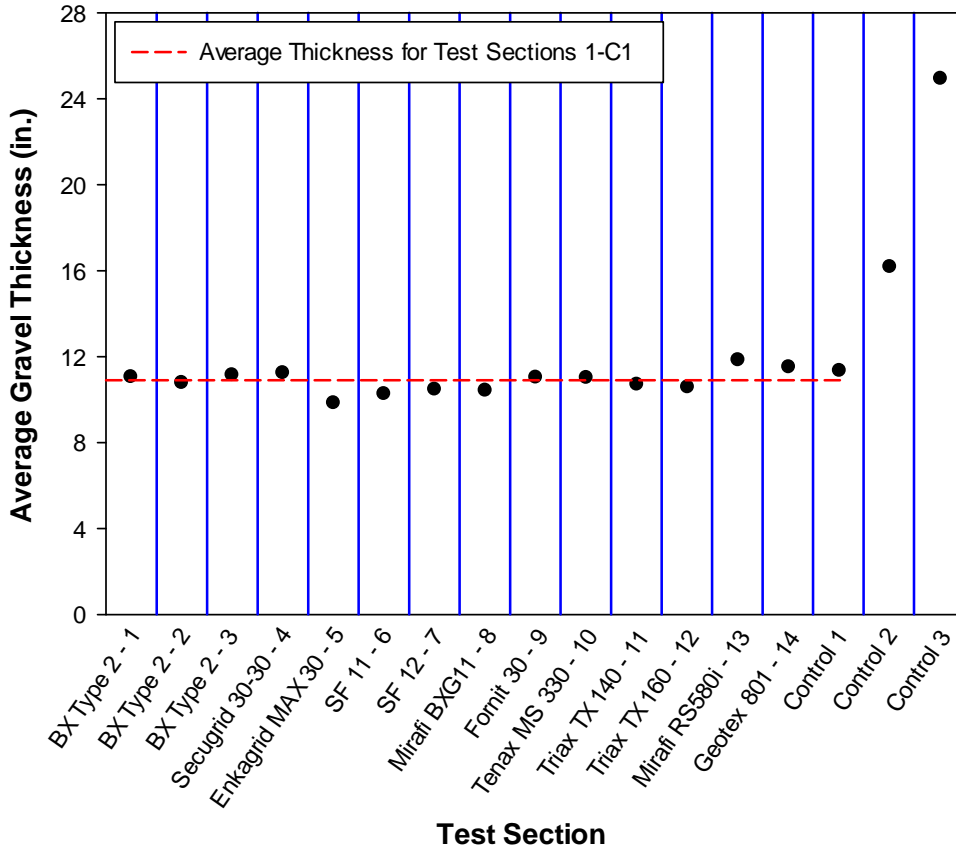
Figure 33: Average base course thickness.

DCP measurements were taken with the dual mass DCP (drop hammer weight of 17.6 lbs.) on the finished surface of the base course in regions *B, D,* and *F* in the west and east rut paths. A correlation equation recommended by the US Army Corps of Engineers for granular soils was used to convert the DCP data to CBR strength (Equation 13, where *DCP* is penetration rate in mm/blow). Penetration data from the upper and lower 2 in. of the base were not used in the calculation of average CBR for each region—granular materials near the surface of the gravel were more easily disturbed, being unbound and the lower 2 in. was close enough to the weak subgrade soil to influence DCP measurements. The variation of CBR along the test plot (as determined from the DCP measurements) is shown in Figure 34. Test sections 1–8 generally showed lower CBR strength than other test sections. The average CBR of the base course was about 20.

$$CBR = \frac{292}{(DCP)^{1.12}}$$ **Equation 13**
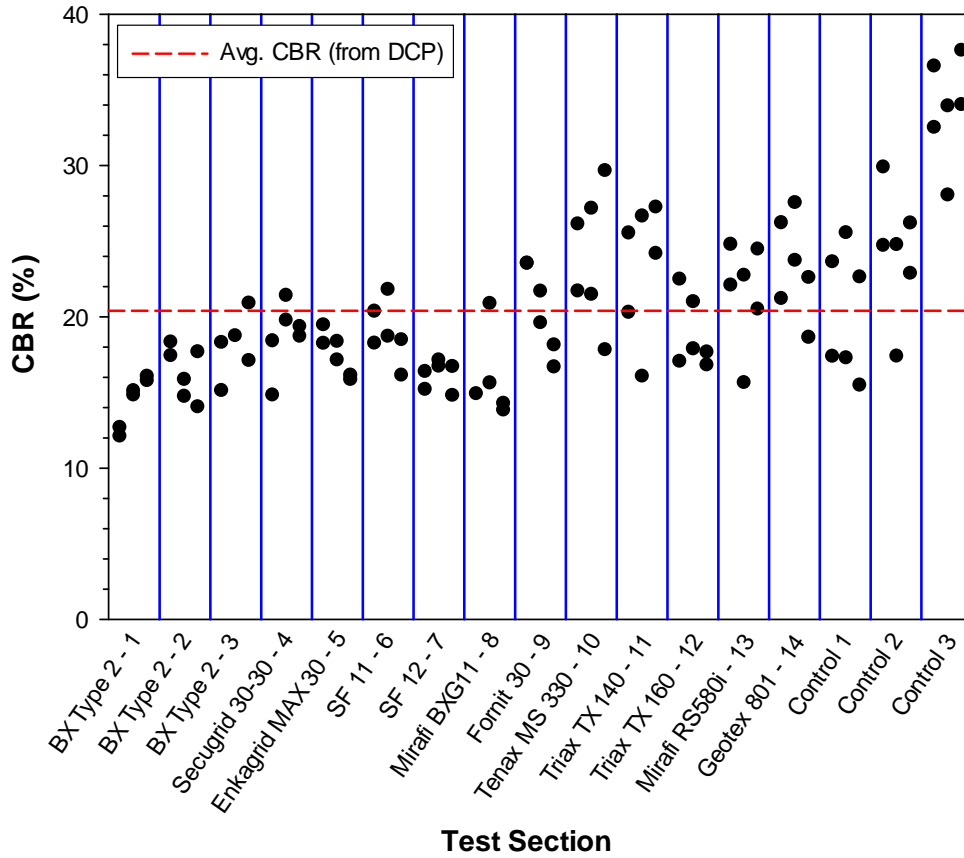
Figure 34: Base course CBR strength from DCP measurements in regions *B, D,* and *F* (west and east rut paths).

LWD measurements were conducted during and after construction of the base course in regions *B, D,* and *F* in the west and east rut path (total of 6 measurements in each test section). The first LWD measurements were made after the first lift of gravel was placed and compacted with one complete pass of the vibratory roller (made up of two individual passes, one up and one back). Three additional complete roller passes were then made (six individual up and back passes) before the second set of LWD measurements were made on the first lift. Final LWD measurements were made after the second lift was placed and compacted with four complete (eight individual) roller passes. Only Control 3 required a third lift and third set of LWD measurements, again, with four complete (eight individual) roller passes.

The average dynamic deflection modulus from the LWD for each test section is shown in Figure 35 (average of the six results from regions *B, D,* and *F*, west and east rut paths). The base course modulus along the test site was fairly consistent after the first lift with an average value of 188 ksf and standard deviation of 25 ksf. The difference in modulus between the first and final roller pass was inconsistent along the test site. Some test sections exhibited stiffer moduli after additional compaction, whereas others showed similar or weaker moduli. The average difference across the test site was only a 3 ksf increase, however the maximum increase was 64 ksf and the maximum decrease in modulus was 47 ksf. Three of the eight test sections that showed an

increase in modulus were the unreinforced control sections. The subgrade likely has some effect on the LWD measurements on base course, particularly with the first lift.
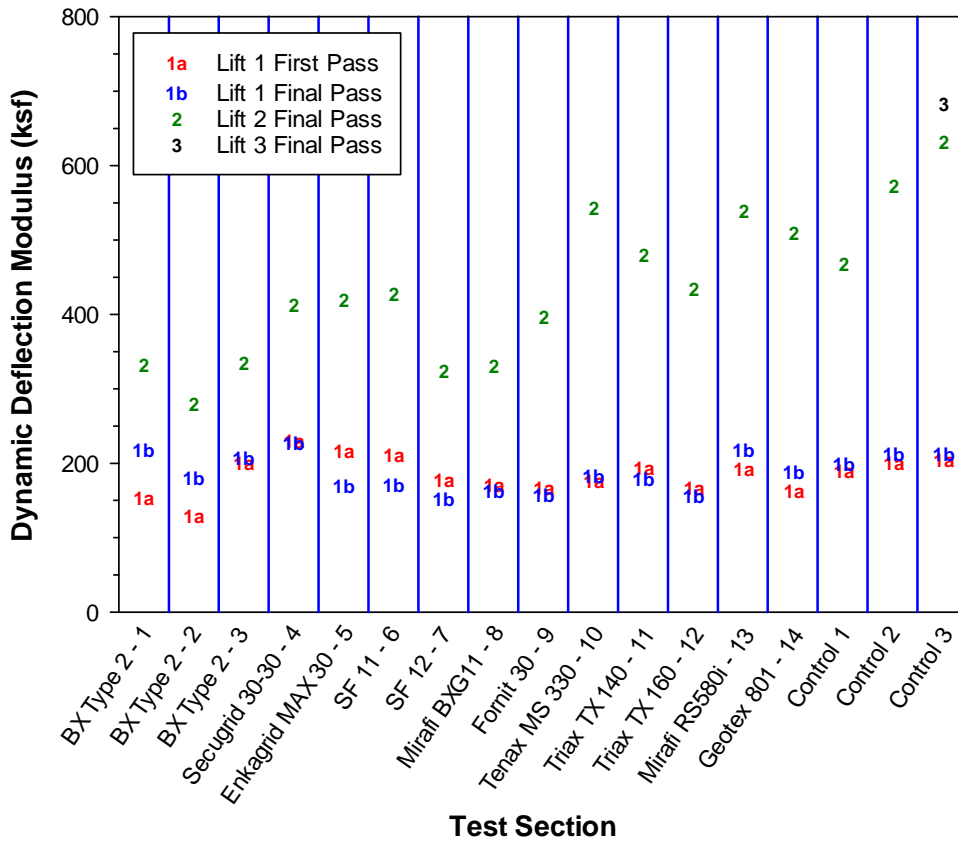
Figure 35: Average LWD measurements during and after base course construction.

The dynamic deflection modulus from the final set of LWD measurements after the base course was fully constructed exhibits similar behavior in comparison to the average CBR of the base course as determined from DCP measurements (Figure 36). The southern test sections are consistently stiffer than the northern test sections.
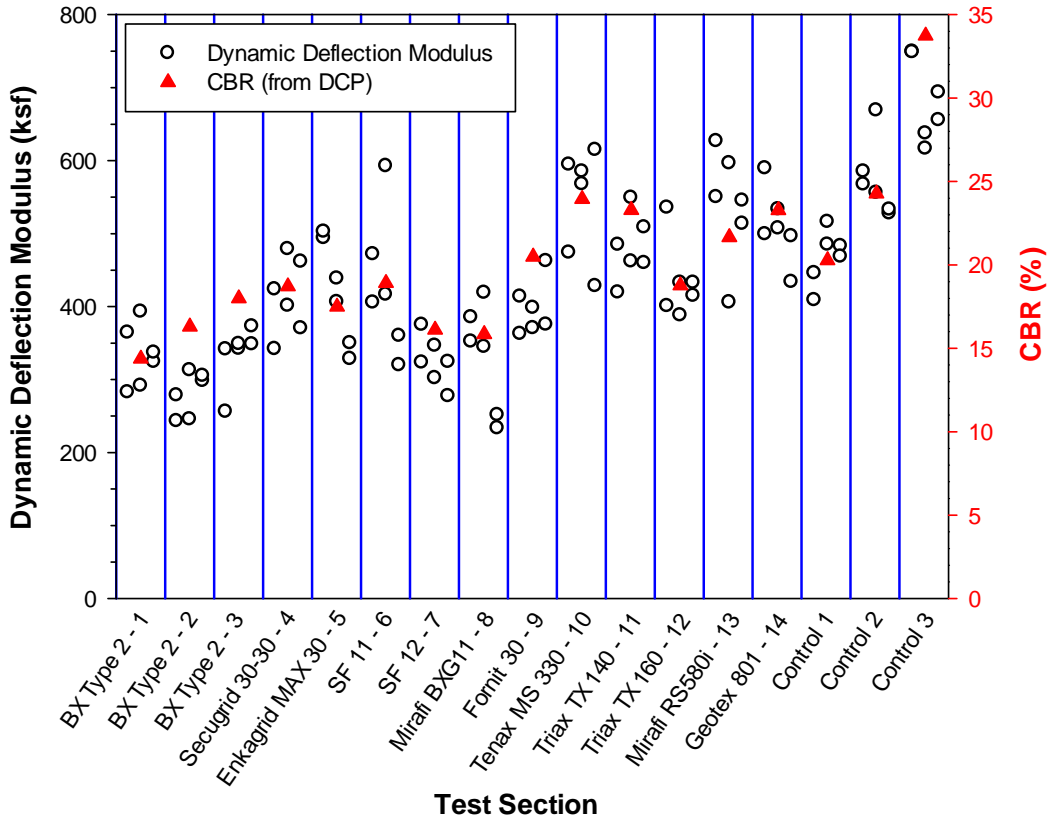
Figure 36: LWD (regions _B, D,_ and _F,_ west and east rut paths) and average CBR from DCP measurements of the completed base course.

In-field CBR tests were conducted after construction of the base course, in substantial accordance to ASTM D4429 using the minimum recommended surcharge of 30 lb. One test was conducted in each test section, located in region _D_ in the east rut. The in-field CBR for each test section is shown in Figure 37. The in-field CBR test results demonstrate a similar trend to the LWD and DCP measurements in that the southern test sections are generally stronger and stiffer than the northern test sections. The in-field CBR results were about 2.64 times greater than the CBR calculated from DCP data. Since only one test was conducted on the final subgrade surface in each test section, the in-field CBR data is not considered as reliable an indicator of overall strength or variability. The rutting behavior was not adjusted based on the stiffness and strength of the base course aggregate layer for two reasons: 1) test sections were not intentionally constructed with different base stiffnesses in order to determine their effect on rut performance, and 2) the stiffness of the base course correlated well with its thickness, as illustrated in Figure 38, and rut performance was adjusted to correct for varying thicknesses, as described in the Analysis and Results section.
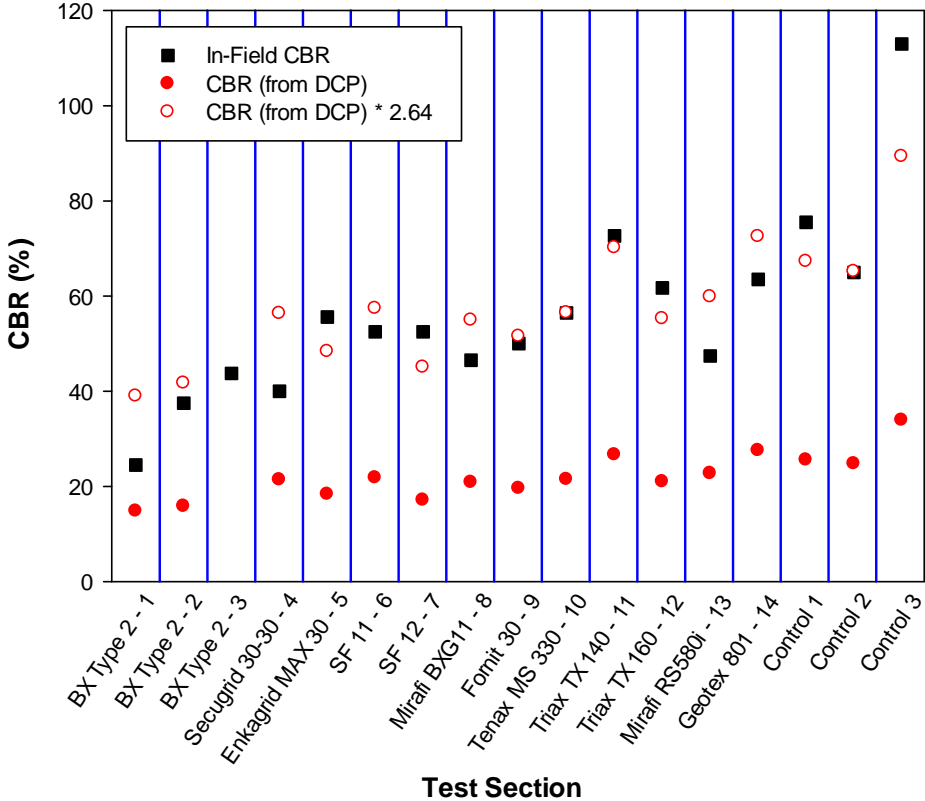
Figure 37: Comparison of base course strength from in-field CBR tests and CBR from DCP in region *D* (east rut path).
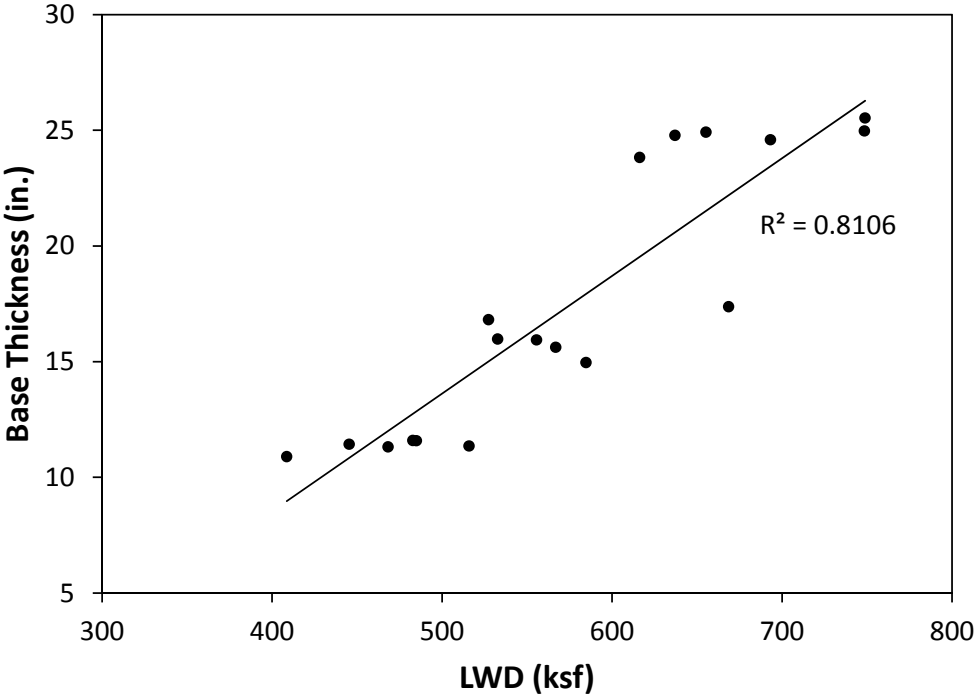
Figure 38: Correlation between stiffness and thickness of the base course.

A nuclear densometer was used to measure density and water content during and after construction of the base course in region *D* in both the east and west rut paths. The average dry unit weight and water content in region *D* of the constructed base course of each test section is shown in Figure 39. All test sections achieved the minimum compaction specification of 95 percent of maximum dry density (determined according to ASTM D 1557, modified Proctor).
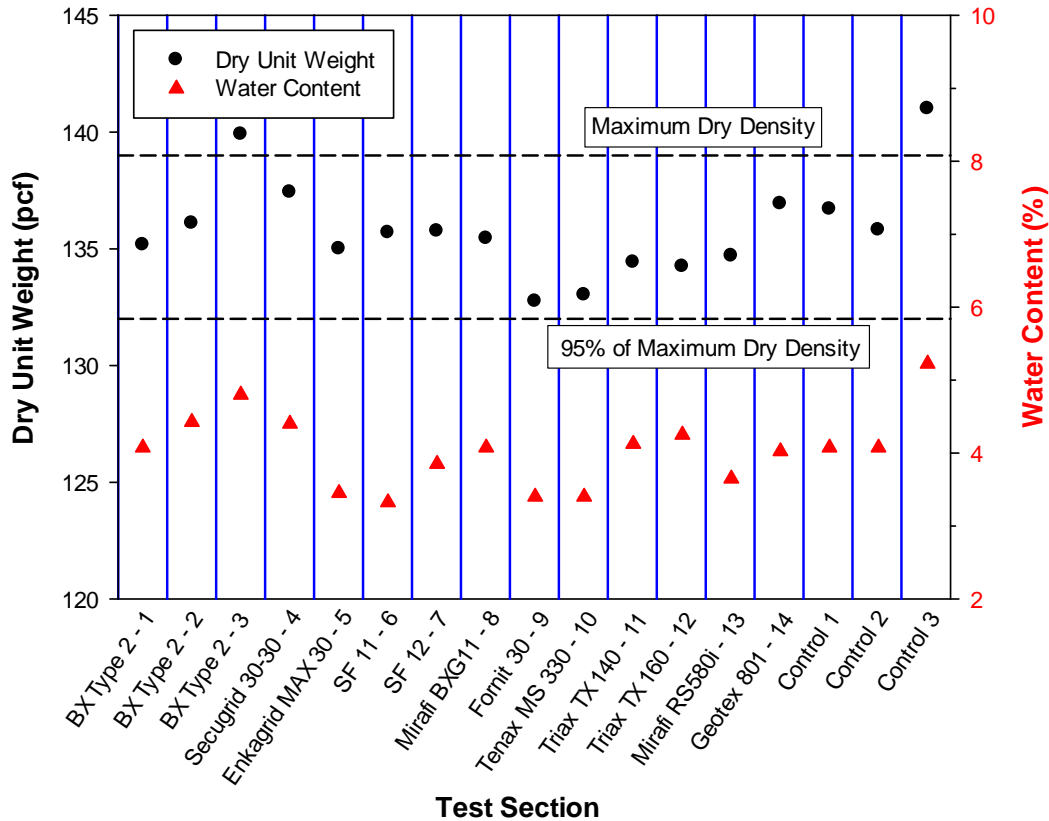
Figure 39: In place density and water content of the base course.

Instrumentation and Data Acquisition Systems

Instrumentation was used in this research project to measure displacement and strain on the geosynthetic (in the cross-machine direction) and pore-water pressure in the subgrade. Linearly variable displacement transducers (LVDTs) were used to measure displacement, resistance strain gages bonded to the surface of the geosynthetics were used to measure strain, and pore-water pressure gages were used to measure pore pressures in the subgrade. Data from the sensors were collected and stored using two CR9000 data loggers from Campbell Scientific, Inc., which were housed in a mobile laboratory located adjacent to the test site.

Six measurements of transverse displacement of the geosynthetic and three measurement of pore pressure in the subgrade were measured at two separate locations within each test section, as illustrated in Figure 40. A cross-sectional of the layout of the sensors at each location is illustrated in Figure 41. All sensors and associated electronics were mounted in watertight

enclosures that were rigidly attached to the existing pavement away from the edge of the test pit to minimize the influence of the presence of these gages in the rut bowl area (Figure 42). The two enclosures were centered in each test section and separated 15 ft from one another. Flexible conduit was used to protect instrumentation cabling. One of the boxes was designated as the "master", which was directly wired to the data acquisition computers that were housed in the mobile laboratory. The other enclosure ("slave") was wired through its corresponding master.
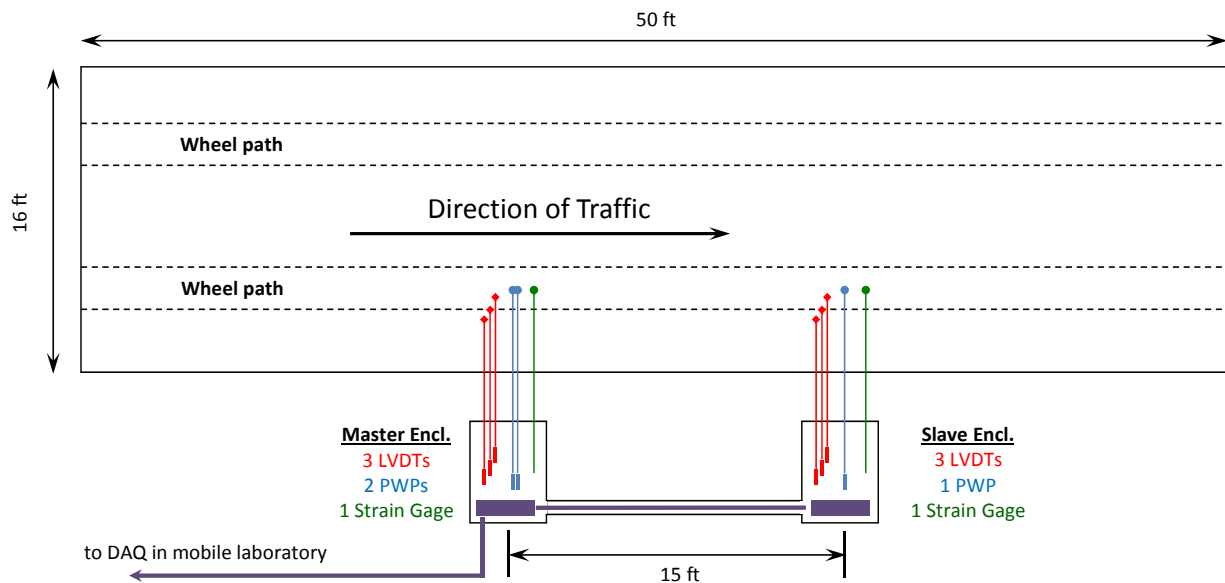
Figure 40: Illustration of instrumentation arrangement within a single test section.
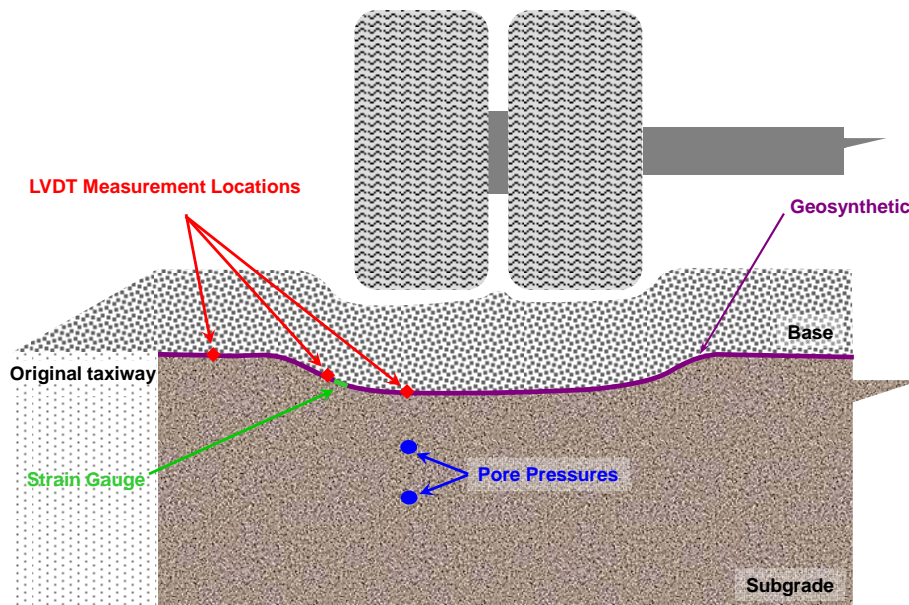
Figure 41: Cross-sectional view of instrumentation layout.

Figure 42: Instrumentation enclosure mounted to pavement.

Displacement Measurements

Six displacement measurements were made in each test section – three measurements at two separate locations – using model HR 1000 LVDTs from Measurement Specialties (Hampton, VA). These sensors were rigidly attached to the bottoms of the enclosures so that the displacement measurements could be made relative to a fixed reference point outside of the test sections. Lead wires were attached to the geosynthetic to bring the point of measurement on the geosynthetic back to the sensor, using the procedure outlined in Cuelho et al. (2008). Rigid plastic tubing was run inside small diameter, schedule 80, PVC pipes to further protect the plastic tubing during trafficking and to plumb the lead wires into the sensor box. A completed lead wire installation and protective tubing arrangement is provided in Figure 43.

Figure 43: Typical lead wire installation with protective tubing.

Resistance Strain Gages

Resistance strain gages were used to measure the strain response on the transverse reinforcing members of the geosynthetic. Gage selection was done mainly based on their size in relation to the size of the elements they need to be mounted on. The EP series of strain gage (from Micro-Measurements – Raleigh, NC) was selected because it accommodates large strain measurements (± 20 percent in some cases).

Instrumenting strain gages on geogrids consists of six main steps: 1) preparing the strain gages, 2) preparing the geogrid surface, 3) attaching the strain gages to the geosynthetic, 4) curing the adhesive, 5) attaching the instrumentation wiring, and 6) applying and curing the protective coating. Strain gaging took place in an enclosed building at the TRANSCEND research facility in Lewistown to minimize influences from wind, sun, water, and airborne contaminants. A detailed description of the procedure used to bond the strain gages to the various geosynthetic products can be found in Morris (2013).

Preparation of the strain gages consisted of attaching wires from the strain gage to bondable terminals. The reason for this step is to prevent potential forces transmitted along the instrumentation wire from damaging the strain gage or affecting its performance during installation and trafficking. Two examples of a typical setup of the gage with jumper wires attached are shown in Figure 44. Special solvents were used to clean the strain gages after this step to remove any foreign matter or solder residues prior to bonding.
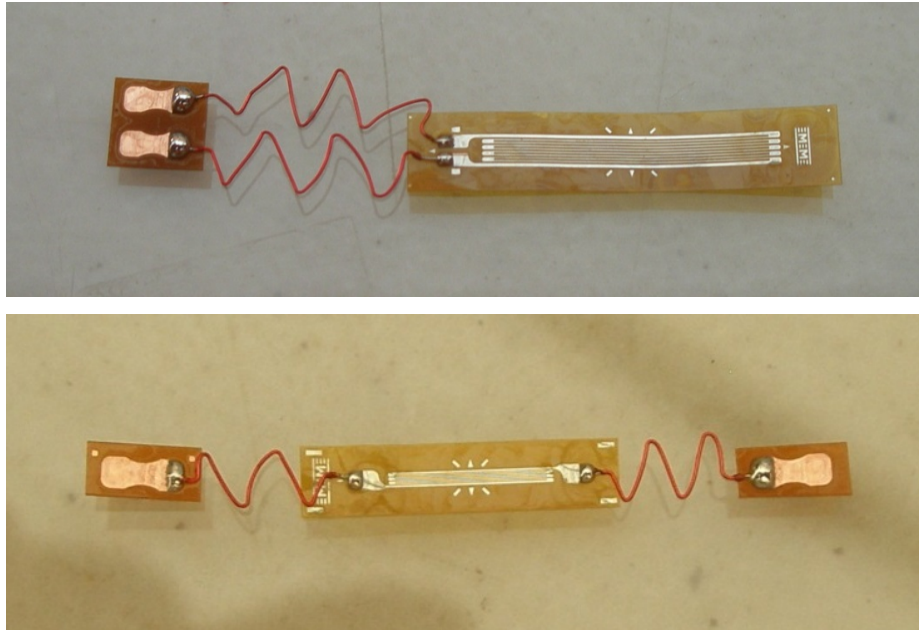
Figure 44: Jumper wires attached to strain gages.

The surface of the geogrid was thoroughly cleaned before applying the adhesive and attaching the strain gage. Preparation of the surface consists of degreasing the surface using a solvent, lightly abrading the surface with sandpaper, and applying chemical conditioning and neutralizing agents. For the woven geogrid products, the protective PVC or polymer coating, applied by the manufacturers to protect the woven grid structure, was removed prior to the cleaning and prepping process. The solvent degreaser removes oils, greases, organic contaminants, and soluble chemical residues. Abrading the surface removes any surface defects of the geogrid, and lightly roughens the surface to facilitate bonding of the adhesive. The conditioning and neutralizing solutions bring the surface to an optimum pH of 7.0 to 7.5.

The strain gages are positioned on the material, the adhesive is applied, and pressure is applied to the gages to create an optimum bond. Two gages were attached to the material at a single location (one on the top of the geosynthetic and one on the bottom) to negate the effects of local bending of the gaged area. Strain gages were attached to the transverse ribs of the geogrids, or in the transverse direction of the geotextile to measure strain in the transverse direction during trafficking. Curing of the adhesive was achieved by elevating the temperature to 150 °F for 6 hours in the gage area. Excess glue was carefully removed using a dremel tool and the lead wires were attached. A strain gage bonded to a geogrid is shown in Figure 45.
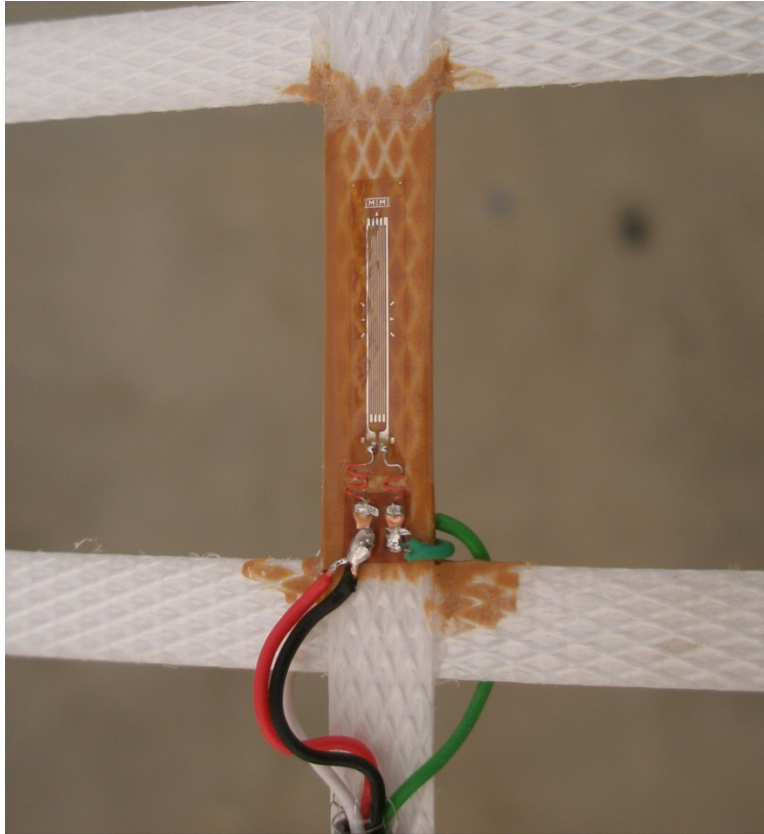
Figure 45: Completed placement and wiring of a strain gage.

A protective coating is then applied to keep water from entering the gaged area and to protect it from physical damage during construction and trafficking. M-Coat J from MicroMeasurments Group (Raleigh, NC) was used for this purpose. A thin piece of Teflon™ is used to separate the exposed gage surface from the coating material, as recommended by the manufacturers. Curing of the protective coating was accelerated by heating the gage area to 125 °F for 2.5 hours. A finished strain gage location is shown in Figure 46.

Figure 46: Completed strain gage installation with protective coating.

The procedure used to bond strain gages to geotextiles was similar, but modified slightly to accommodate the unique surface structure of the materials. To minimize stiffening of the gaged area, a different adhesive (a non-conducting silicone) was used to bond the strain gages to the textiles and also act as the protective coating. A completed strain gage installation on the geotextiles is shown in Figure 47.
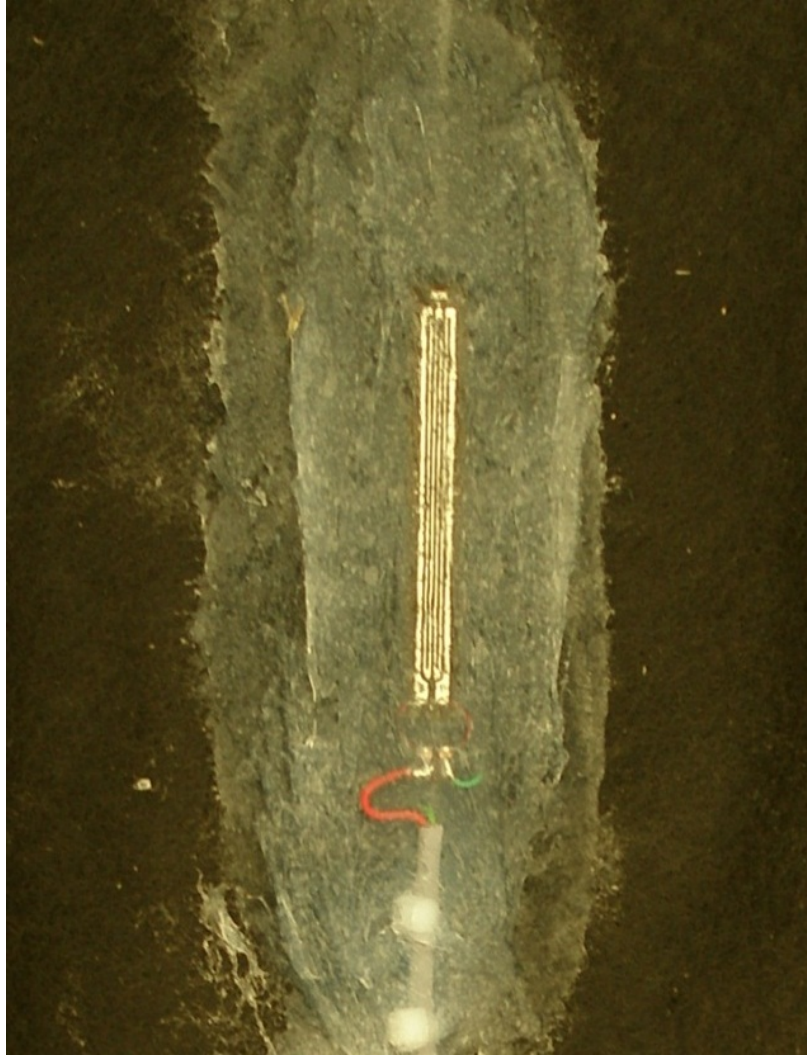
Figure 47: Completed strain gage installation on a non-woven geotextiles.

A three-wire lead wire system was used to negate influence from long lead wires between the strain gage area and the Wheatstone bridge circuitry. Shunt calibration of the strain gage was done to ensure proper operation and determine the baseline measurement for the gages prior to installation.

Further calibration was also necessary to determine how well local measurements of strain obtained by the strain gage matched the global strain response of the geosynthetic. This calibration effort was conducted in the laboratory on wide-width geosynthetic samples that were instrumented with strain gages using the same procedure described above, including environmental protection. Instrumented geosynthetics were tested using a cyclic load protocol that applied 50 sinusoidal pulses at ±0.10 percent strain amplitude at multiple initial strain levels ranging from 0.25 to 10.0 percent permanent strain (total of 750 load cycles). A digital camera was used as a secondary method of verifying the strain response of the geosynthetic near the strain gage. Maximum strain gage readings from the field were generally less than about 4

percent. A single calibration constant was used as a multiplier to synchronize the load-strain response from the strain gage to the global load-strain response. This synchronization process focused on strain responses up to the maximum level of strain measured during trafficking. The calibration factors for each of the materials used in this research are listed in Table 12. Calibration factors less than 1.00 indicated that the strain gages overestimated the global strain. Likewise, calibration factors greater than 1.00 indicated that the strain gages underestimated the global strain.

Table 12: Strain Gage Calibration Factors

Geosynthetic Test Section	Maximum Field Strain (%)	Calibration Factor
BX Type 2	3.20	**0.94**
Secugrid 30/30 Q1	0.64	**0.85**
Enkagrid Max 30	1.34	**1.00**
SF 11	0.74	**1.40**
SF 12	0.36	**1.46**
BXG 11	0.92	**1.16**
Fornit 30	0.54	**1.43**
Tenax MS 330	1.40	**0.94**
TX 140	4.00	**0.80**
TX 160	3.72	**0.84**
RS580i	0.84	**1.75**
Geotex 801	4.22	**1.80**

All of the strain gages installed on the geosynthetics survived construction; however, many of the gages failed during trafficking. Forensic work during the summer of 2013 revealed that the outer coating used to protect the strain gages from water and physical damage was not fully bonded around the edges and water had infiltrated into the gaged area causing them to fail. Strain gage field performance is summarized in Table 13.

Table 13: Strain Gage Survivability

Geosynthetic Test Section	Truck Passes at Failure	
	North Location	South Location
1 – BX Type 2	556[b]	DNF
2 – BX Type 2	303	20
3 – BX Type 2	DNF	DNF
4 – Secugrid 30/30 Q1	303	175
5 – Enkagrid Max 30	405	405
6 – SF 11	303	175
7 – SF 12	1	10
8 – BXG 11	251	40
9 – Fornit 30	40	40
10 – Tenax MS 330	DNF	DNF
11 – TX 140	405	303
12 – TX 160	140	175
13 – RS580i	DNF	DNF
14 – Geotex 801	DNF	DNF

DNF = did not fail

Pore-water Pressure Gages

Pore-water pressure measurements in the subgrade were made using a pressure transducer (0 to 30 psi range) connected to a porous ceramic stone via a rigid plastic tube. The rigid tubing and porous stone extended the point of measurement from the rut area to the pressure sensor which was housed in the enclosures adjacent to the test sections. An extensive laboratory evaluation was undertaken to verify the performance and accuracy of the pressure sensors prior to installing them in the field. This verification process included testing the sensor at various pressures while in a water bath and while embedded in the subgrade soil. In-water tests were used to verify the sensor and associated electronics were working as expected. In-soil tests were conducted by preparing the subgrade to the target strength (CBR = 1.7), and subjecting them to anticipated stresses that were generated during construction and trafficking. Results from these tests indicated that the sensors, when properly prepared, should yield meaningful and accurate responses for analysis purposes.

Based on the laboratory work, a protocol was developed for attaching the porous ceramic stones to the high strength, flexible tubing and de-airing the tubing, sensor and porous stone assembly. The porous ceramic stones are specially made for soil pore-water pressure measurement applications ($k = 7.56 \times 10^{-7}$ cm/s, porosity $\approx 34\%$, effective pore size = 1.7 microns). These stones were attached to the flexible tubing using a special epoxy to prevent leakage of water and entrance of air during their installation and use. The water used to fill the sensor, tubing and saturate the stone was de-aired by boiling and vacuum methods. The ceramic porous stones were

also saturated by boiling them (Figure 48). Vacuum pumps were used to pull the de-aired water through the saturated stone and into the flexible tubing. A brass fitting was used to attach the open end of the flexible tubing to the sensor. This was done under water to prevent any air from penetrating into the system during assembly. This procedure was used to prepare all of the pore-water pressure sensors used in this research project. Great care was given to the de-airing and preparation process to ensure that no bubbles were present in the flexible tubes during installation and use.

Figure 48: Saturation of ceramic porous stones.

Three pore-water pressure measurements were made in each test section, including the controls. Two measurements were made at 6 in. depth and a single measurement was made at 10 in. depth in the wheel path. A small hole was excavated in the subgrade and the saturated stone was covered with a layer of very wet subgrade just prior to being placed at the appropriate depth (Figure 49). This wet soil was needed to prevent the soil from drying out over time. The remainder of the hole was then filled with subgrade and the flexible tubing was run through protective conduit. Using these installation techniques, all pore water pressure sensors were active and in good working condition after construction. During the trafficking phase, however, air bubbles were noticed in several of the sensors. The pore-water pressure sensors were removed in late October to prevent damage to the sensors from below-freezing temperatures.

Figure 49: Installation of pore water pressure sensor in subgrade.

Data Acquisition and Power Systems

The data acquisition system consisted of two CR9000 data loggers from Campbell Scientific Inc. (Logan, UT) that were housed in a mobile laboratory centrally parked near the test site. Data cabling from each of the test sections were routed through flexible conduit and buried adjacent to the test sections to transmit data from and power to the sensors housed in the enclosures. Cabling was connected to circuitry located in the mobile lab to facilitate measurements from each of the sensors (Figure 50). Solar power was planned for this project, but current demand from the sensors and data loggers was too high. After several attempts to make this system work, AC power was eventually installed.

Long term data were recorded from all of the sensors every 30 minutes during the trafficking phase. The data loggers were also used to record dynamic data (at 25 Hz) from all of the sensors during passage of the truck. These dynamic data were recorded during truck passes 1, 2, 3, 5–10, 20, 40, 140, 175, 251, 301–303, 391–395, and 546–548.
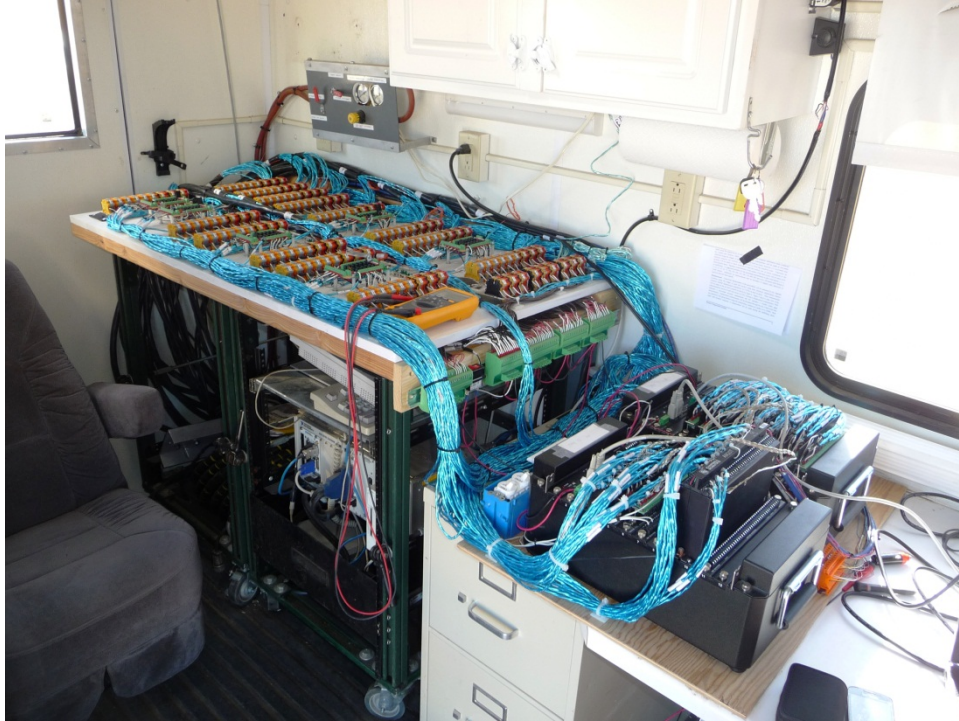
Figure 50: Completion circuitry and data loggers in mobile laboratory.

Trafficking and Data Collection

Trafficking began on September 13th and continued until November 7th, using a three-axle dump truck (Figure 51) that weighed 45,420 lb and had 90 psi tire pressure. Dimensions and weights of the individual axles are shown in Figure 52. Trafficking was always in one direction (from north to south), and the speed was approximately 5 mph to ensure that dynamic loads were not induced in the test sections from any unevenness in the gravel surface. Longitudinal lines were painted on the gravel surface to position the truck during trafficking. These painted lines were also used to mark where rut measurements were to be made. Occasional rainstorms having accumulations greater than one-tenth of an inch over a 24 hour period interrupted trafficking. A total of 1.4 in. of rain fell during trafficking. A history of the precipitation during trafficking is presented in Figure 53. Traffic resumed once the surface of the gravel had dried significantly. Trafficking continued until rut levels reached 3 inches – defined as failure in this project. Photos of Test Section 10 (Tenax MS 330) are presented in Figure 54, Figure 55, Figure 56 and Figure 57 for rut levels of about 0, 1, 2 and 3 inches, respectively. Once 3 inches of rut was attained, repairs were made by placing additional gravel in the rutted areas using a skid-steer loader and leveling the surface (Figure 58). Repairs within test sections were made incrementally, so that un-failed portions of test sections could continue to be trafficked until they reached failure. No further measures of rut were made in areas that were repaired. A history of the rut repair is provided in Appendix F.

Figure 51: Three-axle dump truck used for trafficking.
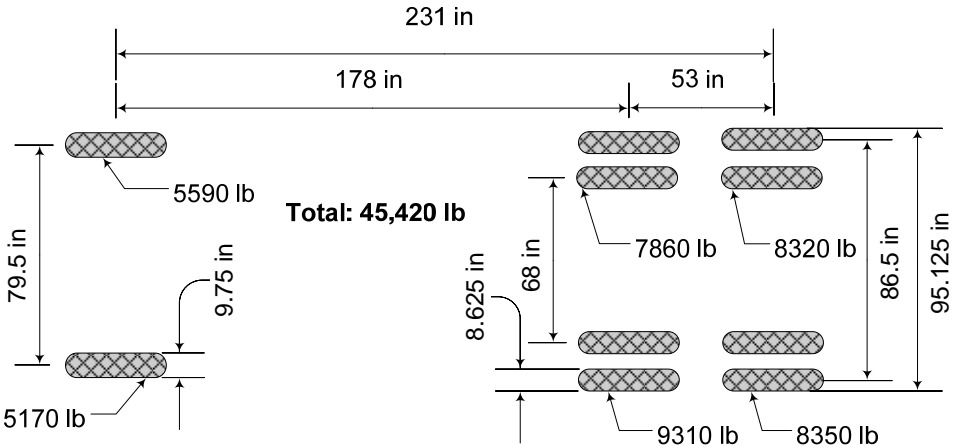
Figure 52: Axle dimensions and associated weights of test vehicle.
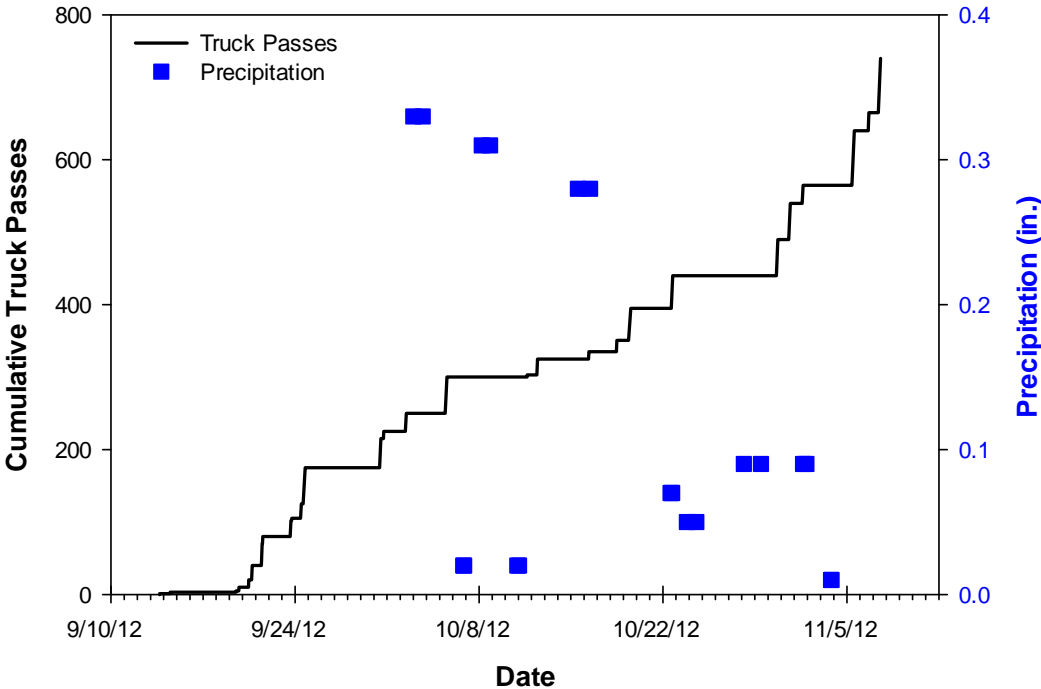
Figure 53: Precipitation events that occurred during trafficking.

Figure 54: Photo of Test Section 10 (Tenax MS 330) at approximately 0 in. of rut.

Figure 55: Photo of Test Section 10 (Tenax MS 330) at approximately 1 in. of rut.

Figure 56: Photo of Test Section 10 (Tenax MS 330) at approximately 2 in. of rut.

Figure 57: Photo of Test Section 10 (Tenax MS 330) at approximately 3 in. of rut.
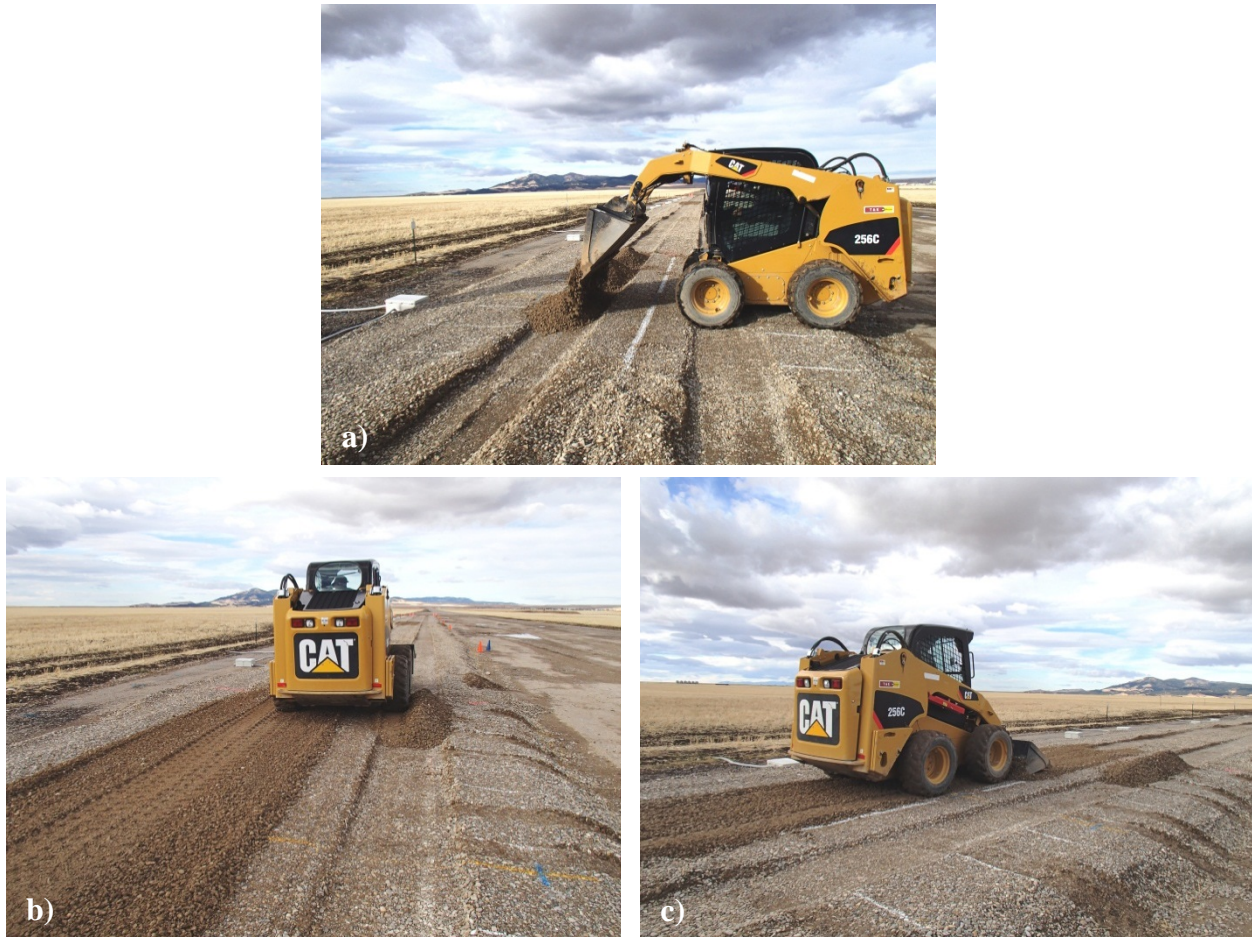
Figure 58: Rut repair: a) adding gravel to the rutted area, b) compacting the new gravel with the skid-steer tractor, and c) final smoothing.

Rut measurements were made at 40-inch intervals along two longitudinal lines that corresponded to the outside rear wheels of the test vehicle using a robotic total station (Leica TPS1205+ with an accuracy of 3 mm + 1.5 ppm). Twenty-eight longitudinal rut measurements were made in each test section at various trafficking levels (14 in the east rut and 14 in the west rut). A summary of the measurements timetable is shown in Table 14. Transverse rut measurements were also made at these same times in two locations in each test section (geographically coincident with the instrumentation locations). Sixteen individual measurements were taken to create a single transverse surface contour.

Table 14: Summary of Rut Measurements

Date Measured	Truck Passes	Notes
9/13/2012	0	
9/14/2012	3	
9/19/2012	10	
9/20/2012	20	
9/20/2012	40	
9/21/2012	70	C1 only
9/23/2012	80	
9/23/2012	102	C1 only
9/24/2012	125	2, 7 and 9 only
9/25/2012	175	
10/2/2012	250	
10/9/2012	300	
10/15/2012	325	
10/18/2012	351	
10/19/2012	395	
10/29/2012	440	
11/1/2012	540	
11/6/2012	640	
11/19/2012	740	

These measurements were used to determine rut as a function of the difference in the elevation of the measurement points over time. Total rut, therefore, was determined by comparing current measurements to a baseline measurement which was made before trafficking. This type of rut is referred to as "elevation rut", as illustrated in Figure 59. The "apparent rut", however, is typically greater and can be defined as the vertical distance from the upper crest of the rut bowl to the bottom of the rut bowl (Figure 59).
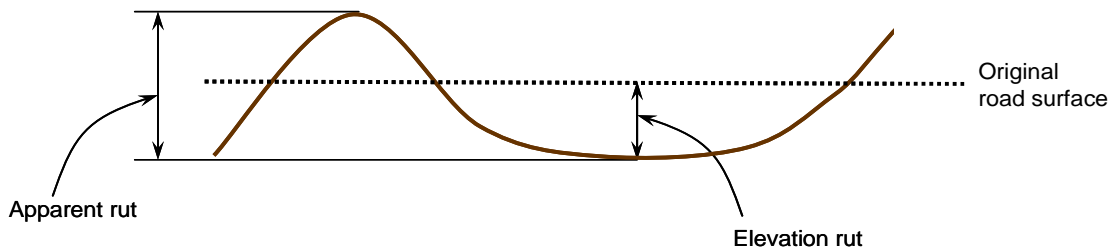
Figure 59: Illustration of rut measurements.

POST-TRAFFICKING FORENSIC INVESTIGATIONS

Post-trafficking, forensic investigations were conducted to evaluate damage to the geosynthetics from construction and from trafficking, to re-evaluate pertinent soil strength characteristics, and to assess mixing of base and subgrade soils from trafficking. Two separate forensic evaluations were conducted: the first immediately after trafficking was completed (week of November 19th, 2012) and the second during the following summer (week of July 8th, 2013). Forensics work during the first visit was limited in scope due to cold weather and focused on investigating areas in each test section that had experienced different levels of longitudinal rut in an attempt to identify reasons for these differences. The second forensic visit was more extensive but occurred after the test sections were exposed to winter conditions and had remained idle for six to eight months, which had allowed the subgrade properties to change and/or equilibrate. During the second visit, large samples of geosynthetic were extracted in areas of the test sections that had experienced approximately 3 inches of longitudinal rut (the maximum level of rut allowed during the experiment before repair).

Several assessments and measurements were made during both of these visits. During the first visit, a small excavator was used to expose the geosynthetic and top of subgrade to make Dynamic Cone Penetrometer (DCP), Lightweight Deflectometer (LWD) and vane shear measurements, and to extract samples near the top of the subgrade to determine moisture content. During the second visit a large sample of geosynthetic (approximately 6 ft long by the width of the test sections) was carefully exhumed from each test section to evaluate damage to the geosynthetic, topographic profiles of the transverse rut at either side of these excavations were made to assess base course thickness, LWD and DCP measurements were taken, soil samples were extracted near the top and bottom of the subgrade layer to evaluate moisture, and multiple samples of base aggregate were collected from above the geosynthetic to evaluate the fines content in the base as a measure of the migration of subgrade material into the base course.

Assessment of Subgrade Soil

The rut behavior within a particular test section was expected to be generally the same. Nevertheless, despite the fact that construction was uniform across the entire test section, differences in the rutting behavior were evident during trafficking. Therefore, the primary goal of the forensic investigations conducted in November 2012, immediately after trafficking was complete, was to collect information to help explain these differences.

A small excavator was used to uncover the geosynthetics and top of subgrade in two to three locations within many of the test sections. Subgrade properties were assessed based on DCP, LWD, and moisture contents taken in the top 3 inches of subgrade. Direct measure of the shear strength of the subgrade was attempted using the hand-held vane shear device; however, the consistency of the subgrade soil made it very difficult to obtain reliable readings. The results of the LWD, DCP and moisture contents are summarized in Table 15. The depth of rut at 300 truck

passes at the point of excavation is also listed in Table 15 to facilitate comparisons between the subgrade properties and rut depth (correlations were made at 300 truck passes because none of the geosynthetic-reinforced test sections had been repaired up to that level of traffic). High rut values listed in Table 15 in Test Sections 11 and 12 (Tensar TX140 and Tensar TX160 test sections, respectively) were caused by full rupture of the materials as seen in the areas excavated during the first forensic investigation.

Table 15: Subgrade Properties from Forensic Analysis Conducted in November 2012

Geosynthetic Test Section	Excavation Location[a]	Rut Depth at 300 Truck Passes (*in.*)	CBR from DCP (%)	Dynamic Deflection Modulus (ksf)	Subgrade Moisture Content (%)
Tensar BX Type 2 (Section 2)	7 – East	1.64	2.56	112	21.2
	4 – East	3.22	1.90	85	22.2
NAUE Secugrid 30/30 Q1 (Section 4)	12 – West	2.85	1.91	118	21.3
	12 – East	1.67	1.43	126	21.7
Colbond Enkagrid Max 30 (Section 5)	9 – West	1.82	2.64	182	19.3
	2 – West[b]	4.00	2.31	97	21.8
Synteen SF 11 (Section 6)	13 – East	4.02	2.58	106	21.7
	5 – East	1.65	2.56	153	22.1
Synteen SF 12 (Section 7)	6 – East[b]	2.69	2.34	115	21.5
	11 – East	5.36	2.51	78	22.7
TenCate Mirafi BXG 11 (Section 8)	11 – East	3.17	2.35	84	22.3
	8 – East	1.48	2.39	80	22.7
Huesker Fornit 30 (Section 9)	10 – West	3.58	2.00	81	22.9
	2 – East	2.99	2.43	110	23.6
Tensar TX 140 (Section 11)	12 – East	1.75	2.59	140	---
	7 – West	7.38[c]	2.52	83	22.0
Tensar TX 160 (Section 12)	6 – East	1.55	2.57	102	22.7
	6 – West	7.67[c]	2.00	82	21.3
TenCate Mirafi RS580i (Section 13)	11 – West	4.18	2.13	83	22.5
	4 – East[b]	1.13	2.37	121	22.8
Propex Geotex 801 (Section 14)	7 – East[b]	1.57	2.54	122	23.0
	11 – East	2.17	2.24	96	21.2

[a] number = longitudinal measurement point along test section – direction = east or west wheel path
[b] small amounts of water accumulation at the interface between subgrade and base course
[c] material fully ruptured at this location resulting in higher rut levels at the point of excavation
--- missing data

Results of the soil tests on the subgrade obtained during the forensic investigations were further analyzed to determine potential correlations between subgrade moisture content, subgrade strength (from the DCP), and subgrade stiffness (from the LWD). The results from this analysis indicated that there is no direct correlation between moisture content or strength and the rut

depth at 300 truck passes. Rutting of the subgrade is primarily indicative of distortional shearing not rutting due to compaction (i.e., volumetric compression) of the subgrade material. Finally, based on this very limited data set, both the DCP and LWD measured an increase in strength and stiffness of about 30 percent when compared to measurements made immediately after construction. Forensic investigations were not conducted in test sections 1, 3, 10, C1, C2 and C3.

Assessments of the base course and subgrade were also made during the second forensic visit in July 2013. A single location that had reached approximately 3 inches of rut in both the east and west wheel tracks (prior to being repaired) was selected for evaluation within each test section. Areas containing the greatest rut levels were used in test sections that did not reach 3 inches of rut before trafficking was terminated.

Once these areas were selected, the base course was carefully removed to facilitate extraction of the geosynthetic and assessments of the subgrade. The base course aggregate was removed using an air nozzle connected to a high-volume air compressor to clear an area approximately 6 ft wide (3 ft on either side of the point of interest), as shown in Figure 60. This method was used in order to minimize damage to the geosynthetics during excavation of the base aggregate. The geosynthetic was then carefully cut out and stored for further evaluation.

Figure 60: Removal of the base course aggregate using compressed air.

After the geosynthetics were removed, measurements of the subgrade soil properties were made using the DCP and LWD, and moisture content samples were taken. DCP and LWD

measurements were made on the top of the subgrade in the west and east ruts along a transverse line (perpendicular to the roadway), the results of which are summarized in Table 16. A trench was then dug to allow moisture samples to be taken near the top and bottom of the subgrade layer in these same locations (Figure 61). Upper subgrade samples were taken about 4 inches from the top of the subgrade and lower subgrade samples were taken about 28 inches below the top of the subgrade.

By the time of the second forensic investigation the test sections had been idle for eight months and had experienced a winter season, which had caused the subgrade to equilibrate and dry out. Moisture contents near the top of the subgrade were all very similar to one another (average moisture content was 16.4 percent) but had lost around 6 percent moisture since the termination of trafficking. Moisture content near the bottom of the subgrade was greater than the top (average moisture content was 18.5 percent), but still lower than during construction (around 22 percent). As a result, DCP and LWD tests on the subgrade also indicated higher strength in the subgrade. Measurements of the dynamic deflection modulus (from the LWD) of the subgrade showed an increase over time (values were around 110 ksf during the second forensic evaluation) when compared to immediately after construction (approximately 60–70 ksf); however, overall not much change had occurred between the first and second forensic evaluations. Correlations between the rut depth at 300 traffic passes and CBR, dynamic deflection modulus, and moisture content were poor as may be expected because the subgrade had changed significantly from when trafficking had ended.

Figure 61: Removal of subgrade from forensic location.

Table 16: Subgrade Properties from Forensic Analysis Conducted in July 2013

Geosynthetic Test Section	Excavation Location[a]	Rut Depth at 300 Truck Passes (*in.*)	CBR from DCP (%)	Dynamic Deflection Modulus (ksf)	Subgrade Moisture Content (%)	
					Upper	Lower
Tensar BX Type 2 (Section 1)	10 – West	2.54	3.29	108	15.4	16.3
	10 – East	2.91	3.73	111	15.4	17.2
Tensar BX Type 2 (Section 2)	9 – West	2.03	2.67	105	16.1	18.7
	9 – East	1.78	2.87	105	15.9	17.3
Tensar BX Type 2 (Section 3)	9 – West	1.79	2.70	86	16.2	18.9
	9 – East	2.33	3.04	93	16.5	19.2
NAUE Secugrid 30/30 Q1 (Section 4)	8 – West	1.74	3.13	86	16.0	17.5
	8 – East	2.02	3.07	98	16.6	18.6
Colbond Enkagrid Max 30 (Section 5)	4 – West	2.21	3.23	148	16.2	19.6
	4 – East	2.91	2.75	88	16.7	19.1
Synteen SF 11 (Section 6)	3 – West	1.92	3.05	91	16.0	20.3
	3 – East	3.11	3.33	220	17.1	18.6
Synteen SF 12 (Section 7)	9 – West	3.52	3.12	79	17.2	18.3
	9 – East	3.63	3.08	85	16.8	18.0
TenCate Mirafi BXG 11 (Section 8)	3 – West	1.78	2.72	134	17.0	19.7
	3 – East	2.28	2.87	116	16.5	18.3
Huesker Fornit 30 (Section 9)	9 – West	2.89	2.73	94	16.1	18.1
	9 – East	3.94	3.08	94	16.4	19.3
Syntec – Tenax MS 330 (Section 10)	9 – West	2.85	2.99	102	16.3	18.9
	9 – East	2.25	2.86	107	16.0	18.8
Tensar TX 140 (Section 11)	3 – West	2.90	2.92	119	16.7	18.7
	3 – East	2.56	3.03	89	16.6	18.7
Tensar TX 160 (Section 12)	12 – West	3.13	2.91	111	15.7	18.4
	12 – East	3.80	2.74	146	16.4	18.5
TenCate Mirafi RS580i (Section 13)	6 – West	1.28	2.77	88	17.0	17.2
	6 – East	1.22	2.77	85	16.4	19.2
Propex Geotex 801 (Section 14)	9 – West	2.01	3.01	90	16.0	19.0
	9 – East	1.92	2.93	217	16.4	18.4
Control 1	4 – West	2.67[b]	3.26	87	16.5	18.4
	4 – East	5.15[b]	2.84	199	15.9	17.3
Control 2	4 – West	2.04	2.79	99	17.2	19.1
	4 – East	1.26	2.69	108	16.9	17.8
Control 3	5 – West	0.90	2.49	74	17.6	18.8
	5 – East	1.26	3.12	99	17.0	18.8

[a] number = longitudinal measurement point along test section – direction = east or west rut wheel path
[b] rut depth at 102 truck passes when ruts were filled in

Assessment of Base Course Aggregate

Assessments of the base course aggregate were also made during both of the forensic visits. These assessments consisted of a topographic survey to compare base thickness before and after trafficking and collection of base aggregate samples to assess migration of fines from the subgrade into the base layer.

During the second visit in the summer of 2013, a topographic survey of the transverse edges of the excavations was taken on top of the base aggregate and again directly below on the subgrade once the base aggregate was removed. Transverse profiles for each test section are provided in Appendix G. The thickness of the base aggregate was determined from these measurements and compared to the thickness at these same points prior to trafficking. These measurements were only made in areas where the ruts had not been repaired. A summary of this data is provided in Table 17. On average, the thickness of the aggregate had decreased by about 0.7 inches. This difference can be attributed to loss of aggregate into the subgrade and compaction and spreading of the aggregate layer during trafficking.

Table 17: Gravel Thickness Comparison Before and After Trafficking

Geosynthetic Test Section	Location[a]	Original Thickness (in.)		Post-Trafficking Thickness (in.)		Thickness Difference (in.)	
		West rut	East rut	West rut	East rut	West	East
Tensar BX Type 2 (Section 1)	9	11.6	10.8	10.7	9.7	0.9	1.1
	10	11.4	11.0	11.2	9.9	0.2	1.1
	11	11.8	10.3	10.4	10.1	1.4	0.2
Tensar BX Type 2 (Section 3)	8	10.7	10.2	9.9	9.2	0.8	1.0
	9	11.2	10.0	11.1	10.2	0.1	-0.2
	10	10.8	11.0	10.2	11.0	0.6	0.0
NAUE Secugrid 30/30 Q1 (Section 4)	7	10.9	10.1	9.7	9.9	1.2	0.2
	8	10.8	9.7	9.4	9.2	1.4	0.5
	9	11.2	9.9	10.0	8.6	1.2	1.3
TenCate Mirafi RS580i (Section 13)	6	12.0	12.3	11.3	12.1	0.7	0.2
Control 2	3	15.3	15.0	14.3	14.3	1.0	0.7
	4	16.0	14.9	---	15.0	---	-0.1
	5	17.3	15.7	16.6	15.1	0.7	0.6
Control 3	4	25.9	25.4	26.1	25.0	-0.2	0.4
	5	26.4	24.8	25.7	24.5	0.7	0.3
	6	25.2	24.8	24.0	24.4	1.2	0.4

[a] longitudinal measurement point along test section
--- missing data

Samples of base aggregate were extracted from the reinforced test sections during the second forensic visit to evaluate migration of fines in to the base layer from construction and trafficking. Three samples were taken from each wheel path (west and east) in each test section (a total of 6 samples per test section). The samples were removed from immediately on top of, at 4 inches above, and at 6 inches above the geosynthetic. This analysis was not conducted on the control test sections because it was too difficult to determine the exact location of the transition between the subgrade and base layers. The volume of material removed for each sample was the same, each being about 1 inch thick by 10 inches wide by 10 inches long. A washed sieve analysis was conducted to determine the amount of fines (percent passing the #200 sieve), and the results are shown in Figure 62. Aggregate samples removed from 4 and 6 inches above the geosynthetic had very similar amounts of fines (around 8.5 and 10 percent). This was similar to the fines content of the stockpile of virgin base aggregate, which was 10 percent. Fines contents in samples from just above the geosynthetic were generally about 5 percent greater. The greatest increase was in Test Section 7 (Synteen SF12) and the smallest increase was in Test Section 13 (TenCate Mirafi RS580i).
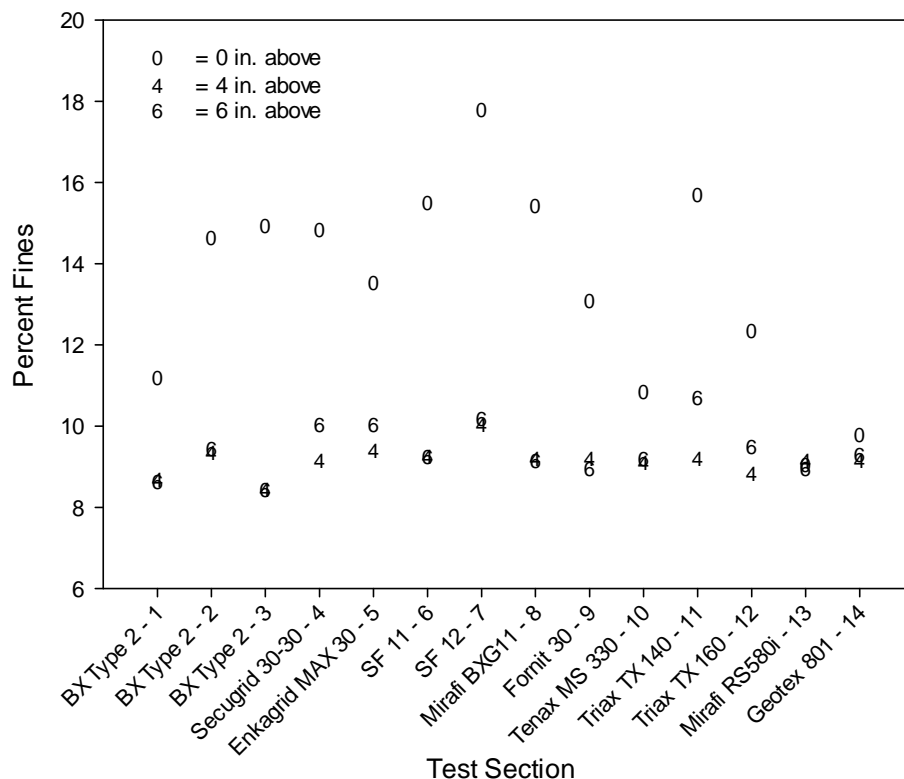

Figure 62: Percent fines in base aggregate samples above geosynthetics.

Assessment of Geosynthetics

The two primary means that geogrids carry load are 1) through the tensile elements (hereafter referred to as ribs) oriented in various directions and 2) the junctions formed by connections between intersecting ribs. Therefore, the primary goal of the qualitative damage assessments of

the geogrid samples was to inspect each junction and rib to determine how intact it was, which is directly related to its ability to carry or transmit load. Damage assessments varied slightly depending on the structural composition of the material. The two textiles (TenCate Mirafi RS580i woven geotextile and Propex Geotex 801 non-woven geotextile) were inspected to verify continuity and integrity of the material. Each extracted geosynthetic sample was about 6 feet long (in the machine direction) by the width of the roll (cross-machine direction).

Junction Damage

Each junction on the geogrid was inspected to determine how "intact" it was. The methodology used to evaluate each junction assigned one of four values (ranging from 0 to 3) corresponding to how intact it was. An outline of the methodology used for the different geogrid structure types is listed in Table 18. Junctions that were noticeably damaged during excavation or transport were not included in the analysis. The overall level of intactness was calculated from the individual scores using Equation 14, where n_0, n_1, n_2, and n_3 correspond to the number of junctions that contained the values 0, 1, 2, and 3, respectively, and n_{tot} is the total number of junctions along a particular rib. Using this method, the average junction intactness was calculated for each material. Intactness was calculated using the entire area of the extracted sample and also using the area of the geogrid within the rutted area, as summarized in Table 19. Photos of each of the extracted samples are provided in Appendix H. The results of these calculations indicate that the junctions were mostly intact for all of the materials. The majority of junction damage was in the rutted area, as shown in Figure 63. Junctions on the integrally-formed, extruded geogrids and the Mirafi BXG11 woven geogrid experienced little to no junction damage based on total area calculation or the rutted area calculation. Although sustaining slightly more junction damage, the Secugrid 30-30 also had very little junction damage. The junctions of the remaining woven geogrid products and the Enkagrid MAX30 welded geogrid sustained the most damage. The Synteen SF12 and Huesker Fornit 30 products sustained the highest junction damage.

Table 18: Scoring Methodology for Junction Damage Assessments

Material Type	Percent Intact	Score	Damage Description
Welded Geogrids	100	3	Junction is completely welded
	50-99	2	More than half of the junction is welded
	1-49	1	Less than half of the junction is welded
	0	0	Junction is completely separated
Woven and Knitted Geogrids	100	3	Cross members are completely fixed
	50-99	2	Cross members are somewhat independent
	1-49	1	Cross members are mostly independent
	0	0	Cross members are totally independent
Integrally-Formed and Extruded Geogrids	100	3	No visible damage
	50-99	2	More than half of the junction is together
	1-49	1	Less than half of the junction is together
	0	0	Junction is completely separated

$$Intactness = \left[\frac{n_0 \cdot 0 + n_1 \cdot 1 + n_2 \cdot 2 + n_3 \cdot 3}{n_{tot} \cdot 3} \right] * 100\% \qquad \textbf{Equation 14}$$

Table 19: Junction Intactness of Extracted Geogrid Samples

Geosynthetic Test Section	Entire Width of Material		Rutted Areas Only	
	Junction Intactness	Range of Values	Junction Intactness	Range of Values
Tensar BX Type 2 (Section 1)	100.0	100.0–100.0	100.0	100.0–100.0
Tensar BX Type 2 (Section 2)	100.0	100.0–100.0	100.0	100.0–100.0
Tensar BX Type 2 (Section 3)	100.0	100.0–100.0	100.0	100.0–100.0
NAUE Secugrid 30/30 Q1 (Section 4)	98.9	87.6–100.0	98.5	87.6–100.0
Colbond Enkagrid Max 30 (Section 5)	96.5	75.5–100.0	94.4	78.4–100.0
Synteen SF 11 (Section 6)	97.6	78.2–100.0	94.4	78.2–100.0
Synteen SF 12 (Section 7)	93.4	61.1–100.0	85.8	61.1–100.0
TenCate Mirafi BXG 11 (Section 8)	99.9	98.4–100.0	99.8	98.4–100.0
Huesker Fornit 30 (Section 9)	94.2	62.5–100.0	86.1	62.5–99.7
Syntec – Tenax MS 330 (Section 10)	99.9	93.6–100.0	99.9	93.6–100.0
Tensar TX 140 (Section 11)	100.0	95.5–100.0	99.9	95.5–100.0
Tensar TX 160 (Section 12)	100.0	100.0–100.0	100.0	100.0–100.0
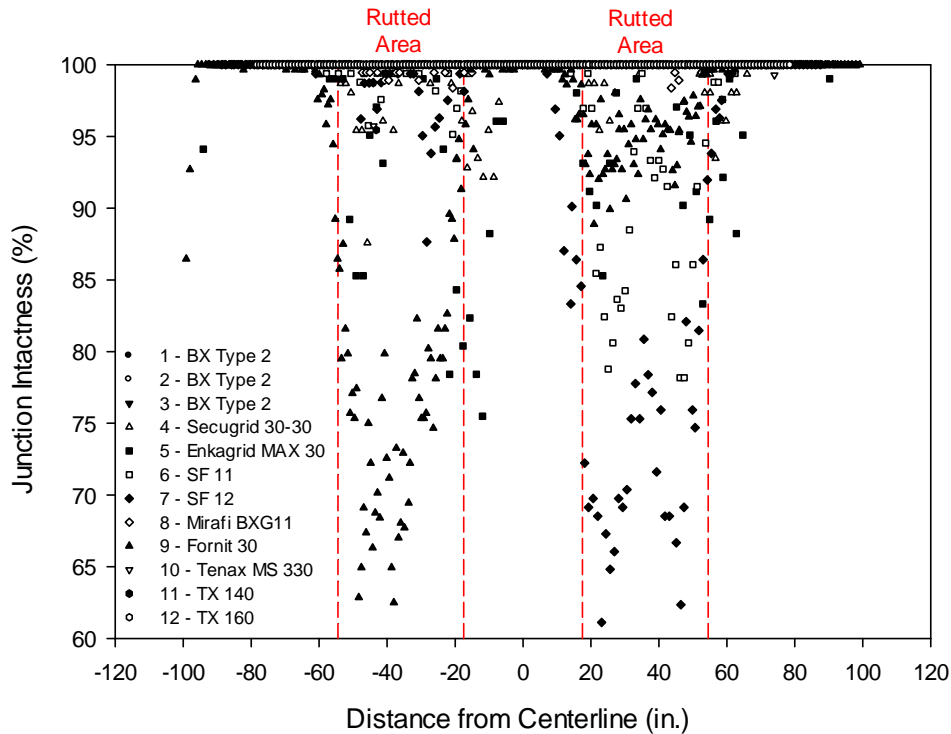
Figure 63: Geogrid junction intactness.

Rib Damage

Similar to the junction damage assessments, rib damage was also assessed on a four-point rating system (using Equation 14) depending on how intact a particular rib was, as summarized in Table 20. Rib damage was separately assessed in both the machine and cross-machine directions, and the results of these assessments are provided in Table 21 and Figure 64 for the machine direction, and Table 22 and Figure 65 for the cross-machine direction. In general, the examination of the ribs yielded similar results as the junction assessments in that most of the damage was located in the rutted area. Individual test sections also yielded similar results in terms of damage levels. The integrally-formed and extruded geogrids, Mirafi BXG11 woven geogrid, and the Enkagrid MAX 30 welded geogrid experienced little to no rib damage in either direction. Although sustaining slightly greater rib damage, Secugrid 30-30 also had very little rib damage. The ribs of the remaining woven geogrid products sustained the most damage. The Synteen SF 11, Synteen SF 12, and Huesker Fornit 30 woven geogrid products sustained the greatest rib damage of all the materials in this study.

Table 20: Scoring Methodology for Rib Damage Assessment

% Intact	Score	Damage Description
100	3	No visible damage
50-99	2	More than half of the rib is intact
1-49	1	Less than half of the rib is intact
0	0	Rib is completely broken

Table 21: Rib Intactness of Extracted Geogrid Samples in the Machine Direction

Geosynthetic Test Section	Entire Width of Material		Rutted Areas Only	
	Rib Intactness	Range of Values	Rib Intactness	Range of Values
Tensar BX Type 2 (Section 1)	100.0	99.5–100.0	100.0	99.5–100.0
Tensar BX Type 2 (Section 2)	100.0	98.7–100.0	100.0	98.7–100.0
Tensar BX Type 2 (Section 3)	100.0	100.0–100.0	100.0	100.0–100.0
NAUE Secugrid 30/30 Q1 (Section 4)	96.4	82.0–100.0	92.0	82.0–100.0
Colbond Enkagrid Max 30 (Section 5)	99.7	96.0–100.0	99.4	96.0–100.0
Synteen SF 11 (Section 6)	93.7	69.8–100.0	86.2	69.8–99.4
Synteen SF 12 (Section 7)	89.1	64.8–100.0	79.3	64.8–94.3
TenCate Mirafi BXG 11 (Section 8)	99.4	95.1–100.0	98.7	95.1–100.0
Huesker Fornit 30 (Section 9)	98.0	86.3–100.0	95.3	86.3–100.0
Syntec – Tenax MS 330 (Section 10)	100.0	97.8–100.0	99.9	97.8–100.0
Tensar TX 140 (Section 11)	99.4	88.9–100.0	98.8	88.9–100.0
Tensar TX 160 (Section 12)	99.8	93.9–100.0	99.5	93.9–100.0
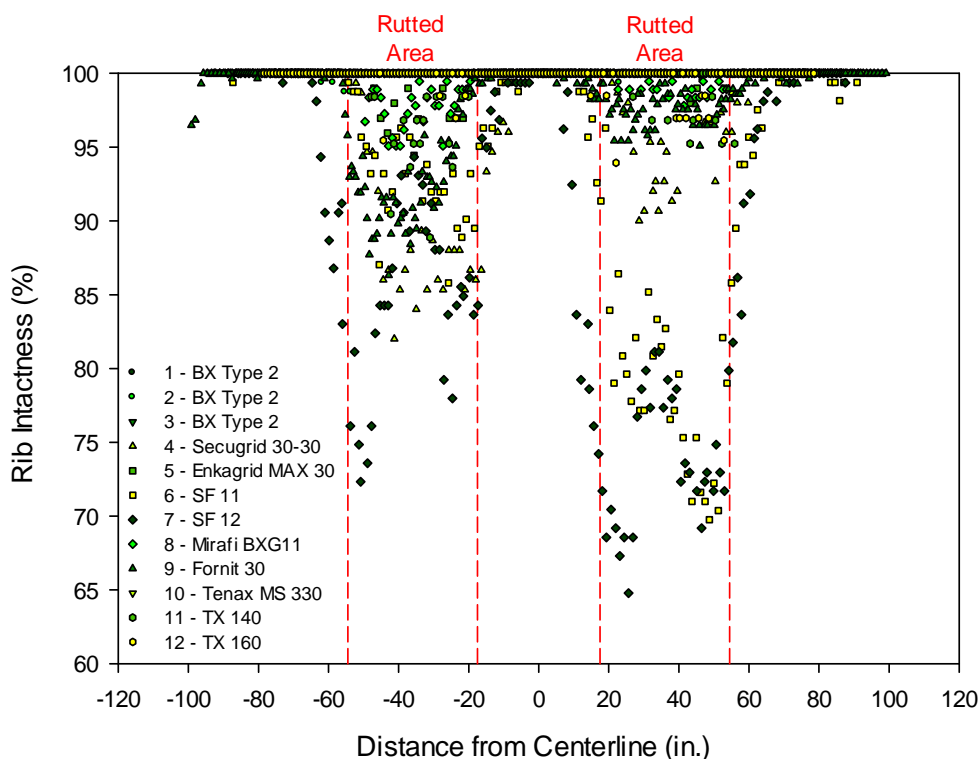
Figure 64: Geogrid rib intactness in the machine direction.

Table 22: Rib Intactness of Extracted Geogrid Samples in the Cross-Machine Direction

| Geosynthetic Test Section	Entire Width of Material		Rutted Areas Only	
	Rib Intactness	Range of Values	Rib Intactness	Range of Values
Tensar BX Type 2 (Section 1)	100.0	100.0–100.0	100.0	100.0–100.0
Tensar BX Type 2 (Section 2)	100.0	100.0–100.0	100.0	100.0–100.0
Tensar BX Type 2 (Section 3)	100.0	100.0–100.0	100.0	100.0–100.0
NAUE Secugrid 30/30 Q1 (Section 4)	97.2	82.4–100.0	94.0	82.4–99.4
Colbond Enkagrid Max 30 (Section 5)	99.8	97.1–100.0	99.6	97.1–100.0
Synteen SF 11 (Section 6)	98.6	85.5–100.0	96.6	85.5–100.0
Synteen SF 12 (Section 7)	98.3	88.9–100.0	96.4	88.9–100.0
TenCate Mirafi BXG 11 (Section 8)	100.0	99.5–100.0	100.0	99.5–100.0
Huesker Fornit 30 (Section 9)	86.7	58.0–100.0	74.9	58.0–91.0
Syntec – Tenax MS 330 (Section 10)	100.0	100.0–100.0	100.0	99.9–100.0
Tensar TX 140 (Section 11)	99.9	95.5–100.0	99.7	95.5–100.0
Tensar TX 160 (Section 12)	99.9	95.7–100.0	99.9	95.7–100.0
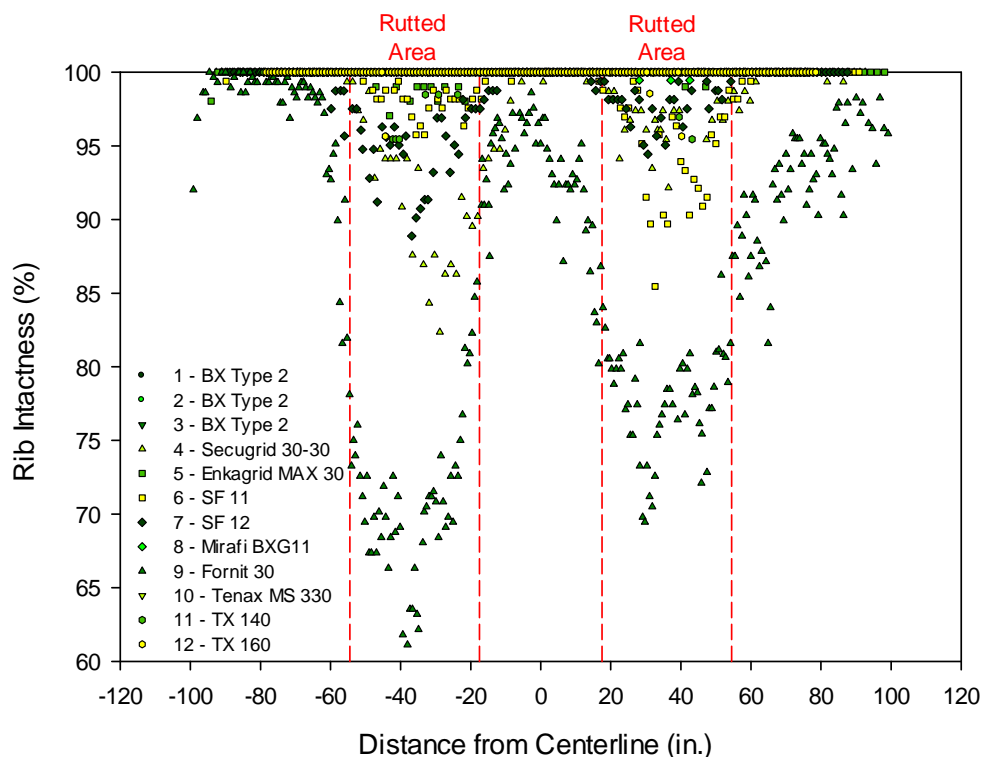
Figure 65: Geogrid rib intactness in the cross-machine direction.

Assessments of Geotextiles

The extracted samples from the woven and non-woven geotextile test sections (TenCate Mirafi RS580i and Propex Geotex801, respectively) sustained no noticeable damage (e.g., tears, holes, significant wear or broken fibers) from construction and trafficking. Pullout of the Mirafi RS580i product was also assessed during the forensic visit in July 2013. The two longitudinal edges of the RS580i textile were exposed by removing the gravel to determine whether the material had shifted toward the wheel track during trafficking. A photograph of the edges of the material (Figure 66) showed that pullout did not occur. To further verify this, a topographic survey was taken of the two exposed edges. Analysis of this data indicated that the width of the material was very similar to the original roll width and, on average, the edges did not deviate from one another more than a quarter of an inch.

Figure 66: Edges of Mirafi RS580i geotextile showing no pullout a) east edge, b) west edge.

General Observations

Most of the geosynthetics that were exhumed from the test sections were distorted in the rutted area due to the torsion of the drive wheels on the test vehicle as it propelled its way along the test site. The geosynthetics were horizontally distorted in the opposite direction of traffic as depicted in Figure 67. An assessment of this distortion was made on the extracted geosynthetic samples by using a long straight edge and measuring the maximum horizontal deviation in the material at multiple locations in the machine direction. Distortion of the non-woven geotextile was estimated based on visual clues along the surface of the extracted sample. The average horizontal distortion in each of the wheel paths is summarized in Table 23 for each of the test sections. In general, the integrally-formed and extruded geogrids exhibited the least amount of distortion, followed closely by the welded geogrids and woven geotextile. Out of all of the geogrids, the woven products experienced the most distortion, but the non-woven geotextile had the greatest amount of distortion in all. An attempt was made to correlate distortion to rut behavior; however, there seemed to be little correlation between the level of horizontal distortion and rut (for rut depths at 300 truck passes).

Figure 67: Typical horizontal distortion in the rutted area from trafficking.

Table 23: Distortion of Geosynthetics Due to Trafficking

Geosynthetic Test Section	Excavation Location[a]	Rut Depth at 300 Truck Passes (in.)	Average Distortion (in.)
Tensar BX Type 2 (Section 1)	10 – West	2.54	0.4
	10 – East	2.91	0.3
Tensar BX Type 2 (Section 2)	9 – West	2.03	0.8
	9 – East	1.78	0.4
Tensar BX Type 2 (Section 3)	9 – West	1.79	0.2
	9 – East	2.33	0.1
NAUE Secugrid 30/30 Q1 (Section 4)	8 – West	1.74	0.6
	8 – East	2.02	0.4
Colbond Enkagrid Max 30 (Section 5)	4 – West	2.21	0.6
	4 – East	2.91	0.5
Synteen SF 11 (Section 6)	3 – West	1.92	1.2
	3 – East	3.11	0.8
Synteen SF 12 (Section 7)	9 – West	3.52	1.7
	9 – East	3.63	1.8
TenCate Mirafi BXG 11 (Section 8)	3 – West	1.78	0.9
	3 – East	2.28	1.0
Huesker Fornit 30 (Section 9)	9 – West	2.89	1.5
	9 – East	3.94	1.7
Syntec – Tenax MS 330 (Section 10)	9 – West	2.85	0.4[b]
	9 – East	2.25	0.7[b]
Tensar TX 140 (Section 11)	3 – West	2.90	0.0
	3 – East	2.56	0.0
Tensar TX 160 (Section 12)	12 – West	3.13	0.0
	12 – East	3.80	0.0
TenCate Mirafi RS580i (Section 13)	6 – West	1.28	1.1
	6 – East	1.22	0.9
Propex Geotex 801 (Section 14)	9 – West	2.01	3.9
	9 – East	1.92	3.9

[a] longitudinal measurement point along test section – direction = east or west wheel path
[b] average of all three layers (avg. top-east = 0.9 in., avg. top-west = 0.6 in., avg. mid-east = 0.7 in., avg. mid-west = 0.1 in., avg. bot-east = 0.4 in., avg. bot-west = 0.4 in.)

Several of the test sections also showed evidence of the tension membrane effect. After the base course was removed, the geosynthetic in the wheel path of several of the test sections was taut and, due to the tension in the material, became elevated from the permanent rut contour in the surface of the subgrade, as shown in the example in Figure 68.

Figure 68: Example of tension in geosynthetic in the wheel path.

Tensile Strength

Three samples were cut from each of the exhumed geosynthetics in the cross-machine direction in order to evaluate changes in tensile strength after construction and trafficking. One sample was removed from the west wheel path, one from the center area between the wheel paths, and one from the east wheel path. Samples were removed from areas containing little to no rib damage (i.e., abraded, broken or partially severed ribs). The results of these tensile tests are summarized in Table 24 along with average tensile properties of the virgin materials. Individual results from each of the test sections are provided in Appendix I. The results indicated that the majority of the strength at 2 percent strain increased and the ultimate strengths decreased when compared to the virgin materials. These changes are likely because the geosynthetics were permanently stretched due to the rutting making their apparent 2 percent strength greater in the post-trafficking tests, while abrasion, wear and other superficial damage caused an overall decrease in the ultimate strength. The greatest strength loss was measured in the Synteen SF 12 and Huesker Fornit 30 woven geogrids, and overall, the integrally-formed grids showed the smallest loss of strength.

Table 24: Cross-Machine Tensile Strength of Extracted Geogrid Samples

Geosynthetic Test Section	West Wheel Path Strength[a] (lb/ft)			Center Strength[a] (lb/ft)			East Wheel Path Strength[a] (lb/ft)			Virgin Material Strength[a] (lb/ft)		
	2%	5%	Ult.	2%	5%	Ult.	2%	5%	Ult.	2%	5%	Ult.
Tensar BX Type 2 (Sect. 1)	870	1590	1871	877	1590	1939	857	1569	1857	822	1494	1946
Tensar BX Type 2 (Sect. 2)	857	[b]	1528	863	1583	1699	843	[b]	1275	822	1494	1946
Tensar BX Type 2 (Sect. 3)	836	1549	1809	877	1590	1823	863	[b]	1507	822	1494	1946
NAUE Secugrid 30/30 Q1	939	1788	2056	973	1891	2645	946	1788	1891	946	1830	2713
Colbond Enkagrid MAX 30	863	1672	1672	898	1816	2343	870	1720	1747	857	1775	2378
Synteen SF 11	637	911	3056	644	932	3529	624	918	2535	617	925	3782
Synteen SF 12	719	980	2713	740	1042	4200	733	1069	2782	987	1446	5818
TenCate Mirafi BXG11	761	1316	2378	747	1240	3501	740	1213	3207	740	1281	3221
Huesker Fornit 30	850	1014	1309	939	1891	2152	610	[b]	719	946	1939	2618
SynTec Tenax MS 330[c]	740	1295	1562	678	1309	2056	733	1412	1740	692	1343	2248
Tensar TX140	343	[b]	528	329	658	685	343	658	678	322	665	843
Tensar TX160	397	740	761	384	754	822	377	[b]	692	391	747	884
TenCate Mirafi RS580i	1597	3577	5030	1576	3618	5961	1645	3645	5338	1501	3440	6112
Propex Geotex 801	NT	NT	NT	NT	NT	NT	NT	NT	NT	[d]	[d]	255[e]

[a] ASTM D4595 and ASTM D6637
[b] failure occurred before 5% strain
[c] tested by WTI as a composite, i.e., not separately
[d] data was difficult to interpret at low strain values
[e] grab tensile strength (ASTM D4632) in pounds as tested by SGI Testing Services, LLC
NT = not tested

Summary and Conclusions of Post-Trafficking Forensic Investigations

Two forensic investigations were conducted as part of this project: one immediately after trafficking had terminated and a second eight months later. During each of these visits, construction equipment was used to remove the base and subgrade layers so that large samples of the geosynthetic could be removed to assess damage and evaluate tensile properties, and to facilitate strength, stiffness and moisture measurements of the base and subgrade. The excavation of the base course, geosynthetic and subgrade provided a good opportunity to evaluate the shape of the rut in the two wheel paths, distortion of the geosynthetic from trafficking and rut accumulation, pullout, and other qualitative assessments. Select images obtained during the second forensic investigation are shown in Appendix J to provide a brief photographic record of each test section.

The information collected during the two separate forensic investigations indicated the following.

- A limited number of stiffness measurements made on the surface of the subgrade and base course during the forensic investigations revealed potential correlations to rut performance, indicating that the LWD device may potentially be used to help predict performance of geosynthetics when used in subgrade stabilization applications.

- On average, the thickness of the aggregate had decreased by about 0.7 inches, which can mostly likely be attributed to compaction and spreading of the aggregate layer during trafficking.

- Fines contents in aggregate samples from just above the geosynthetic were generally about 5 percent greater than in samples higher up in the base course. The greatest increase was in Test Section 7 (Synteen SF12) and the smallest increase was in Test Section 13 (TenCate Mirafi RS580i).

- Junctions were mostly intact for all of the materials, and the majority of junction damage was in the rutted area. Junctions on the integrally-formed, extruded geogrids and the Mirafi BXG11 woven geogrid experienced little to no junction damage. The junctions of the Synteen SF11 woven geogrid and the Enkagrid MAX30 welded geogrid sustained moderate damage, and the Synteen SF12 and Huesker Fornit 30 products sustained the highest junction damage.

- Most of the damage to the ribs was located in the rutted area. The integrally-formed and extruded geogrids, Mirafi BXG11 woven geogrid, and the Enkagrid MAX 30 welded geogrid experienced little to no rib damage in either direction. The ribs of the remaining woven geogrid products sustained the most damage. The Synteen SF 11, Synteen SF 12, and Huesker Fornit 30 woven geogrid products sustained the greatest rib damage of all the materials in this study.

- The geotextiles (TenCate Mirafi RS580i and Propex Geotex801) sustained no noticeable damage (e.g., tears, holes, significant wear or broken fibers) from construction and trafficking.

- TenCate Mirafi RS580i did not pullout during trafficking.

- All of the geosynthetics exhibited horizontal distortion from trafficking. The Tensar TX140 and TX160 products had no distortion. The level of distortion did not correlate to rutting behavior.

- Post-trafficking assessments of the tensile properties of the geosynthetics indicated that the majority of the geosynthetic strengths at 2 percent strain

increased and the ultimate strengths decreased when compared to the virgin materials. The greatest tensile strength loss was measured in the Synteen SF 12 and Huesker Fornit 30 woven geogrids, and overall, the integrally-formed grids showed the smallest loss of strength.

ANALYSIS AND RESULTS

The analysis for this project utilized data from a variety of sources to characterize the behavior and determine the relative performance of the individual test sections. Longitudinal rut measurements during trafficking were corrected based on data collected from test sections that were purposefully constructed with varying subgrade strengths and base course thicknesses. A statistical analysis was conducted using a t-test to determine and/or verify the validity and comparability of the longitudinal rut data. Once corrected and verified, a regression analysis was conducted to determine potential relationships between multiple geosynthetic material properties and the performance of the test sections. Transverse rut profiles and displacement and strain data in the transverse direction were also utilized to further characterize and understand the behavior of the test sections and geosynthetic material as a function of traffic. Finally, results of the pore-water pressure measurements are presented and discussed as they relate to the performance of the test sections.

Rut Analysis

Longitudinal and transverse rut measurements were the primary means used to determine the behavior and relative performance of each test section. Rut behavior is mainly affected by four factors: 1) the strength of the subgrade, 2) the depth of the base course, 3) the strength of the base course, and 4) the presence of the geosynthetic. The field test sections were constructed to have the same subgrade strength (with the intentional exception of Test Sections 1 and 2), the same base thickness (with the intentional exception of the Control 2 and Control 3 test sections), and the same base course strength to minimize differences between test sections and facilitate a more direct comparison between individual test sections. Despite efforts during construction to eliminate differences in subgrade strength and base course thickness, small variations were inevitable. An empirical correction procedure was implemented to adjust the rut response for these two properties so that direct performance comparisons between test sections were more accurate. Rut data was not adjusted based on base course strength and stiffness because 1) strength and stiffness properties were not measured at every rut measurement point, and 2) there were no controls where these properties were purposefully varied to determine their effect on performance. When adjustments for subgrade strength and base course thickness are applied to the rut data, the remaining behavioral differences between the reinforced test sections can more confidently be attributed to the geosynthetic reinforcement.

Subgrade Strength Adjustment

Rut depth at the 28 longitudinal measurements locations within each test section naturally varied from one another during trafficking based on the cumulative support provided by the subgrade, geosynthetic and base aggregate. To evaluate the effect of subgrade strength on the rut response, Test Sections 1, 2 and 3 were built with the same geogrid reinforcement (Tensar BX Type 2) and same base thickness, but had different subgrade strengths. Test Sections 1 and 2 were

purposefully constructed with subgrade strengths different from the remaining test sections to evaluate the effect subgrade strength had on rutting behavior. As expected, Test Section 2, having the weakest subgrade strength, had the fastest rut accumulation, while Test Section 1, which had the strongest subgrade strength, showed the slowest rut accumulation. To more accurately evaluate the effect that subgrade strength had on rut behavior, it was necessary to use select data from Test Sections 1, 2 and 3 that had the same base course thickness (within a tolerance of ±0.50 in.), as well as the same subgrade strength within an individual test section (within a tolerance of ±0.05 CBR). The average base course thickness for the first three test sections based on the select points was 10.9 inches, and the average subgrade strengths based on vane shear measurements at select measurement points for Test Sections 1, 2 and 3 were 2.17, 1.64 and 1.79, respectively. Figure 69, which shows average rut as a function of truck passes for Test Sections 1, 2 and 3, was generated using only the select points.
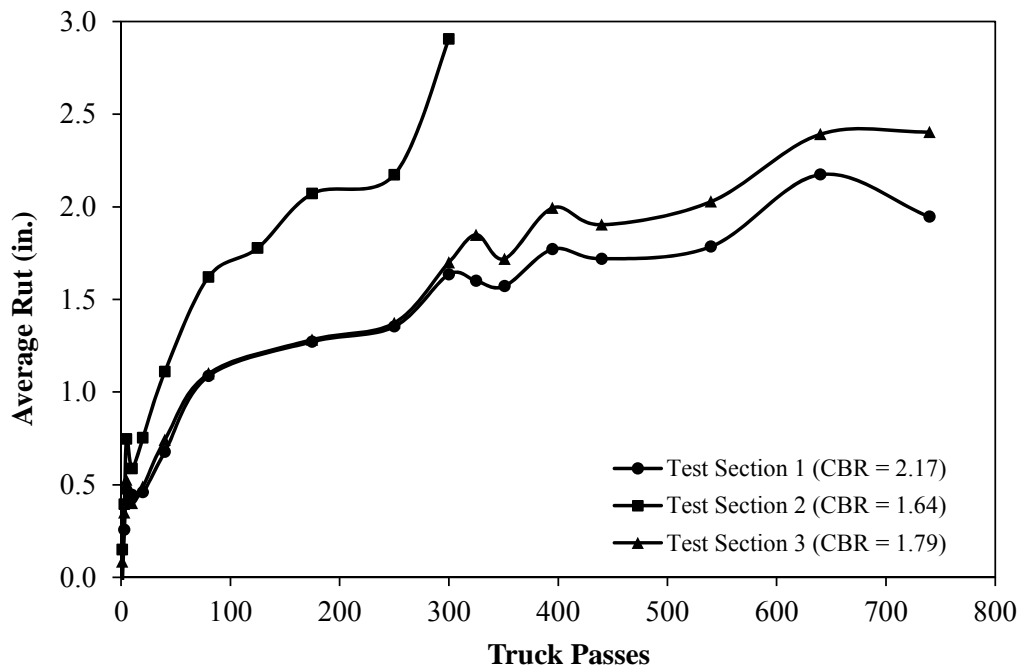

Figure 69: Average rut response for Test Sections 1, 2 and 3 based on select measurement points.

Referring to Figure 69, the rut response of Test Sections 1 and 3 were very similar, especially at lower traffic levels, even though the subgrade strength was an average of 0.37 CBR stronger in Test Section 1 versus Test Section 3. In contrast, the weaker subgrade strength in Test Section 2 affected the rut behavior more dramatically when compared to Test Sections 1 and 3. Multiplicative factors of 1.08 and 0.65 were applied to the rut data from Test Sections 1 and 2, respectively, to match the rut responses to Test Section 3 (recall that Test Sections 3 through 14 and Controls 1, 2 and 3 were constructed to have the same subgrade strength). The adjusted rut responses using the multiplicative factors are shown in Figure 70. Individual rut measurements from Test Sections 3 through 14 and Controls 1, 2 and 3 were then corrected using adjustment

factors based on the bi-linear relationship illustrated in Figure 71, where subgrade strengths above 1.79 were multiplied by factors ranging from 1.00 to about 1.08, and subgrade strengths lower than 1.79 were multiplied by factors ranging from 1.00 to about 0.65 depending on the actual strength of the subgrade at that measurement point. Linear interpolation was used to determine adjustment factors between the end points of the bi-linear line in Figure 71. The rut data from all of the test sections was adjusted based on subgrade strength prior to adjustments for base thickness. The methodology for adjusting the rut responses based on base course thickness is described in the following subsection.
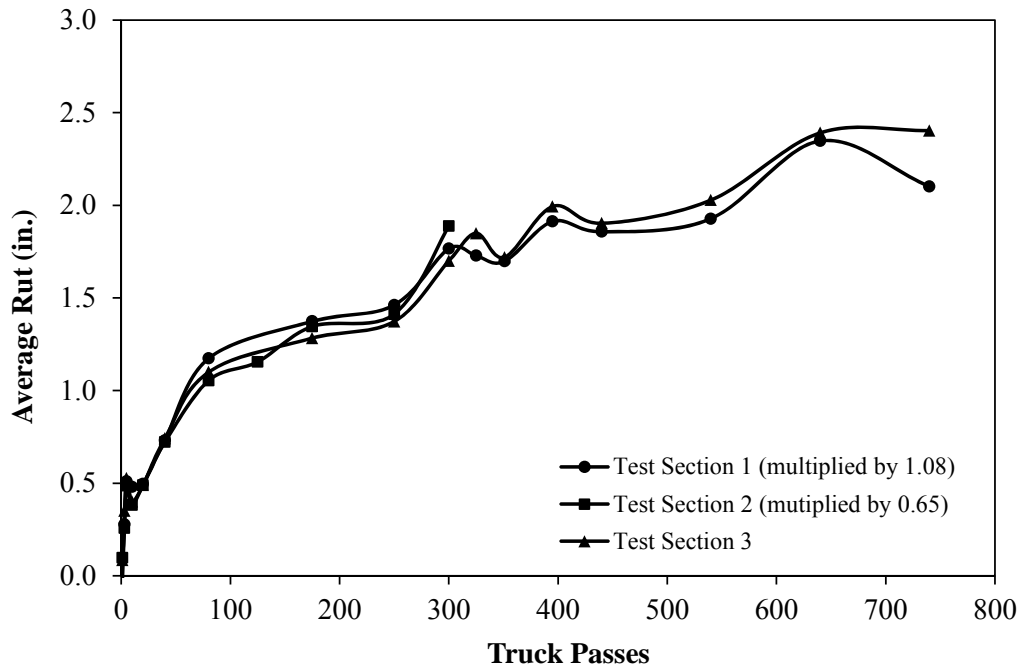
Figure 70: Adjusted rut response for Test Sections 1, 2, and 3 based on select measurement points.
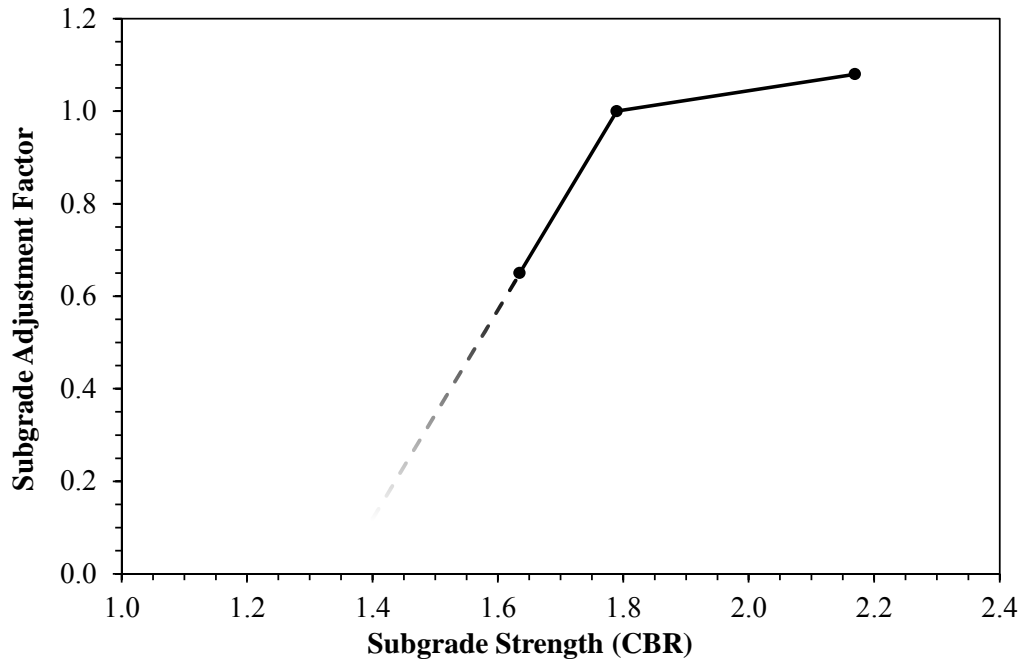
Figure 71: Adjustment factors for subgrade strength variations.

Base Course Thickness Adjustment

The three control test sections (containing no geosynthetic reinforcement) were purposefully constructed with different base aggregate depths to determine the effect that base course thickness had on rutting behavior. In this case, Control 1, having the shallowest gravel depth, had the highest rut accumulation and Control 3, which had the deepest gravel depth, had the lowest rut accumulation, as shown in Figure 72 (note that the rut responses shown in Figure 72 were adjusted for differences in subgrade strength). The average gravel thickness was 11.3 in. for Control 1, 16.3 in. for Control 2 and 24.9 in. for Control 3. The average gravel depth for Test Sections 1 through 14 was 10.9 in. (slightly less than the base thickness of Control 1); therefore, points were selected from Control 1 that had base thicknesses of 10.9 ±0.5 in. for analytical purposes. Similarly, select points from Control 2 consisted of base thicknesses of 16.3 ±0.5 in. Using the select points, a best-fit line was used to estimate the rut response for the Control 1 test section and best-fit power curve (form of the equation is $y = a \cdot x^b$) was used to estimate the rut response for the Control 2 test section, as shown in Figure 73. Control 3 was not needed in this analysis because individual gravel depth measurements in the test sections did not exceed about 13 in. To correct for base thicknesses less than the select points in Control 1 (10.9 in.), a linear function could be used, but when gravel depths were greater than Control 1 the relationship of rut to traffic transitioned to a power function.
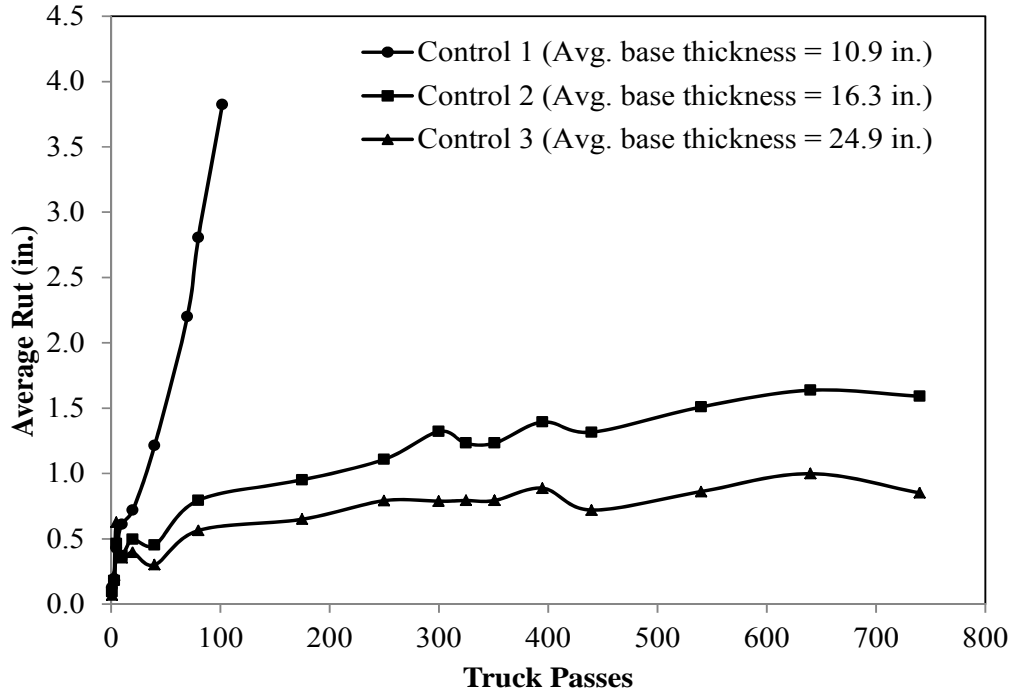
Figure 72: Average rut response for Control test sections (subgrade strength corrections applied).
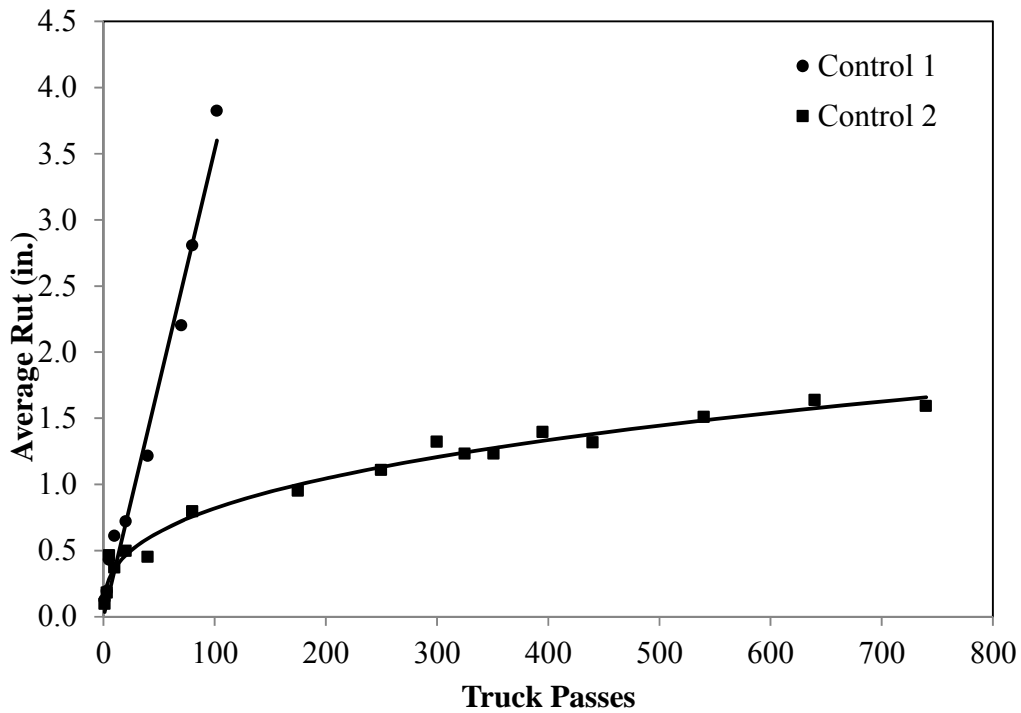

Figure 73: Best-fit estimations of average rut response for Control 1 and Control 2 test sections based on select measurement points.

Control test sections having average base course thicknesses between 10.9 and 16.3 inches were not tested; therefore, the shape of the rut response is unknown for gravel thicknesses other than what was tested. To complicate matters, the shape of these curves also differed, with shallow gravel depths having a more linear response and deeper gravel depths following a power distribution. An analysis based on the 1993 AASHTO design equation for flexible pavements (Equation 15 (Huang, 2004)) was used to help estimate the shape of the rut response for gravel depths greater than 10.9 in. (covering the upper range of base aggregate depths measured during construction).

$$log\,W_{18} = Z_R S_0 + 9.36\,log(SN + 1) - 0.20 + \frac{log\left[\frac{(4.2 - p_t)}{(4.2 - 1.5)}\right]}{0.4 + \frac{1094}{(SN + 1)^{5.19}}} + 2.32logM_R - 8.07$$

Equation 15

where,

Z_R = -1.282

S_0 = 0.45

p_t = 1.5

M_R = 2,685 psi (where M_R = 1500*CBR, and the average subgrade strength = 1.79 CBR)

Inputting these parameters into Equation 15 yielded the following simplified equation:

$$log\,W_{18} = 9.36\,log(SN + 1) - 0.903 \qquad \textbf{Equation 16}$$

Solving Equation 16 for W_{18} (equivalent single-axle loads or ESALs) based on structural numbers (*SN*) for base course depths between 0.0 and 16.3 in. yielded the curve shown in Figure 74. Structural number is directly related to the base thickness and ESALs are directly related to truck passes. A power curve was used to fit the curve generated by the simplified AASHTO equation. It was preferable to use a power function to fit the rut performance data because it allowed values of zero as the independent variable. From this it was determined that the best-fit power curve can be used to estimate the shape of the relationship between base thickness and truck passes at various rut depths.
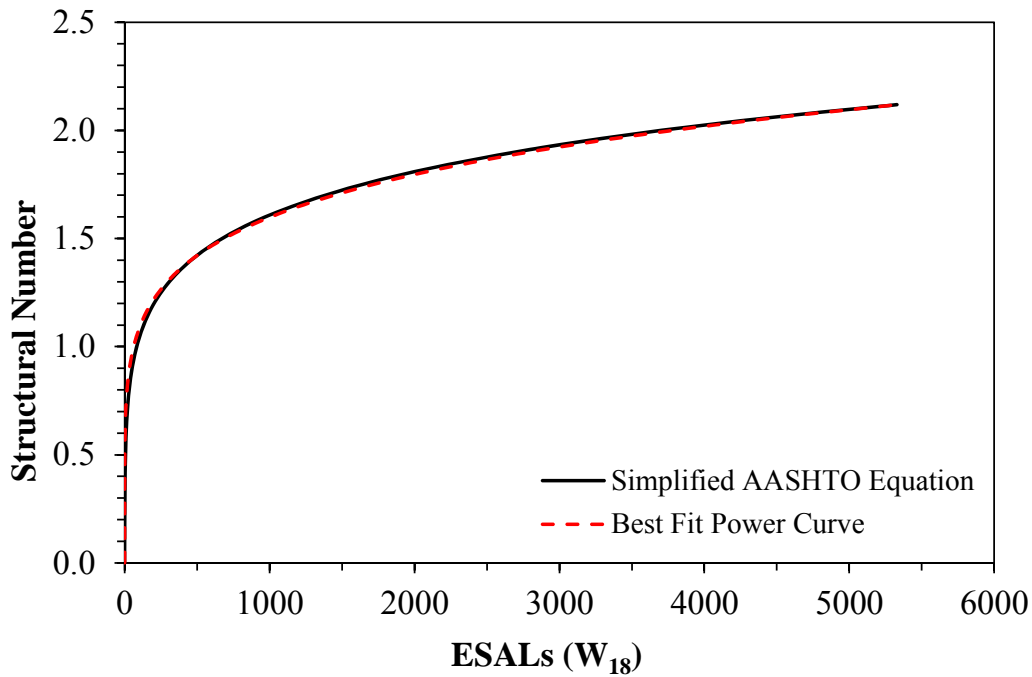
Figure 74: Power curve estimation of simplified AASHTO equation.

To determine the relationship between base thickness and truck passes at various rut depths, a series of best-fit curves were created based on three known points (first point was 0 truck passes for 0.0 in. base thickness, second point was truck passes for 10.9 in. of base aggregate from the Control 1 test section, and the third known point was truck passes for 16.3 in. of base aggregate from the Control 2 test section), as illustrated in Figure 75. This data was then rearranged to show the relationship of rut depth to truck passes for a variety of base course depths, as shown in Figure 76. Referring to Figure 76, relationships that fall within the shaded region between the 10.9 in. line and 16.3 in. line have a power curve shape while relationships that fall to the left of the 10.9 in. line follow a linear trend. A unique relationship (and therefore a unique set of coefficients for the linear or power trend lines) exists for each base course thickness depending on where it falls on the graph presented in Figure 76. Corrections were made by adding or subtracting the number of truck passes to the individual rut performance curves (Figure 76) based on the base thickness at that particular point. Corrections to account for various base course thicknesses were not made to the rut depth (as was done in the subgrade adjustment analysis) because the rut corrections were much too sensitive to base course thickness. Base thicknesses that were shallower than 10.9 in. were adjusted by adding truck passes and base thicknesses that were thicker than 10.9 in. were adjusted by subtracting truck passes.
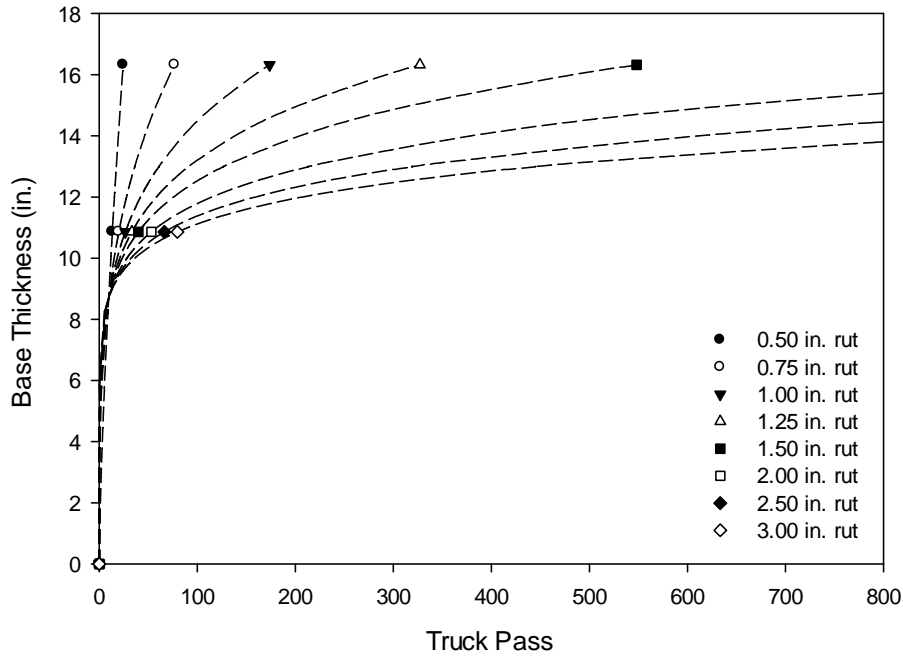
**Figure 75: Power curve estimation of base course thickness versus truck pass relationships.**
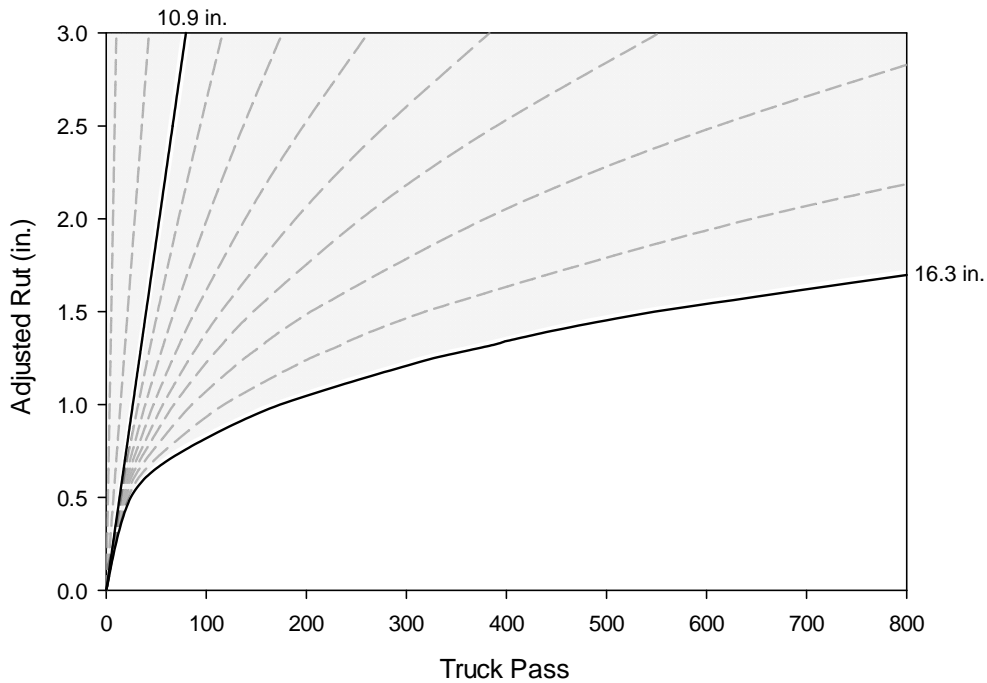
Figure 76: Base course thickness adjustment illustration.

Longitudinal Rut Analysis

Using the method described in the previous section, individual rut measurements were adjusted and averaged together within a particular test section to create the corrected rut responses presented in Figure 77 for each of the test sections. Individual rut measurements that were

greater than one standard deviation away from the mean were not used in the analysis. Test Sections 1 and 2 are not shown on these graphs because they were constructed for the sole purpose to formulate the corrections necessary to make direct comparisons between the remaining test sections; however, the control test sections are shown to compare performance of reinforced versus unreinforced test sections with varying depths of base course. Rut responses having steeper slopes (i.e., to the left on the graph) exhibited the poorest performance, while rut responses that were shallower (i.e., lower and to the right) showed the best performance. The woven geotextile (Mirafi RS580i) performed the best, followed by BX Type 2, Secugrid 30-30 Q1 and the non-woven geotextile (Geotex 801). The poorest performance was observed in the Fornit 30, SF12 and TX160 geogrids.
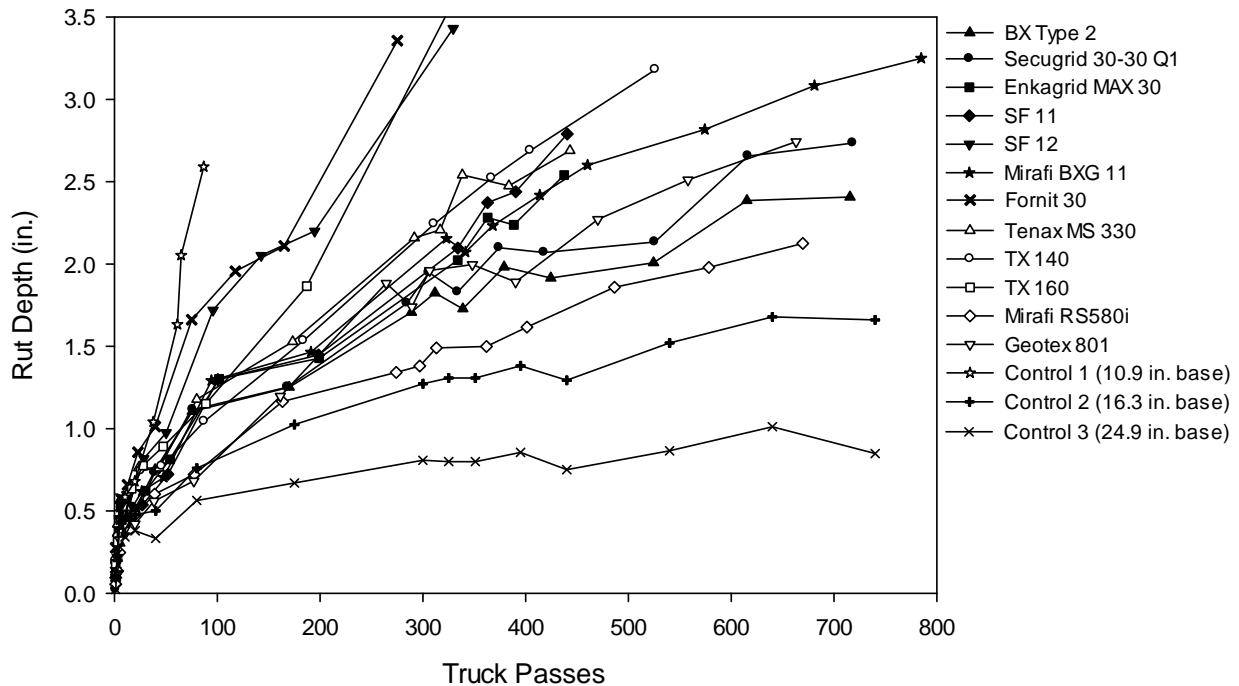
Figure 77: Corrected rut response for all test sections.

While qualitative assessments are valuable in generally describing differences in performance between test sections, they are of limited use in situations when these differences are less pronounced. Additionally, data scatter may make it difficult to confidently state whether one test section clearly performed better than another. Therefore, quantitative comparisons between test sections were made using a two sample t-test. This test evaluates the statistical significance of the differences in the means of two sample populations (in this case, the mean rut depth). The results of this test can be expressed in a variety of forms, and the decision was made to use the p-value for each comparison. The p-value for the test ranges between 0 and 1; values approaching 0 indicate greater probability that the sample means are different, while values approaching 1 indicate greater probability that the means are the same.

The mean for each test section was compared to all other test sections for truck passes 1, 3, 5, 10, 20, 40, 80, 175, 300, 325, 351, 395, 440, 540, 640, and 740 using this methodology. Altogether, 1,589 comparisons were possible. The degree of similarity and difference is arbitrary, and depends on how one chooses to consider the data being compared. For the purposes of this study, two means were considered more similar if the p-value was between 0 and 0.25; likewise, two means were considered more different if the p-value was between 0.75 and 1.00. Using these criteria, the results revealed that, overall, the comparisons of the means were different from one another 84.8 percent of the time. Conversely, the means were similar to one another 4.1 percent of the time. The remaining 11.1 percent of the values had p-values between 0.25 and 0.75. Similarities between test sections were random and indicated no definite trends. This result also indicates that the rut responses, while sometimes similar to one another in Figure 77, are generally different enough to facilitate direct comparisons of their relative performance. The p-values for all the comparisons of the mean rut depths are provided in Appendix K.

Further analysis of the longitudinal rut responses was conducted using the performance data presented in Figure 77 to determine which geosynthetic material properties were most related to the performance of a particular test section. This analysis was conducted at various rut depths (1.0, 2.0 and 2.5 inches) to determine whether different material properties affected performance at various levels of rut. The following material properties were considered in this analysis:

- Wide-width tensile strength at 2% in the machine and cross-machine directions
- Wide-width tensile strength at 5% in the machine and cross-machine directions
- Ultimate wide-width tensile strength in the machine and cross-machine directions
- Cyclic tensile stiffness at 0.5, 1.0, 1.5, 2.0, 3.0 and 4.0 percent in the machine and cross-machine directions
- Resilient interface shear stiffness in the cross-machine direction
- Junction strength in the cross-machine direction
- Junction stiffness in the cross-machine direction, determined by taking the secant stiffness of the junction strength response at 0.05 in. of displacement
- Aperture stability modulus

A simple linear regression analysis was conducted to determine which of the properties listed above was most related to the performance of the test sections. Linear regression was selected because there were too few points to clearly indicate a more sophisticated regression equation and it provided sufficient information to be able to compare data fit between individual analyses or to observe changes or trends in data fit for multiple variables. In this analysis, the number of truck passes for a particular test section was adjusted by subtracting the number of truck passes in Control 1 to determine N_{add}, the number of additional truck passes a particular test section experienced in comparison to Control 1. That allowed the y-intercept to be set to zero because the absence of geosynthetic reinforcement would result in no benefit to the test section. R-

squared (the coefficient of determination) is commonly used as the indicator of how well the data points fit the regression line, and was used in this analysis as the parameter to determine how well a particular material property can be used as a potential predictor of field performance. R-squared values approaching 1.0 indicate a better fit, while values less than that (including negative values) indicate poorer correlations. Negative r-squared values indicate that the linear regression analysis would have yielded a slope in the opposite direction (i.e., negative versus positive) if the y-intercept was unrestricted. The regression analysis was conducted at 1.0, 2.0 and 2.5 in. of rut; rut greater than 2.5 in. was not experienced in some of the test sections. Test Sections 3 and 13 (BX Type 2 and Mirafi RS580i, respectively) did not reach 2.5 in. of rut, so predicted values were used in the regression analysis at this rut level. The results from these analyses are shown in Table 25.

Table 25: R-Squared Results of Linear Regression Analysis Using Data from All Test Sections

	Cross-machine direction*			Machine direction*		
	1.0 in. rut	2.0 in. rut	2.5 in. rut	1.0 in. rut	2.0 in. rut	2.5 in. rut
Wide-width strength @ 2%	-0.520	-0.437	-0.479	-0.855	-0.382	-0.560
Wide-width strength @ 5%	0.078	0.083	0.119	-0.769	-0.362	-0.545
Ultimate wide-width strength	-0.073	-0.372	-0.377	**0.511**	0.289	0.305
Cyclic modulus @ 0.5%	-0.739	-0.629	-0.706	-1.381	-0.772	-1.114
Cyclic modulus @ 1.0%	0.012	-0.075	-0.044	-1.241	-0.727	-1.037
Cyclic modulus @ 1.5%	0.122	-0.009	0.037	-1.035	-0.566	-0.828
Cyclic modulus @ 2.0%	0.102	-0.045	-0.005	-0.959	-0.517	-0.766
Cyclic modulus @ 3.0%	0.055	-0.112	-0.081	-0.836	-0.503	-0.754
Cyclic modulus @ 4.0%	0.034	-0.125	-0.103	-0.693	-0.417	-0.647
Resilient interface shear stiffness	-1.327	-0.589	-0.588	---	---	---
Junction strength[a]	0.065	**0.601**	**0.649**	---	---	---
Junction stiffness[a]	0.176	**0.720**	**0.680**	---	---	---
Aperture stability modulus[a,b]	-0.447	-0.208	-0.297	-0.447	-0.208	-0.297

* bolded values indicate R-squared values greater than 0.500
--- material tests not conducted in the machine direction
[a] junction strength and stiffness, and aperture stability modulus of the Tenax MS 330 product was not included in this analysis because it was difficult to determine this property based on the fact that it consisted of three layers
[b] aperture stability modulus is not direction dependent so values are the same for machine and cross-machine directions

Referring to Table 25, the geosynthetic material property that was most related to performance was the strength and stiffness of the junctions in the cross-machine direction, and the strength and stiffness of the junction correlated better with performance as rut increased, as shown in Figure 78. R-squared values in the machine direction are all negative with the exception of the ultimate wide-width strength which showed better correlation at lower levels of rut.
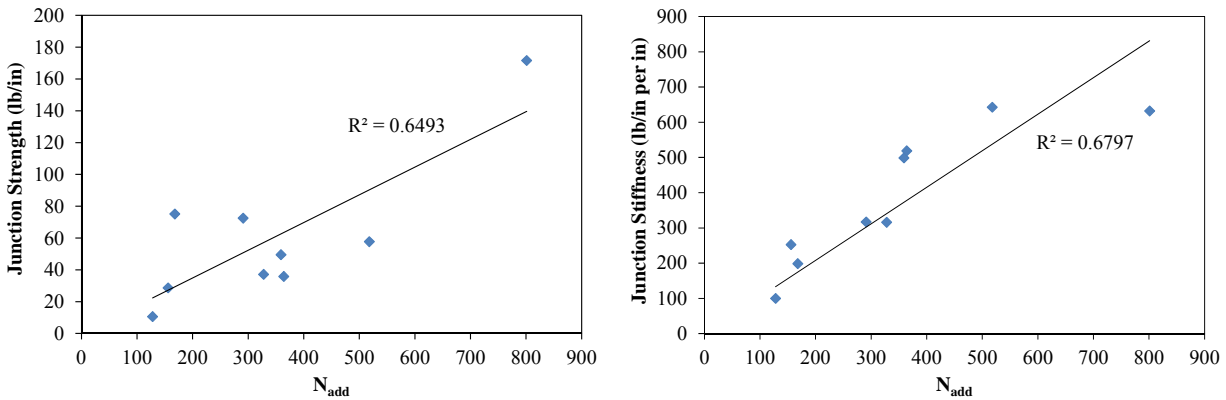
Figure 78: Results of a) junction strength and b) junction stiffness regression analysis at 2.5 in. rut.

A second linear regression analysis was conducted excluding data from geosynthetics that performed poorly – Test Section 7 (Synteen SF 12) and Test Section 9 (Huesker Fornit 30). Knowing that the primary property linked to performance in these test sections was junction stiffness, these products were unable to transmit stresses into the cross-machine structural elements because the junctions were too weak. By eliminating products other potential links between the geosynthetic properties and test section performance became more apparent. The R-squared values for this revised analysis are summarized in Table 26. These results indicate that by excluding materials that did not perform well based on their weaker junctions, the tensile strength in the material is also a good indicator of performance. This is most apparent in the wide-width tensile strengths at 5 percent and the cyclic stiffness values. Interestingly, the ultimate wide-width tensile strength in the machine direction also correlates to rut performance. R-squared values are reduced for junction strength and stiffness because of the missing data.

Table 26: R-Squared Results of Linear Regression Analysis Using Select Data

	Cross-machine direction*			Machine direction*		
	1.0 in. rut	2.0 in. rut	2.5 in. rut	1.0 in. rut	2.0 in. rut	2.5 in. rut
Wide-width strength @ 2%	0.436	**0.691**	**0.577**	-0.529	-0.041	-0.236
Wide-width strength @ 5%	**0.609**	**0.667**	**0.668**	-0.415	0.011	-0.197
Ultimate wide-width strength	**0.612**	0.456	0.379	**0.678**	**0.515**	**0.509**
Cyclic modulus @ 0.5%	0.269	**0.590**	0.429	-0.933	-0.286	-0.660
Cyclic modulus @ 1.0%	**0.633**	**0.680**	**0.659**	-0.749	-0.196	-0.536
Cyclic modulus @ 1.5%	**0.676**	**0.673**	**0.670**	-0.566	-0.060	-0.350
Cyclic modulus @ 2.0%	**0.683**	**0.666**	**0.657**	-0.501	-0.023	-0.300
Cyclic modulus @ 3.0%	**0.672**	**0.643**	**0.623**	-0.372	0.003	-0.275
Cyclic modulus @ 4.0%	**0.644**	**0.638**	**0.605**	-0.281	0.042	-0.213
Resilient interface shear stiffness	-0.912	0.146	0.053	---	---	---
Junction strength[a]	-0.234	0.481	**0.545**	---	---	---
Junction stiffness[a]	-0.407	**0.611**	**0.505**	---	---	---
Aperture stability modulus[b]	-0.181	0.063	-0.065	-0.181	0.063	-0.065

* bolded values indicate R-squared values greater than 0.500
--- material tests not conducted in the machine direction
[a] junction strength and stiffness of the Tenax MS 330 product was not included in this analysis because it was difficult to determine this property based on the fact that it consisted of three layers
[b] aperture stability modulus is not direction dependent so values are the same for machine and cross-machine directions

A linear regression analysis was also conducted using data from Phase I of this project (Cuelho and Perkins, 2009). Six of the test sections from Phase I used the same geosynthetics as this project (BX Type 2, Secugrid 30-30 Q1, Enkagrid MAX 30, SF11, Mirafi BXG11 and Geotex 801). These test sections had very similar subgrade strengths but contained an average of approximately 8 in. of gravel. Performance data was analyzed with respect to the material properties listed above at 1.0, 2.0, 3.0 and 4.0 in. of rut. The results of this analysis are listed in Table 27.

Table 27: R-Squared Results of Linear Regression Analysis Using Phase I Performance Data

	Cross-machine direction				Machine direction			
	1.0 in. rut	2.0 in. rut	3.0 in. rut	4.0 in. rut	1.0 in. rut	2.0 in. rut	3.0 in. rut	4.0 in. rut
Wide-width strength @ 2%	-4.779	-1.776	**0.710**	**0.635**	-0.488	-0.223	0.443	**0.577**
Wide-width strength @ 5%	-0.886	-0.065	**0.787**	**0.688**	-0.543	-0.277	0.366	0.477
Ultimate wide-width strength	-5.588	-3.974	-2.030	-0.961	-5.604	-3.926	-1.386	-0.361
Cyclic modulus @ 0.5%	-6.535	-2.984	0.348	**0.607**	-0.831	-0.400	0.466	**0.647**
Cyclic modulus @ 1.0%	-8.630	-4.158	0.026	**0.507**	-1.326	-0.730	0.343	**0.570**
Cyclic modulus @ 1.5%	-11.05	-5.550	-0.414	0.278	-1.526	-0.869	0.298	**0.566**
Cyclic modulus @ 2.0%	-11.84	-6.198	-0.647	0.261	-1.883	-1.084	0.232	**0.522**
Cyclic modulus @ 3.0%	-13.11	-7.254	-1.278	-0.139	-2.511	-1.584	-0.016	0.427
Cyclic modulus @ 4.0%	-13.83	-7.782	-1.617	-0.395	-2.422	-1.526	-0.027	0.386
Resilient interface shear stiffness	-1.343	-0.399	-0.193	-0.622	---	---	---	---
Junction strength	0.436	**0.562**	0.243	-0.044	---	---	---	---
Junction stiffness	-1.416	0.180	**0.839**	0.153	---	---	---	---
Aperture stability modulus[a]	**0.553**	0.337	0.358	0.386	**0.553**	0.337	0.358	0.386

* bolded values indicate R-squared values greater than 0.500
--- material tests not conducted in the machine direction
[a] aperture stability modulus is not direction dependent so values are the same for machine and cross-machine directions

Considering a similar approach as before, the regression analysis using performance data from the Phase I project indicates, overall, that tensile strength in both material directions relate to performance at higher levels of rut, while junction strength relates to performance at lower levels of rut – the relationship with junction strength peaks at 2.0 in. of rut, while junction stiffness peaks at 3.0 in. of rut. Aperture stability modulus is also related to early performance of the Phase I test sections.

In summary, the performance of geosynthetics as subgrade stabilization is dependent on the constructed properties of the road being stabilized. In situations where there is less structural benefit from the gravel base course layer and more benefit is expected of the geosynthetic (as in Phase I), stiffness and tensile strength play a greater role in rut suppression, especially given the rapid deterioration of these test sections under traffic load. In addition, the strength and stiffness of the junctions in the cross-machine direction plays a role, but diminishes as rut develops. Conversely, in situations where there is more base course and rut development is less rapid (as in this project), the role of junction stiffness and strength is more apparent as reliance on this property for performance increases as a function of rut. Coupled with this is the early dependence on the stiffness of the geosynthetic as loads are transmitted into the material, especially in the cross-machine direction as the geosynthetic confines the base aggregate as it spreads laterally under the applied load. Once the material has been engaged in this way, further

transmission of lateral loads are borne by members in the machine direction of the material as they transmit the load into the cross-machine load bearing members (i.e., junction strength and stiffness). An analysis of the behavior of the test sections in the transverse direction is presented in the next section to more thoroughly investigate and discuss these behaviors.

Practitioners who wish to use these geosynthetics as subgrade stabilization should consider minimum values for geosynthetic material properties that correlated well with performance of the test sections. The material properties most related to the performance (identified as R-squared values greater than 0.500 in Table 25, Table 26, and Table 27) included junction stiffness and strength in the cross-machine direction, wide-width tensile strength at 2 percent and 5 percent, and cyclic tension stiffness. Minimum values for these properties may be categorized by the severity of the site conditions, ranging from moderate to severe, as demonstrated in the two phases of this project. Moderate and severe conditions are subjective but can be estimated by considering the strength of the subgrade, the thickness of the base course, ground pressures associated with construction equipment, traffic levels and acceptable rut depths. Keep in mind that these properties are mutually important. For example, geogrids that have good junction strength but low tensile strength may not perform well. Likewise, geogrids with higher tensile strength and lower junction strength also may not perform well. Despite the fact that the woven and non-woven geotextiles performed well in these test sections, it is unknown which material properties are directly responsible for their performance. Intuitively, however, surface friction properties and tensile strength of the materials plays an important role. Selecting products (like the ones used in this study) that have sufficient surface roughness and/or tensile strength is suggested.

Transverse Rut Analysis

The transverse behavior of the test sections was characterized using transverse rut measurements (taken perpendicular to traffic), displacement measurements, and strain measurements. Transverse rut measurements were taken at two locations (referred to as north and south) within each test section during trafficking (geographically coincident with the instrumented locations). Transverse rut measurements were made using the robotic total station at the same schedule as the longitudinal rut measurements. Nineteen individual measurements points were taken to create a single transverse surface contour. A set of transverse profiles were created for each measurement location using data from multiple truck passes, as shown in the example in Figure 79 for Test Section 10 (Tenax MS 330), north location. Transverse profiles for all of the test sections are provided in Appendix L.

Referring to Figure 79, successive passes of the test vehicle induced deeper and deeper ruts until it reached a depth of 3 in. when it was filled in to facilitate further trafficking. Bearing capacity failure is evident based on the heaving of the road surface adjacent to the wheel path. Heave is defined as the difference between apparent rut and elevation rut, as illustrated in Figure 80. The apparent rut was determined by analyzing the transverse rut profiles and then subtracting the

elevation rut to determine heave. Heave was then plotted with respect to truck passes, as shown in the example in Figure 81 for Test Section 10 (Tenax MS 330). For the purposes of this analysis, the initiation of heave was defined as the point at which 0.5 in. of heave occurred. Using this criterion, the number of truck passes at 0.5 in. of heave was determined for all of the test sections. Heave occurred at different traffic levels within each test section, but most began around 100 to 300 truck passes, and test sections that began to heave earlier generally reached 2 in. of rut earlier, as illustrated in Figure 82, with the exception of Test Section 13 (Mirafi RS580i). Possible explanations for this difference are 1) the woven textile behaves differently from the other tests sections and is not comparable in terms of its heave and rut characteristics, or 2) heave characteristics are based on limited data and may not reflect the average response from the entire test section.
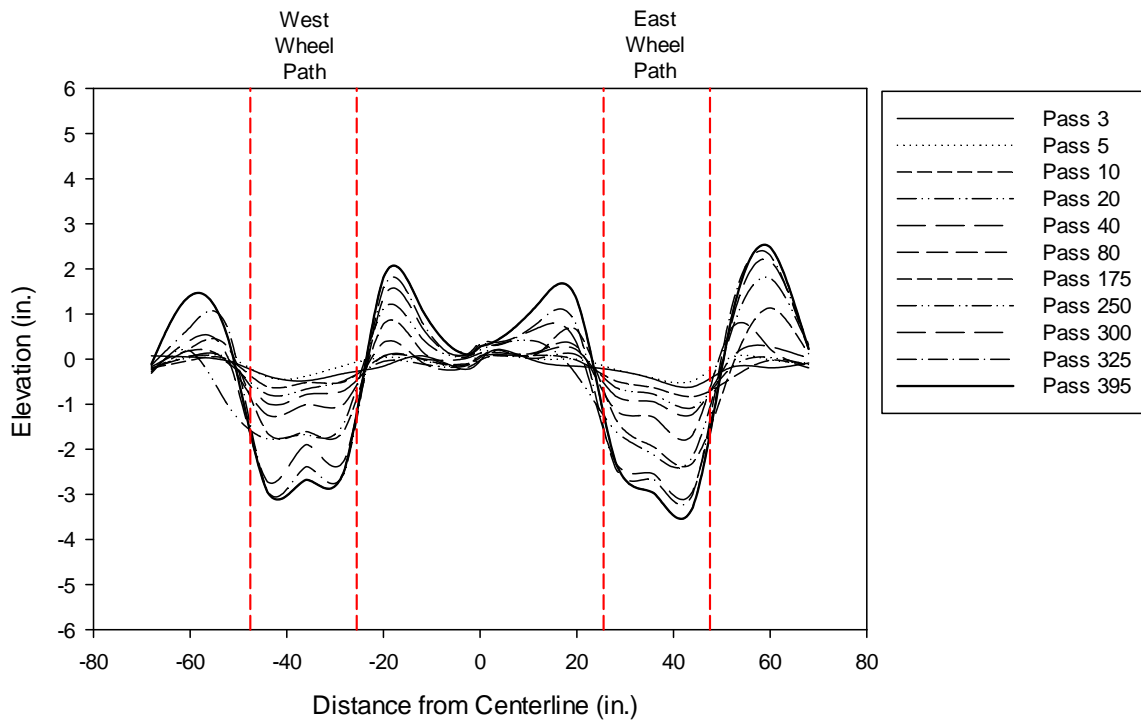
Figure 79: Transverse rut profiles for Test Section 10 (Tenax MS 330), north location.
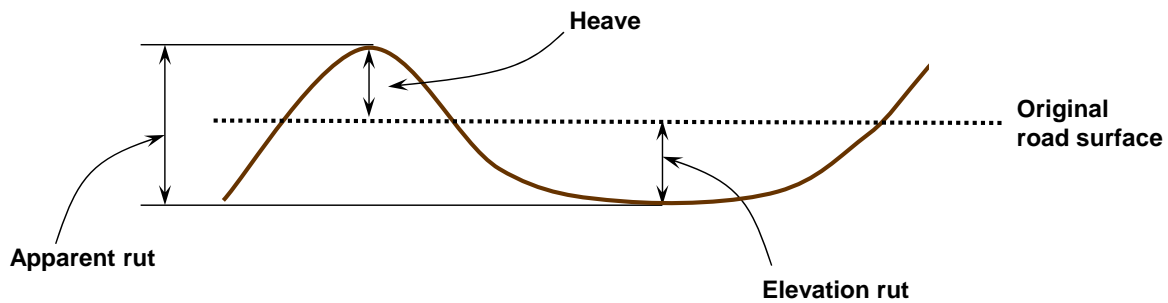
Figure 80: Illustration of heave.
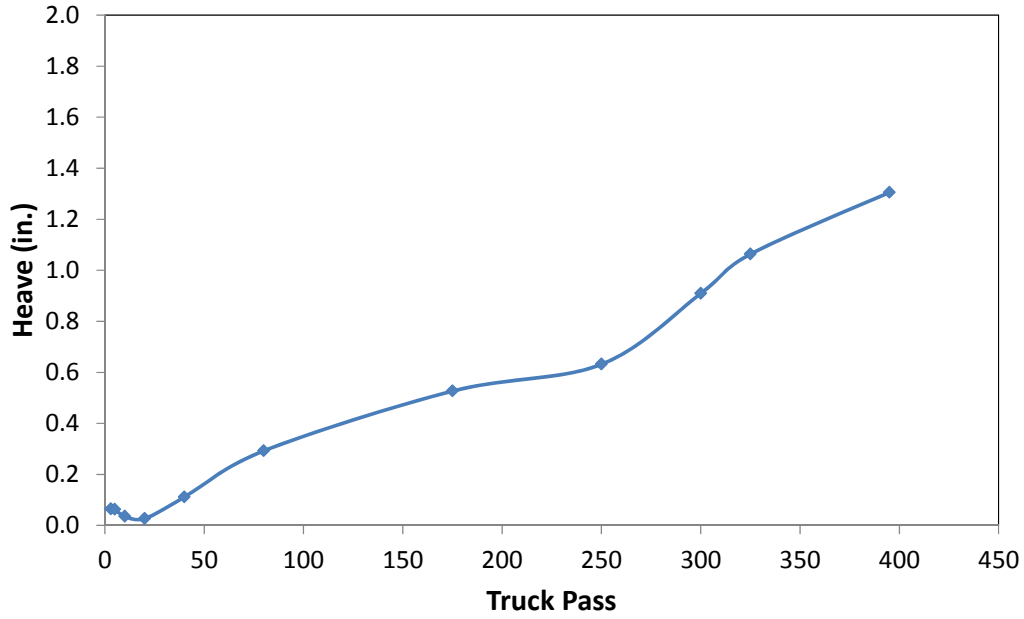
Figure 81: Heave as a function of truck pass for Test Section 10 (Tenax MS 330).
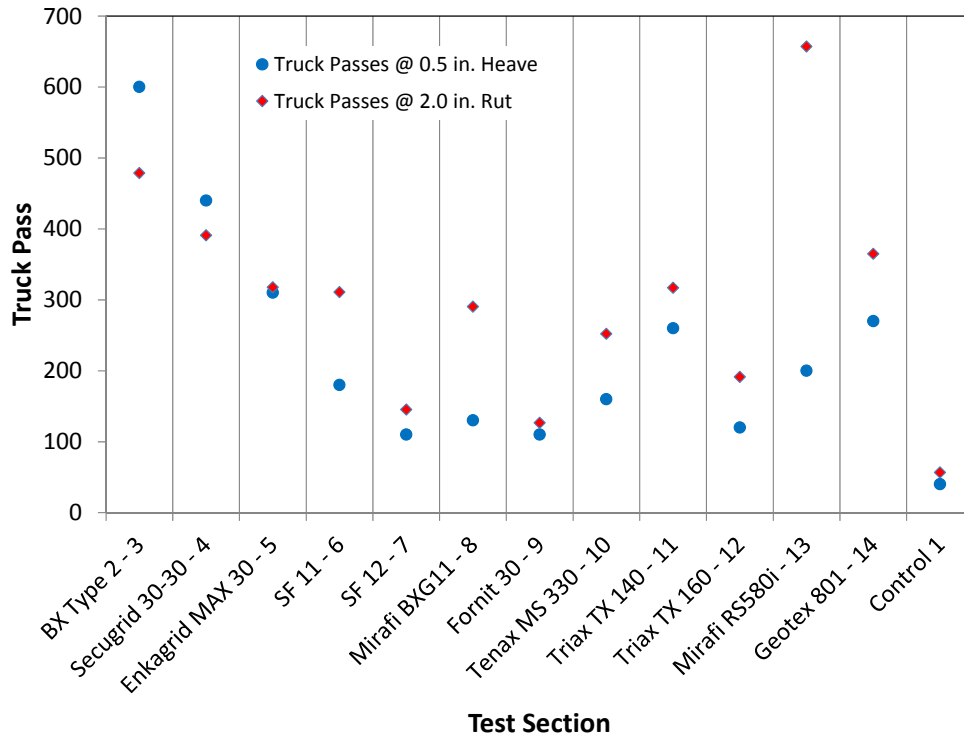
Figure 82: Heave and longitudinal rut comparison for all test sections.

Displacement Analysis

Long-term and dynamic displacement data were collected during trafficking to characterize movement and strain in the material at two locations along the west edge of the wheel path. The first displacement measurement point was furthest to the west outside of the wheel path (LVDT 1 measurement), the second measurement was near the edge of the wheel path (LVDT 2 measurement), and the third measurement point was directly under the outside tire of the dual wheel (LVDT 3 measurement), as illustrated in the plan view presented in Figure 83. Three strain calculations were possible using these measurements and knowing the original distance between these points. $Strain_{1-2}$ is the strain between LVDT 1 and LVDT 2, $Strain_{2-3}$ is the strain between LVDT 2 and LVDT 3, and $Strain_{1-3}$ is the overall strain between LVDT 1 and LVDT 3. The following sign convention was used: positive displacement moves to the left (westward) in Figure 83 and positive strain indicates tension. Note that the LVDTs only sense movement in a single direction and are not able to discern movement of the actual measurement point in three directions. As trafficking began, the base course aggregate began to engage the geosynthetic reinforcement as the gravel particles at the bottom of the base layer began to spread laterally under the load. The geosynthetic resisted this spreading of the aggregate by confining the particle movement primarily through interaction with the intersecting members of the grid structure or the surface friction of the textile materials. As the rut depth increased under increased truck passes, however, distortion of the rut bowl caused the gravel to gradually lose its ability to spread laterally which in turn caused the stresses in the base course layer to become more vertical, resembling punching shear. Stresses from the loaded wheels became more vertical through the base course and the area of influence at the interface between the base and subgrade was decreased thereby increasing stresses on the top of the subgrade. As the subgrade and base were continually shoved away from the center of the rutted area under continued traffic loading, the primary mechanism of support from the geosynthetics transitioned from lateral confinement to tensioned membrane (refer to Figure 1). This transition is also evident by the heaving of the subgrade and base on either side of the rut bowl (as described above) and changes in the displacement and strain characteristics.
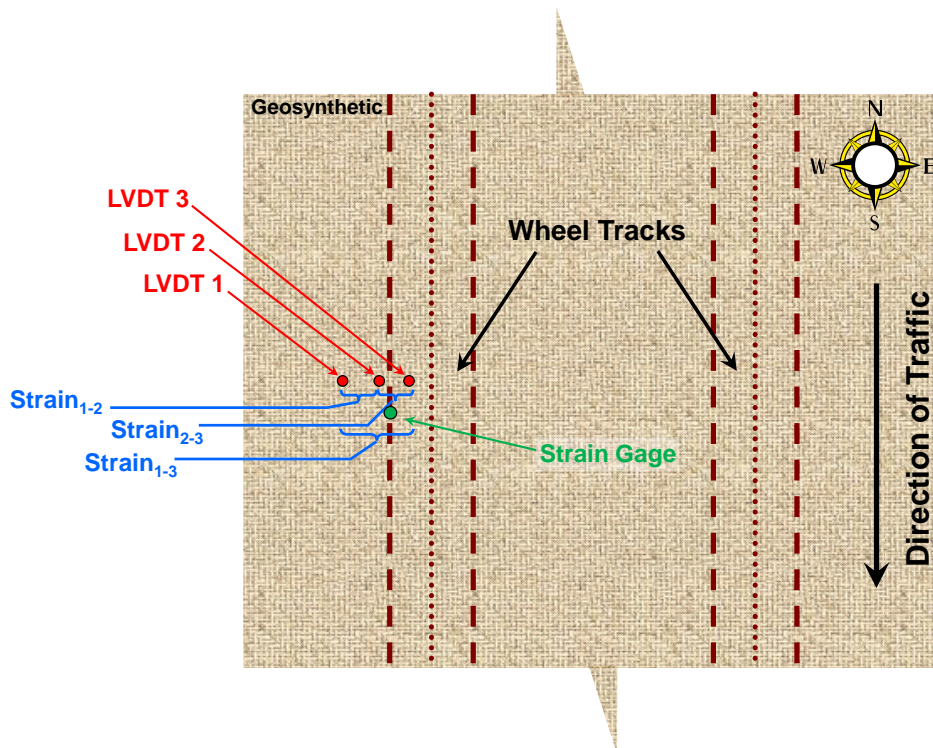
Figure 83: Illustration of displacement and strain measurements and corresponding strain calculation.

Displacement of the geosynthetic as progressive rutting takes place is evident in the displacement history for each test section. Problems with the data acquisition system resulted in loss of long-term data during trafficking; however, dynamic data collected at various times during trafficking were appended together to create a continuous data trace where accumulated time between truck passes is removed to allow several truck passes to be shown on a single plot. Dynamic data were collected for truck passes 1, 2, 3, 6, 7, 8, 9, 10, 20, 40, 80, 140, 175, 251, 301, 302, 303, 401, 402, 403, 404, 405, 556, 557 and 558. A history of the dynamic displacement measurements for Test Section 7 (Synteen SF 12) at the north instrumentation location is shown in Figure 84. The complete displacement history for all of the test sections is shown in Appendix M.
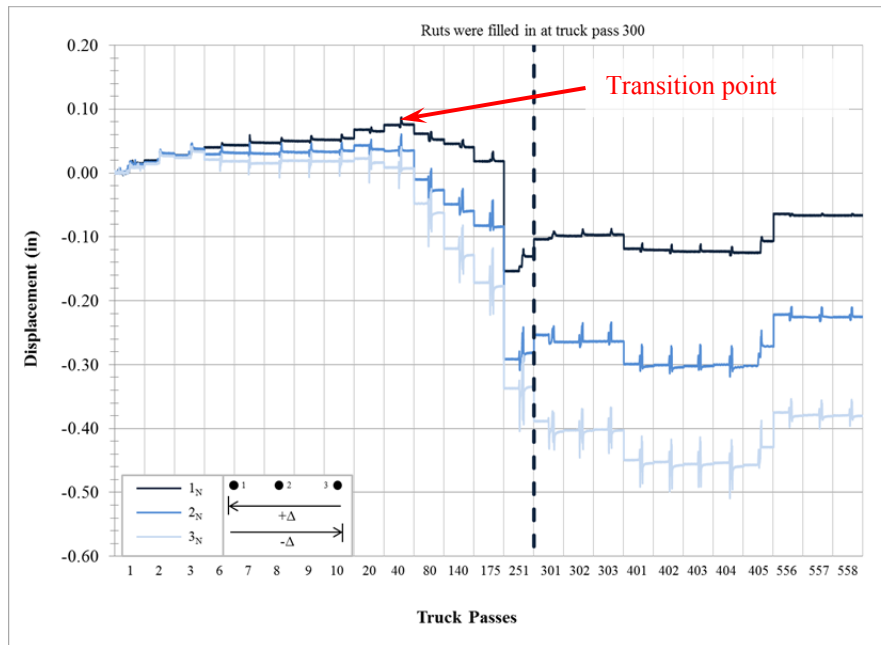
Figure 84: LVDT dynamic displacement results – Test Section 7-North.

Referring to Figure 84, early displacements generally accumulate in a positive direction indicating global movement of the geosynthetic to the west (away from the rutted area). After about 40 truck passes the sensors begin to move toward the rutted area as the geosynthetic is pulled down into the forming rut, as illustrated in Figure 85. This reversal of the direction in movement is coincident with the point of inflection from positive to negative slope in the displacement responses. Lateral movement of the LVDT measurement points were generally illustrated in Figure 85 using the displacement data presented in Figure 84. Similar behavior was evident in several of the test sections, with some test sections making this transition at lower or higher numbers of truck passes. This behavior suggests a transition between lateral confinement of the base course by the geosynthetic to membrane support involving deeper rutting and the tensioned-membrane effect. A graphical illustration of the point of transition for all of the test sections based on displacement data (primarily from LVDT 3 directly under the wheel at the bottom of the rut bowl) is shown in Figure 86. Changes in displacement revealed similar results to the heave and longitudinal rut response, namely, those test sections where the direction of the displacements transitioned earlier also reached higher levels of longitudinal rut earlier. This transition generally occurred at or before about 2 inches of longitudinal rut. It wasn't possible to determine the transition point for the TX140 material using the displacement data.

Dynamic displacement responses were small (from approximately 0.01 to 0.05 in. for a single truck pass). Accumulated displacements differed for the different test sections and, overall, the minimum and maximum values were approximately -0.25 and 1.0 in., respectively.
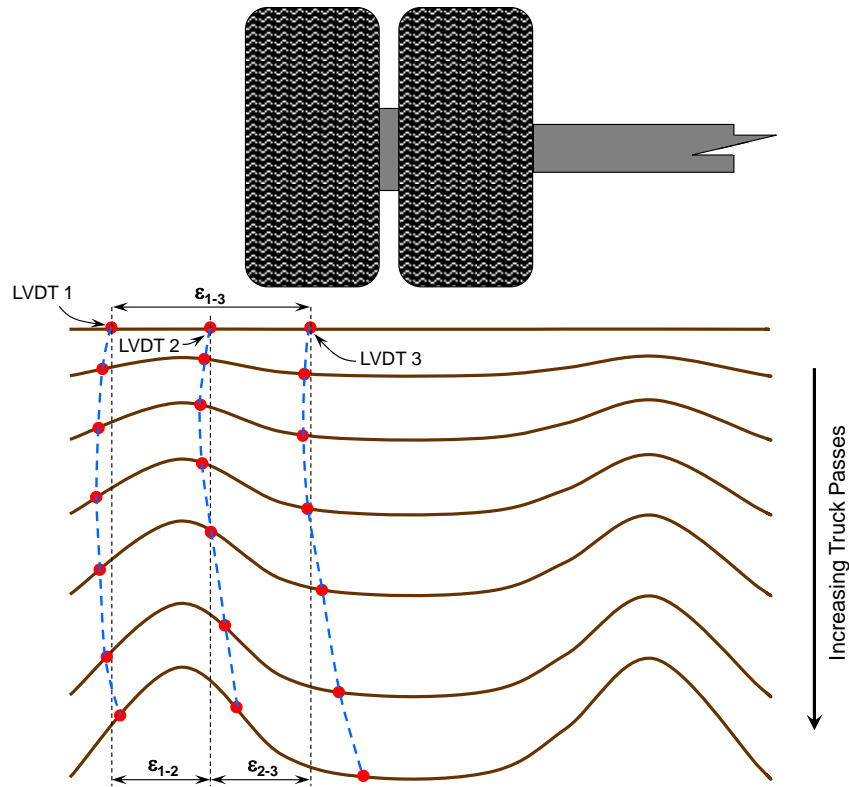
Figure 85: Distortion of the instrumented area due to rut formation.
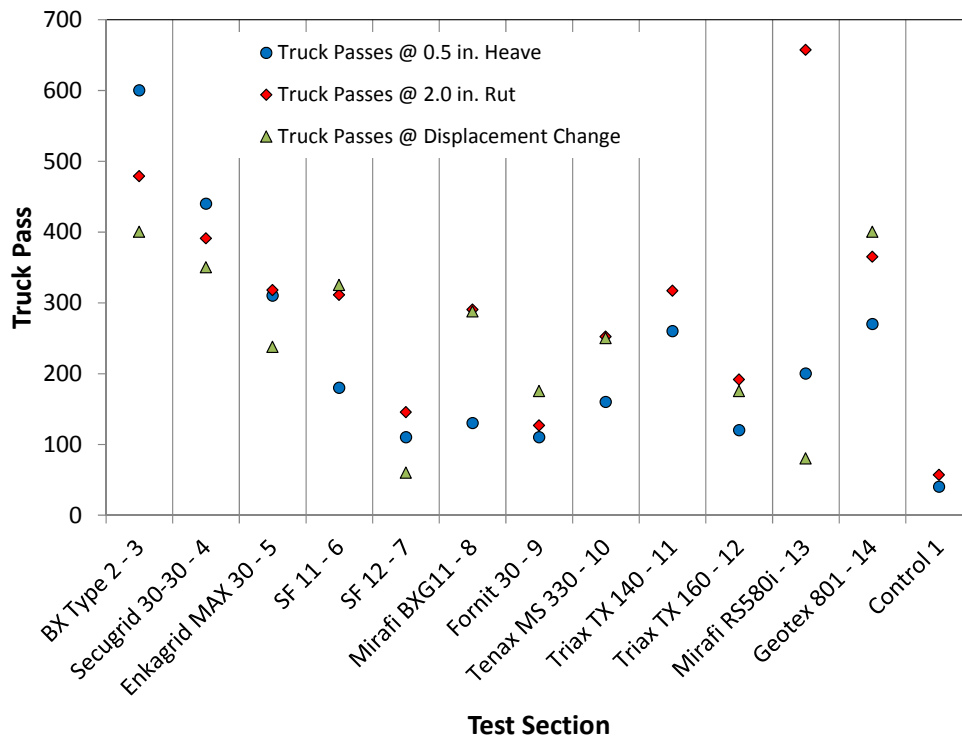
Figure 86: Heave, longitudinal rut, and change in displacement comparison for all test sections.

Strain Analysis

Similar to the displacement data, dynamic strain data (from the bonded strain gages) was used to create a continuous data trace where accumulated time between truck passes is removed to allow several truck passes to be shown on a single plot. Strain was measured in two locations within each test section near the edge of the outside wheel of the truck on the west rut (as illustrated in Figure 41 and Figure 83). An example of a representative strain record is shown in Figure 87, from Test Section 3 (Tensar BX Type 2). Dynamic strain responses from all of the test sections are summarized in Appendix N. Considering all of the test sections, maximum strains from the dynamic strain data ranged from about 0.3 to 2.8 percent. Maximum dynamic strains from a single truck pass ranged from about 0.3 percent to 1.5 percent. Similar results were obtained from the long-term strain data, which showed that maximum accumulated strains ranged from about 0.3 to 3.0 percent. A summary of the cumulative strain data is tabulated in Table 28. Long-term strain responses during trafficking for all of the test sections are summarized in Appendix O. The greatest strain levels were observed in Test Section 14 (Geotex 801, non-woven textile). Considering the long-term strain data, the greatest strains in the geogrids were observed in the Tensar products, with the greatest in the TX140 and TX160 geogrids. The least strain was observed in the Mirafi RS580i geotextile and NAUE Secugrid 30-30 geogrid. Working strain levels in this experiment were generally around the 2 to 5 percent range which corresponded well with typical design properties used for these materials.
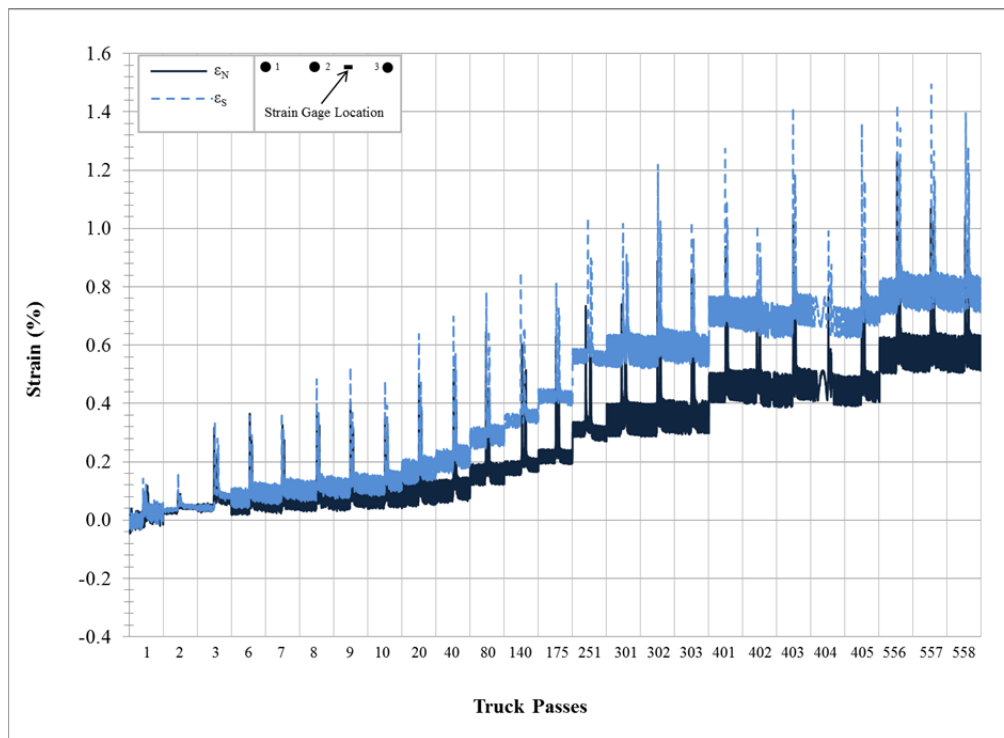
Figure 87: Dynamic strain response from Test Section 3 (Tensar BX Type 2).

Table 28: Cumulative Strain Levels During Trafficking from Bonded Strain Gages

Geosynthetic Test Section	Maximum Cumulative Strain[a] (%)		Maximum Dynamic Strain (%)
	From Dynamic Data[b]	From Long-Term Data	
BX Type 2 (Section 1)	0.8	1.1	0.8
BX Type 2 (Section 2)	2.1	1.8	1.3
BX Type 2 (Section 3)	0.8	1.1	0.6
Secugrid 30/30 Q1 (Section 4)	0.3[c]	0.3[c]	0.3
Enkagrid Max 30 (Section 5)	0.8	0.5	0.4
SF 11 (Section 6)	0.6	0.6	0.6
SF 12 (Section 7)	0.2[c]	---	0.4
Mirafi BXG 11 (Section 8)	0.6	0.7	0.8
Fornit 30 (Section 9)	0.3[c]	---	0.5
Tenax MS 330 (Section 10)	0.6	0.7	0.7
TX 140 (Section 11)	0.8	1.8	0.6
TX 160 (Section 12)	2.0	1.9	1.1
Mirafi RS580i (Section 13)	0.4	0.5	0.5
Geotex 801 (Section 14)	2.8	3.0	1.5

[a] from data prior to ruts being filled in
[b] dynamic data was collected only through truck pass 558
[c] sensors stopped prematurely
--- difficult to determine from strain data

Strain was also determined using the LVDTs, as discussed above and illustrated in Figure 83. Strains calculated from the displacement data varied widely, but generally were less than about 2 percent, with the exception of Test Section 14 (Geotex 801) which experienced strains of up to 9 percent as discerned from the long-term data (Table 29). Strain responses determined from the dynamic LVDT data are summarized in Appendix P, and strain responses determined from the long-term LVDT data are summarized in Appendix Q. Strain calculated using LVDT positions 2 and 3 ($Strain_{2-3}$) overlap the bonded strain gage areas. Comparisons of strain between the two measurement methods reveals similar general trends; however, a direct comparison is problematic because the LVDT measurement point was able to move in three dimensions and the LVDT measurements spanned a gage length of around 8 in. compared to a bonded strain gage length of 0.25 to 0.5 in. for the geogrids and 2.0 inches for the geotextiles.

Table 29: Long-Term Strain Levels During Trafficking from LVDT Displacement Gages

Geosynthetic Test Section	Maximum Strain from Dynamic Data[a] (%)		Maximum Strain from Long-Term Data (%)	
	$Strain_{1-2}$	$Strain_{2-3}$	$Strain_{1-2}$	$Strain_{2-3}$
BX Type 2 (Section 1)	0.9	0.3	0.8	0.4
BX Type 2 (Section 2)	2.2	2.2	1.3	1.0
BX Type 2 (Section 3)	0.4	0.5	0.6	0.5
Secugrid 30/30 Q1 (Section 4)	0.7	0.8	1.1	1.1
Enkagrid Max 30 (Section 5)	1.2	0.1	0.1	1.5
SF 11 (Section 6)	0.9	1.6	1.1	1.8
SF 12 (Section 7)	2.4	1.1	1.8	1.1
Mirafi BXG 11 (Section 8)	1.5	0.9	1.8	0.8
Fornit 30 (Section 9)	0.9	0.7	1.0	0.6
Tenax MS 330 (Section 10)	0.9	0.5	0.9	0.5
TX 140 (Section 11)	1.3	2.0	0.5	1.5
TX 160 (Section 12)	1.8	1.7	2.6	1.0
Mirafi RS580i (Section 13)	1.6	0.6	2.0	0.5
Geotex 801 (Section 14)	2.6	8.0	4.6	9.0

[a] dynamic data was collected only through truck pass 558

Pore-Water Pressure Analysis

Previous work by Christopher et al. (2009) involving the construction of unpaved roads on a weak subgrade in a large box and loaded with a 40 kN cyclic load applied to a 300 mm diameter plate showed a strong correlation between the excess pore water pressure developed in the subgrade and the rutting performance of the test section when different reinforcement products were used. Analytical work by Christopher et al. (2009) resulted in a relationship between the undrained shear strength of the subgrade and the excess pore water pressure resulting from the simulated traffic loading. In general, as excess pore-water pressure increases, effective stress decreases and undrained shear strength decreases, which results in less traffic carrying capacity of the road. Excess pore water pressure is a result of the stresses applied to the subgrade. Since reinforcement reduces the stresses experienced by the subgrade, reinforcement in turn should decrease the excess pore water pressure developed.

In the first phase of this study (Cuelho and Perkins, 2009), pore water pressure was measured in the subgrade of the test sections and showed static values ranging between 0.04 and 1.8 psi at the end of trafficking. Using the analytical equations of Christopher et al. (2009), a decrease in subgrade CBR ranging between 0.01 and 0.23 was predicted.

In the current study, three pore water pressure sensors were placed in each test section to further the understanding of how pore-water pressures generated by traffic loading relate to roadway performance and the role of geosynthetics in controlling excess pore water pressure. Two sensors were placed at a depth of 6 in. into the subgrade. A third sensor was placed at a depth of 10 in. All sensors were placed to align under the center of the outermost rear wheel (refer to Figure 41).

Long-term pore-water pressure data was collected on the same schedule as the strain and displacement data. Dynamic response was measured at selected truck passes as the truck travelled down the test sections. An example of dynamic response is illustrated in Figure 88 for Test Section 3 (BX Type 2), truck pass 9. In this test section, the pore-water pressure increases in response to each of the three truck axle passes. An overall increase in pore-water pressure of approximately 0.1 psi is observed due to the passage of the truck. Figure 89 shows values of pore-water pressure in this test section after the truck passes shown and illustrates how pore-water pressure continues to build up with increasing truck passes. Similar individual plots for all of the test sections are provided in Appendix R. A summary of all pore-water pressure data from all test sections for each sensor location is shown in Figure 90, Figure 91, and Figure 92 for the north 10 in. deep, north 6 in. deep, and south 6 in. deep measurement points, respectively. Referring to these figures, it can be observed that by truck pass 175, the increase in static pore water pressure ranged from 0.13 to 4.8 psi between all the test sections and measurement points.
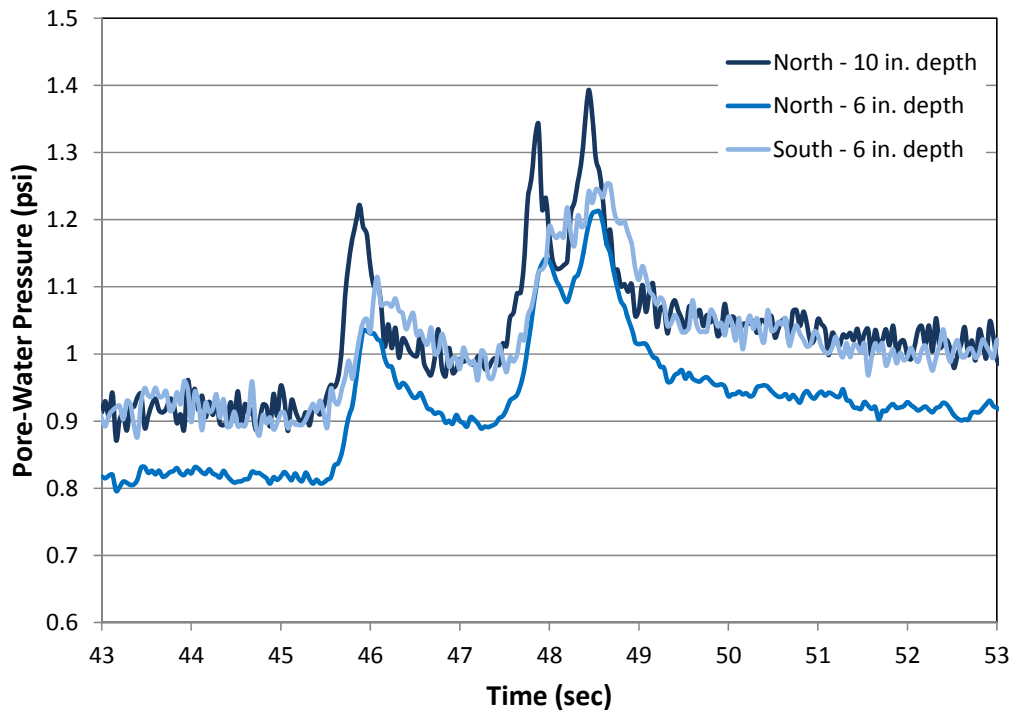
Figure 88: Dynamic pore-water pressure response in Test Section 3, truck pass 9.
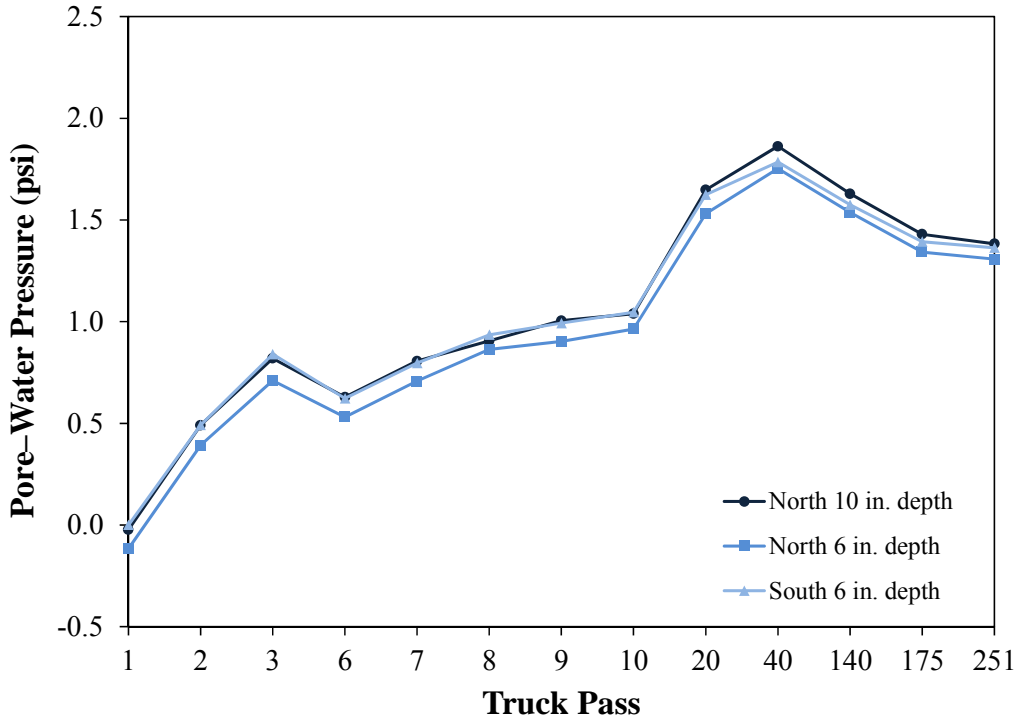
Figure 89: Cumulative pore-water pressure in Test Section 3 after passage of the truck.
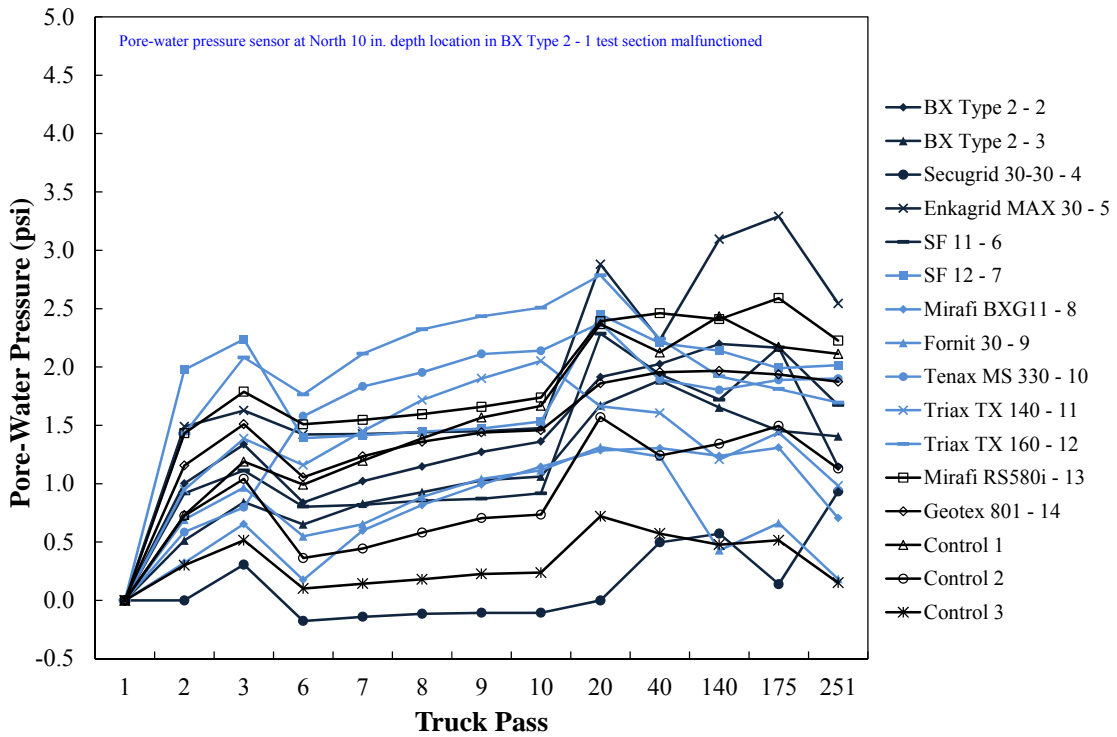
Figure 90: Cumulative pore-water pressure in all test sections after passage of the truck, as measured by north, 10 in. deep sensor.
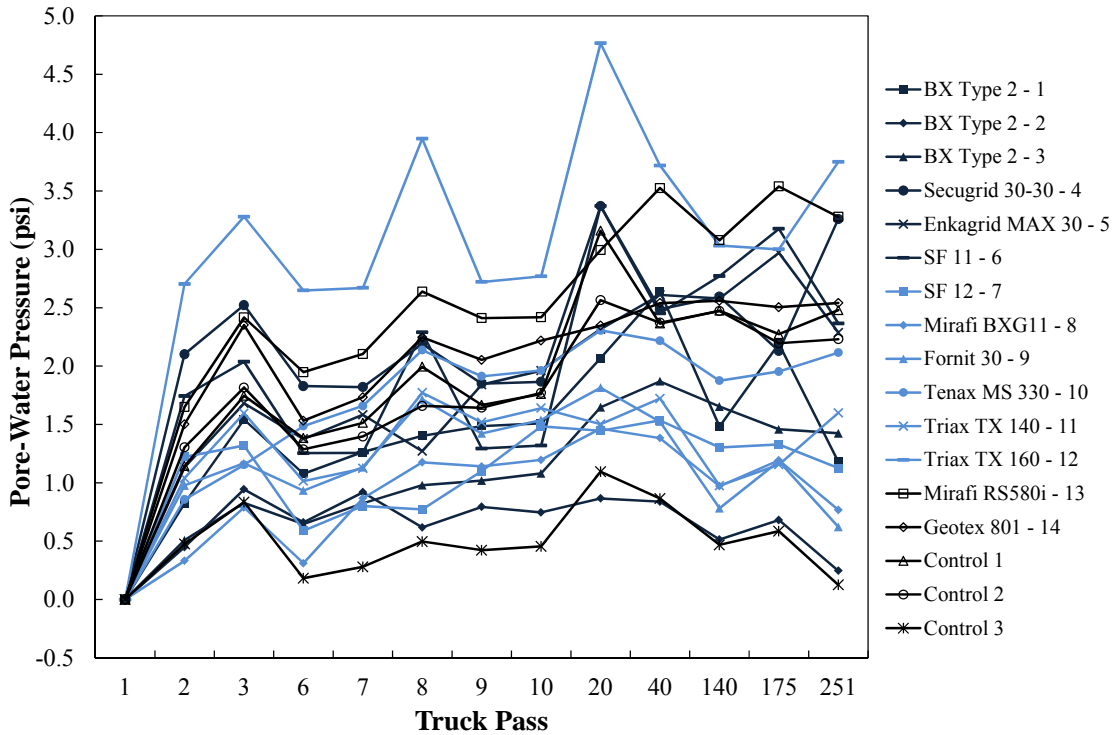
Figure 91: Cumulative pore-water pressure in all test sections after passage of the truck, as measured by north, 6 in. deep sensor.
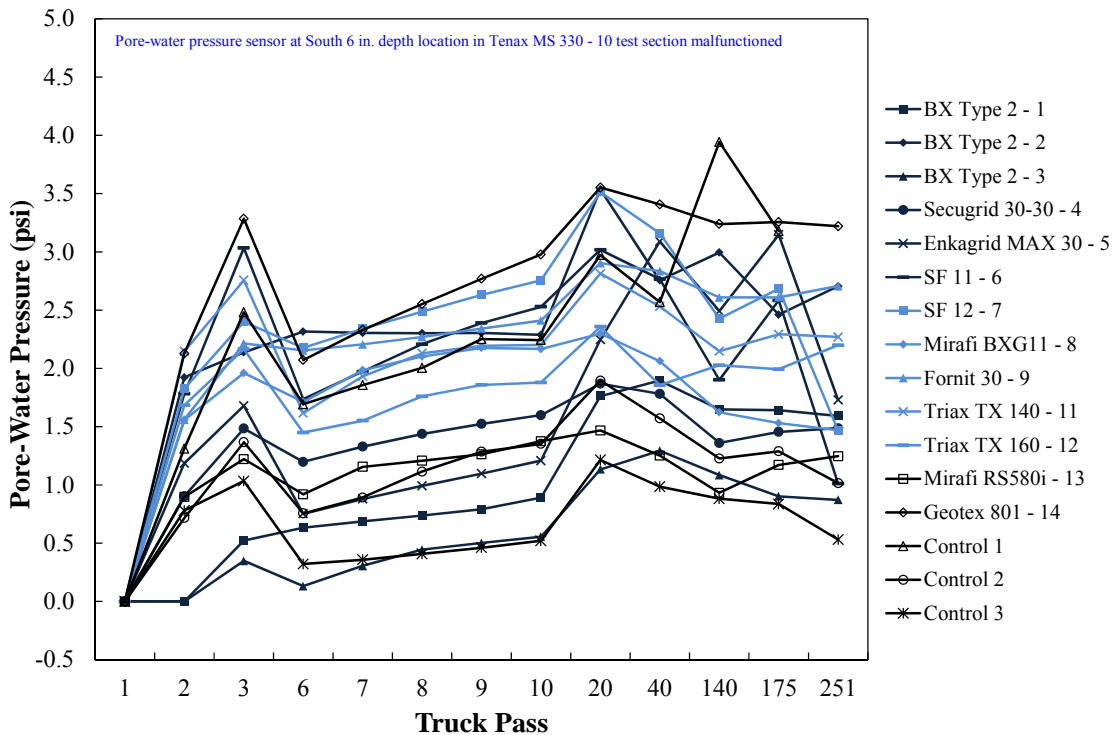
Figure 92: Cumulative pore-water pressure in all test sections after passage of the truck, as measured by south, 6 in. deep sensor.

The elapsed time between traffic passes has an influence on the magnitude of static pore-water pressure build up in the subgrade. The pore-water pressure in Test Section 8 between truck passes 175 and 250 is shown in Figure 93. The data shows that pore water pressure builds up during periods of traffic loading and then slowly dissipates during periods when no traffic is applied. Since all test sections experienced the same schedule of traffic loading, the effect of wait periods should be essentially the same for all test sections.
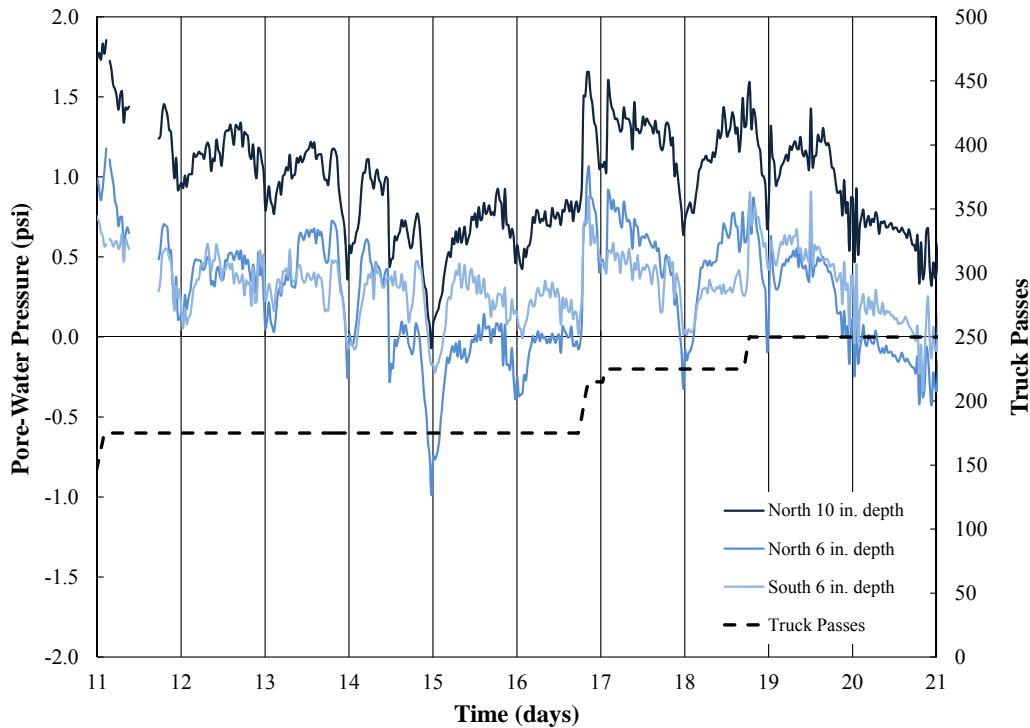
Figure 93: Pore-water pressure in Test Section 8 (TenCate Mirafi BXG11) for truck passes 175-250.

The analytical equation developed by Christopher et al. (2009) is shown as Equation 17, where Δs_u is the change in undrained shear strength due to an increase in static pore water given by u_e and with each having the same set of units. In this study, vane shear test results were compared to CBR measurements to develop a relationship between the two, which is given by Equation 18 (in units of psi).

$$\Delta s_u = \frac{u_e}{1.4} \qquad \qquad \textbf{Equation 17}$$

$$s_u = 4.472CBR + 0.8028 \qquad \qquad \textbf{Equation 18}$$

Combining Equations 17 and 18, a decrease in subgrade CBR was calculated for each test section at truck pass 175, where an average value of excess pore-water pressure from the three sensors in a given test section were used in equation 17. The results from this analysis are

summarized in Table 30 and Figure 94. Table 31 provides the values of excess pore water pressure used to obtain the loss of CBR given in Table 30. In Figure 94, each bar shows the average decrease in subgrade CBR while the error band corresponds to plus or minus one standard deviation from the mean.

Table 30: Predicted Loss in Subgrade CBR in each Test Section Due to Pore-Water Pressure Accumulation by Truck Pass 175

Test Section	North – 10 in. depth	North – 6 in. depth	South – 6 in. depth	Average	Standard Deviation
BX Type 2 (Section 1)	---	0.41	0.10	0.25	0.216
BX Type 2 (Section 2)	0.26	0.32	0.21	0.27	0.057
BX Type 2 (Section 3)	0.20	0.20	0.01	0.14	0.113
Secugrid 30/30 Q1 (Section 4)	-0.15	0.16	0.10	0.04	0.161
Enkagrid Max 30 (Section 5)	0.33	0.44	0.38	0.38	0.054
SF 11 (Section 6)	0.14	0.30	0.35	0.27	0.109
SF 12 (Section 7)	0.14	0.16	0.31	0.20	0.090
Mirafi BXG 11 (Section 8)	0.18	0.30	0.20	0.23	0.064
Fornit 30 (Section 9)	0.16	0.26	0.26	0.23	0.056
Tenax MS 330 (Section 10)	0.23	0.30	---	0.26	0.048
TX 140 (Section 11)	0.18	0.27	0.34	0.26	0.083
TX 160 (Section 12)	0.22	0.29	0.29	0.27	0.045
Mirafi RS580i (Section 13)	0.24	0.45	0.25	0.31	0.116
Geotex 801 (Section 14)	0.25	0.28	0.43	0.32	0.098
Control 1	0.22	0.25	0.43	0.30	0.115
Control 2	0.10	0.20	0.19	0.16	0.051
Control 3	-0.06	-0.01	-0.03	-0.04	0.024

--- missing data

Table 31: Pore-Water Pressure Accumulations in Subgrade in Each Test Section by Truck Pass 175

Test Section	North – 10 in. depth	North – 6 in. depth	South – 6 in. depth	Average	Standard Deviation
BX Type 2 (Section 1)	---	3.67	1.76	2.71	1.351
BX Type 2 (Section 2)	2.76	3.16	2.44	2.78	0.359
BX Type 2 (Section 3)	2.40	2.38	1.16	1.98	0.711
Secugrid 30/30 Q1 (Section 4)	0.21	2.11	1.73	1.35	1.005
Enkagrid Max 30 (Section 5)	3.21	3.89	3.50	3.53	0.338
SF 11 (Section 6)	2.02	3.02	3.33	2.79	0.683
SF 12 (Section 7)	1.99	2.16	3.04	2.39	0.566
Mirafi BXG 11 (Section 8)	2.26	3.01	2.40	2.56	0.402
Fornit 30 (Section 9)	2.15	2.78	2.73	2.55	0.349
Tenax MS 330 (Section 10)	2.56	2.99	-	2.77	0.303
TX 140 (Section 11)	2.22	2.82	3.25	2.76	0.518
TX 160 (Section 12)	2.47	2.97	2.96	2.80	0.282
Mirafi RS580i (Section 13)	2.65	3.92	2.67	3.08	0.729
Geotex 801 (Section 14)	2.67	2.90	3.83	3.13	0.616
Control 1	2.52	2.66	3.84	3.01	0.723
Control 2	1.78	2.36	2.30	2.15	0.319
Control 3	0.75	1.05	0.91	0.90	0.150

--- missing data
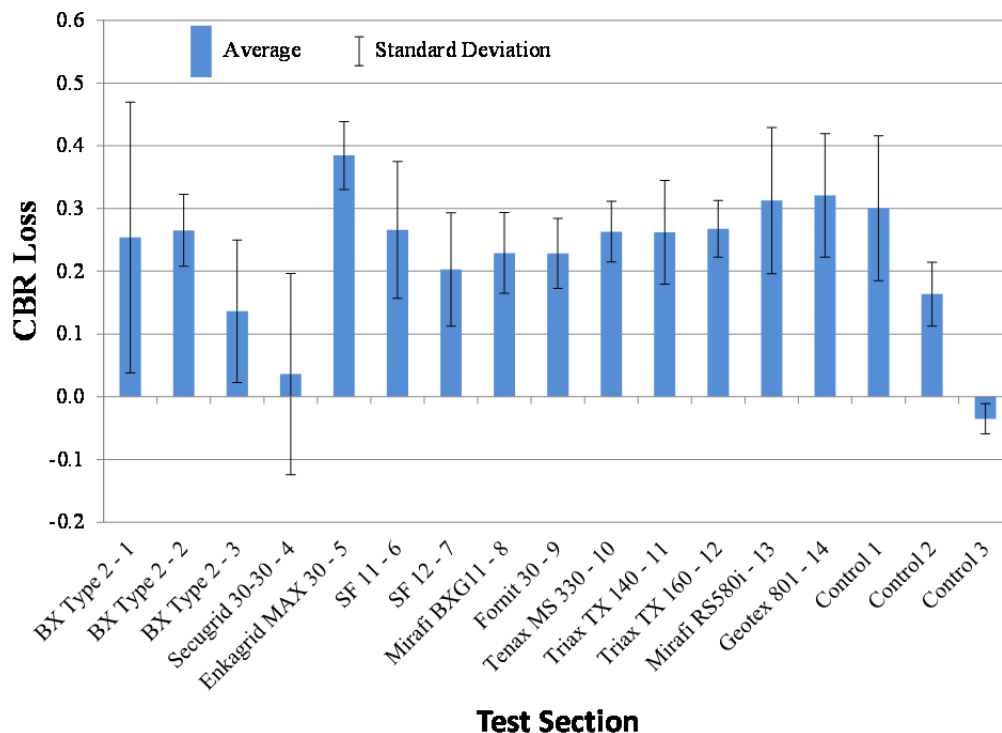
Figure 94: Predicted change in subgrade CBR in each test section due to pore-water pressure accumulation by truck pass 175.

Control 1, Control 2 and Control 3 contained increasing thickness of base aggregate and no reinforcement. The pore-water pressure measurements and corresponding predictions of subgrade CBR loss show decreasing values as the base thickness increases. This is consistent with sections of greater structural cross section producing less stress on the subgrade and less pore water pressure increase. Test Sections 1, 2 and 3 which were all reinforced with BX Type 2 but were constructed on subgrades of different initial CBR strengths. Large standard deviations in the data from these test sections made it difficult to draw definitive conclusions regarding the influence of initial subgrade strength on pore-water pressure development. Furthermore, a simple linear regression analysis indicated that there is not a clear trend as to pore-water pressure development and rut performance of the remainder of the reinforced test sections.

Performance Evaluation

Performance of the test sections is based upon the ability of the geosynthetics to help support a given number of truck passes over the weak subgrade, which is measured by changes in longitudinal rut. Two evaluation methods that can be used to compare the relative performance of the test sections are the base course reduction (BCR) analysis and the traffic benefit ratio (TBR) analysis. Using the results of these analyses in conjunction with the material properties of the geosynthetic can help geosynthetic users select material properties that are associated with a particular level of performance.

Base Course Reduction Analysis

The BCR factor can be used to compare the base course thickness between reinforced and unreinforced test sections that perform equally (Equation 1). In order to accomplish this, however, unreinforced test sections would need to be built to match the performance of each of the reinforced test sections. In this experiment, Control 1 and Control 2 were constructed to understand the performance of unreinforced test sections. Using the information from the base course adjustment analysis, as summarized in Figure 76, the predicted performance of control test sections constructed with gravel thicknesses between 10.9 in. (average base thickness of select points in Control 1) and 16.3 in. (average base thickness of Control 2) could be determined. To perform the BCR analysis, unique power curves were used to generate predicted rut performance for unreinforced "controls" that matched the entire rut response of each of the reinforced test sections (summarized in Figure 77). The performance of the predicted "controls" was based on estimated base thicknesses between 10.9 and 16.3 in. For example, to calculate the BCR for Test Section 3, the longitudinal rut response presented in Figure 77 for this test section was fitted using a power curve. The position of the power curve with respect to the rut response associated with Control 1 and Control 2 was associated with a particular base course thickness (as illustrated in Figure 76). In the case of Test Section 3, the base course thickness of a hypothetical unreinforced test section that would perform as well as Test Section 3 was 14.25 in. Using equation 1, the difference in base course thickness between the reinforced test section and the unreinforced test section was 3.4 in. ($D_{\Delta} = D_{unreinforced} - D_{reinforced} = 14.3\text{-}10.9 = 3.4$ in.). Dividing 3.4 in. by the thickness of the unreinforced test section ($D_{unreinforced} = 14.3$ in.) and multiplying by 100 to express the result in percent yields a BCR of 31.2 for Test Section 3. The results of this analysis are summarized in Table 32, and indicate that the greatest reduction in base thickness is approximately 26.9 percent (TenCate Mirafi RS580i) corresponding to a difference of 4.0 in. of gravel; the least was 10.2 percent (Huesker Fornit 30) corresponding to 1.2 in. of gravel. These comparisons are valid for situations where additional gravel would be sufficient to allow heavy construction equipment to operate on the weak subgrade without excessive rutting or other deformations. The BCR analysis does not take into consideration other potential long-term benefits of geosynthetics beyond their ability to stabilize weak subgrades during construction, such as, separation, filtration, reinforcement, etc.

Table 32: Summary of Base Course Reduction Factors

Test Section	D_Δ (in.)	BCR (%)
BX Type 2 (Section 3)	3.4	23.8
Secugrid 30/30 Q1 (Section 4)	3.0	21.9
Enkagrid Max 30 (Section 5)	2.6	19.6
SF 11 (Section 6)	2.5	19.0
SF 12 (Section 7)	1.4	11.7
Mirafi BXG 11 (Section 8)	2.6	19.3
Fornit 30 (Section 9)	1.2	10.2
Tenax MS 330 (Section 10)	2.3	17.7
TX 140 (Section 11)	2.3	17.4
TX 160 (Section 12)	1.6	13.1
Mirafi RS580i (Section 13)	4.0	26.9
Geotex 801 (Section 14)	2.9	21.3

Traffic Benefit Ratio

An alternative way to compare the relative performance of each test section when compared to the control is to calculate the TBR. TBR is the ratio of the number of truck passes for a reinforced test section to the number of truck passes for an unreinforced test section. This analysis was conducted at varying levels of longitudinal rut depth (1.0, 2.0 and 2.5 in.); however, the overall performance ranking of the test sections did not change as a function of rut depth. The same power curve fit that was used in the BCR analysis was used in the TBR analysis to generally smooth out the rut responses and estimate the longitudinal rut in those test sections that had not yet reached 2.0 or 2.5 inches of rut. The results of this analysis are summarized in Table 33. Similar to the results of the BCR analysis, the greatest traffic benefit was realized in Test Section 13 (TenCate Mirafi RS580i) and the least benefit was with the Huesker Fornit 30 product (Test Section 9). On average, geosynthetics helped support around six to seven times more traffic passes when evaluated at 2.5 inches of rut.

Table 33: Traffic Benefit Ratio Summary

Test Section	TBR at 1.0" rut depth	TBR at 2.0" rut depth	TBR at 2.5" rut depth
BX Type 2 (Section 3)	3.4	7.9	10.4
Secugrid 30/30 Q1 (Section 4)	3.0	6.6	8.4
Enkagrid Max 30 (Section 5)	2.7	5.2	6.5
SF 11 (Section 6)	2.6	4.9	6.1
SF 12 (Section 7)	1.7	2.6	2.9
Mirafi BXG 11 (Section 8)	2.6	5.1	6.3
Fornit 30 (Section 9)	1.6	2.3	2.5
Tenax MS 330 (Section 10)	2.4	4.4	5.4
TX 140 (Section 11)	2.4	4.3	5.2
TX 160 (Section 12)	1.9	2.9	3.4
Mirafi RS580i (Section 13)	4.1	10.8	14.8
Geotex 801 (Section 14)	2.9	6.2	7.9

Performance Summary

The performance of geosynthetics as subgrade stabilization is dependent on the constructed properties of the road being stabilized. In situations where there is less structural benefit from the gravel base course layer and more benefit is expected of the geosynthetic (as in Phase I), stiffness and tensile strength play a greater role in rut suppression, especially given the rapid deterioration of these test sections under traffic load. In addition, the strength and stiffness of the junctions in the cross-machine direction plays a role, but diminishes as rut continues to increase. Conversely, in situations where there is more base course and rut development is less rapid (as in this project), the role of junction stiffness and strength is more apparent as reliance on this property for performance increases as a function of rut. Coupled with this is the early dependence on the stiffness of the geosynthetic as loads are transmitted into the material, especially in the cross-machine direction as the geosynthetic confines the base aggregate as it spreads laterally under the applied load. Once the material has been engaged in this way, further transmission of lateral loads are borne by members in the machine direction of the material as they transmit the load into the cross-machine load bearing members (i.e., junction strength and stiffness).

The principal elements of this project are summarized in Table 34 which contains the performance results of the individual test sections, the properties of the geosynthetics most related to their performance, and the constructed properties of the subgrade and base course. Based on the level of performance desired, individual agencies can utilize the information contained in Table 34 as a guide to determine baseline requirements for geosynthetics in

subgrade stabilization applications. Attention should primarily focus on junction strength and stiffness properties and tensile strength properties for this application.

Table 34: Summary of Test Section Performance and Material Characteristics

	Tensar BX Type 2	Secugrid 30-30 Q1	Enkagrid MAX 30	Synteen SF 11	Synteen SF 12	Mirafi BXG11	Fornit 30	Tenax MS 330	Tensar TX 140	Tensar TX 160	TenCate RS580i	Geotex 801	Information Source
Performance													
BCR (%)	23.8	21.9	19.6	19.0	11.7	19.3	10.2	17.7	17.4	13.1	26.9	21.3	Table 32
TBR @ 2 in. rut	7.9	6.6	5.2	4.9	2.6	5.1	2.3	4.4	4.3	2.9	10.8	6.2	Table 33
TP @ 1 in. rut[a]	96	86	75	73	49	74	46	68	67	53	115	83	Figure 77[a]
TP @ 2 in. rut[a]	449	371	297	280	146	288	129	250	242	165	611	351	Figure 77[a]
TP @ 2.5 in. rut[a]	737	595	462	433	207	447	180	380	367	237	1046	559	Figure 77[a]
Avg. junction intactness (%)	100	98.5	94.4	94.4	85.8	99.8	86.1	99.9	99.9	100	N/A	N/A	Table 19
Avg. XMD rib intactness (%)	100	94.0	99.6	96.6	96.4	100	74.9	100	99.7	99.9	N/A	N/A	Table 22
Avg. 2% XMD strength loss (%)[b]	-3.3	0.4	-1.2	-2.2	26.4	-1.4	22.8	-6.4	-6.4	0.9	-8.0	NT	Table 24
Overall performance ranking	2	3	5	7	11	6	12	8	9	10	1	4	N/A
Geosynthetics													
2% XMD strength (lb/ft)	822	946	857	617	987	740	946	692	322	391	1501	25[c]	Table 5
5% XMD strength (lb/ft)	1494	1830	1775	925	1446	1281	1939	1343	665	747	3440	73[c]	Table 5
2% XMD cyclic modulus (kip/ft)	62	79	69	58	91	67	76	54	28	31	157	NT	Figure 10
XMD junction strength (lb/in)	172	58	50	37	29	36	11	66[d]	72	75	N/A	N/A	Table 8
XMD junction stiff. (lb/in/in)	632	642	498	315	252	518	99.2	157[d]	316	198	N/A	N/A	App. D
Subgrade													
Avg. strength (psf)[e]	1225	1236	1202	1204	1254	1236	1235	1209	1195	1210	1133	1165	Figure 24
Avg. density (pcf)[f]	102.3	105.0	102.7	104.5	103.7	102.6	103.8	105.4	103.2	103.3	103.5	103.7	Figure 29
Water content (%)	25.2	22.4	23.1	22.9	22.5	23.1	23.1	21.5	22.9	22.5	22.6	22.2	Figure 29
Base Course													
Avg. thickness (in.)[g]	11.0	11.1	9.9	10.3	10.4	10.3	10.9	11.2	10.8	10.6	11.8	11.5	Figure 33
Avg. strength (CBR)[h]	18.1	18.7	17.5	18.9	16.1	15.7	20.5	24.0	23.3	18.8	21.7	23.3	Figure 34
Avg. dynamic stiffness (ksf)[i]	335	413	420	427	324	331	397	544	480	434	539	510	Figure 35
Avg. density (pcf)[f]	139.9	137.4	135.0	135.7	135.8	135.5	132.8	133.0	134.4	134.3	134.7	136.9	Figure 39
Water content (%)[f]	4.8	4.4	3.5	3.3	3.9	4.1	3.4	3.4	4.1	4.3	3.7	4.0	Figure 39

[a] Values were determined using the power curve estimations used in the BCR and TBR analyses; values greater than 740 are predicted
[b] Positive values indicate strength loss; negative values indicate strength gain
[c] Results of wide-width tests on the Propex Geotex 801 geotextile having a 1 in. gage length
[d] Junction strength and stiffness are for a single layer of material (three layer material)
[e] Undrained shear strength determine by in-field vane shear during construction (performance differences due to variance of subgrade strength was adjusted based on the performance of Test Section 1 and 2)
[f] From in-field nuclear density measurements
[g] Performance differences due to variance of base course thickness was adjusted based on the performance of Control 1, Control 2, and Control 3 test sections
[h] Base course strength determined by DCP measurements prior to trafficking
[i] Dynamic stiffness of base course as determined by LWD measurements prior to trafficking
N/A = not applicable
NT = not tested

SUMMARY, CONCLUSIONS AND RECOMMENDATIONS

This research project was initiated as a follow-on study to the study completed by Cuelho and Perkins in 2009 (Phase I). In that study, it was found that geosynthetic-reinforced test sections constructed on a weak subgrade and topped with a relatively thin layer of base aggregate carried very few passes of a fully-loaded three-axle dump truck. Results from that study indicated that, under those conditions, the tensile strength of the geosynthetic reinforcement was primarily linked to performance and that current design methodologies for subgrade stabilization applications had inadequately predicted the depth of base course needed to stabilize the roadway. To further investigate the performance of geosynthetics under less severe conditions, new test sections were constructed with thicker base course. In addition, a broader set of material tests were conducted to more thoroughly evaluate the potential relationship between geosynthetic material properties and the relative performance of the test sections.

Summary

Full-scale test sections were constructed, trafficked and monitored at TRANSCEND, a full-scale transportation research facility managed by the Western Transportation Institute, to compare the relative operational performance of geosynthetics used as subgrade stabilization. In all, 17 test sections were constructed – 14 containing geosynthetic reinforcement and three without. Each test section was 50 ft. long. Subgrade soil was prepared and installed in a trench 16 ft. wide, 3 ft. deep and 860 ft. long. The average constructed strength of the subgrade was 1.79 CBR with the exception of two test sections reinforced with BX Type 2 geogrid, one of which purposely was constructed to 2.17 CBR and the other at 1.64 CBR. These test sections were constructed to determine the effect that subgrade strength had on the performance of the test sections. Reinforced test sections were constructed with an average base course thickness of 10.9 in. The base thickness was primarily based on results of the cyclic plate load test reinforced with BX Type 2 geogrid topped with 10 in. of base course. The Control 2 and Control 3 test sections were purposely constructed with thicker base course (16.3 in. and 24.9 in., respectively) to evaluate the effect of base thickness on test section performance. Information from the test sections that were purposely constructed with different subgrade strength and base course thickness were used to correct any variability in the remaining reinforced test sections.

Strength and consistency of the subgrade during construction was monitored using a variety of methods including vane shear, LWD, DCP, moisture content, in-field CBR, and nuclear densometer. The subgrade was built in 6 layers each approximately 6 in. deep. Placement was accomplished using a large excavator, final smoothing was done with a skid-steer tractor and a smooth-drum roller was used to compact the layer. Once the subgrade was built to the top of the trench, the subgrade was smoothed and the geosynthetics and instrumentation were installed. The base course aggregate was prepared to the proper moisture content and carefully placed on top of the geosynthetics in two lifts using a skid steer tractor. A large screed was used to create a

uniform thickness of gravel over the test sections and a smooth-drum vibratory roller was used to compact the base aggregate. In addition to a topographic survey, the final surface of the base course was measured using DCP, nuclear densometer, LWD and CBR.

A fully-loaded, three-axle dump truck was used to traffic the test sections. Measurements of longitudinal rut, transverse rut, geosynthetic displacement, geosynthetic strain and subgrade pore-water pressure were taken during trafficking. Trafficking of the test sections ran from mid-September to early November 2012. The speed of the truck was about 5 mph and always in one direction. Trafficking continued until rut levels reached approximately 3 in. – defined as failure in this project. Repairs to the rut were made by placing additional gravel in the rutted areas using a skid-steer loader and leveling the surface once a significant portion of a test section reached 3 in. of rut. This allowed the remaining un-failed portions of the test sections to be further trafficked.

Longitudinal rut measurements were periodically made at 40-inch intervals along the two rut paths formed by the truck. In addition, transverse rut measurements were made in two locations within each test section coincident with the instrumentation. Rut measurements were based on changes in elevation of the measurement points over time as compared to a baseline measurement made before trafficking. The accumulation of rut as a function of truck passes revealed that the woven geotextile (Mirafi RS580i) performed the best, followed by BX Type 2 geogrid, Secugrid 30-30 Q1 geogrid and the non-woven geotextile (Geotex 801). The poorest performance was observed in the Fornit 30, SF 12 and TX160 geogrids. Quantitative comparisons between test sections were made using a two sample t-test to determine whether the average rut in the various test sections are truly different from one another. Overall, the comparisons of the means were different from one another 84.8 percent of the time and any similarities between test sections were random and indicated no definite trends.

Further analysis of the longitudinal rut data was conducted to determine which geosynthetic material properties were most related to the performance of a particular test section. This analysis was conducted at various rut depths (1.0, 2.0 and 2.5 inches) to determine whether different material properties affected performance at various levels of rut. A linear regression analysis was performed using wide-width tensile strength and stiffness, cyclic tensile stiffness, resilient interface shear stiffness, junction strength and stiffness, and aperture stability modulus. Overall, the analysis of rut from this project revealed that strength and stiffness of the junctions in the cross-machine direction and wide-width tensile strength at 2 and 5 percent were chiefly related to the performance of the geogrid-reinforced test sections.

The performance of geosynthetics as subgrade stabilization is dependent on the constructed properties of the road being stabilized. In situations where there is less structural benefit from the gravel base course layer and more benefit is expected of the geosynthetic (as in Phase I), stiffness and tensile strength play a greater role in rut suppression, especially given the rapid deterioration of these test sections under traffic load. In addition, the strength and stiffness of the

junctions in the cross-machine direction plays a role, but diminishes as rut continues to increase. Conversely, in situations where there is more base course and rut development is less rapid (as in this project), the role of junction stiffness and strength is more apparent as reliance on this property for performance increases as a function of rut. Coupled with this is the early dependence on the stiffness of the geosynthetic as loads are transmitted into the material, especially in the cross-machine direction as the geosynthetic confines the base aggregate as it spreads laterally under the applied load. Once the material has been engaged in this way, further transmission of lateral loads are borne by members in the machine direction of the material as they transmit the load into the cross-machine load bearing members (i.e., junction strength and stiffness).

The transverse behavior of the test sections was characterized using transverse rut measurements (taken perpendicular to traffic), displacement measurements, and strain measurements. Bearing capacity failure was evident based on the heaving of the road surface adjacent to the wheel path. Heave occurred at different traffic levels within each test section, but most began around 100 to 300 truck passes, and test sections that began to heave earlier generally approached failure earlier. Near saturation moisture contents in the subgrade indicates that rutting of the subgrade is primarily due to distortional shearing and not compaction (i.e., volumetric compression).

Long-term and dynamic displacement and strain data were collected during trafficking to further characterize the transverse behavior of the test sections through the movement and strain in the material at two locations along the west edge of the wheel path. Early displacements generally accumulate in a positive direction indicating global movement of the geosynthetic to the west (away from the rutted area). After about 40 truck passes the sensors begin to move toward the rutted area as the geosynthetic is pulled down into the forming rut. This reversal of the direction in movement is coincident with the point of inflection from positive to negative slope in the displacement responses. Similar behavior was evident in several of the test sections, with some test sections making this transition at lower or higher numbers of truck passes. This behavior indicates a transition between lateral confinement of the base course by the geosynthetic to membrane support involving deeper rutting and the tensioned-membrane effect. Changes in displacement revealed similar results to the heave and longitudinal rut response, namely, those test sections where the direction of the displacements transitioned earlier also reached higher levels of longitudinal rut earlier. This transition generally occurred at or before about 2 in. of longitudinal rut.

Strain from the strain gages was measured in two locations within each test section near the edge of the outside wheel of the truck on the west rut path. Considering all of the test sections, maximum strains from the dynamic strain data ranged from about 0.3 to 2.8 percent. Maximum dynamic strains from a single truck pass ranged from about 0.3 percent to 1.5 percent. Similar results were obtained from the long-term strain data, which showed that maximum accumulated strains ranged from about 0.3 to 3.0 percent.

Two forensic investigations were conducted as part of this project: one immediately after trafficking had terminated and a second eight months later. During each of these visits, construction equipment was used to remove the base and subgrade layers so that large samples of the geosynthetic could be removed to assess damage and evaluate tensile properties, and to facilitate strength, stiffness and moisture measurements of the base and subgrade. The excavation of the base course, geosynthetic and subgrade provided a good opportunity to evaluate the shape of the rut in the two wheel paths, distortion of the geosynthetic from trafficking and rut accumulation, pullout, and other qualitative assessments.

Conclusions

The following conclusions were made from the work performed during this project:

- A linear regression analysis to characterize the relationship between geosynthetic material properties and the rut performance of the test sections indicated that junction strength and stiffness of the geosynthetic, wide-width strength, and cyclic stiffness in the cross-machine direction correlate reasonably well with rut performance.

- A similar analysis using data from test sections from Phase I (Cuelho and Perkins, 2009) constructed with thinner base aggregate revealed that correlations between rut performance and junction stiffness peaked at about 3 in. of rut, and that correlations between rut and wide-width tensile strength in the cross-machine direction at 2 and 5 percent and cyclic stiffness at 0.5 to 2 percent increased as rut increased.

- The transverse rut analysis indicated that the primary mechanism of reinforcement was lateral confinement at lower rut levels and transitioned to membrane support after about 2 in. of rut or less than 300 truck passes, as evident in the heave characteristics and also supported by the analysis using displacement and strain instrumentation.

- The results of the base course reduction (BCR) analysis indicated that the greatest reduction in base thickness was approximately 26.9 percent (TenCate Mirafi RS580i) corresponding to a difference of 4.0 in. of gravel; the least was 10.2 percent (Huesker Fornit 30) corresponding to 1.2 in. of gravel. These comparisons are valid for situations where additional gravel would be sufficient to allow heavy construction equipment to operate on the weak subgrade without excessive rutting or other damage.

- The results of the traffic benefit ratio (TBR) analysis indicated that the greatest benefit was achieved by using the TenCate Mirafi RS580i geotextile, resulting in an improvement of almost 11 times the traffic level when compared to the

unreinforced test section (Control 1). The smallest TBR was in the Huesker Fornit 30 test section (TBR = 2.3).

- The woven geotextile (TenCate Mirafi RS580i) performed the best, but further research is needed to more clearly determine which material properties are associated with its performance. Surface friction properties and tensile strength of these materials likely contributes to their good performance. It is suggested that geotextiles with sufficient surface roughness and/or tensile strength be selected for this application. This product did not pull out during trafficking.

- Likewise, the non-woven geotextile (Propex Geotex 801), although the weakest product in terms of tensile strength, performed better than many of the geogrid products. Further research is also needed to determine the reasons for its good performance.

- A limited number of stiffness measurements made on the surface of the subgrade and base course during the forensic investigations revealed potential correlations to rut performance, indicating that the LWD device may potentially be used to help predict performance of geosynthetics when used in subgrade stabilization applications.

- From the samples of geosynthetic extracted during the forensic investigations, junctions were mostly intact for all of the materials, and the majority of junction damage was in the rutted area. Junctions on the integrally-formed, extruded geogrids and the Mirafi BXG11 woven geogrid experienced little to no junction damage. The junctions of the Synteen SF11 woven geogrid and the Enkagrid MAX30 welded geogrid sustained moderate damage, and the Synteen SF12 and Huesker Fornit 30 products sustained the highest junction damage.

- Most of the damage to the ribs was located in the rutted area. The integrally-formed and extruded geogrids, Mirafi BXG11 woven geogrid, and the Enkagrid MAX 30 welded geogrid experienced little to no rib damage in either direction. The ribs of the remaining woven geogrid products sustained the most damage. The Synteen SF11, Synteen SF12, and Huesker Fornit 30 woven geogrid products sustained the greatest rib damage of all the materials in this study. Forensic excavations of the Tensar TX140 and TX160 materials conducted immediately after trafficking in areas of high rut revealed that these materials had ruptured.

- The geotextiles (TenCate Mirafi RS580i and Propex Geotex801) sustained no noticeable damage (e.g., tears, holes, significant wear or broken fibers) from construction and trafficking. Continuity of the geotextile products ensured their ability to separate the subgrade and base course layers over time, thereby

minimize intermixing of layers and preserving the structural integrity of the base course.

- Post-trafficking assessments of the tensile properties of the geosynthetics indicated that the majority of the geosynthetic strengths at 2 percent strain increased and the ultimate strengths decreased when compared to the virgin materials. The greatest tensile strength loss was measured in the Synteen SF12 and Huesker Fornit 30 woven geogrids, and overall, the integrally-formed grids showed the smallest loss of strength.

- Based on data from the control test sections, the pore-water pressure measurements and corresponding predictions of subgrade CBR loss show decreasing values as the base thickness increases. A simple linear regression analysis indicated that there is not a clear trend as to pore-water pressure development and performance of the geosynthetics.

Recommendations

The results of this study indicated that strength and stiffness of the junctions and tensile members mainly contribute to the performance of geosynthetics when used as subgrade stabilization, and the relative contribution of these material properties depends on the thickness of the base course aggregate layer and the anticipated rut depth. Practitioners who wish to use geosynthetics as subgrade stabilization should consider specifying minimum values for material properties that correlated with good performance of the test sections. These minimum values can be categorized by the severity of the site conditions, ranging from moderate to severe, as demonstrated in the two phases of this project. Further work is necessary to more confidently specify minimum values for geosynthetic material properties associated with good rut performance. The specified properties are mutually important, and products having only one of the specified properties may not perform well. Further research is necessary to determine the combined effect of these properties as they relate to subgrade stabilization of a greater variety of base thicknesses and subgrade strengths. Information from that research could be used to augment or determine specific design parameters for a wider range of subgrade stabilization applications. Despite the fact that the woven and non-woven geotextiles performed well in the field study, it is unknown which material properties are directly responsible for their performance. Intuitively, surface friction properties and tensile strength of the materials plays an important role however, additional work is needed to evaluate the effect individual geotextile properties have on their performance in subgrade stabilization applications.

REFERENCES

Christopher, B., Perkins, S., Lacina, B., and Marr, A. (2009) "Pore Water Pressure Influence on Geosynthetic Stabilized Subgrade Performance." Proceedings: Geosynthetics 2009, February 25-27, Salt Lake City, UT, pp. 215-221.

Cuelho, E., Christopher, B., Perkins, S. (2008) "Small Strain and Displacement Monitoring Methods for Geosynthetics under Monotonic and Cyclic Loading" Proceedings: Geoamericas 2008 Conference, IFAI, March 2-5, Cancun, Mexico.

Cuelho, E. and Perkins, S. (2009) "Field Investigation of Geosynthetics Used for Subgrade Stabilization" Final report to the Montana Department of Transportation, FHWA/MT-09-003/8193, 140 pp.

Fannin, R.J. and Sigurdsson, O. (1996) "Field Observations on Stabilization of Unpaved Roads with Geosynthetics." Journal of Geotechnical Engineering. Vol. 122, no. 7, pp. 544-553.

Haliburton, T., Lawmaster, J. and McGuffey, V. (1981). Use of Engineering Fabrics in Transportation Related Applications, Federal Highway Administration, FHWA DTFH61-80-C-00094.

Holtz, R., Christopher, B. and Berg, R. (2008) Geosynthetic Design and Construction Guidelines. U.S. Department of Transportation, Federal Highway Administration, Washington DC, Report No. FHWA-NHI-07-092, 592 pp.

Huang, Y. (2004) *Pavement Analysis and Design*, 2nd Edition, Prentice Education Inc., Upper Saddle River, NJ, 775p.

Hufenus, R., Rueegger, R., Banjac, R., Mayor, P., Springman, S.M., and Bronnimann, R. (2006) Full-Scale Field Tests on Geosynthetic Reinforced Unpaved Roads on Soft Subgrade. Geotextiles and Geomembranes. vol. 24, no. 1, pp. 21–37.

Kessler Soils Engineering Products (2010) User's Manual for K-100 Models Dynamic Cone Penetrometer.

Kinney, T. (2000) Standard Test Method for Determining the "Aperture Stability Modulus" of a Geogrid, Seattle, Shannon & Wilson, Inc.

Morris, Z. (2013) "Evaluation of Transverse Behavior of Geosynthetics When Used For Subgrade Stabilization," Thesis submitted in partial fulfilment of Master's degree, Montana State University, Bozeman, MT.

Peck, R.B., Hanson, W.E., and Thornburn, T.H. (1974) *Foundation Engineering*, 2nd ed., Wiley, New York.

Perkins, S. and Christopher, B. (2010) "Development of Design Charts for Unpaved Road Using NAUE Geosynthetics: Phases I, II & III," Final report to NAUE GmbH & Co. KG.

Tingle, J. and Webster, S. (2003) "Corps of Engineers Design of Geosynthetic-Reinforced Unpaved Roads" Transportation Research Record 1849, pp.193-201.

APPENDIX A – WIDE-WIDTH TENSION LOAD-DISPLACEMENT REULTS
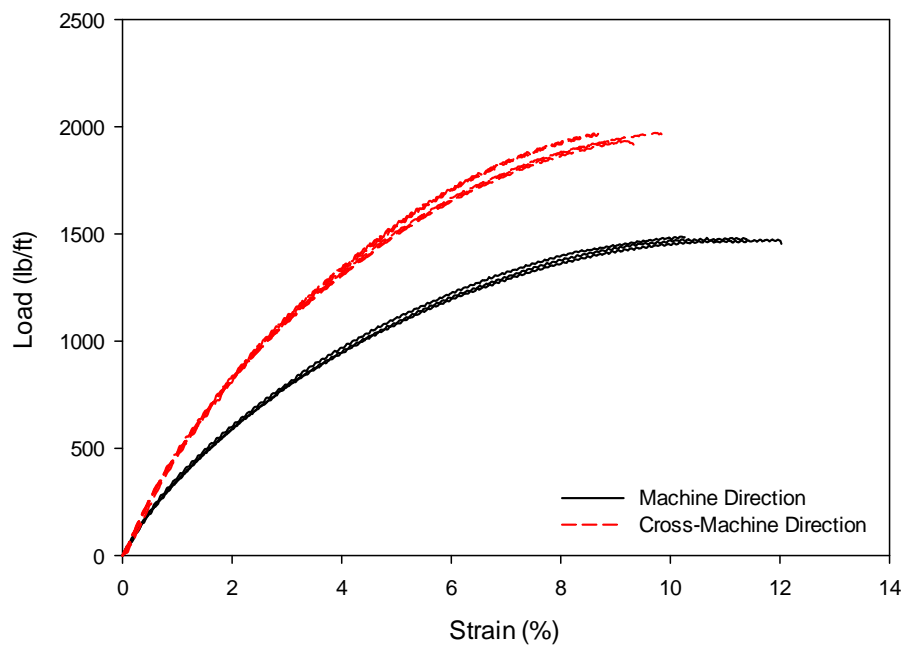
Figure A-1: Wide-width tension results for Tensar BX Type 2.
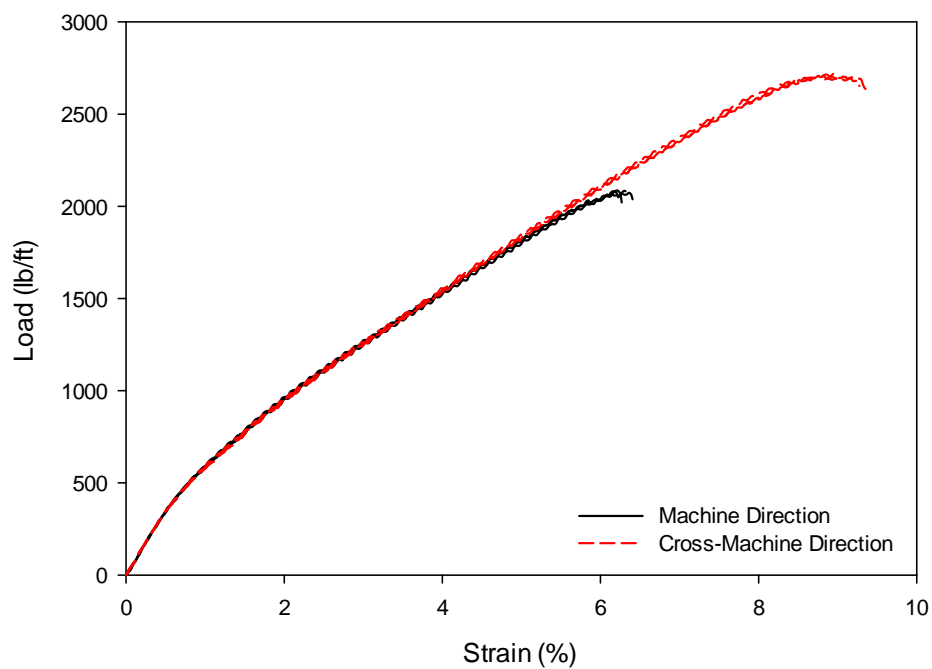
Figure A-2: Wide-width tension results for NAUE Secugrid 30/30 Q1.
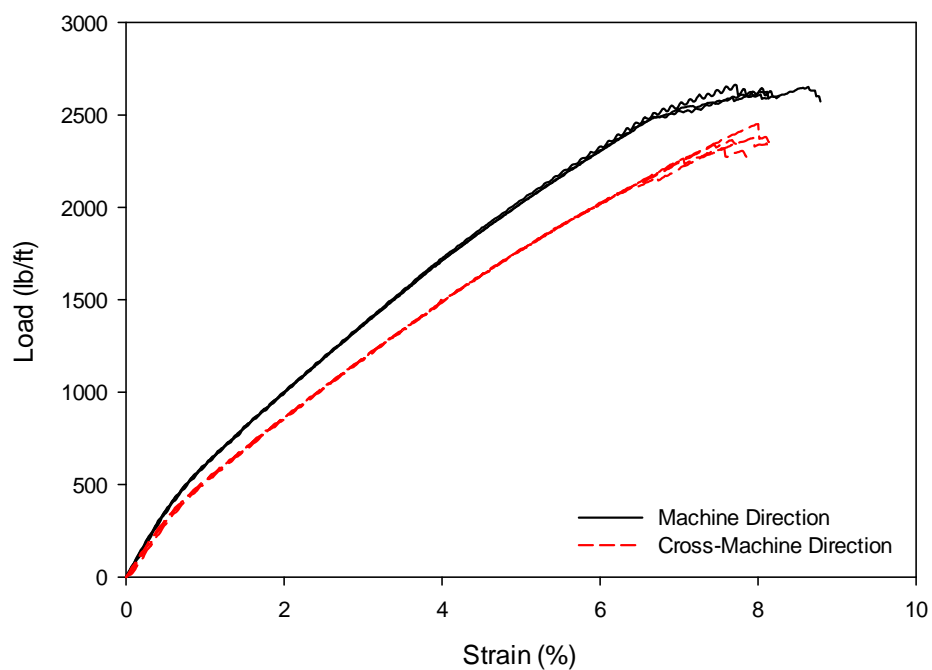
Figure A-3: Wide-width tension results for Colbond Enkagrid Max 30.
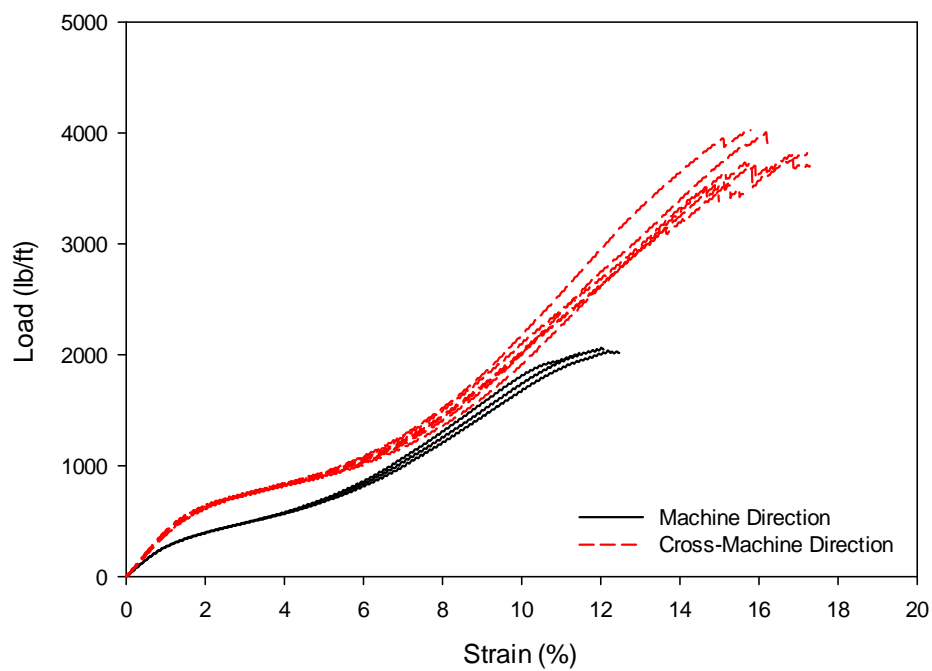
Figure A-4: Wide-width tension results for Synteen SF-11.
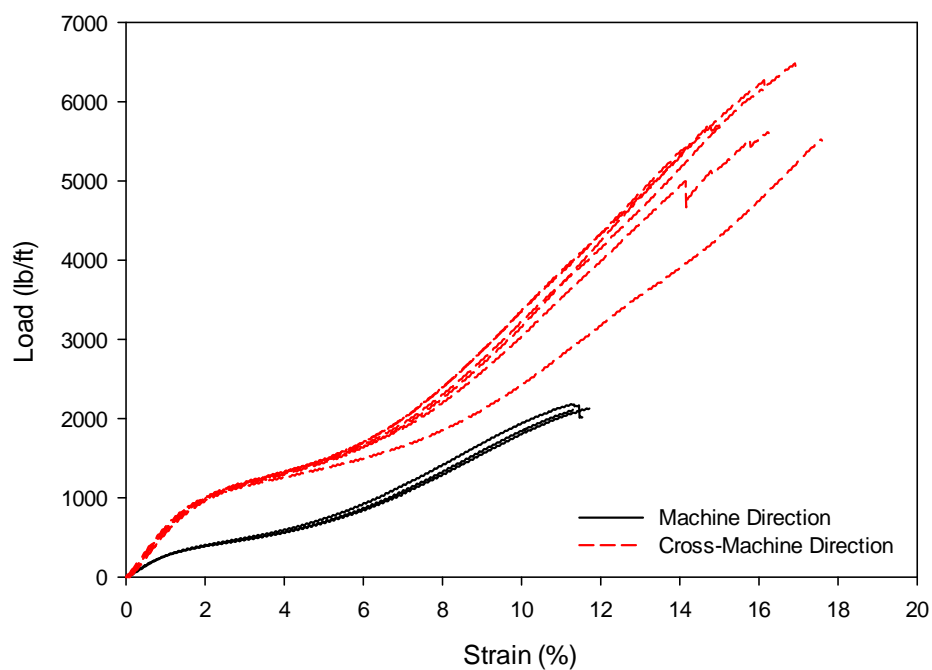
Figure A-5: Wide-width tension results for Synteen SF-12.
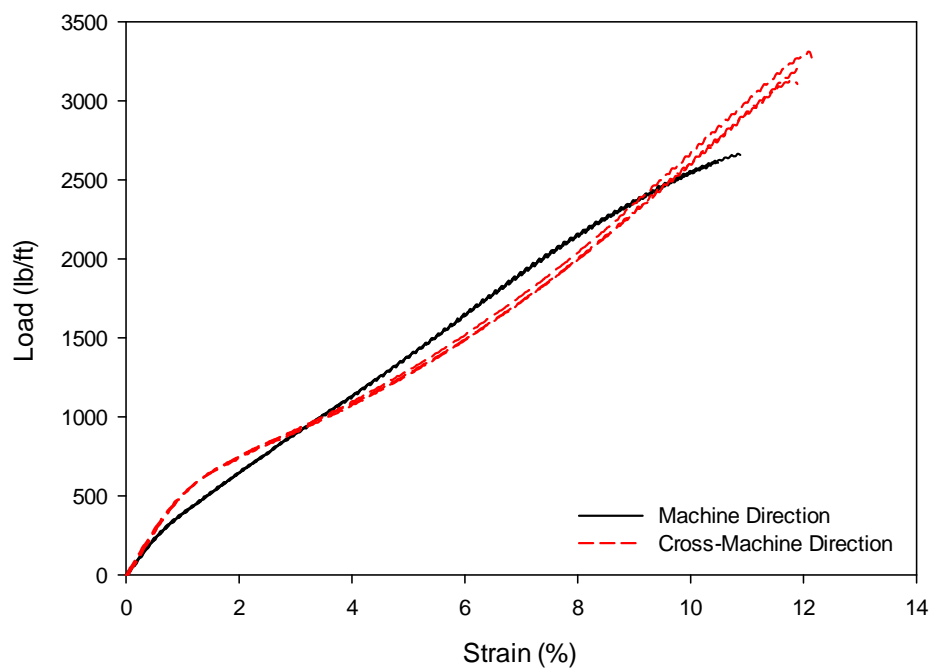
Figure A-6: Wide-width tension results for TenCate Mirafi BXG-11.
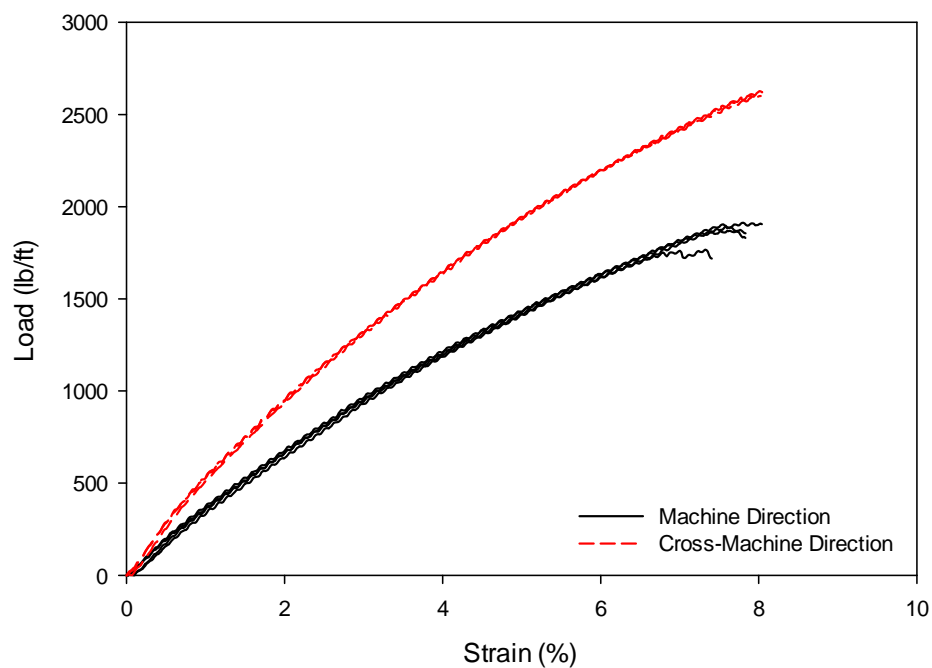
Figure A-7: Wide-width tension results for Huesker Fornit 30.
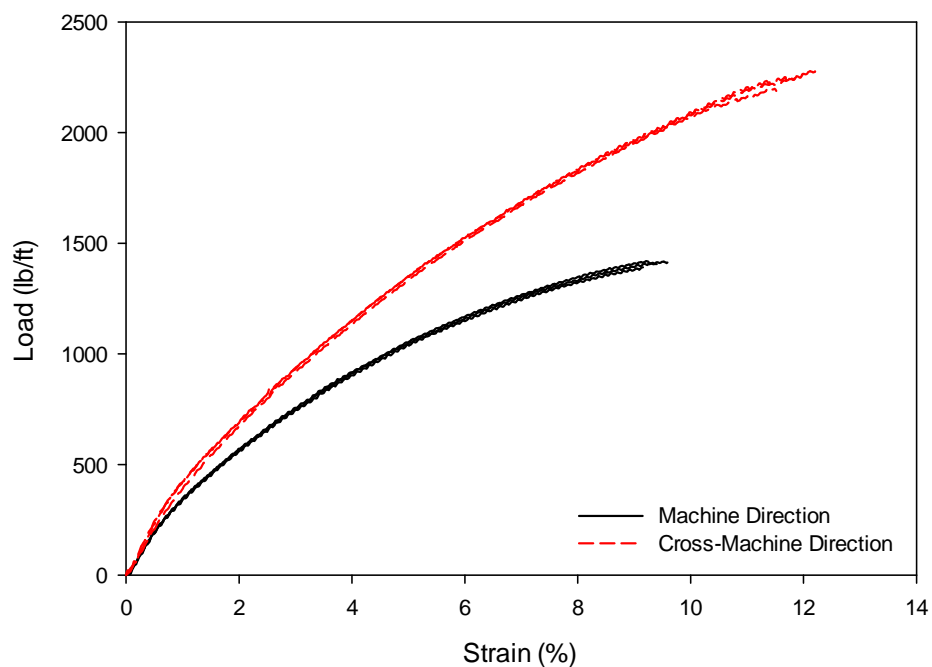
Figure A-8: Wide-width tension results for SynTec Tenax MS 330.
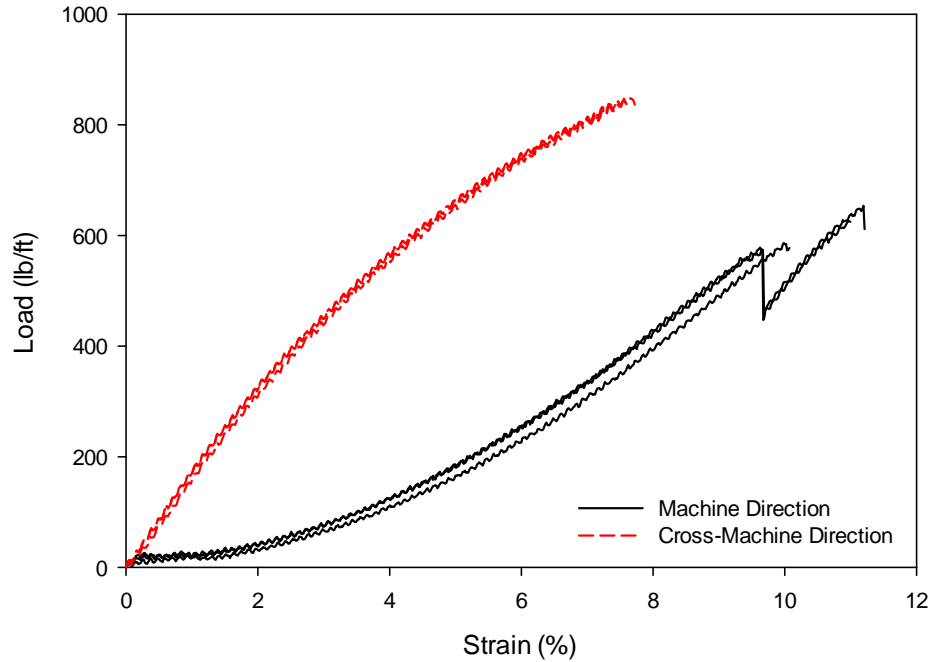
Figure A-9: Wide-width tension results for Tensar TX 140.
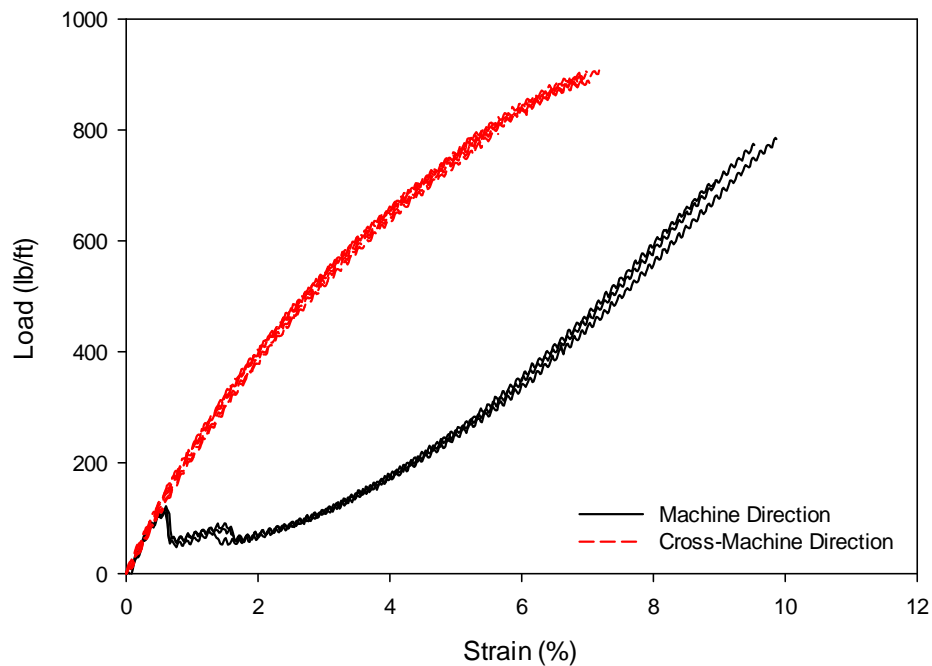
Figure A-10: Wide-width tension results for Tensar TX-160.
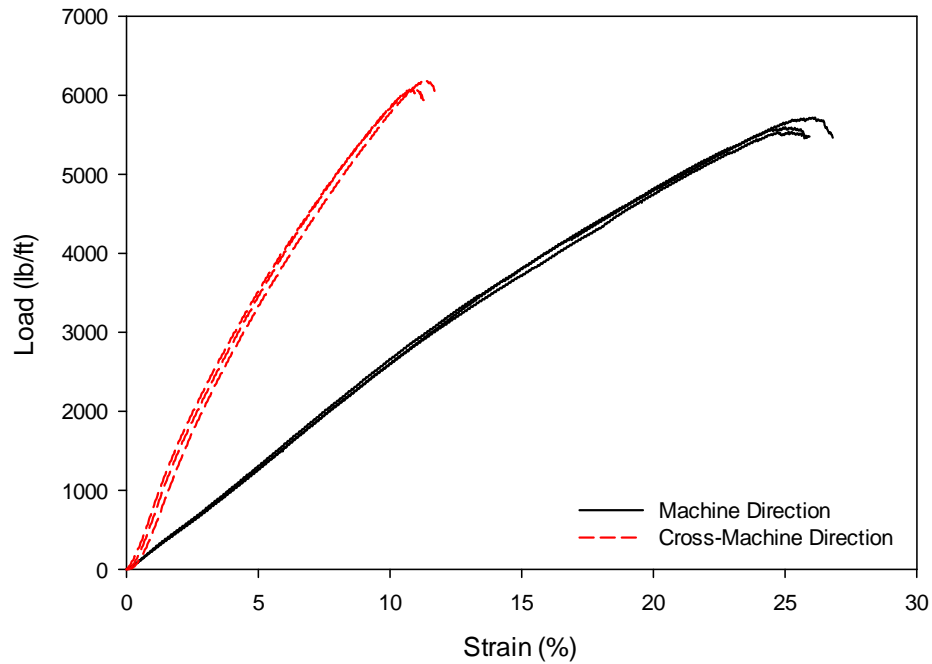
Figure A-11: Wide-width tension results for TenCate Mirafi RS580i.
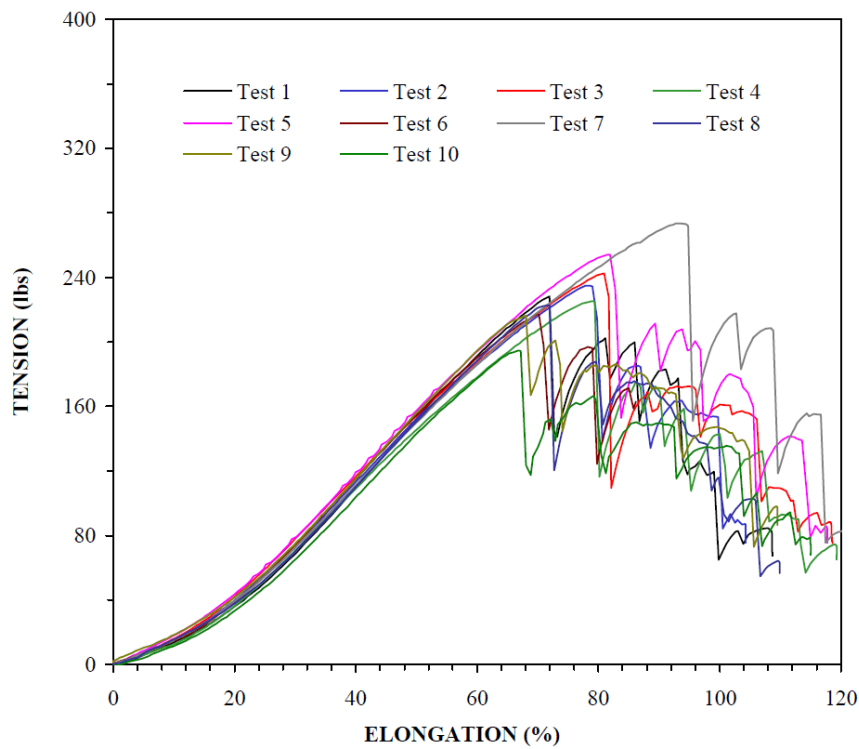
Figure A-12: Grab tensile strength in the machine direction for Propex Geotex 801.
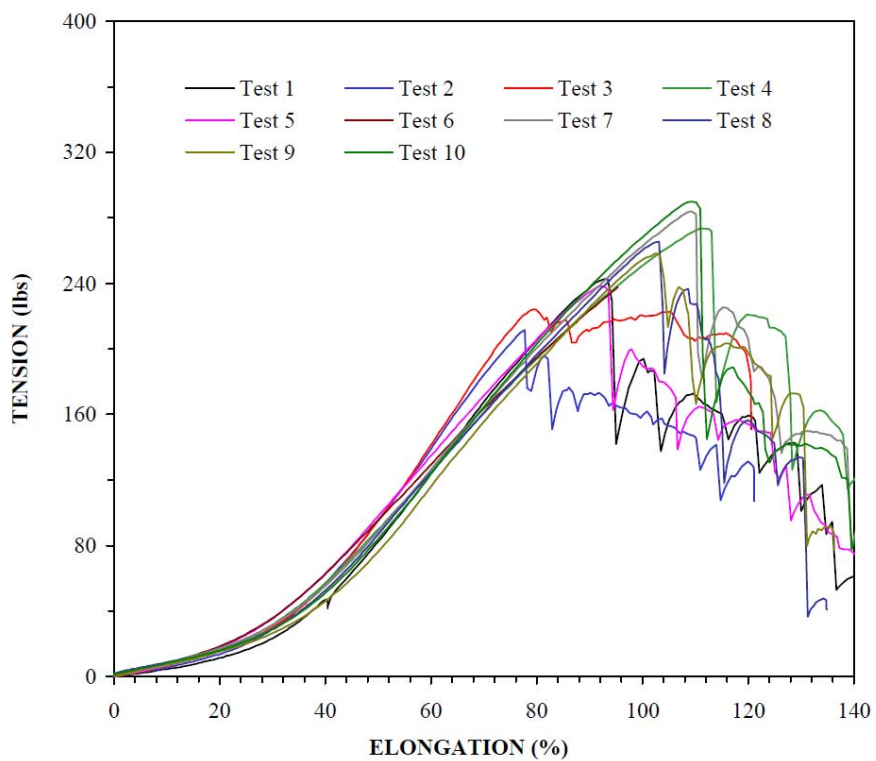
Figure A-13: Grab tensile strength in the cross-machine direction for Propex Geotex 801).

APPENDIX B – CYCLIC TENSILE STIFFNESS LOAD-DISPLACEMENT RESULTS
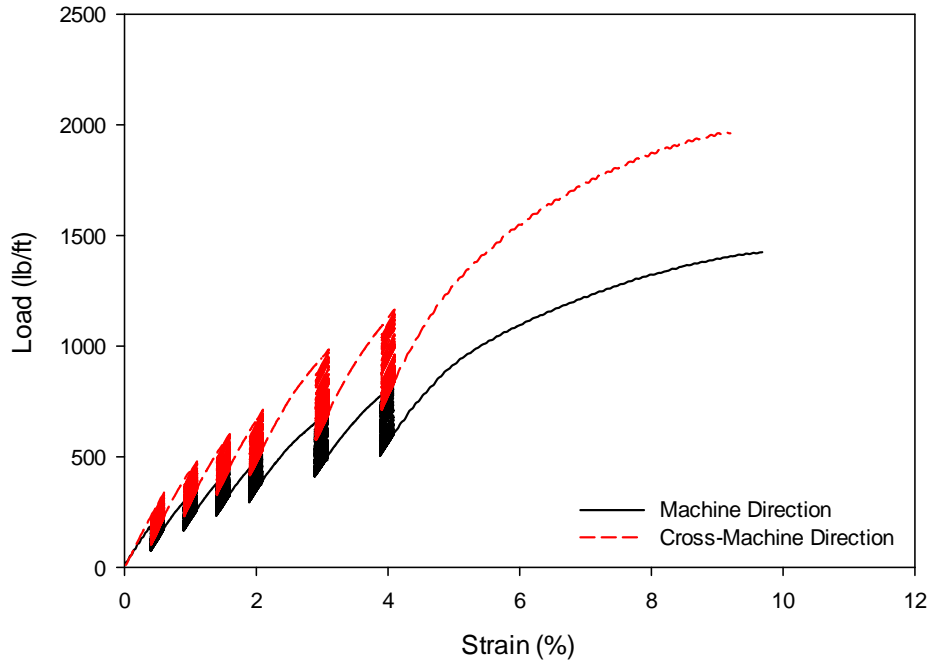
Figure B-1: Cyclic tensile stiffness for Tensar BX Type 2.
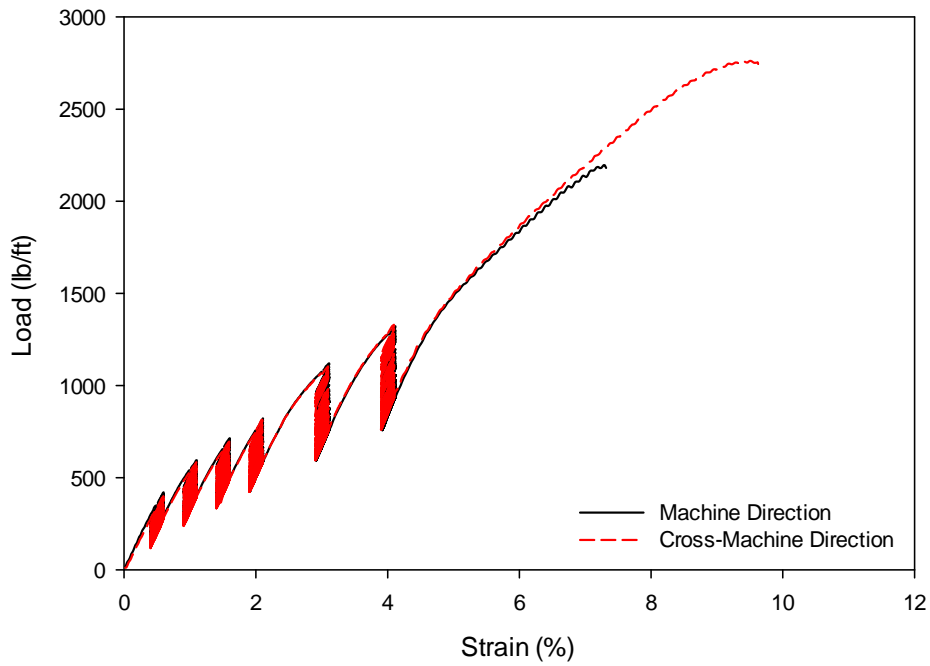
Figure B-2: Cyclic tensile stiffness for NAUE Secugrid 30/30 Q1.
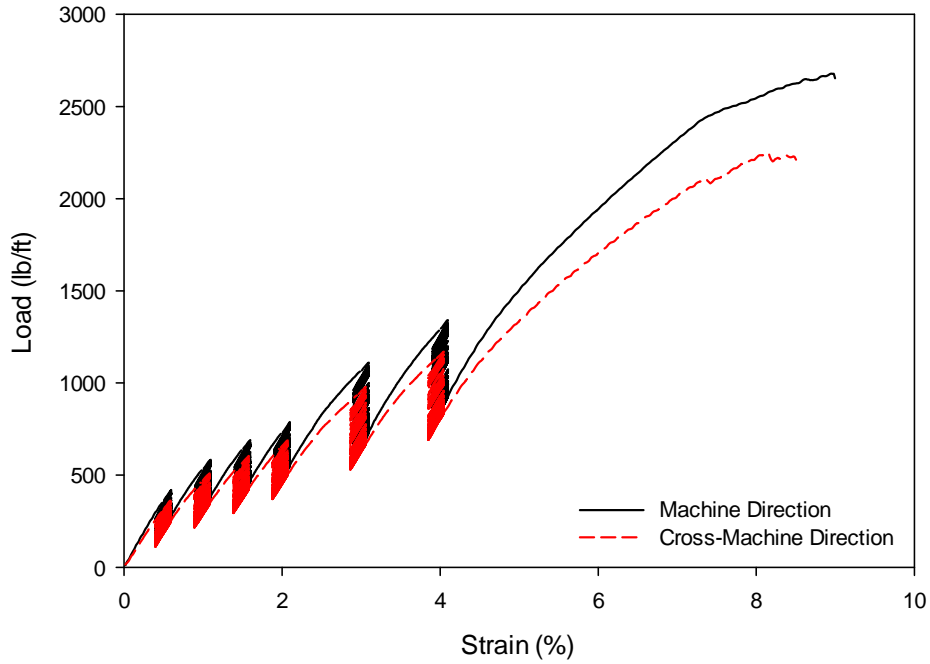
Figure B-3: Cyclic tensile stiffness for Colbond Enkagrid Max 30.
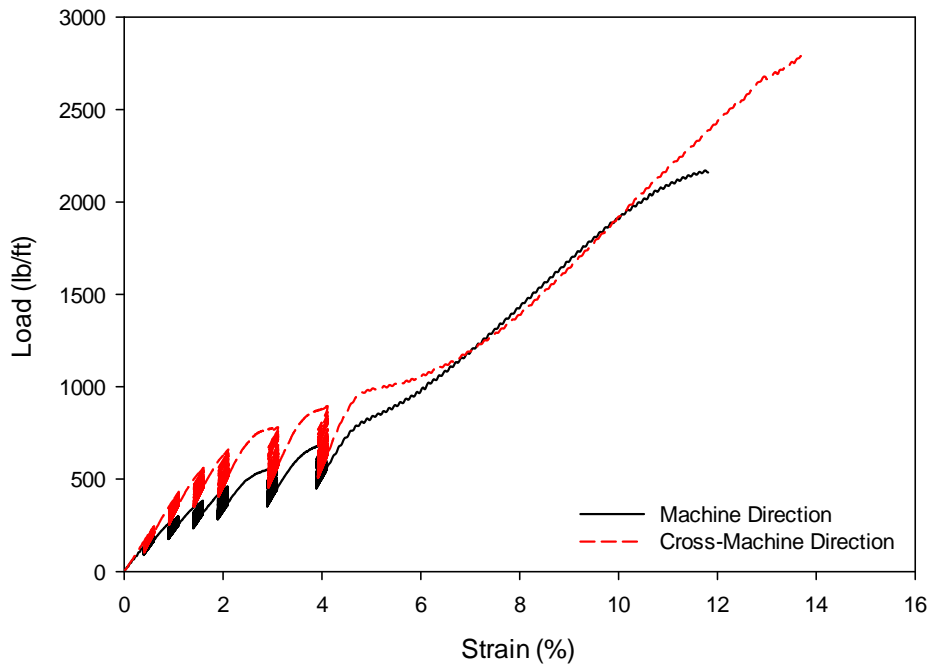
Figure B-4: Cyclic tensile stiffness for Synteen SF 11.
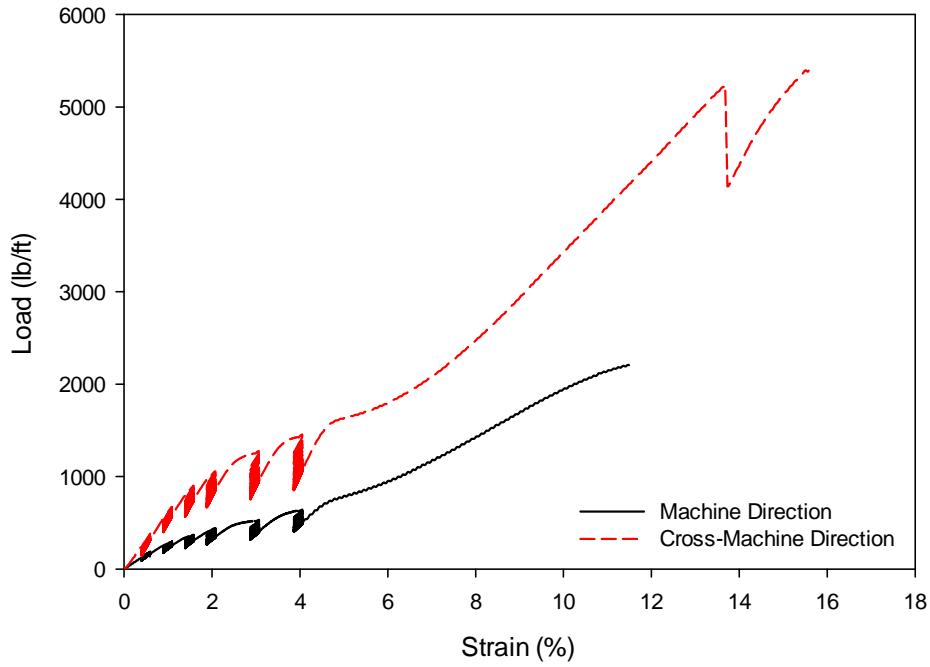
Figure B-5: Cyclic tensile stiffness for Synteen SF 12.
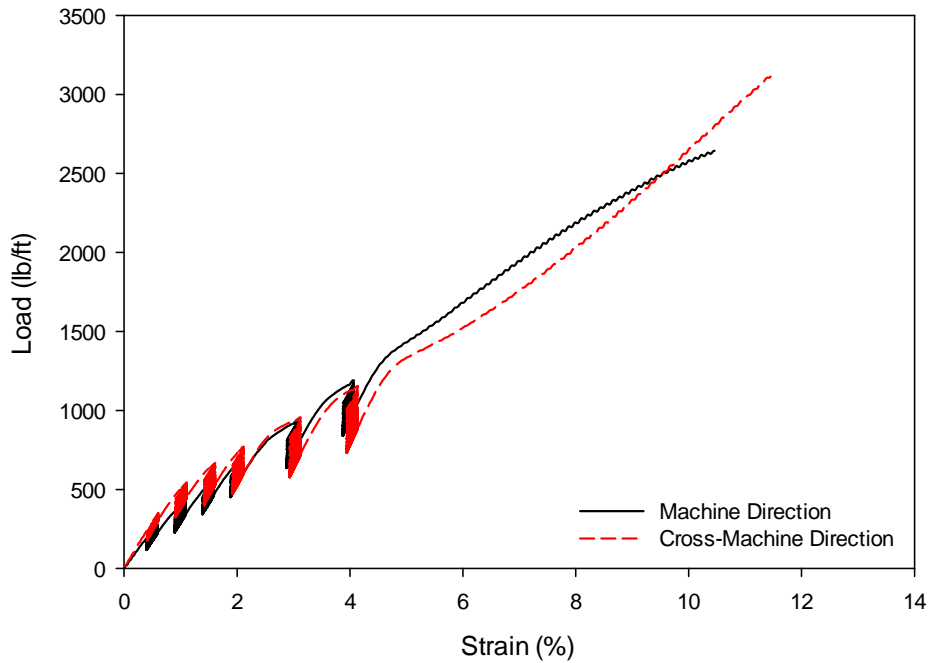
Figure B-6: Cyclic tensile stiffness for TenCate Mirafi BXG 11.
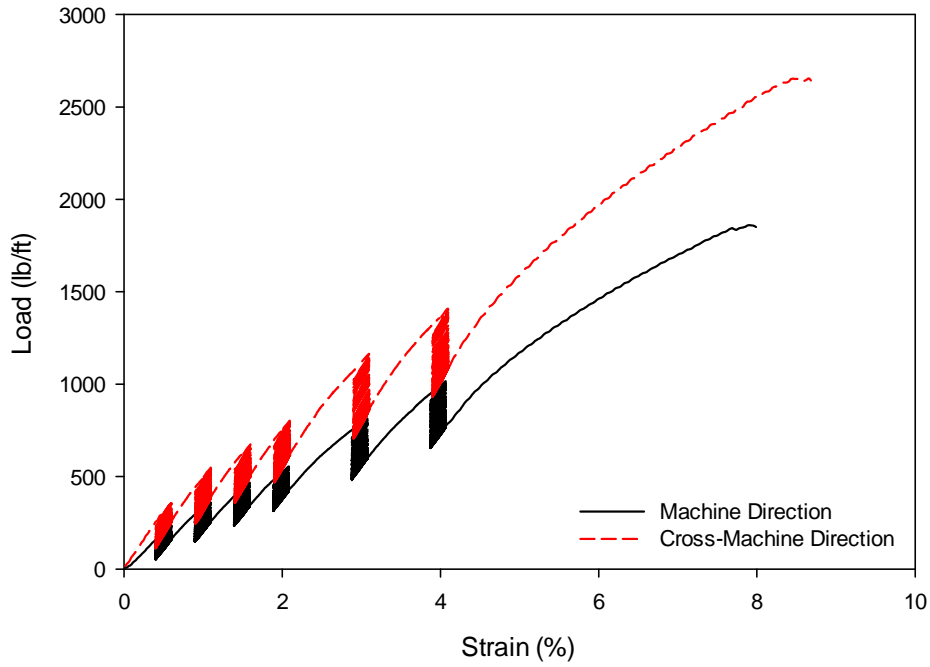
Figure B-7: Cyclic tensile stiffness for Huesker Fornit 30.
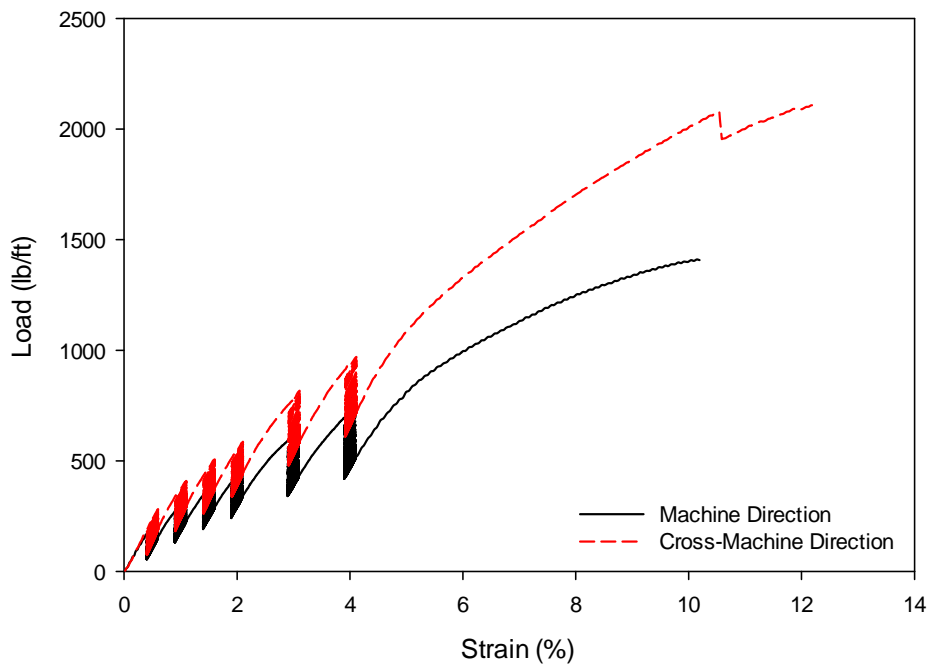
Figure B-8: Cyclic tensile stiffness for SynTec Tenax MS330.
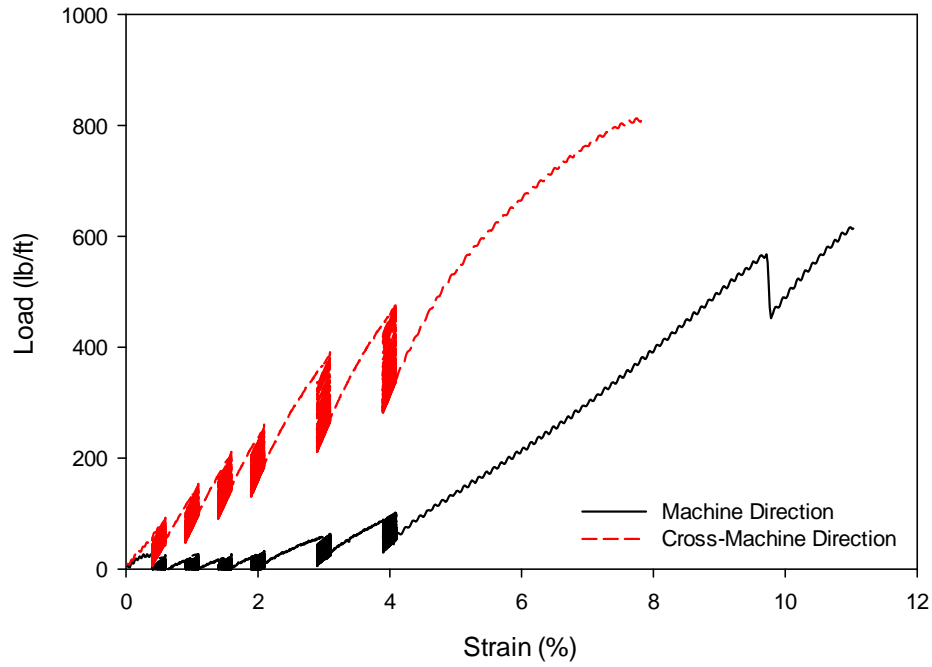
Figure B-9: Cyclic tensile stiffness for Tensar TX 140.
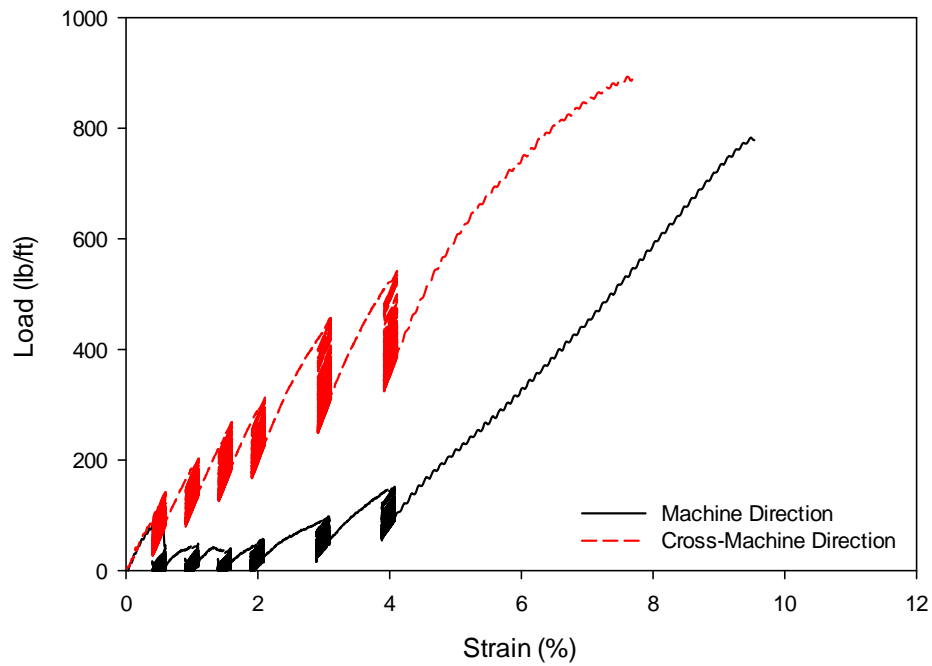
Figure B-10: Cyclic tensile stiffness for Tensar TX 160.
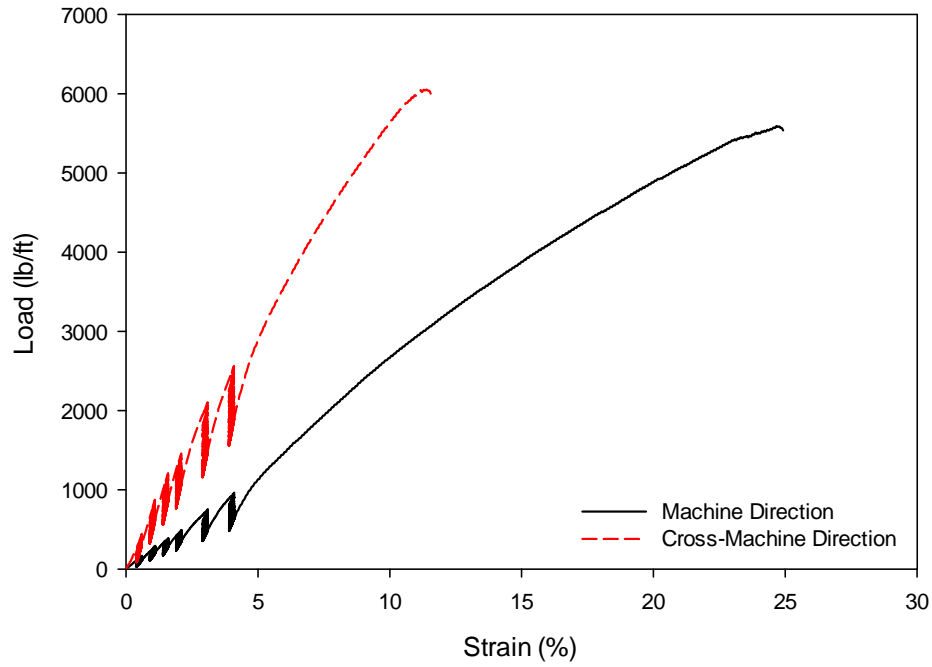
Figure B-11: Cyclic tensile stiffness for TenCate Mirafi RS580i.

APPENDIX C – RESILIENT INTERFACE SHEAR STIFFNESS PLOTS
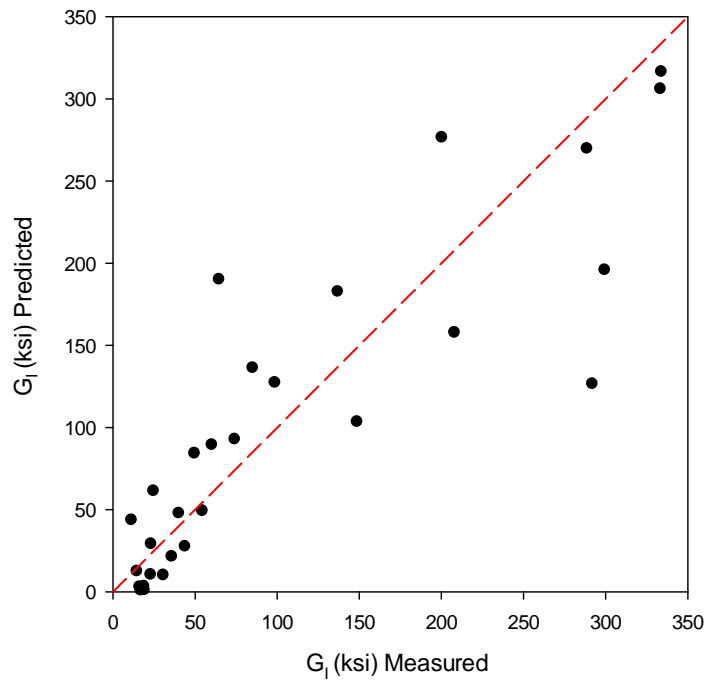
Figure C-1: Resilient interface shear stiffness for Tensar BX Type 2.
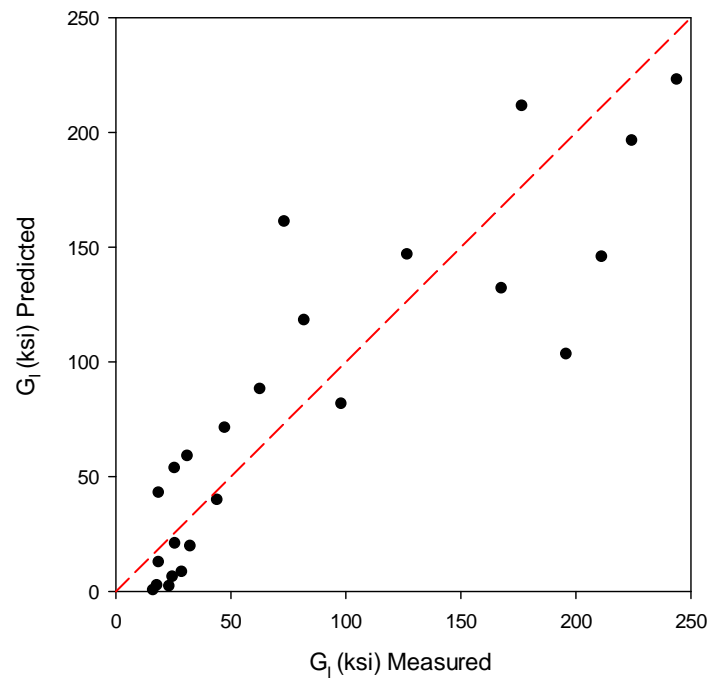
Figure C-2: Resilient interface shear stiffness for NAUE Secugrid 30/30 Q1.
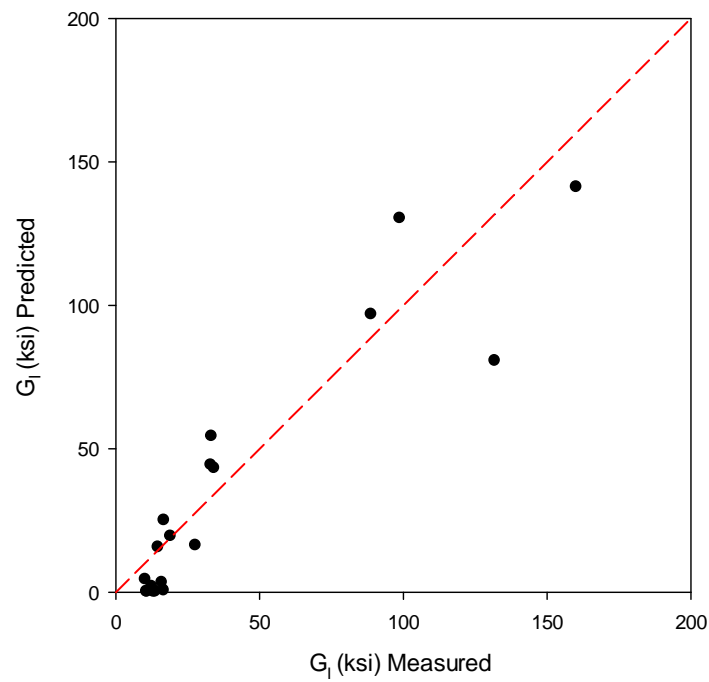
Figure C-3: Resilient interface shear stiffness for Colbond Enkagrid Max 30.
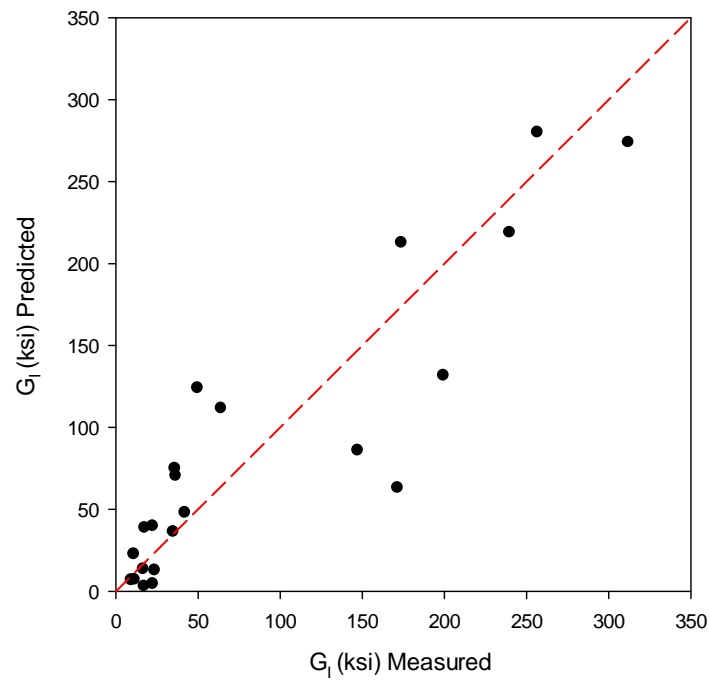
Figure C-4: Resilient interface shear stiffness for Synteen SF 11.
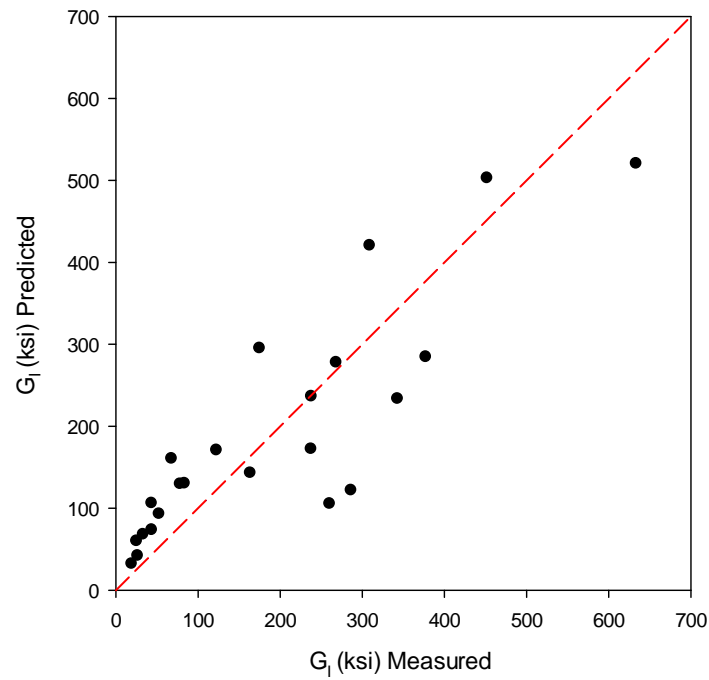
Figure C-5: Resilient interface shear stiffness for Synteen SF 12.
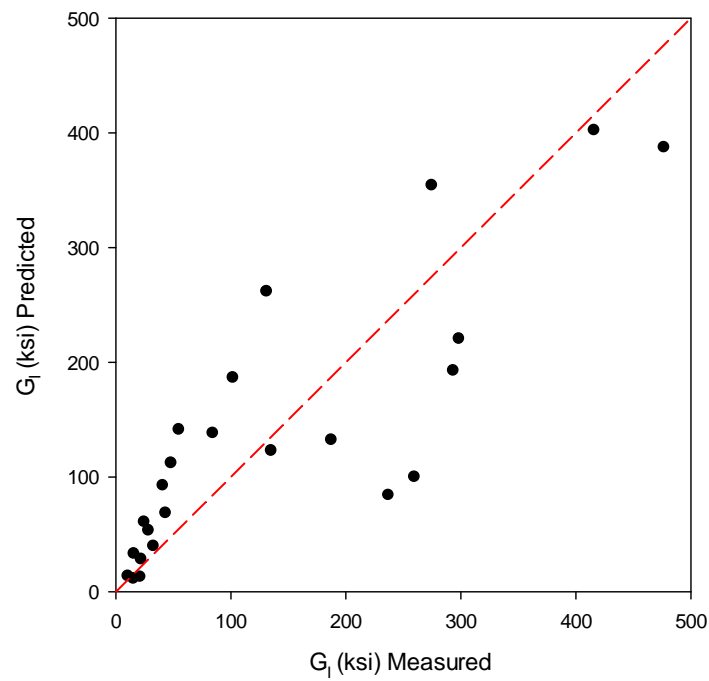
Figure C-6: Resilient interface shear stiffness for TenCate Mirafi BXG 11.
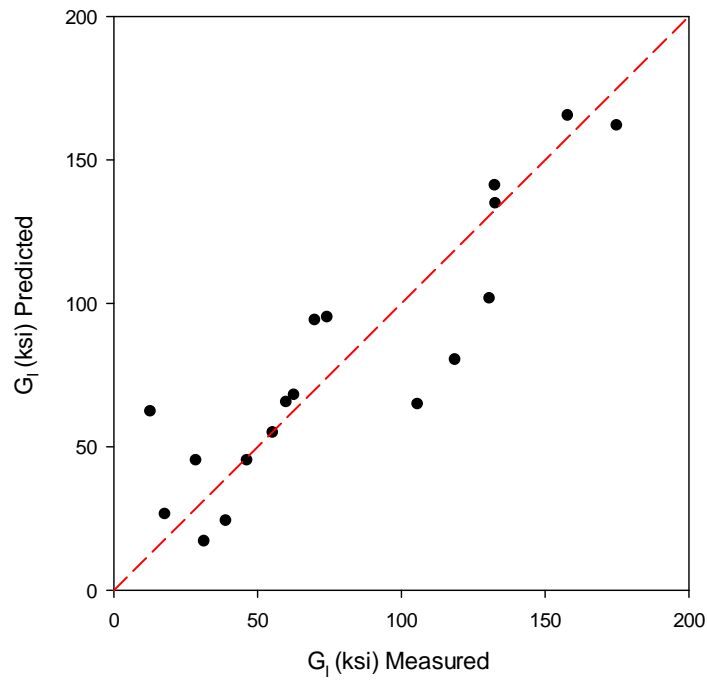
Figure C-7: Resilient interface shear stiffness for Huesker Fornit 30.
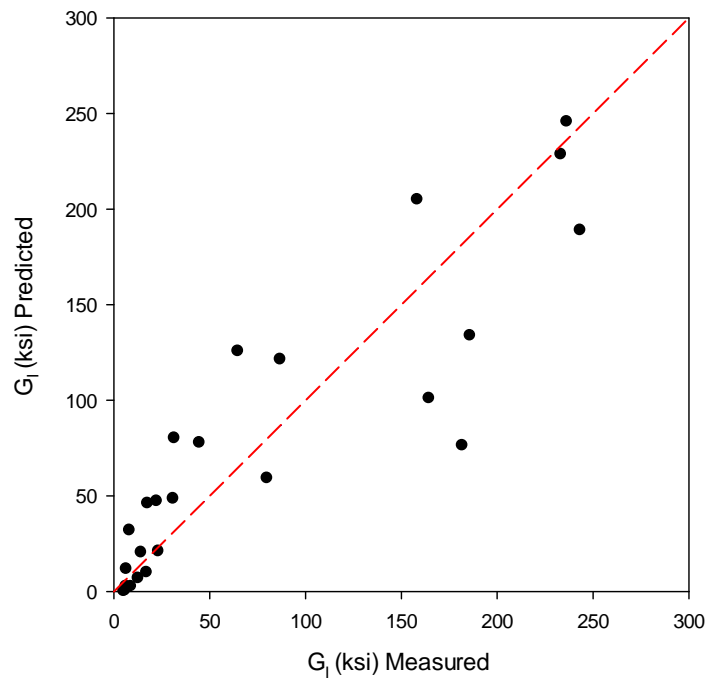
Figure C-8: Resilient interface shear stiffness for SynTec Tenax MS330.
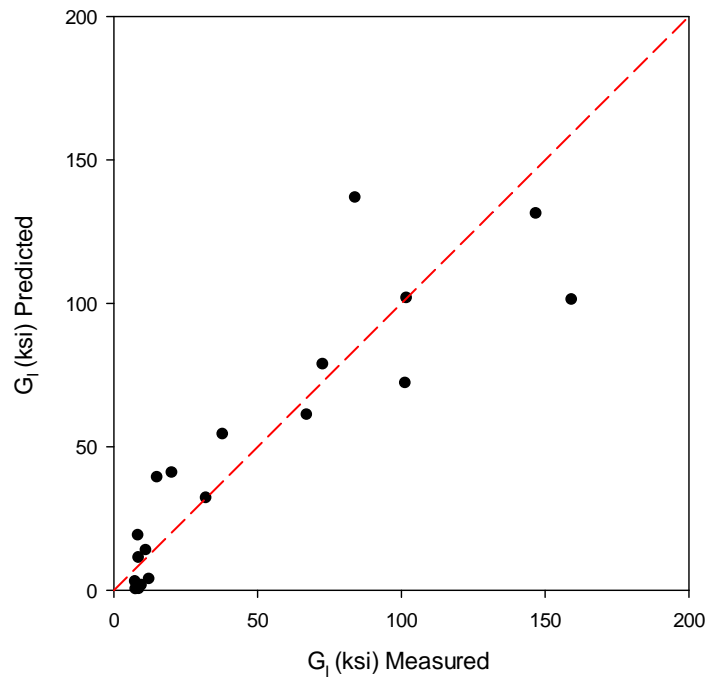
Figure C-9: Resilient interface shear stiffness for Tensar TX 140.
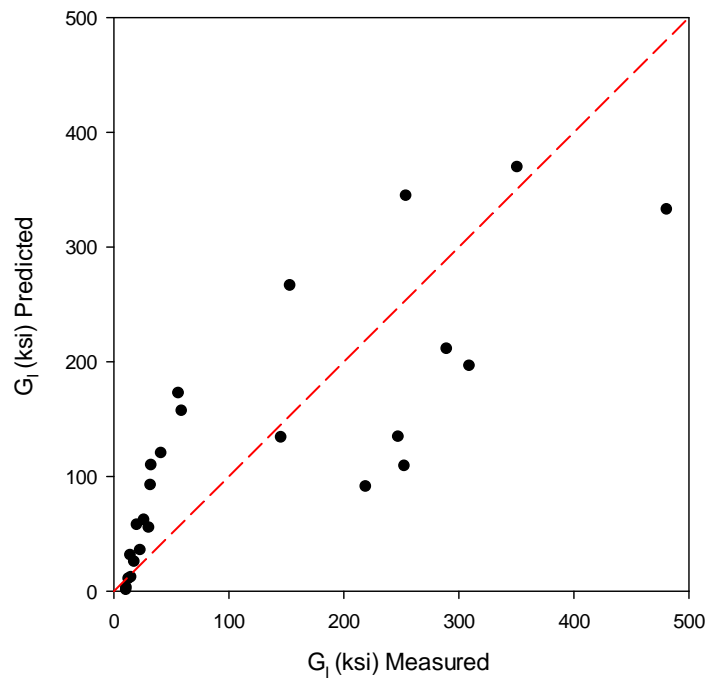
Figure C-10: Resilient interface shear stiffness for Tensar TX 160.
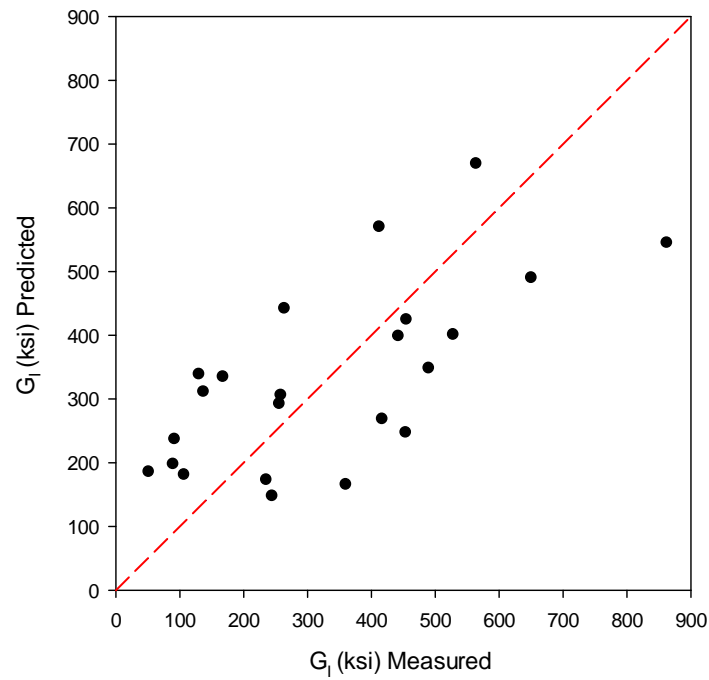
Figure C-11: Resilient interface shear stiffness for TenCate Mirafi RS580i.
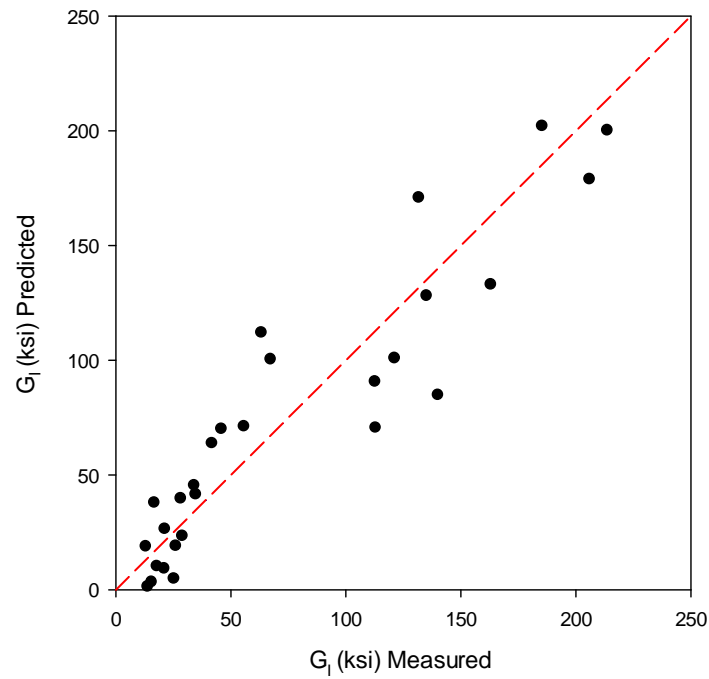
Figure C-12: Resilient interface shear stiffness for Propex Geotex 801.

APPENDIX D – JUNCTION STRENGTH LOAD-DISPLACEMENT RESULTS
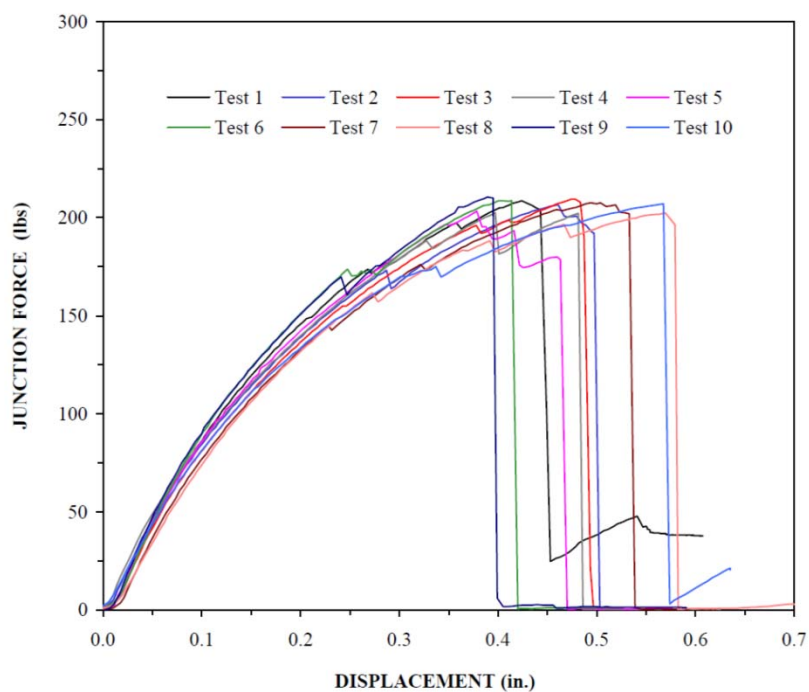
Figure D-1: Junction strength for Tensar BX Type 2.
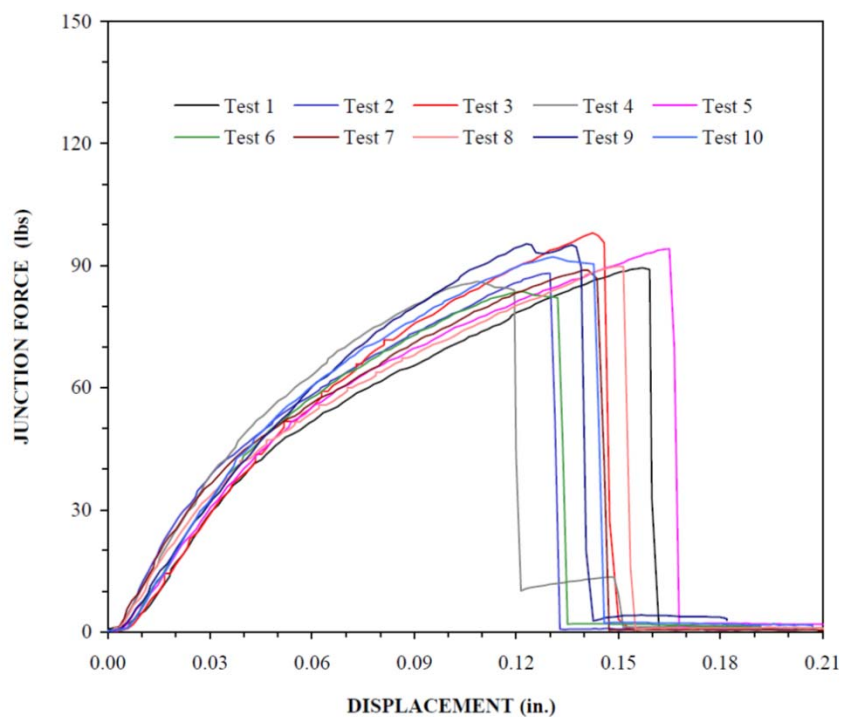
Figure D-2: Junction strength for NAUE Secugrid 30/30 Q1.
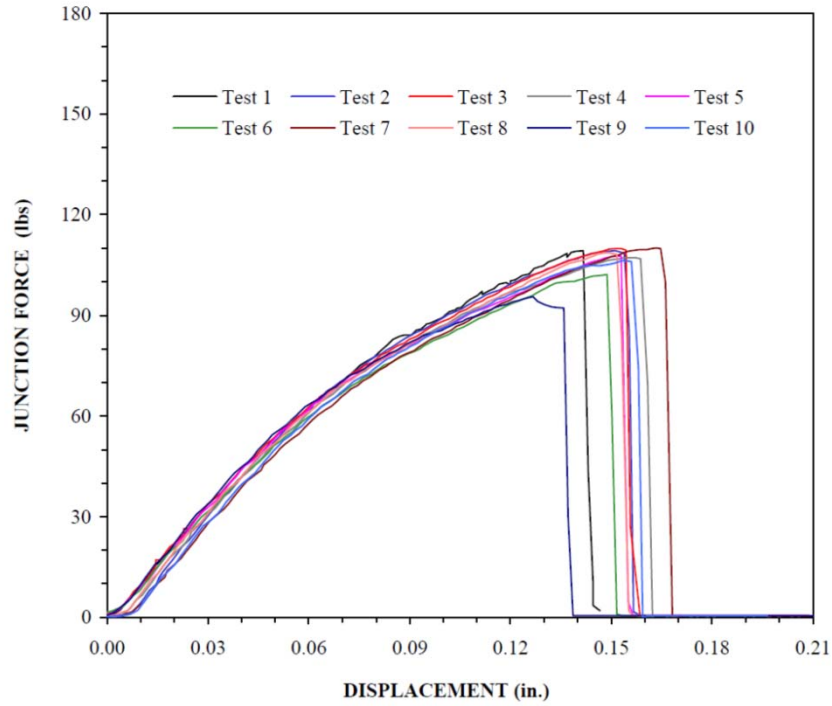
Figure D-3: Junction strength for Colbond Enkagrid Max 30.
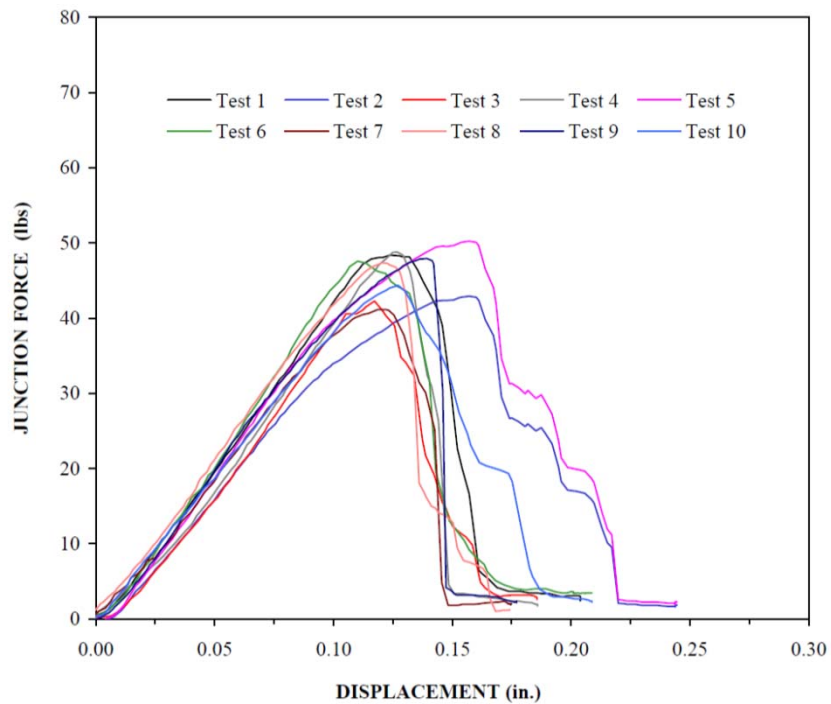
Figure D-4: Junction strength for Synteen SF 11.
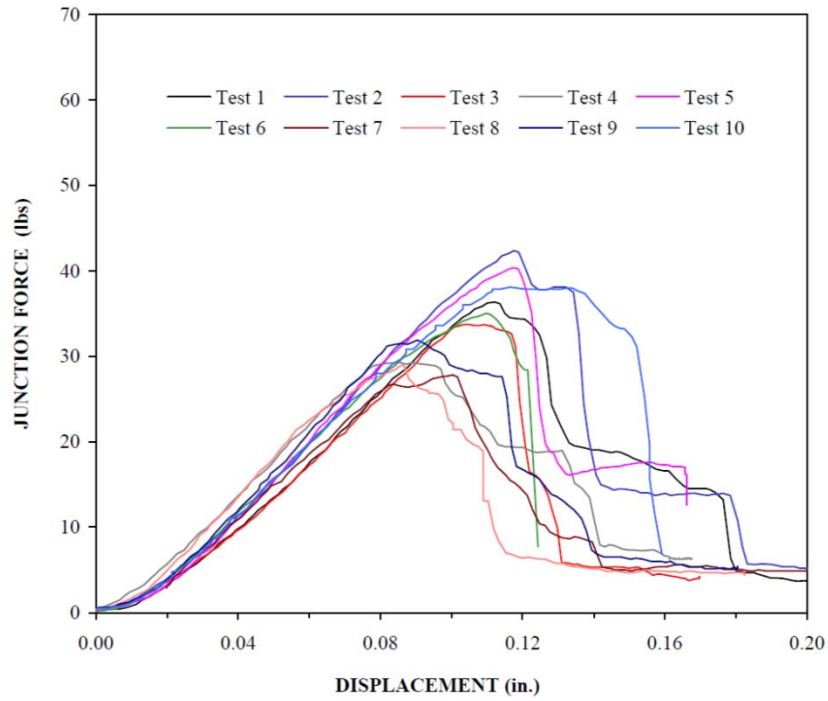
Figure D-5: Junction strength for Synteen SF 12.
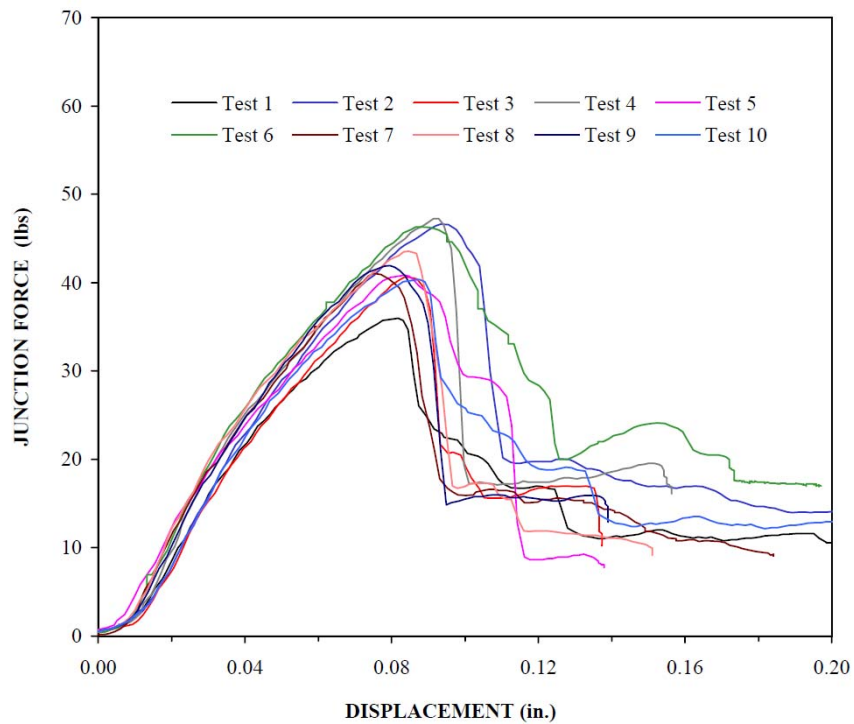
Figure D-6: Junction strength for TenCate Mirafi BXG 11.
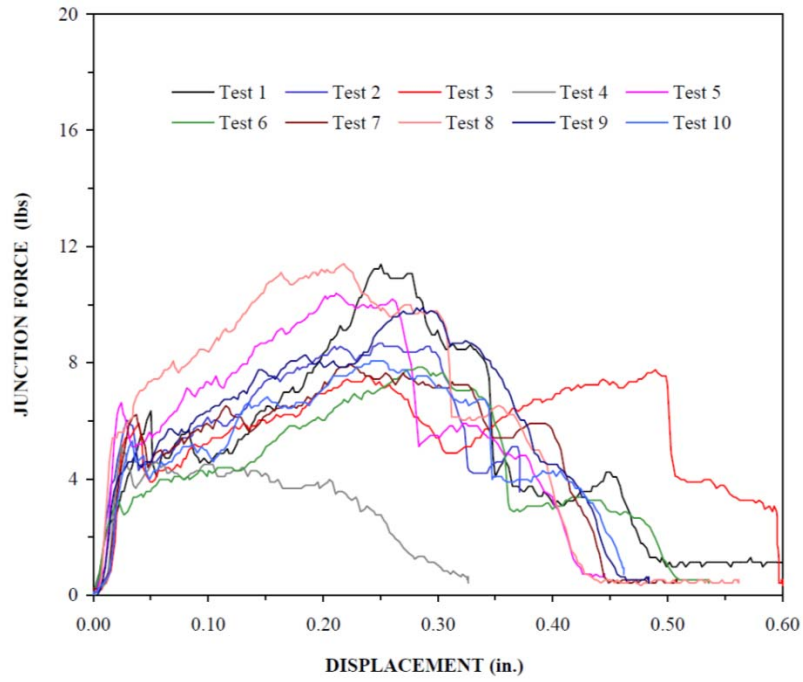
Figure D-7: Junction strength for Huesker Fornit 30.
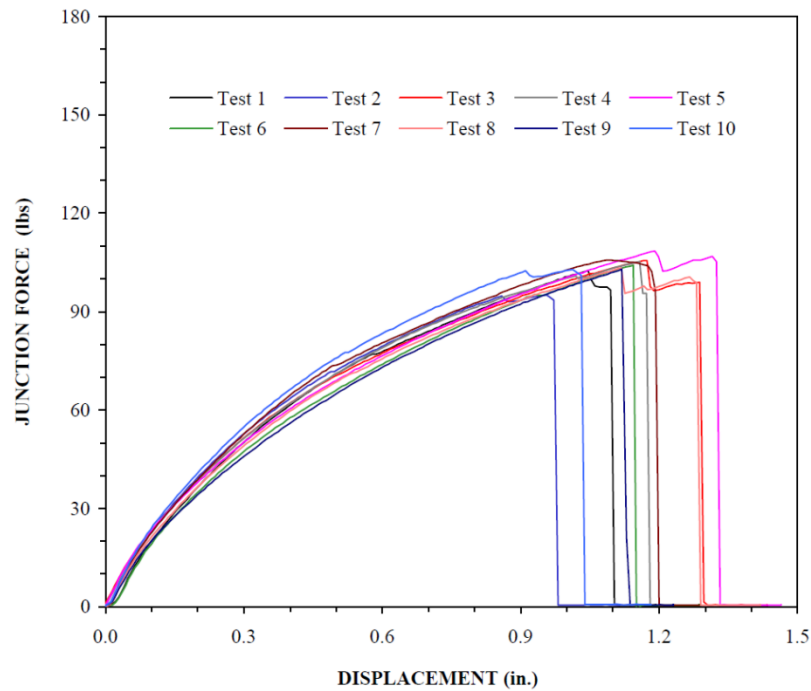
Figure D-8: Junction strength for SynTec Tenax MS330.
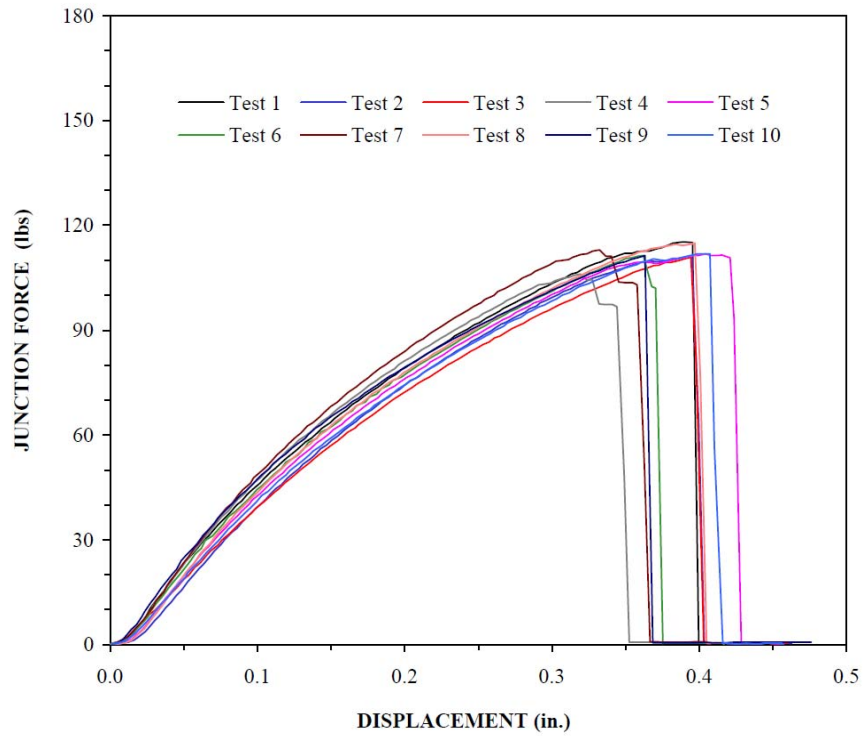
Figure D-9: Junction strength for Tensar TX 140.
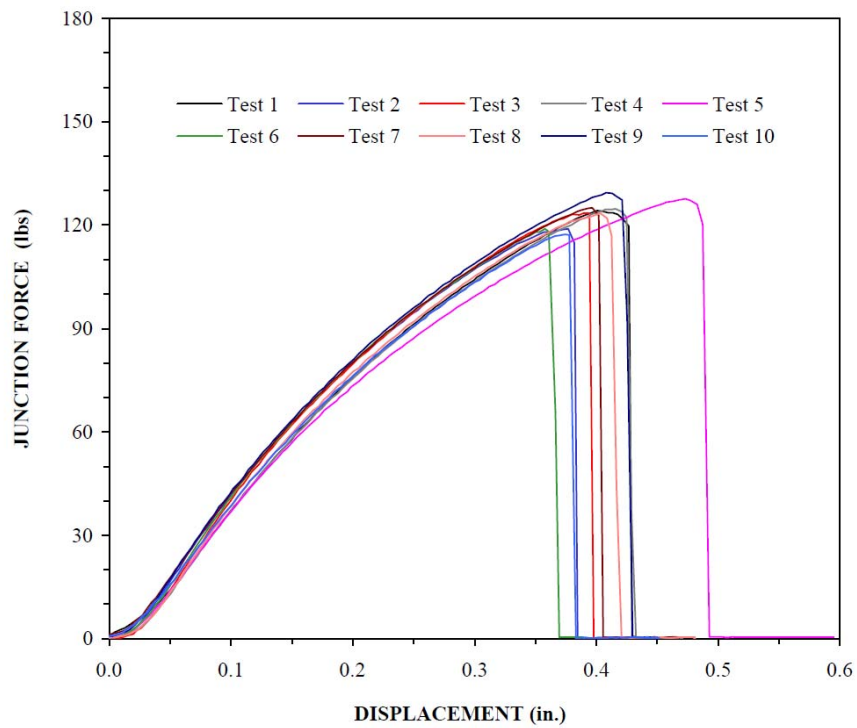
Figure D-10: Junction strength for Tensar TX 160.

APPENDIX E – APERTURE STABILITY MODULUS PLOTS
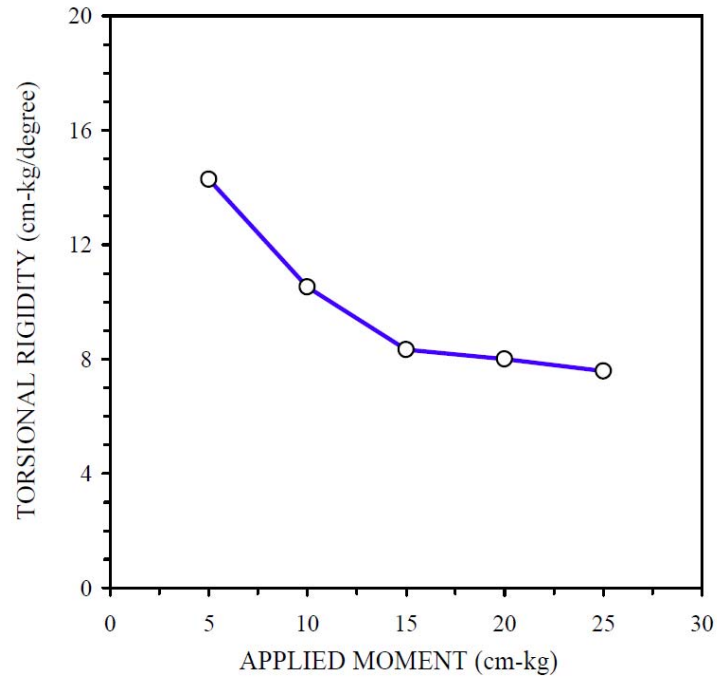
Figure E-1: Aperture stability modulus for Tensar BX Type 2.
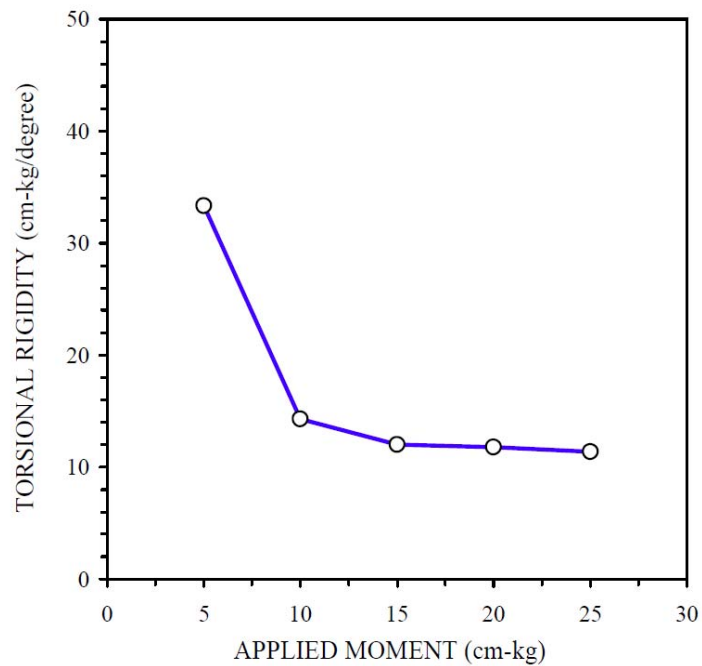
Figure E-2: Aperture stability modulus for NAUE Secugrid 30/30 Q1.
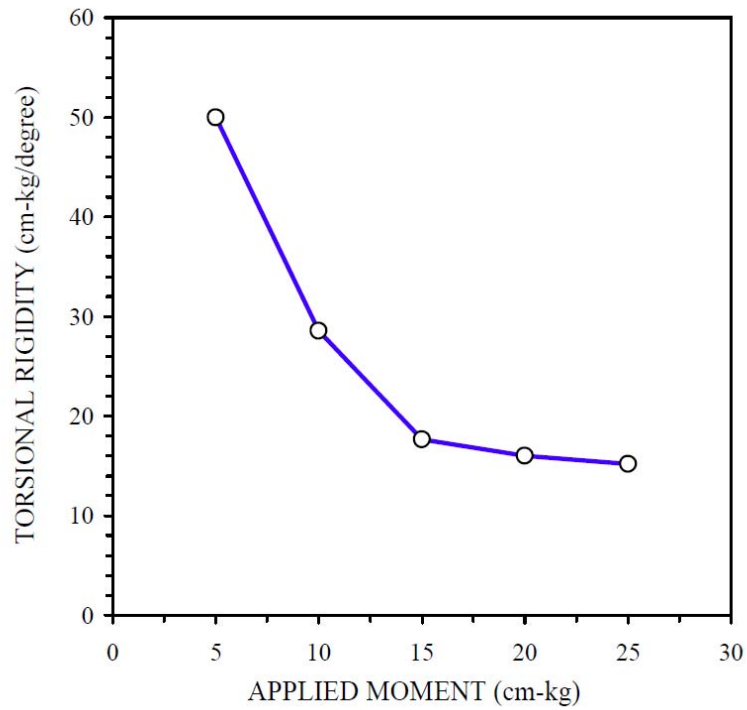
Figure E-3: Aperture stability modulus for Colbond Enkagrid Max 30.
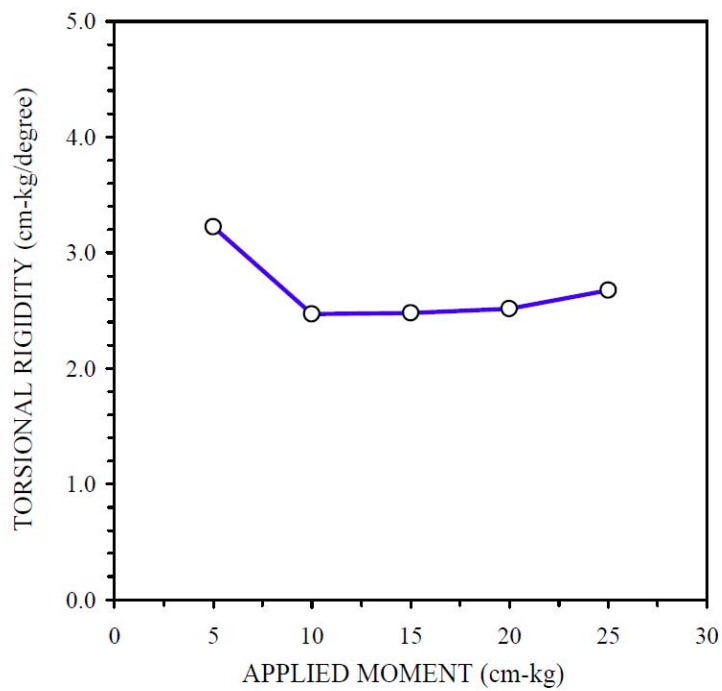
Figure E-4: Aperture stability modulus for Synteen SF 11.
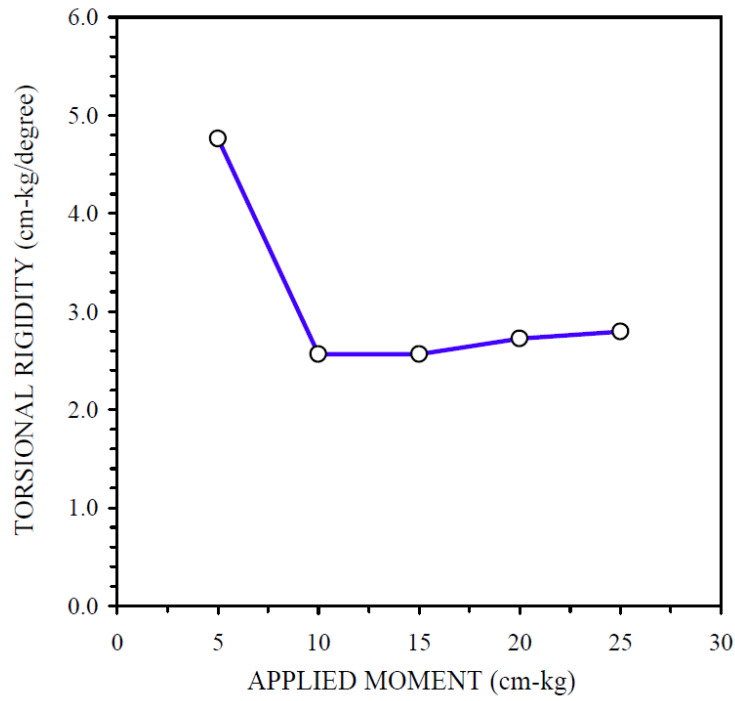
Figure E-5: Aperture stability modulus for Synteen SF 12.
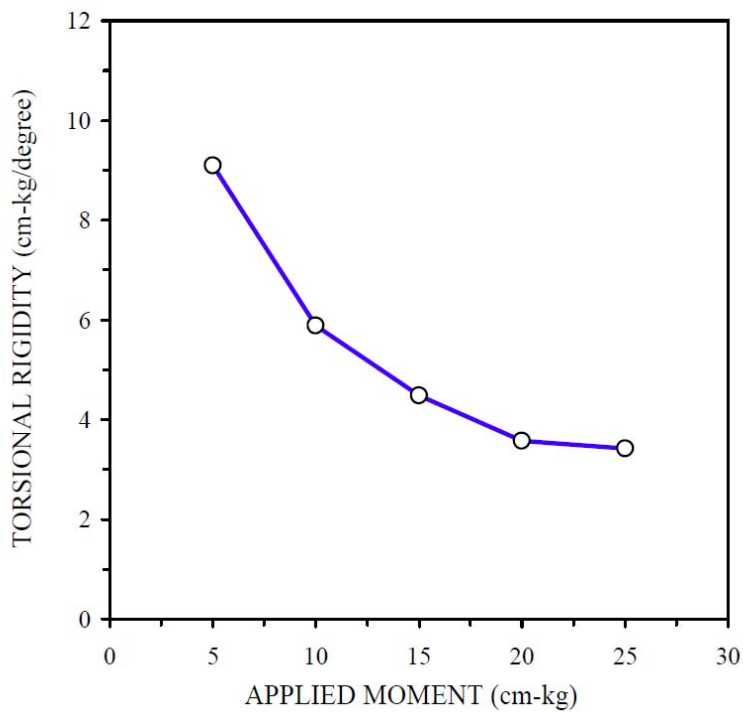
Figure E-6: Aperture stability modulus for TenCate Mirafi BXG 11.
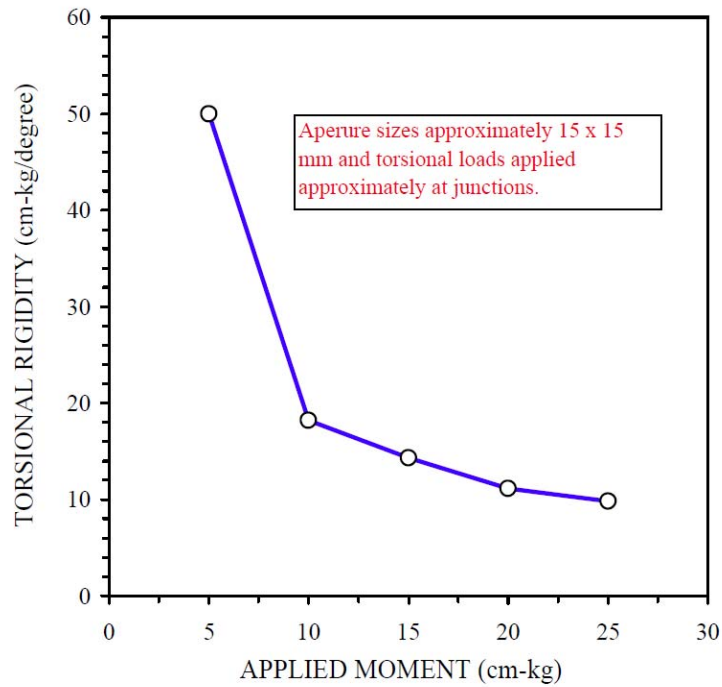
Figure E-7: Aperture stability modulus for Huesker Fornit 30.
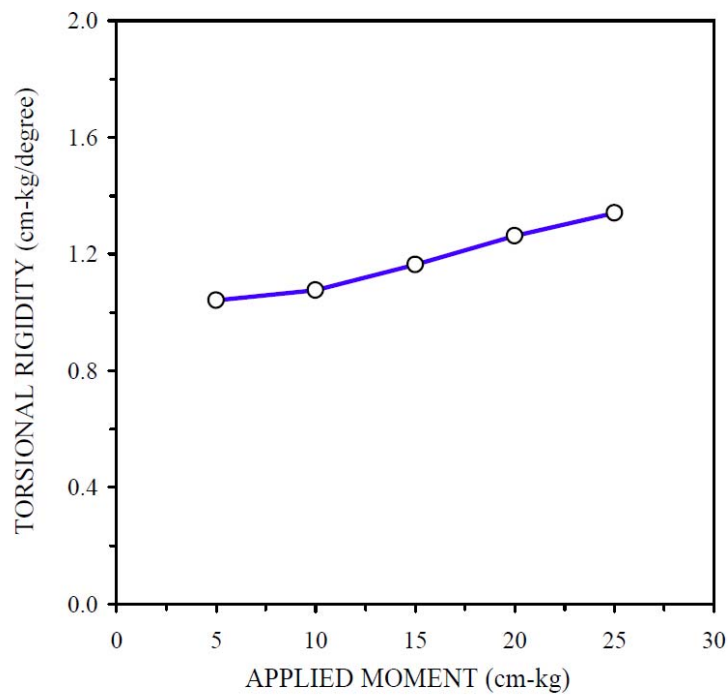
Figure E-8: Aperture stability modulus for SynTec Tenax MS330.
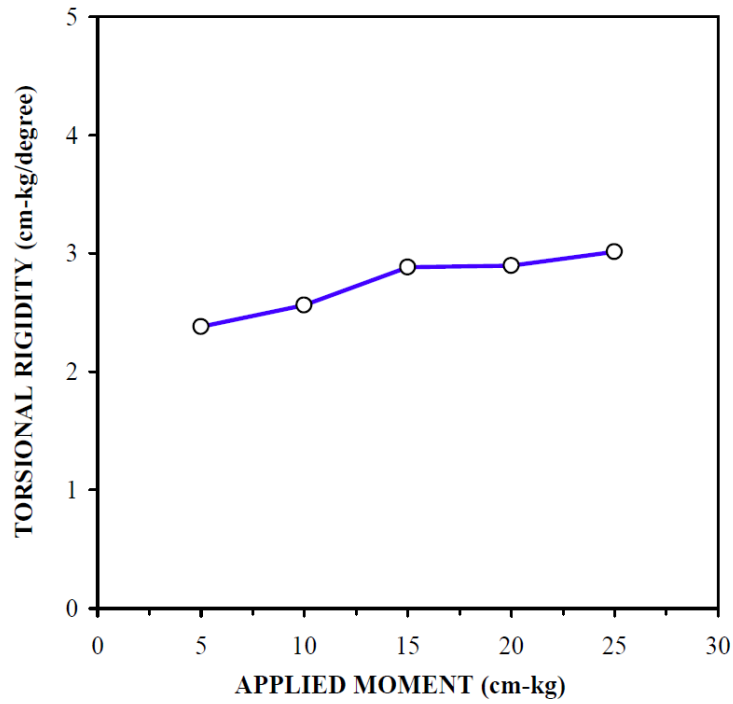
Figure E-9: Aperture stability modulus for Tensar TX 140.
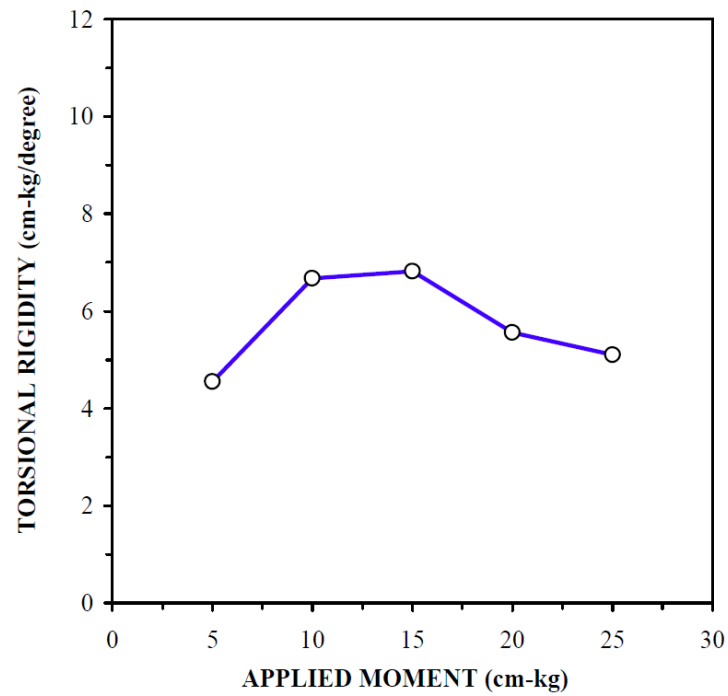
Figure E-10: Aperture stability modulus for Tensar TX 160.

APPENDIX F – HISTORY OF RUT REPAIR FOR ALL TEST SECTIONS

The following tables provide a visual history of th e rut repair for all of the test sections during trafficking. Twenty-eight rut m easurements were made in each test section (14 in the east rut and 14 in the west rut). Each of these m easurements is represente d by a single box in the following tables. Boxe s that are shaded indicate when ruts were filled and m easurements in those areas were ended.

Test Section IFG-1															
Truck Pass	Rut	Measurement Point													
		1	2	3	4	5	6	7	8	9	10	11	12	13	14
0	E														
	W														
3	E														
	W														
10	E														
	W														
20	E														
	W														
40	E														
	W														
70	E														
	W														
80	E														
	W														
102	E														
	W														
125	E														
	W														
175	E														
	W														
250	E														
	W														
300	E														
	W														
325	E														
	W														
351	E														
	W														
395	E														
	W														
440	E														
	W														
540	E														
	W														
640	E														
	W														
740	E														
	W														

Test Section IFG-2															
Truck Pass	Rut	Measurement Point													
		1	2	3	4	5	6	7	8	9	10	11	12	13	14
0	E														
	W														
3	E														
	W														
10	E														
	W														
20	E														
	W														
40	E														
	W														
70	E														
	W														
80	E														
	W														
102	E														
	W														
125	E														
	W														
175	E														
	W														
250	E														
	W														
300	E														
	W														
325	E														
	W														
351	E														
	W														
395	E														
	W														
440	E														
	W														
540	E														
	W														
640	E														
	W														
740	E														
	W														

Test Section IFG-3																
Truck Pass	Rut	Measurement Point													
		1	2	3	4	5	6	7	8	9	10	11	12	13	14
0	E														
	W														
3	E														
	W														
10	E														
	W														
20	E														
	W														
40	E														
	W														
70	E														
	W														
80	E														
	W														
102	E														
	W														
125	E														
	W														
175	E														
	W														
250	E														
	W														
300	E														
	W														
325	E														
	W														
351	E														
	W														
395	E														
	W														
440	E														
	W														
540	E														
	W														
640	E														
	W														
740	E														
	W														

Test Section WeG-4																
Truck Pass	Rut	Measurement Point													
		1	2	3	4	5	6	7	8	9	10	11	12	13	14
0	E														
	W														
3	E														
	W														
10	E														
	W														
20	E														
	W														
40	E														
	W														
70	E														
	W														
80	E														
	W														
102	E														
	W														
125	E														
	W														
175	E														
	W														
250	E														
	W														
300	E														
	W														
325	E														
	W														
351	E														
	W														
395	E														
	W														
440	E														
	W										■	■	■	■	■
540	E														
	W										■	■	■	■	■
640	E														
	W										■	■	■	■	■
740	E														
	W										■	■	■	■	■

Test Section WeG-5															
Truck Pass	Rut	Measurement Point													
		1	2	3	4	5	6	7	8	9	10	11	12	13	14
0	E														
	W														
3	E														
	W														
10	E														
	W														
20	E														
	W														
40	E														
	W														
70	E														
	W														
80	E														
	W														
102	E														
	W														
125	E														
	W														
175	E														
	W														
250	E														
	W														
300	E														
	W														
325	E														
	W														
351	E														
	W														
395	E														
	W														
440	E														
	W														
540	E														
	W														
640	E														
	W														
740	E														
	W														

Test Section WoG-6															
Truck Pass	Rut	Measurement Point													
		1	2	3	4	5	6	7	8	9	10	11	12	13	14
0	E														
	W														
3	E														
	W														
10	E														
	W														
20	E														
	W														
40	E														
	W														
70	E														
	W														
80	E														
	W														
102	E														
	W														
125	E														
	W														
175	E														
	W														
250	E														
	W														
300	E														
	W														
325	E														
	W														
351	E														
	W														
395	E														
	W														
440	E														
	W														
540	E														
	W														
640	E														
	W														
740	E														
	W														

Test Section WoG-7		Measurement Point													
Truck Pass	**Rut**	1	2	3	4	5	6	7	8	9	10	11	12	13	14
0	E														
0	W														
3	E														
3	W														
10	E														
10	W														
20	E														
20	W														
40	E														
40	W														
70	E														
70	W														
80	E														
80	W														
102	E														
102	W														
125	E														
125	W														
175	E														
175	W														
250	E														
250	W														
300	E	▦	▦	▦	▦	▦	▦	▦	▦	▦	▦	▦	▦	▦	▦
300	W	▦	▦	▦	▦	▦	▦	▦	▦	▦	▦	▦	▦	▦	▦
325	E	▦	▦	▦	▦	▦	▦	▦	▦	▦	▦	▦	▦	▦	▦
325	W	▦	▦	▦	▦	▦	▦	▦	▦	▦	▦	▦	▦	▦	▦
351	E	▦	▦	▦	▦	▦	▦	▦	▦	▦	▦	▦	▦	▦	▦
351	W	▦	▦	▦	▦	▦	▦	▦	▦	▦	▦	▦	▦	▦	▦
395	E	▦	▦	▦	▦	▦	▦	▦	▦	▦	▦	▦	▦	▦	▦
395	W	▦	▦	▦	▦	▦	▦	▦	▦	▦	▦	▦	▦	▦	▦
440	E	▦	▦	▦	▦	▦	▦	▦	▦	▦	▦	▦	▦	▦	▦
440	W	▦	▦	▦	▦	▦	▦	▦	▦	▦	▦	▦	▦	▦	▦
540	E	▦	▦	▦	▦	▦	▦	▦	▦	▦	▦	▦	▦	▦	▦
540	W	▦	▦	▦	▦	▦	▦	▦	▦	▦	▦	▦	▦	▦	▦
640	E	▦	▦	▦	▦	▦	▦	▦	▦	▦	▦	▦	▦	▦	▦
640	W	▦	▦	▦	▦	▦	▦	▦	▦	▦	▦	▦	▦	▦	▦
740	E	▦	▦	▦	▦	▦	▦	▦	▦	▦	▦	▦	▦	▦	▦
740	W	▦	▦	▦	▦	▦	▦	▦	▦	▦	▦	▦	▦	▦	▦

Test Section WoG-8		Measurement Point													
Truck Pass	**Rut**	1	2	3	4	5	6	7	8	9	10	11	12	13	14
0	E														
0	W														
3	E														
3	W														
10	E														
10	W														
20	E														
20	W														
40	E														
40	W														
70	E														
70	W														
80	E														
80	W														
102	E														
102	W														
125	E														
125	W														
175	E														
175	W														
250	E														
250	W														
300	E										▦	▦	▦	▦	▦
300	W										▦	▦	▦	▦	▦
325	E										▦	▦	▦	▦	▦
325	W										▦	▦	▦	▦	▦
351	E										▦	▦	▦	▦	▦
351	W										▦	▦	▦	▦	▦
395	E										▦	▦	▦	▦	▦
395	W										▦	▦	▦	▦	▦
440	E	▦	▦	▦						▦	▦	▦	▦	▦	▦
440	W	▦	▦			▦	▦	▦		▦	▦	▦	▦	▦	▦
540	E	▦	▦							▦	▦	▦	▦	▦	▦
540	W	▦	▦							▦	▦	▦	▦	▦	▦
640	E	▦	▦			▦	▦	▦	▦	▦	▦	▦	▦	▦	▦
640	W	▦	▦	▦		▦	▦	▦		▦	▦	▦	▦	▦	▦
740	E	▦	▦	▦	▦	▦				▦	▦	▦	▦	▦	▦
740	W	▦	▦	▦	▦	▦				▦	▦	▦	▦	▦	▦

Test Section KnG-9																
Truck Pass	Rut	Measurement Point													
		1	2	3	4	5	6	7	8	9	10	11	12	13	14
0	E														
	W														
3	E														
	W														
10	E														
	W														
20	E														
	W														
40	E														
	W														
70	E														
	W														
80	E														
	W														
102	E														
	W														
125	E														
	W														
175	E														
	W														
250	E														
	W														
300	E	■	■	■	■	■	■	■	■	■	■	■	■	■	■
	W	■	■	■	■	■	■	■	■	■	■	■	■	■	■
325	E	■	■	■	■	■	■	■	■	■	■	■	■	■	■
	W	■	■	■	■	■	■	■	■	■	■	■	■	■	■
351	E	■	■	■	■	■	■	■	■	■	■	■	■	■	■
	W	■	■	■	■	■	■	■	■	■	■	■	■	■	■
395	E	■	■	■	■	■	■	■	■	■	■	■	■	■	■
	W	■	■	■	■	■	■	■	■	■	■	■	■	■	■
440	E	■	■	■	■	■	■	■	■	■	■	■	■	■	■
	W	■	■	■	■	■	■	■	■	■	■	■	■	■	■
540	E	■	■	■	■	■	■	■	■	■	■	■	■	■	■
	W	■	■	■	■	■	■	■	■	■	■	■	■	■	■
640	E	■	■	■	■	■	■	■	■	■	■	■	■	■	■
	W	■	■	■	■	■	■	■	■	■	■	■	■	■	■
740	E	■	■	■	■	■	■	■	■	■	■	■	■	■	■
	W	■	■	■	■	■	■	■	■	■	■	■	■	■	■

Test Section ExG-10																
Truck Pass	Rut	Measurement Point													
		1	2	3	4	5	6	7	8	9	10	11	12	13	14
0	E														
	W														
3	E														
	W														
10	E														
	W														
20	E														
	W														
40	E														
	W														
70	E														
	W														
80	E														
	W														
102	E														
	W														
125	E														
	W														
175	E														
	W														
250	E														
	W														
300	E														
	W														
325	E														
	W														
351	E														
	W														
395	E	■	■	■	■	■									
	W	■	■	■	■	■	■	■							
440	E	■	■	■	■	■	■	■	■	■	■	■	■	■	■
	W	■	■	■	■	■	■	■	■	■	■	■	■	■	■
540	E	■	■	■	■	■	■	■	■	■	■	■	■	■	■
	W	■	■	■	■	■	■	■	■	■	■	■	■	■	■
640	E	■	■	■	■	■	■	■	■	■	■	■	■	■	■
	W	■	■	■	■	■	■	■	■	■	■	■	■	■	■
740	E	■	■	■	■	■	■	■	■	■	■	■	■	■	■
	W	■	■	■	■	■	■	■	■	■	■	■	■	■	■

Test Section IFG-11

Truck Pass	Rut	1	2	3	4	5	6	7	8	9	10	11	12	13	14
0	E														
	W														
3	E														
	W														
10	E														
	W														
20	E														
	W														
40	E														
	W														
70	E														
	W														
80	E														
	W														
102	E														
	W														
125	E														
	W														
175	E														
	W														
250	E														
	W														
300	E														
	W														
325	E														
	W														
351	E														
	W														
395	E														
	W														
440	E														
	W														
540	E														
	W														
640	E														
	W														
740	E														
	W														

Test Section IFG-12

Truck Pass	Rut	1	2	3	4	5	6	7	8	9	10	11	12	13	14
0	E														
	W														
3	E														
	W														
10	E														
	W														
20	E														
	W														
40	E														
	W														
70	E														
	W														
80	E														
	W														
102	E														
	W														
125	E														
	W														
175	E														
	W														
250	E														
	W														
300	E														
	W														
325	E														
	W														
351	E														
	W														
395	E														
	W														
440	E														
	W														
540	E														
	W														
640	E														
	W														
740	E														
	W														

Test Section WoT-13		Measurement Point													
Truck Pass	Rut	1	2	3	4	5	6	7	8	9	10	11	12	13	14
0	E														
	W														
3	E														
	W														
10	E														
	W														
20	E														
	W														
40	E														
	W														
70	E														
	W														
80	E														
	W														
102	E														
	W														
125	E														
	W														
175	E														
	W														
250	E														
	W														
300	E														
	W							▓	▓	▓	▓	▓	▓	▓	▓
325	E														
	W							▓	▓	▓	▓	▓	▓	▓	▓
351	E														
	W							▓	▓	▓	▓	▓	▓	▓	▓
395	E														
	W							▓	▓	▓	▓	▓	▓	▓	▓
440	E														
	W							▓	▓	▓	▓	▓	▓	▓	▓
540	E														
	W							▓	▓	▓	▓	▓	▓	▓	▓
640	E							▓	▓	▓	▓	▓	▓	▓	▓
	W	▓	▓					▓	▓	▓	▓	▓	▓	▓	▓
740	E							▓	▓	▓	▓	▓	▓	▓	▓
	W	▓	▓					▓	▓	▓	▓	▓	▓	▓	▓

Test Section NWoT-14		Measurement Point													
Truck Pass	Rut	1	2	3	4	5	6	7	8	9	10	11	12	13	14
0	E														
	W														
3	E														
	W														
10	E														
	W														
20	E														
	W														
40	E														
	W														
70	E														
	W														
80	E														
	W														
102	E														
	W														
125	E														
	W														
175	E														
	W														
250	E														
	W														
300	E														
	W	▓	▓	▓							▓	▓	▓	▓	▓
325	E	▓	▓	▓							▓	▓	▓	▓	▓
	W	▓	▓	▓											
351	E														
	W	▓	▓	▓						▓	▓	▓	▓	▓	▓
395	E	▓	▓	▓						▓	▓	▓	▓	▓	▓
	W	▓	▓	▓						▓	▓	▓	▓	▓	▓
440	E	▓	▓	▓						▓	▓	▓	▓	▓	▓
	W	▓	▓			▓	▓			▓	▓	▓	▓	▓	▓
540	E	▓	▓	▓						▓	▓	▓	▓	▓	▓
	W	▓	▓	▓		▓	▓			▓	▓	▓	▓	▓	▓
640	E	▓	▓	▓				▓	▓	▓	▓	▓	▓	▓	▓
	W	▓	▓	▓				▓	▓	▓	▓	▓	▓	▓	▓
740	E	▓	▓	▓		▓	▓	▓	▓	▓	▓	▓	▓	▓	▓
	W	▓	▓	▓	▓	▓	▓	▓	▓	▓	▓	▓	▓	▓	▓

Test Section Control 1															
Truck Pass	Rut	Measurement Point													
		1	2	3	4	5	6	7	8	9	10	11	12	13	14
0	E														
	W														
3	E														
	W														
10	E														
	W														
20	E														
	W														
40	E														
	W														
70	E														
	W														
80	E														
	W														
102	E														
	W														
125	E														
	W														
175	E														
	W														
250	E														
	W														
300	E														
	W														
325	E														
	W														
351	E														
	W														
395	E														
	W														
440	E														
	W														
540	E														
	W														
640	E														
	W														
740	E														
	W														

Test Section Control 2															
Truck Pass	Rut	Measurement Point													
		1	2	3	4	5	6	7	8	9	10	11	12	13	14
0	E														
	W														
3	E														
	W														
10	E														
	W														
20	E														
	W														
40	E														
	W														
70	E														
	W														
80	E														
	W														
102	E														
	W														
125	E														
	W														
175	E														
	W														
250	E														
	W														
300	E														
	W														
325	E														
	W														
351	E														
	W														
395	E														
	W														
440	E														
	W														
540	E														
	W														
640	E														
	W														
740	E														
	W														

Test Section Control 3															
Truck Pass	Rut	Measurement Point													
		1	2	3	4	5	6	7	8	9	10	11	12	13	14
0	E														
	W														
3	E														
	W														
10	E														
	W														
20	E														
	W														
40	E														
	W														
70	E														
	W														
80	E														
	W														
102	E														
	W														
125	E														
	W														
175	E														
	W														
250	E														
	W														
300	E														
	W														
325	E														
	W														
351	E														
	W														
395	E														
	W														
440	E														
	W														
540	E														
	W														
640	E														
	W														
740	E														
	W														

APPENDIX G – TOPOGRAPHIC SURVEY PLOTS FOR SUBGRADE AND BASE COURSE DURING FORENSIC INVESTIGATIONS
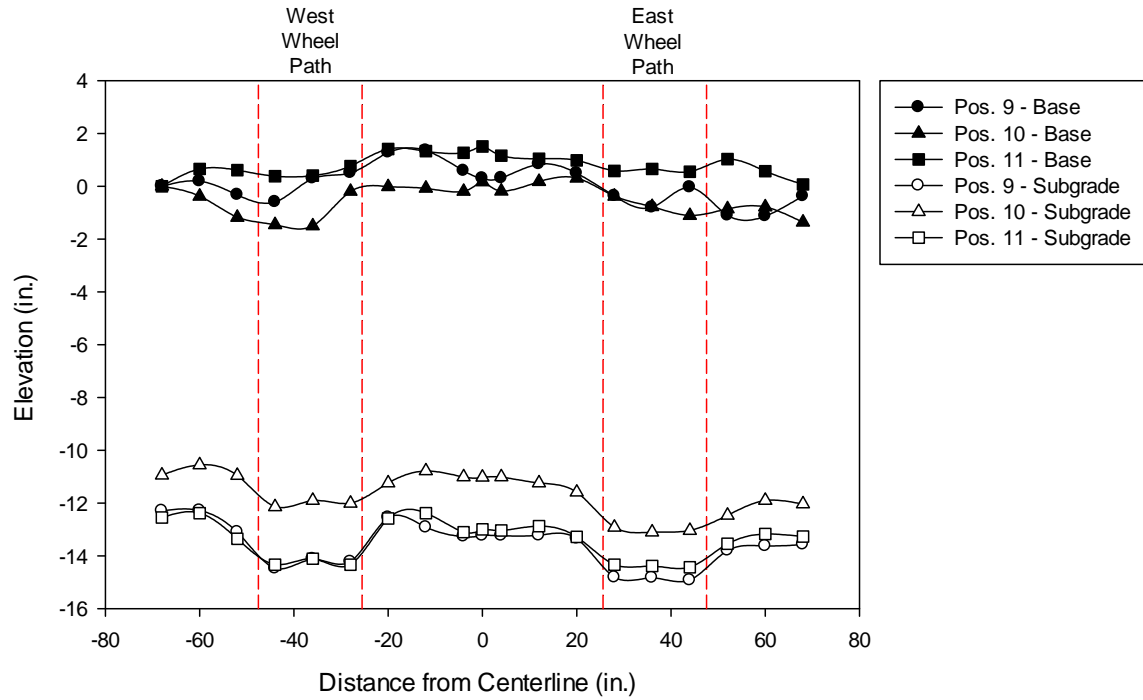
Figure G-1: Forensic topographic survey in Test Section 1 (Tensar BX Type 2, CBR = 2.17).
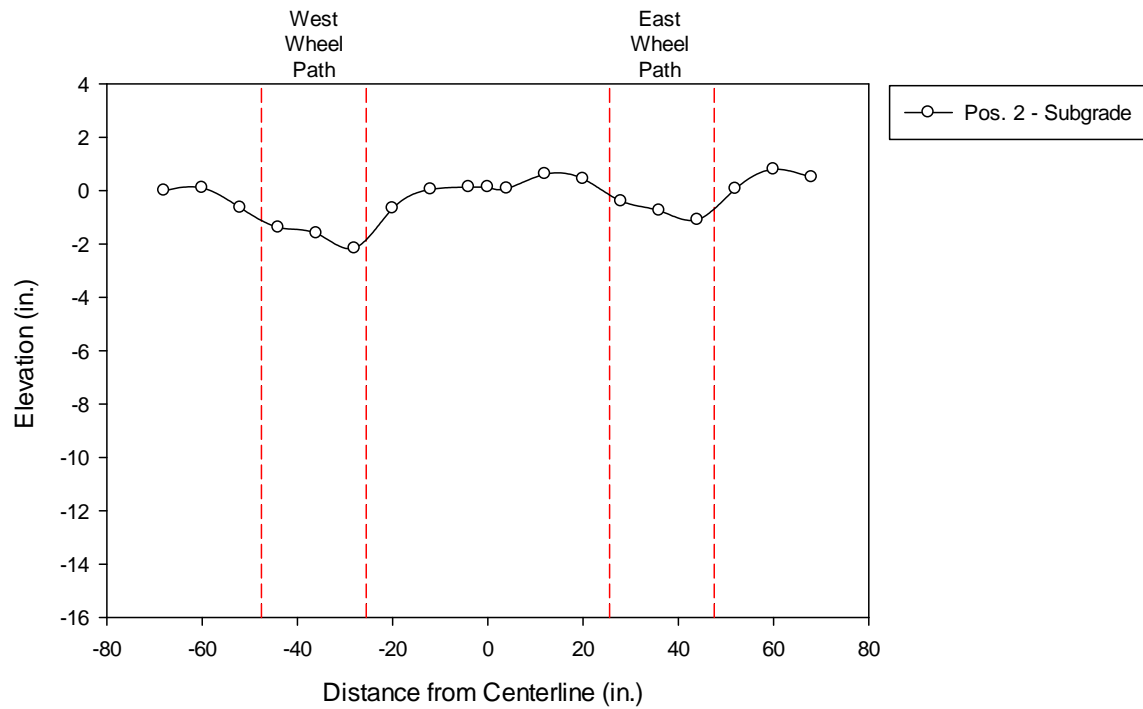
Figure G-2: Forensic topographic survey in Test Section 2 (Tensar BX Type 2, CBR = 1.64).
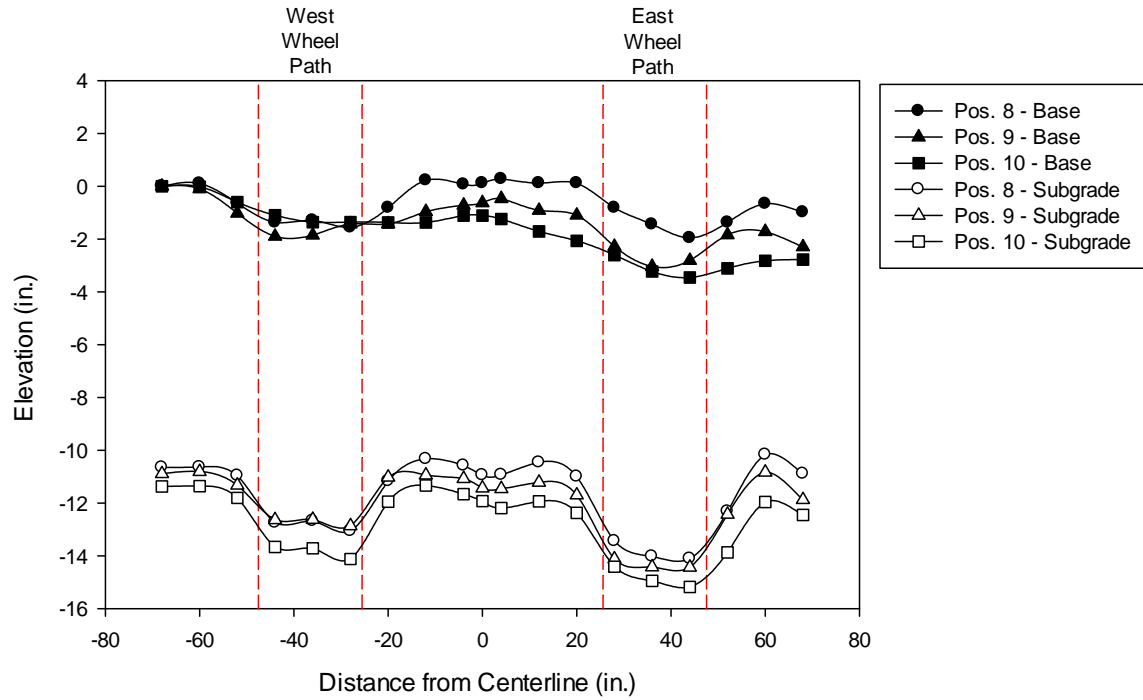
Figure G-3: Forensic topographic survey in Test Section 3 (Tensar BX Type 2, CBR = 1.79).
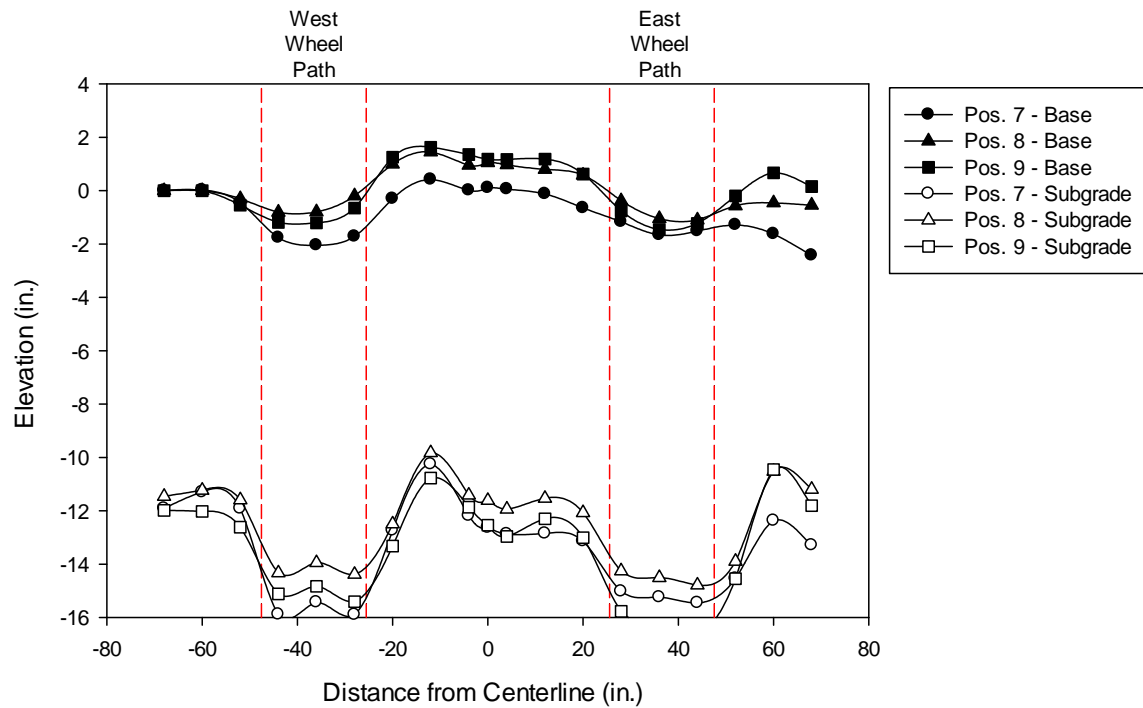
Figure G-4: Forensic topographic survey in Test Section 4 (NAUE Secugrid 30-30 Q1).
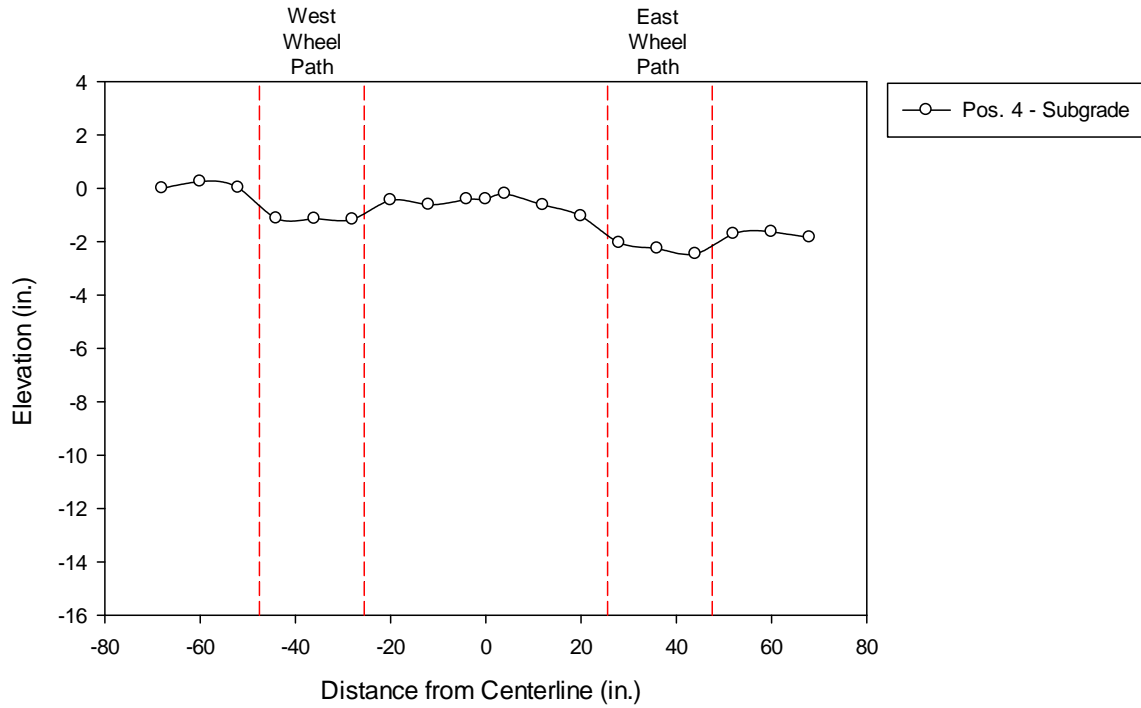
Figure G-5: Forensic topographic survey in Test Section 5 (Colbond Enkagrid MAX 30).
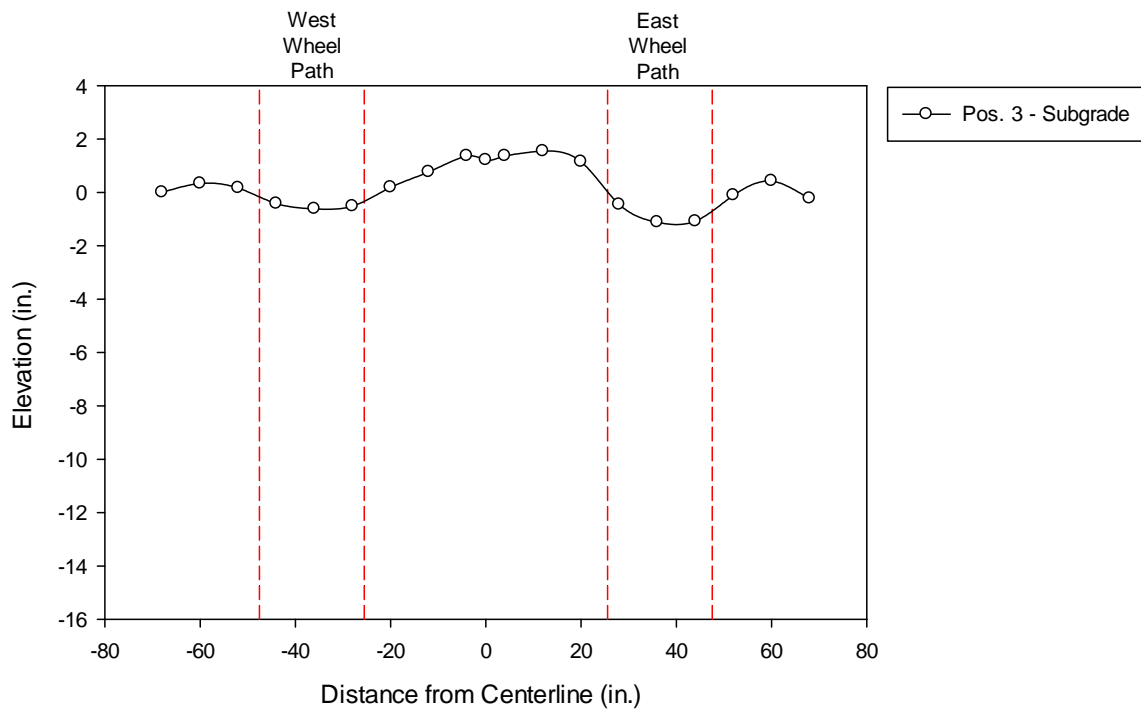
Figure G-6: Forensic topographic survey in Test Section 6 (Synteen SF11).
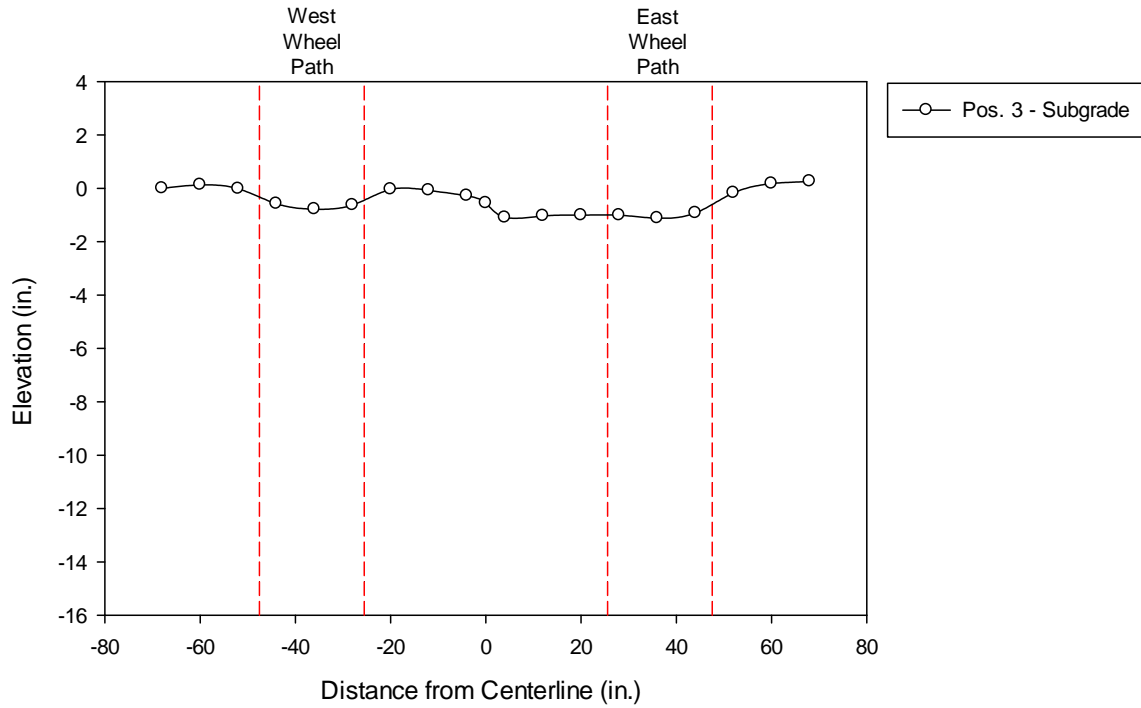
Figure G-7: Forensic topographic survey in Test Section 8 (TenCate Mirafi BXG11).
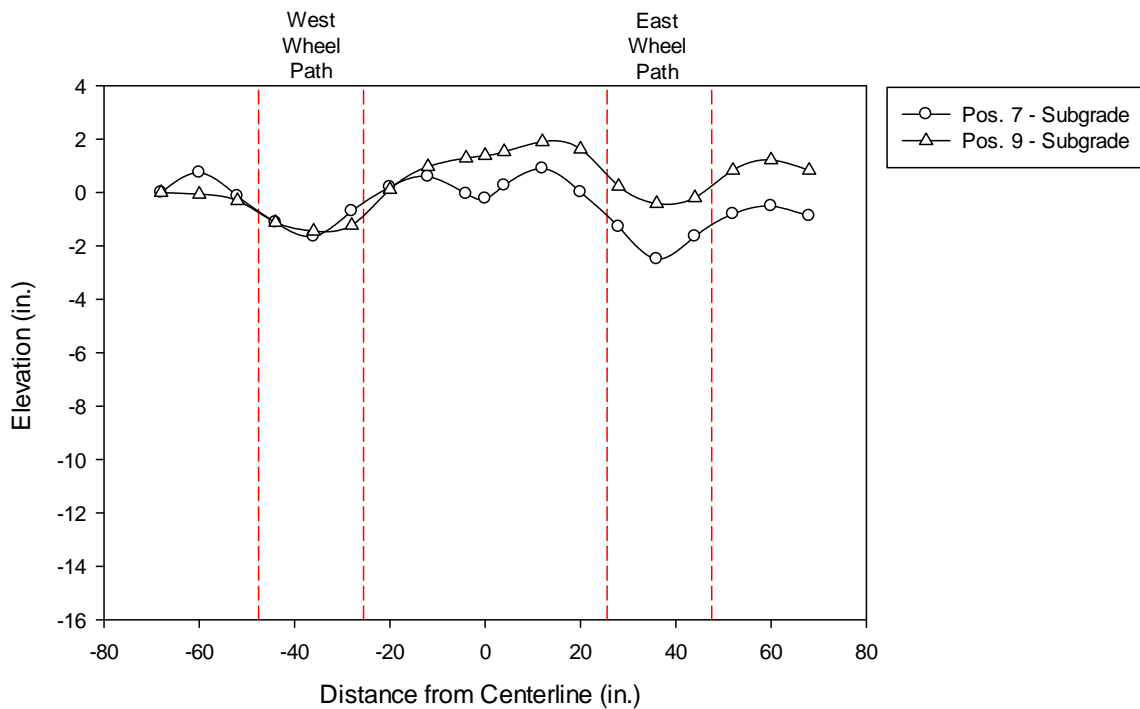
Figure G-8: Forensic topographic survey in Test Section 9 (Huesker Fornit 30).
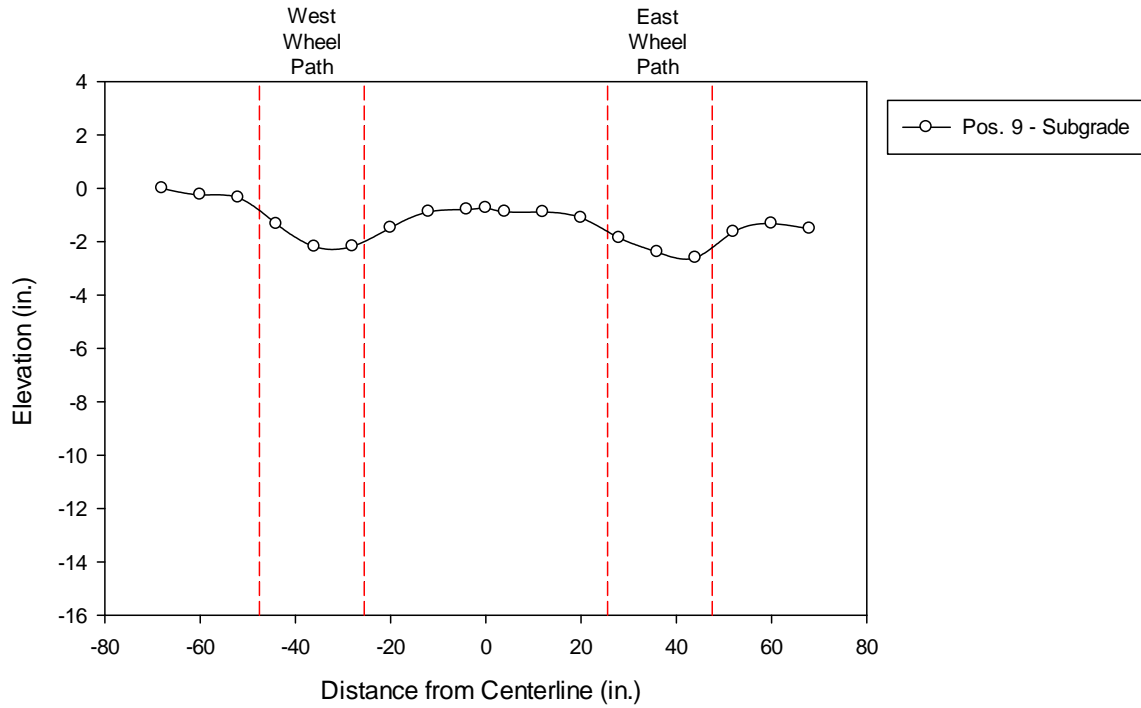
Figure G-9: Forensic topographic survey in Test Section 10 (Syntec Tenax MS 330).
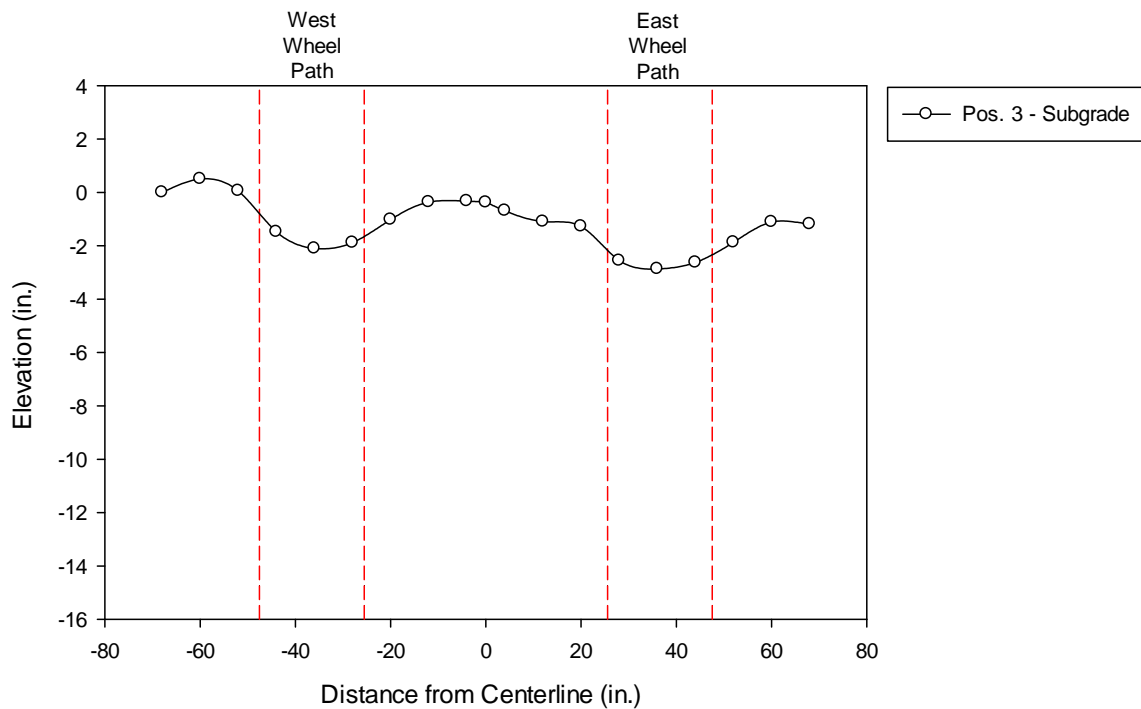
Figure G-10: Forensic topographic survey in Test Section 11 (Tensar TX140).
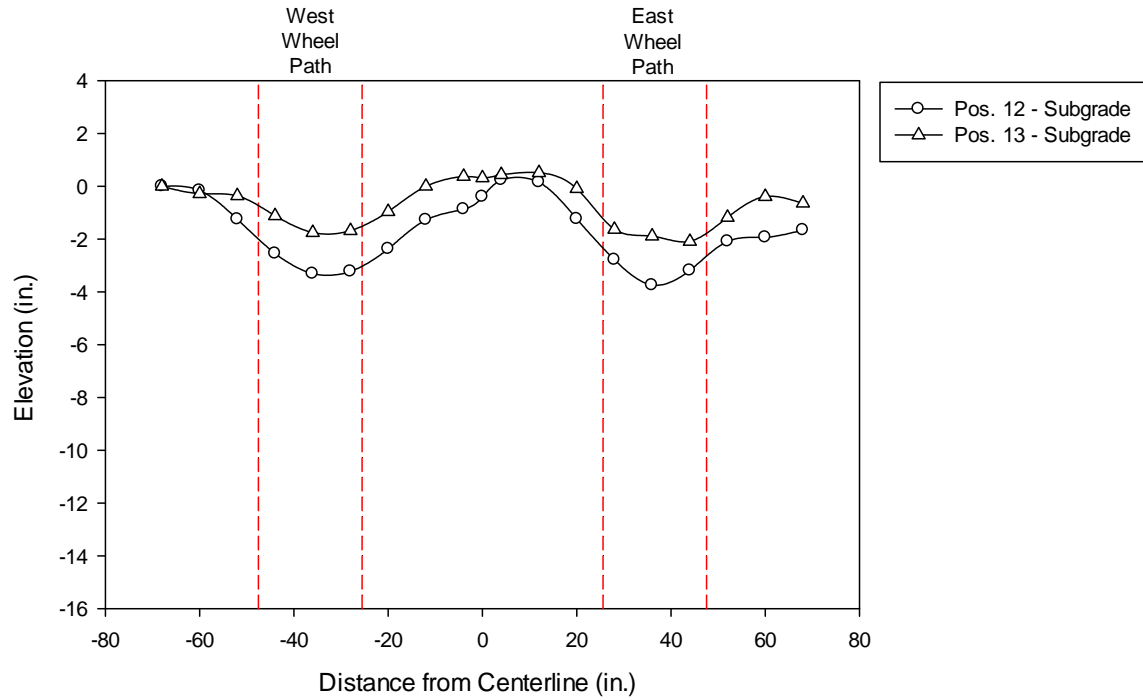
Figure G-11: Forensic topographic survey in Test Section 12 (Tensar TX160).
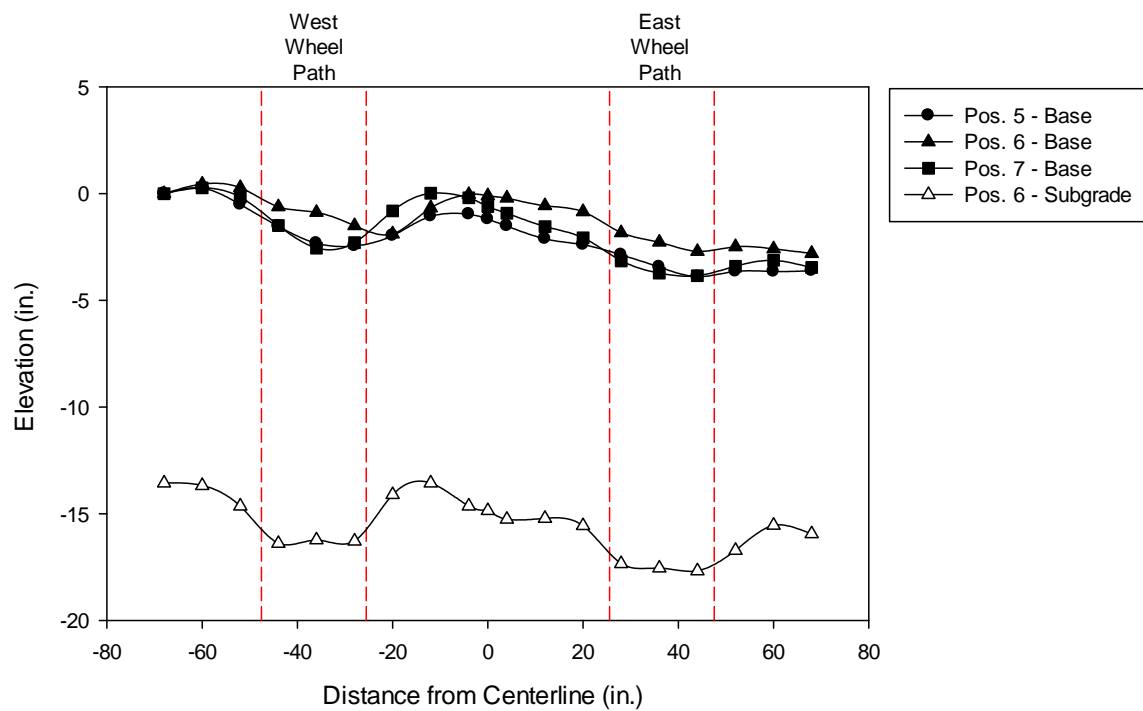
Figure G-12: Forensic topographic survey in Test Section 13 (TenCate Mirafi RS580i).
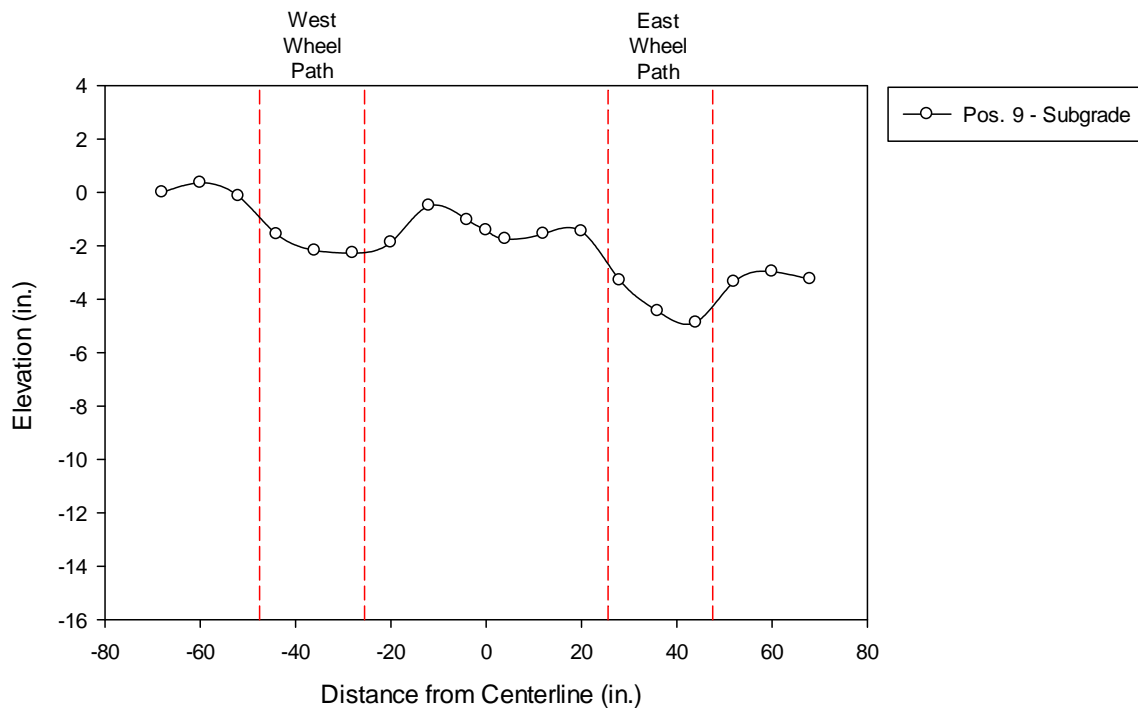
Figure G-13: Forensic topographic survey in Test Section 14 (Propex Geotex 801).
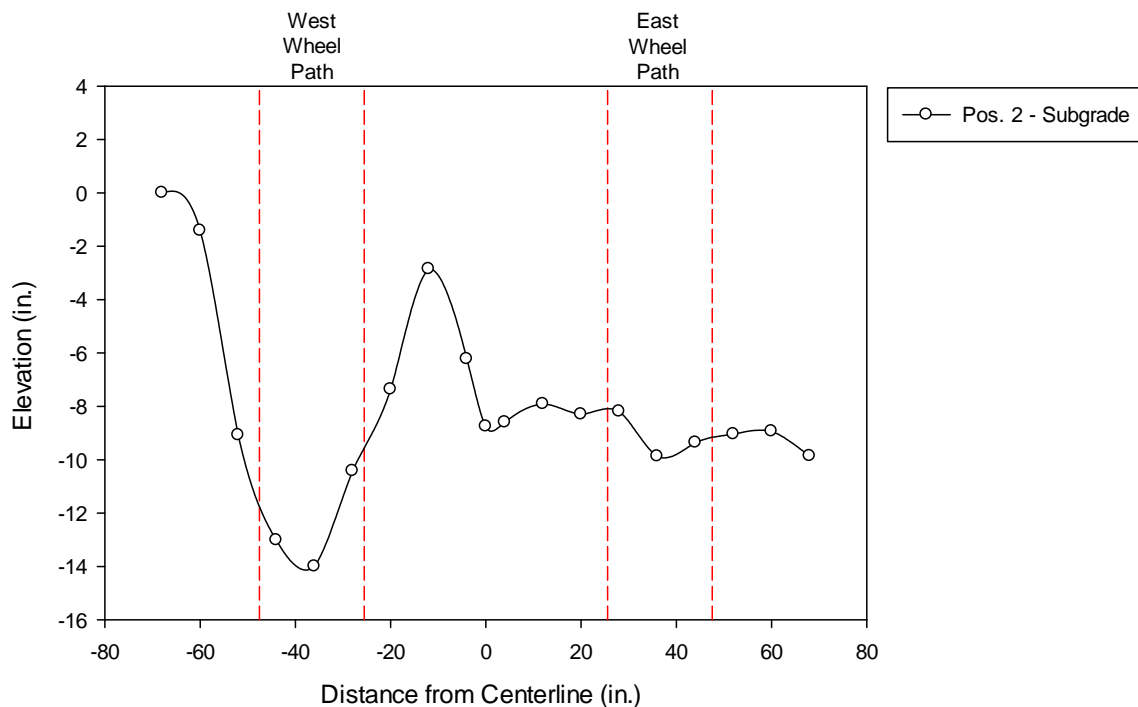
Figure G-14: Forensic topographic survey in Test Section Control 1.
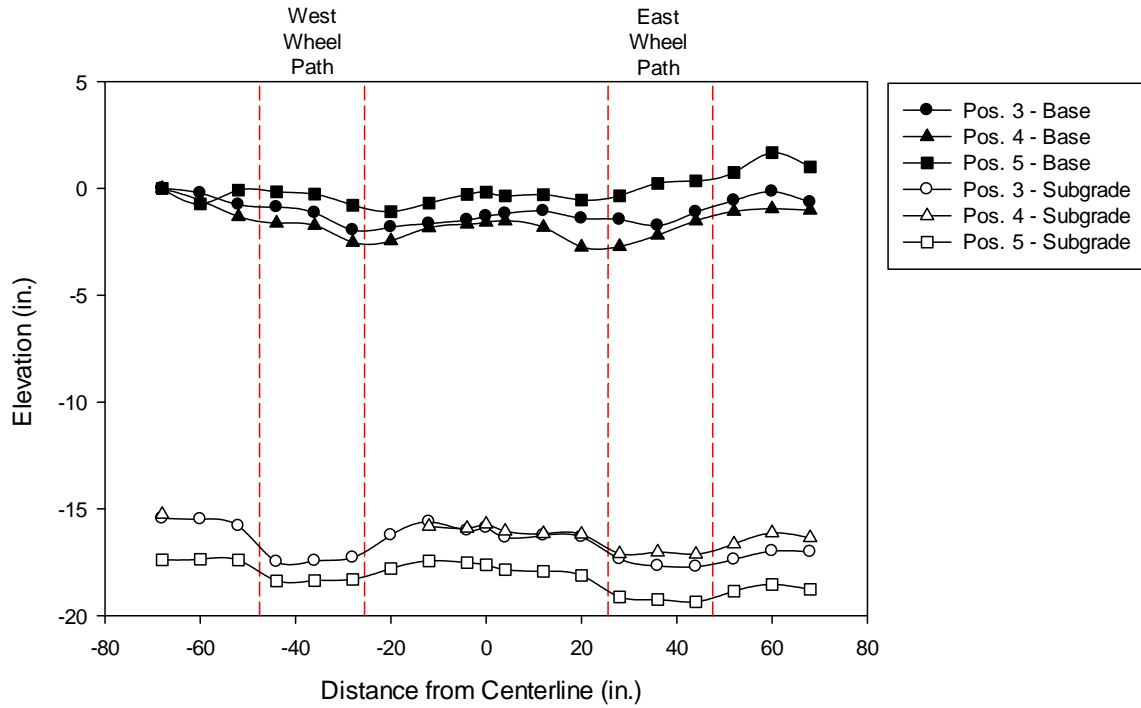
Figure G-15: Forensic topographic survey in Test Section Control 2.
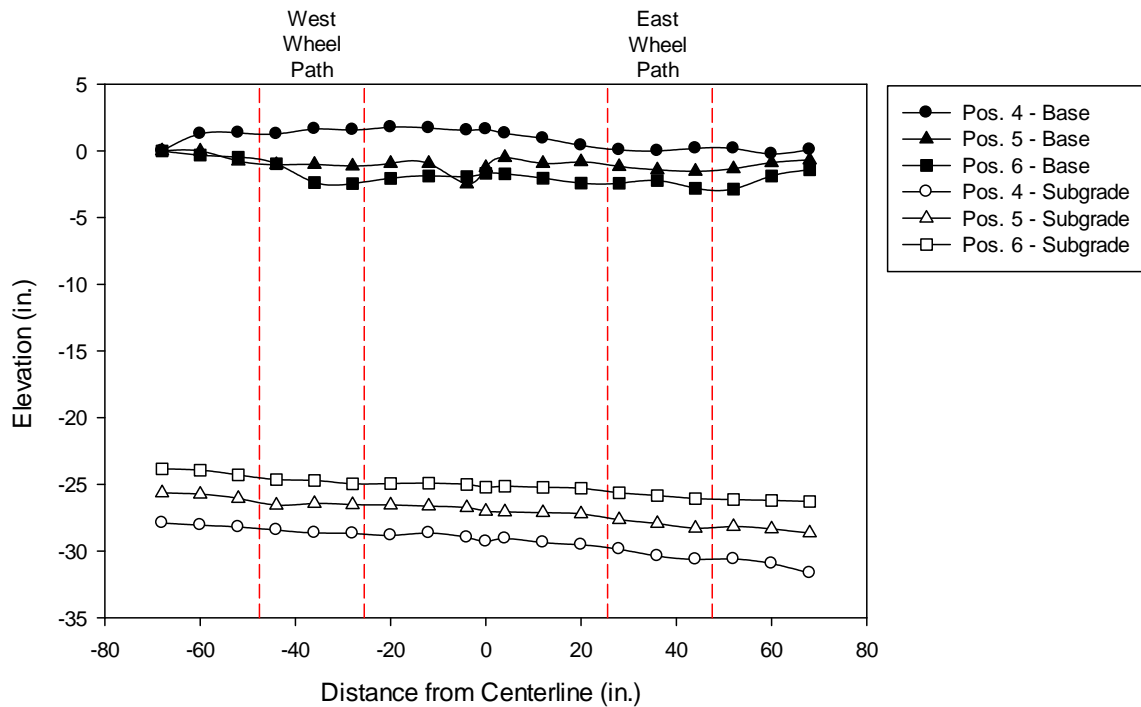
Figure G-16: Forensic topographic survey in Test Section Control 3.

APPENDIX H – PHOTOS OF EXHUMED GEOSYNTHETIC SAMPLES

Figure H-1: Photos of exhumed geosynthetic from Test Section 1 – Tensar BX Type 2.

Figure H-2: Photos of exhumed geosynthetic from Test Section 2 – Tensar BX Type 2.

Figure H-3: Photos of exhumed geosynthetic from Test Section 3 – Tensar BX Type 2.

Figure H-4: Photos of exhumed geosynthetic from Test Section 4 – NAUE Secugrid 30-30 Q1.

Figure H-5: Photos of exhumed geosynthetic from Test Section 5 – Colbond Enkagrid MAX 30.

Figure H-6: Photos of exhumed geosynthetic from Test Section 6 – Synteen SF 11.

Figure H-7: Photos of exhumed geosynthetic from Test Section 7 – Synteen SF 12.

Figure H-8: Photos of exhumed geosynthetic from Test Section 8 – TenCate Mirafi BXG11.

Figure H-9: Photos of exhumed geosynthetic from Test Section 9 – Huesker Fornit 30.

Figure H-10: Photos of exhumed geosynthetic from Test Section 10 – Syntec Tenax MS330.

Figure H-11: Photos of exhumed geosynthetic from Test Section 11 – Tensar TX140.

Figure H-12: Photos of exhumed geosynthetic from Test Section 12 – Tensar TX160.
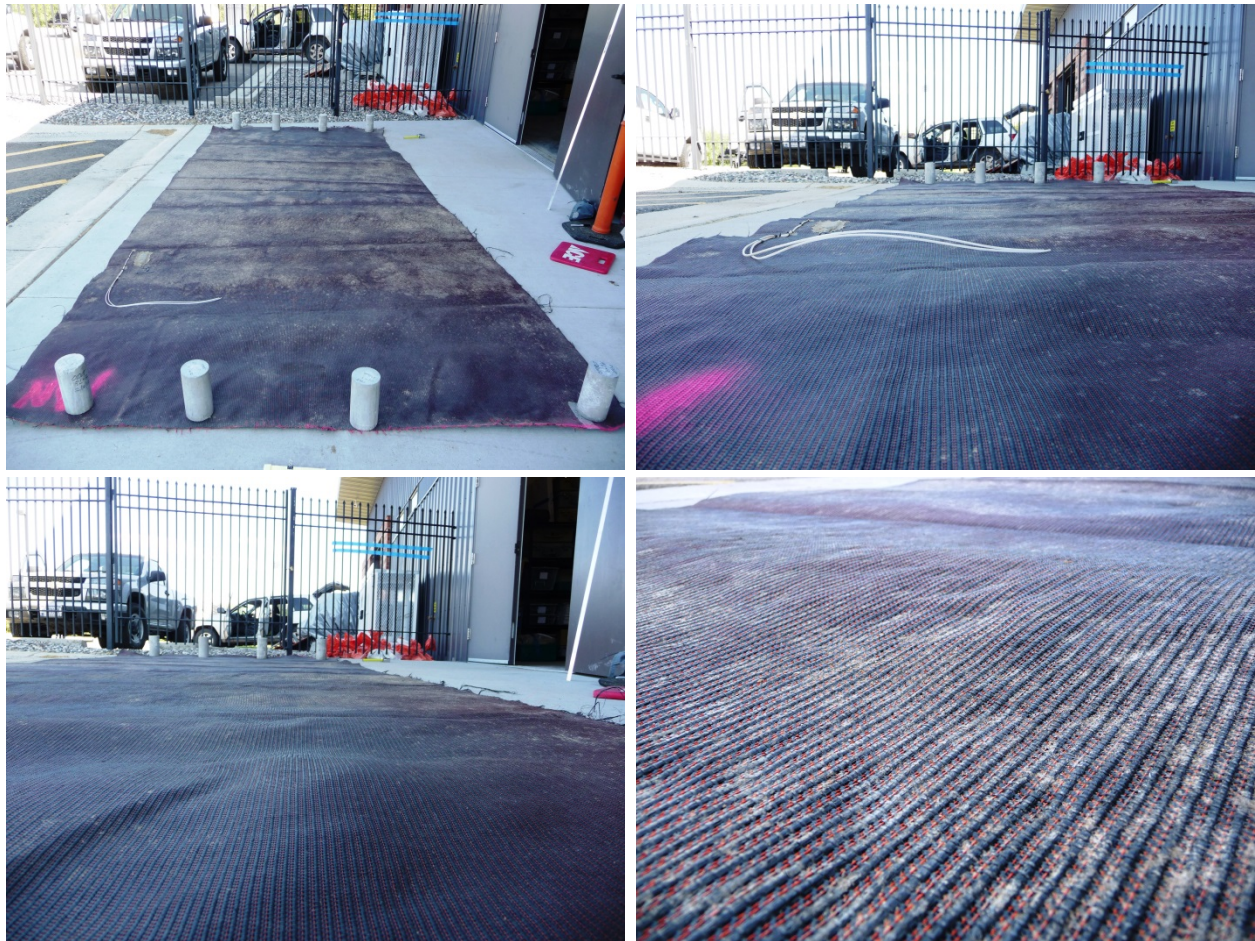
Figure H-13: Photos of exhumed geosynthetic from Test Section 13 – TenCate Mirafi RS580i.
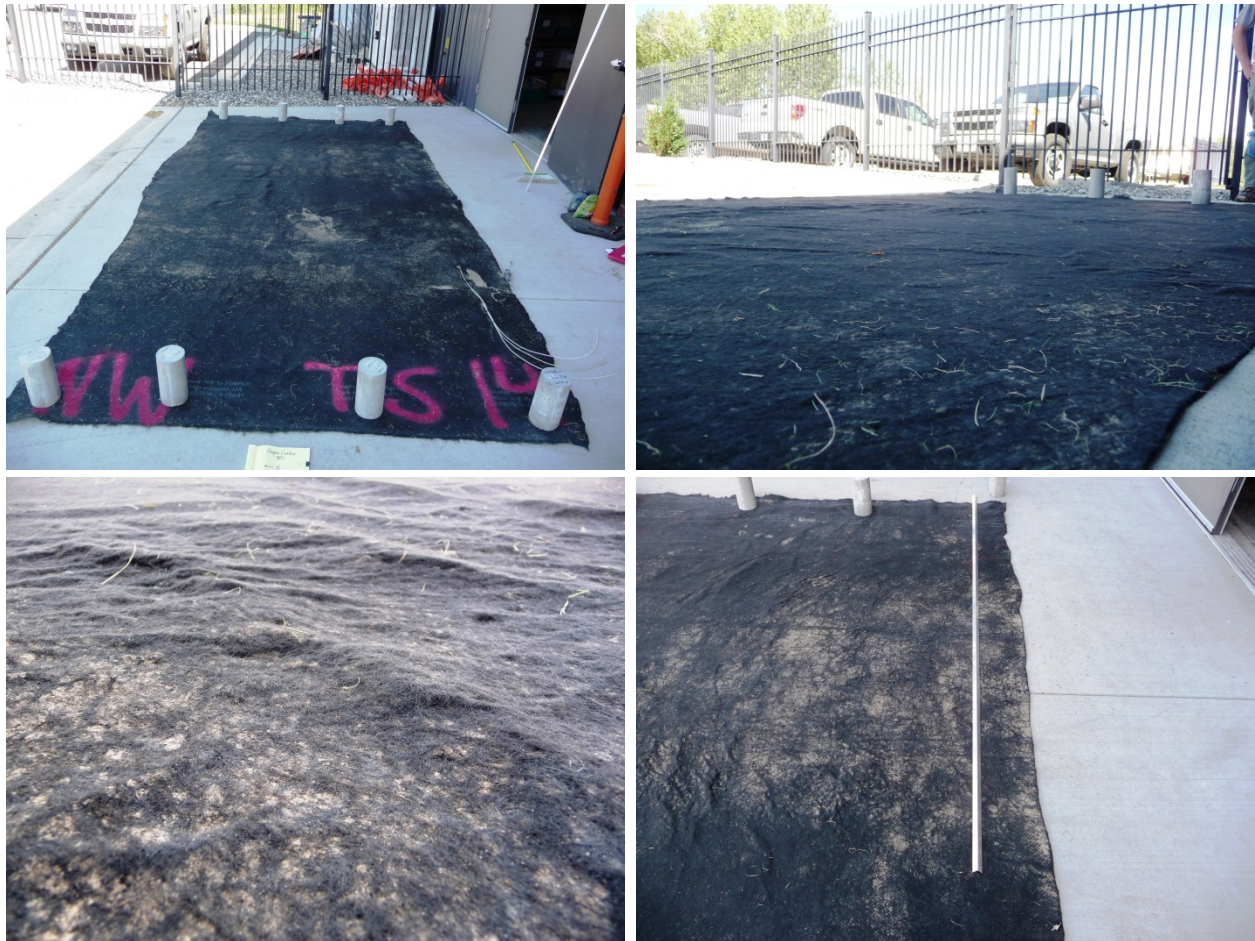
Figure H-14: Test Section 14 – Propex Geotex 801.

APPENDIX I – TENSILE STRENGTH TEST RESULTS FROM EXHUMED GEOSYNTHETICS
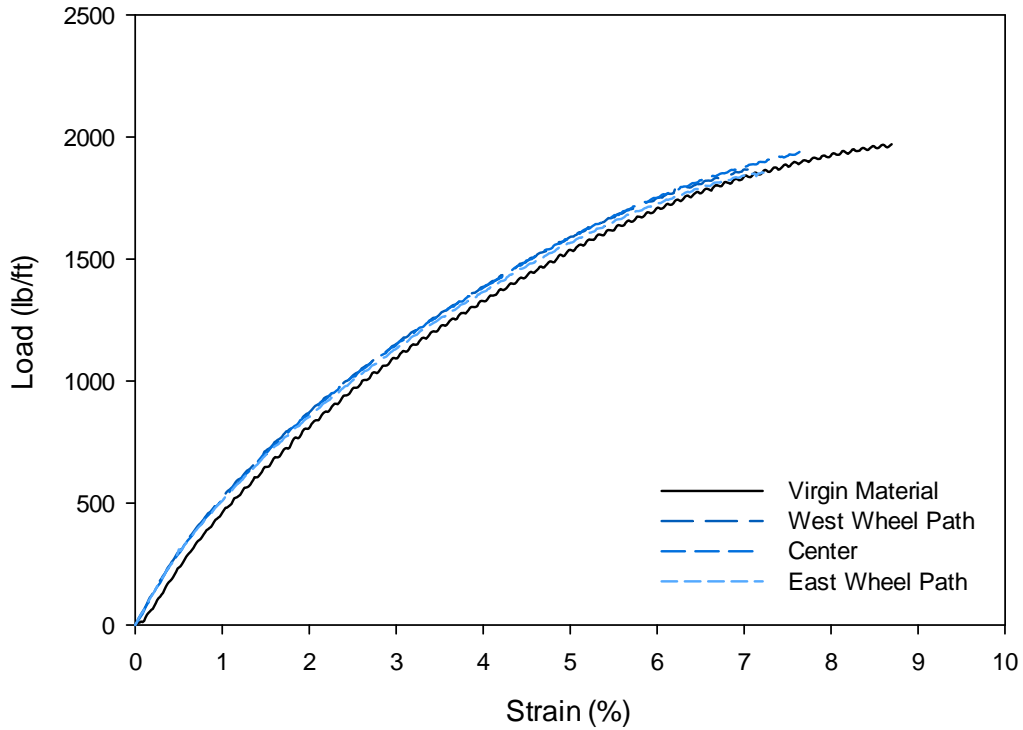
Figure I-1: Tensile strength of exhumed geosynthetic from Test Section 1 – Tensar BX Type 2.
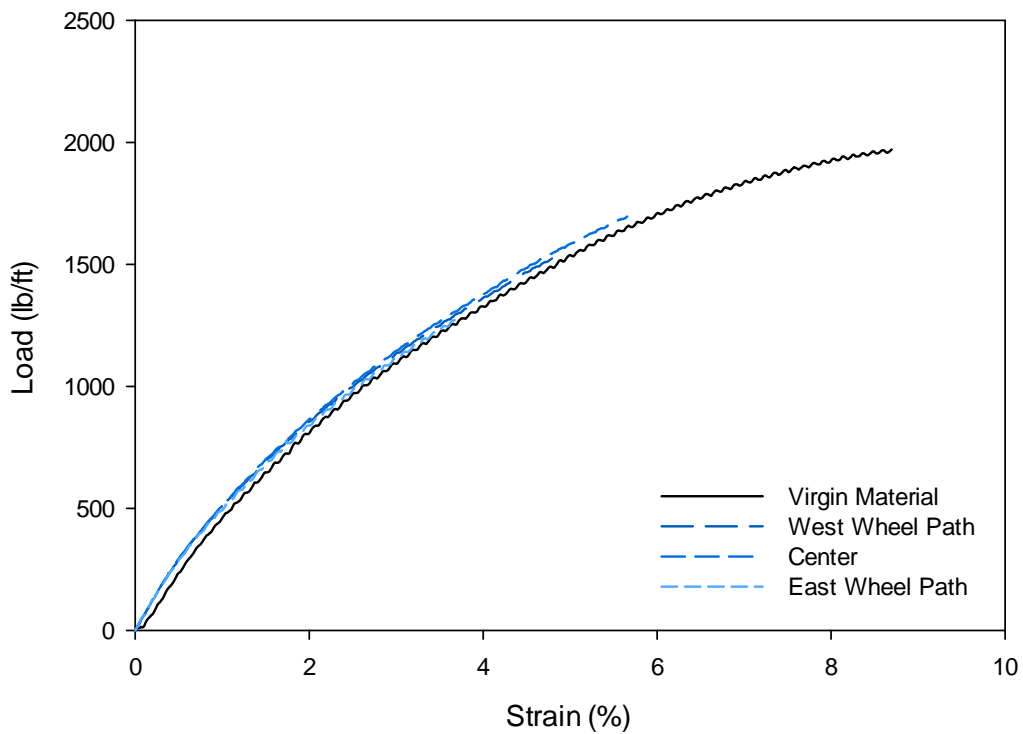
Figure I-2: Tensile strength of exhumed geosynthetic from Test Section 2 – Tensar BX Type 2.
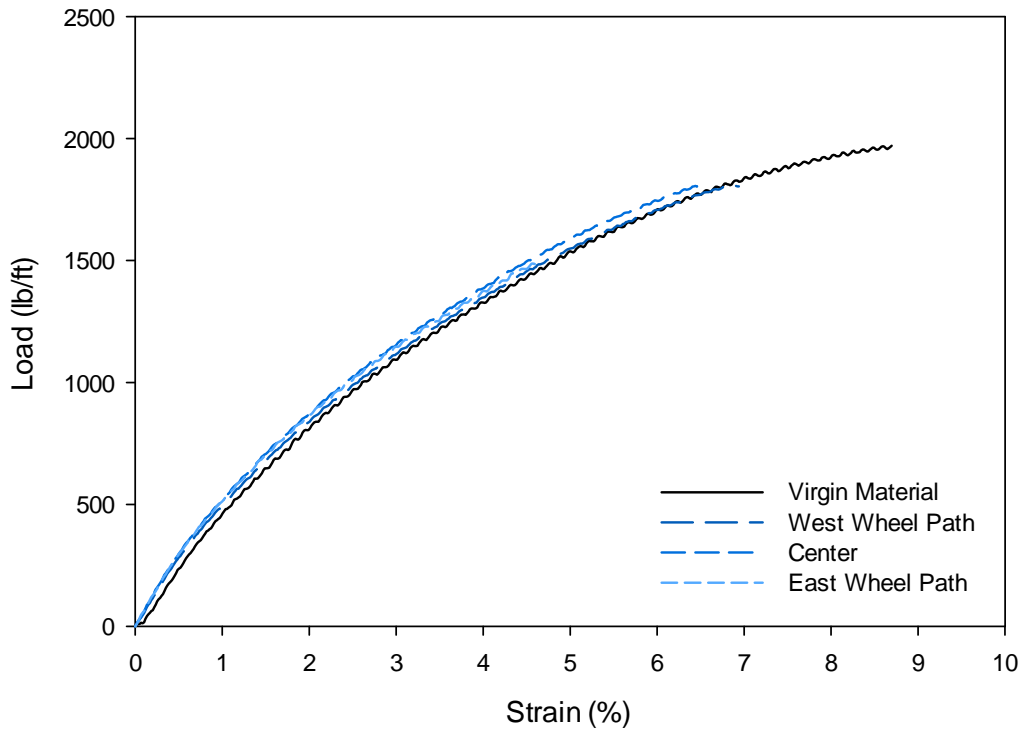
Figure I-3: Tensile strength of exhumed geosynthetic from Test Section 3 – Tensar BX Type 2.
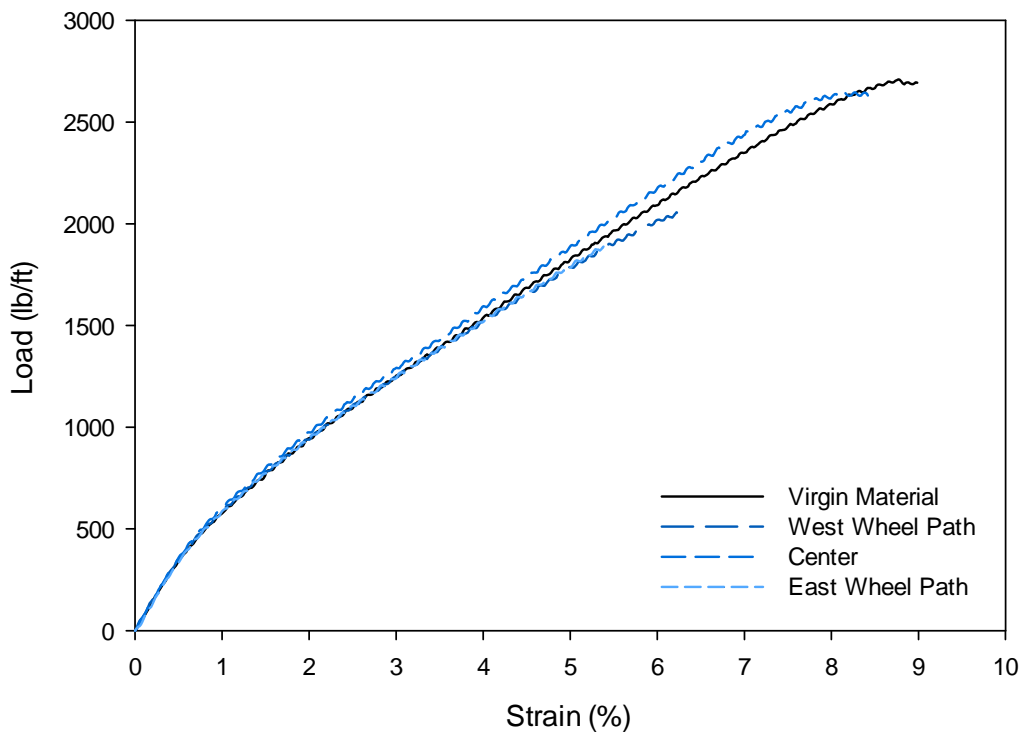
Figure I-4: Tensile strength of exhumed geosynthetic from Test Section 4 – NAUE Secugrid 30-30 Q1.
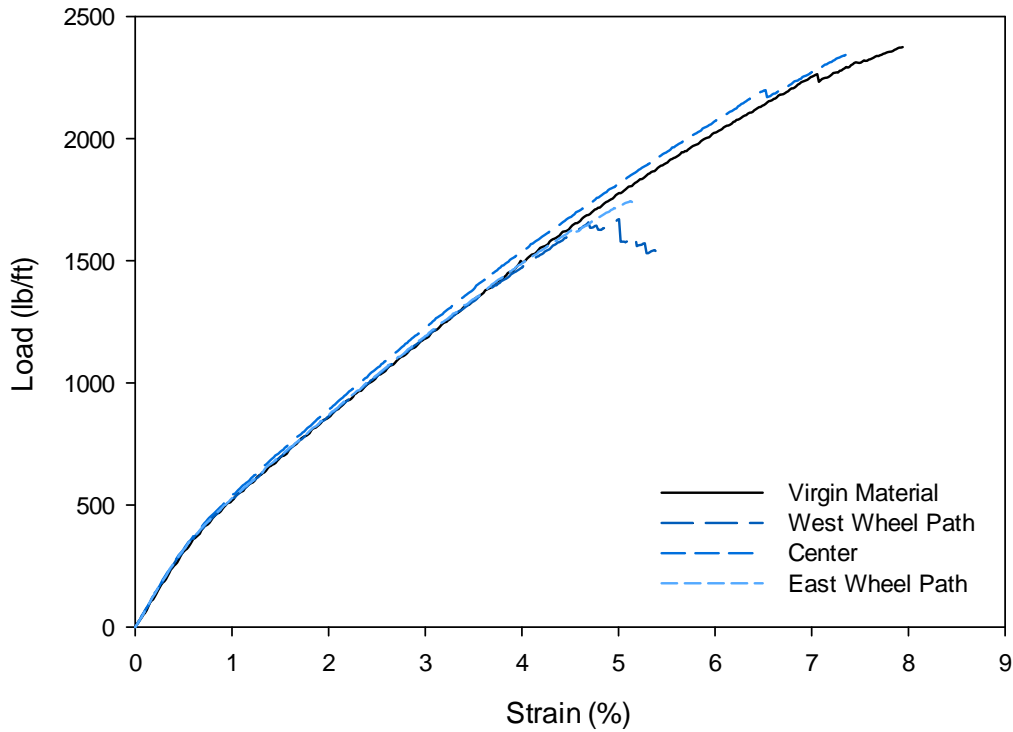
Figure I-5: Tensile strength of exhumed geosynthetic from Test Section 5 – Colbond Enkagrid MAX 30.
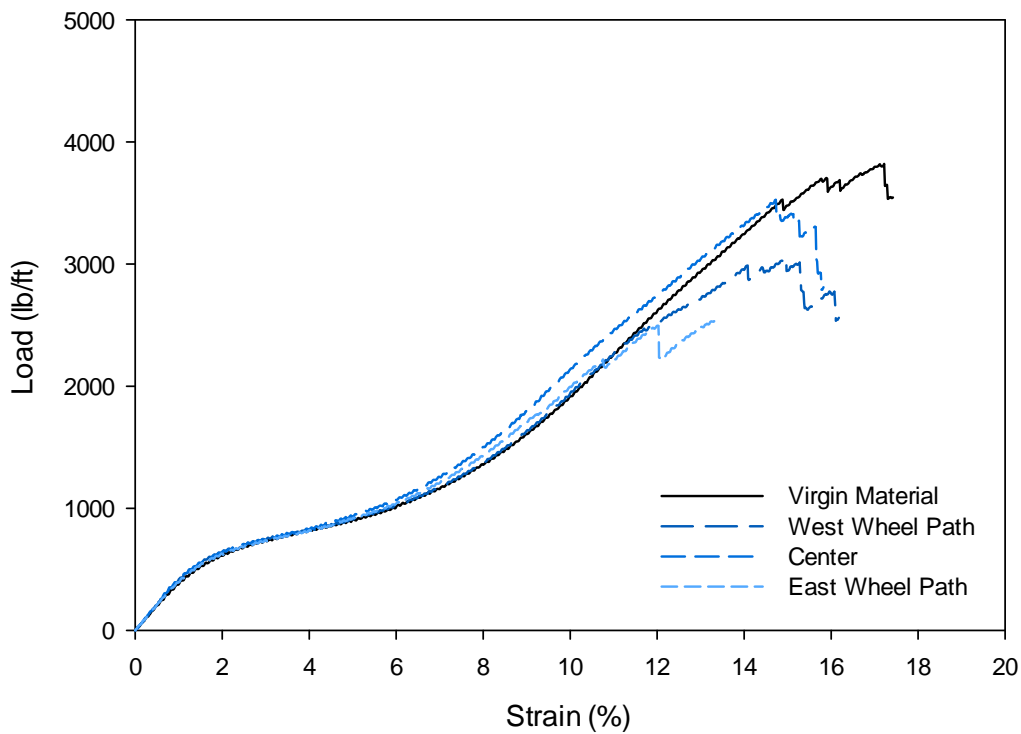
Figure I-6: Tensile strength of exhumed geosynthetic from Test Section 6 – Synteen SF 11.
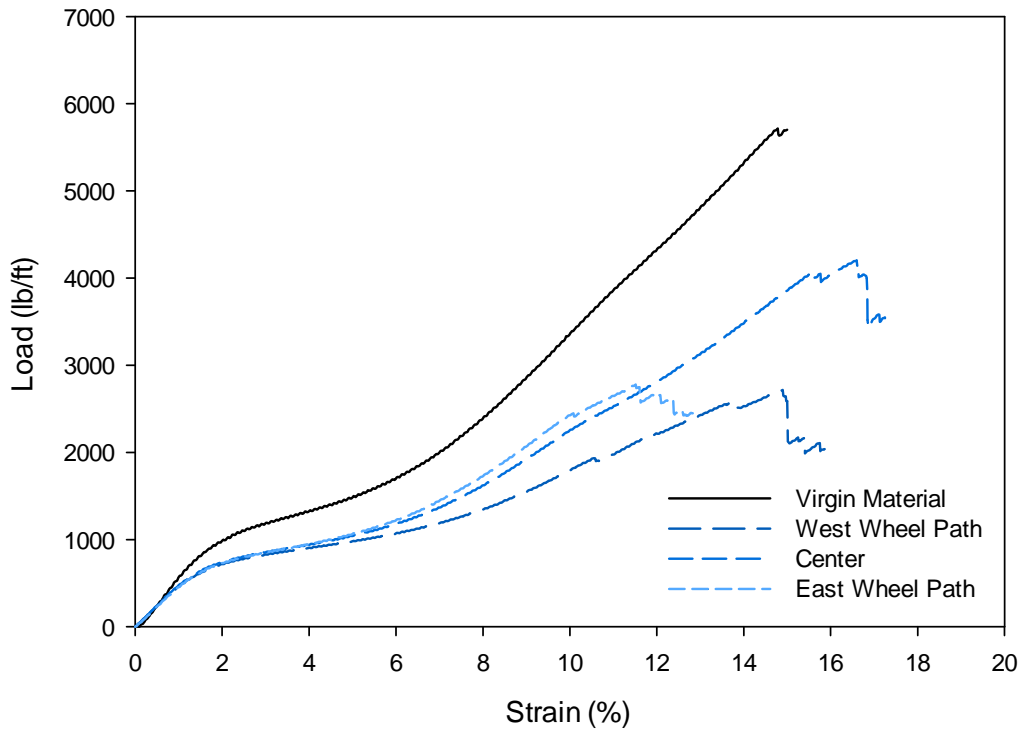
Figure I-7: Tensile strength of exhumed geosynthetic from Test Section 7 – Synteen SF 12.
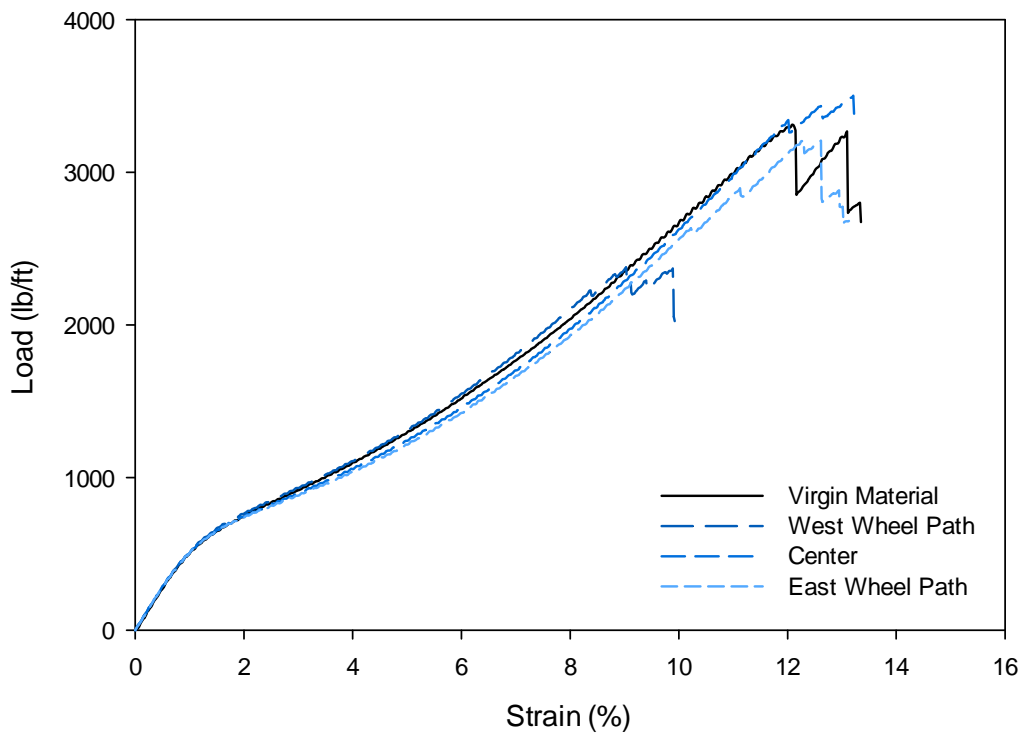
Figure I-8: Tensile strength of exhumed geosynthetic from Test Section 8 – TenCate Mirafi BXG11.
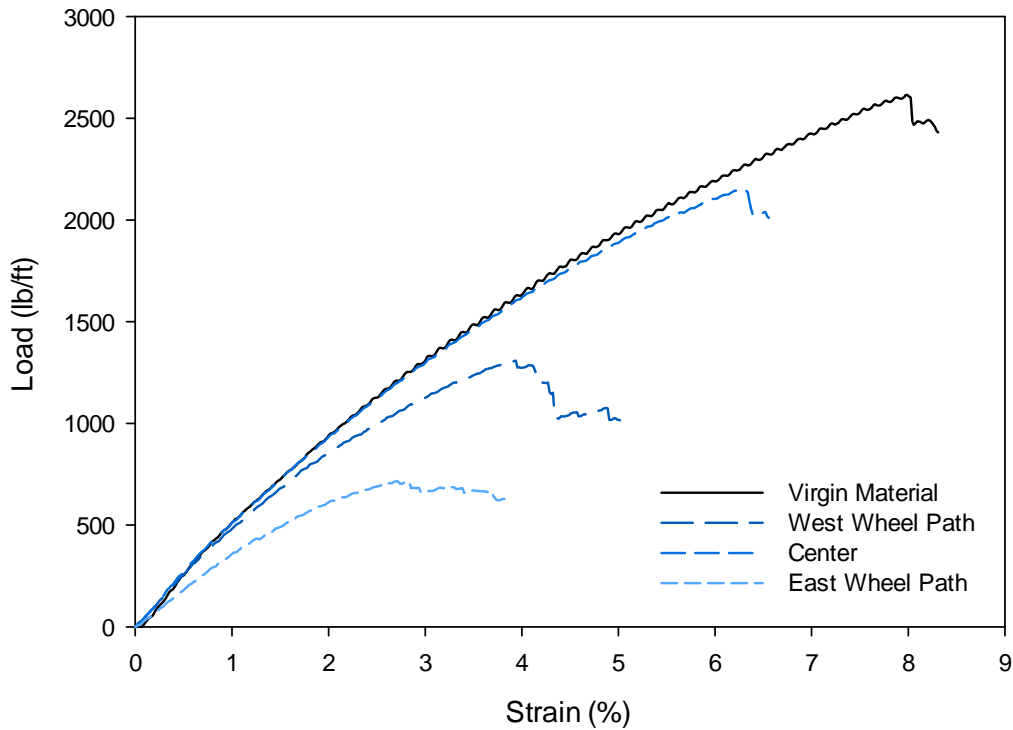
Figure I-9: Tensile strength of exhumed geosynthetic from Test Section 9 – Huesker Fornit 30.
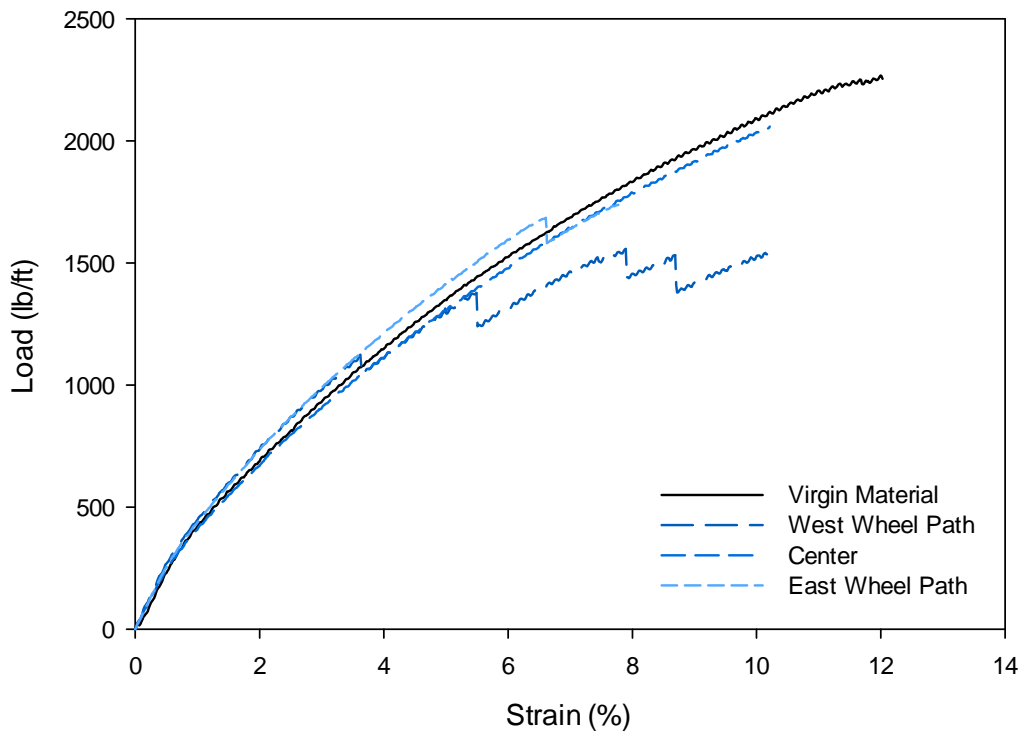
Figure I-10: Tensile strength of exhumed geosynthetic from Test Section 10 – Syntec Tenax MS 330.
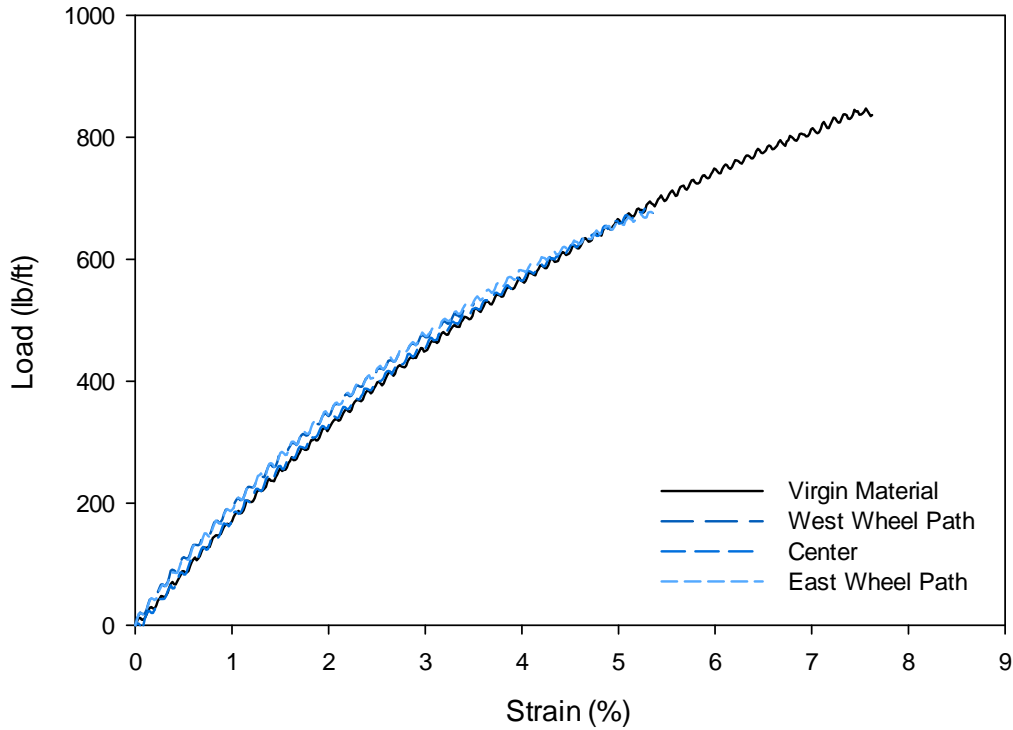
Figure I-11: Tensile strength of exhumed geosynthetic from Test Section 11 – Tensar TX140.
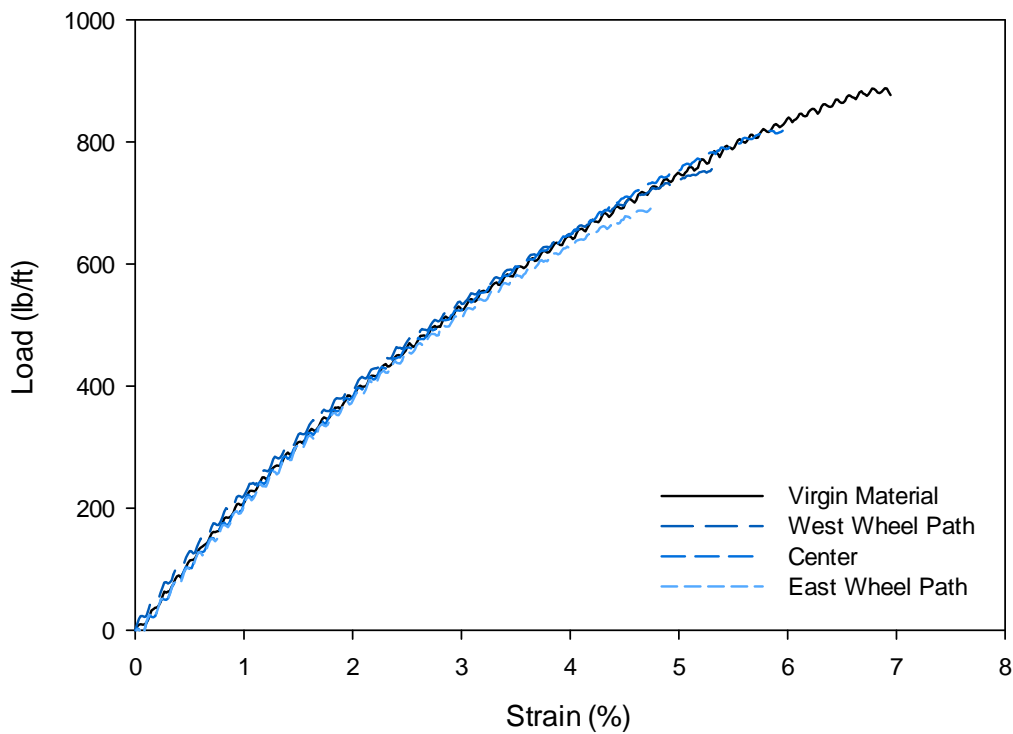
Figure I-12: Tensile strength of exhumed geosynthetic from Test Section 12 – Tensar TX160.
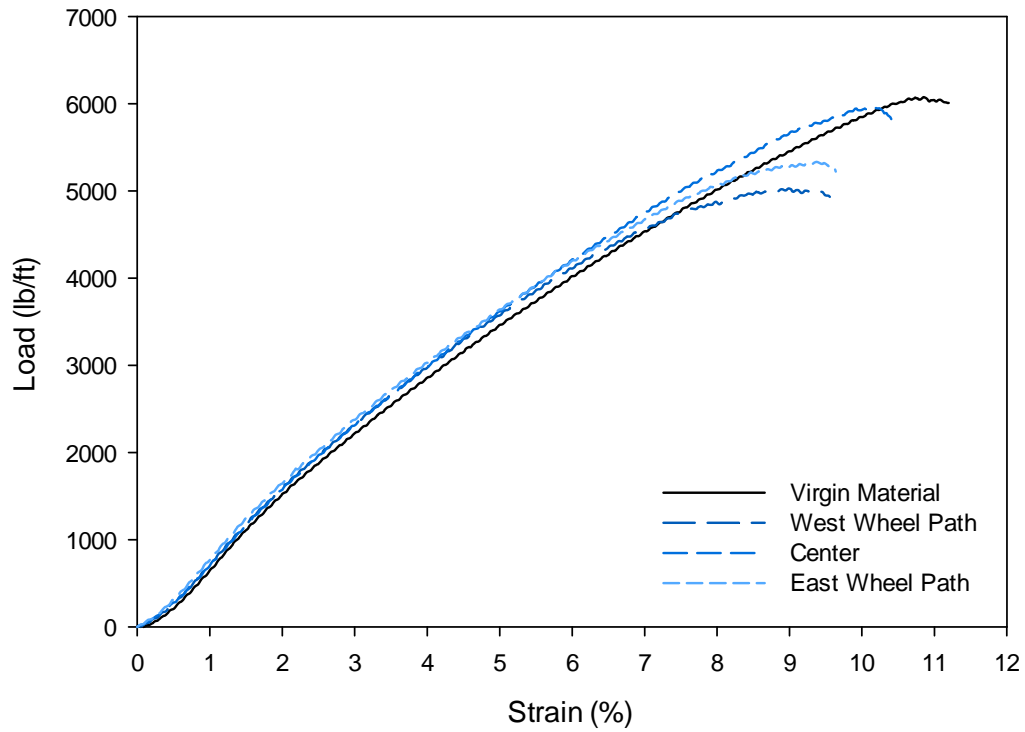
Figure I-13: Tensile strength of exhumed geosynthetic from Test Section 13 – TenCate Mirafi RS580i.

APPENDIX J – PHOTOS OF FORENSIC WORK
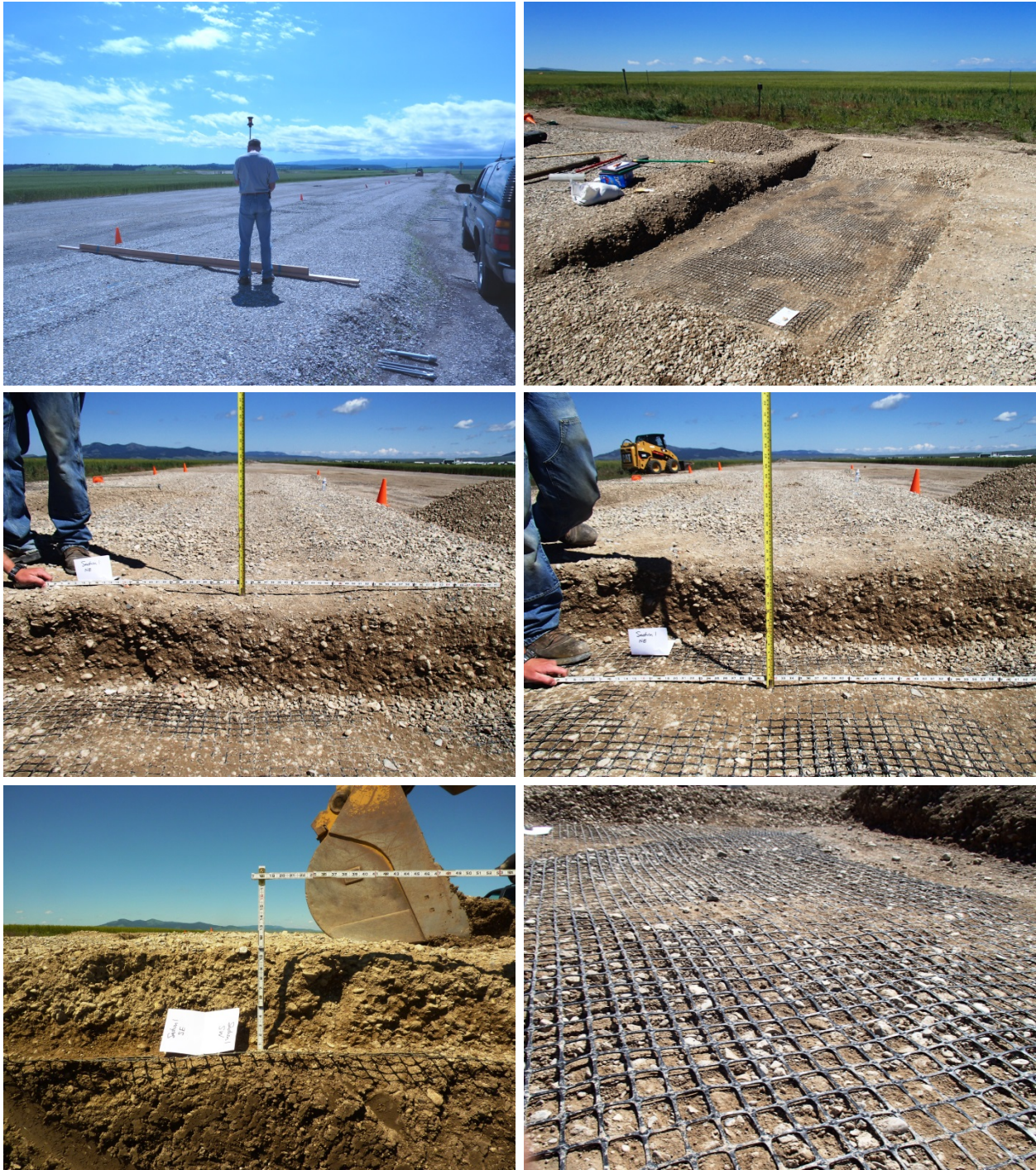
Figure J-1: Photos of forensic work in Test Section 1 – Tensar BX Type 2.

Figure J-2: Photos of forensic work in Test Section 2 – Tensar BX Type 2.

Figure J-3: Photos of forensic work in Test Section 3 – Tensar BX Type 2.

Figure J-4: Photos of forensic work in Test Section 4 – NAUE Secugrid 30-30 Q1.

Figure J-5: Photos of forensic work in Test Section 5 – Colbond Enkagrid MAX 30.
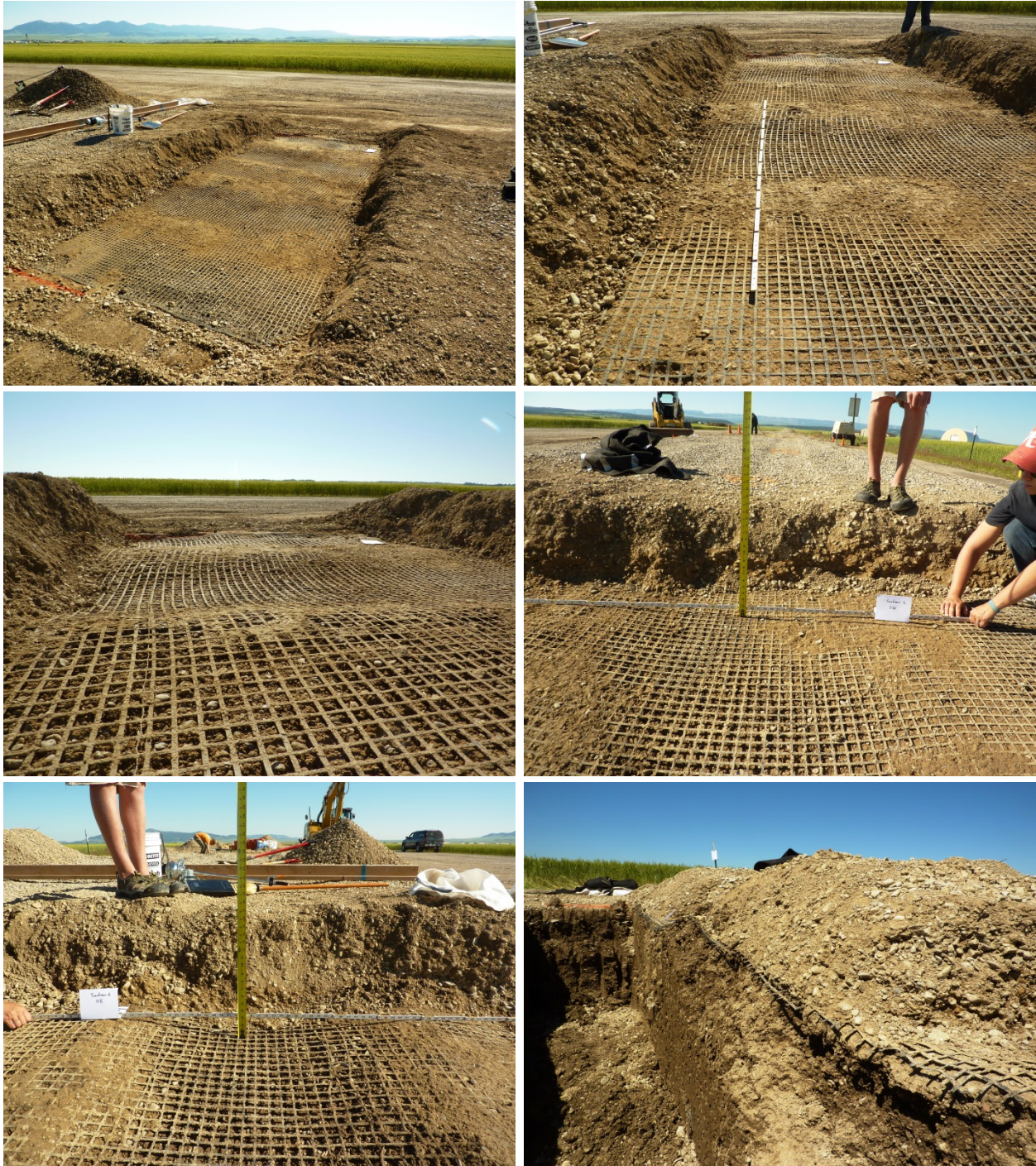
Figure J-6: Photos of forensic work in Test Section 6 – Synteen SF 11.

Figure J-7: Photos of forensic work in Test Section 7 – Synteen SF 12.

Figure J-8: Photos of forensic work in Test Section 8 – TenCate Mirafi BXG11.
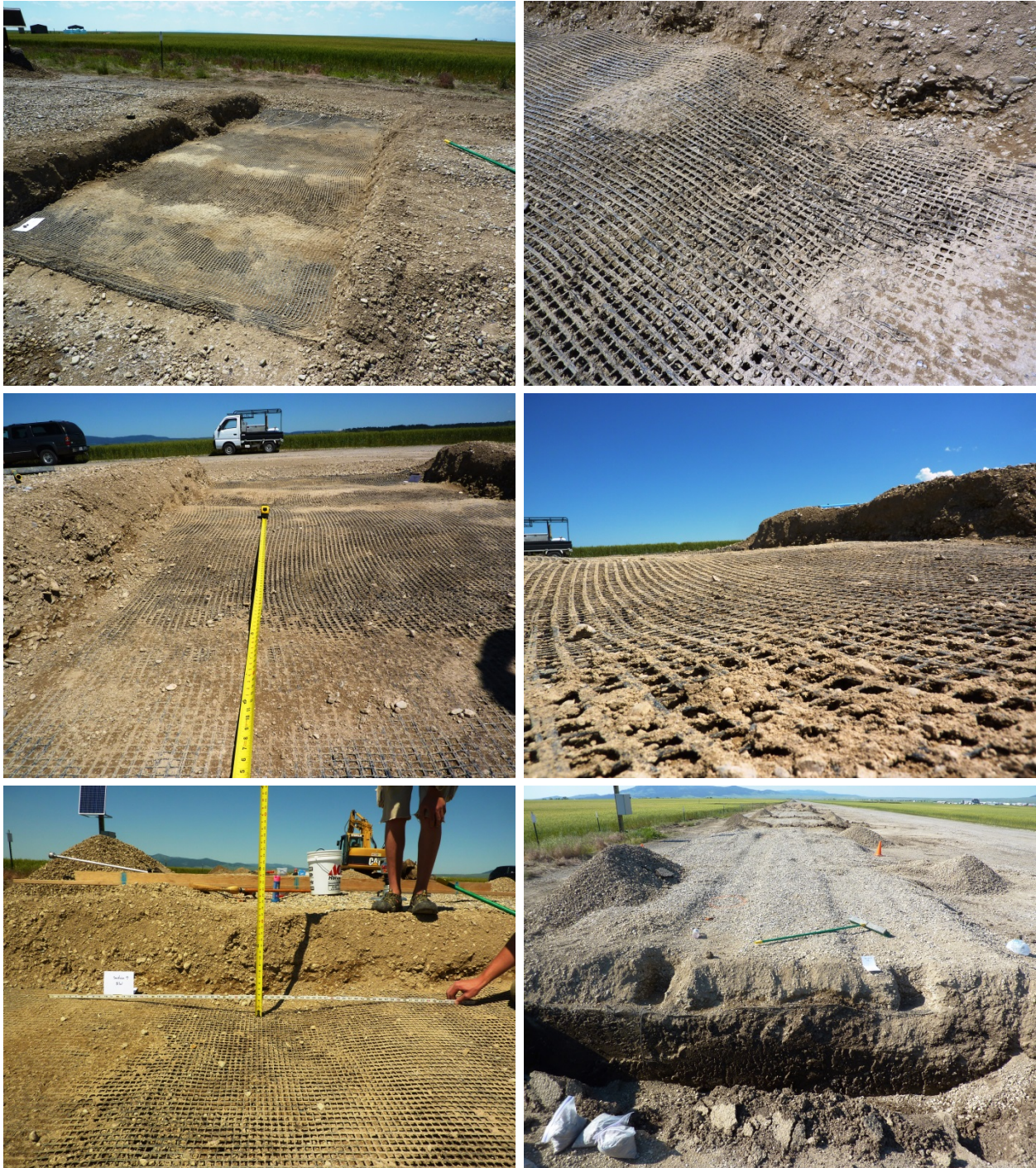
Figure J-9: Photos of forensic work in Test Section 9 – Huesker Fornit 30.
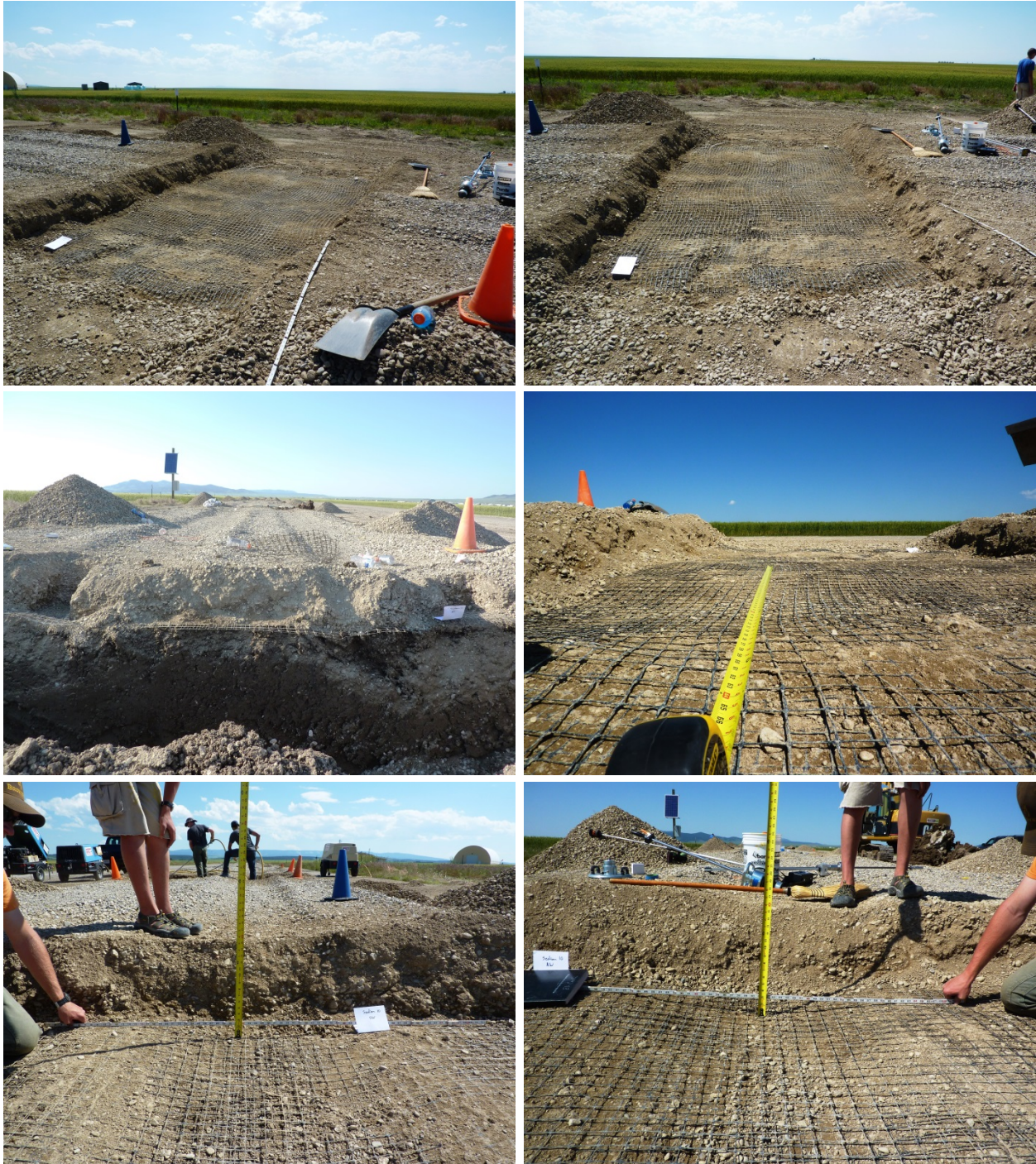
Figure J-10: Photos of forensic work in Test Section 10 – Syntec Tenax MS 330.

Figure J-11: Photos of forensic work in Test Section 11 – Tensar TX140.

Figure J-12: Photos of forensic work in Test Section 12 – Tensar TX160.

Figure J-13: Photos of forensic work in Test Section 13 – TenCate Mirafi RS580i.

Figure J-14: Photos of forensic work in Test Section 14 – Propex Geotex 801.
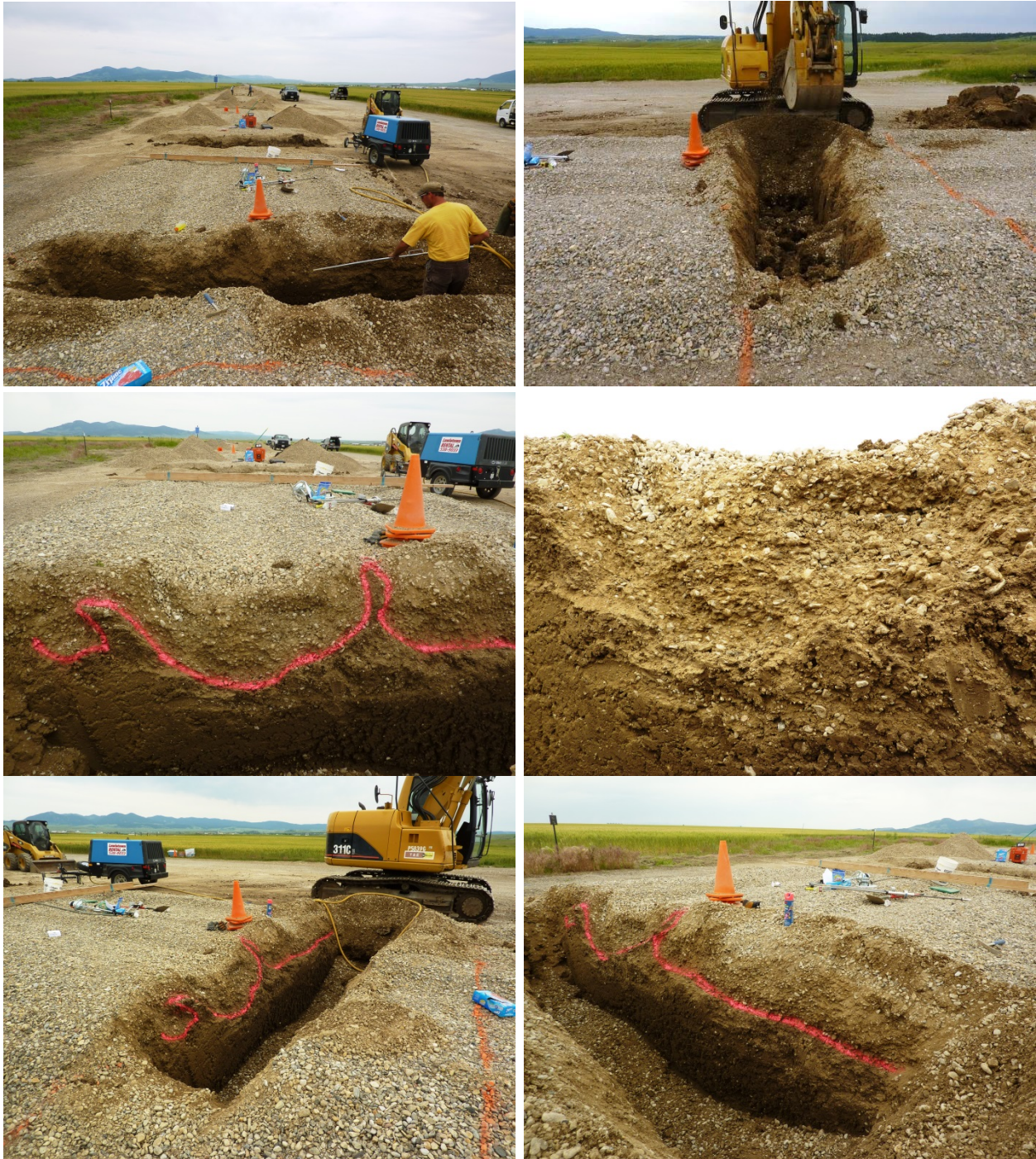
Figure J-15: Photos of forensic work in Control 1 Test Section.

Figure J-16: Photos of forensic work in Control 2 Test Section.

Figure J-17: Photos of forensic work in Control 3 Test Section.

APPENDIX K – SUMMARY OF STATISTICS RESULTS FOR LONGITUDINAL RUT ANALYSIS

Key:

similar (p > 0.75)
between (0.25 < p < 0.75)
different (p < 0.25)

Test Section Comparison	Truck Pass															
	1	3	5	10	20	40	80	175	300	325	351	395	440	540	640	740
1-2	0.0054	0.3861	0.4684	0.0063	0.2703	0.4130	0.5917	0.1736	0.0045	0.0677	N/A	N/A	N/A	N/A	N/A	N/A
1-3	0.0024	0.0004	0.0711	0.4754	0.0360	0.1665	0.3514	0.7244	0.0457	0.0022	0.0051	0.0056	0.0037	0.0103	0.0039	0.0000
1-4	0.1228	0.0479	0.2992	0.0074	0.2425	0.4907	0.2278	0.6990	0.0065	0.0001	0.0002	0.0001	0.0001	0.0002	0.0000	0.0000
1-5	0.0001	0.0001	0.0389	0.9549	0.0000	0.0085	0.0000	0.0070	0.0000	0.0000	0.0000	0.0000	N/A	N/A	N/A	N/A
1-6	0.0009	0.0000	0.1090	0.9844	0.0128	0.7119	0.0003	0.0169	0.0001	0.0000	0.0000	0.0000	N/A	N/A	N/A	N/A
1-7	0.0000	0.0000	0.0035	0.0109	0.0000	0.0000	0.0000	0.0000	0.0000	0.0000	N/A	N/A	N/A	N/A	N/A	N/A
1-8	0.0000	0.0000	0.5962	0.7759	0.0000	0.9710	0.0000	0.0007	0.0000	0.0004	0.0000	0.0000	0.0000	0.0160	0.0118	0.0054
1-9	0.0000	0.0000	0.2198	0.0000	0.0000	0.0000	0.0000	0.0000	0.0000	0.0000	N/A	N/A	N/A	N/A	N/A	N/A
1-10	0.0000	0.0000	0.0002	0.0173	0.0000	0.0639	0.0094	0.0000	0.0000	0.0000	0.0000	0.0000	0.0000	N/A	N/A	N/A
1-11	0.0000	0.0015	0.0002	0.0001	0.0000	0.2317	0.8487	0.0009	0.0002	N/A	N/A	0.0012	0.0004	0.0002	0.0008	0.0031
1-12	0.0000	0.0090	0.0271	0.0000	0.0000	0.0103	0.2651	0.0000	0.0000	N/A	N/A	N/A	N/A	N/A	N/A	N/A
1-13	0.0133	0.0571	0.0000	0.5436	0.1826	0.0470	0.0000	0.5444	0.1887	0.0447	0.7899	0.0322	0.7724	0.5403	0.4192	0.2083
1-14	0.0004	0.0300	0.0007	0.3685	0.8726	0.0000	0.0000	0.5579	0.0040	0.1374	0.0006	0.0569	0.1367	0.0153	0.0949	0.1103
1-C1	0.0002	0.6036	0.5592	0.0009	0.0000	0.0002	0.0015	0.0006	0.0024	N/A	N/A	N/A	N/A	N/A	N/A	N/A
1-C2	0.0014	0.9246	0.8653	0.9781	0.1937	0.0000	0.0000	0.0003	0.0000	0.0002	0.0032	0.0000	0.0000	0.0002	0.0000	0.0377
1-C3	0.0907	0.3624	0.0156	0.0079	0.3517	0.0000	0.0000	0.0000	0.0000	0.0000	0.0000	0.0000	0.0000	0.0000	0.0000	0.0000
2-3	0.4109	0.0001	0.0067	0.1169	0.1806	0.0517	0.2196	0.1126	0.0001	0.9981	N/A	N/A	N/A	N/A	N/A	N/A
2-4	0.1005	0.0876	0.0372	0.6785	0.9054	0.1870	0.1508	0.1056	0.0000	0.3322	N/A	N/A	N/A	N/A	N/A	N/A
2-5	0.0412	0.0000	0.0022	0.0059	0.0000	0.0033	0.0001	0.0014	0.0000	0.0013	N/A	N/A	N/A	N/A	N/A	N/A
2-6	0.2907	0.0000	0.0084	0.0056	0.0614	0.3369	0.0006	0.0032	0.0000	0.0013	N/A	N/A	N/A	N/A	N/A	N/A
2-7	0.0002	0.0000	0.0000	0.0000	0.0000	0.0000	0.0000	0.0000	0.0000	0.0000	N/A	N/A	N/A	N/A	N/A	N/A
2-8	0.0045	0.0000	0.7659	0.0011	0.0000	0.4770	0.0001	0.0002	0.0000	0.1066	N/A	N/A	N/A	N/A	N/A	N/A
2-9	0.0000	0.0000	0.0242	0.0000	0.0000	0.0000	0.0000	0.0000	0.0000	0.0000	N/A	N/A	N/A	N/A	N/A	N/A
2-10	0.0000	0.0000	0.0000	0.0000	0.0000	0.0205	0.0143	0.0000	0.0000	0.0045	N/A	N/A	N/A	N/A	N/A	N/A
2-11	0.0000	0.0005	0.0001	0.0000	0.0000	0.0978	0.7876	0.0002	0.0000	N/A	N/A	N/A	N/A	N/A	N/A	N/A
2-12	0.0002	0.0073	0.0604	0.0000	0.0000	0.0045	0.1776	0.0000	0.0000	N/A	N/A	N/A	N/A	N/A	N/A	N/A
2-13	0.5606	0.0000	0.0000	0.0266	0.6323	0.1510	0.0000	0.6930	0.8575	0.0000	N/A	N/A	N/A	N/A	N/A	N/A
2-14	0.1869	0.0001	0.0000	0.0086	0.1192	0.0001	0.0000	0.1215	0.0000	0.2895	N/A	N/A	N/A	N/A	N/A	N/A
2-C1	0.0490	0.7158	0.7683	0.0000	0.0000	0.0001	0.0008	0.0001	0.0003	N/A	N/A	N/A	N/A	N/A	N/A	N/A
2-C2	0.2270	0.3722	0.5230	0.0086	0.6484	0.0000	0.0000	0.0148	0.4035	0.0000	N/A	N/A	N/A	N/A	N/A	N/A
2-C3	0.0701	0.8914	0.0000	0.6094	0.0018	0.0000	0.0000	0.0000	0.0000	0.0000	N/A	N/A	N/A	N/A	N/A	N/A
3-4	0.0338	0.0318	0.2951	0.0899	0.2339	0.6370	0.8357	0.9770	0.4431	0.1195	0.1787	0.1831	0.0987	0.2305	0.0190	0.0217
3-5	0.3514	0.1010	0.8301	0.4977	0.0025	0.1065	0.0007	0.0163	0.0006	0.0000	0.0000	0.0000	N/A	N/A	N/A	N/A
3-6	0.9391	0.1849	0.7117	0.4631	0.5083	0.5546	0.0050	0.0309	0.0027	0.0001	0.0000	0.0000	N/A	N/A	N/A	N/A
3-7	0.0069	0.0000	0.3896	0.0043	0.5083	0.0000	0.0000	0.0000	0.0000	0.0000	N/A	N/A	N/A	N/A	N/A	N/A
3-8	0.0698	0.0029	0.0081	0.3216	0.0045	0.2171	0.0012	0.0020	0.0001	0.0330	0.0002	0.0023	0.0001	0.0295	0.0234	0.0118
3-9	0.0000	0.0000	0.4258	0.0000	0.0000	0.0001	0.0000	0.0000	0.0000	0.0000	N/A	N/A	N/A	N/A	N/A	N/A
3-10	0.0006	0.0661	0.0000	0.0066	0.0000	0.7435	0.1490	0.0000	0.0000	0.0000	0.0000	0.0000	0.0000	N/A	N/A	N/A
3-11	0.0005	0.4650	0.0000	0.0001	0.0000	0.7128	0.3811	0.0020	0.0021	N/A	N/A	0.0059	0.0015	0.0010	0.0019	0.0053
3-12	0.0059	0.1067	0.0002	0.0000	0.0000	0.0463	0.5922	0.0000	0.0000	N/A	N/A	N/A	N/A	N/A	N/A	N/A
3-13	0.1832	0.0000	0.0000	0.7900	0.4262	0.0048	0.0000	0.4100	0.0326	0.0001	0.0360	0.0001	0.0158	0.2421	0.0052	0.0888
3-14	0.8277	0.0000	0.0000	0.9015	0.0039	0.0000	0.0000	0.2679	0.0741	0.2948	0.0208	0.8926	0.8478	0.1007	0.5356	0.3768
3-C1	0.3427	0.0002	0.0005	0.0001	0.0003	0.0011	0.0030	0.0006	0.0068	N/A	N/A	N/A	N/A	N/A	N/A	N/A
3-C2	0.6961	0.0007	0.0150	0.3896	0.4427	0.0000	0.0000	0.0000	0.0000	0.0000	0.0000	0.0000	0.0000	0.0000	0.0000	0.0000
3-C3	0.0221	0.0003	0.6543	0.0421	0.0001	0.0000	0.0000	0.0000	0.0000	0.0000	0.0000	0.0000	0.0000	0.0000	0.0000	0.0000
4-5	0.0014	0.0017	0.1834	0.0074	0.0000	0.0748	0.0008	0.0162	0.0037	0.0009	0.0001	0.0002	N/A	N/A	N/A	N/A
4-6	0.0131	0.0008	0.4627	0.0069	0.0834	0.8530	0.0060	0.0312	0.0092	0.0020	0.0001	0.0001	N/A	N/A	N/A	N/A
4-7	0.0000	0.0000	0.0184	0.0000	0.0000	0.0001	0.0000	0.0000	0.0000	0.0000	N/A	N/A	N/A	N/A	N/A	N/A
4-8	0.0002	0.0000	0.0485	0.0021	0.0001	0.5135	0.0013	0.0019	0.0006	0.2858	0.0023	0.0200	0.0015	0.0401	0.0731	0.0601
4-9	0.0000	0.0000	0.7936	0.0000	0.0000	0.0001	0.0000	0.0000	0.0003	0.0000	N/A	N/A	N/A	N/A	N/A	N/A
4-10	0.0000	0.0002	0.0000	0.0000	0.0000	0.4457	0.1934	0.0000	0.0000	0.0045	0.0000	0.0004	0.0001	N/A	N/A	N/A
4-11	0.0000	0.1184	0.0000	0.0000	0.0000	0.5147	0.2868	0.0020	0.0053	N/A	N/A	0.0191	0.0058	0.0015	0.0073	0.0206
4-12	0.0000	0.4639	0.0004	0.0000	0.0000	0.0335	0.6767	0.0000	0.0000	N/A	N/A	N/A	N/A	N/A	N/A	N/A
4-13	0.2265	0.0000	0.0000	0.0157	0.7261	0.0109	0.0000	0.3995	0.0146	0.0000	0.0035	0.0000	0.0005	0.0353	0.0000	0.0023
4-14	0.0054	0.0000	0.0000	0.0053	0.1195	0.0000	0.0000	0.2463	0.2144	0.0157	0.1694	0.3635	0.1868	0.3360	0.4759	0.9805
4-C1	0.0021	0.0538	0.0185	0.0000	0.0000	0.0005	0.0035	0.0006	0.0106	N/A	N/A	N/A	N/A	N/A	N/A	N/A
4-C2	0.0173	0.0430	0.1615	0.0052	0.7379	0.0000	0.0000	0.0000	0.0000	0.0000	0.0000	0.0000	0.0000	0.0000	0.0000	0.0000
4-C3	0.9566	0.1076	0.0569	0.9047	0.0030	0.0000	0.0000	0.0000	0.0000	0.0000	0.0000	0.0000	0.0000	0.0000	0.0000	0.0000
5-6	0.3049	0.4699	0.5380	0.9387	0.0356	0.0883	0.9480	0.8348	0.5750	0.4934	0.1829	0.1444	N/A	N/A	N/A	N/A
5-7	0.0178	0.0276	0.5225	0.0077	0.0000	0.0035	0.0000	0.0000	0.0736	0.0000	N/A	N/A	N/A	N/A	N/A	N/A
5-8	0.2379	0.5273	0.0026	0.7239	0.8924	0.0158	0.8460	0.6197	0.2554	0.0960	0.9719	0.3957	N/A	N/A	N/A	N/A
5-9	0.0000	0.0044	0.2881	0.0000	0.0000	0.0024	0.0000	0.0000	0.3850	0.0000	N/A	N/A	N/A	N/A	N/A	N/A
5-10	0.0007	0.7030	0.0000	0.0120	0.0001	0.1287	0.0118	0.1256	0.1316	0.4285	0.0046	0.5657	N/A	N/A	N/A	N/A
5-11	0.0005	0.0284	0.0000	0.0001	0.0076	0.4592	0.0004	0.2608	0.1990	N/A	N/A	0.9052	N/A	N/A	N/A	N/A
5-12	0.0154	0.0050	0.0000	0.0000	0.0015	0.2832	0.0900	0.0010	0.0001	N/A	N/A	N/A	N/A	N/A	N/A	N/A
5-13	0.0076	0.0000	0.0000	0.4975	0.0002	0.0001	0.0000	0.0154	0.0000	0.0000	0.0000	0.0000	N/A	N/A	N/A	N/A
5-14	0.3305	0.0000	0.0000	0.2504	0.0000	0.0000	0.0000	0.0000	0.1447	0.0000	0.0059	0.0001	N/A	N/A	N/A	N/A
5-C1	0.9326	0.0000	0.0000	0.0001	0.1609	0.0072	0.0505	0.0054	0.0713	N/A	N/A	N/A	N/A	N/A	N/A	N/A
5-C2	0.6593	0.0000	0.0036	0.9231	0.0003	0.0000	0.0000	0.0000	0.0000	0.0000	0.0000	0.0000	N/A	N/A	N/A	N/A
5-C3	0.0004	0.0000	0.8796	0.0025	0.0000	0.0000	0.0000	0.0000	0.0000	0.0000	0.0000	0.0000	N/A	N/A	N/A	N/A

Test Section Comparison	Truck Pass															
	1	3	5	10	20	40	80	175	300	325	351	395	440	540	640	740
6-7	0.0021	0.0002	0.1528	0.0110	0.0000	0.0002	0.0000	0.0000	0.4315	0.0000	N/A	N/A	N/A	N/A	N/A	N/A
6-8	0.0421	0.0532	0.0103	0.7905	0.0513	0.7109	0.9264	0.8497	0.6905	0.0545	0.2174	0.0506	N/A	N/A	N/A	N/A
6-9	0.0000	0.0000	0.6426	0.0000	0.0000	0.0001	0.0001	0.0000	0.9218	0.0000	N/A	N/A	N/A	N/A	N/A	N/A
6-10	0.0001	0.5963	0.0000	0.0174	0.0000	0.4115	0.0497	0.3340	0.6199	0.2006	0.4851	0.0575	N/A	N/A	N/A	N/A
6-11	0.0001	0.0343	0.0000	0.0001	0.0002	0.4589	0.0019	0.4243	0.4449	N/A	N/A	0.1915	N/A	N/A	N/A	N/A
6-12	0.0019	0.0029	0.0001	0.0000	0.0000	0.0347	0.1268	0.0034	0.0002	N/A	N/A	N/A	N/A	N/A	N/A	N/A
6-13	0.0940	0.0000	0.0000	0.4520	0.1039	0.0144	0.0000	0.0098	0.0001	0.0000	0.0000	0.0000	N/A	N/A	N/A	N/A
6-14	0.8678	0.0000	0.0000	0.2247	0.0000	0.0000	0.0000	0.0000	0.0298	0.0000	0.0000	0.0000	N/A	N/A	N/A	N/A
6-C1	0.3040	0.0000	0.0004	0.0002	0.0011	0.0003	0.0481	0.0068	0.1144	N/A	N/A	N/A	N/A	N/A	N/A	N/A
6-C2	0.7139	0.0000	0.0262	0.9921	0.1186	0.0000	0.0000	0.0000	0.0000	0.0000	0.0000	0.0000	N/A	N/A	N/A	N/A
6-C3	0.0060	0.0000	0.2747	0.0024	0.0000	0.0000	0.0000	0.0000	0.0000	0.0000	0.0000	0.0000	N/A	N/A	N/A	N/A
7-8	0.2673	0.0197	0.0000	0.0133	0.0000	0.0000	0.0000	0.0000	0.6885	0.0000	N/A	N/A	N/A	N/A	N/A	N/A
7-9	0.0001	0.2113	0.0470	0.0011	0.3775	0.5808	0.4808	0.2935	0.3651	0.7207	N/A	N/A	N/A	N/A	N/A	N/A
7-10	0.2285	0.0004	0.0000	0.6373	0.1166	0.0000	0.0000	0.0000	0.6417	0.0000	N/A	N/A	N/A	N/A	N/A	N/A
7-11	0.2601	0.0000	0.0000	0.0555	0.1002	0.0029	0.0000	0.0000	0.7994	N/A	N/A	N/A	N/A	N/A	N/A	N/A
7-12	0.8187	0.0000	0.0000	0.0077	0.3635	0.2783	0.0000	0.1406	0.0003	N/A	N/A	N/A	N/A	N/A	N/A	N/A
7-13	0.0000	0.0000	0.0000	0.0004	0.0000	0.0000	0.0000	0.0000	0.0000	0.0000	N/A	N/A	N/A	N/A	N/A	N/A
7-14	0.0012	0.0000	0.0000	0.0000	0.0000	0.0000	0.0000	0.0000	0.0020	0.0000	N/A	N/A	N/A	N/A	N/A	N/A
7-C1	0.0336	0.0000	0.0000	0.1270	0.0017	0.4181	0.5989	0.9972	0.2084	N/A	N/A	N/A	N/A	N/A	N/A	N/A
7-C2	0.0260	0.0000	0.0007	0.0082	0.0000	0.0000	0.0000	0.0000	0.0000	N/A	N/A	N/A	N/A	N/A	N/A	N/A
7-C3	0.0000	0.0000	0.4747	0.0000	0.0000	0.0000	0.0000	0.0000	0.0000	N/A	N/A	N/A	N/A	N/A	N/A	N/A
8-9	0.0000	0.0023	0.0313	0.0000	0.0000	0.0000	0.0000	0.0000	0.7025	0.0000	N/A	N/A	N/A	N/A	N/A	N/A
8-10	0.0292	0.1283	0.0000	0.0214	0.0002	0.1110	0.0184	0.2812	0.9660	0.2552	0.0167	0.6800	0.5817	N/A	N/A	N/A
8-11	0.0300	0.0002	0.0000	0.0001	0.0068	0.2490	0.0006	0.4436	0.6219	N/A	N/A	0.5531	0.6361	0.1958	0.0560	0.0202
8-12	0.2097	0.0000	0.0238	0.0000	0.0014	0.0125	0.1110	0.0018	0.0003	N/A	N/A	N/A	N/A	N/A	N/A	N/A
8-13	0.0008	0.0000	0.0000	0.3036	0.0004	0.0391	0.0000	0.0065	0.0000	0.0000	0.0000	0.0000	0.0000	0.0147	0.0143	0.0039
8-14	0.0382	0.0000	0.0000	0.1253	0.0000	0.0000	0.0000	0.0000	0.0070	0.0004	0.0071	0.0010	0.0001	0.0195	0.0569	0.1871
8-C1	0.3070	0.0000	0.9415	0.0006	0.1414	0.0002	0.0447	0.0084	0.1611	N/A	N/A	N/A	N/A	N/A	N/A	N/A
8-C2	0.1818	0.0000	0.7092	0.7929	0.0007	0.0000	0.0000	0.0000	0.0000	0.0000	0.0000	0.0000	0.0000	0.0013	0.0017	0.0024
8-C3	0.0001	0.0000	0.0001	0.0014	0.0000	0.0000	0.0000	0.0000	0.0000	0.0000	0.0000	0.0000	0.0000	0.0003	0.0002	0.0003
9-10	0.0021	0.0001	0.0000	0.0002	0.0309	0.0000	0.0000	0.0000	0.5919	0.0000	N/A	N/A	N/A	N/A	N/A	N/A
9-11	0.0008	0.0000	0.0000	0.1198	0.0298	0.0017	0.0000	0.0001	0.4365	N/A	N/A	N/A	N/A	N/A	N/A	N/A
9-12	0.0004	0.0000	0.0003	0.5766	0.1252	0.1531	0.0000	0.4802	0.0002	N/A	N/A	N/A	N/A	N/A	N/A	N/A
9-13	0.0000	0.0000	0.0000	0.0000	0.0000	0.0000	0.0000	0.0000	0.0000	0.0000	N/A	N/A	N/A	N/A	N/A	N/A
9-14	0.0000	0.0000	0.0000	0.0000	0.0000	0.0000	0.0000	0.0000	0.0215	0.0000	N/A	N/A	N/A	N/A	N/A	N/A
9-C1	0.0000	0.0000	0.0041	0.0389	0.0001	0.7294	0.8627	0.6466	0.1239	N/A	N/A	N/A	N/A	N/A	N/A	N/A
9-C2	0.0000	0.0000	0.0851	0.0000	0.0000	0.0000	0.0000	0.0000	0.0000	0.0000	N/A	N/A	N/A	N/A	N/A	N/A
9-C3	0.0000	0.0000	0.0884	0.0000	0.0000	0.0000	0.0000	0.0000	0.0000	0.0000	N/A	N/A	N/A	N/A	N/A	N/A
10-11	0.8704	0.0082	0.7485	0.0148	0.6654	0.8327	0.0425	0.9536	0.6098	N/A	N/A	0.7527	0.9993	N/A	N/A	N/A
10-12	0.3695	0.0005	0.0649	0.0018	0.7578	0.0546	0.7589	0.0050	0.0002	N/A	N/A	N/A	N/A	N/A	N/A	N/A
10-13	0.0000	0.0000	0.0262	0.0014	0.0000	0.0018	0.0000	0.0012	0.0000	0.0000	0.0000	0.0000	0.0000	N/A	N/A	N/A
10-14	0.0000	0.0000	0.3995	0.0000	0.0000	0.0000	0.0000	0.0000	0.0061	0.0000	0.0000	0.0002	0.0000	N/A	N/A	N/A
10-C1	0.0020	0.0000	0.0000	0.0590	0.0494	0.0012	0.0089	0.0174	0.1655	N/A	N/A	N/A	N/A	N/A	N/A	N/A
10-C2	0.0026	0.0000	0.0002	0.0212	0.0000	0.0000	0.0000	0.0000	0.0000	0.0000	0.0000	0.0000	0.0000	N/A	N/A	N/A
10-C3	0.0000	0.0000	0.0000	0.0000	0.0000	0.0000	0.0000	0.0000	0.0000	0.0000	0.0000	0.0000	0.0000	N/A	N/A	N/A
11-12	0.4231	0.3517	0.0555	0.3394	0.5373	0.1429	0.2676	0.0158	0.0011	N/A	N/A	N/A	N/A	N/A	N/A	N/A
11-13	0.0000	0.0000	0.0390	0.0000	0.0000	0.0008	0.0000	0.0010	0.0000	N/A	N/A	0.0001	0.0001	0.0022	0.0018	0.0083
11-14	0.0000	0.0000	0.2149	0.0000	0.0000	0.0000	0.0000	0.0000	0.0005	N/A	N/A	0.0013	0.0002	0.0015	0.0061	0.0587
11-C1	0.0017	0.0002	0.0000	0.7009	0.1191	0.0016	0.0011	0.0183	0.2613	N/A	N/A	N/A	N/A	N/A	N/A	N/A
11-C2	0.0024	0.0011	0.0001	0.0000	0.0000	0.0000	0.0000	0.0000	0.0000	N/A	N/A	0.0000	0.0000	0.0001	0.0001	0.0016
11-C3	0.0000	0.0003	0.0000	0.0000	0.0000	0.0000	0.0000	0.0000	0.0000	N/A	N/A	0.0000	0.0000	0.0000	0.0000	0.0002
12-13	0.0000	0.0000	0.0001	0.0000	0.0000	0.0000	0.0000	0.0000	0.0000	N/A	N/A	N/A	N/A	N/A	N/A	N/A
12-14	0.0012	0.0000	0.0952	0.0000	0.0000	0.0000	0.0000	0.0000	0.0000	N/A	N/A	N/A	N/A	N/A	N/A	N/A
12-C1	0.0276	0.0064	0.0050	0.1544	0.0263	0.0703	0.0060	0.3785	0.0046	N/A	N/A	N/A	N/A	N/A	N/A	N/A
12-C2	0.0211	0.0097	0.0140	0.0000	0.0000	0.0000	0.0000	0.0000	0.0000	N/A	N/A	N/A	N/A	N/A	N/A	N/A
12-C3	0.0000	0.0127	0.0000	0.0000	0.0000	0.0000	0.0000	0.0000	0.0000	N/A	N/A	N/A	N/A	N/A	N/A	N/A
13-14	0.0436	0.5112	0.0012	0.8024	0.0223	0.0850	0.1511	0.4855		0.0003	0.0001	0.0003	0.0613	0.0193	0.0311	0.1292
13-C1	0.0112	0.0038	0.0000	0.0000	0.0000	0.0000	0.0000	0.0002	0.0003	N/A	N/A	N/A	N/A	N/A	N/A	N/A
13-C2	0.0909	0.1215	0.0000	0.4863	0.9984	0.0043	0.2423	0.0009	0.1454	0.1657	0.0015	0.0278	0.0000	0.0000	0.0000	0.0019
13-C3	0.1819	0.0003	0.0000	0.0133	0.0002	0.0000	0.0000	0.0000	0.0000	0.0000	0.0000	0.0000	0.0000	0.0000	0.0000	0.0000
14-C1	0.3316	0.0007	0.0000	0.0000	0.0000	0.0000	0.0000	0.0003	0.0266	N/A	N/A	N/A	N/A	N/A	N/A	N/A
14-C2	0.7934	0.0529	0.0005	0.3681	0.1259	0.0702	0.0153	0.0000	0.0000	0.0000	0.0000	0.0000	0.0001	0.0001	0.0001	0.0051
14-C3	0.0017	0.0000	0.0140	0.0575	0.0000	0.0000	0.0000	0.0000	0.0000	0.0000	0.0000	0.0000	0.0000	0.0000	0.0000	0.0004
C1-C2	0.6277	0.5303	0.6704	0.0001	0.0000	0.0000	0.0000	0.0000	0.0000	N/A	N/A	N/A	N/A	N/A	N/A	N/A
C1-C3	0.0008	0.5996	0.0001	0.0000	0.0000	0.0000	0.0000	0.0000	0.0000	N/A	N/A	N/A	N/A	N/A	N/A	N/A
C2-C3	0.0111	0.2106	0.0013	0.0069	0.0020	0.0000	0.0000	0.0000	0.0000	0.0000	0.0000	0.0000	0.0000	0.0000	0.0000	0.0000

APPENDIX L – TRANSVERSE RUT PROFILES DURING TRAFFICKING
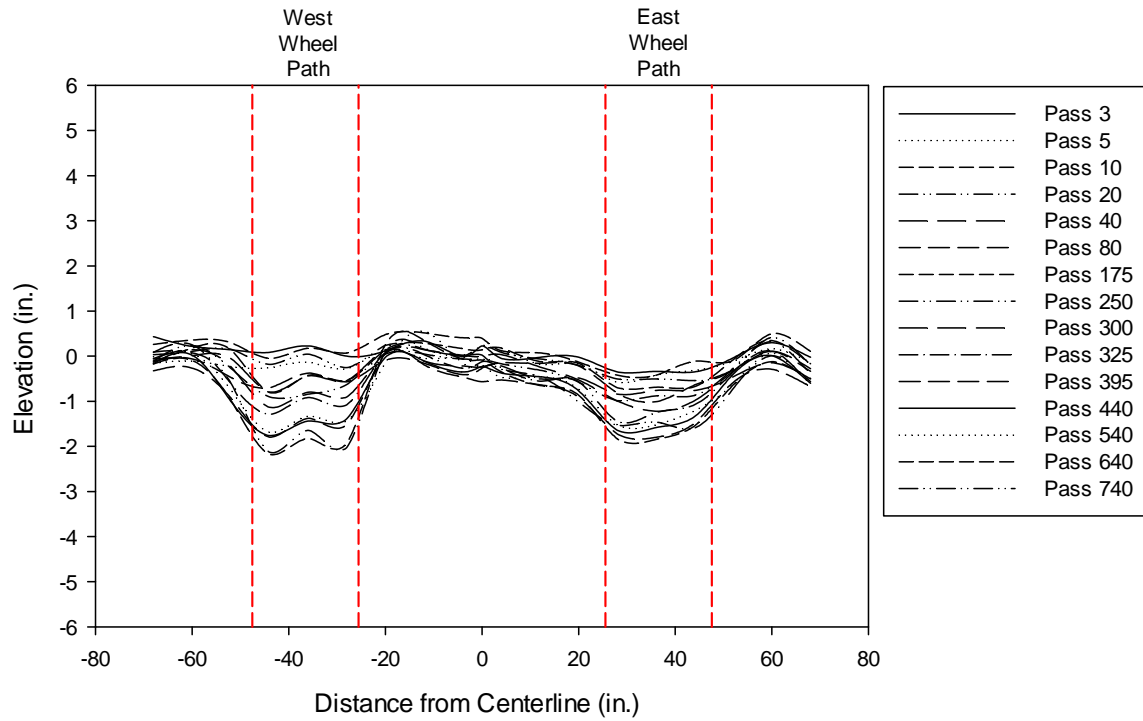
Figure L-1: Transverse rut profiles for Test Section 1, north (Tensar BX Type 2, CBR = 2.17).
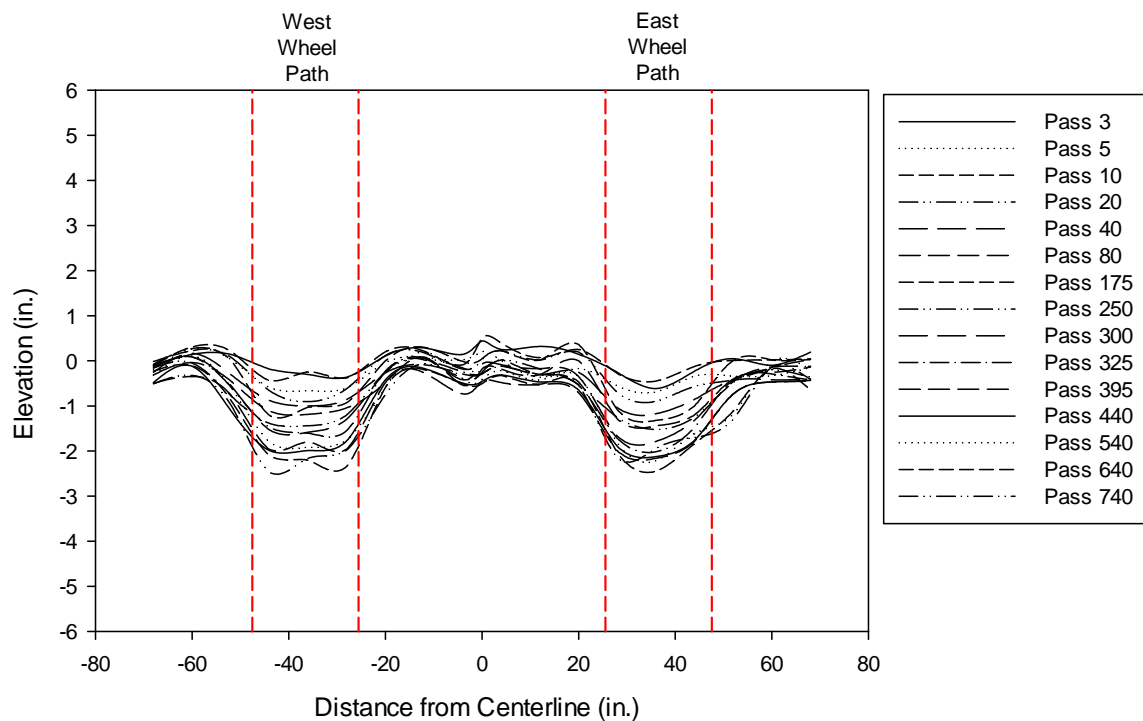
Figure L-2: Transverse rut profiles for Test Section 1, south (Tensar BX Type 2, CBR = 2.17).
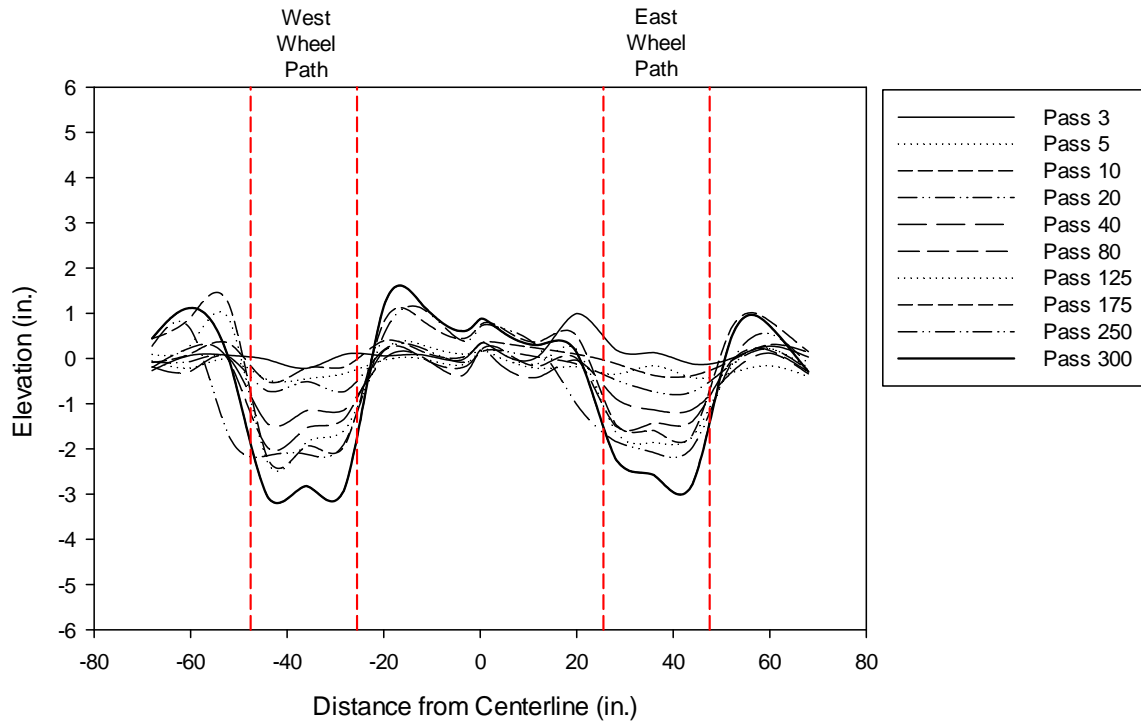
Figure L-3: Transverse rut profiles for Test Section 2, north (Tensar BX Type 2, CBR = 1.64)
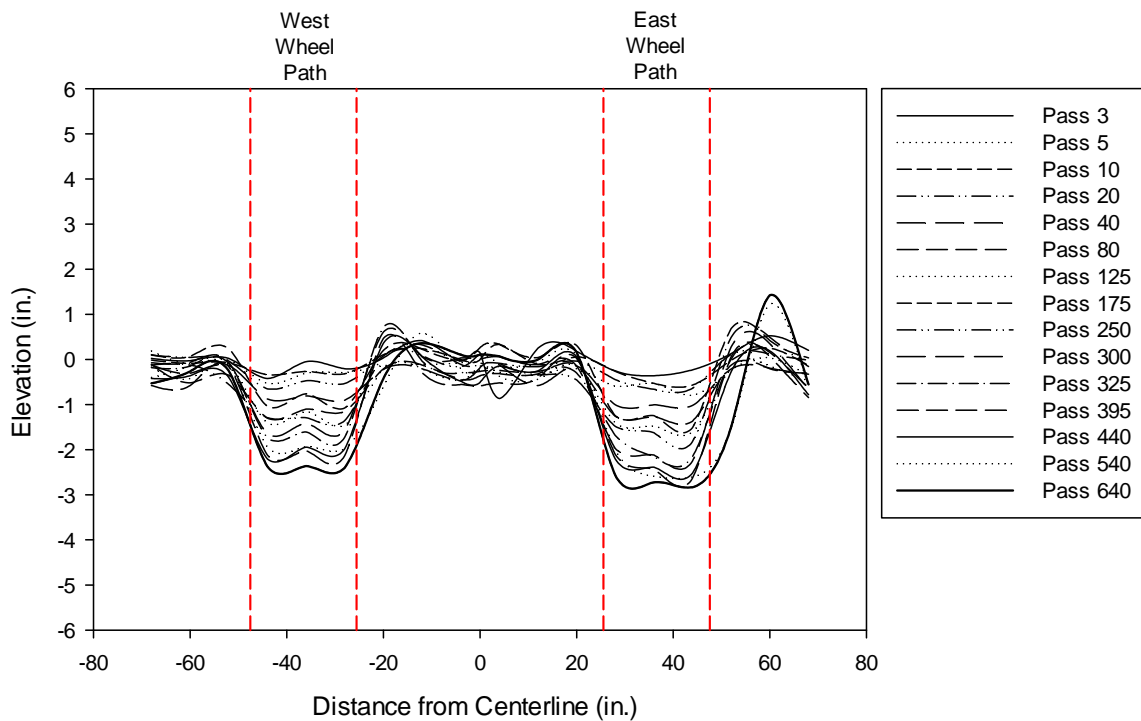
**Figure L-4: Transverse rut profiles for Test Section 2, south (Tensar BX Type 2, CBR = 1.64).**
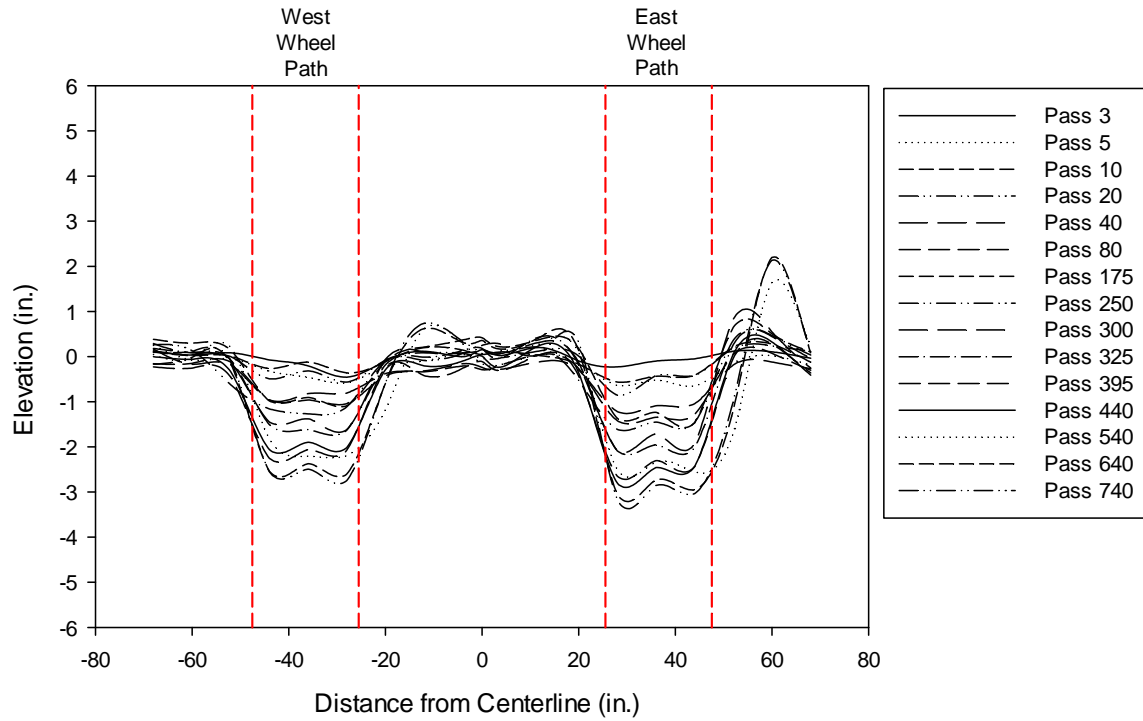
**Figure L-5: Transverse rut profiles for Test Section 3, north (Tensar BX Type 2, CBR = 1.79)**
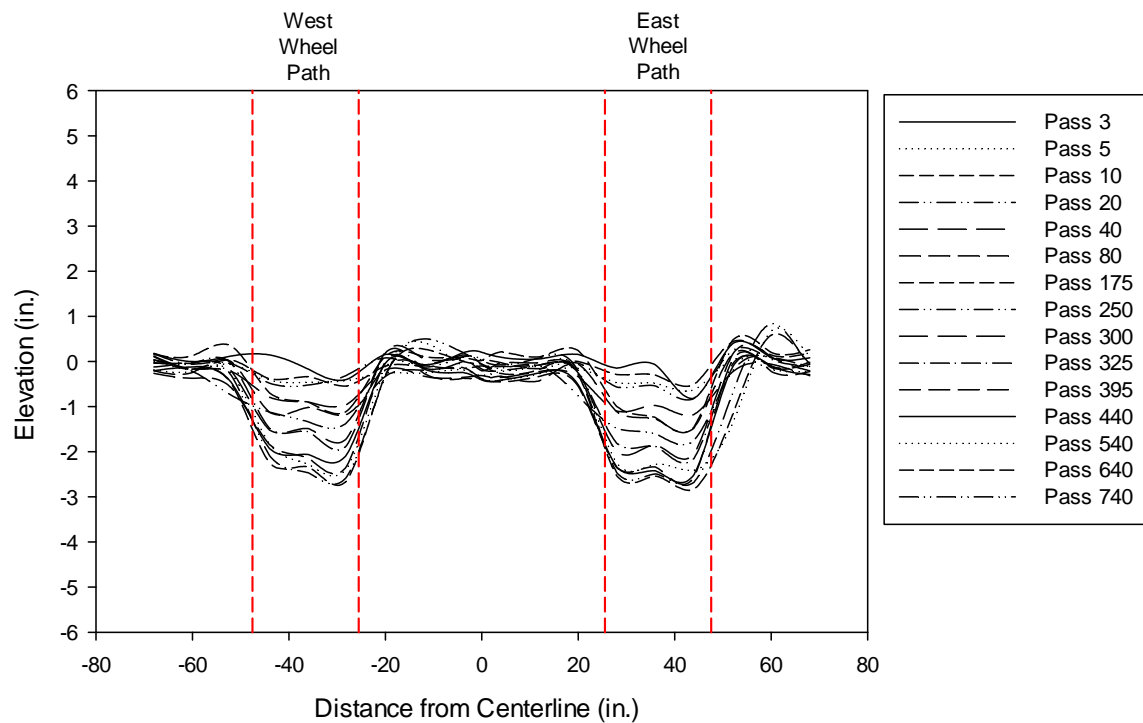
**Figure L-6: Transverse rut profiles for Test Section 3, south (Tensar BX Type 2, CBR = 1.79).**
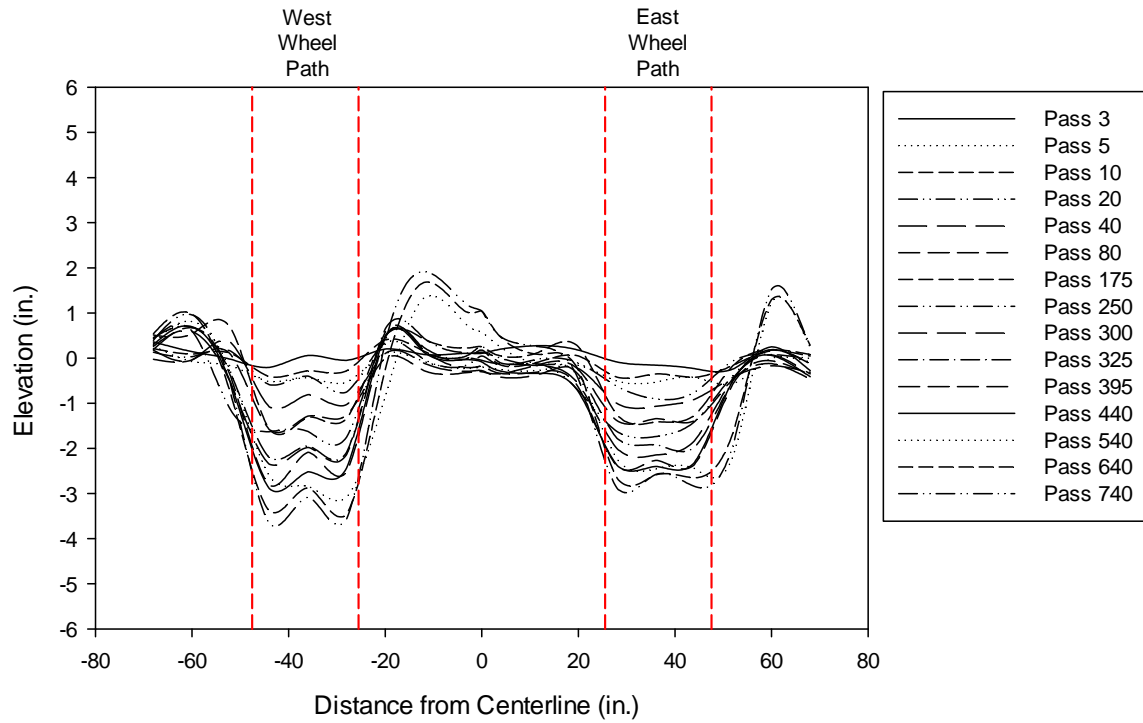
Figure L-7: Transverse rut profiles for Test Section 4, north (NAUE Secugrid 30-30 Q1).
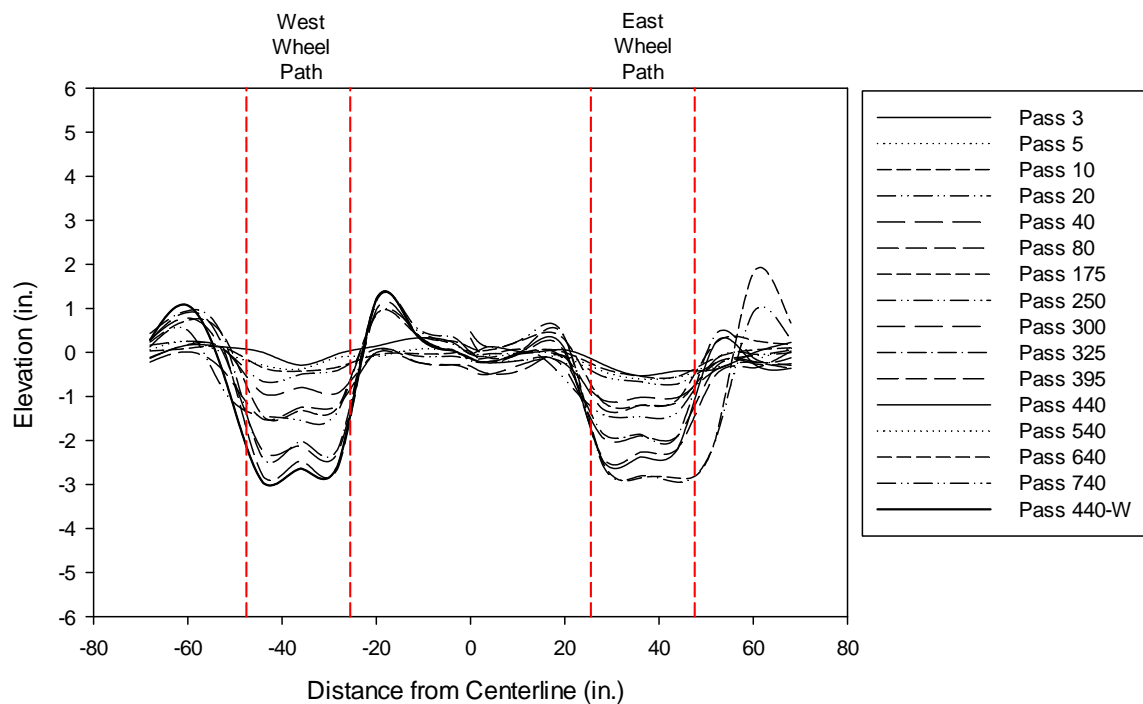

Figure L-8: Transverse rut profiles for Test Section 4, south (NAUE Secugrid 30-30 Q1).
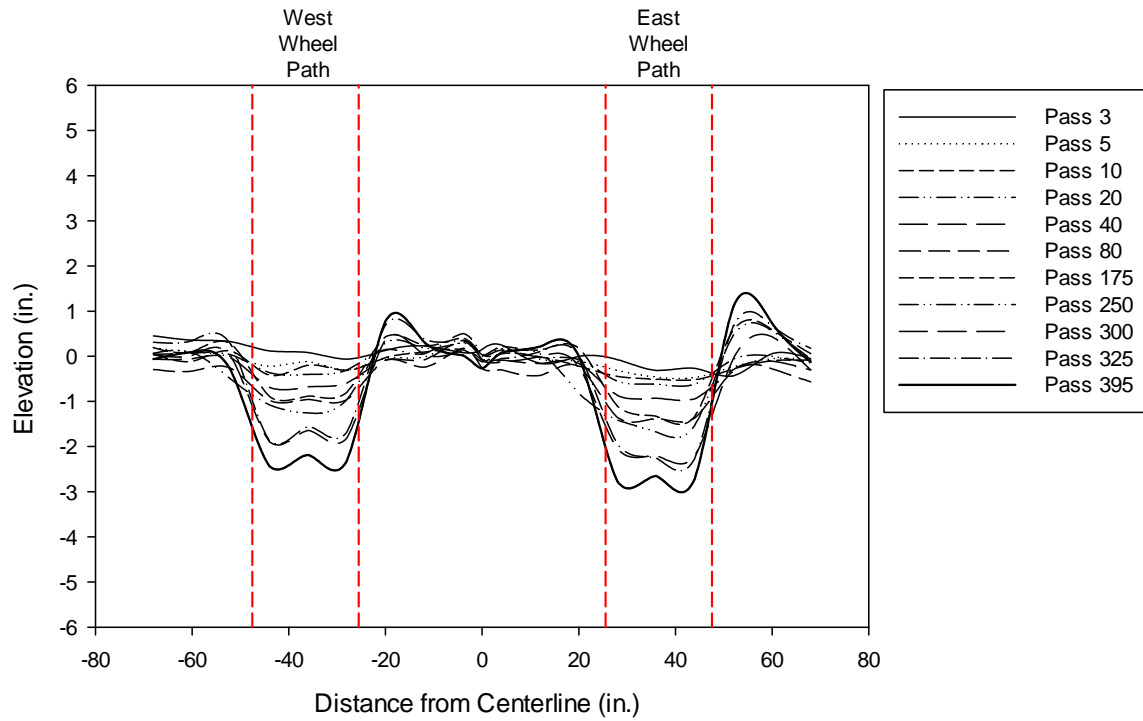
Figure L-9: Transverse rut profiles for Test Section 5, north (Colbond Enkagrid MAX 30).
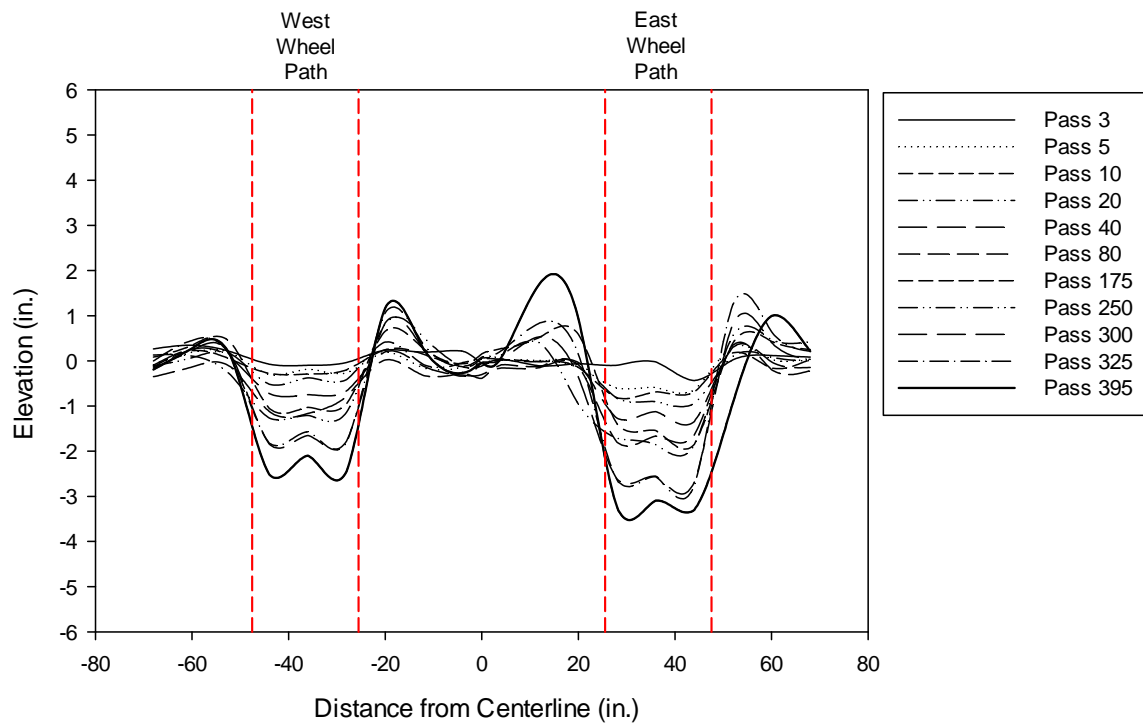
Figure L-10: Transverse rut profiles for Test Section 5, south (Colbond Enkagrid MAX 30).
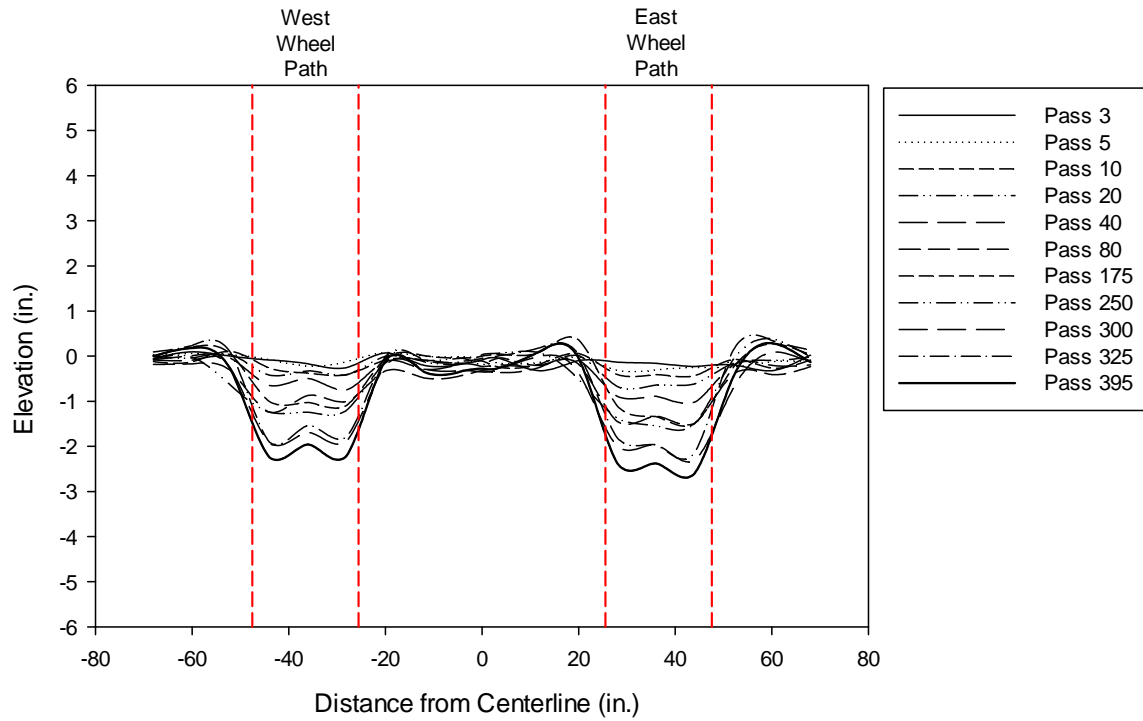
Figure L-11: Transverse rut profiles for Test Section 6, north (Synteen SF11).
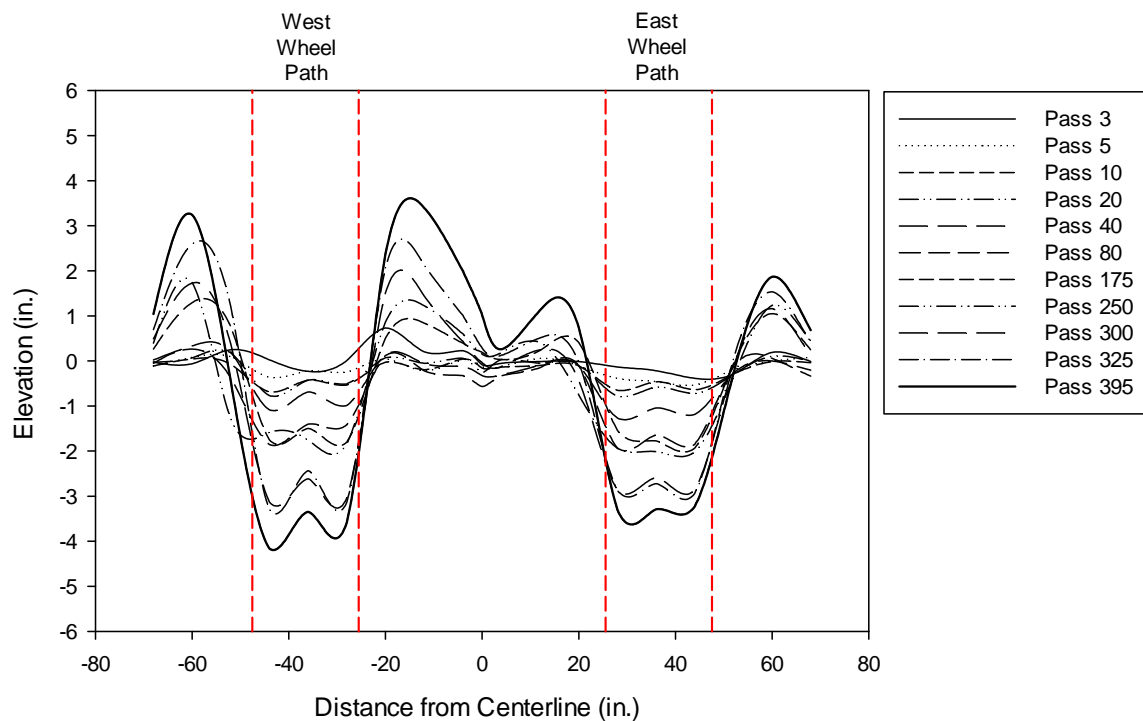
Figure L-12: Transverse rut profiles for Test Section 6, south (Synteen SF11).
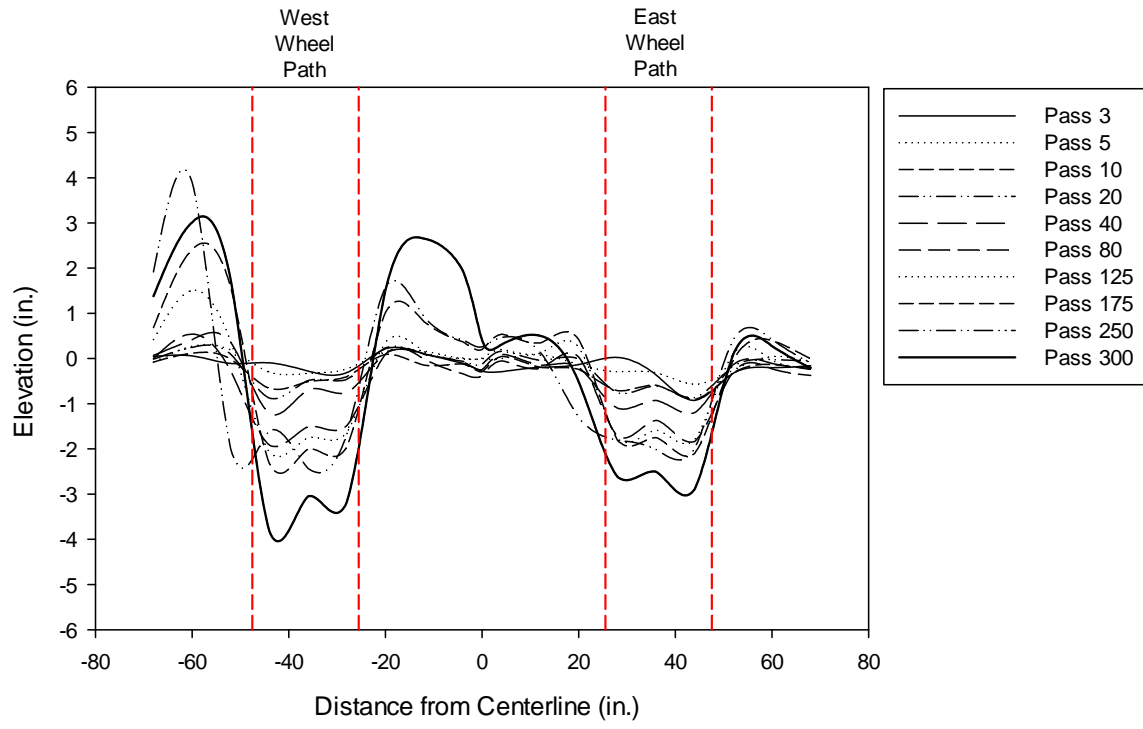
Figure L-13: Transverse rut profiles for Test Section 7, north (Synteen SF12).
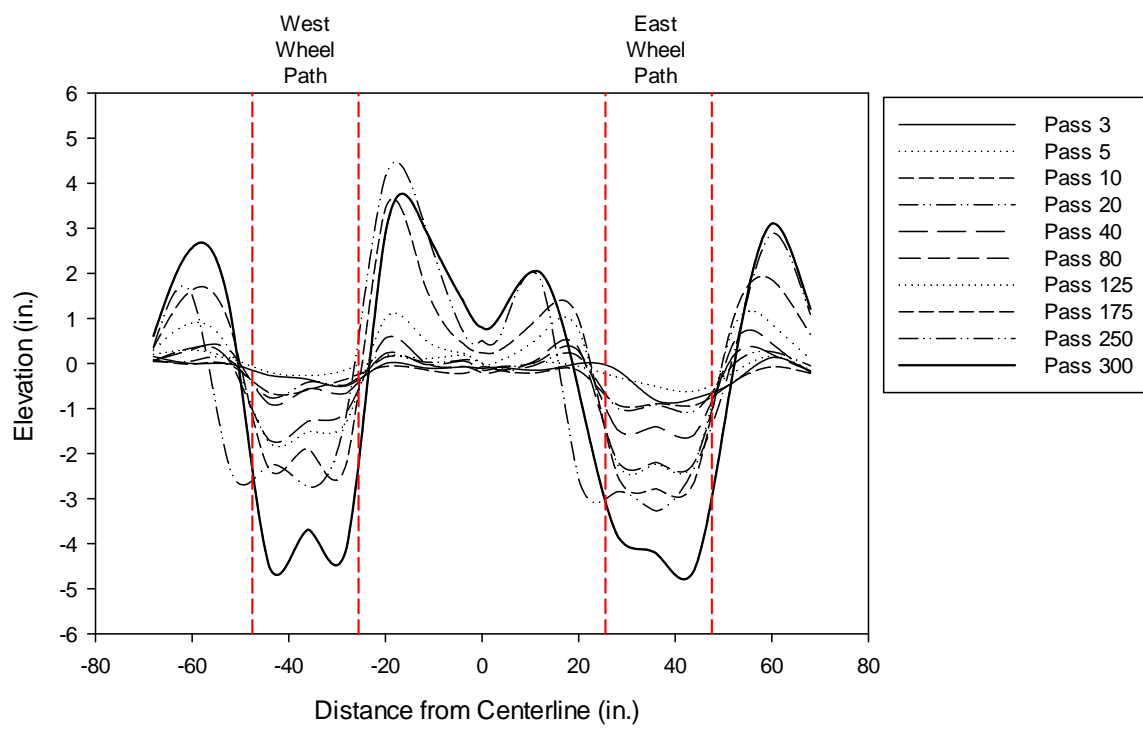
Figure L-14: Transverse rut profiles for Test Section 7, south (Synteen SF12).
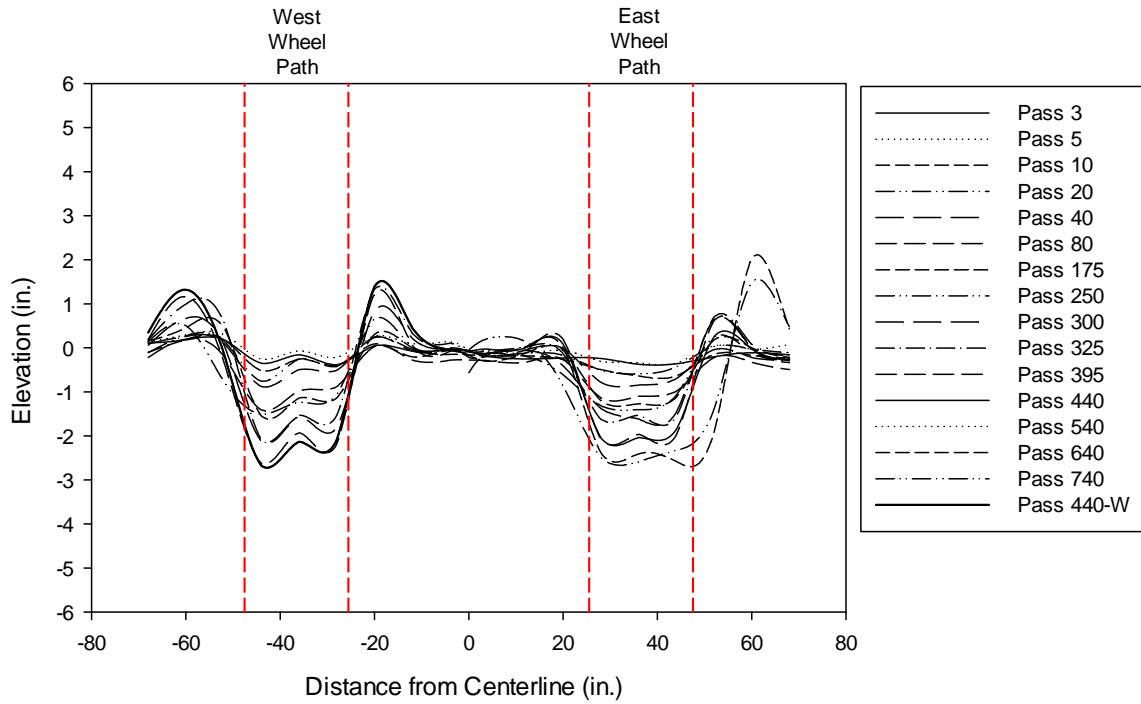
Figure L-15: Transverse rut profiles for Test Section 8, north (TenCate Mirafi BXG11).
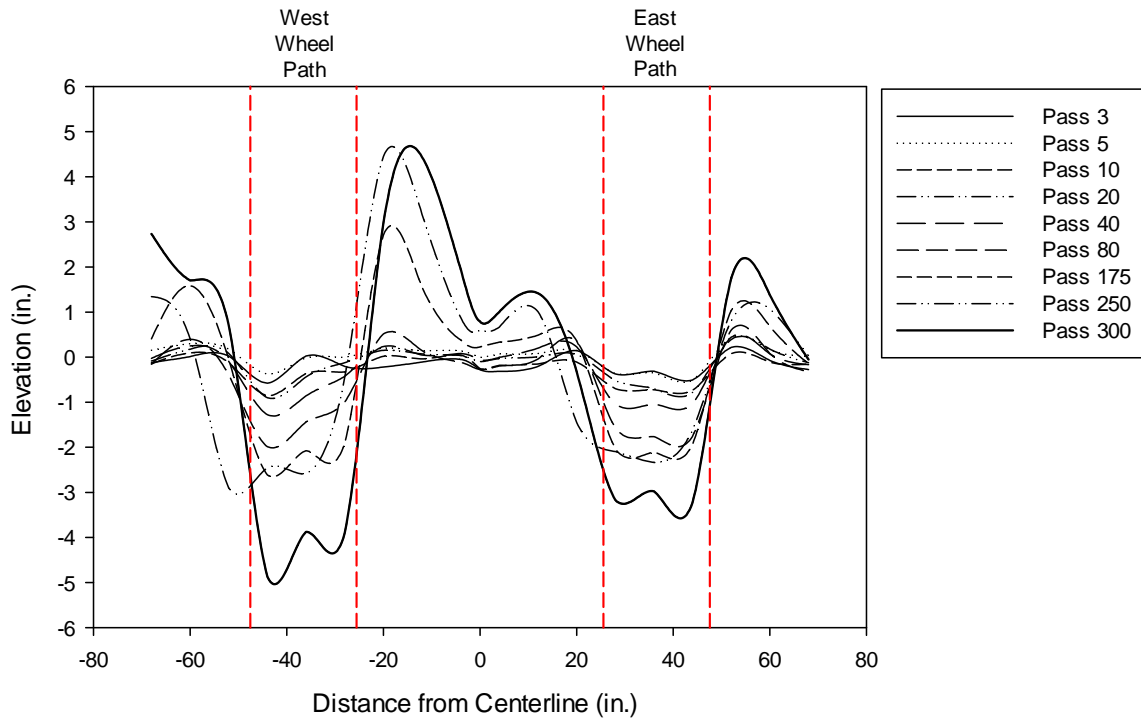
Figure L-16: Transverse rut profiles for Test Section 8, south (TenCate Mirafi BXG11).
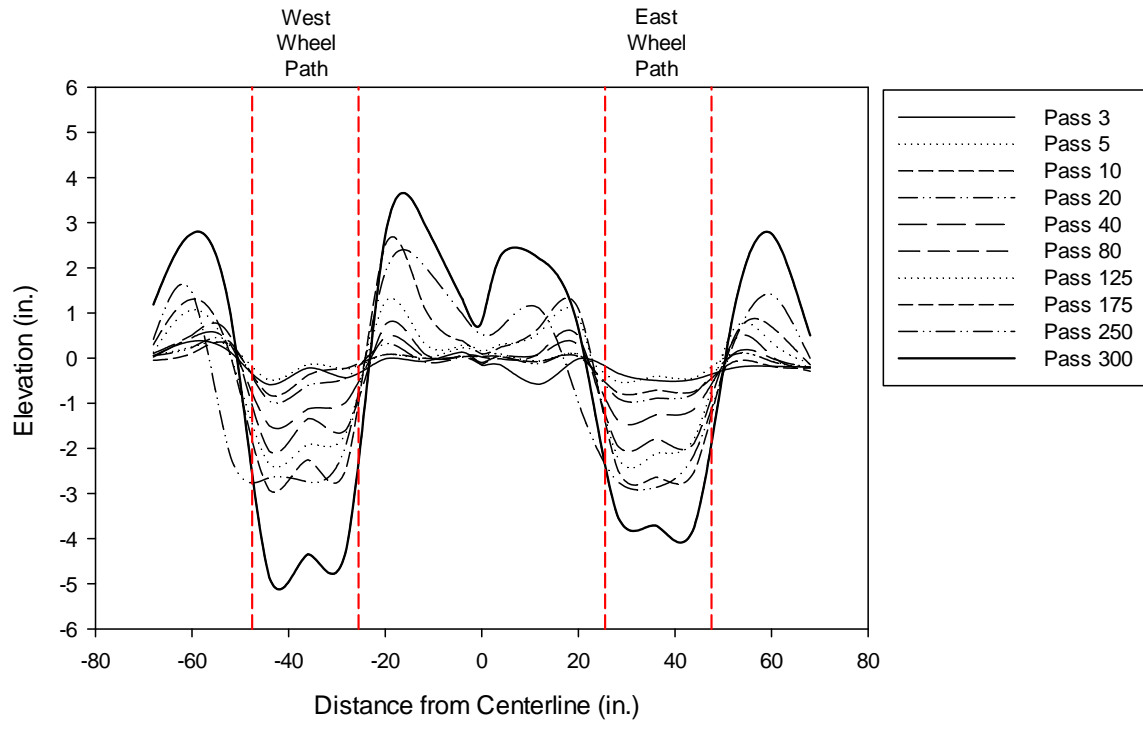
Figure L-17: Transverse rut profiles for Test Section 9, north (Huesker Fornit 30).
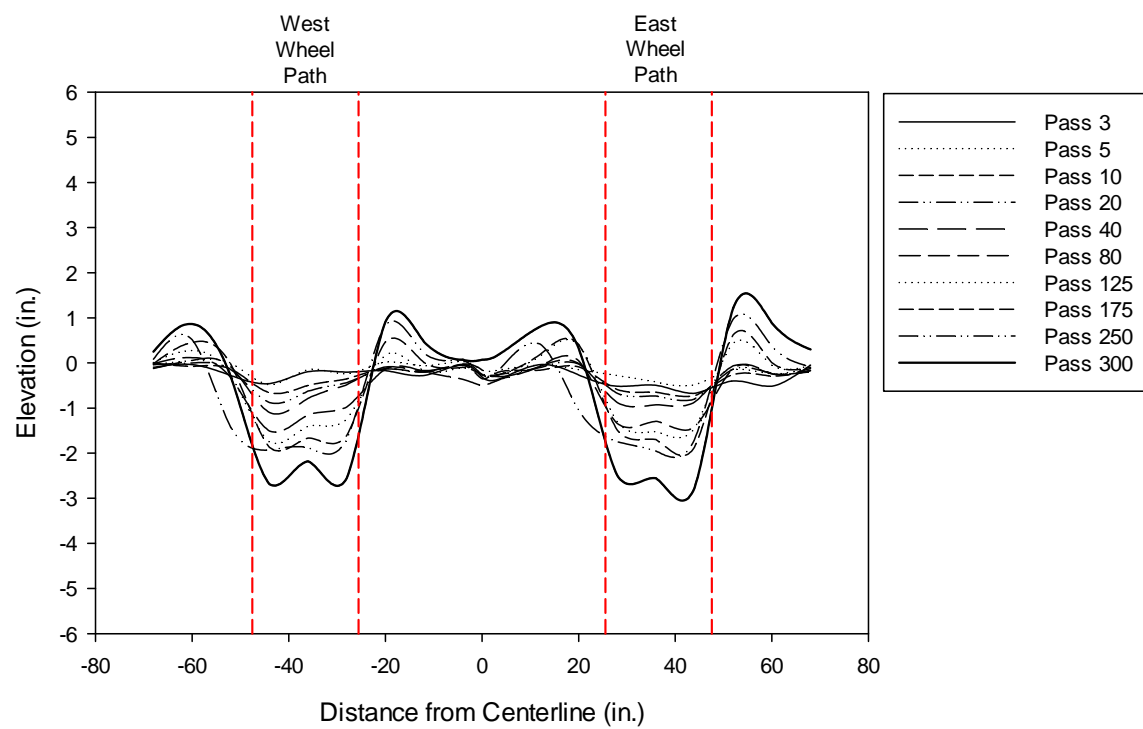
Figure L-18: Transverse rut profiles for Test Section 9, south (Huesker Fornit 30).
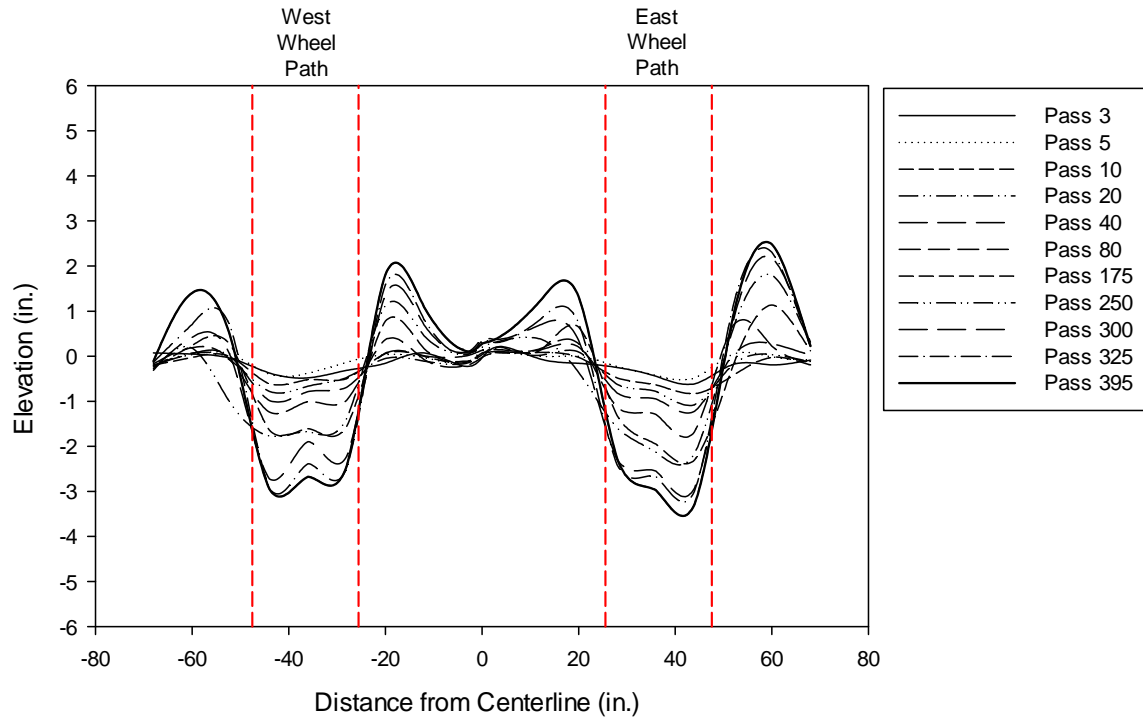
Figure L-19: Transverse rut profiles for Test Section 10, north (Syntec Tenax MS 330).
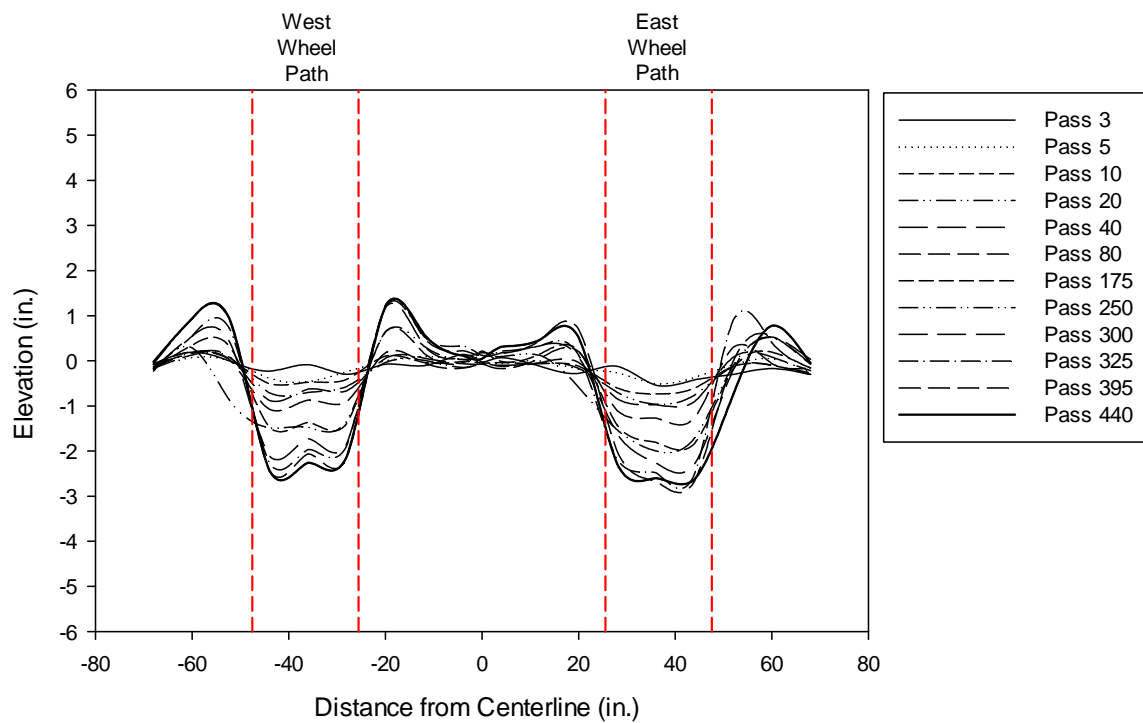
Figure L-20: Transverse rut profiles for Test Section 10, south (Syntec Tenax MS 330).
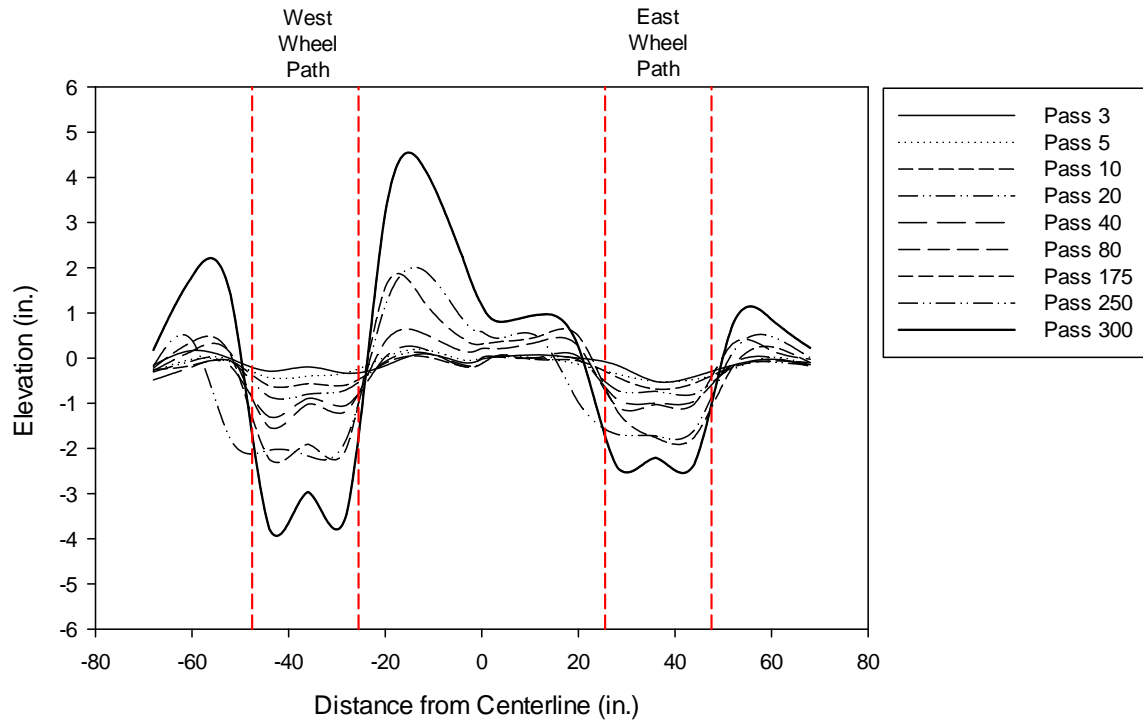
Figure L-21: Transverse rut profiles for Test Section 11, north (Tensar TX140).
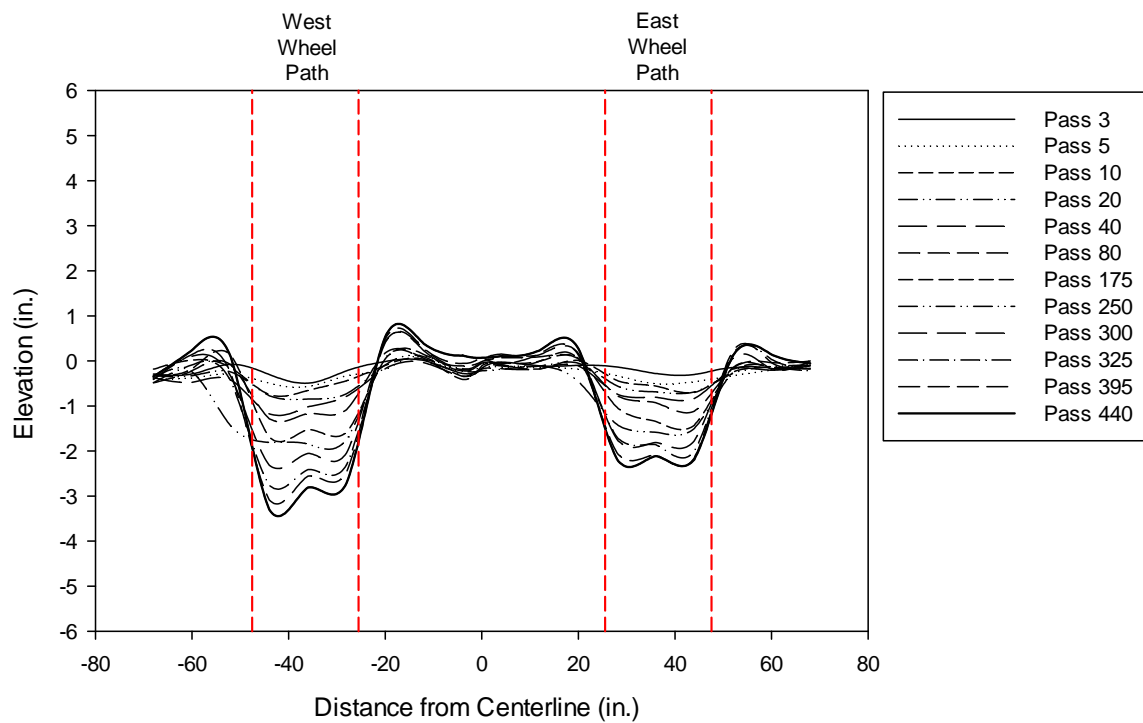
Figure L-22: Transverse rut profiles for Test Section 11, south (Tensar TX140).
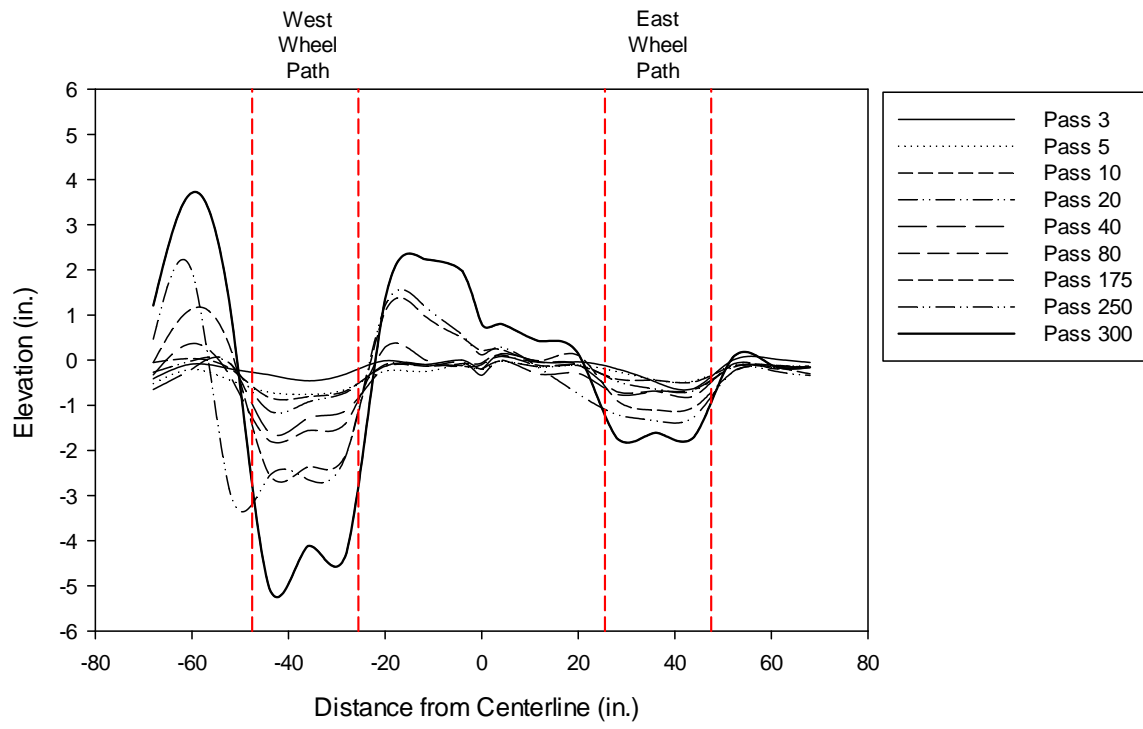
Figure L-23: Transverse rut profiles for Test Section 12, north (Tensar TX160).
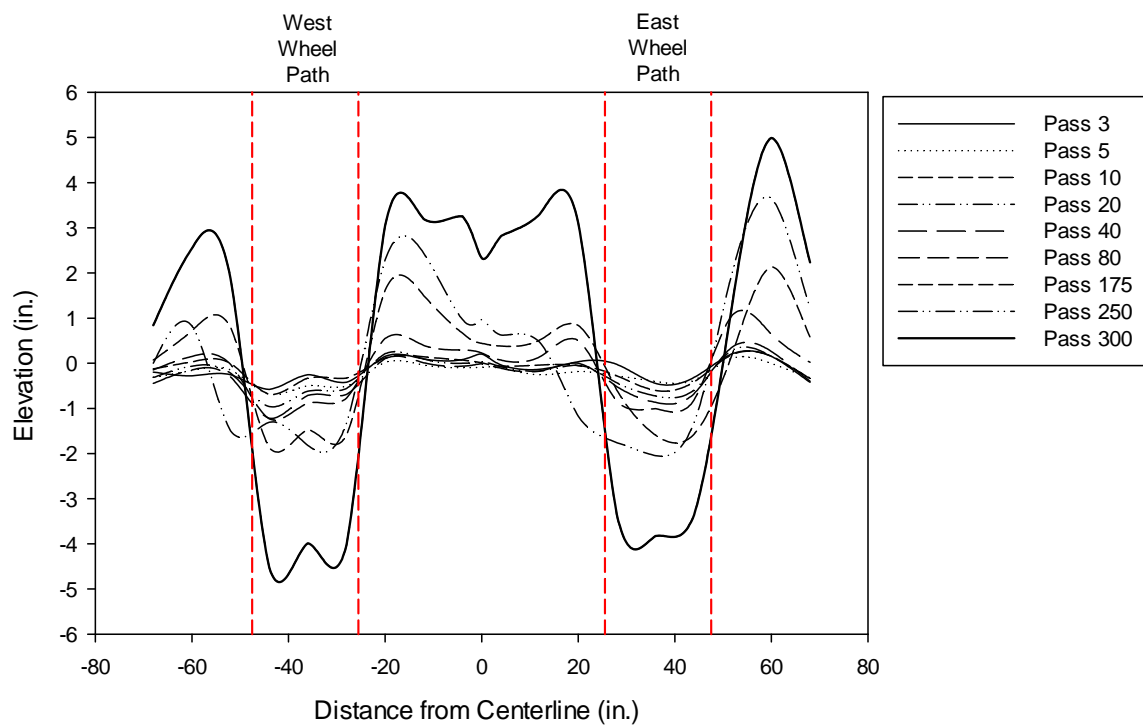
Figure L-24: Transverse rut profiles for Test Section 12, south (Tensar TX160).
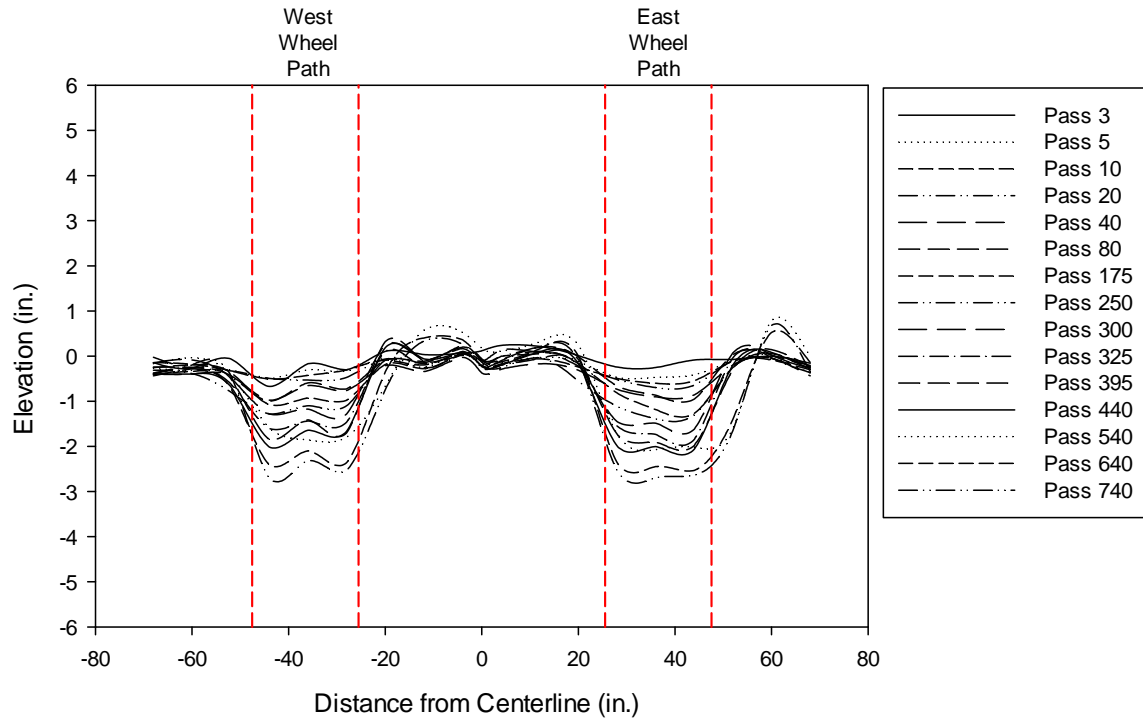
Figure L-25: Transverse rut profiles for Test Section 13, north (TenCate Mirafi RS580i).
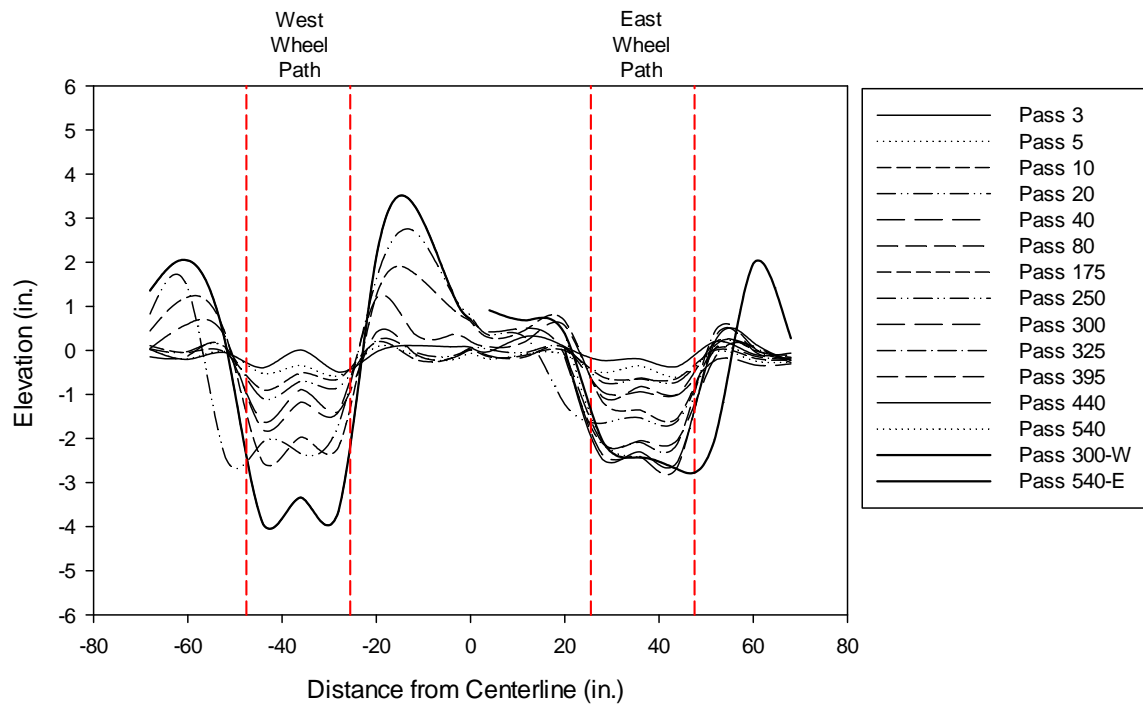
Figure L-26: Transverse rut profiles for Test Section 13, south (TenCate Mirafi RS580i).
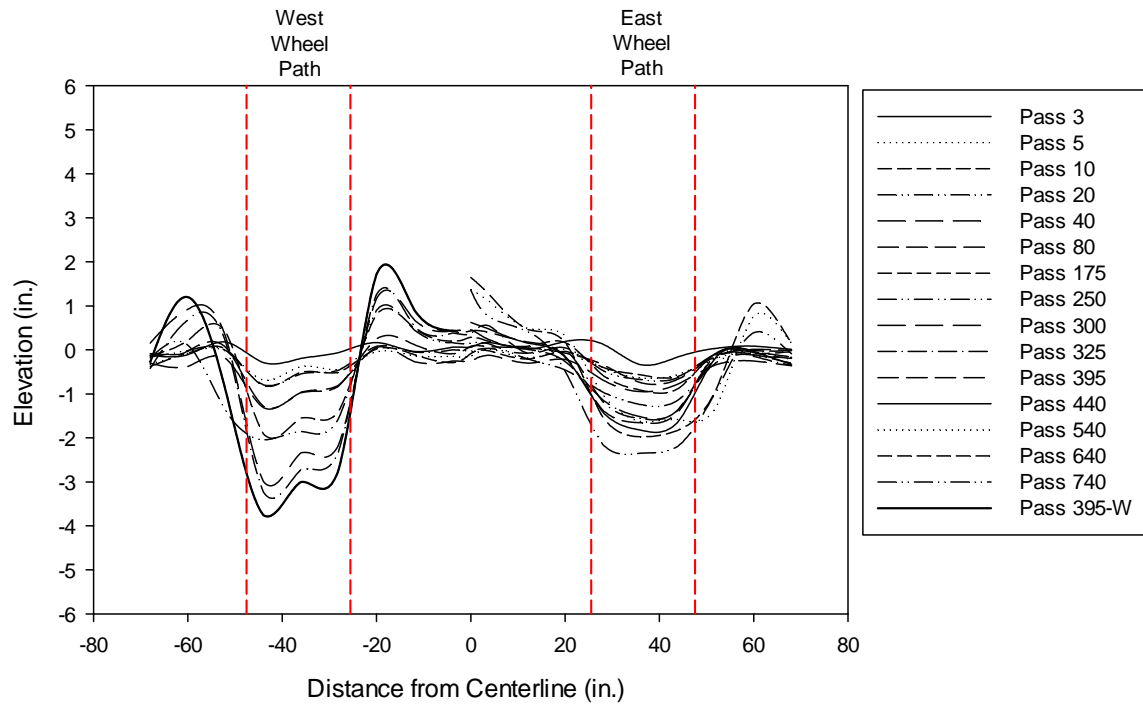
Figure L-27: Transverse rut profiles for Test Section 14, north (Propex Geotex 801).
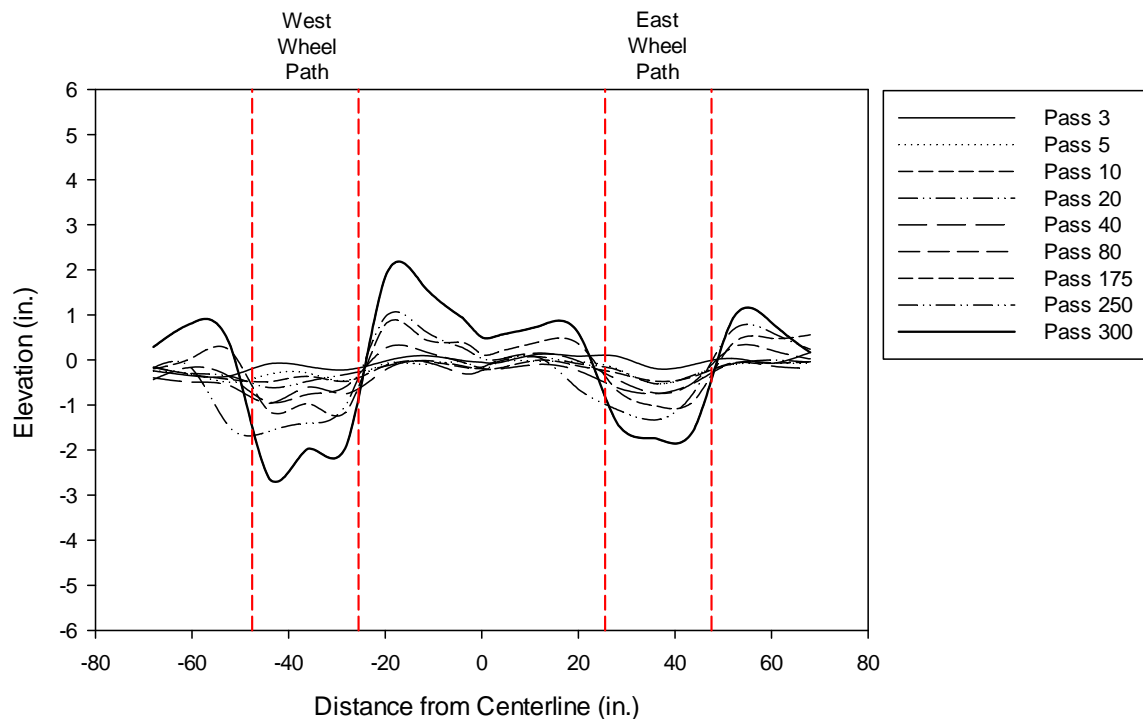
Figure L-28: Transverse rut profiles for Test Section 14, south (Propex Geotex 801).
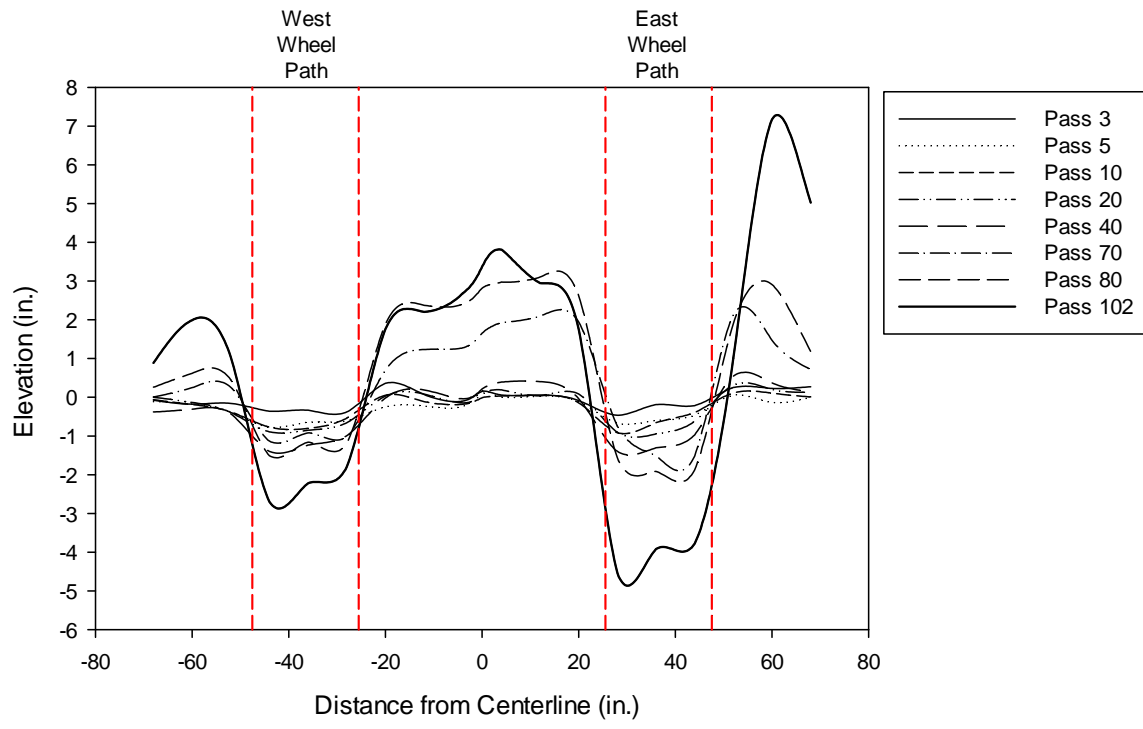
Figure L-29: Transverse rut profiles for Test Section Control 1, north.
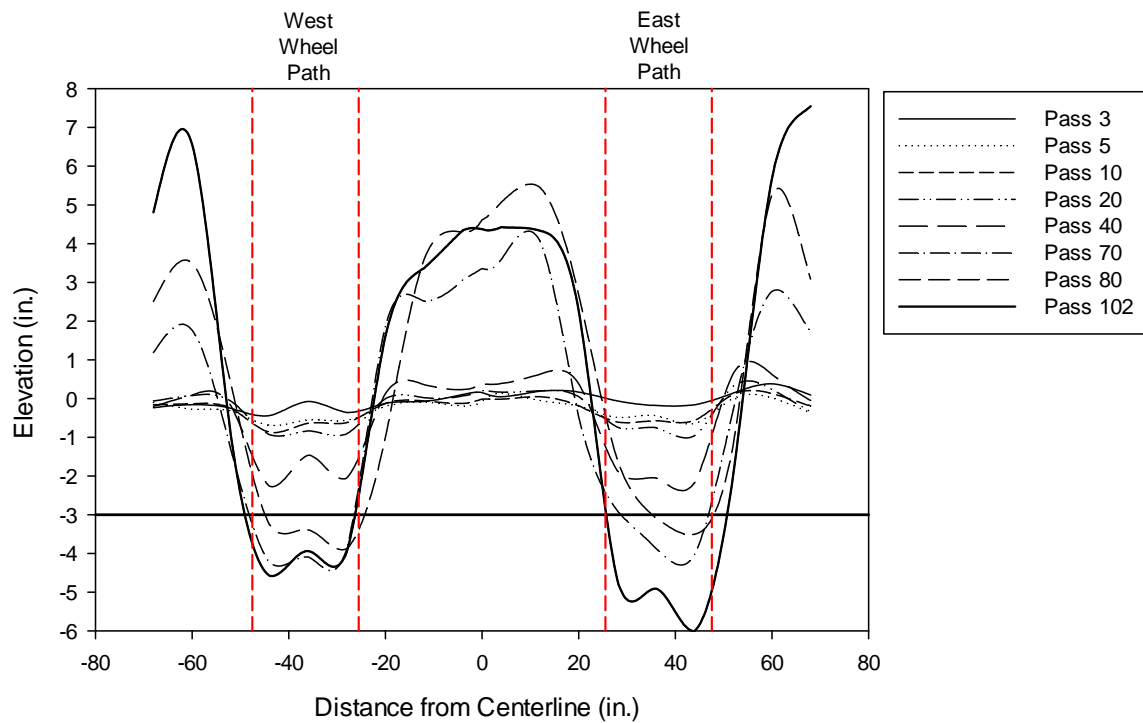
Figure L-30: Transverse rut profiles for Test Section Control 1, south.
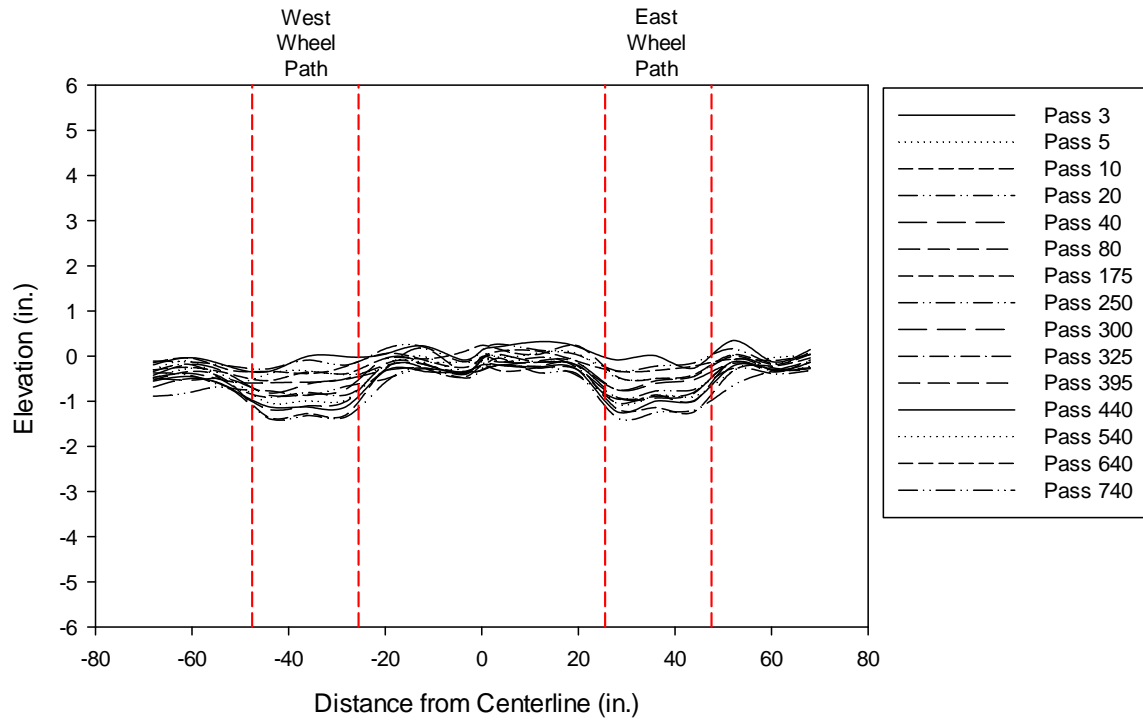
Figure L-31: Transverse rut profiles for Test Section Control 2, north.
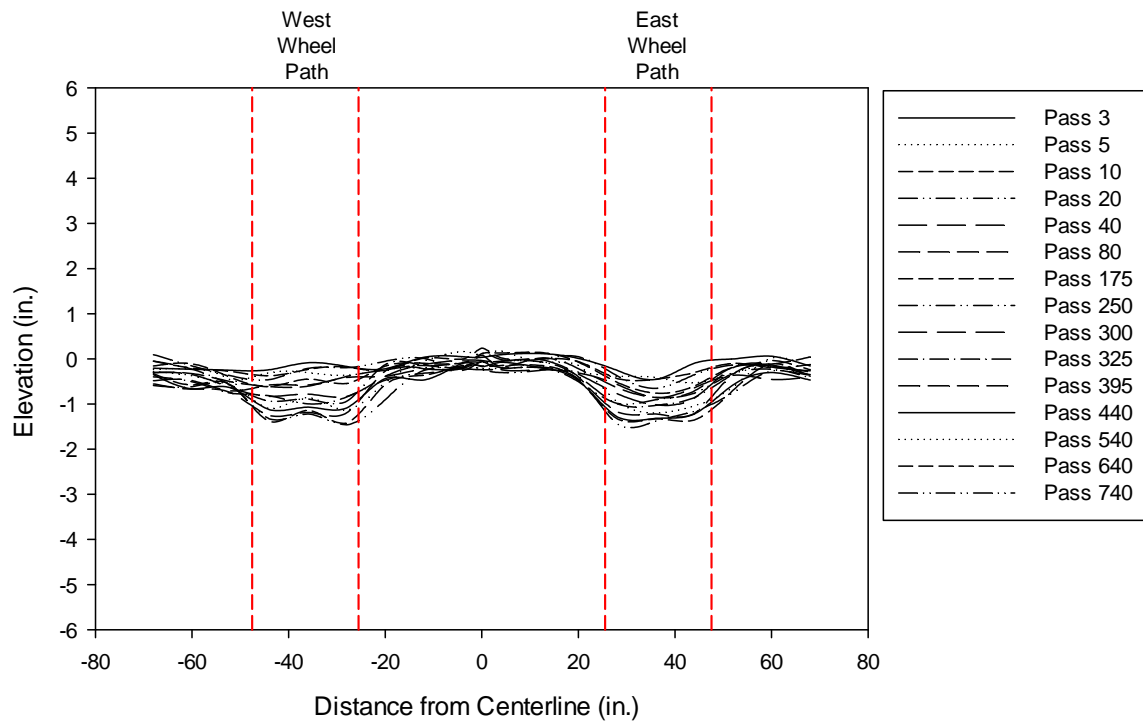
Figure L-32: Transverse rut profiles for Test Section Control 2, south.
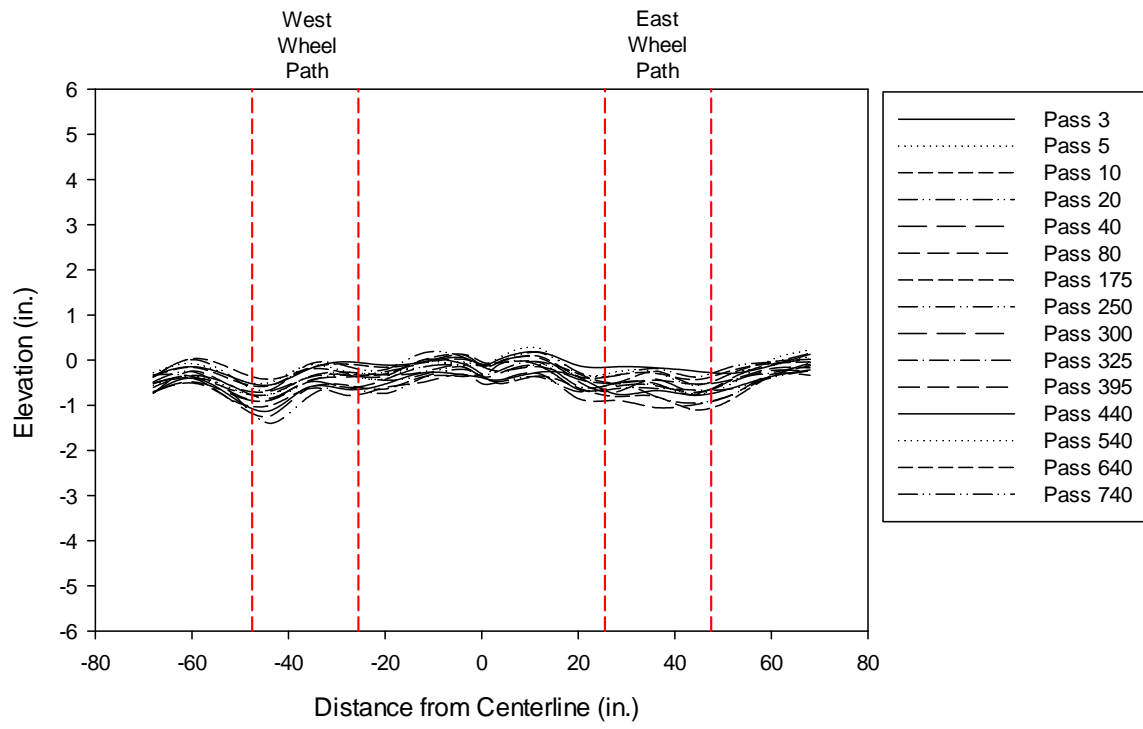
Figure L-33: Transverse rut profiles for Test Section Control 3, north.
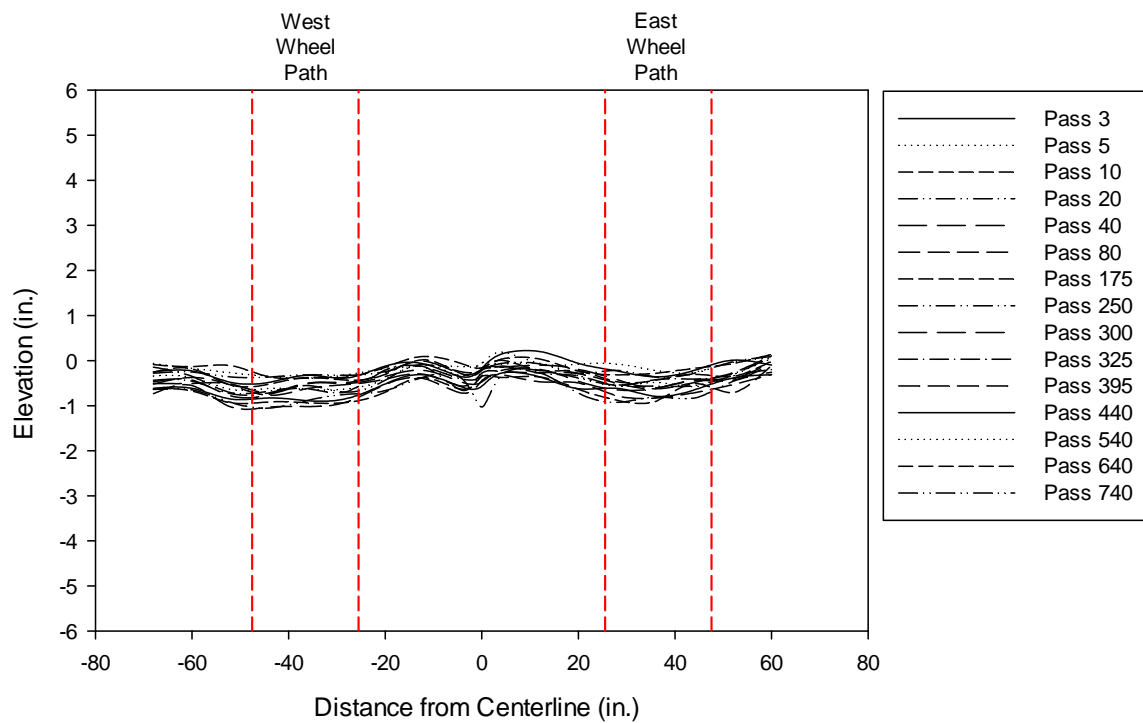
Figure L-34: Transverse rut profiles for Test Section Control 3, south.

APPENDIX M – LVDT DISPLACEMENT RESULTS
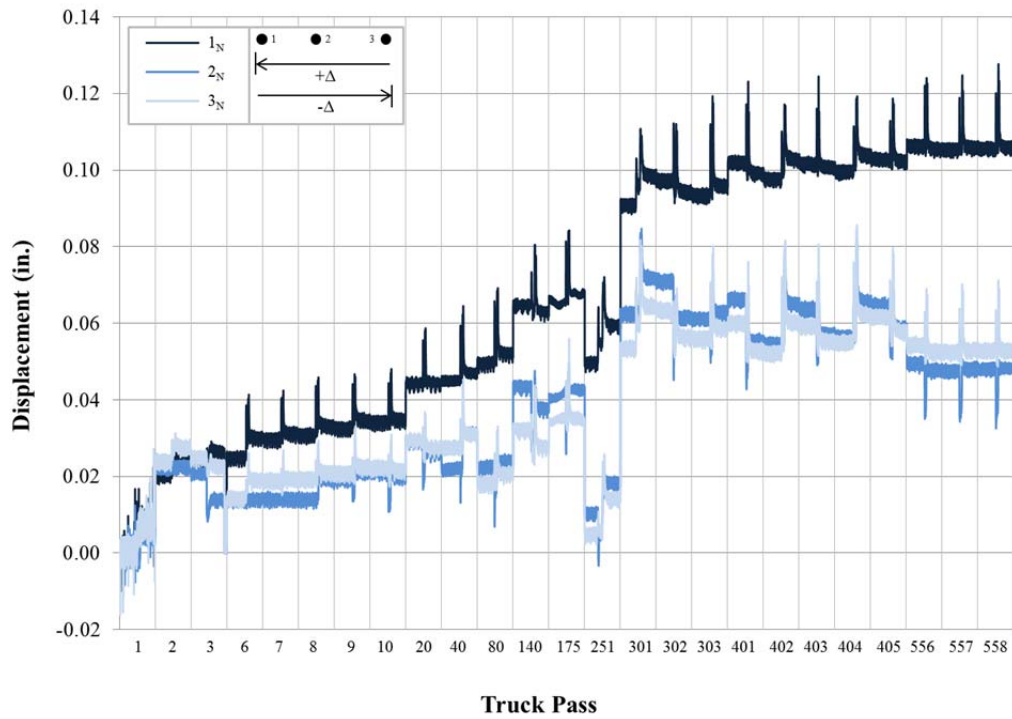
Figure M-1: Dynamic displacements for Test Section 1, north (Tensar BX Type 2, CBR = 2.17).
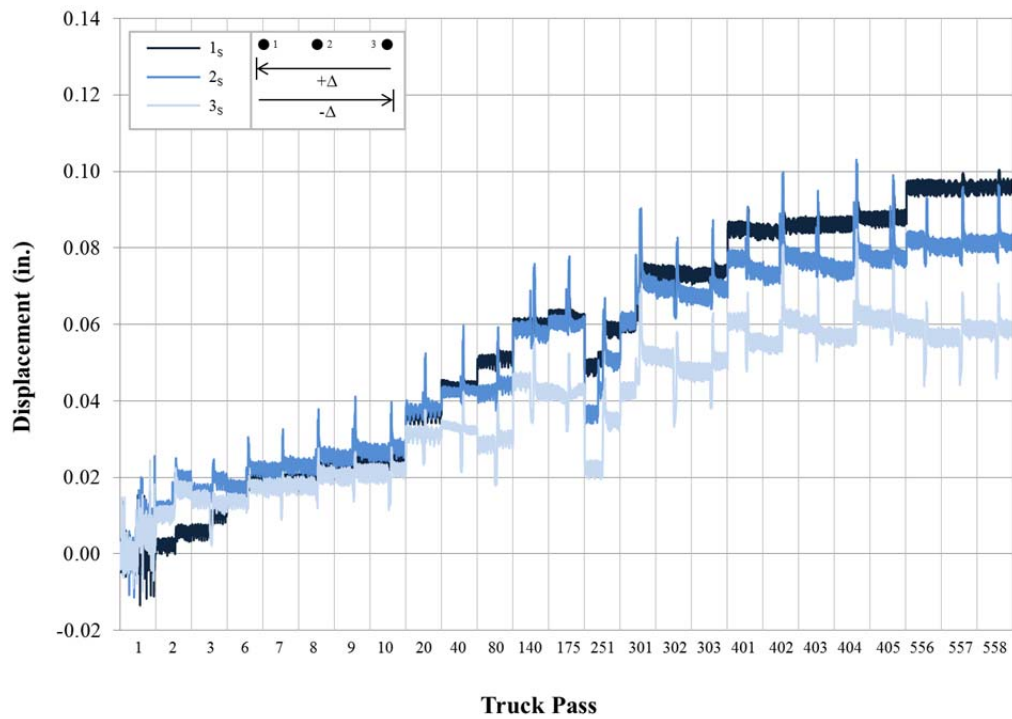
Figure M-2: Dynamic displacements for Test Section 1, south (Tensar BX Type 2, CBR = 2.17).
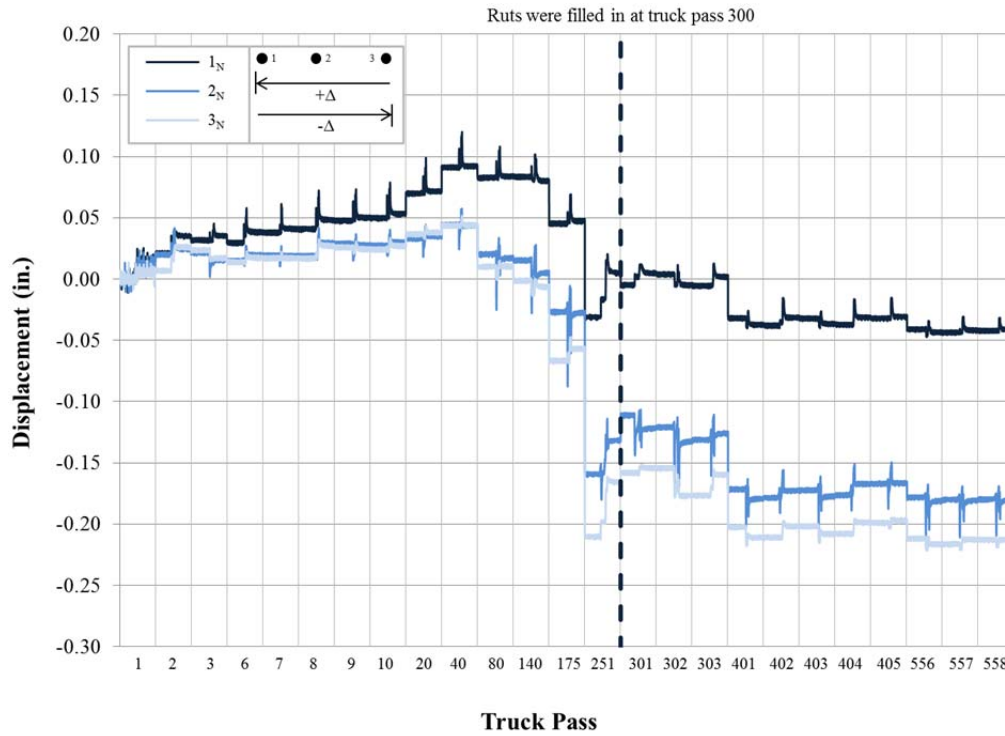
Figure M-3: Dynamic displacements for Test Section 2, north (Tensar BX Type 2, CBR = 1.64).
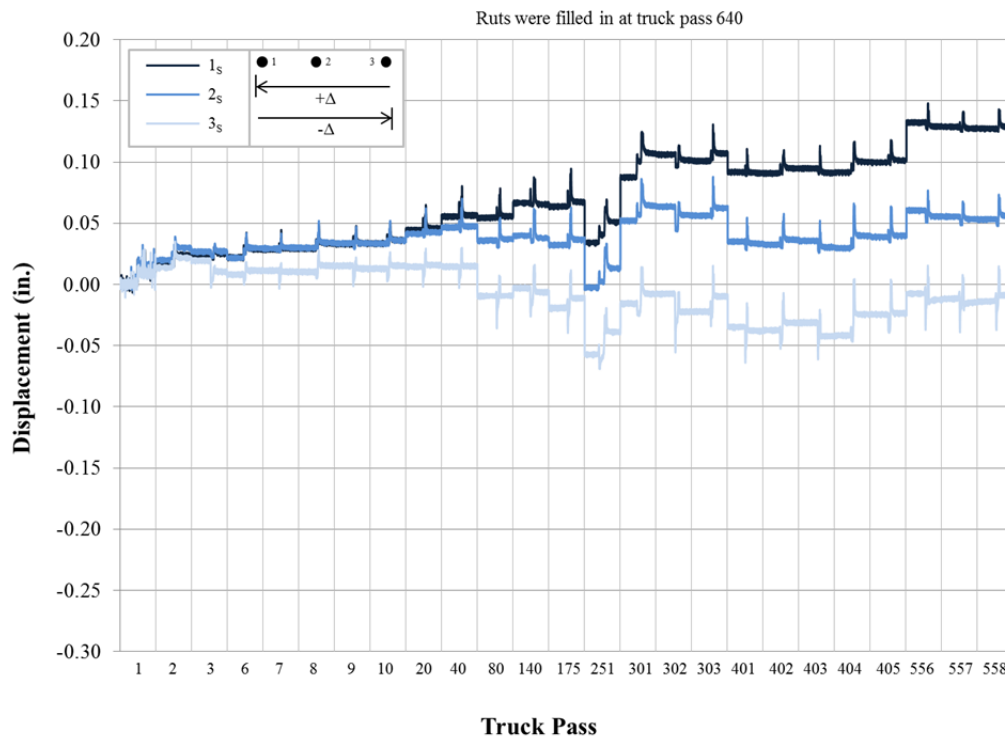
Figure M-4: Dynamic displacements for Test Section 2, south (Tensar BX Type 2, CBR = 1.64).
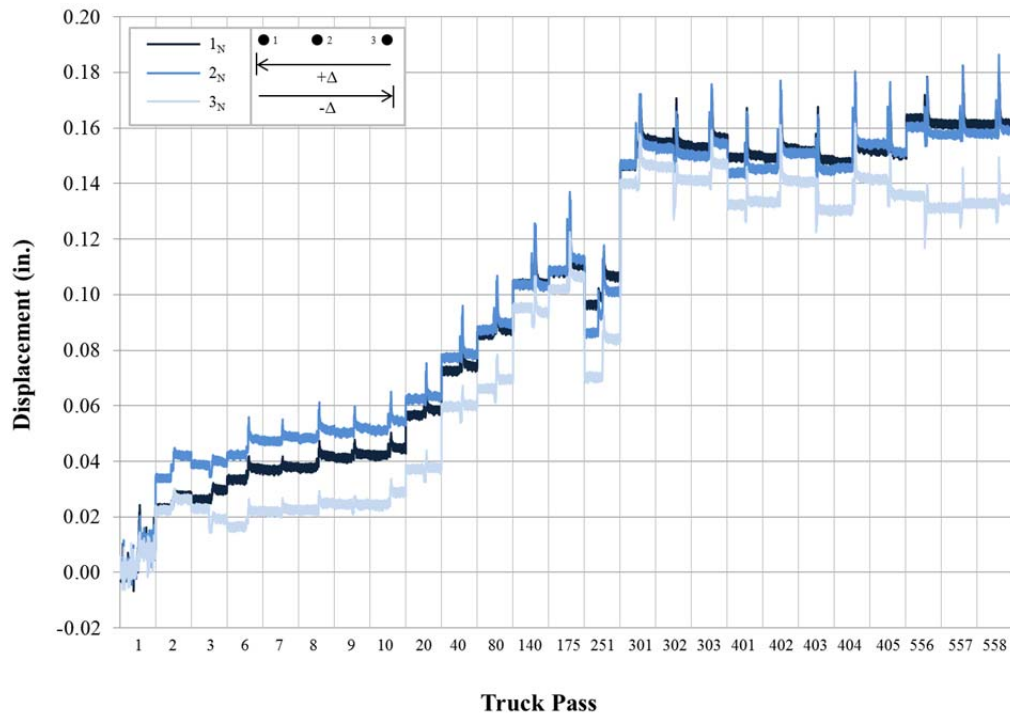
Figure M-5: Dynamic displacements for Test Section 3, north (Tensar BX Type 2, CBR = 1.79).
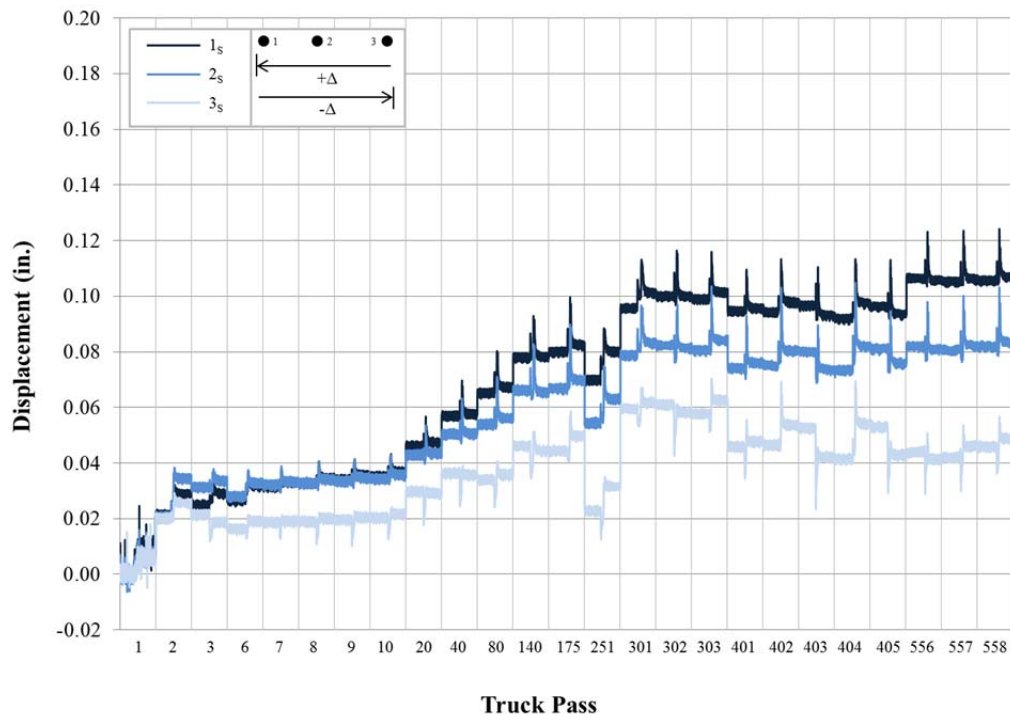
Figure M-6: Dynamic displacements for Test Section 3, south (Tensar BX Type 2, CBR = 1.79).
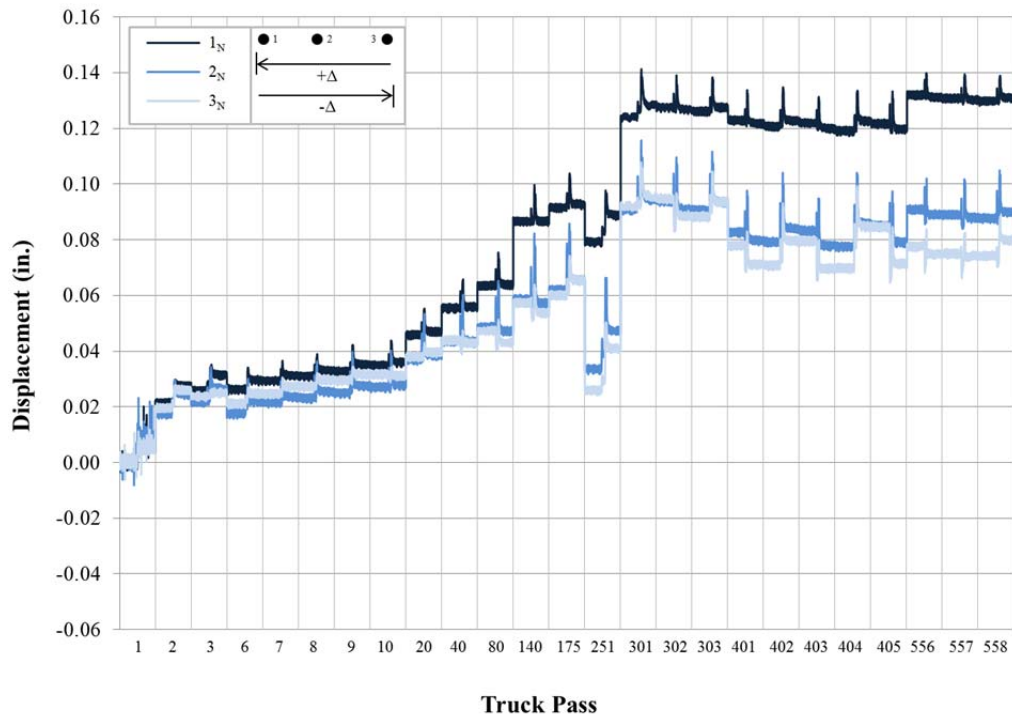
Figure M-7: Dynamic displacements for Test Section 4, north (NAUE Secugrid 30-30 Q1).
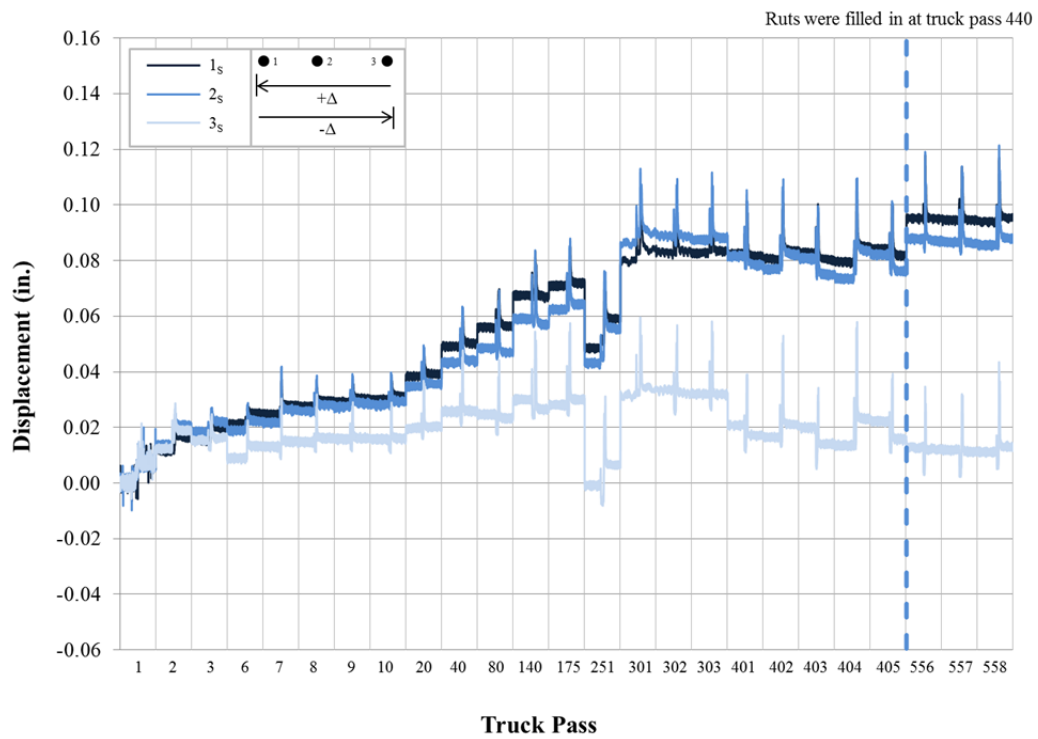
Figure M-8: Dynamic displacements for Test Section 4, south (NAUE Secugrid 30-30 Q1).
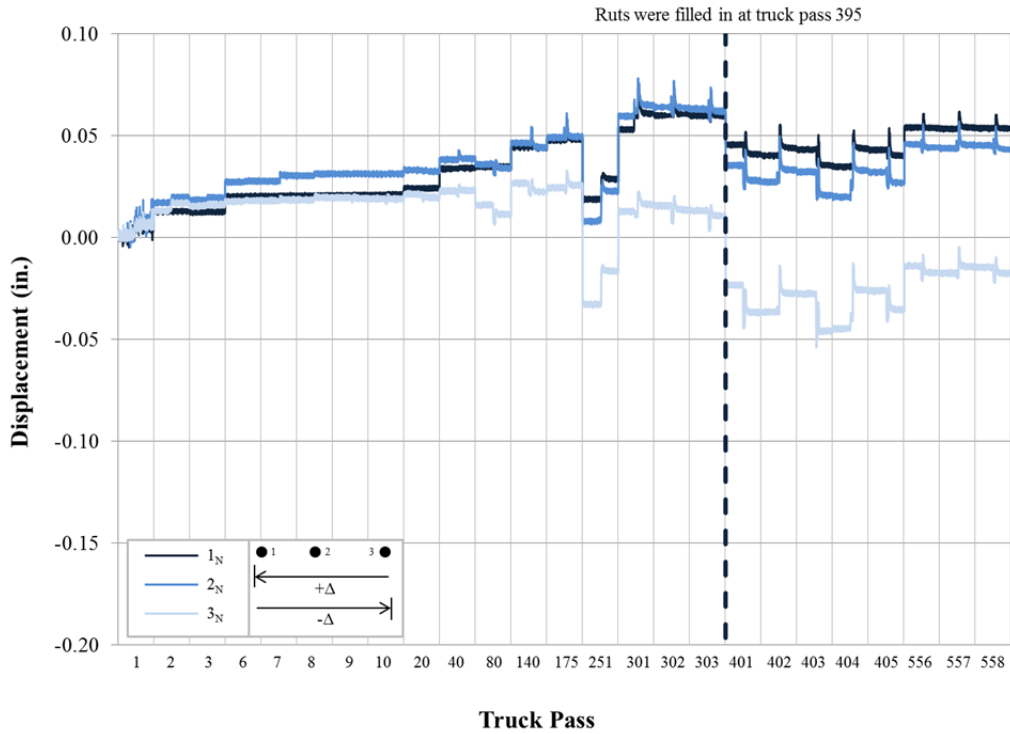
Figure M-9: Dynamic displacements for Test Section 5, north (Colbond Enkagrid MAX 30).
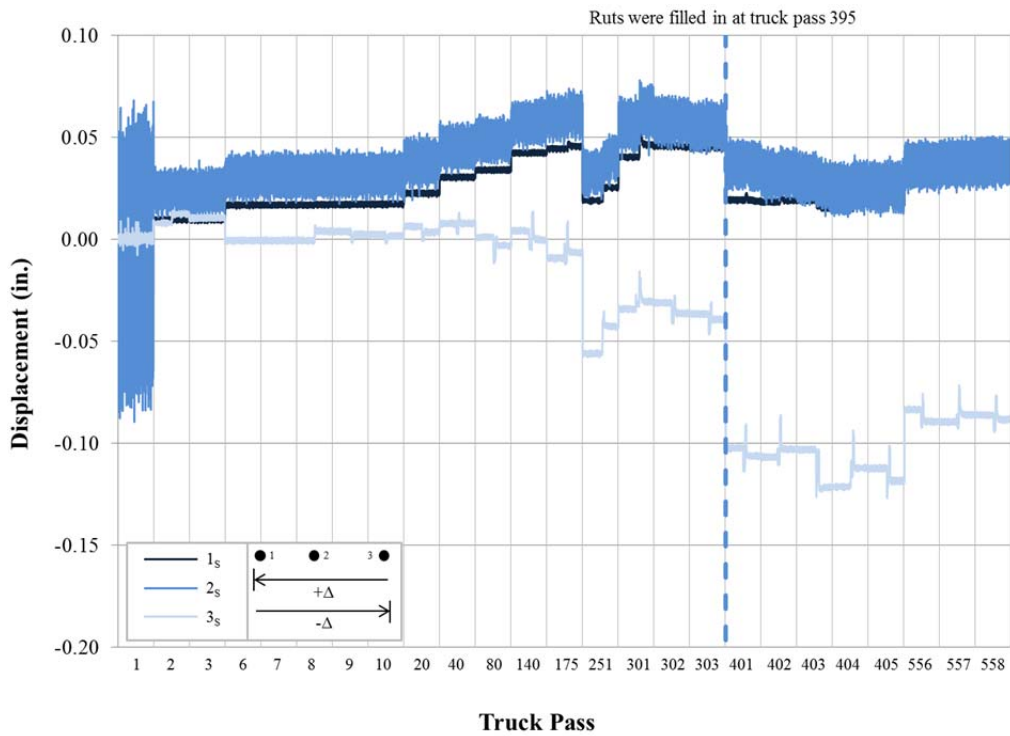
Figure M-10: Dynamic displacements for Test Section 5, south (Colbond Enkagrid MAX 30).
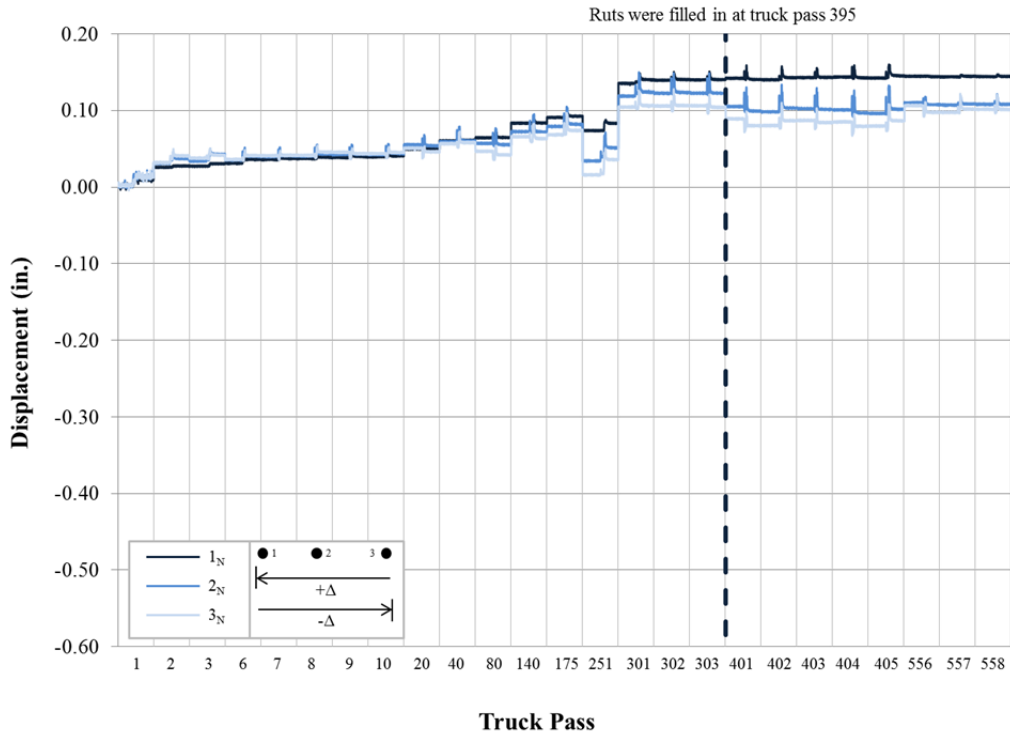
Figure M-11: Dynamic displacements for Test Section 6, north (Synteen SF11).
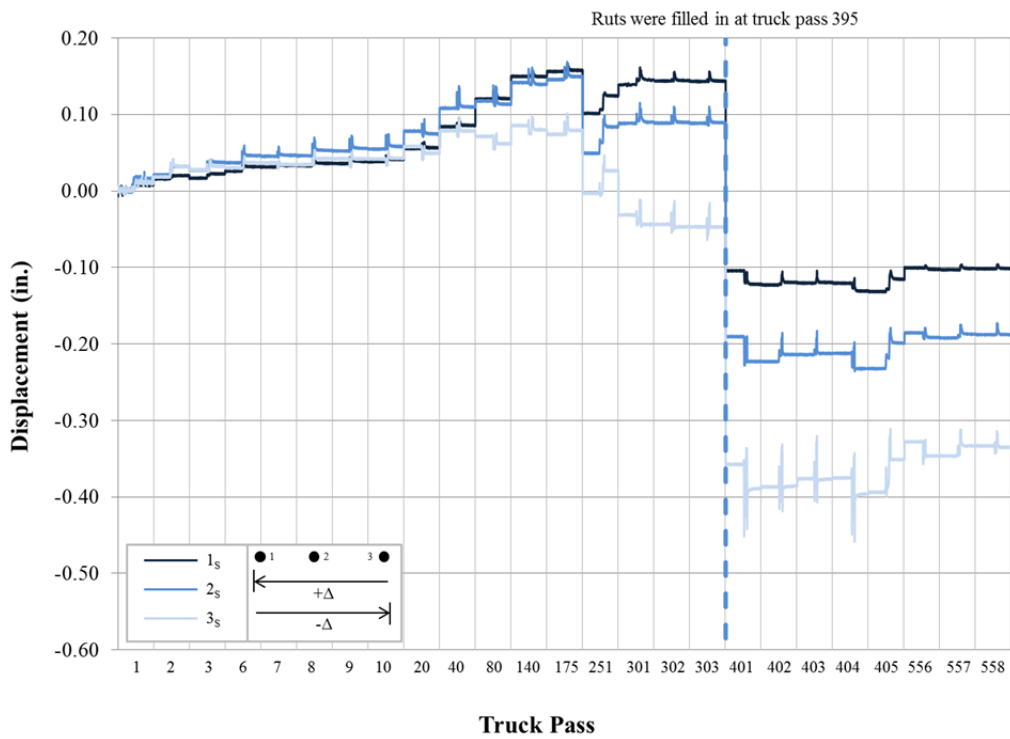
Figure M-12: Dynamic displacements for Test Section 6, south (Synteen SF11).
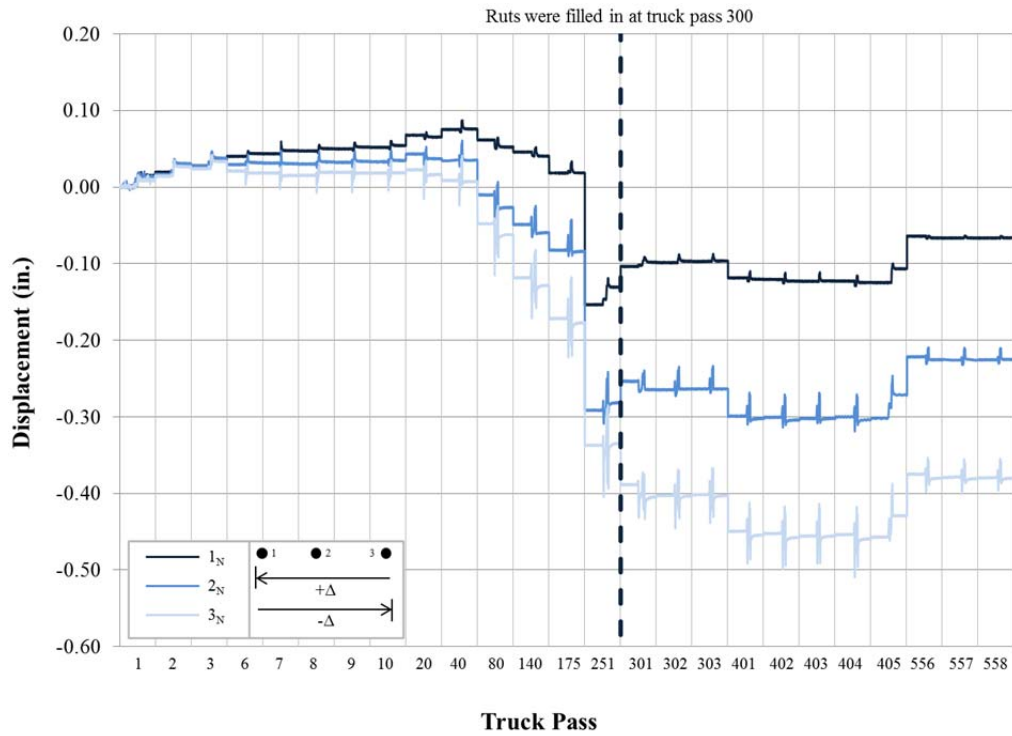
Figure M-13: Dynamic displacements for Test Section 7, north (Synteen SF12).
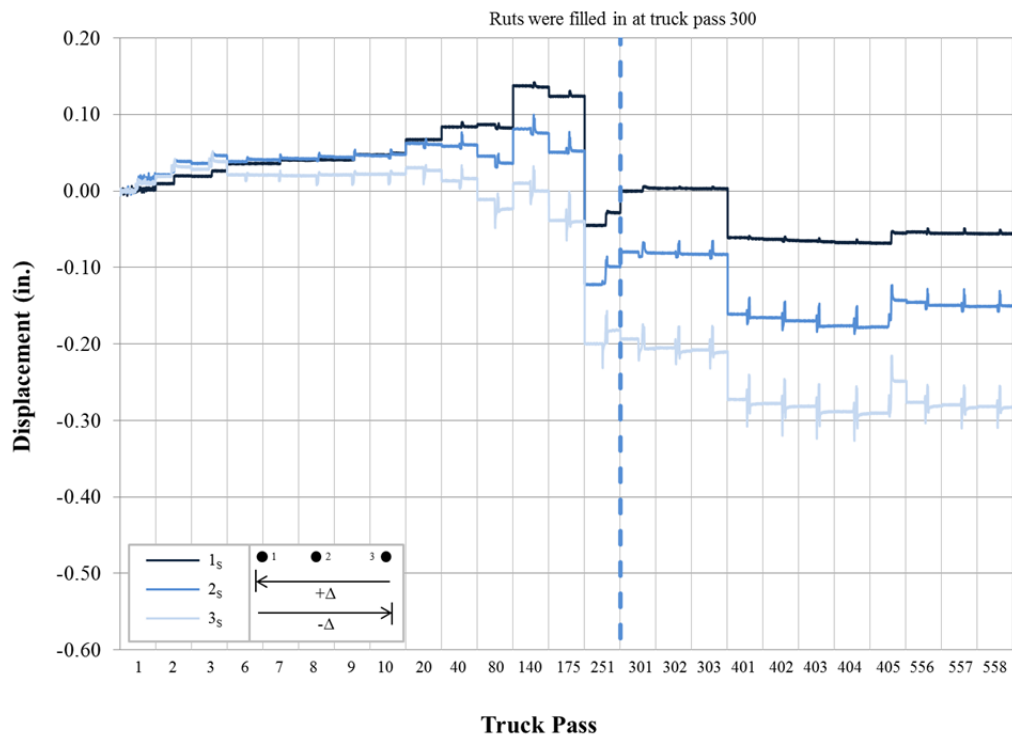
Figure M-14: Dynamic displacements for Test Section 7, south (Synteen SF12).
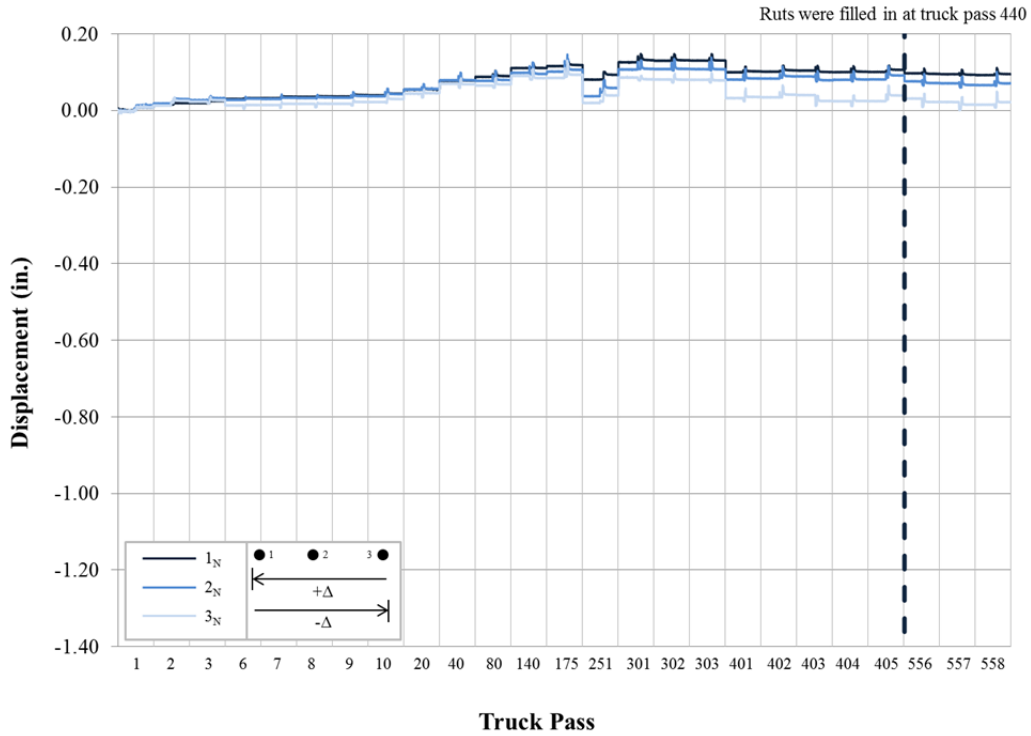
Figure M-15: Dynamic displacements for Test Section 8, north (TenCate Mirafi BXG11).
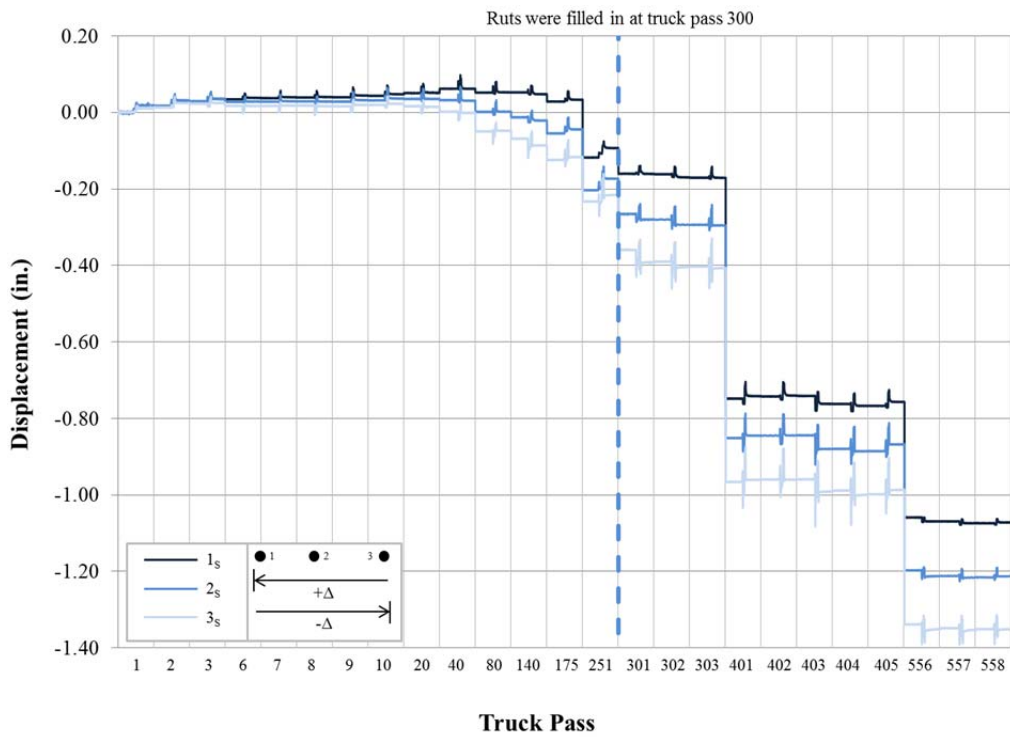
Figure M-16: Dynamic displacements for Test Section 8, south (TenCate Mirafi BXG11).
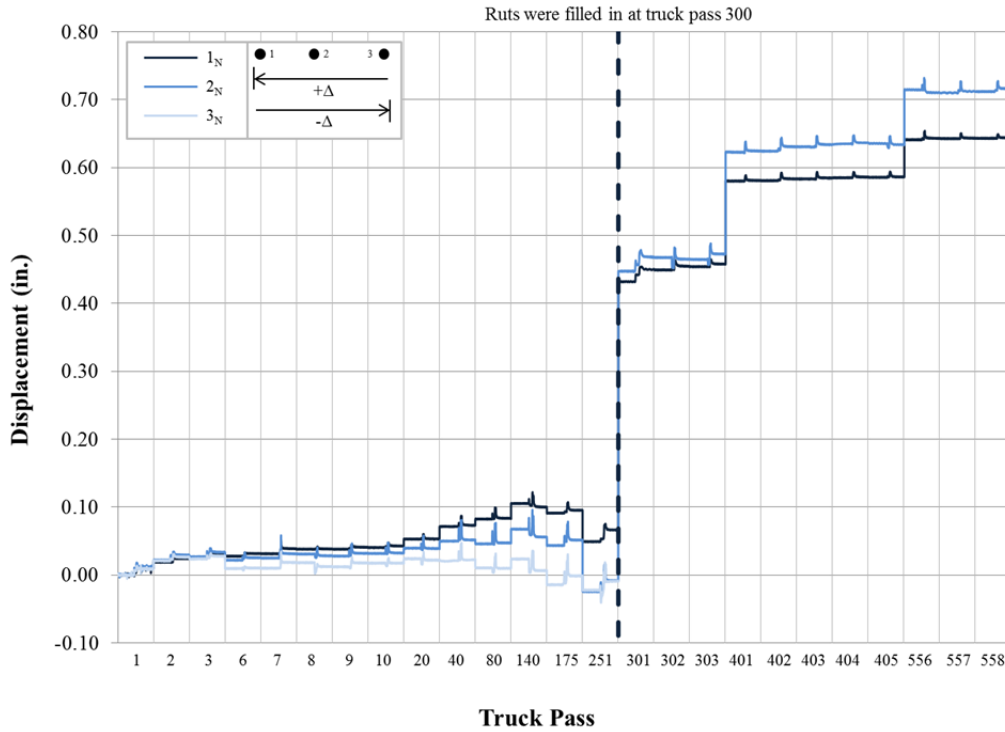
Figure M-17: Dynamic displacements for Test Section 9, north (Huesker Fornit 30).
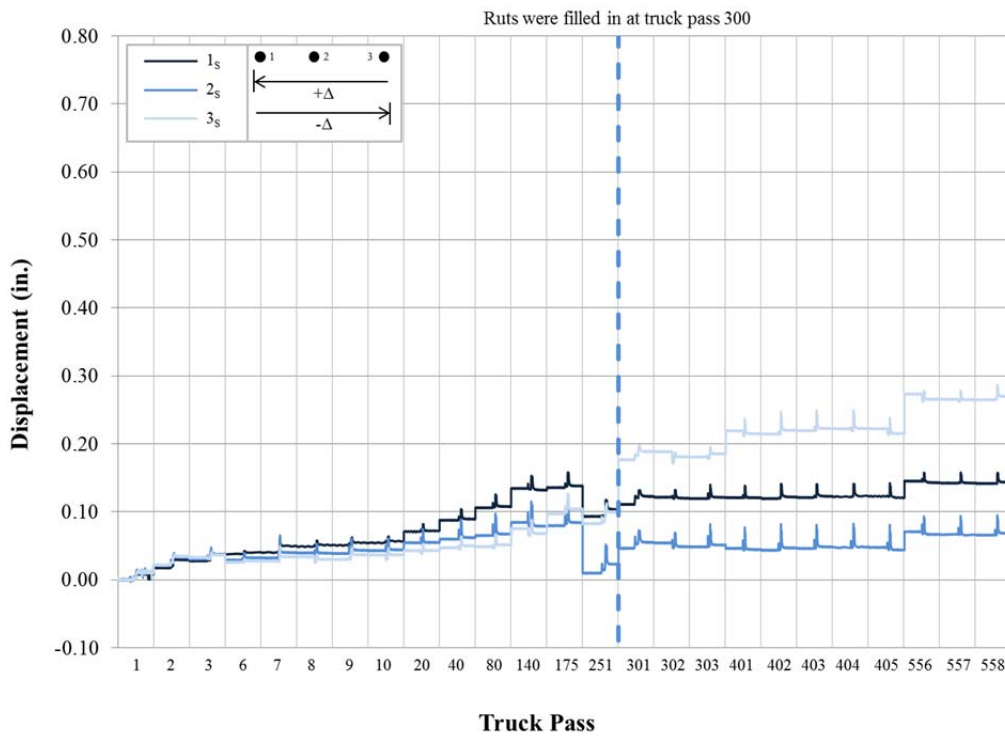
Figure M-18: Dynamic displacements for Test Section 9, south (Huesker Fornit 30).
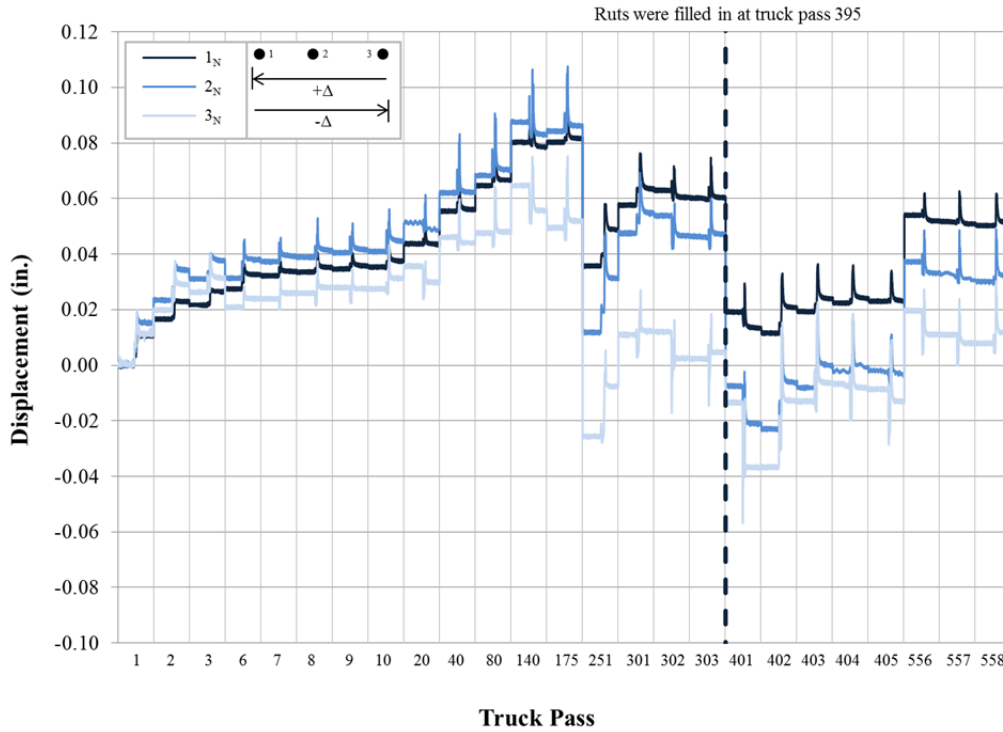
Figure M-19: Dynamic displacements for Test Section 10, north (SynTec Tenax MS 330).
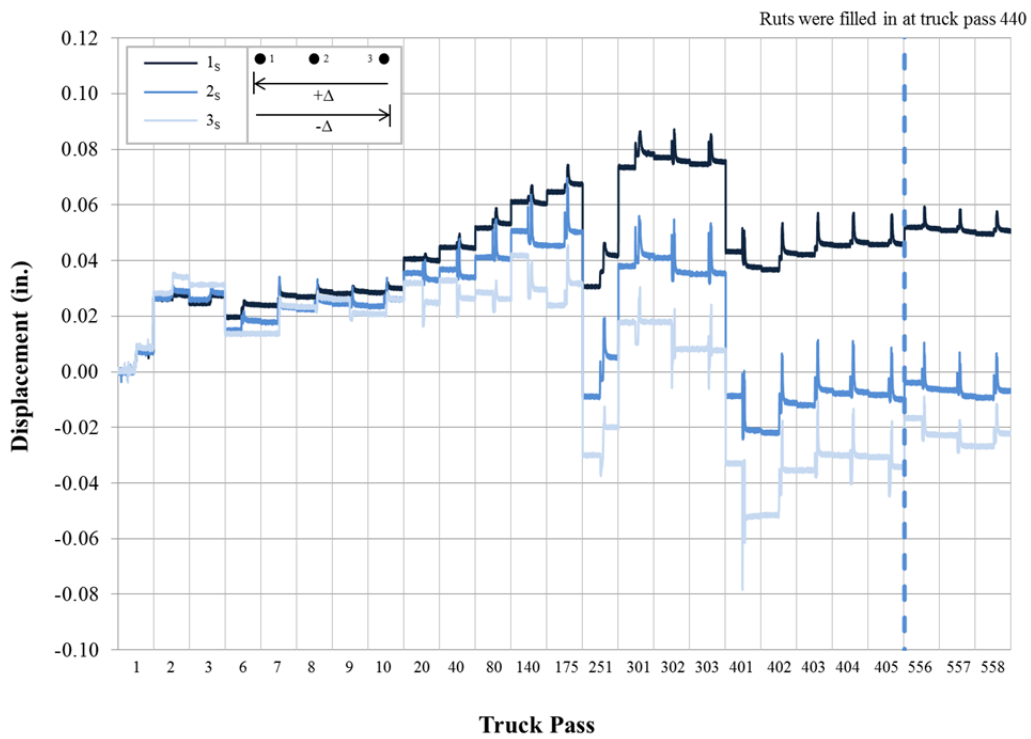
Figure M-20: Dynamic displacements for Test Section 10, south (SynTec Tenax MS 330).
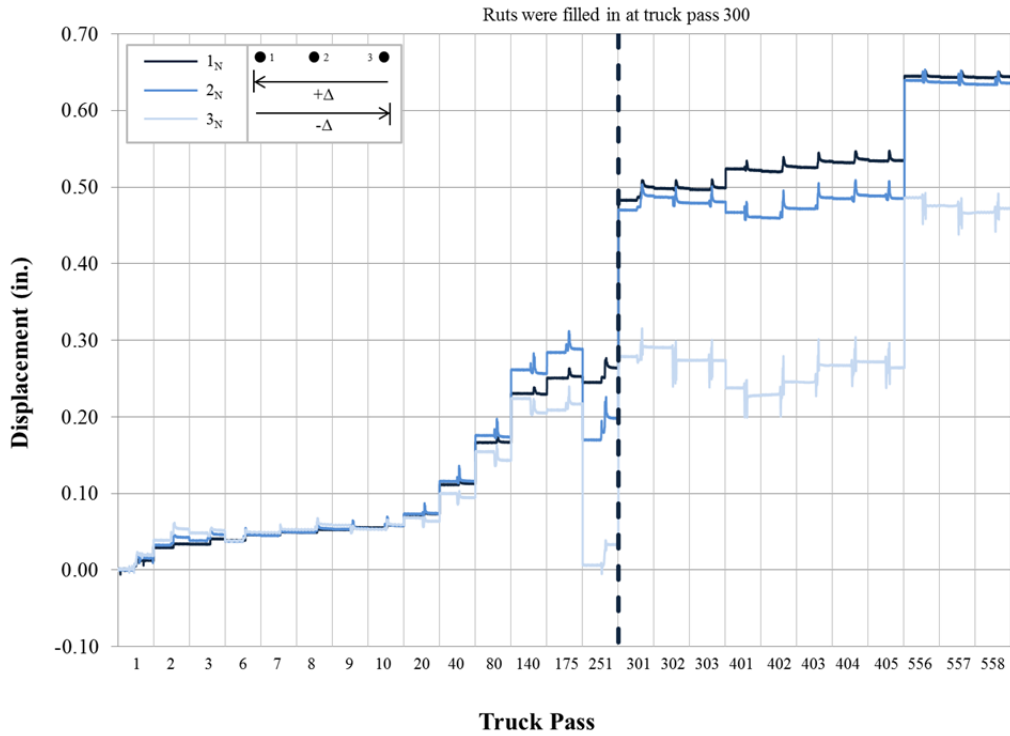
Figure M-21: Dynamic displacements for Test Section 11, north (Tensar TX140).
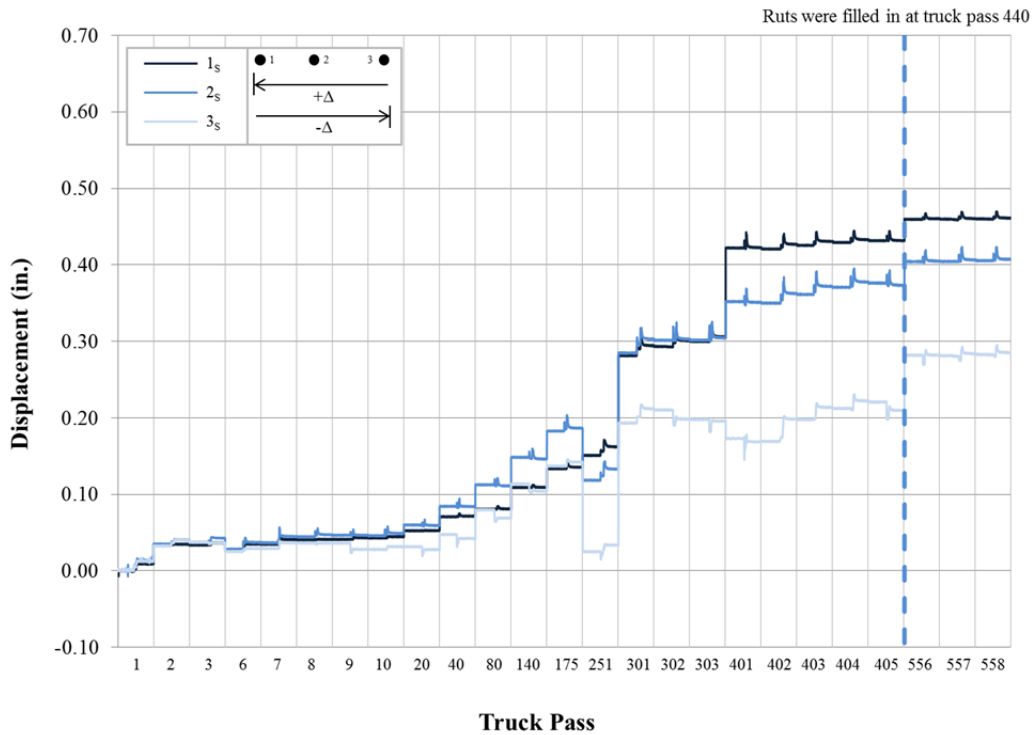
Figure M-22: Dynamic displacements for Test Section 11, south (Tensar TX140).
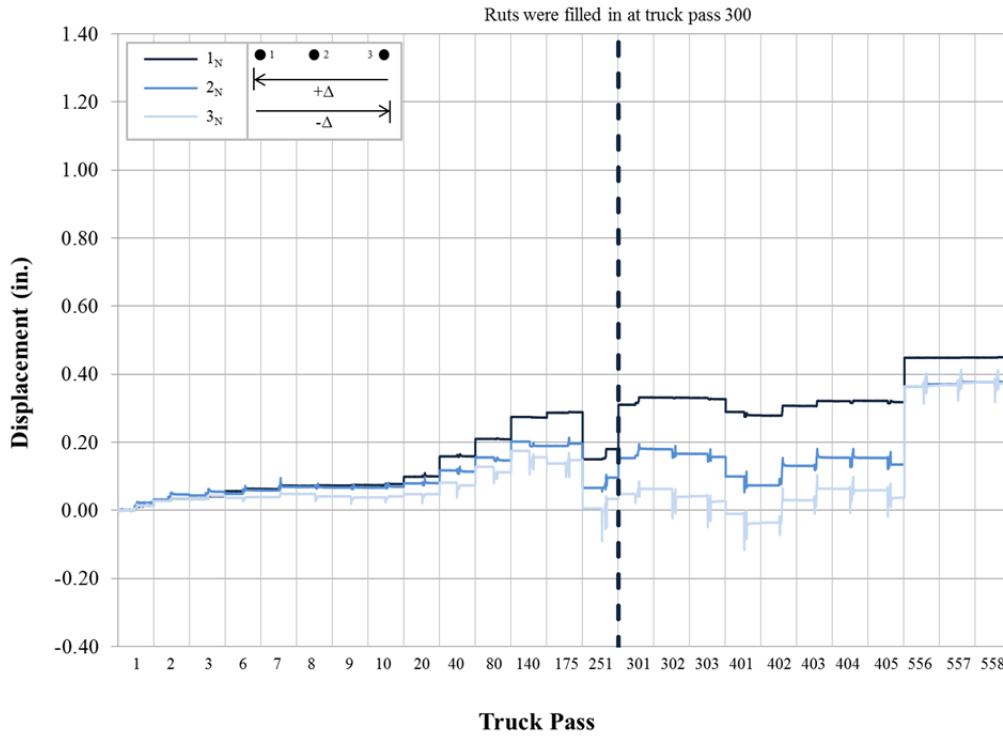
Figure M-23: Dynamic displacements for Test Section 12, north (Tensar TX160).
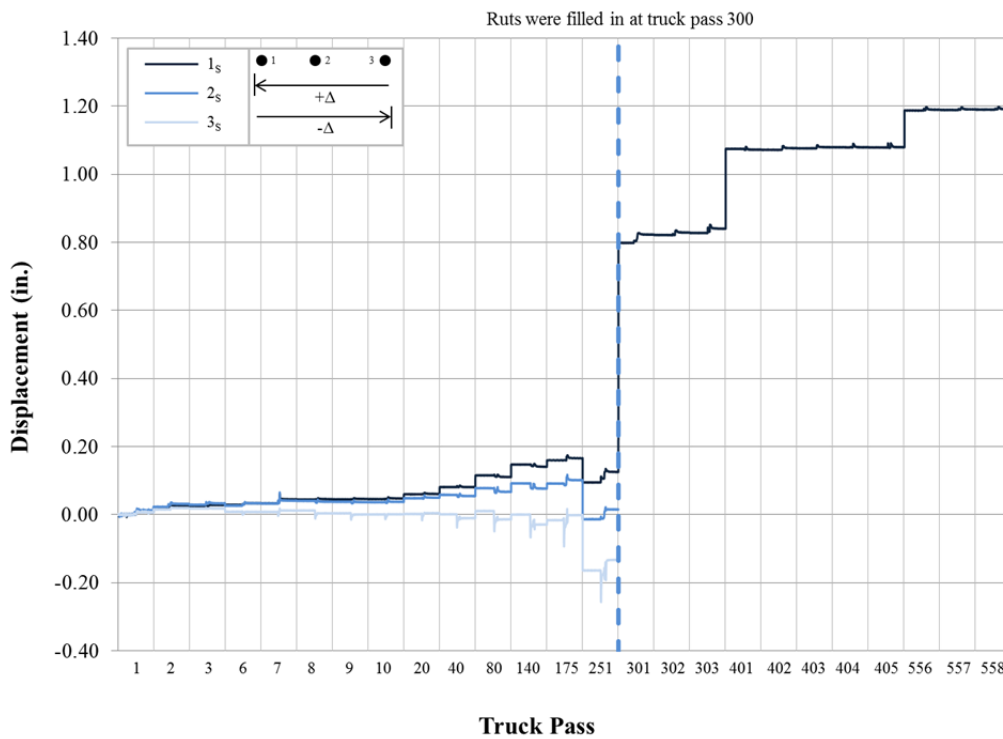
Figure M-24: Dynamic displacements for Test Section 12, south (Tensar TX160).
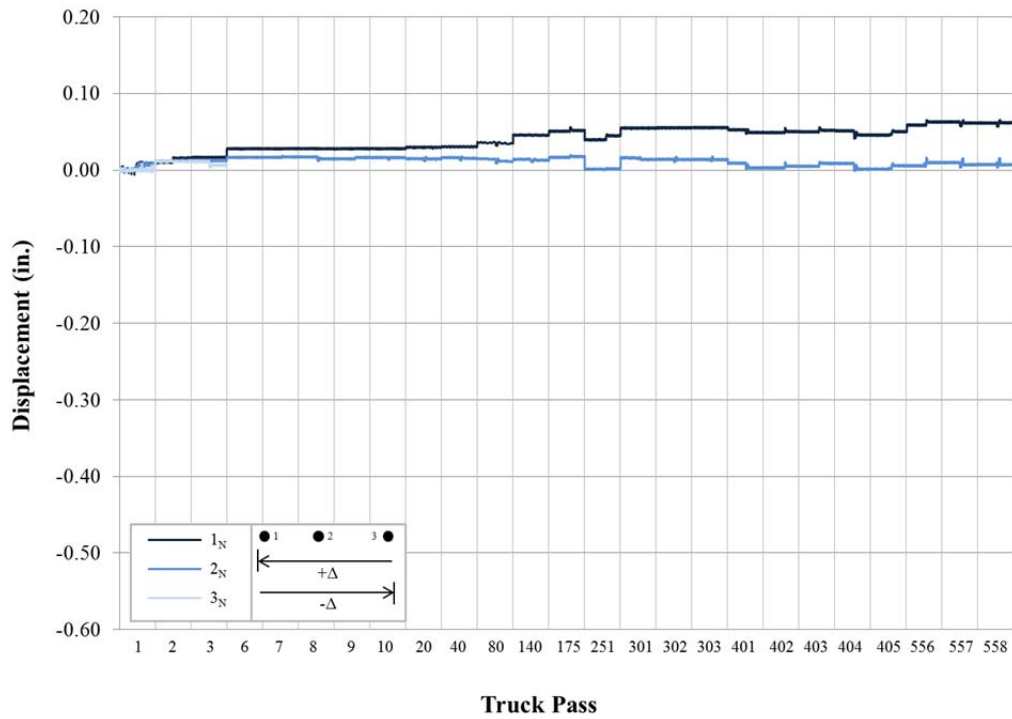
Figure M-25: Dynamic displacements for Test Section 13, north (TenCate Mirafi RS580i).
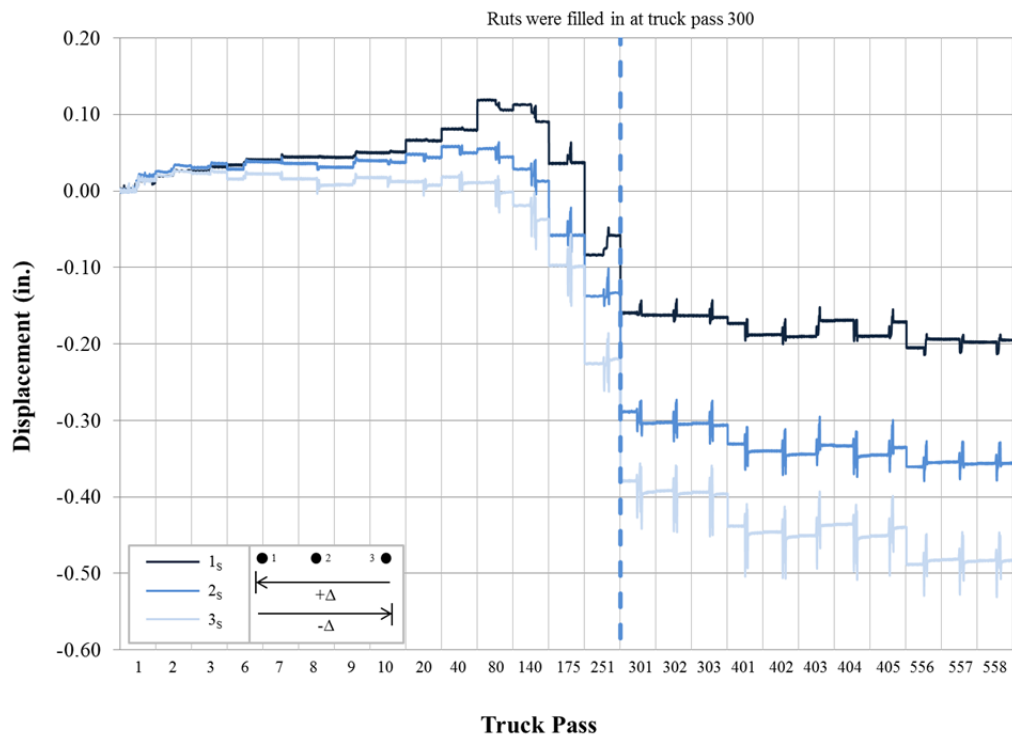
Figure M-26: Dynamic displacements for Test Section 13, south (TenCate Mirafi RS580i).
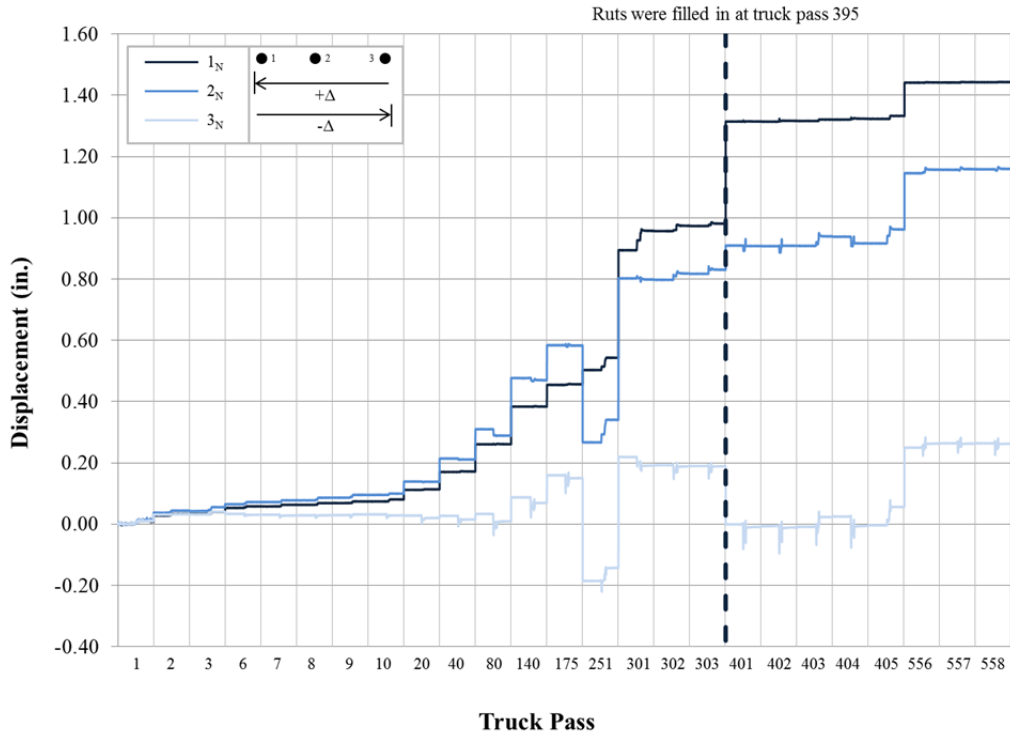
**Figure M-27: Dynamic displacements for Test Section 14, north (Propex Geotex 801).**
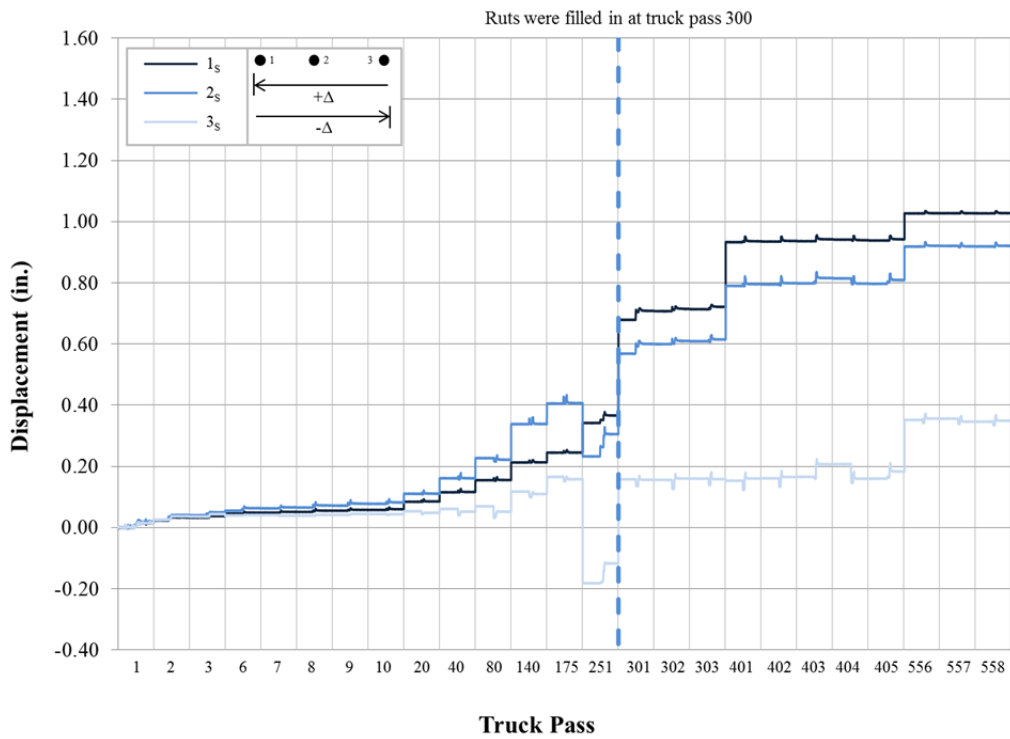
Figure M-28: Dynamic displacements for Test Section 14, south (Propex Geotex 801).

APPENDIX N – DYNAMIC STRAIN RESULTS FROM STRAIN GAGES
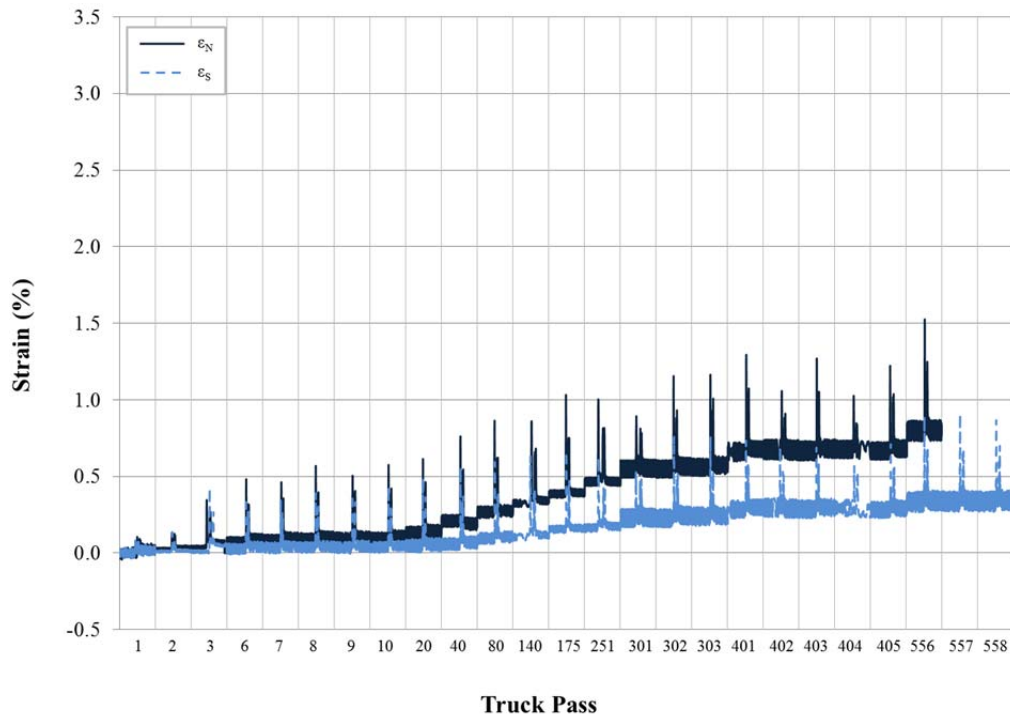
Figure N-1: Dynamic strain gage results for Test Section 1 (Tensar BX Type 2, CBR = 2.17).
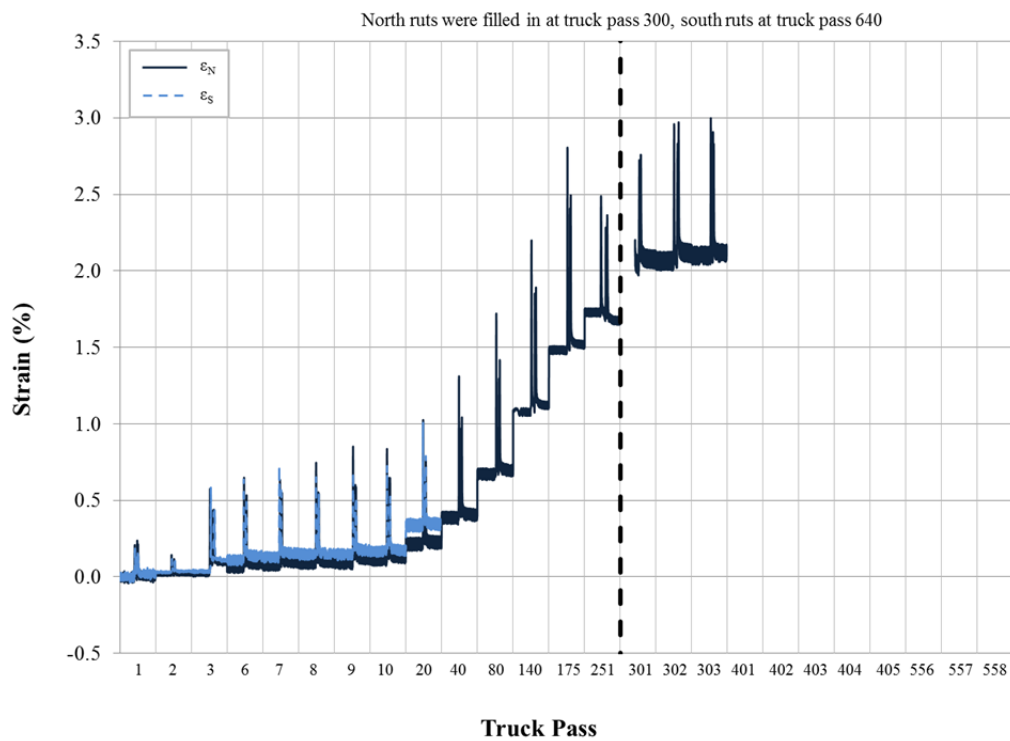
Figure N-2: Dynamic strain gage results for Test Section 2 (Tensar BX Type 2, CBR = 1.64).
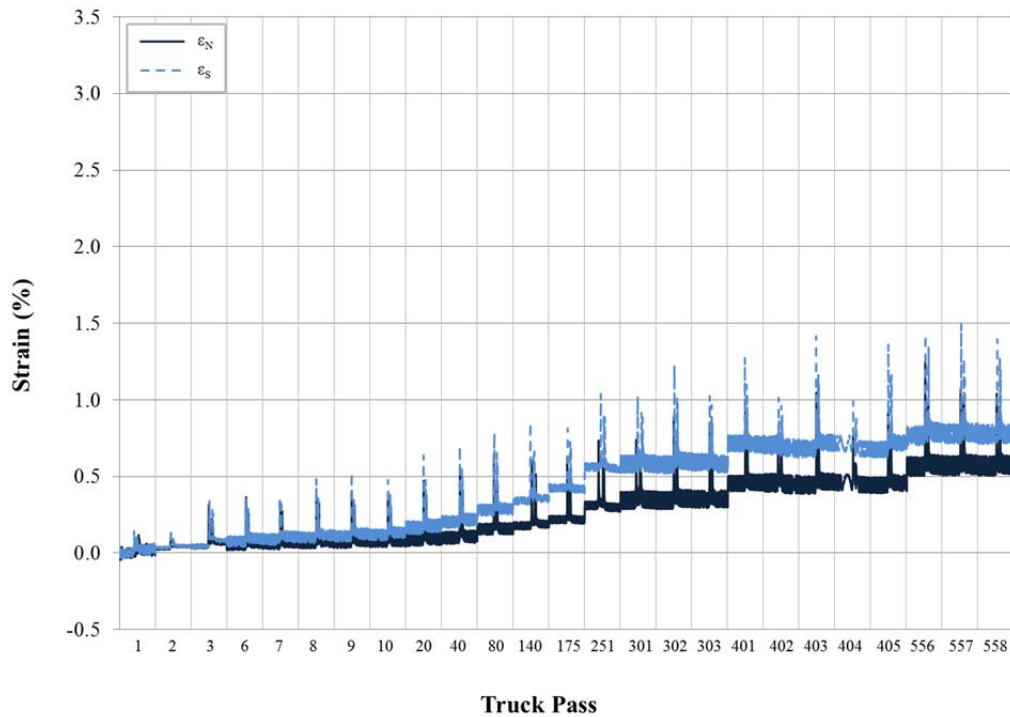
Figure N-3: Dynamic strain gage results for Test Section 3 (Tensar BX Type 2, CBR = 1.79).

South ruts were filled in at truck pass 440
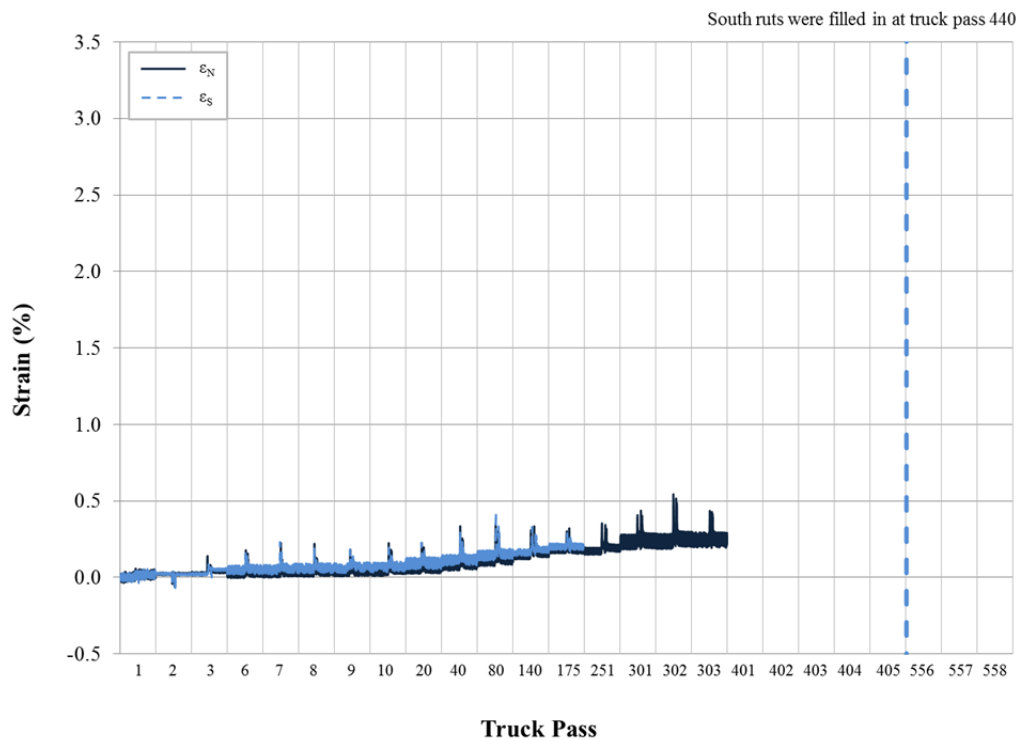
Figure N-4: Dynamic strain gage results for Test Section 4 (NAUE Secugrid 30-30 Q1).
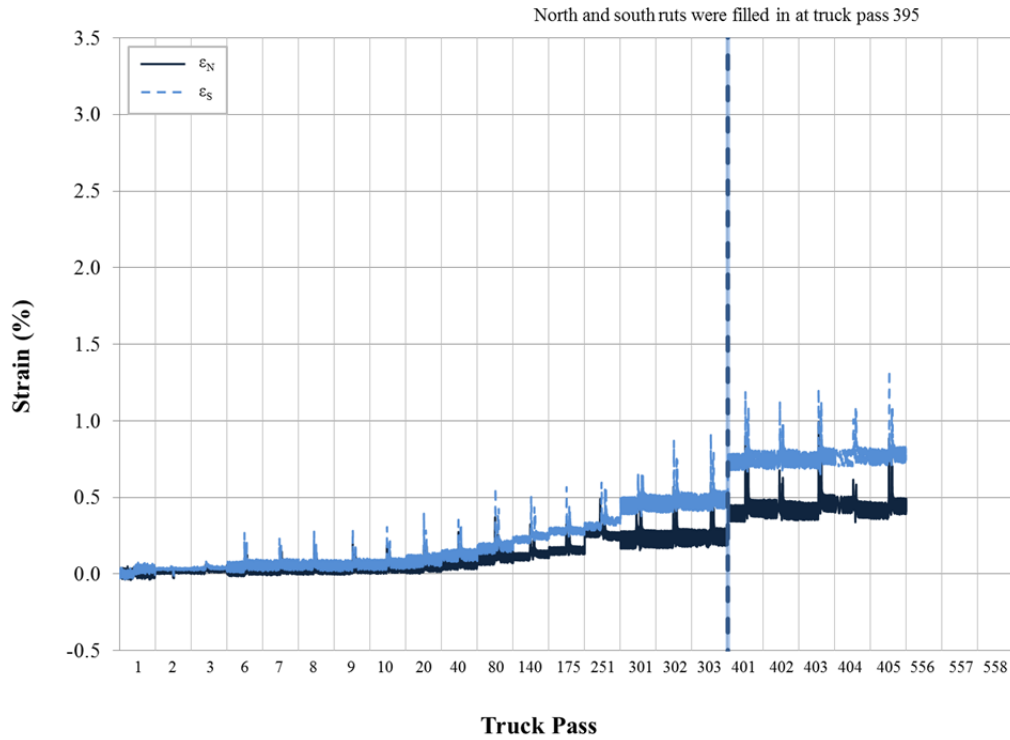
Figure N-5: Dynamic strain gage results for Test Section 5 (Colbond Enkagrid MAX 30).
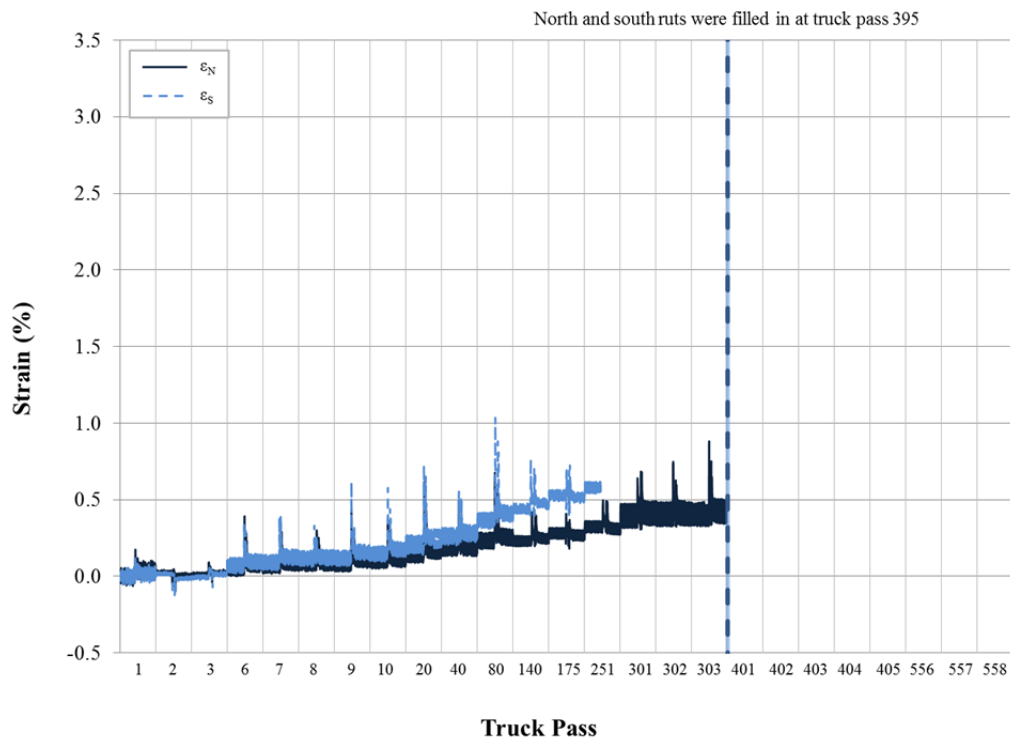
Figure N-6: Dynamic strain gage results for Test Section 6 (Synteen SF11).
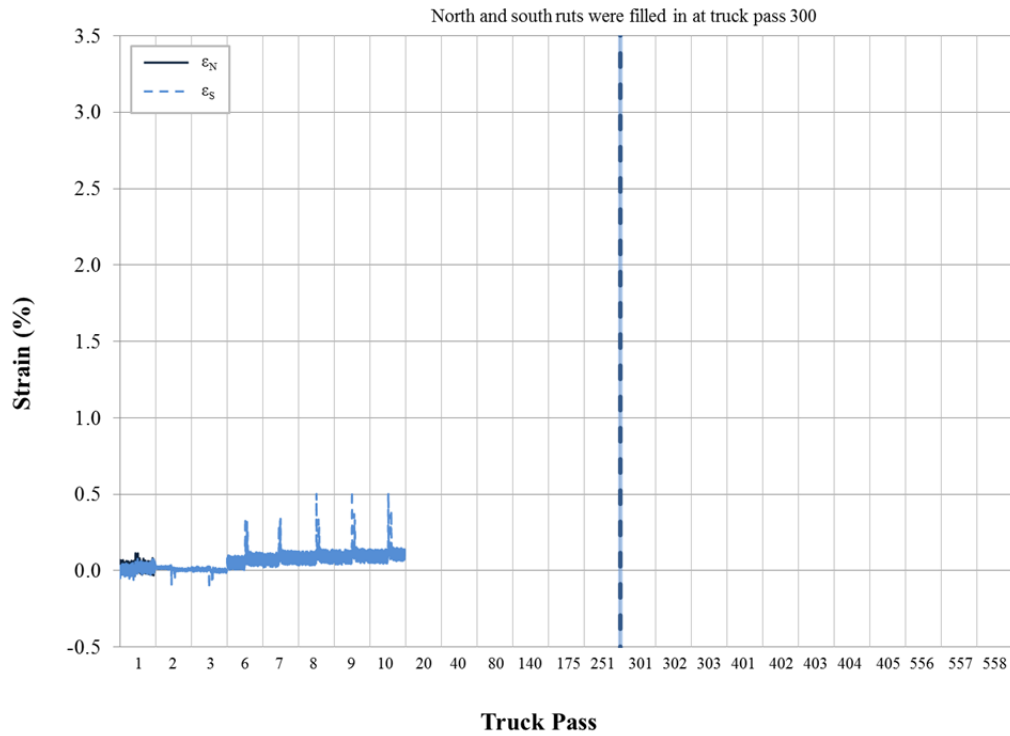
Figure N-7: Dynamic strain gage results for Test Section 7 (Synteen SF12).
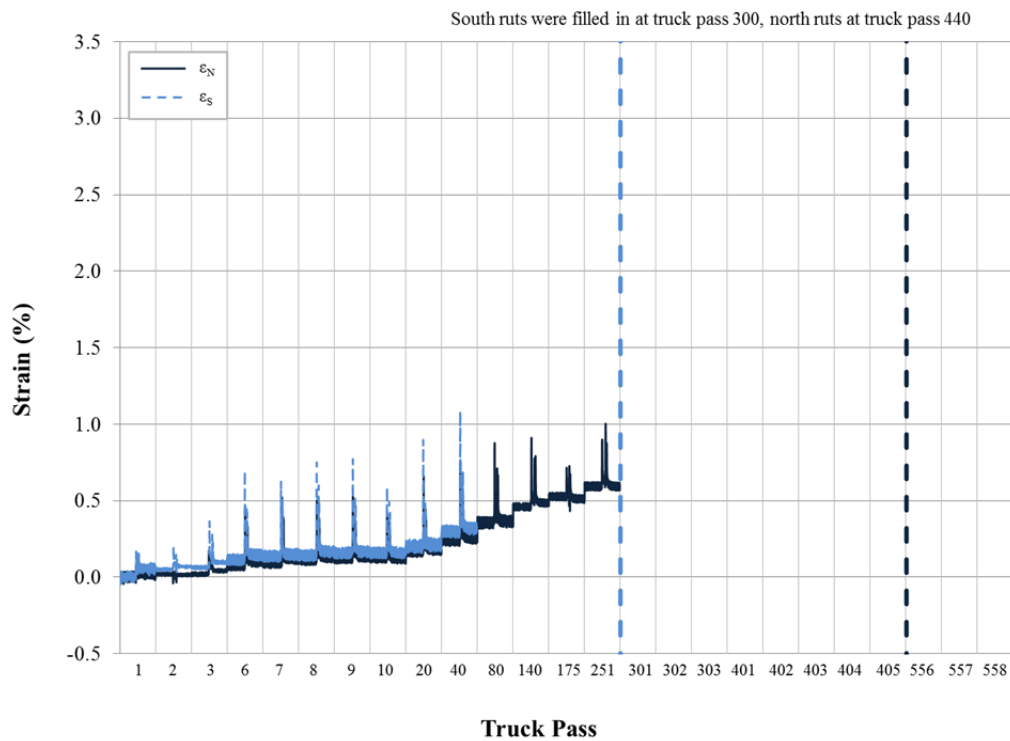
Figure N-8: Dynamic strain gage results for Test Section 8 (TenCate Mirafi BXG11).
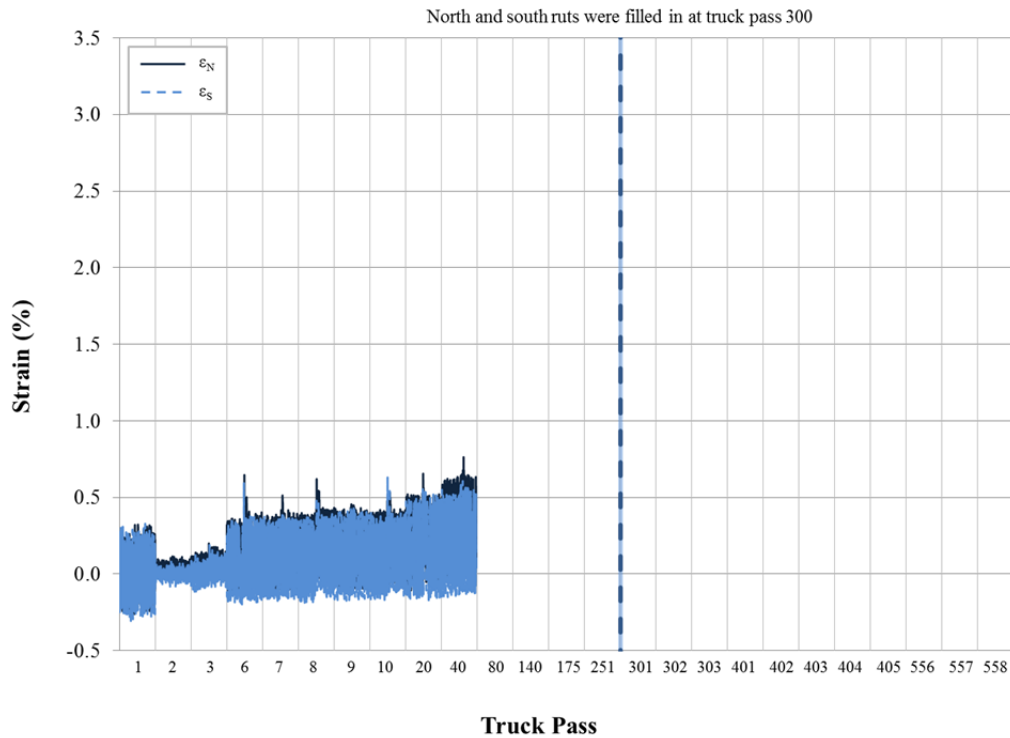
Figure N-9: Dynamic strain gage results for Test Section 9 (Huesker Fornit 30).
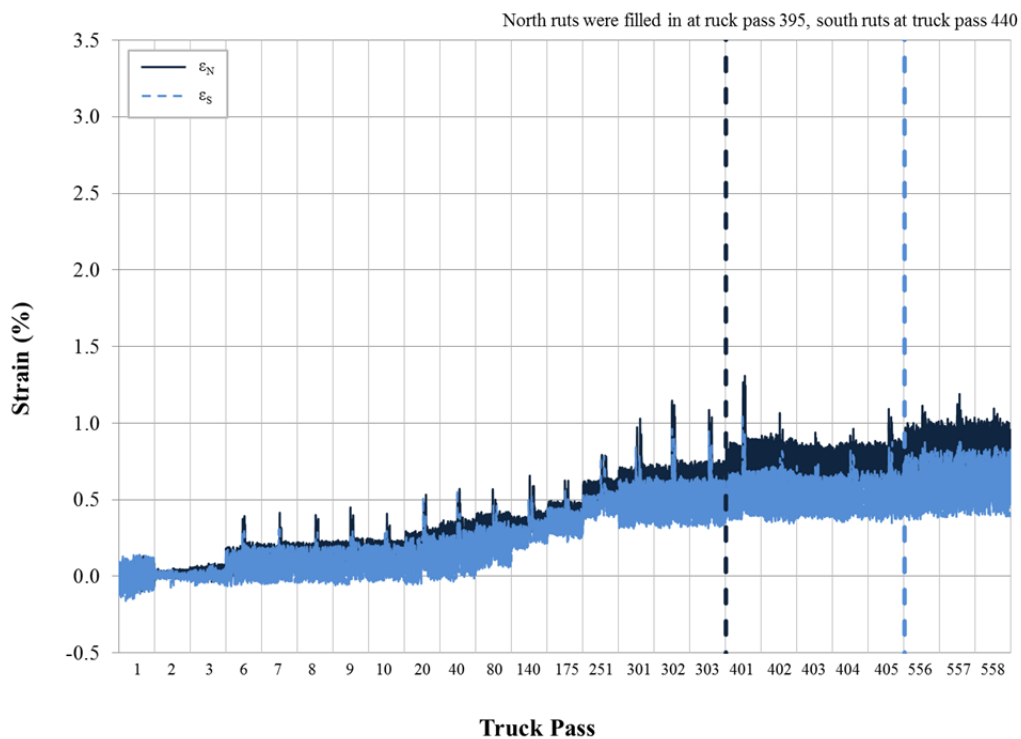
Figure N-10: Dynamic strain gage results for Test Section 10 (SynTec Tenax MS 330).
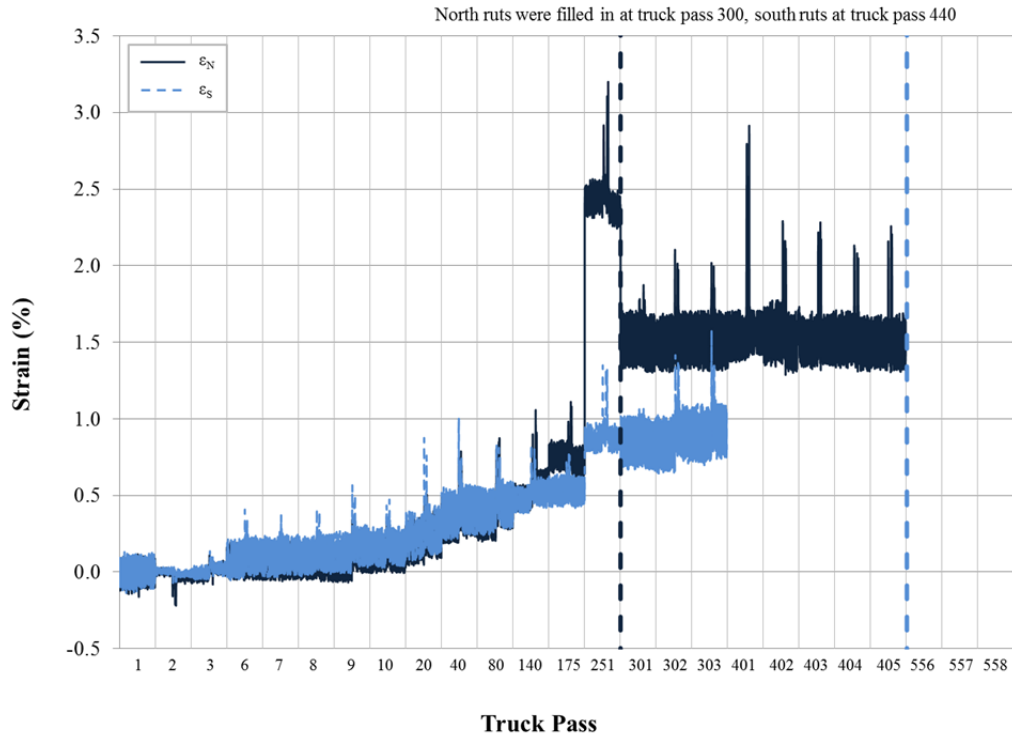
Figure N-11: Dynamic strain gage results for Test Section 11 (Tensar TX140).
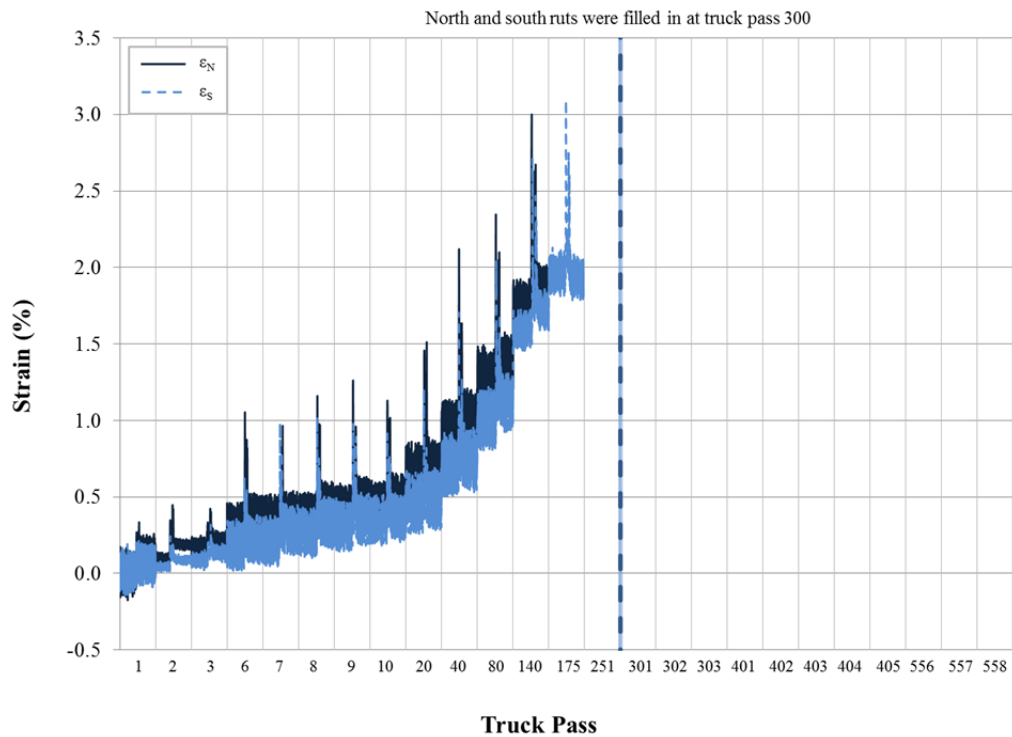
Figure N-12: Dynamic strain gage results for Test Section 12 (Tensar TX160).
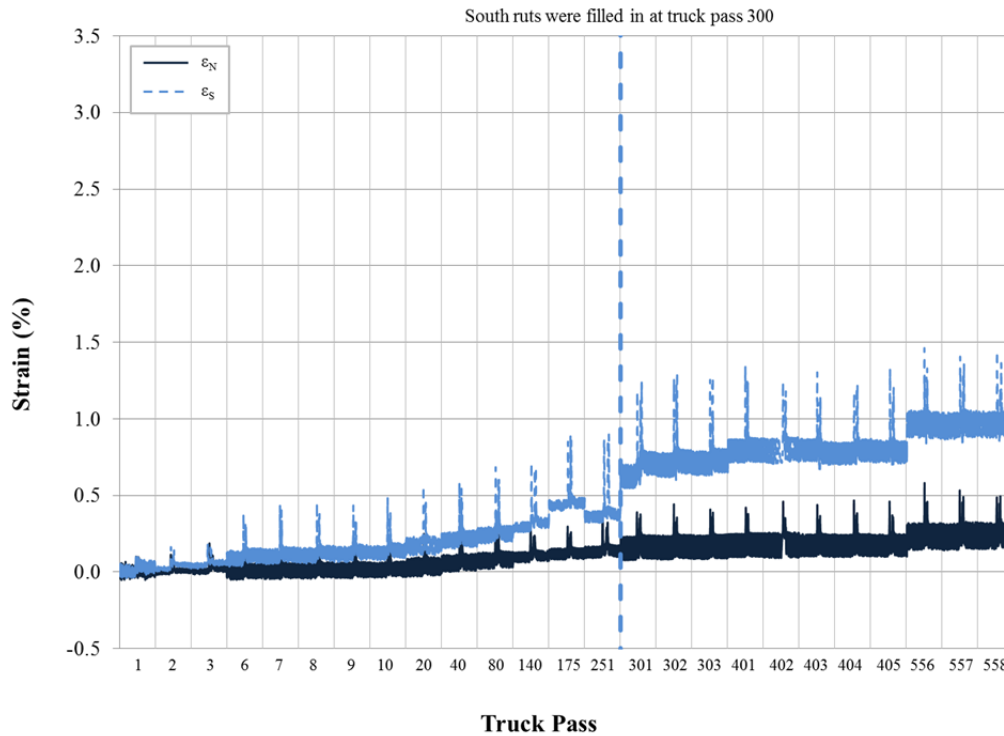
Figure N-13: Dynamic strain gage results for Test Section 13 (TenCate Mirafi RS580i).
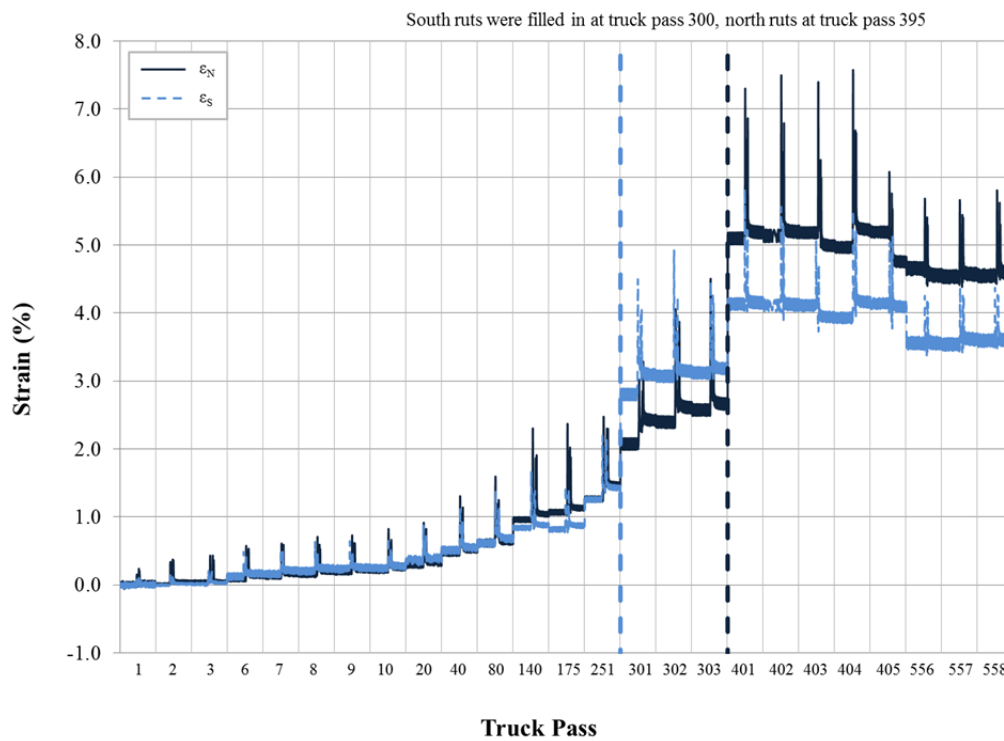
Figure N-14: Dynamic strain gage results for Test Section 14 (Propex Geotex 801).

APPENDIX O – CUMULATIVE STRAIN RESULTS FROM STRAIN GAGES
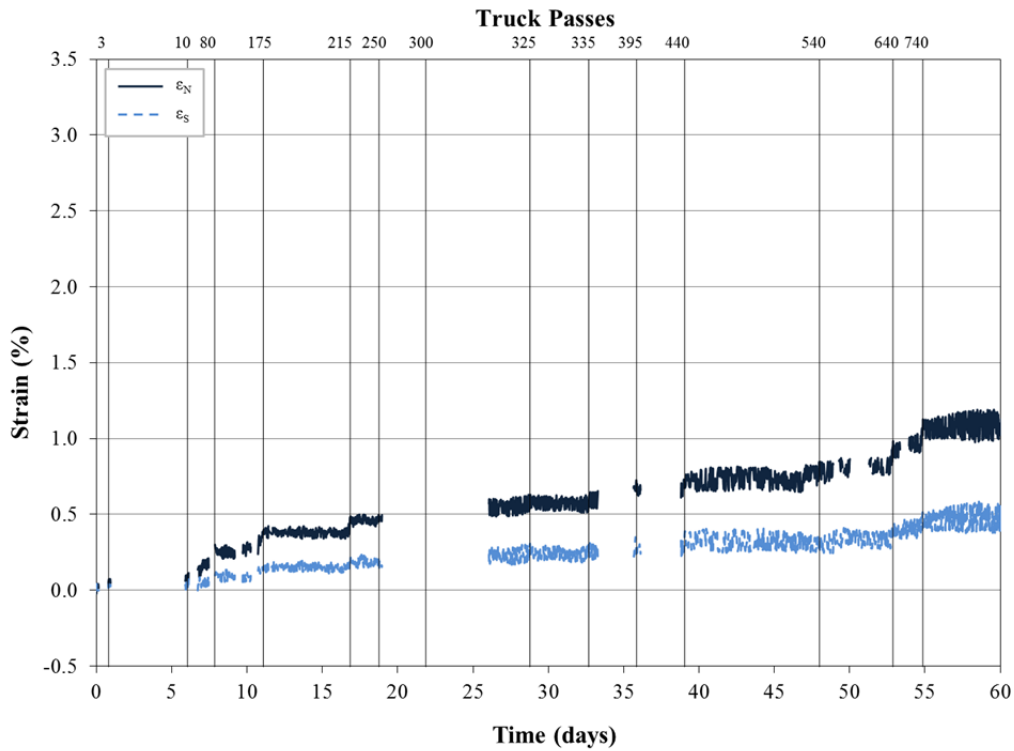
Figure O-1: Cumulative strain gage results for Test Section 1 (Tensar BX Type 2, CBR = 2.17).
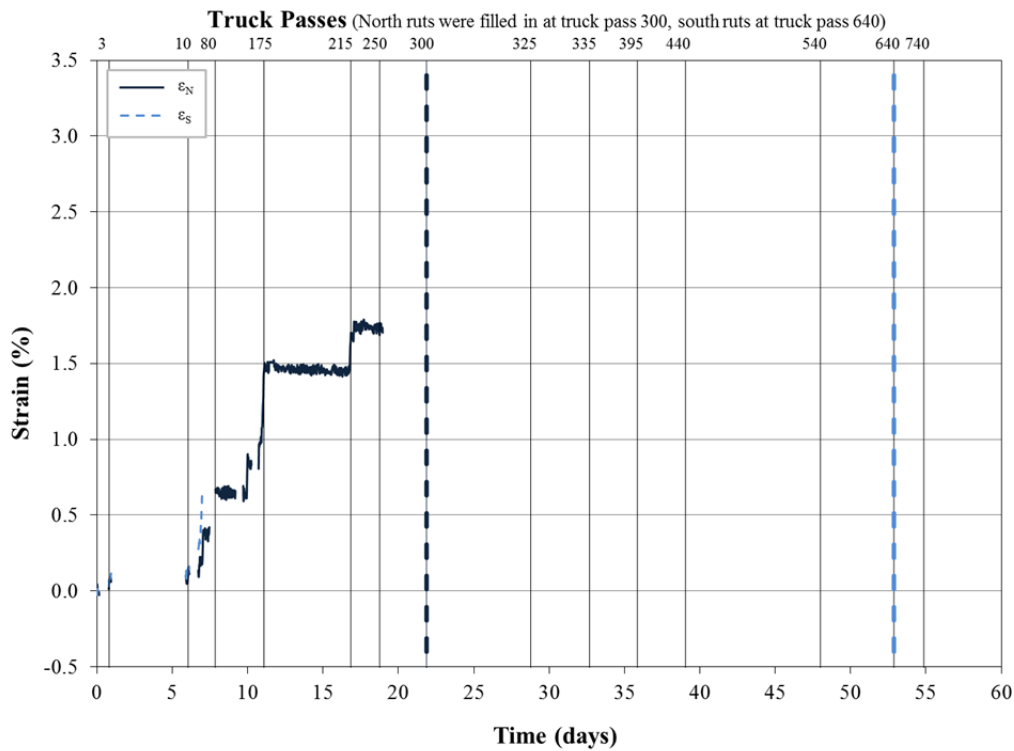
Figure O-2: Cumulative strain gage results for Test Section 2 (Tensar BX Type 2, CBR = 1.64).
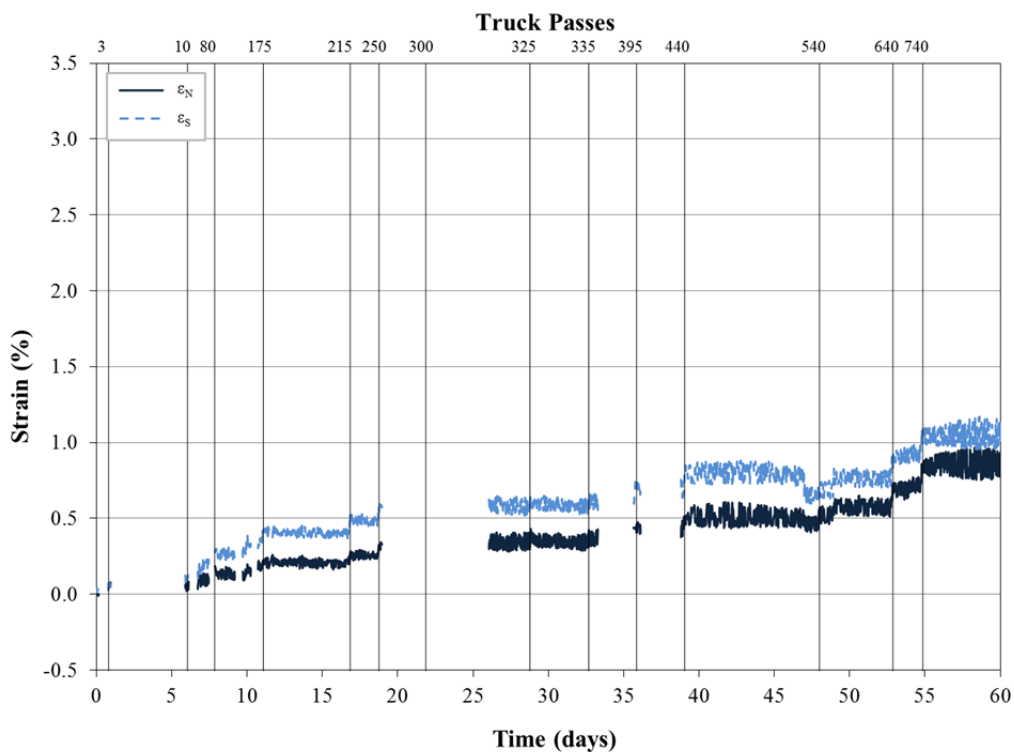
Figure O-3: Cumulative strain gage results for Test Section 3 (Tensar BX Type 2, CBR = 1.79).
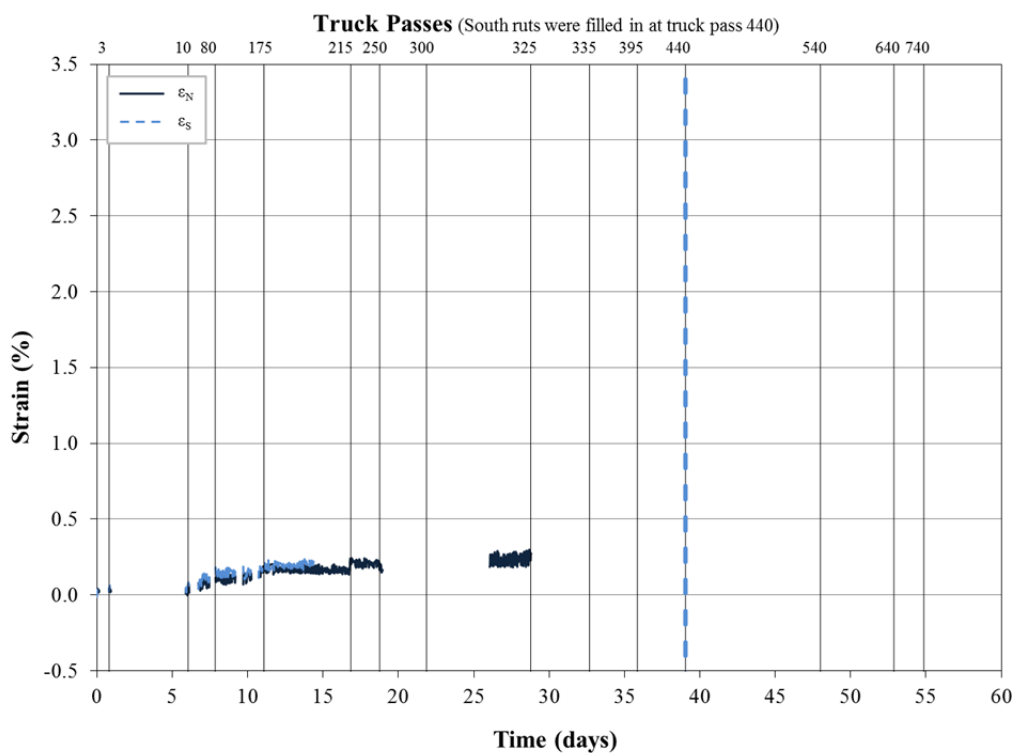
Figure O-4: Cumulative strain gage results for Test Section 4 (NAUE Secugrid 30-30 Q1).
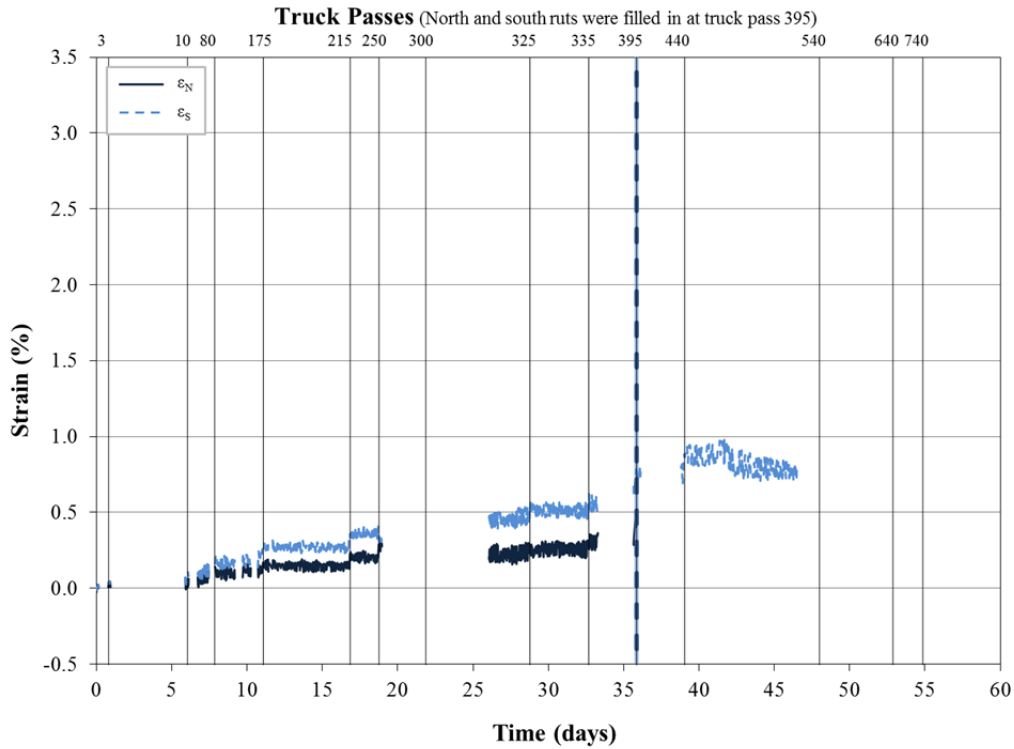
Figure O-5: Cumulative strain gage results for Test Section 5 (Colbond Enkagrid MAX 30).
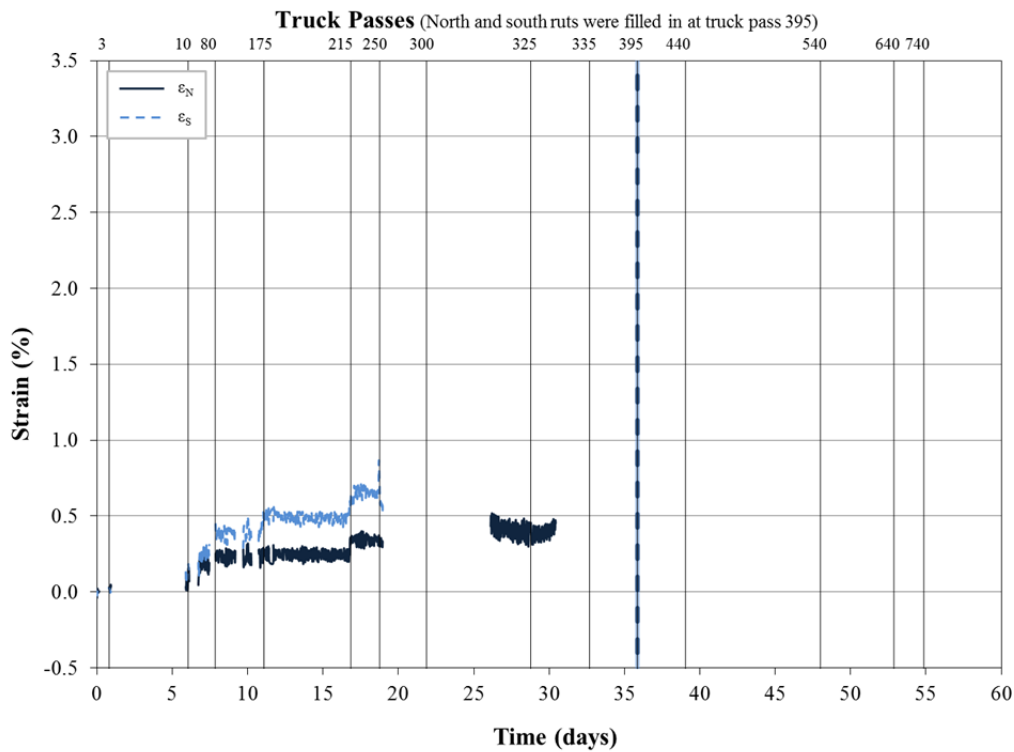
Figure O-6: Cumulative strain gage results for Test Section 6 (Synteen SF11).
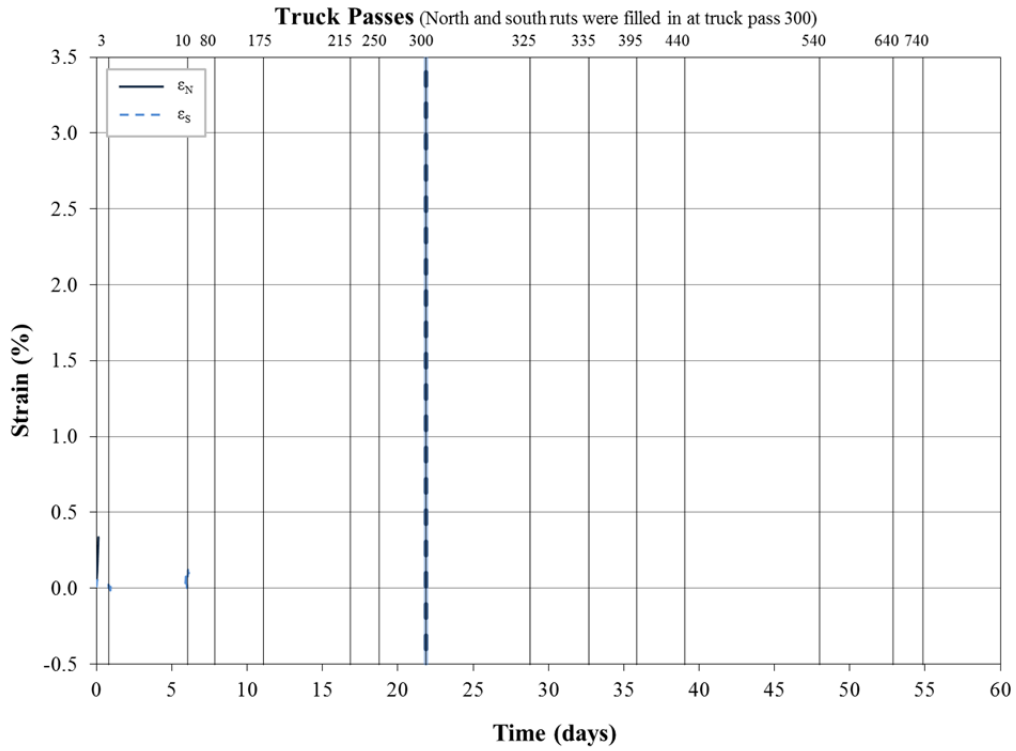
Figure O-7: Cumulative strain gage results for Test Section 7 (Synteen SF12).
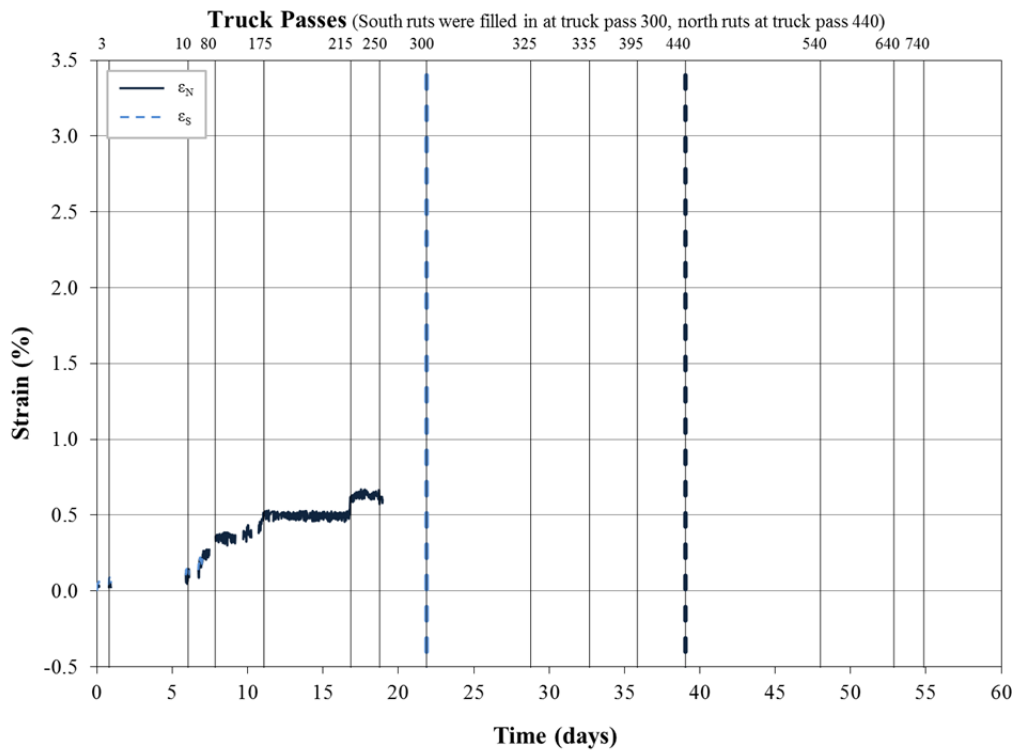
Figure O-8: Cumulative strain gage results for Test Section 8 (TenCate Mirafi BXG11).
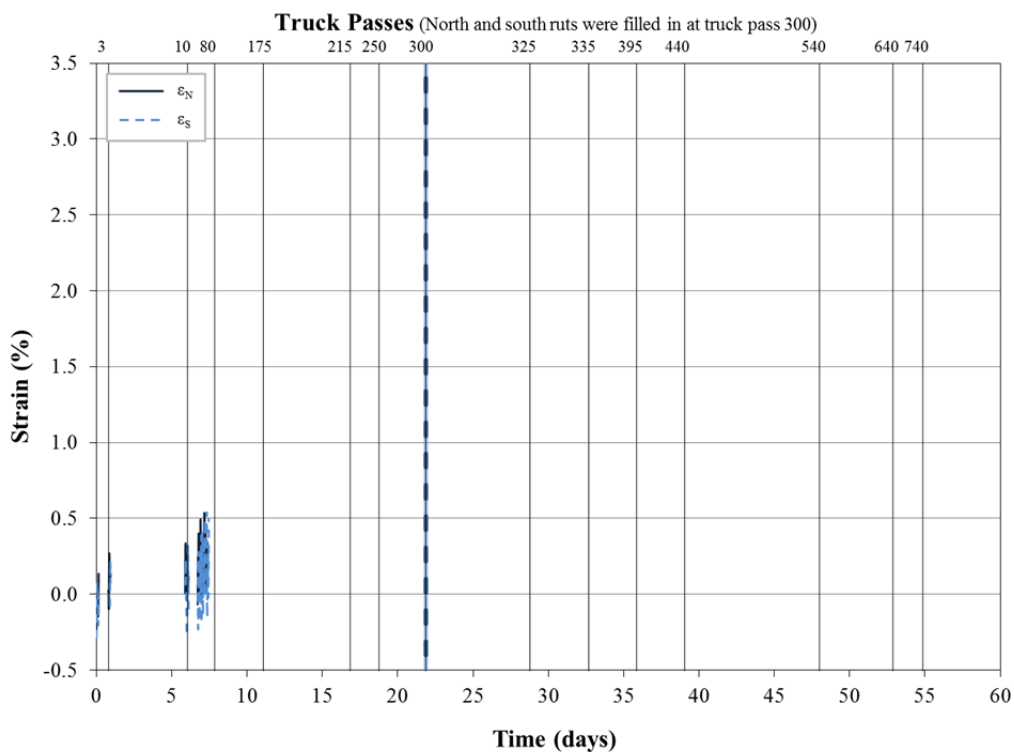
Figure O-9: Cumulative strain gage results for Test Section 9 (Huesker Fornit 30).
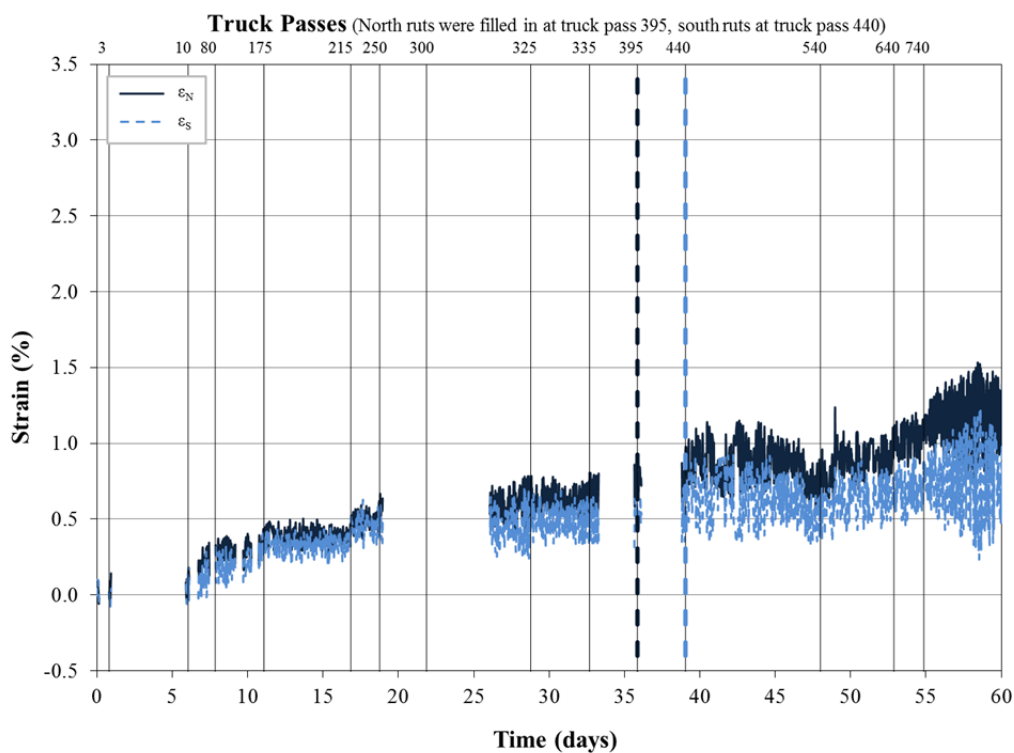
Figure O-10: Cumulative strain gage results for Test Section 10 (SynTec Tenax MS 330).
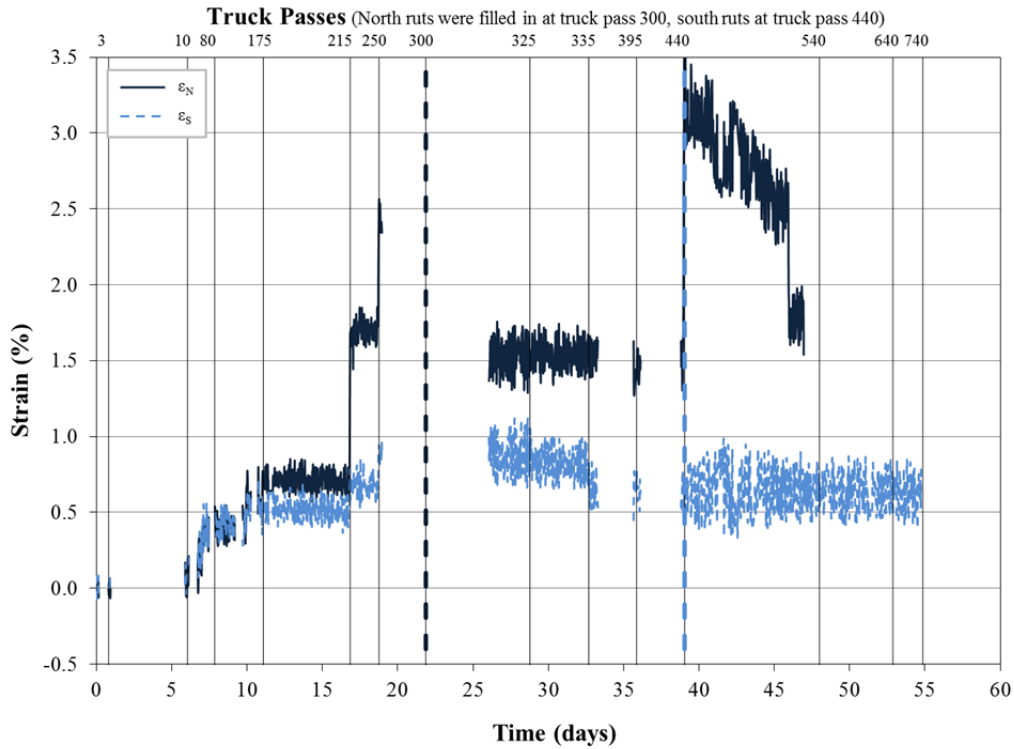
Figure O-11: Cumulative strain gage results for Test Section 11 (Tensar TX140).
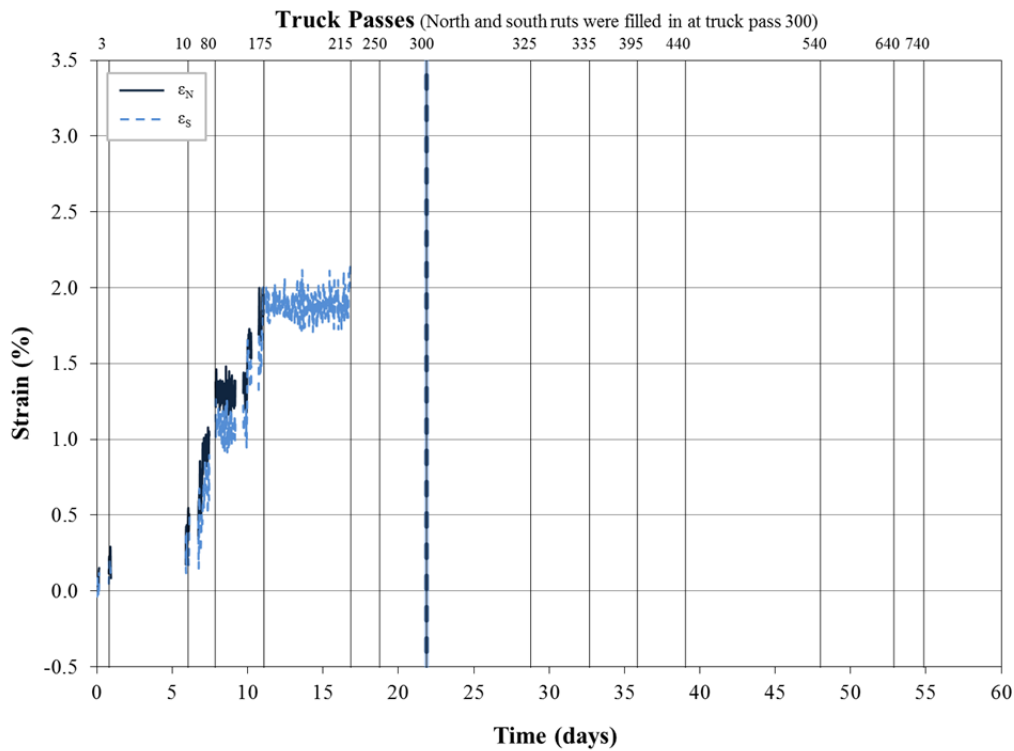
Figure O-12: Cumulative strain gage results for Test Section 12 (Tensar TX160).
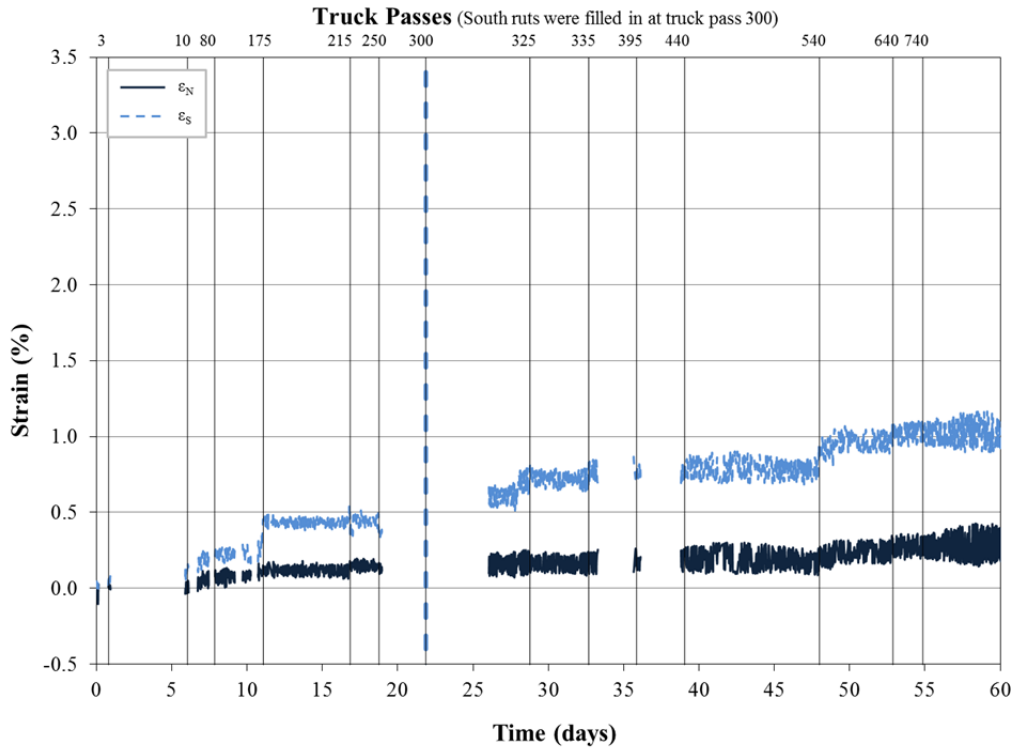
Figure O-13: Cumulative strain gage results for Test Section 13 (TenCate Mirafi RS580i).
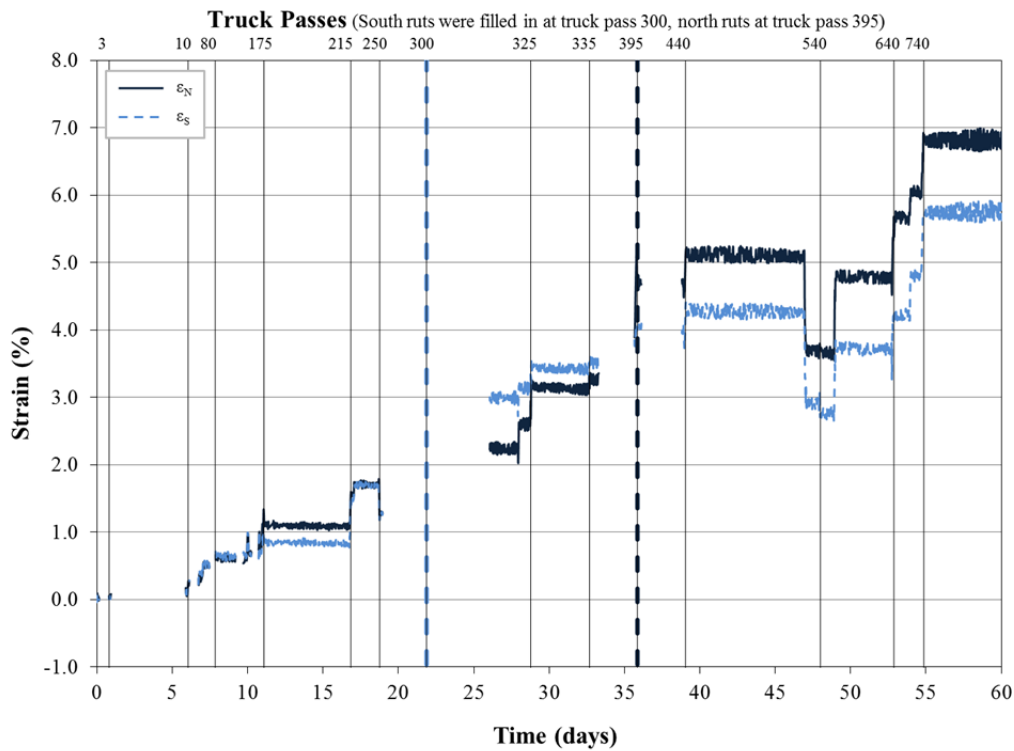
Figure O-14: Cumulative strain gage results for Test Section 14 (Propex Geotex 801).

APPENDIX P – DYNAMIC STRAIN RESULTS FROM LVDTS
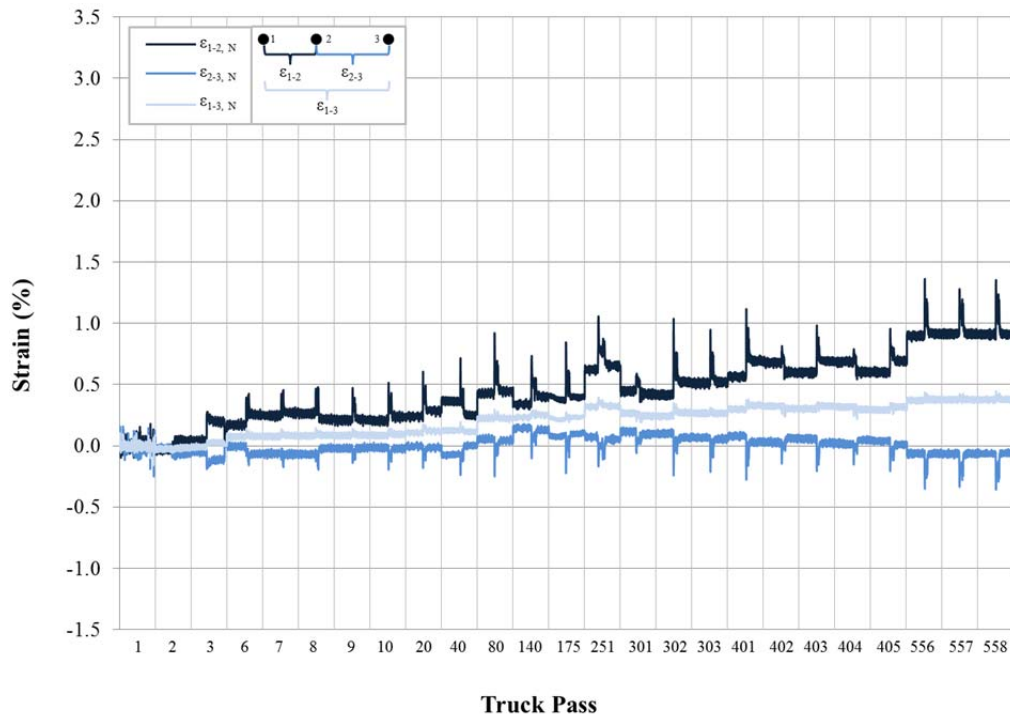
Figure P-1: Dynamic LVDT strain for Test Section 1, north (Tensar BX Type 2, CBR = 2.17).
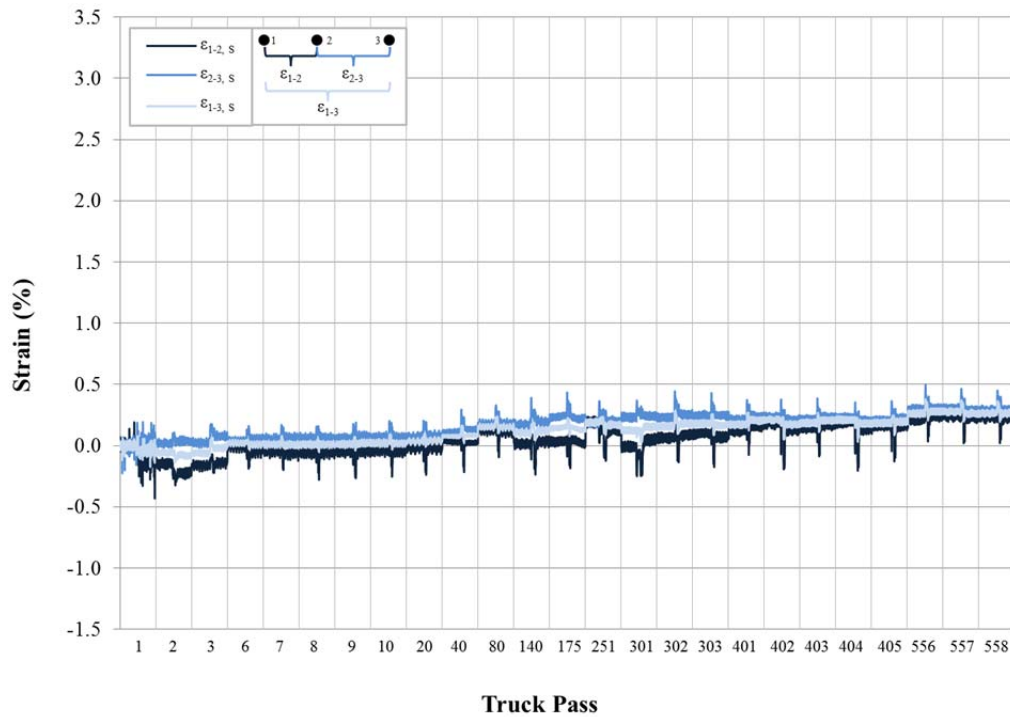
Figure P-2: Dynamic LVDT strain for Test Section 1, south (Tensar BX Type 2, CBR = 2.17).
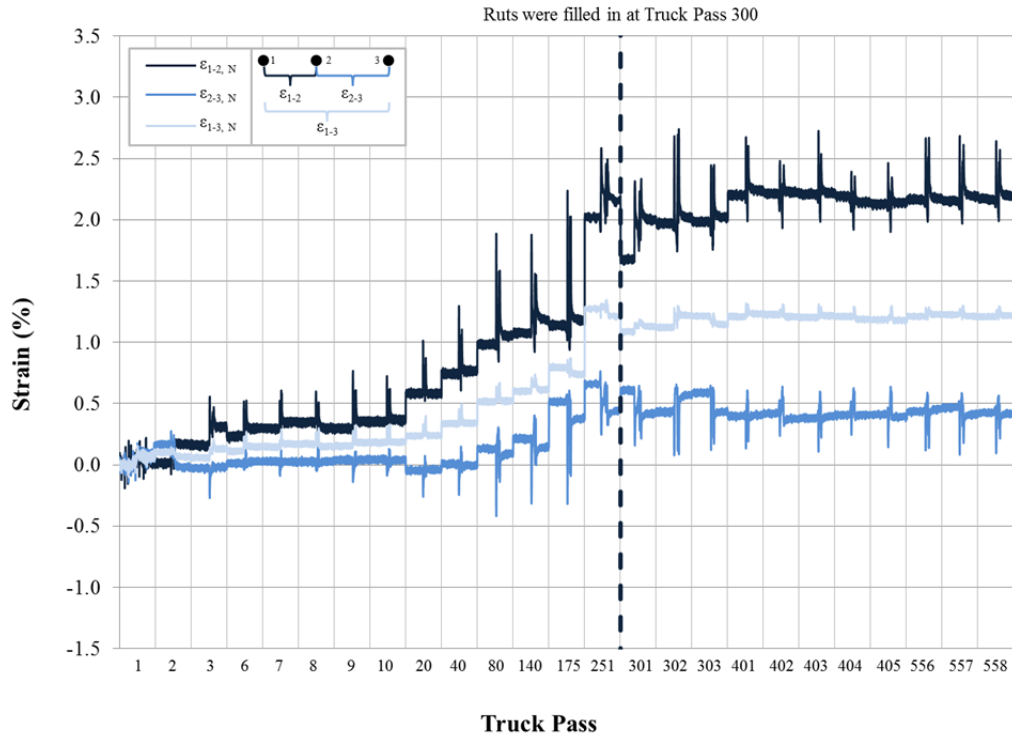
Figure P-3: Dynamic LVDT strain for Test Section 2, north (Tensar BX Type 2, CBR = 1.64).
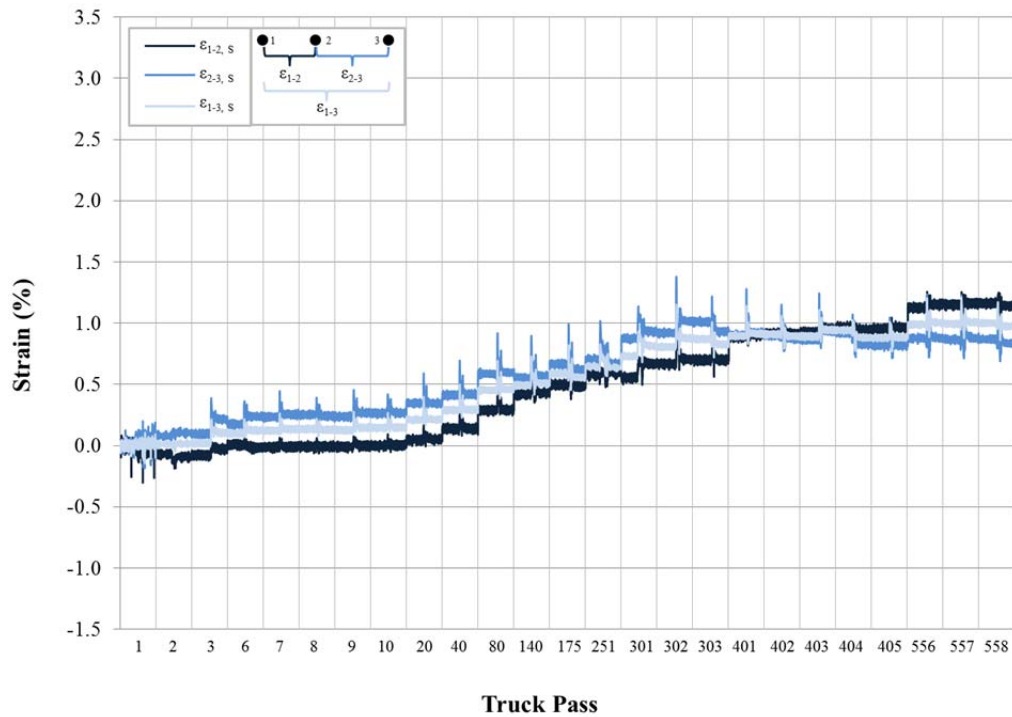
Figure P-4: Dynamic LVDT strain for Test Section 2, south (Tensar BX Type 2, CBR = 1.64).
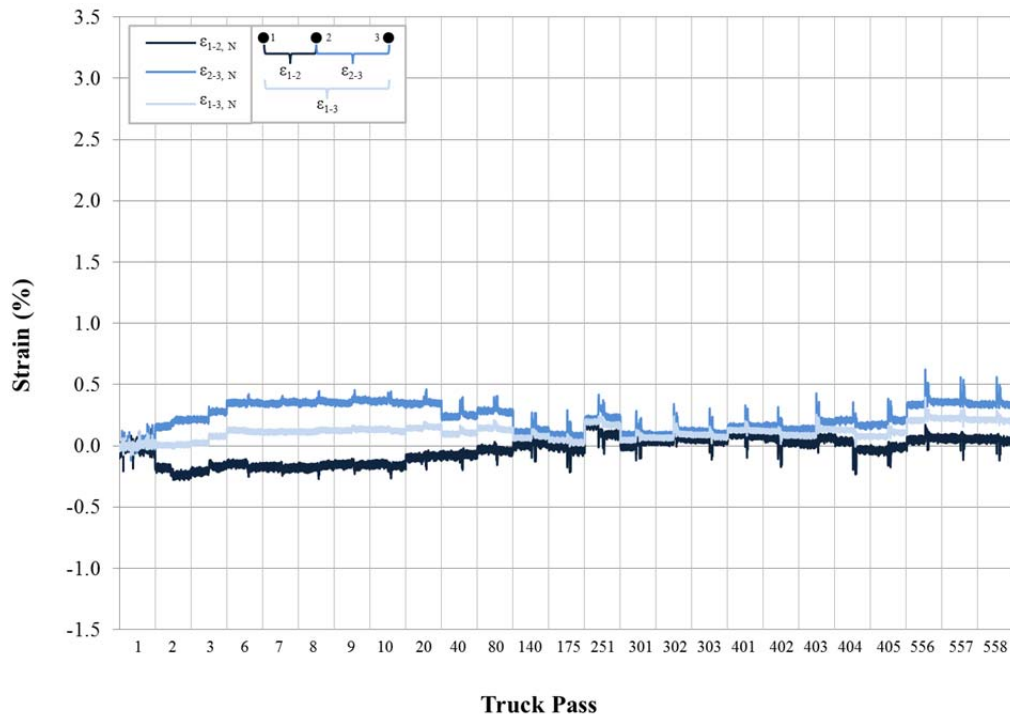
Figure P-5: Dynamic LVDT strain for Test Section 3, north (Tensar BX Type 2, CBR = 1.79).
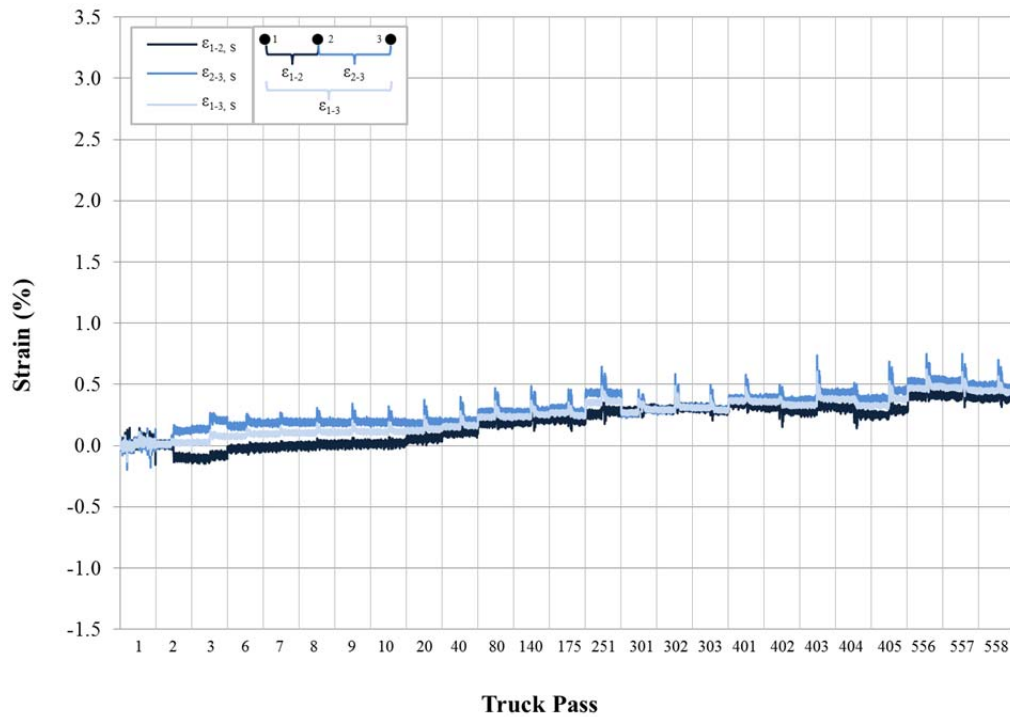
Figure P-6: Dynamic LVDT strain for Test Section 3, south (Tensar BX Type 2, CBR = 1.79).
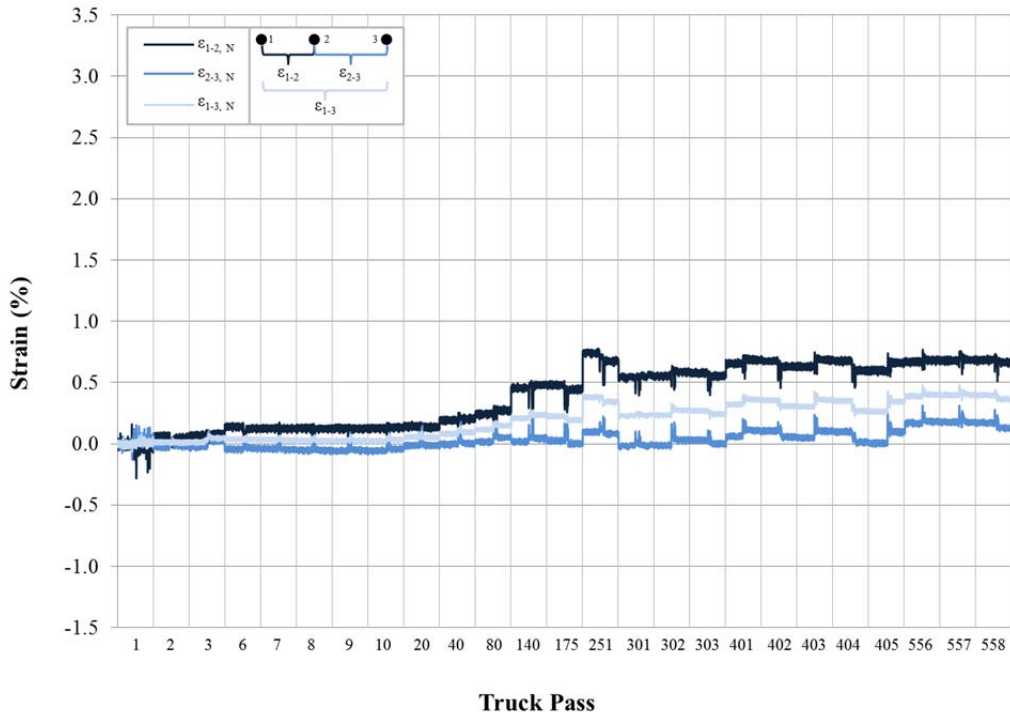
Figure P-7: Dynamic LVDT strain for Test Section 4, north (NAUE Secugrid 30-30 Q1).
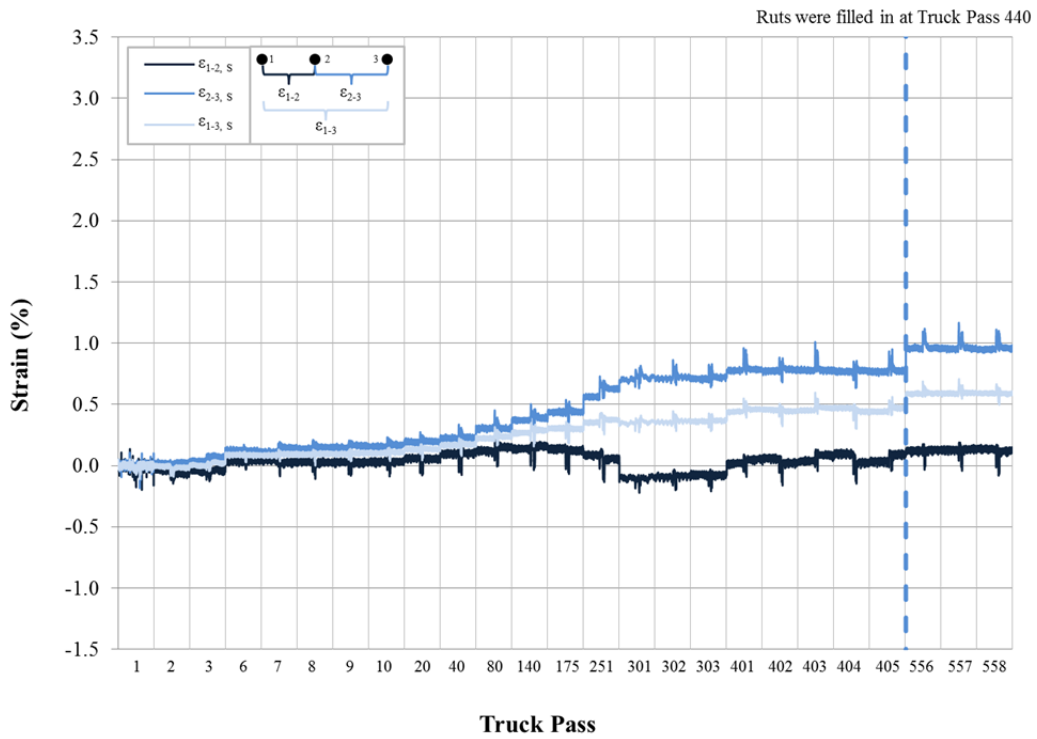
Figure P-8: Dynamic LVDT strain for Test Section 4, south (NAUE Secugrid 30-30 Q1).
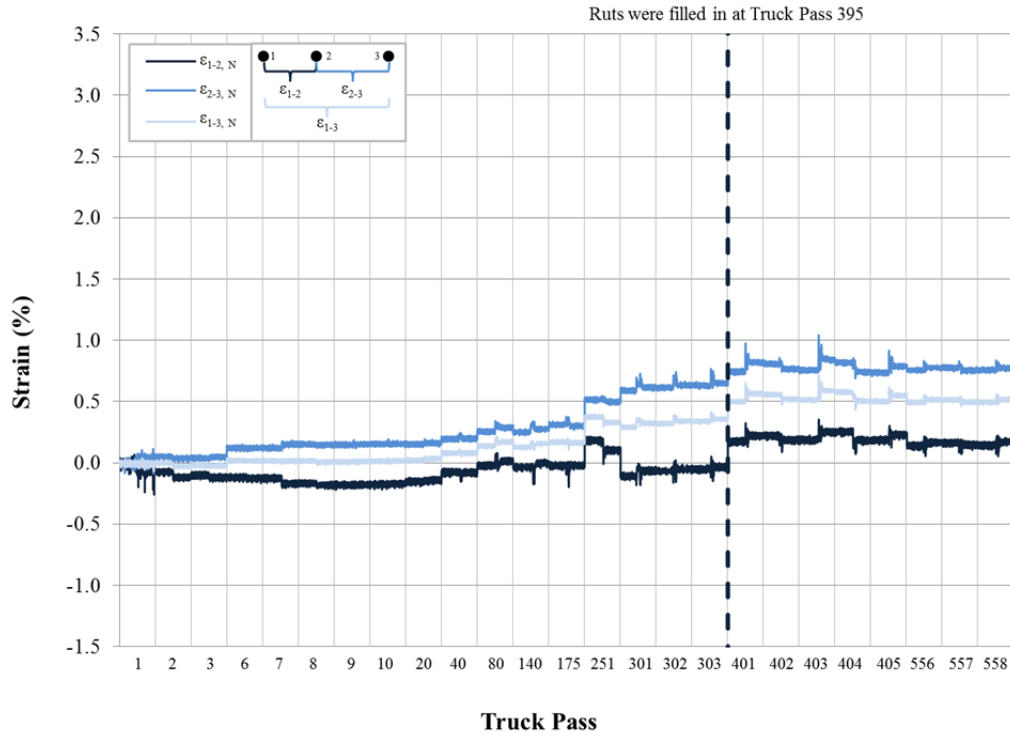
Figure P-9: Dynamic LVDT strain for Test Section 5, north (Colbond Enkagrid MAX 30).
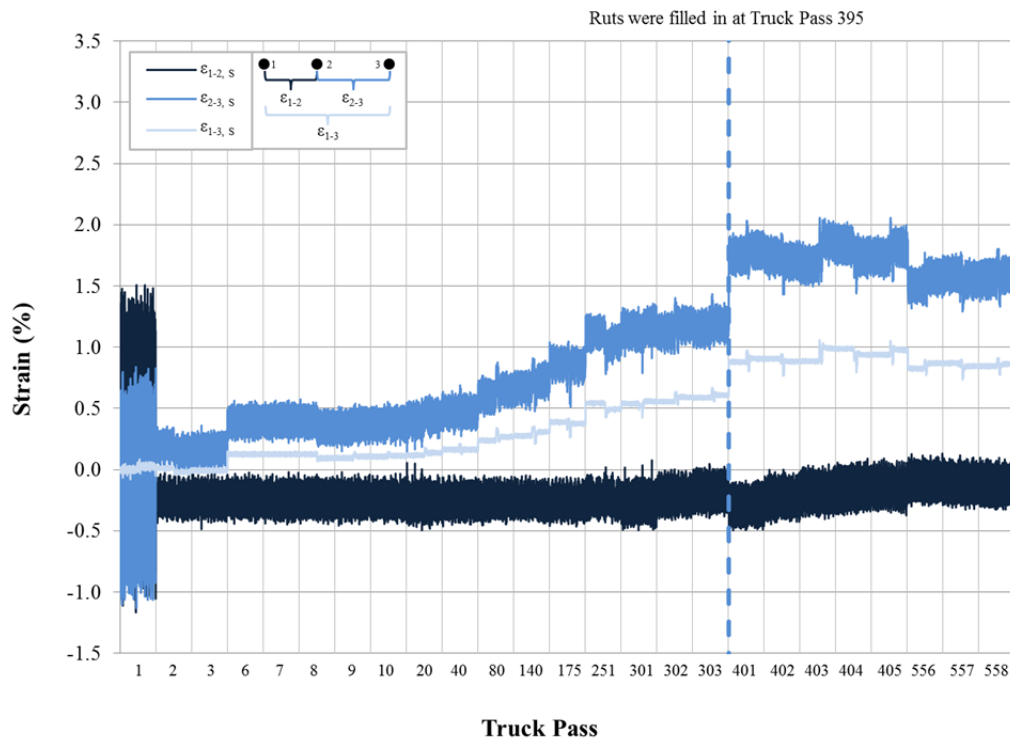
Figure P-10: Dynamic LVDT strain for Test Section 5, south (Colbond Enkagrid MAX 30).
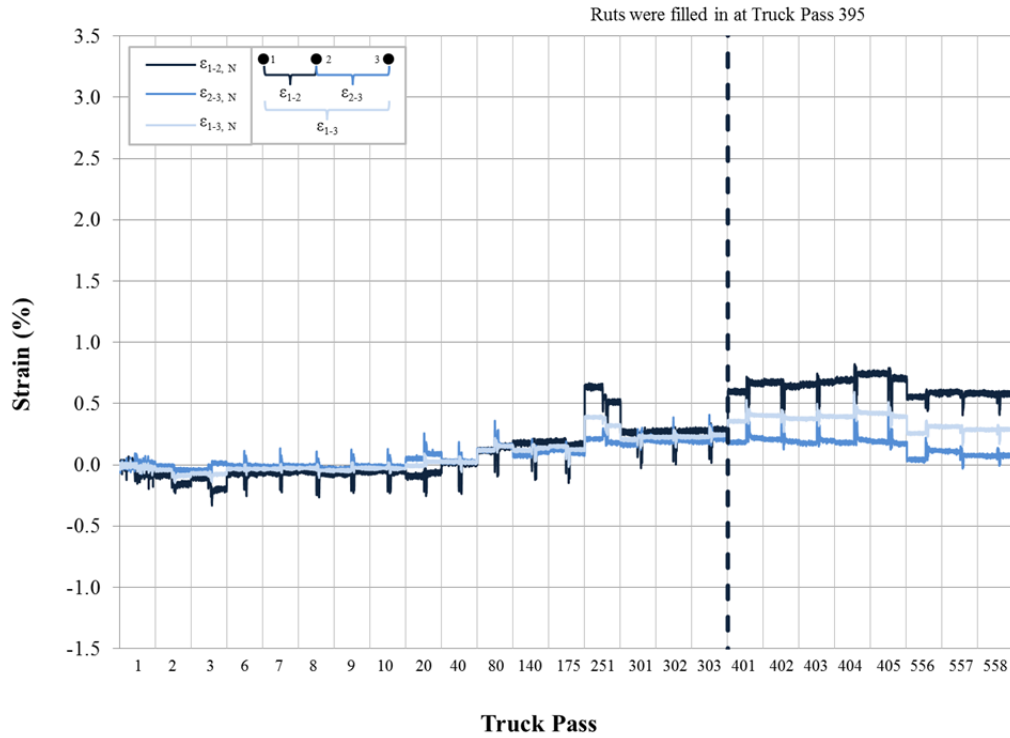
Figure P-11: Dynamic LVDT strain for Test Section 6, north (Synteen SF11).
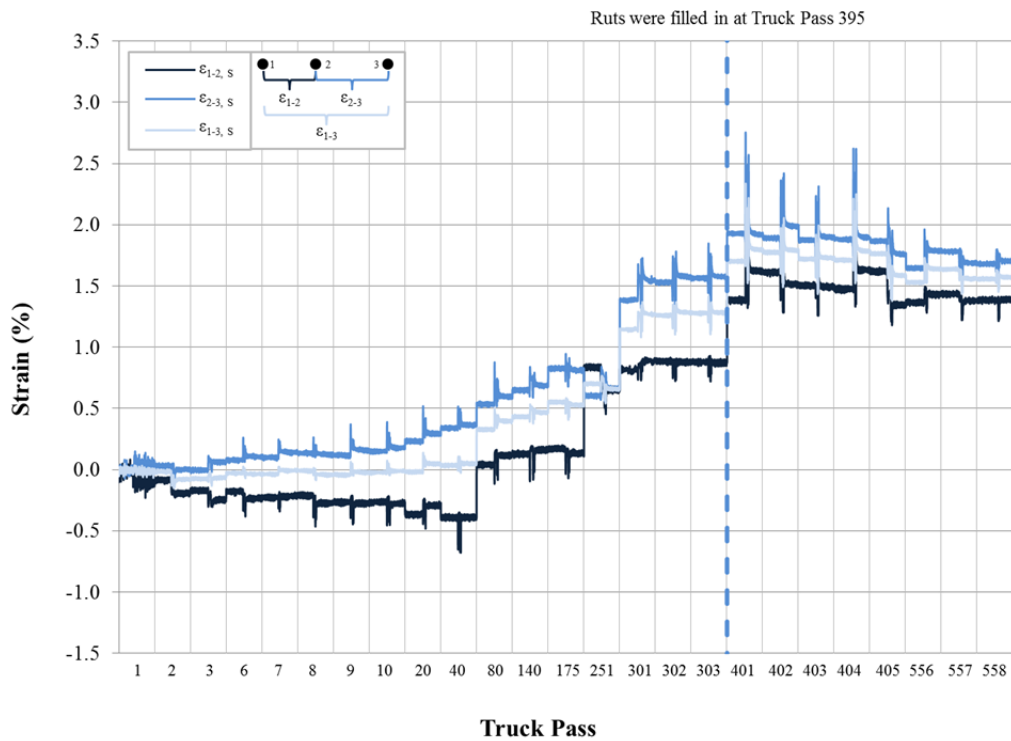
Figure P-12: Dynamic LVDT strain for Test Section 6, south (Synteen SF11).
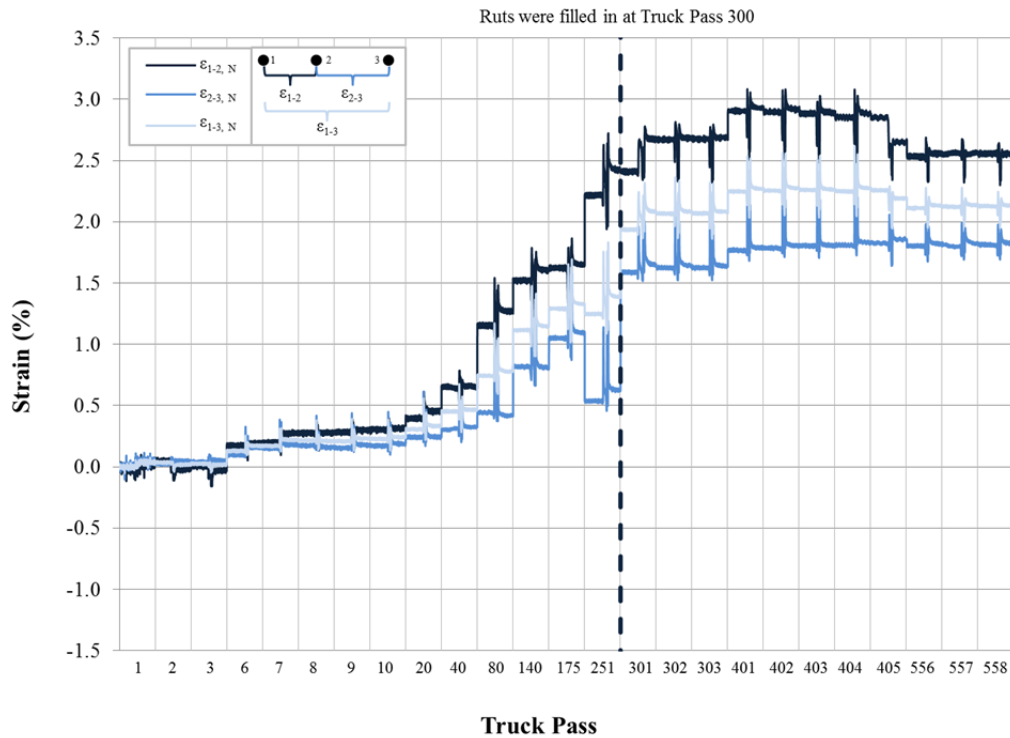
Figure P-13: Dynamic LVDT strain for Test Section 7, north (Synteen SF12).
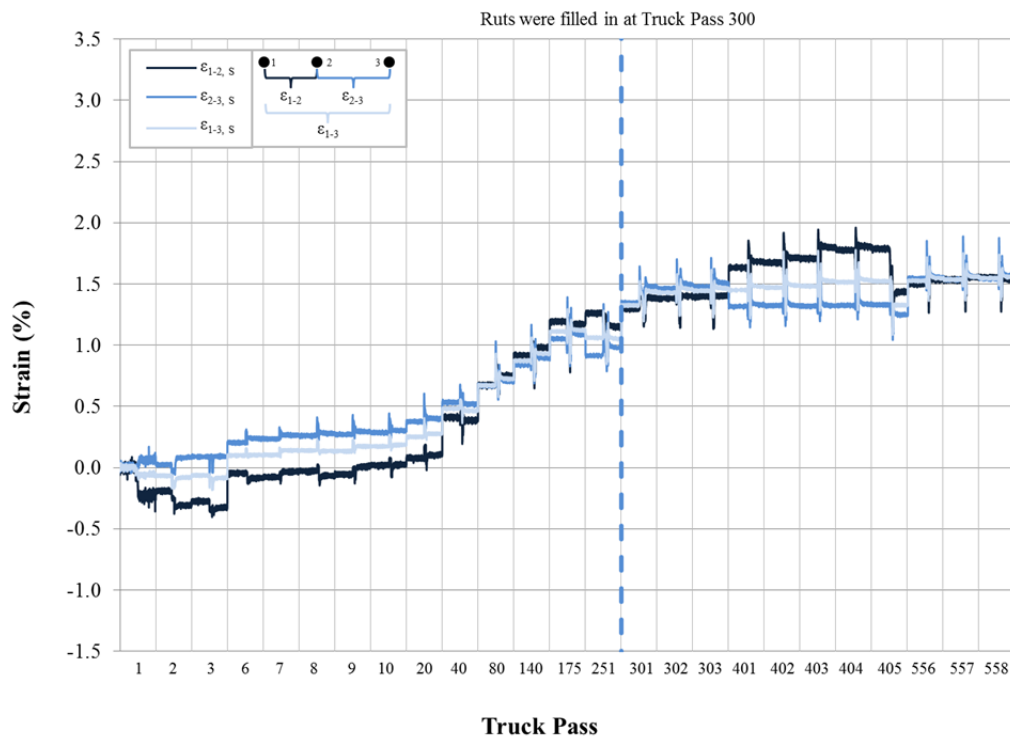
Figure P-14: Dynamic LVDT strain for Test Section 7, south (Synteen SF12).
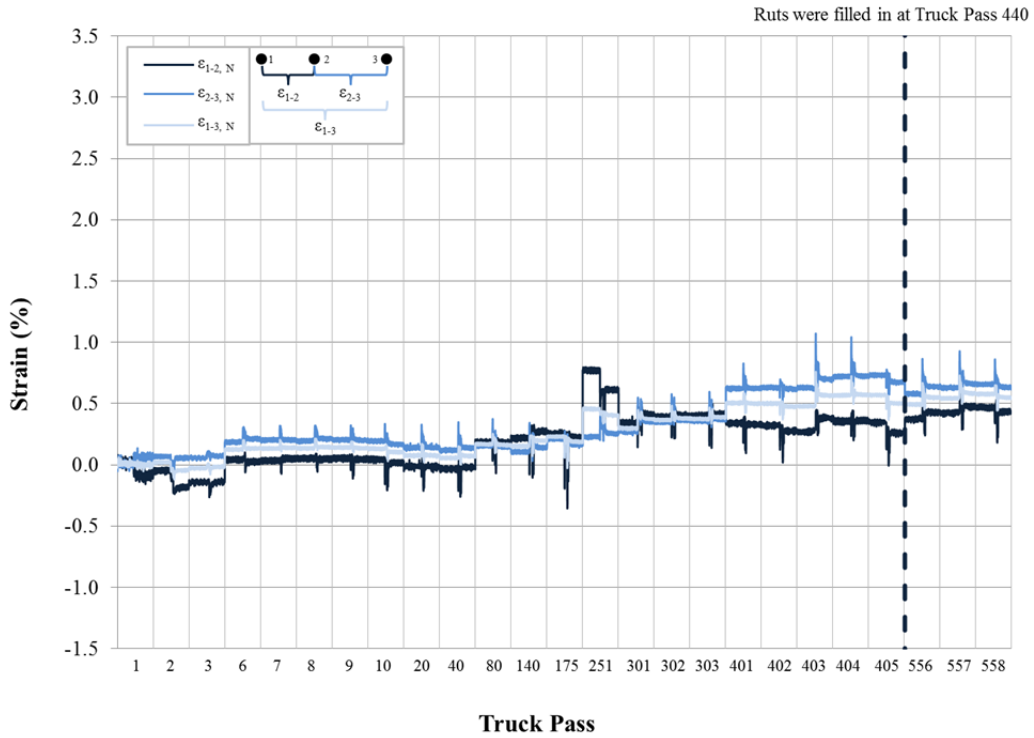
Figure P-15: Dynamic LVDT strain for Test Section 8, north (TenCate Mirafi BXG11).
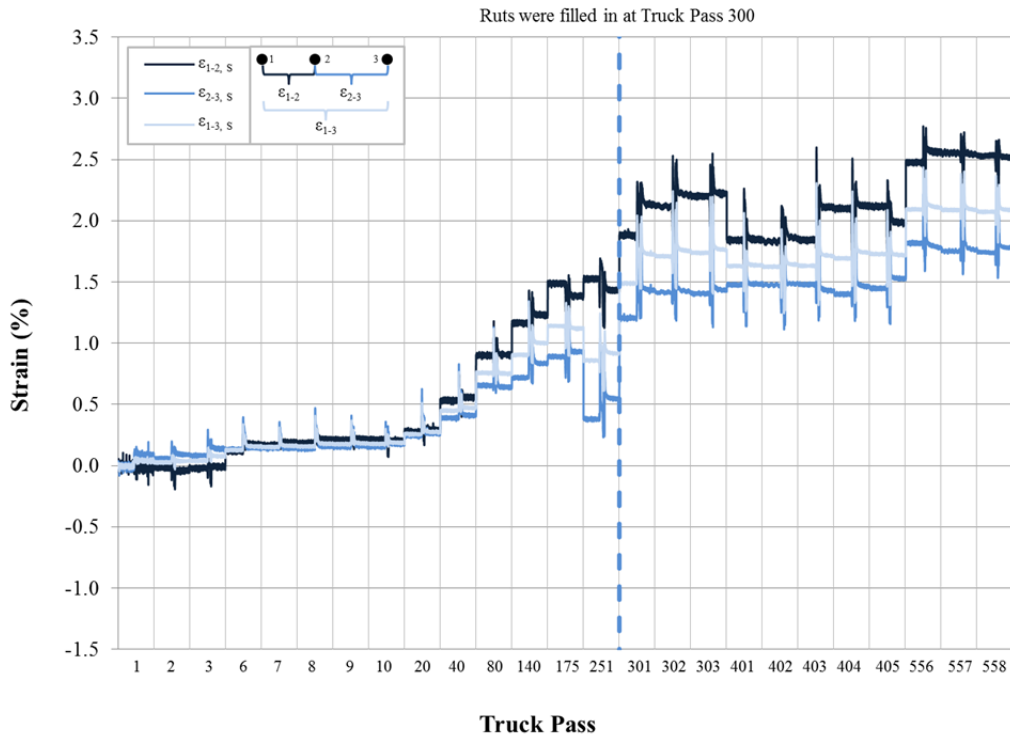
Figure P-16: Dynamic LVDT strain for Test Section 8, south (TenCate Mirafi BXG11).
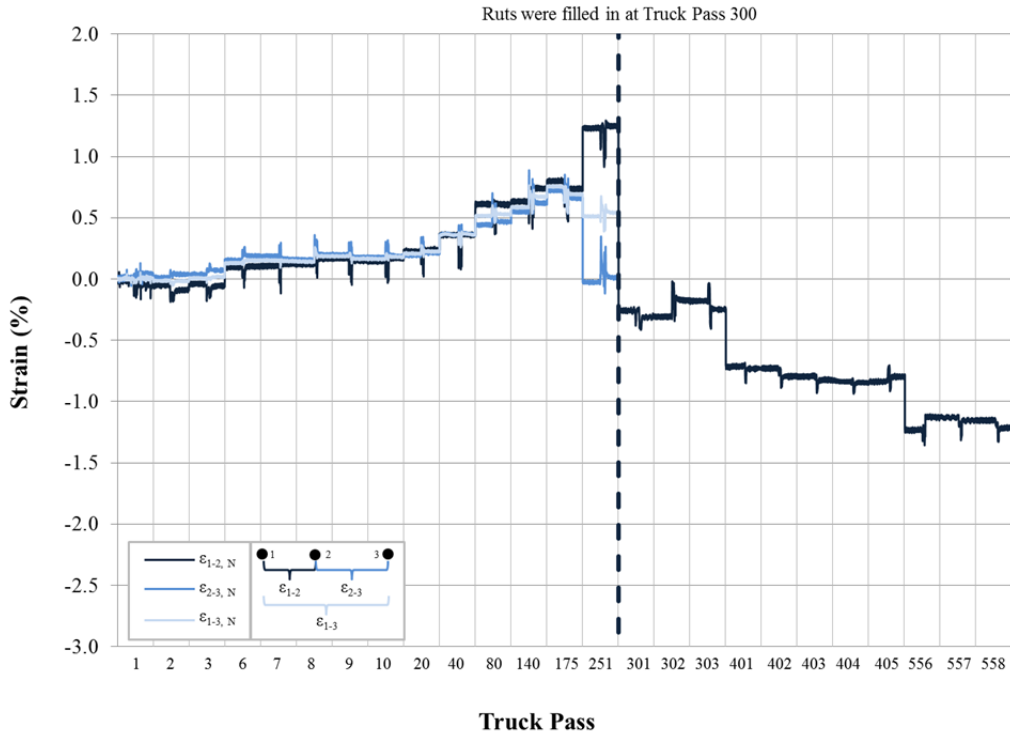
Figure P-17: Dynamic LVDT strain for Test Section 9, north (Huesker Fornit 30).
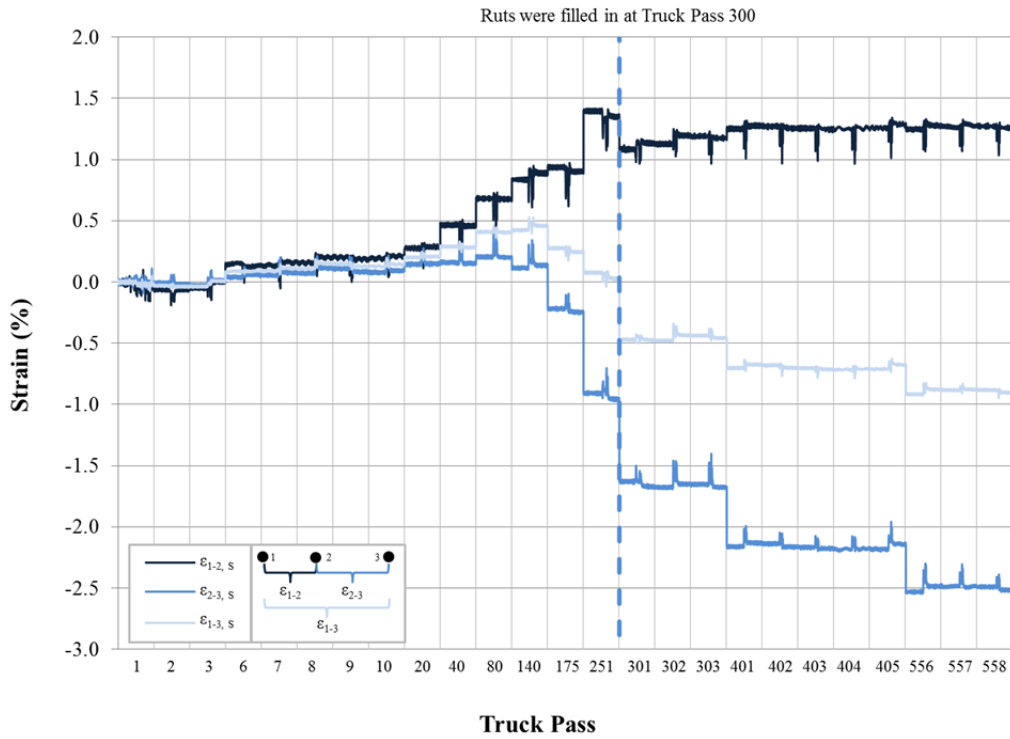
Figure P-18: Dynamic LVDT strain for Test Section 9, south (Huesker Fornit 30).
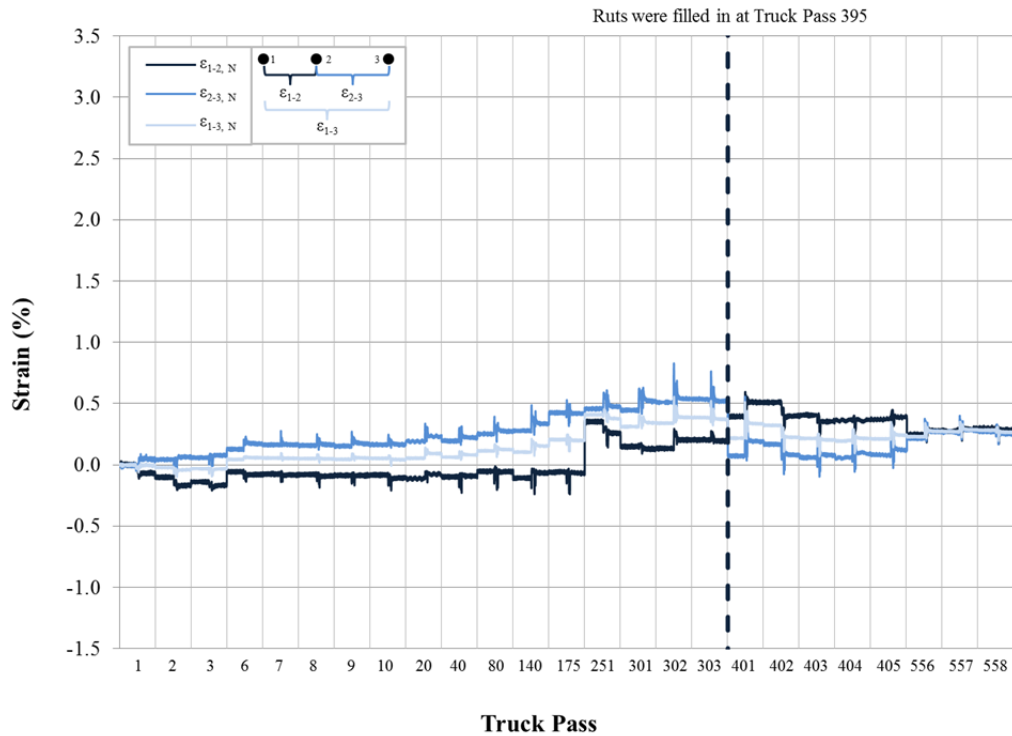
Figure P-19: Dynamic LVDT strain for Test Section 10, north (SynTec Tenax MS 330).
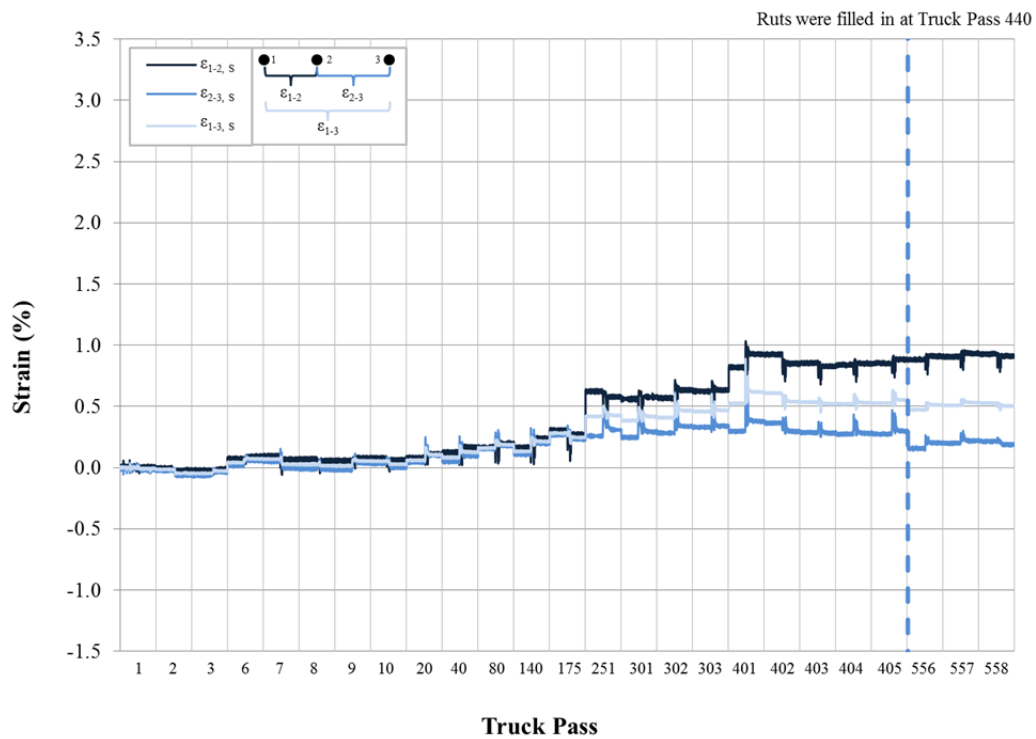
Figure P-20: Dynamic LVDT strain for Test Section 10, south (SynTec Tenax MS 330).
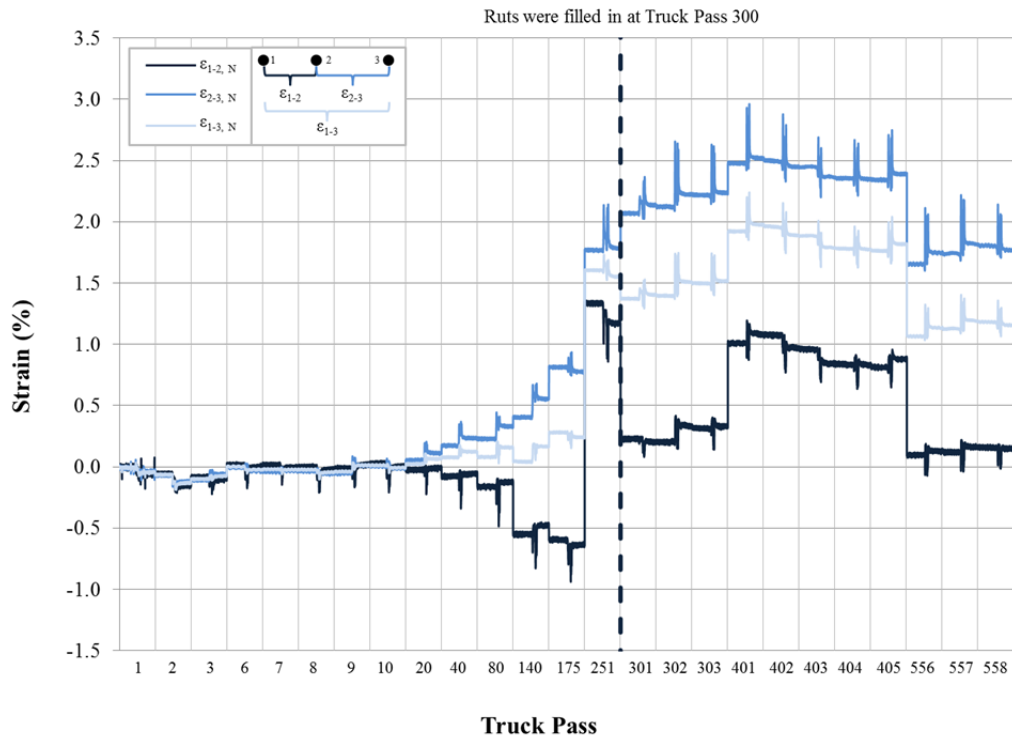
**Figure P-21: Dynamic LVDT strain for Test Section 11, north (Tensar TX140).**
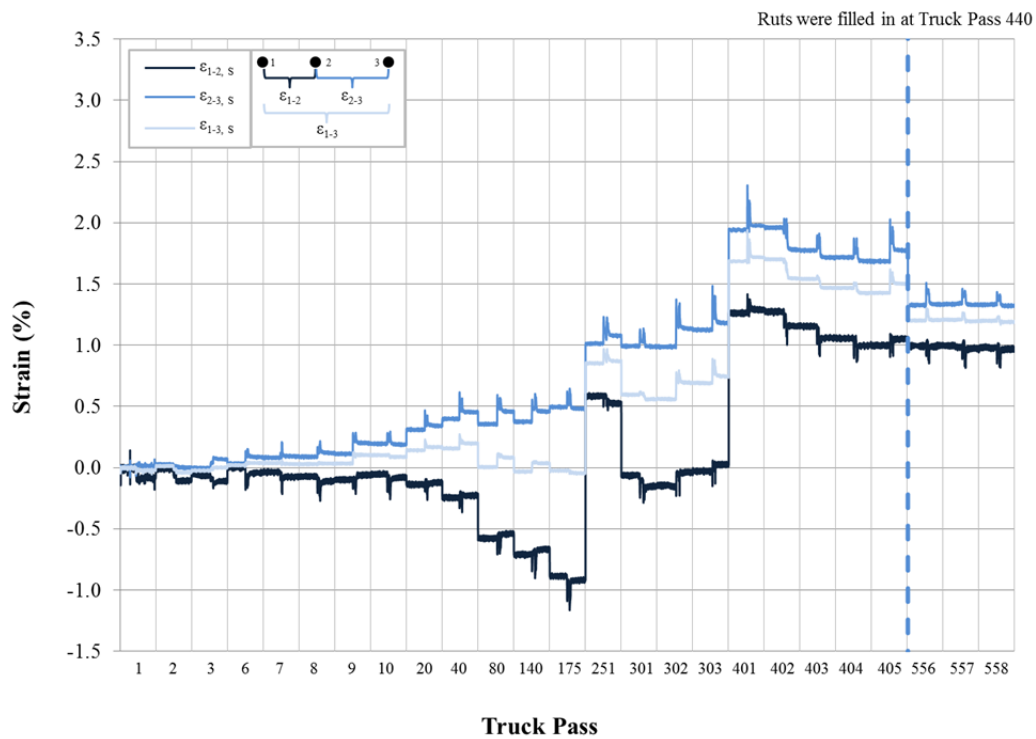
**Figure P-22: Dynamic LVDT strain for Test Section 11, south (Tensar TX140).**
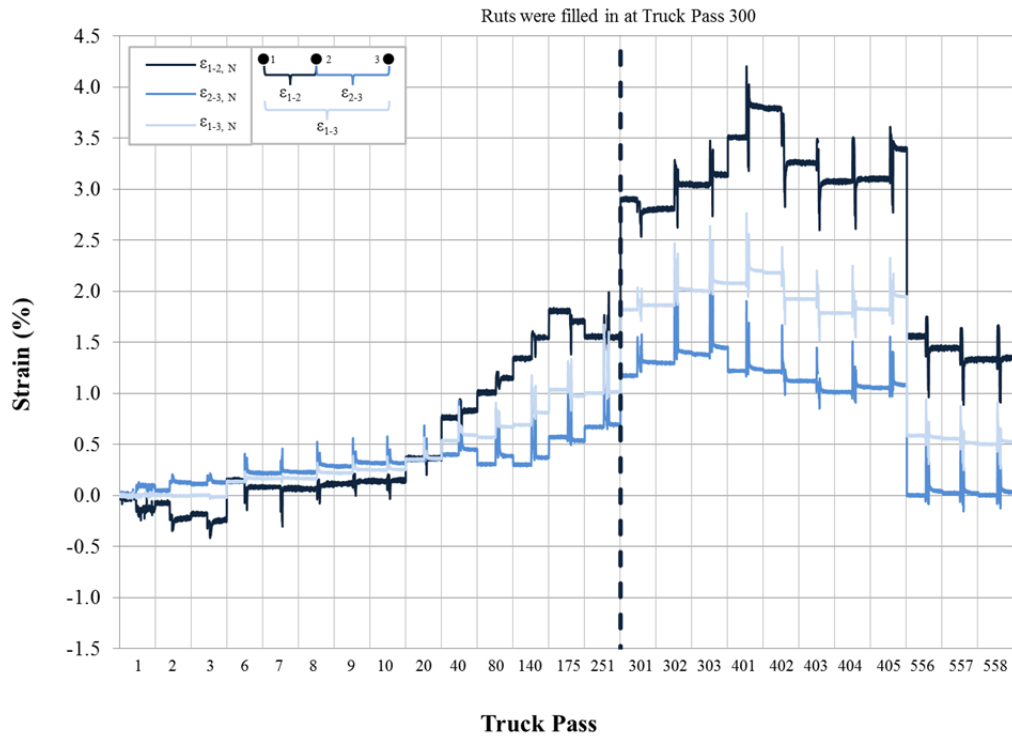
**Figure P-23: Dynamic LVDT strain for Test Section 12, north (Tensar TX160).**
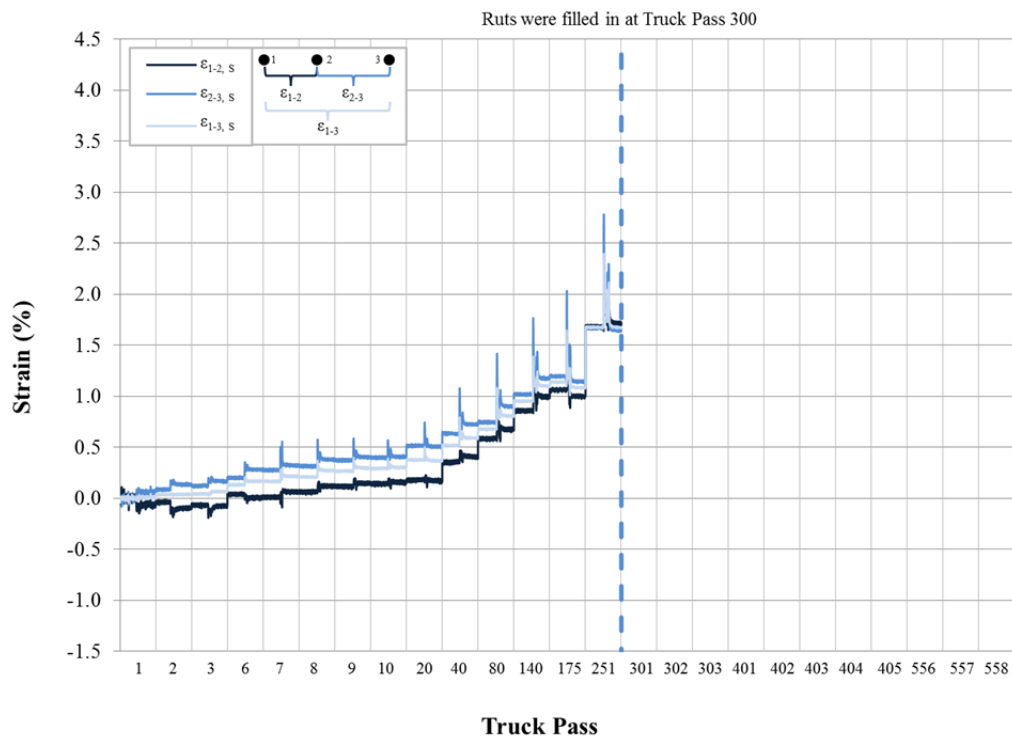
**Figure P-24: Dynamic LVDT strain for Test Section 12, south (Tensar TX160).**
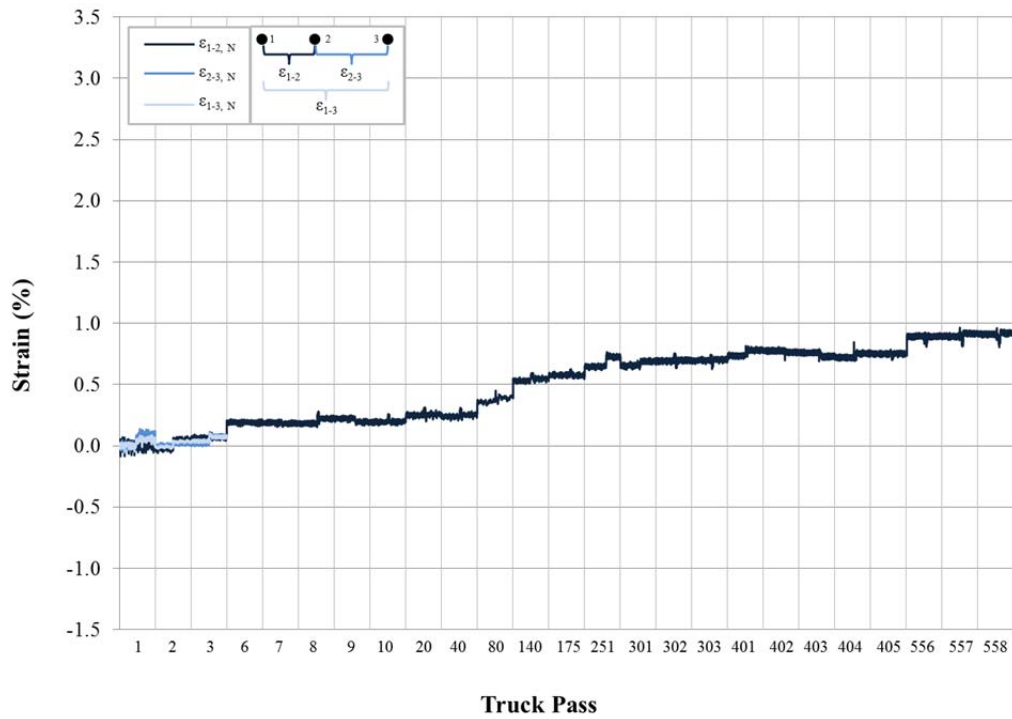
**Figure P-25: Dynamic LVDT strain for Test Section 13, north (TenCate Mirafi RS580i).**
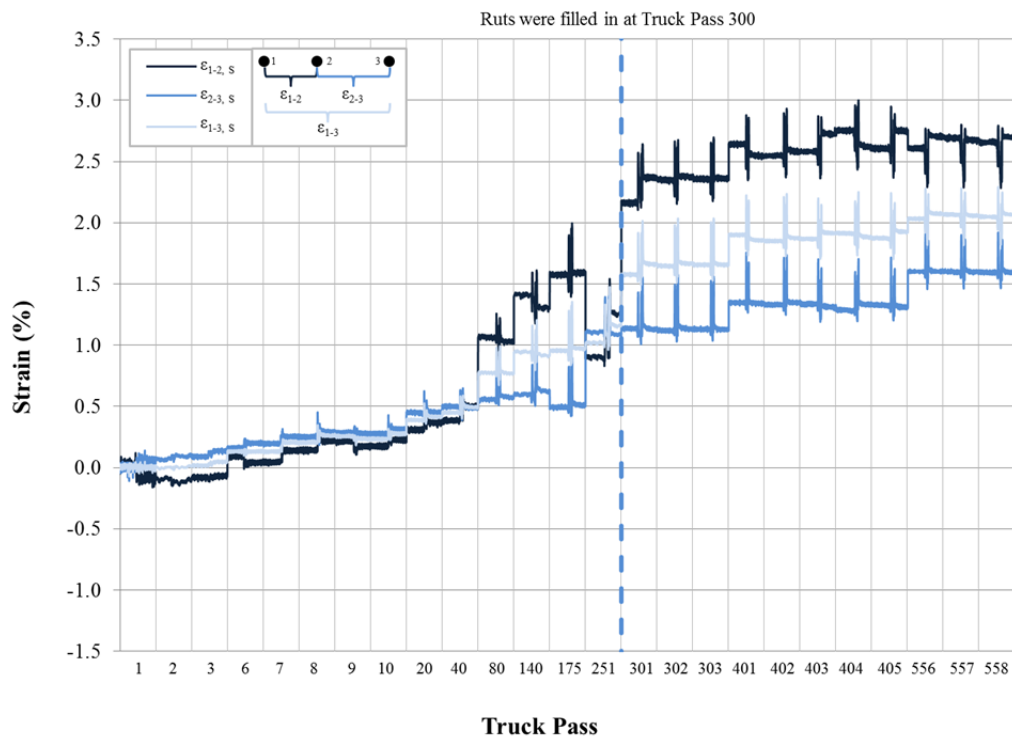
Figure P-26: Dynamic LVDT strain for Test Section 13, south (TenCate Mirafi RS580i).
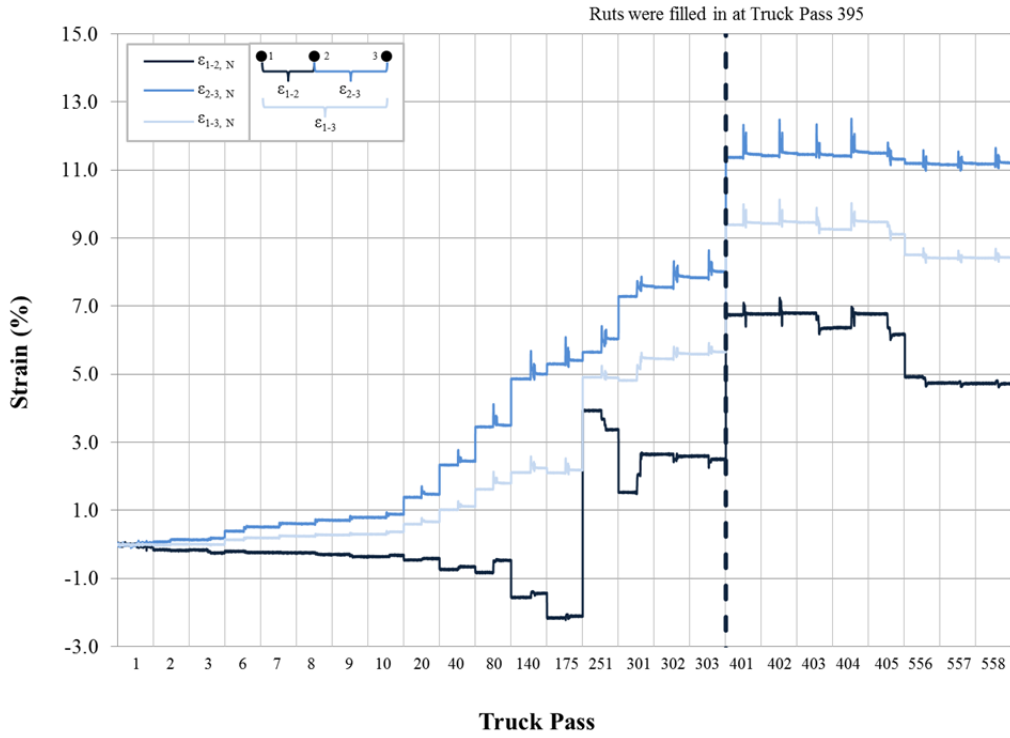
**Figure P-27: Dynamic LVDT strain for Test Section 14, north (Propex Geotex 801).**
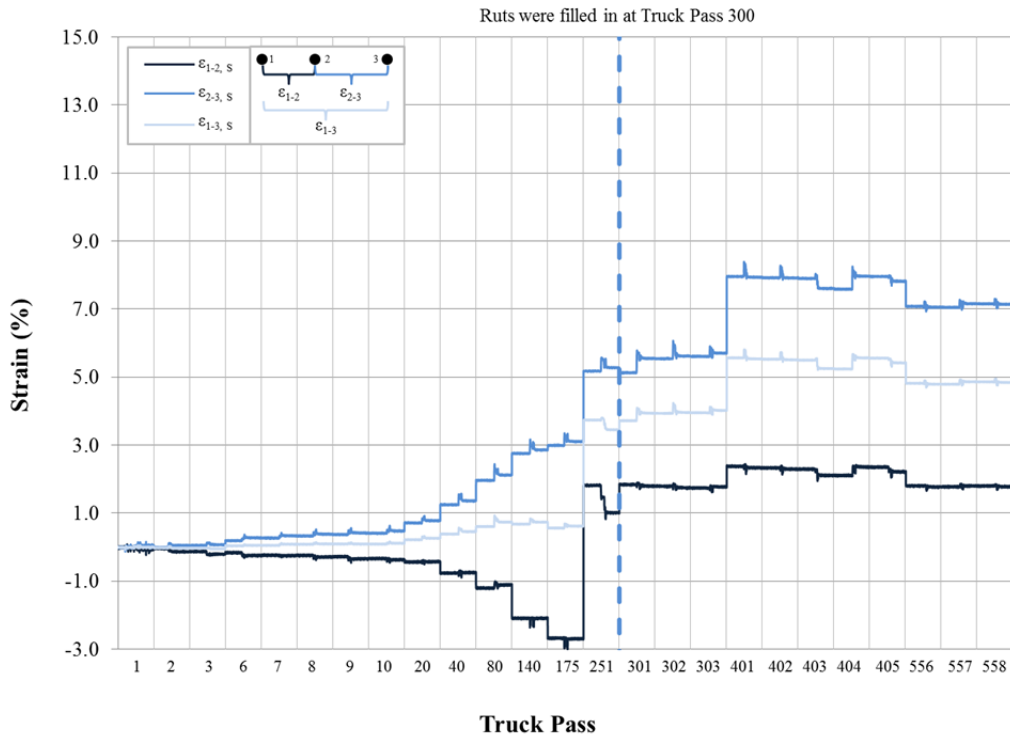
Figure P-28: Dynamic LVDT strain for Test Section 14, south (Propex Geotex 801).

APPENDIX Q – CUMULATIVE STRAIN RESULTS FROM LVDTS
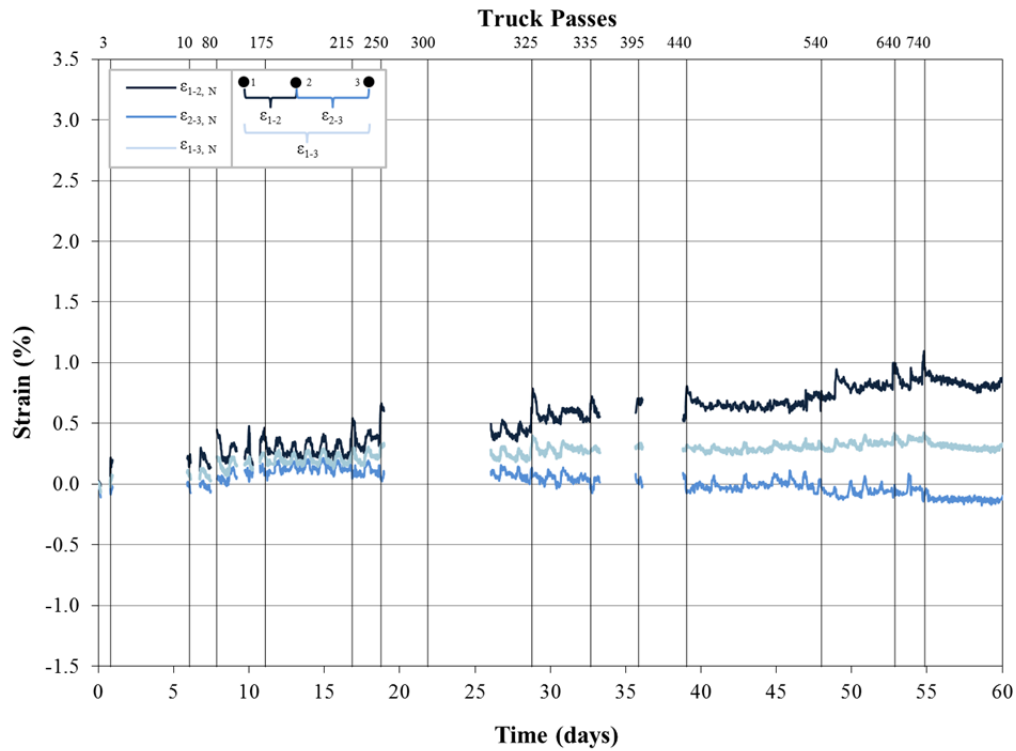
Figure Q-1: Cumulative LVDT strain for Test Section 1, north (Tensar BX Type 2, CBR = 2.17).
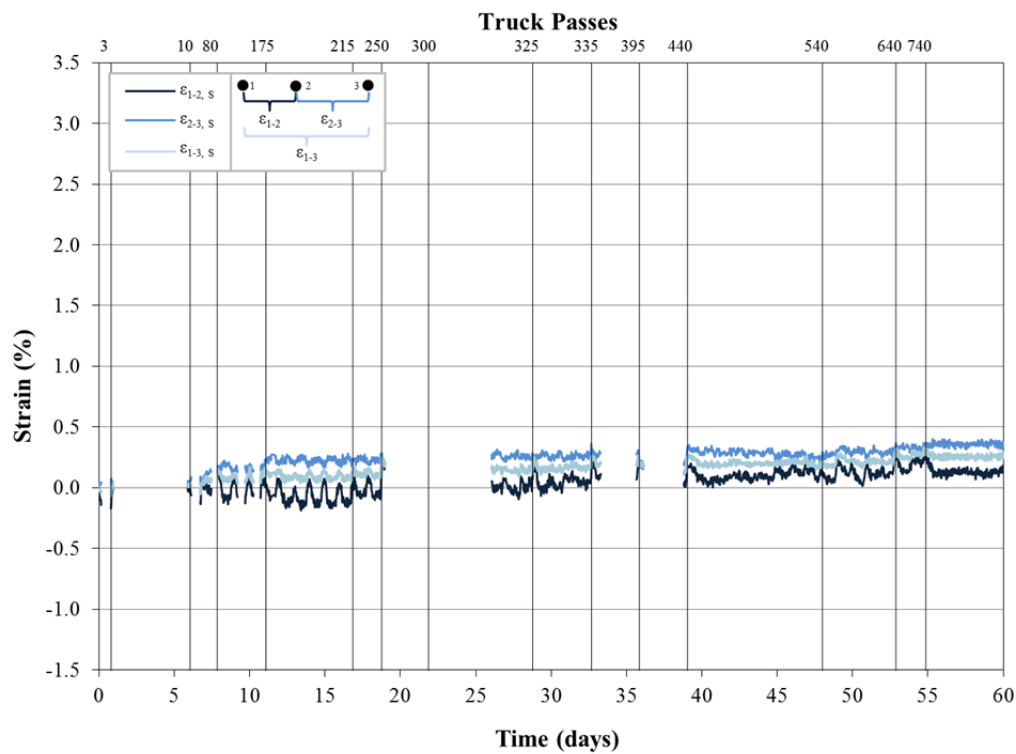
Figure Q-2: Cumulative LVDT strain for Test Section 1, south (Tensar BX Type 2, CBR = 2.17).
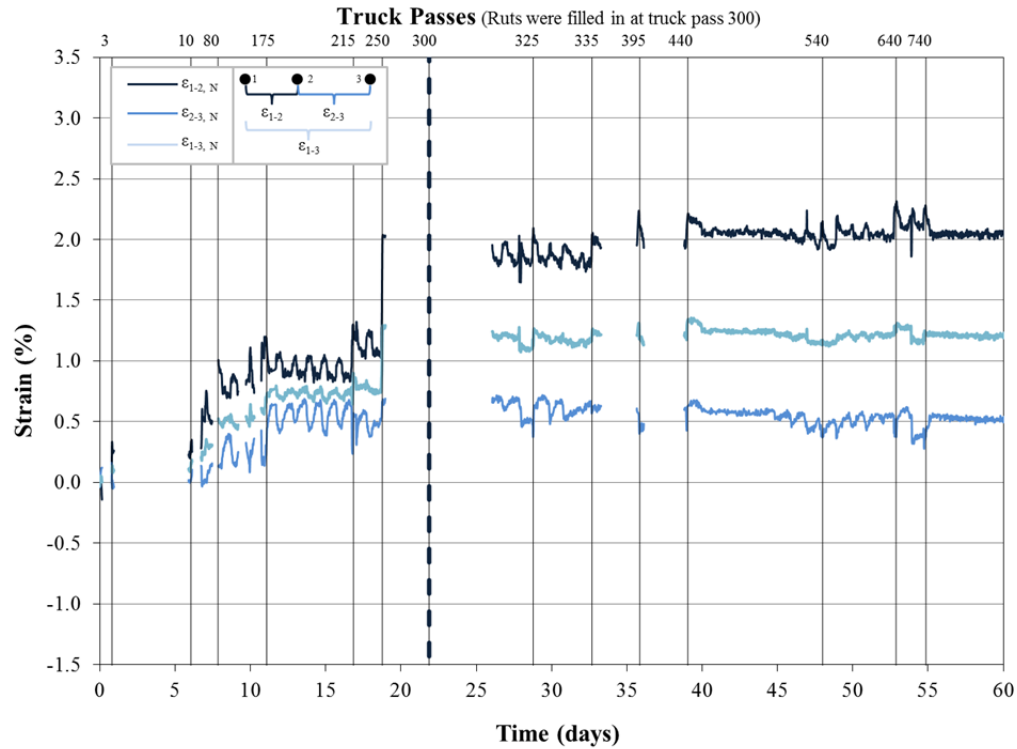
Figure Q-3: Cumulative LVDT strain for Test Section 2, north (Tensar BX Type 2, CBR = 1.64).
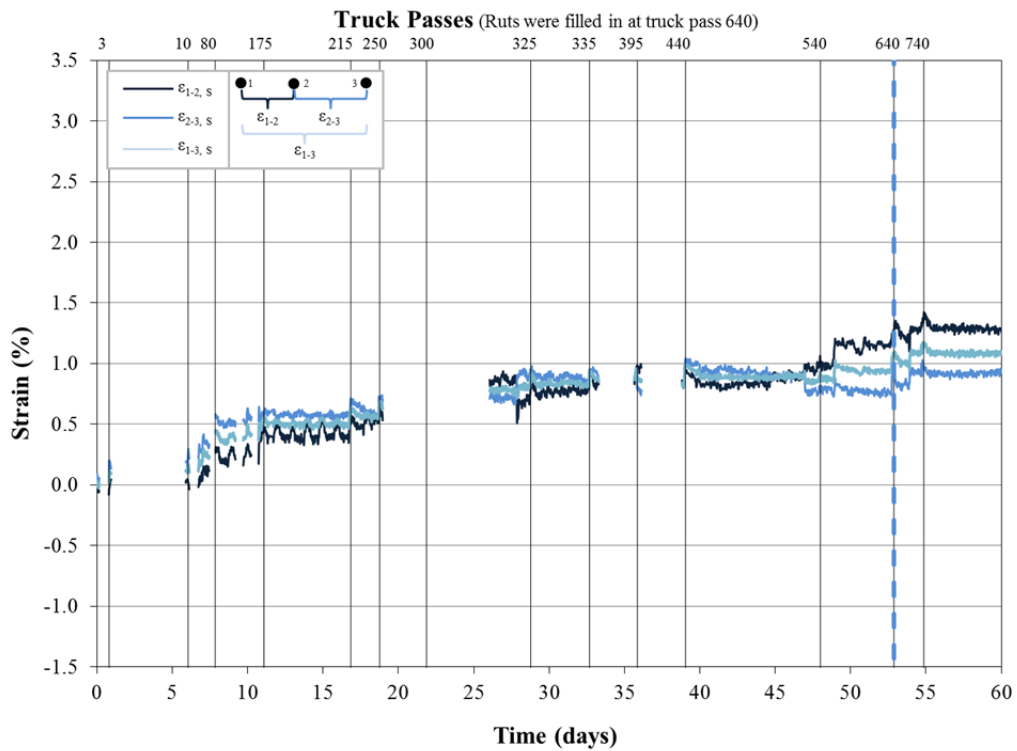
Figure Q-4: Cumulative LVDT strain for Test Section 2, south (Tensar BX Type 2, CBR = 1.64).
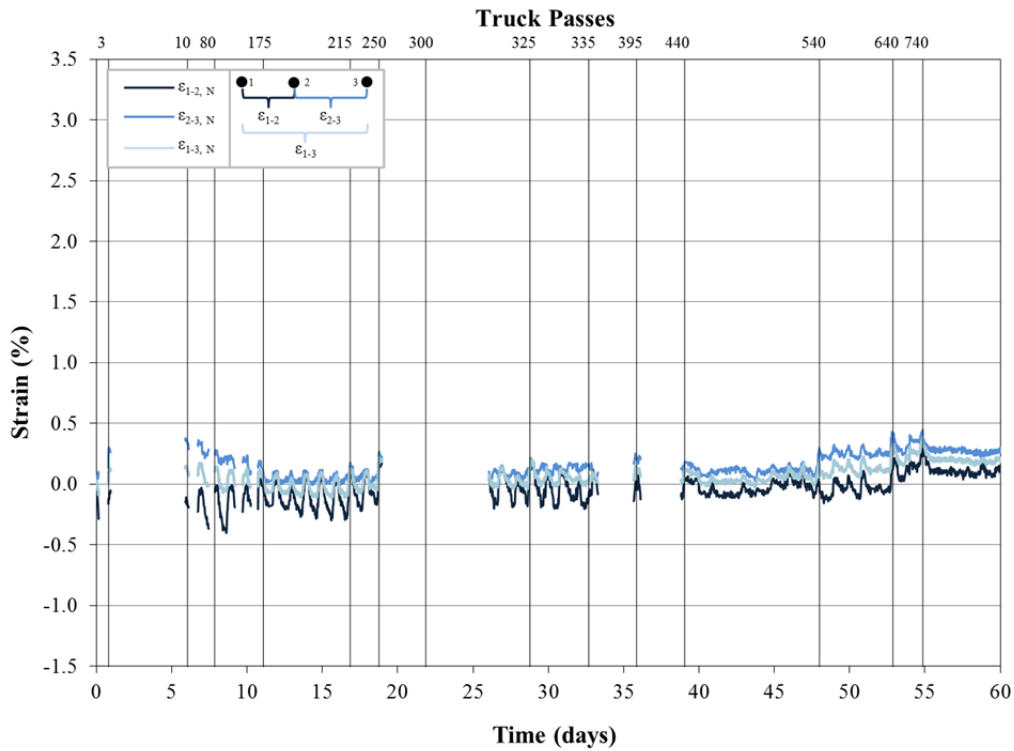
Figure Q-5: Cumulative LVDT strain for Test Section 3, north (Tensar BX Type 2, CBR = 1.79).
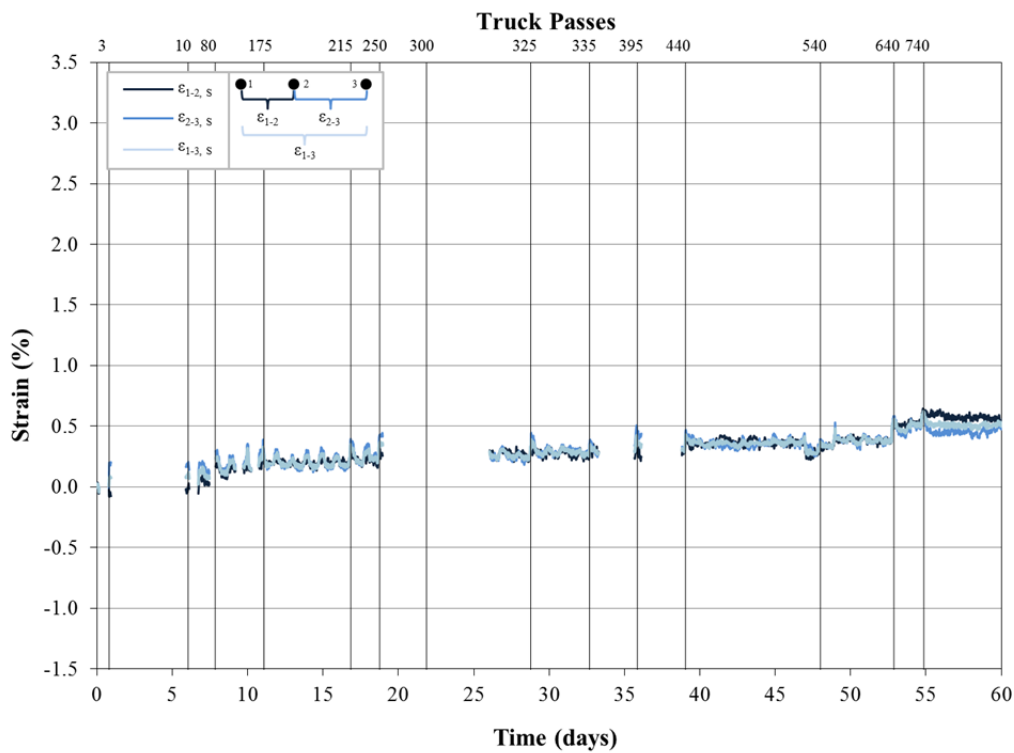
Figure Q-6: Cumulative LVDT strain for Test Section 3, south (Tensar BX Type 2, CBR = 1.79).
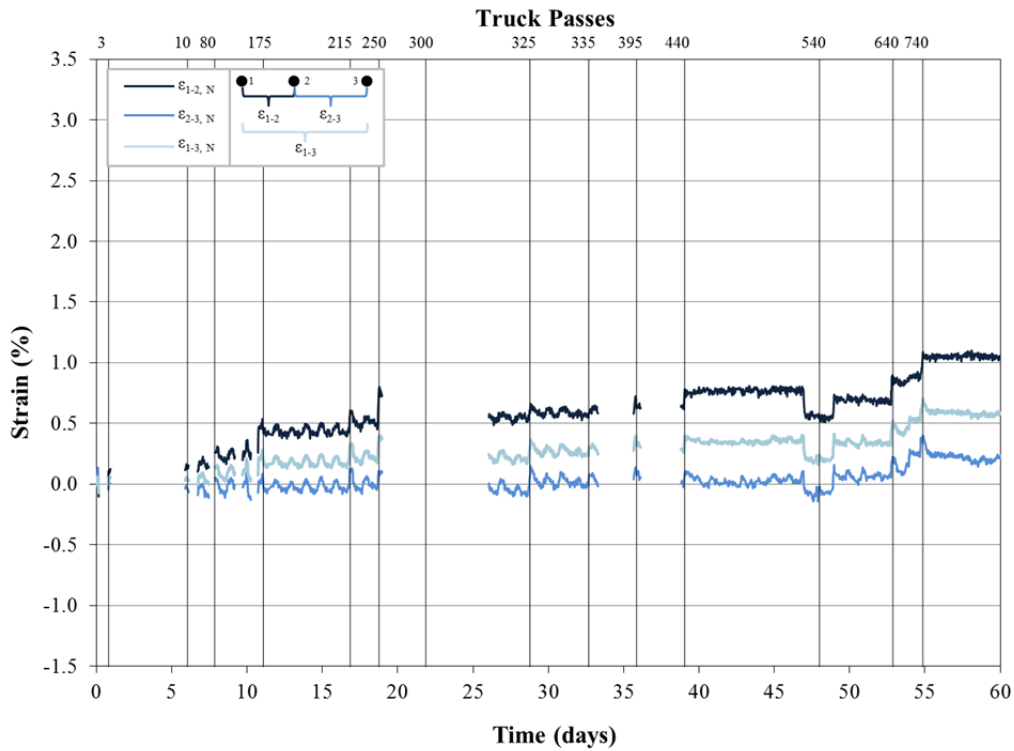
Figure Q-7: Cumulative LVDT strain for Test Section 4, north (NAUE Secugrid 30-30 Q1).
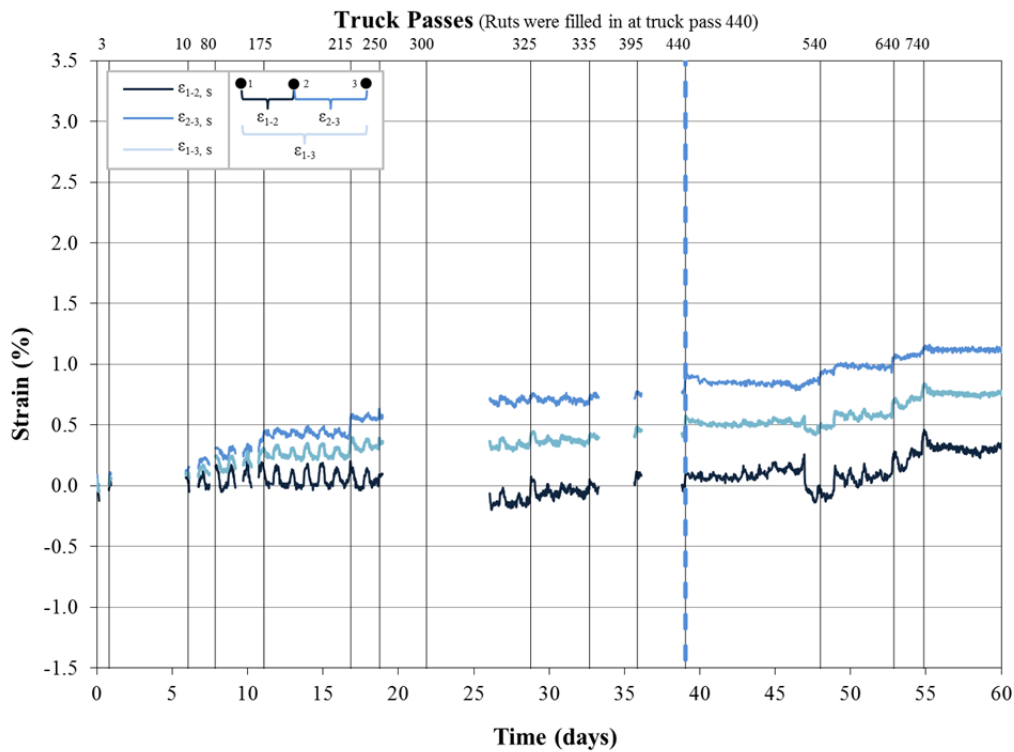
Figure Q-8: Cumulative LVDT strain for Test Section 4, south (NAUE Secugrid 30-30 Q1).
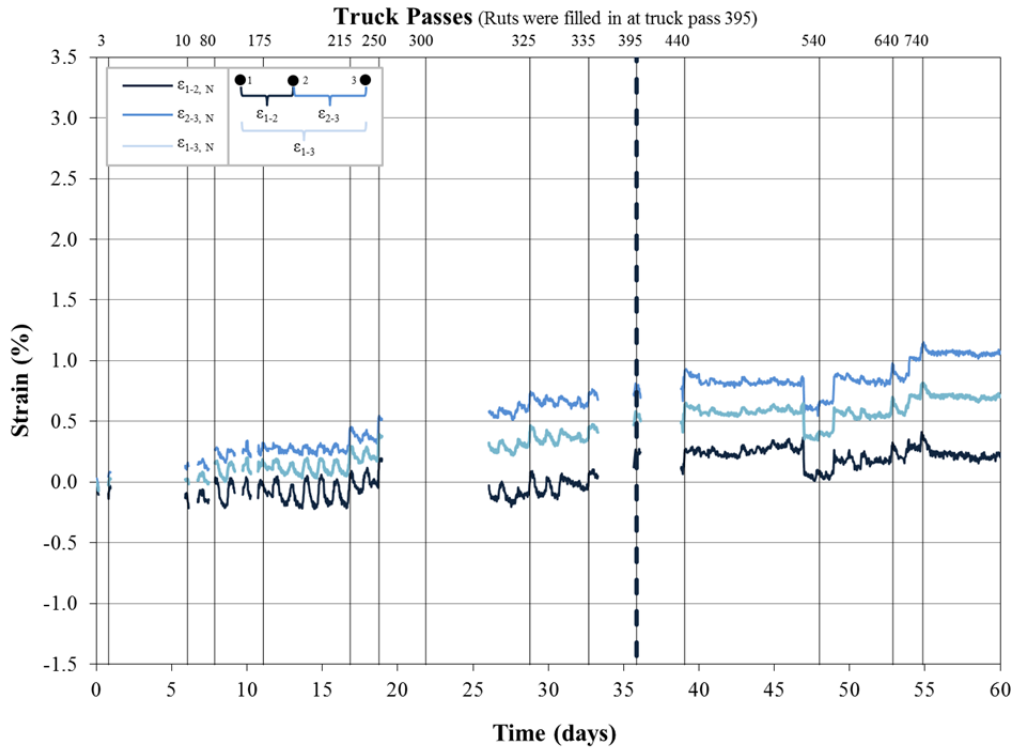
Figure Q-9: Cumulative LVDT strain for Test Section 5, north (Colbond Enkagrid MAX 30).
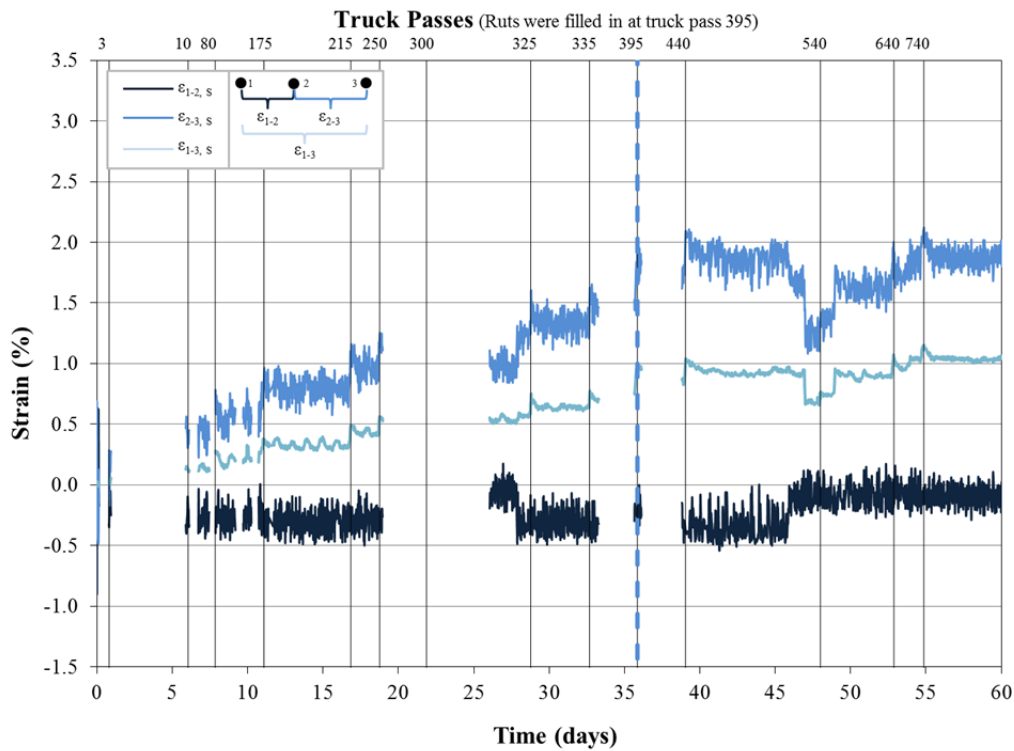
Figure Q-10: Cumulative LVDT strain for Test Section 5, south (Colbond Enkagrid MAX 30).
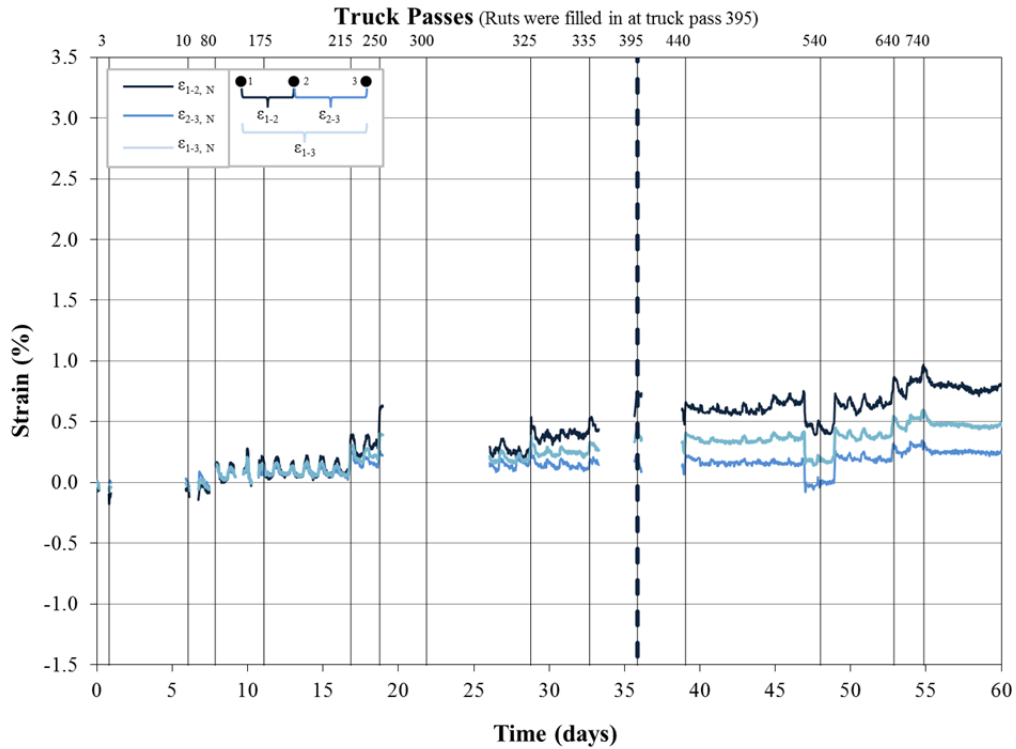
Figure Q-11: Cumulative LVDT strain for Test Section 6, north (Synteen SF11).
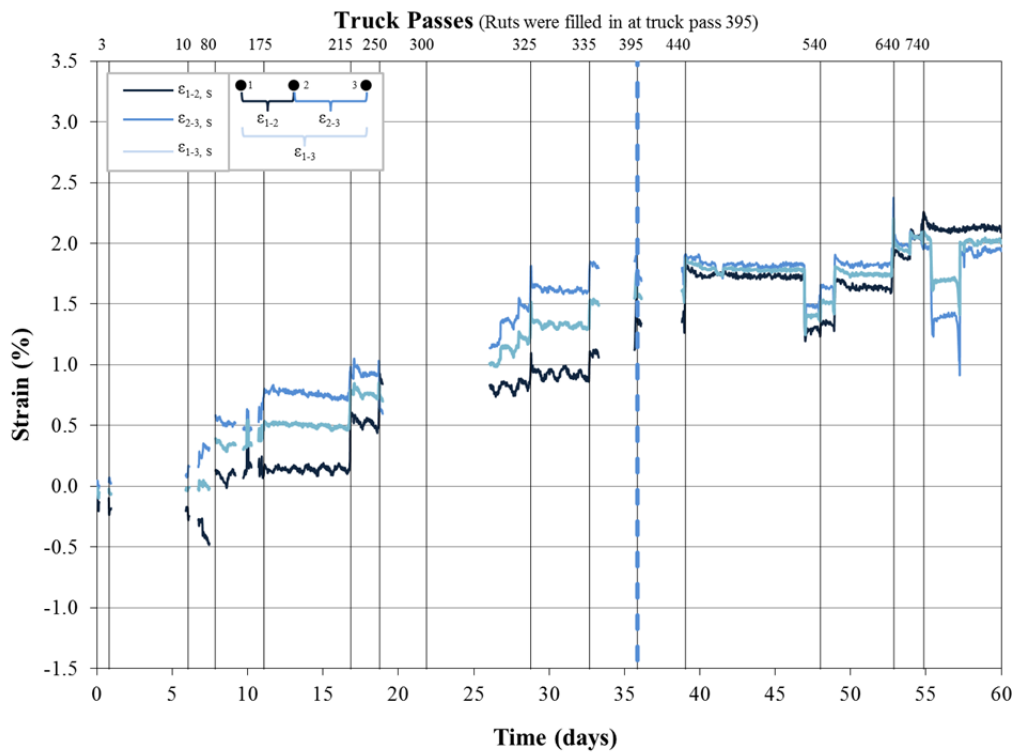
Figure Q-12: Cumulative LVDT strain for Test Section 6, south (Synteen SF11).
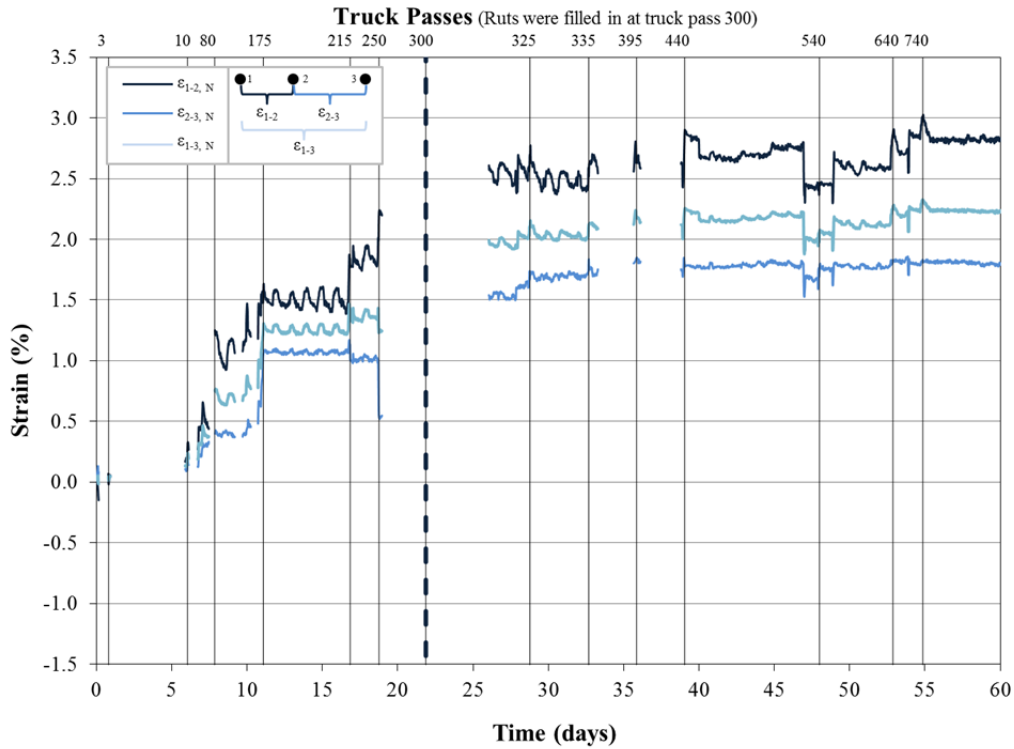
Figure Q-13: Cumulative LVDT strain for Test Section 7, north (Synteen SF12).
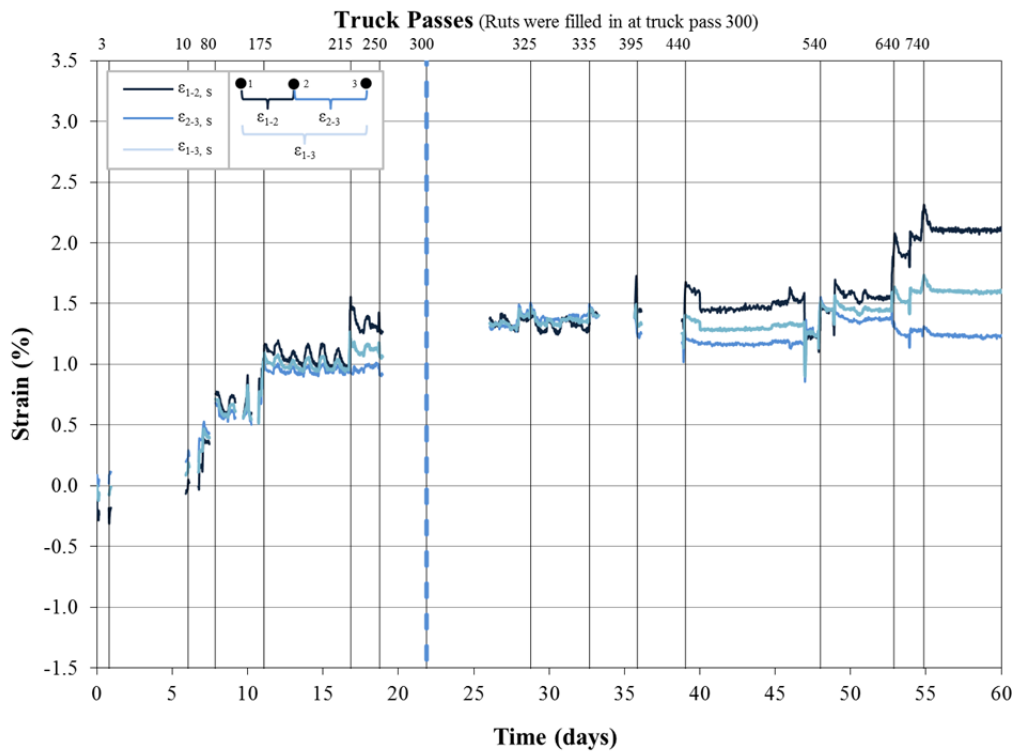
Figure Q-14: Cumulative LVDT strain for Test Section 7, south (Synteen SF12).
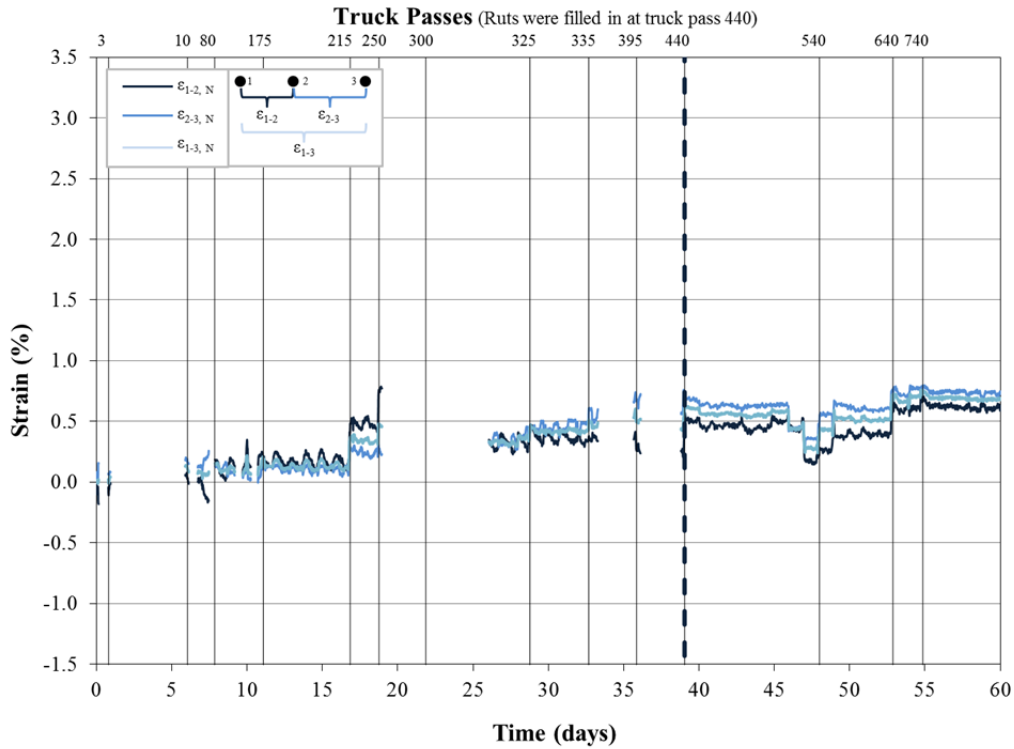
Figure Q-15: Cumulative LVDT strain for Test Section 8, north (TenCate Mirafi BXG11).
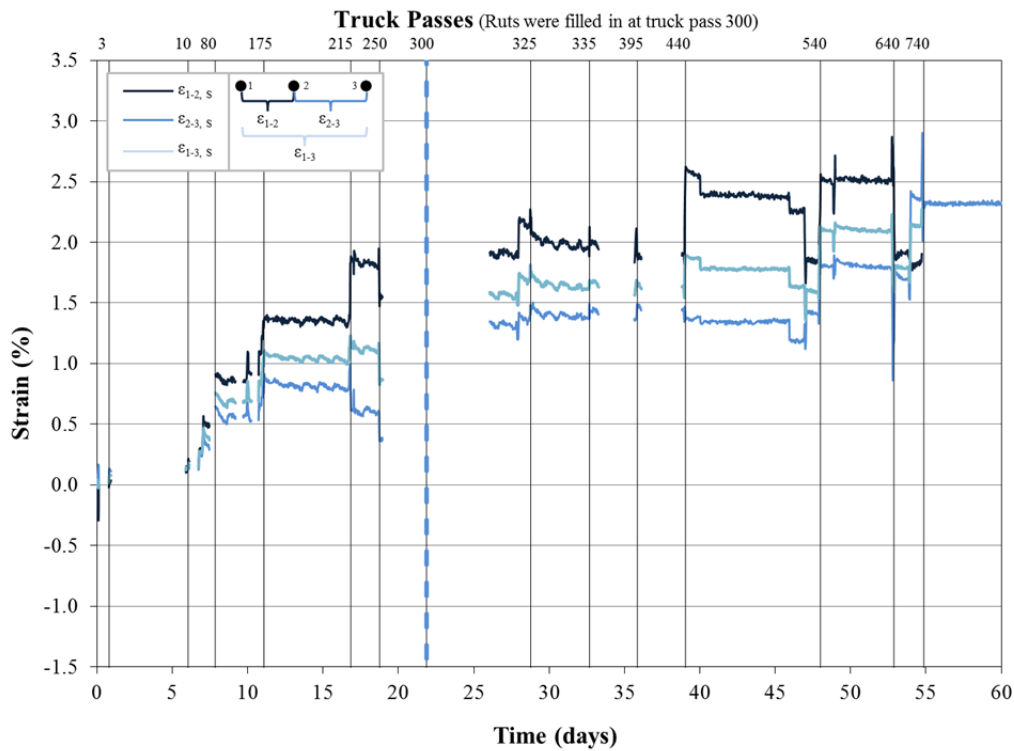
Figure Q-16: Cumulative LVDT strain for Test Section 8, south (TenCate Mirafi BXG11).
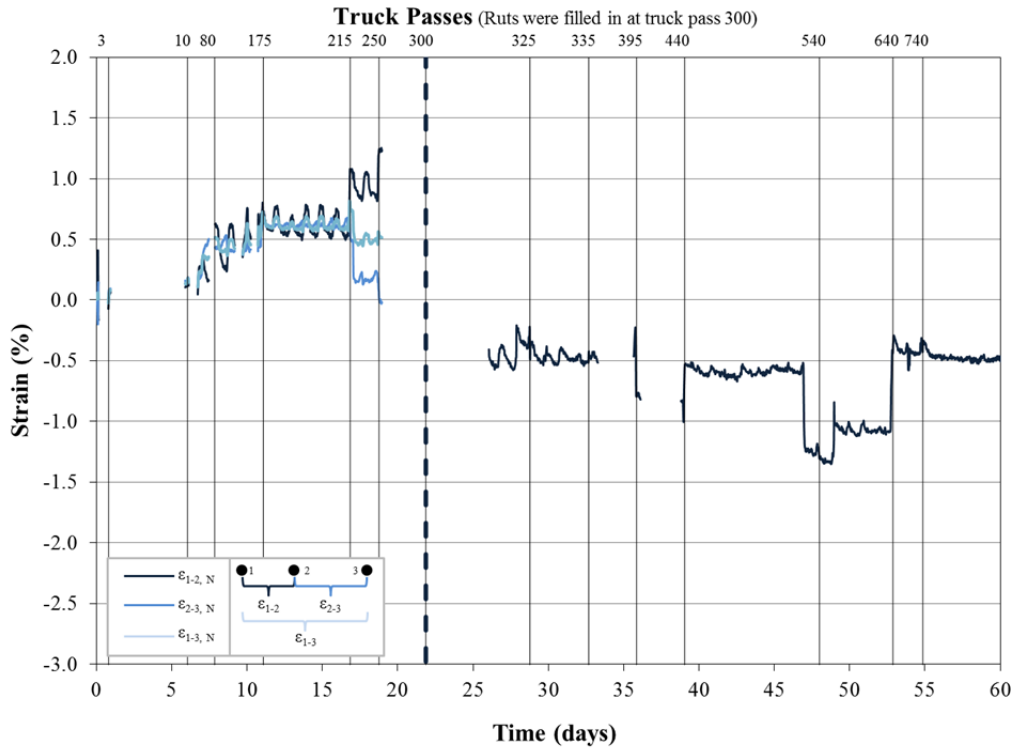
Figure Q-17: Cumulative LVDT strain for Test Section 9, north (Huesker Fornit 30).
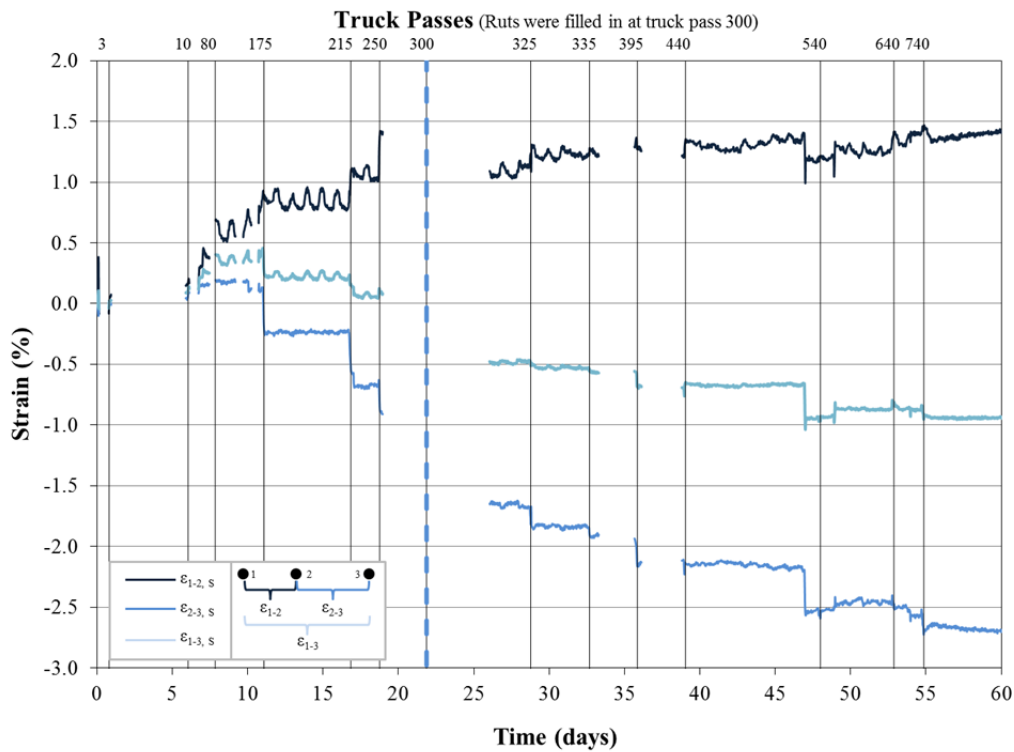
Figure Q-18: Cumulative LVDT strain for Test Section 9, south (Huesker Fornit 30).
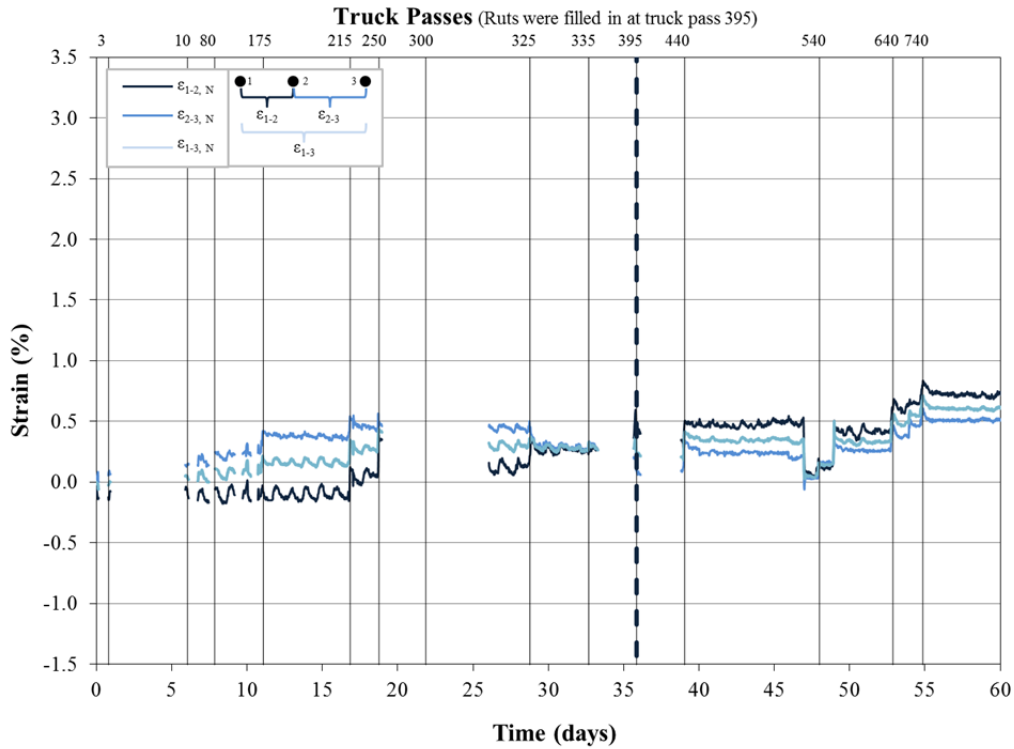
Figure Q-19: Cumulative LVDT strain for Test Section 10, north (SynTec Tenax MS 330).
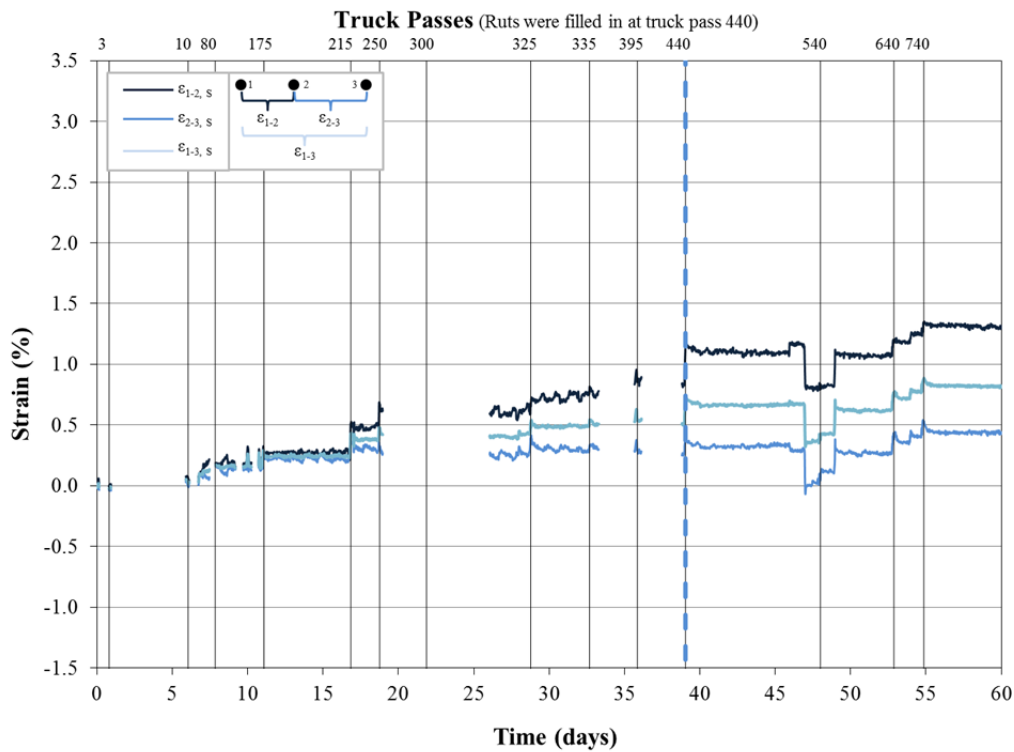
Figure Q-20: Cumulative LVDT strain for Test Section 10, south (SynTec Tenax MS 330).
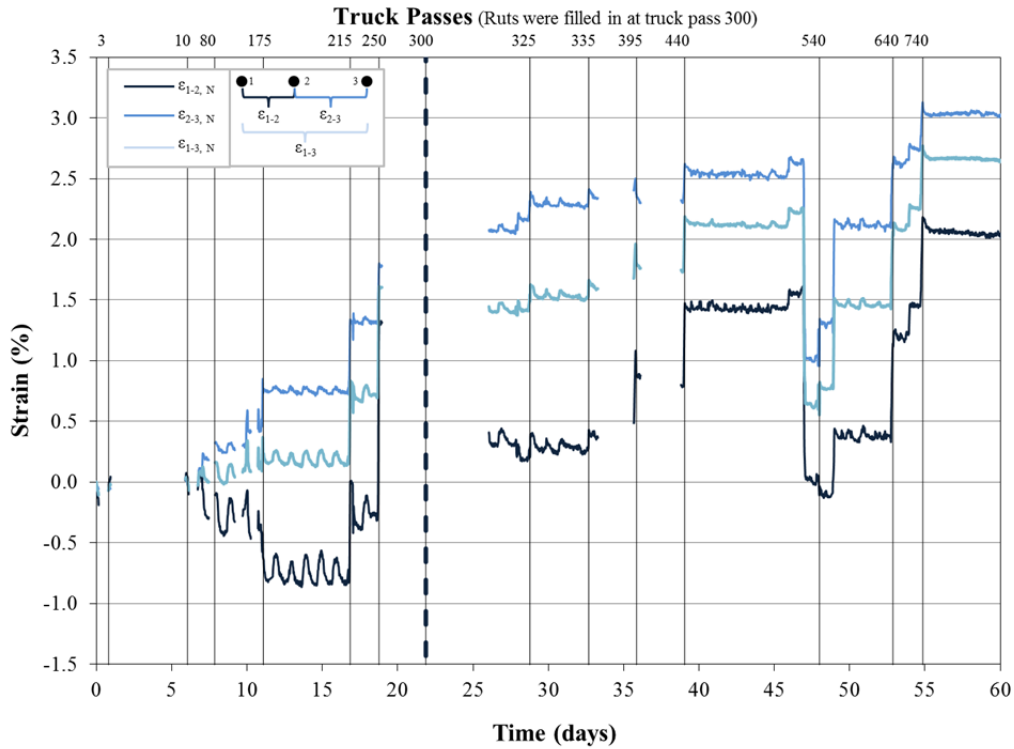
Figure Q-21: Cumulative LVDT strain for Test Section 11, north (Tensar TX140).
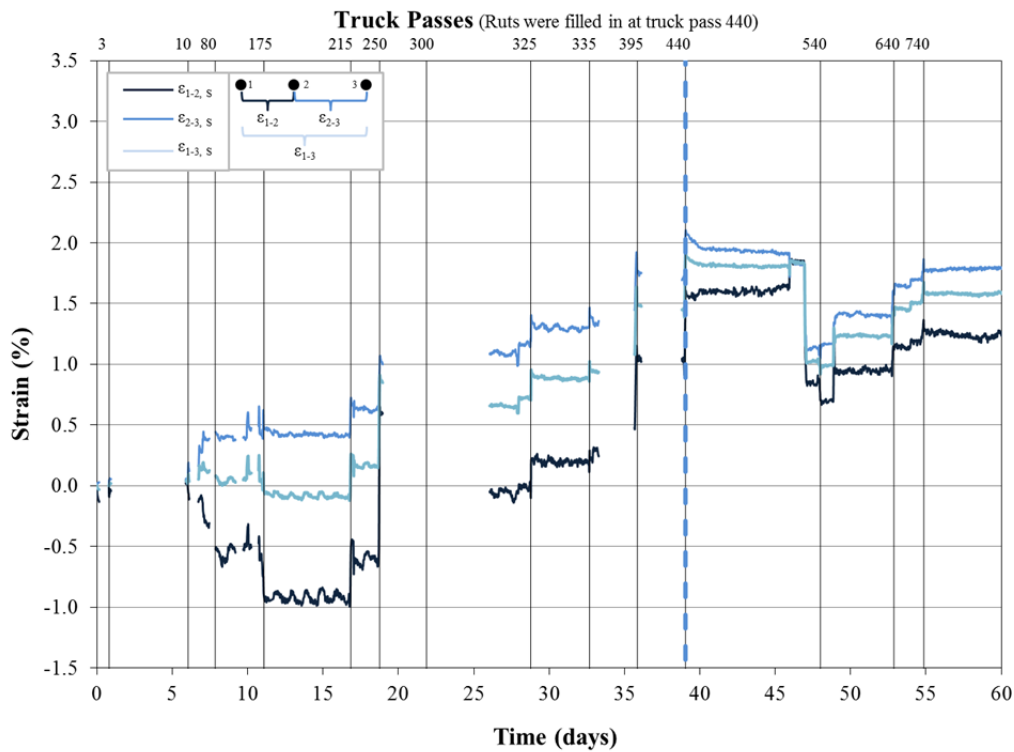
Figure Q-22: Cumulative LVDT strain for Test Section 11, south (Tensar TX140).
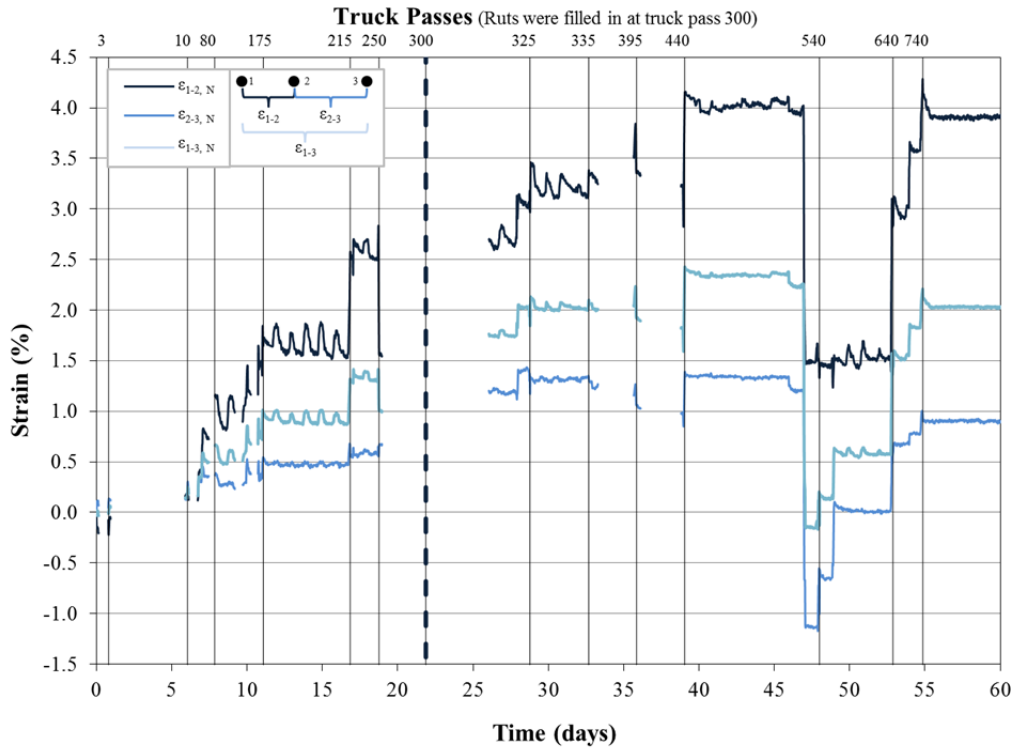
Figure Q-23: Cumulative LVDT strain for Test Section 12, north (Tensar TX160).
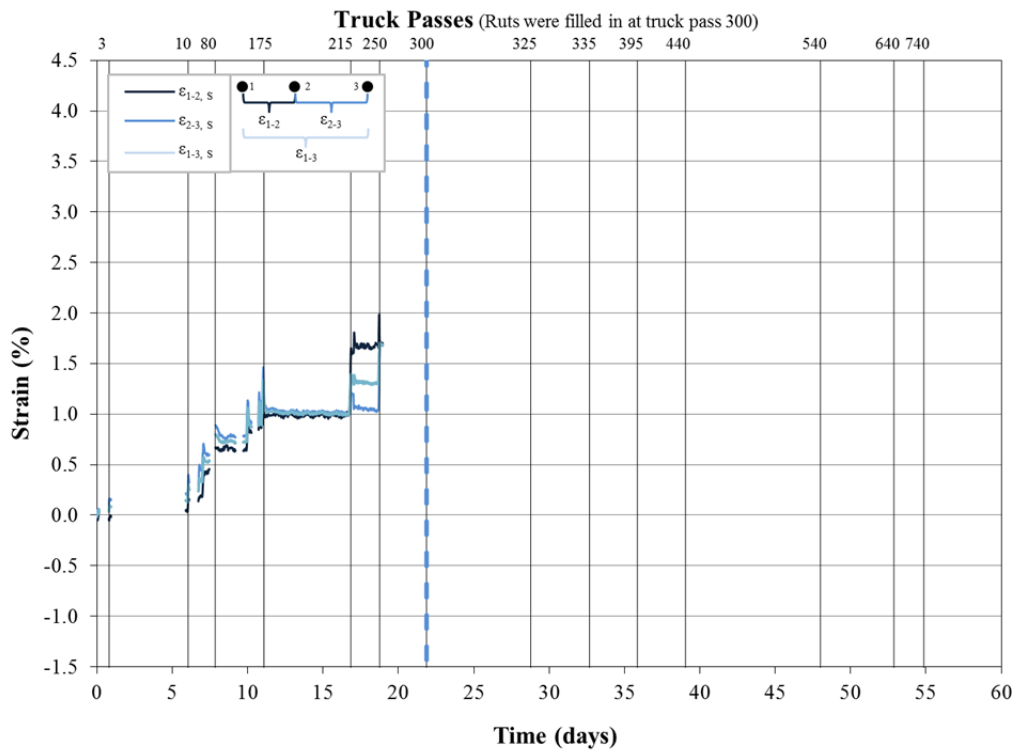
Figure Q-24: Cumulative LVDT strain for Test Section 12, south (Tensar TX160).
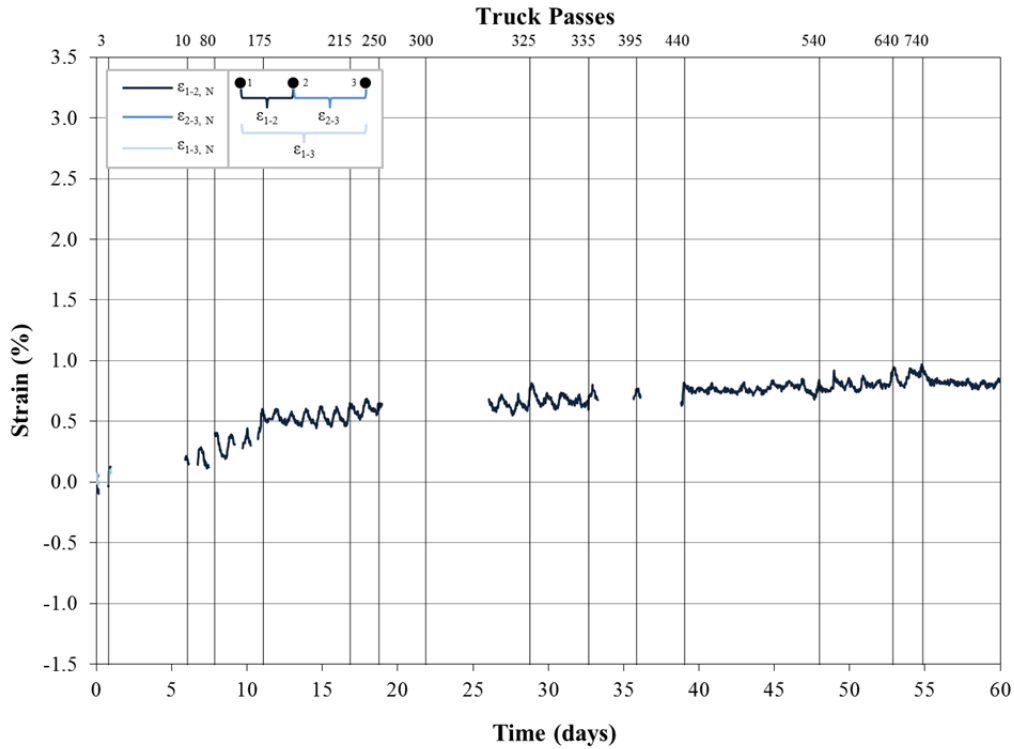
Figure Q-25: Cumulative LVDT strain for Test Section 13, north (TenCate Mirafi RS580i).
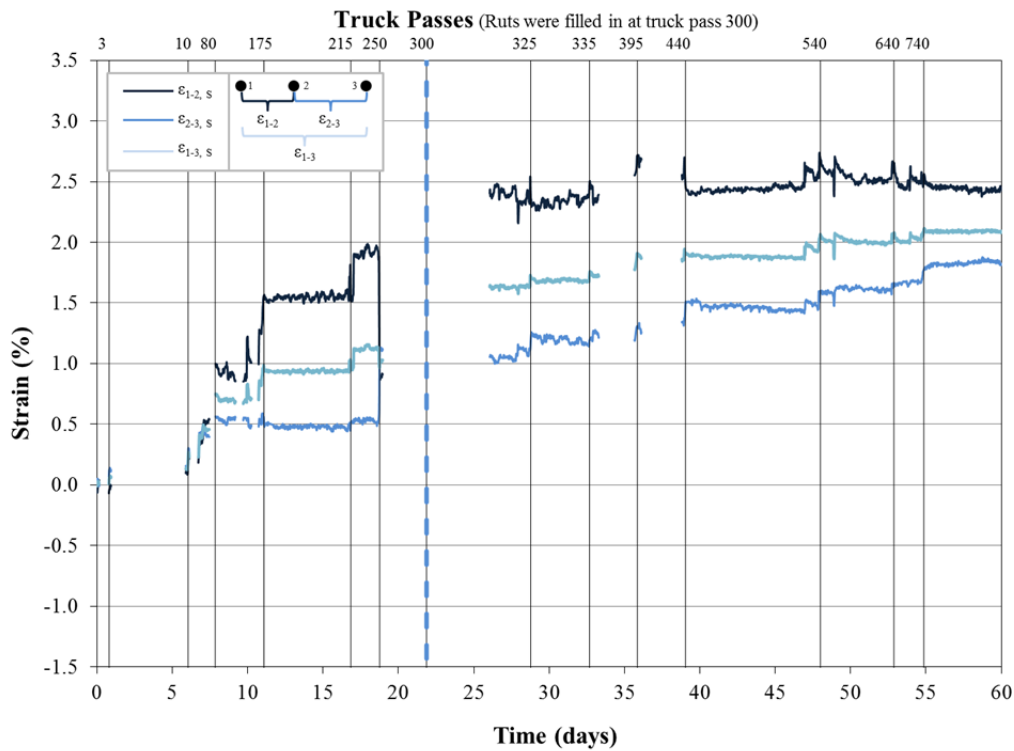
Figure Q-26: Cumulative LVDT strain for Test Section 13, south (TenCate Mirafi RS580i).
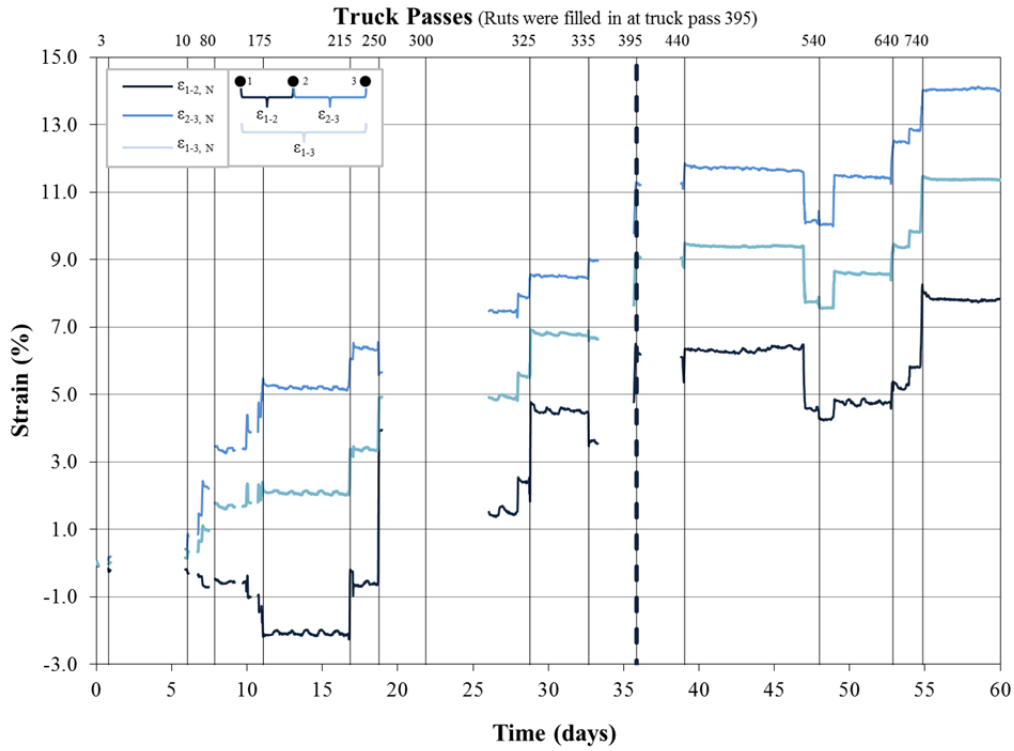
Figure Q-27: Cumulative LVDT strain for Test Section 14, north (Propex Geotex 801).
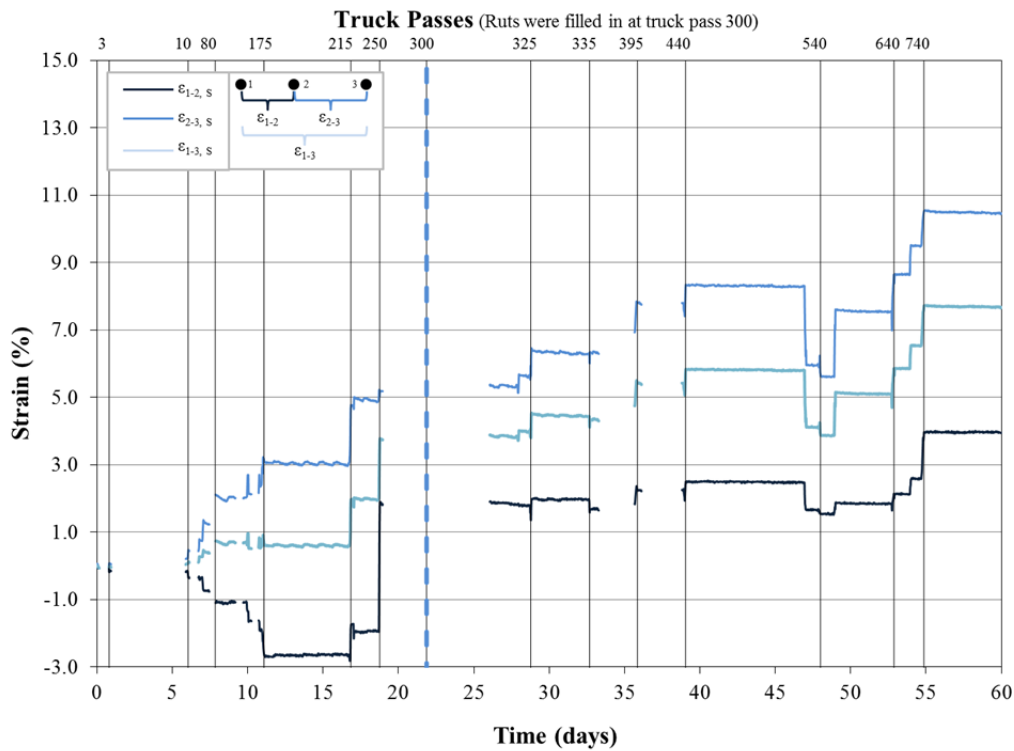
Figure Q-28: Cumulative LVDT strain for Test Section 14, south (Propex Geotex 801).

APPENDIX R – CUMULATIVE PORE-WATER PRESSURE RESULTS
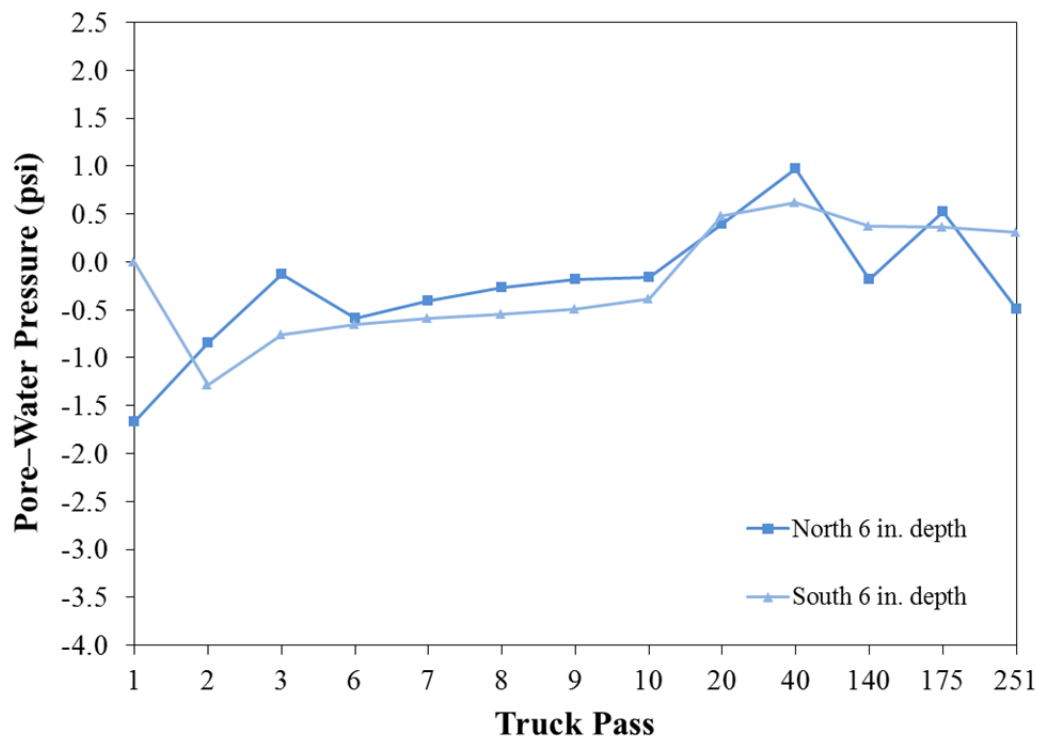
Figure R-1: Dynamic pore-water pressure for Test Section 1 (Tensar BX Type 2, CBR = 2.17).
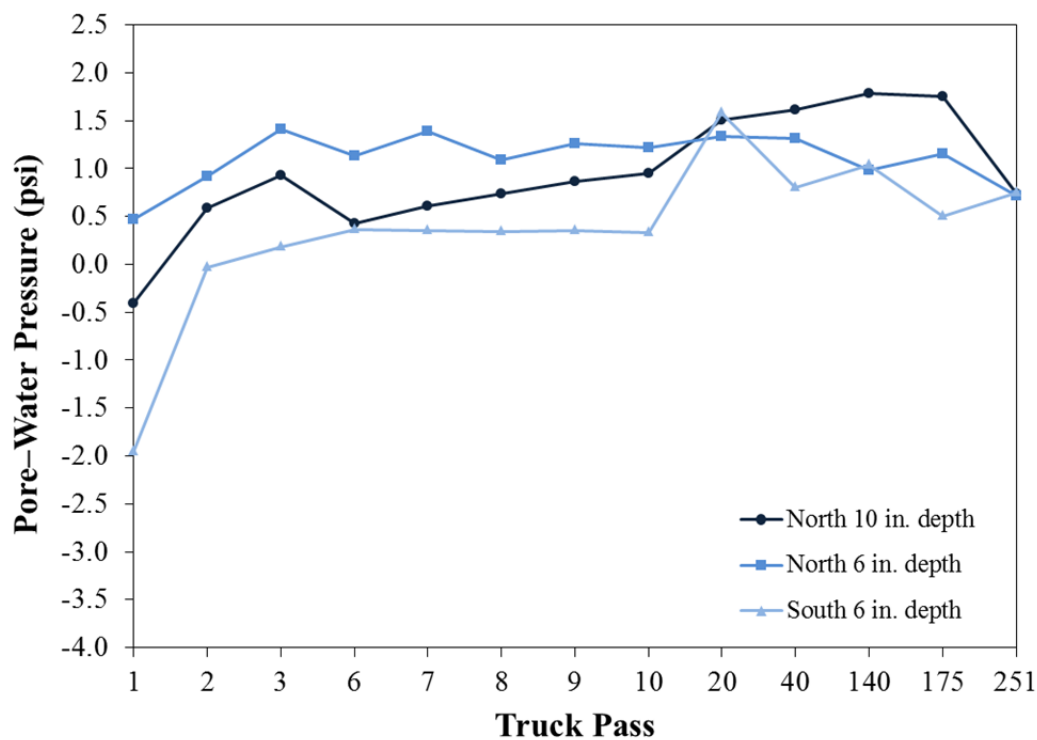

Figure R-2: Dynamic pore-water pressure for Test Section 2 (Tensar BX Type 2, CBR = 1.64).
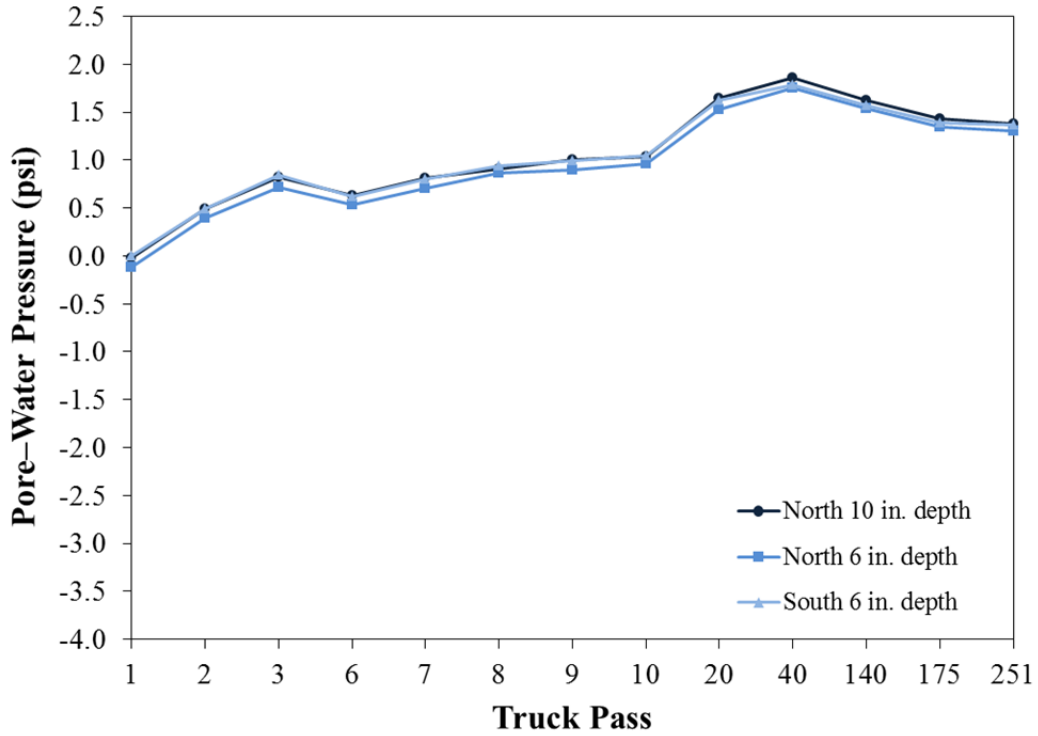
Figure R-3: Dynamic pore-water pressure for Test Section 3 (Tensar BX Type 2, CBR = 1.79).
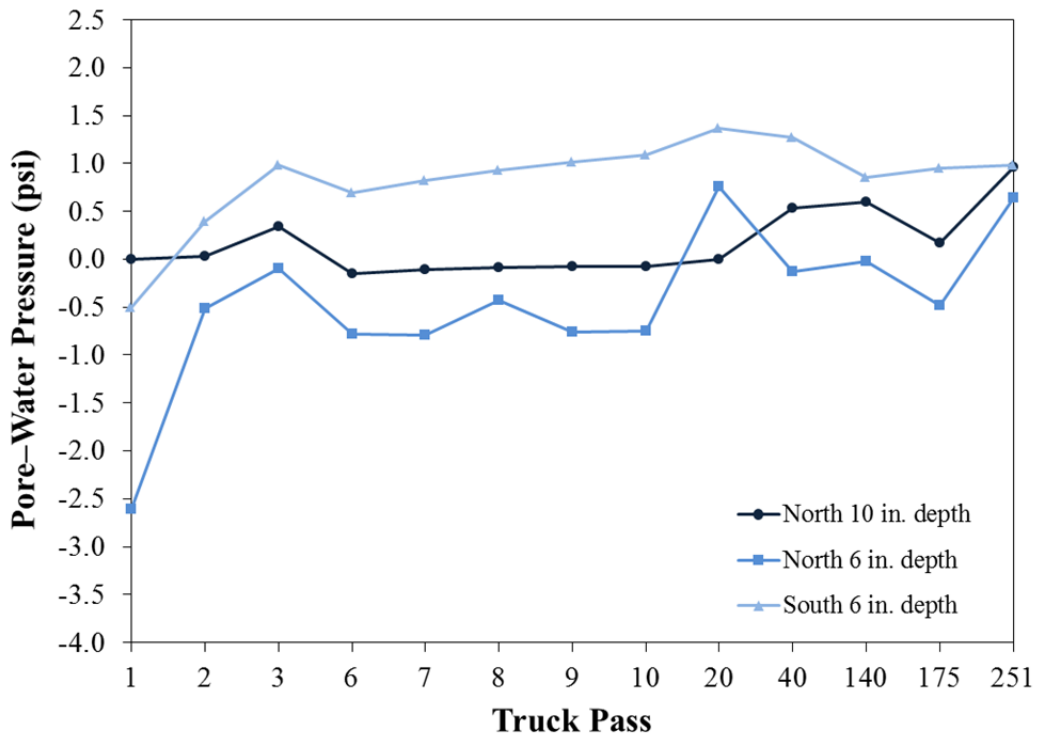
Figure R-4: Dynamic pore-water pressure for Test Section 4 (NAUE Secugrid 30-30 Q1).
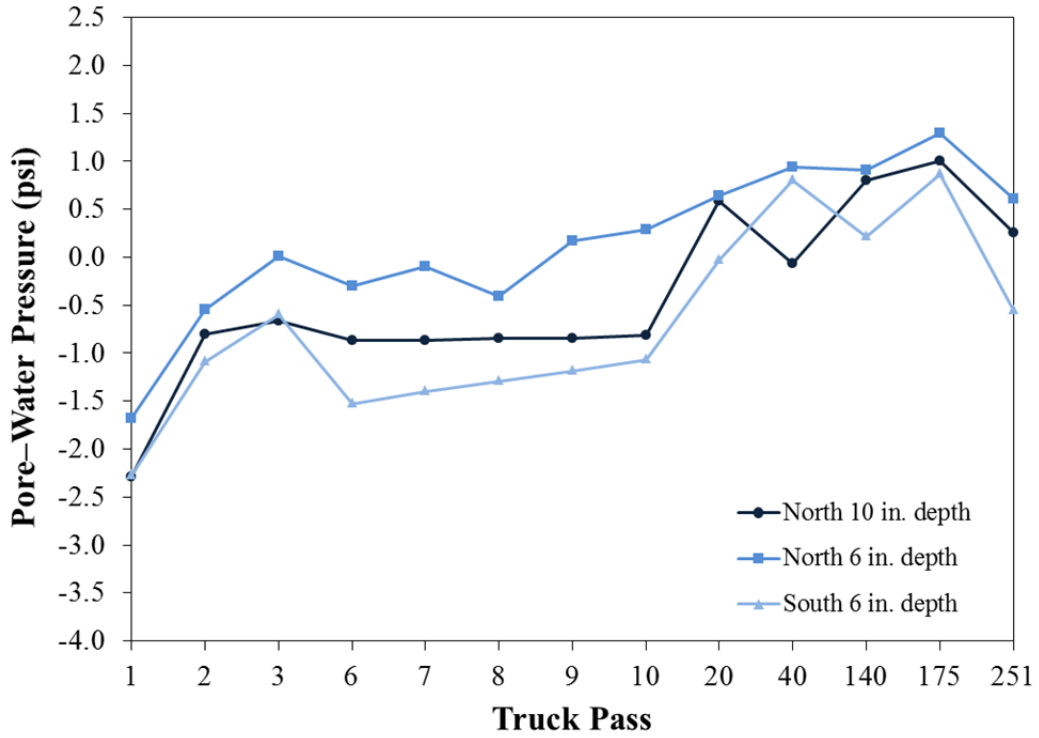
Figure R-5: Dynamic pore-water pressure for Test Section 5 (Colbond Enkagrid MAX 30).
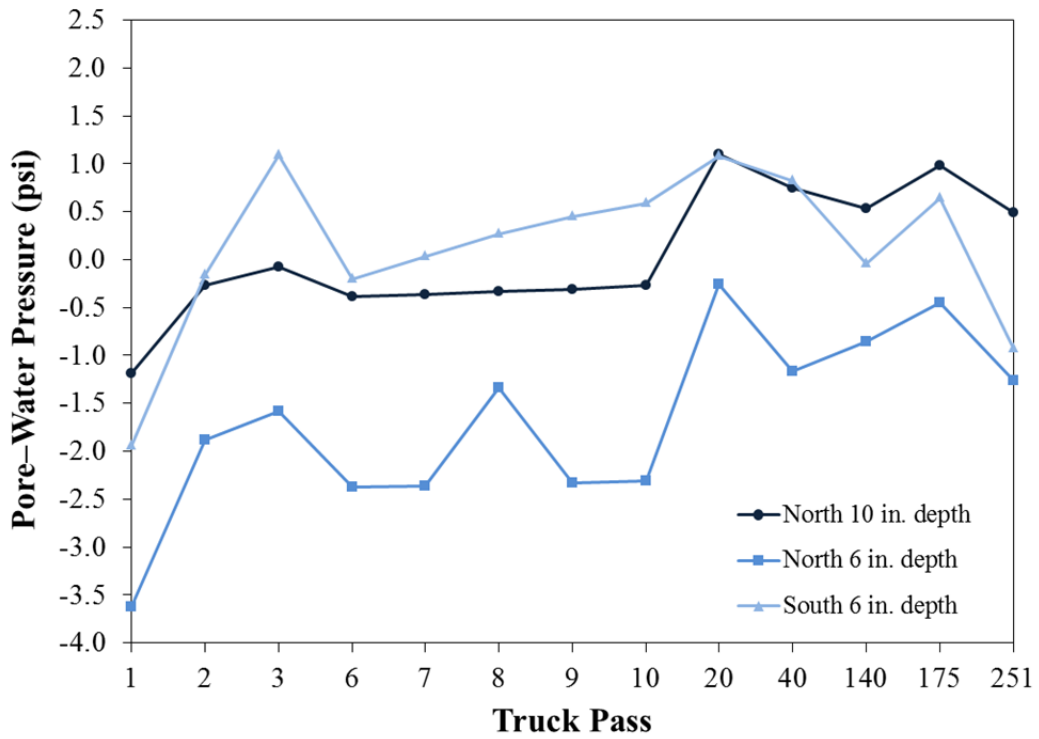
Figure R-6: Dynamic pore-water pressure for Test Section 6 (Synteen SF11).
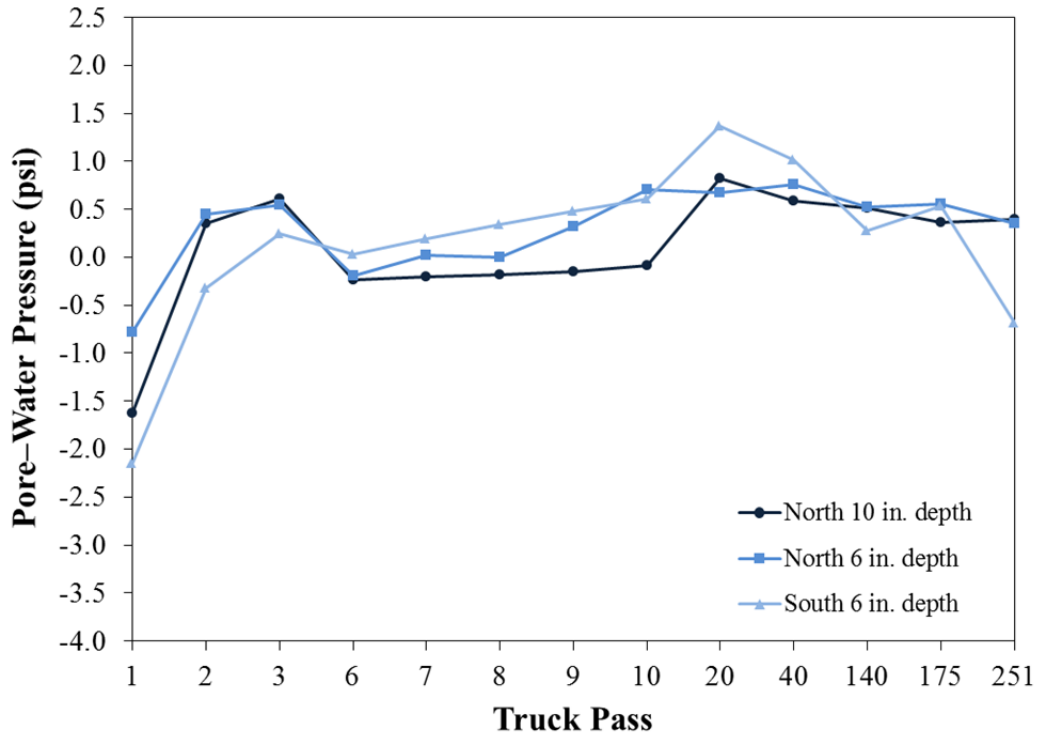
**Figure R-7: Dynamic pore-water pressure for Test Section 7 (Synteen SF12).**
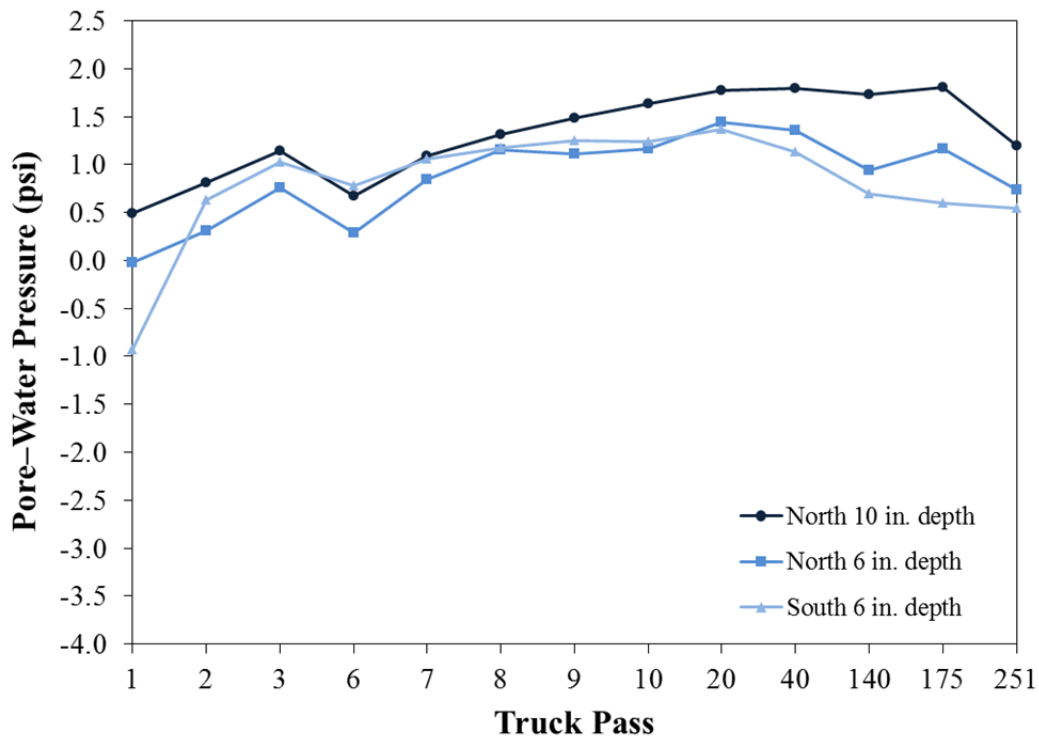
Figure R-8: Dynamic pore-water pressure for Test Section 8 (TenCate Mirafi BXG11).
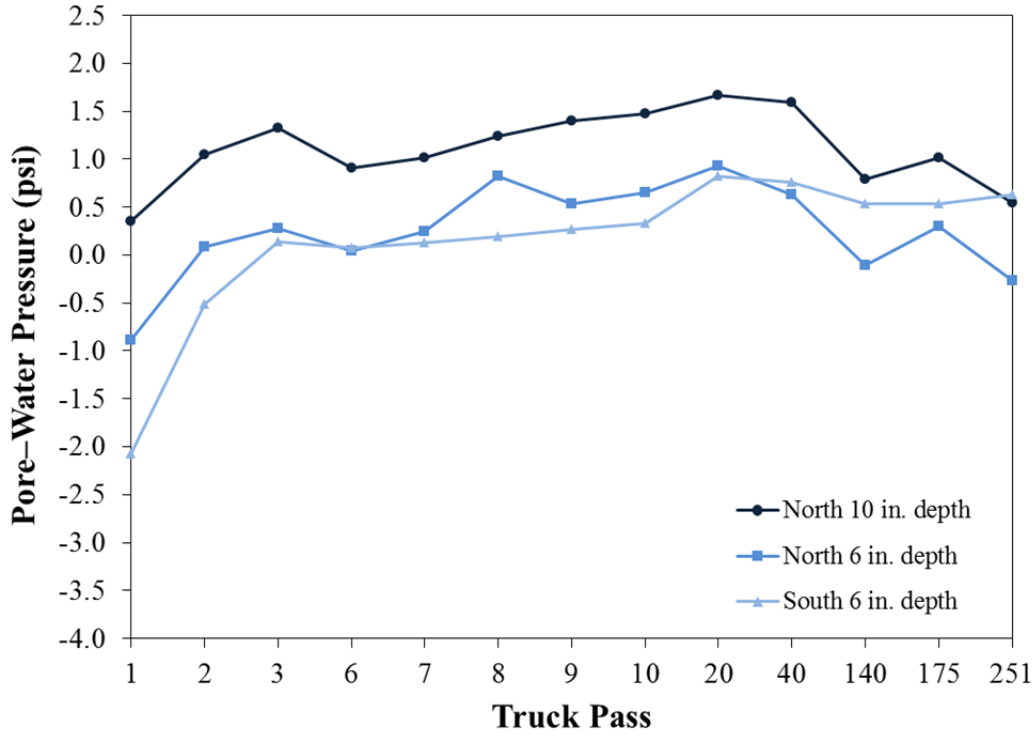
Figure R-9: Dynamic pore-water pressure for Test Section 9 (Huesker Fornit 30).
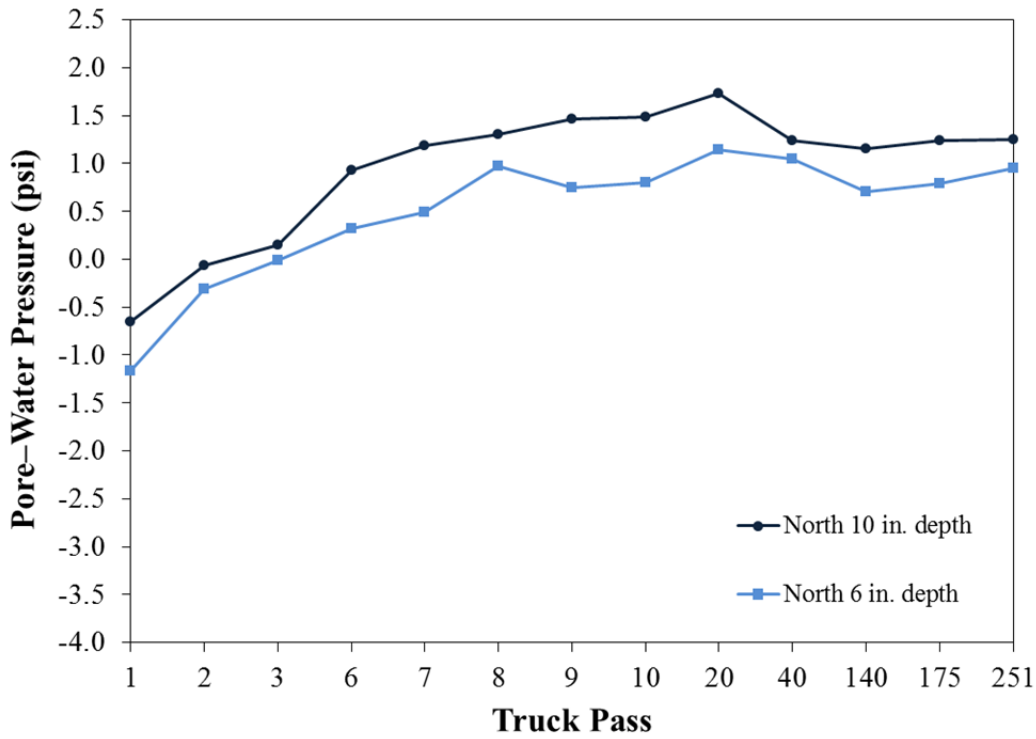
Figure R-10: Dynamic pore-water pressure for Test Section 10 (SynTec Tenax MS 330).
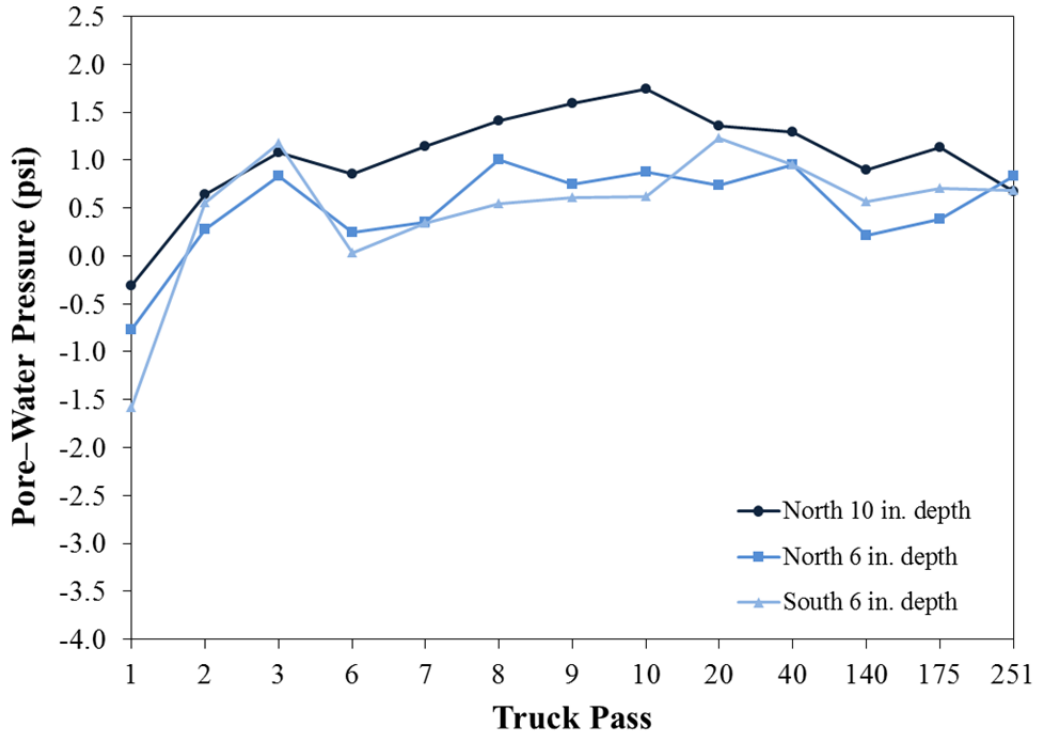
Figure R-11: Dynamic pore-water pressure for Test Section 11 (Tensar TX140).
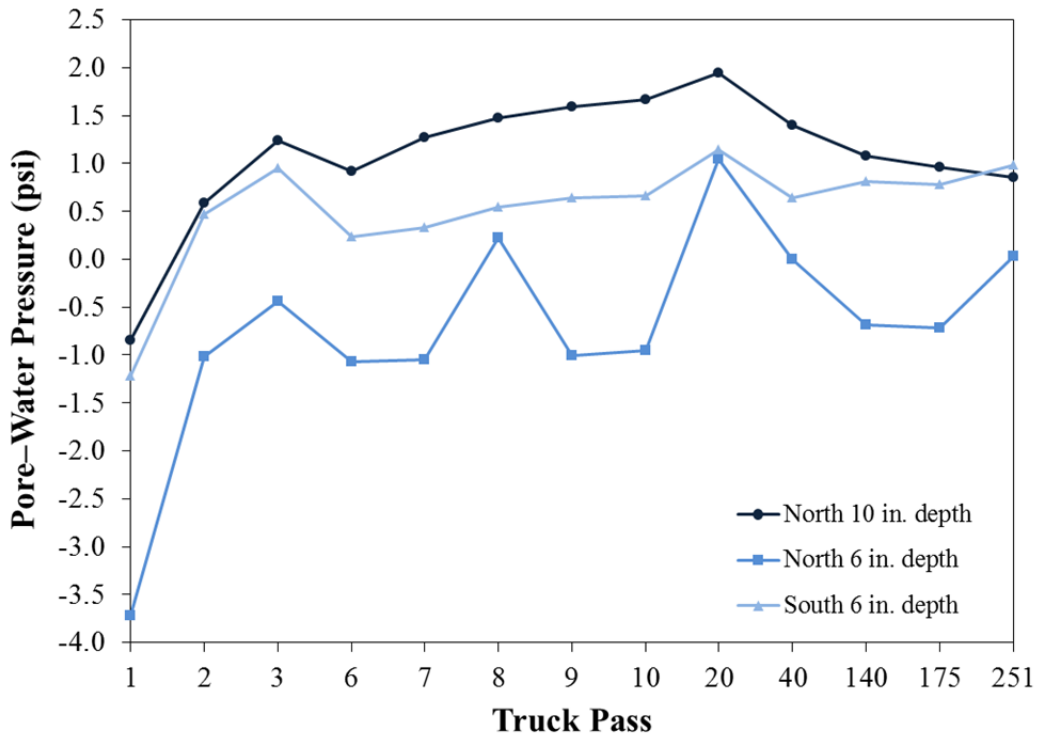
Figure R-12: Dynamic pore-water pressure for Test Section 12 (Tensar TX160).
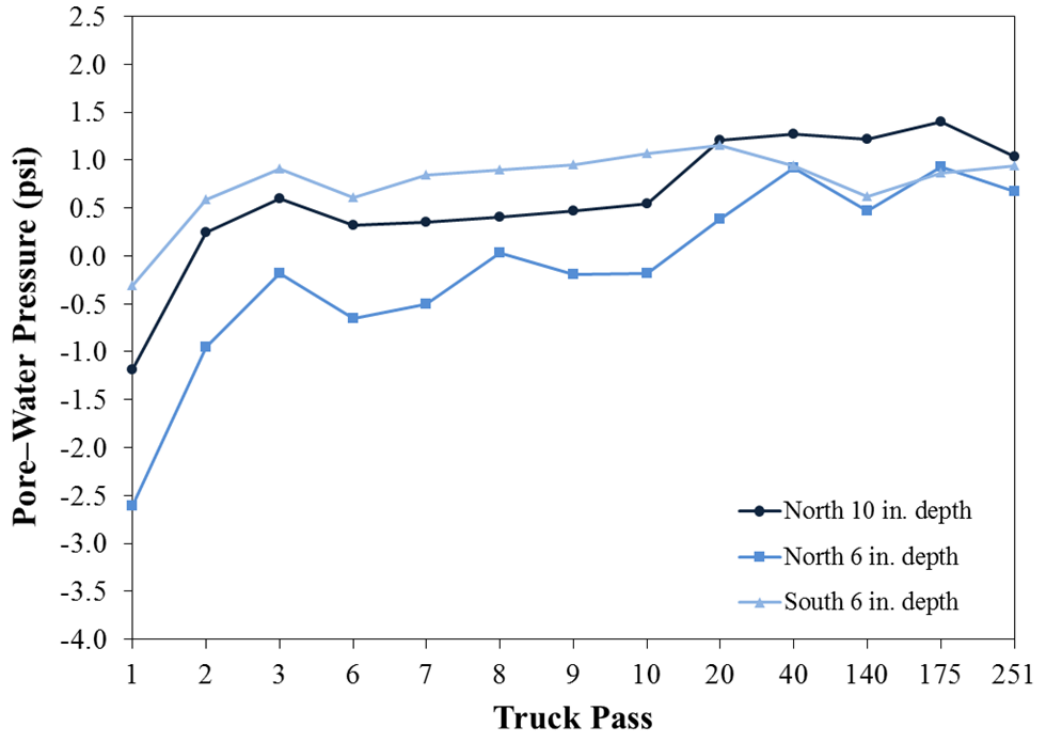
Figure R-13: Dynamic pore-water pressure for Test Section 13 (TenCate Mirafi RS580i).
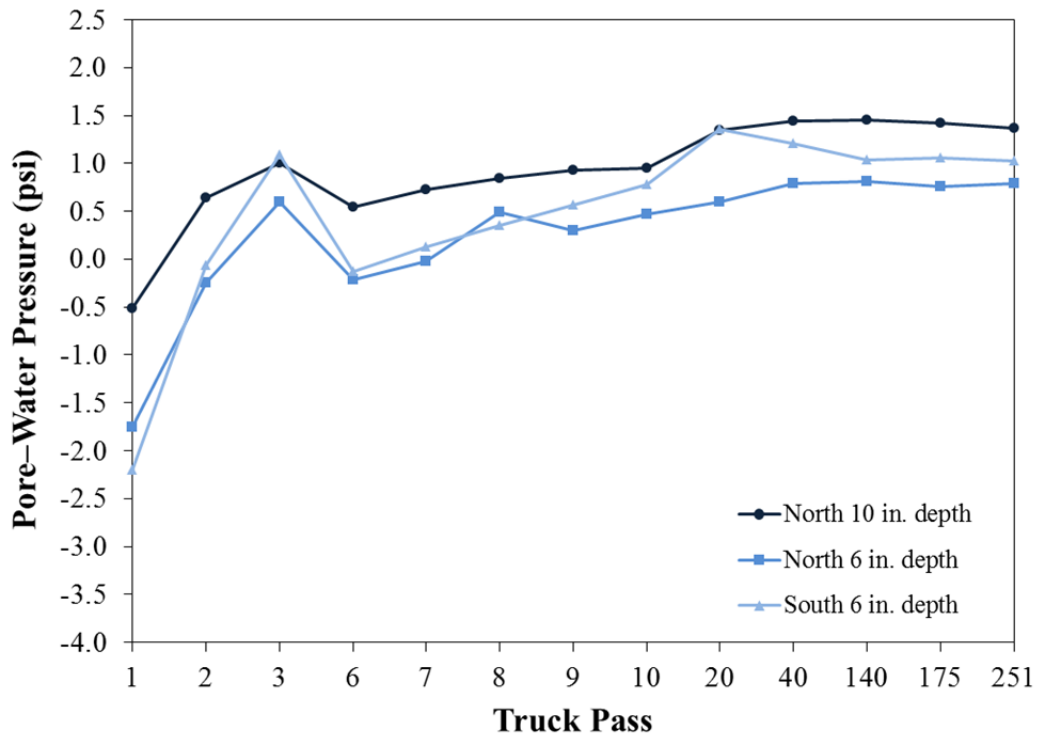

**Figure R-14: Dynamic pore-water pressure for Test Section 14 (Propex Geotex 801).**
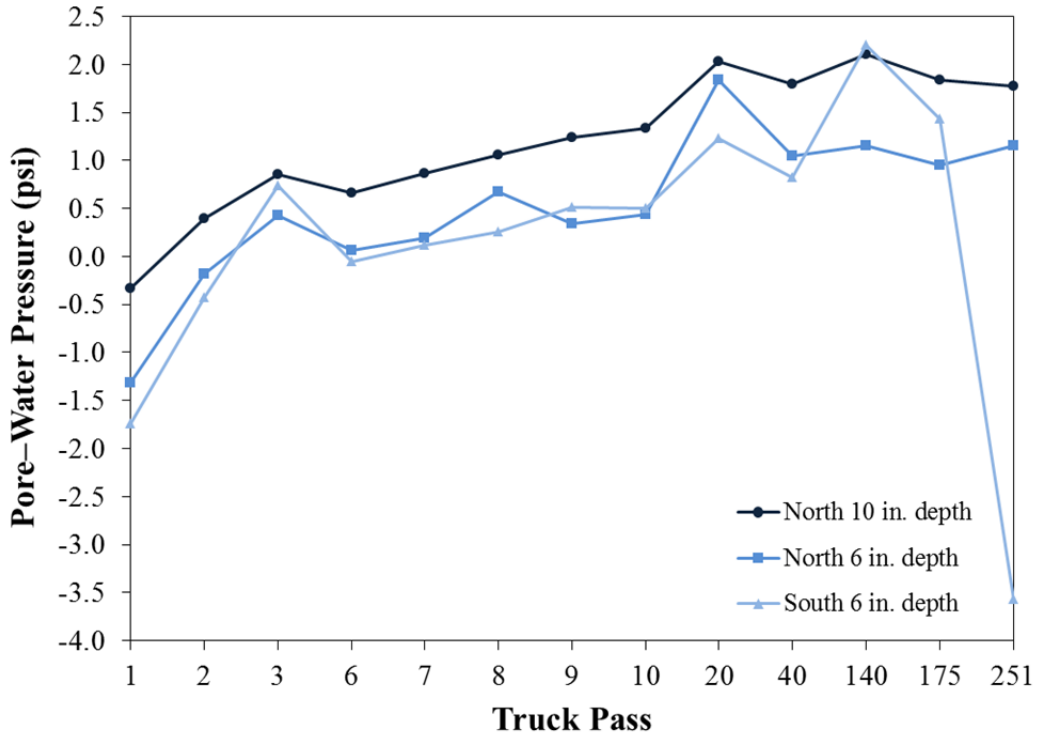
**Figure R-15: Dynamic pore-water pressure for Test Section Control 1.**
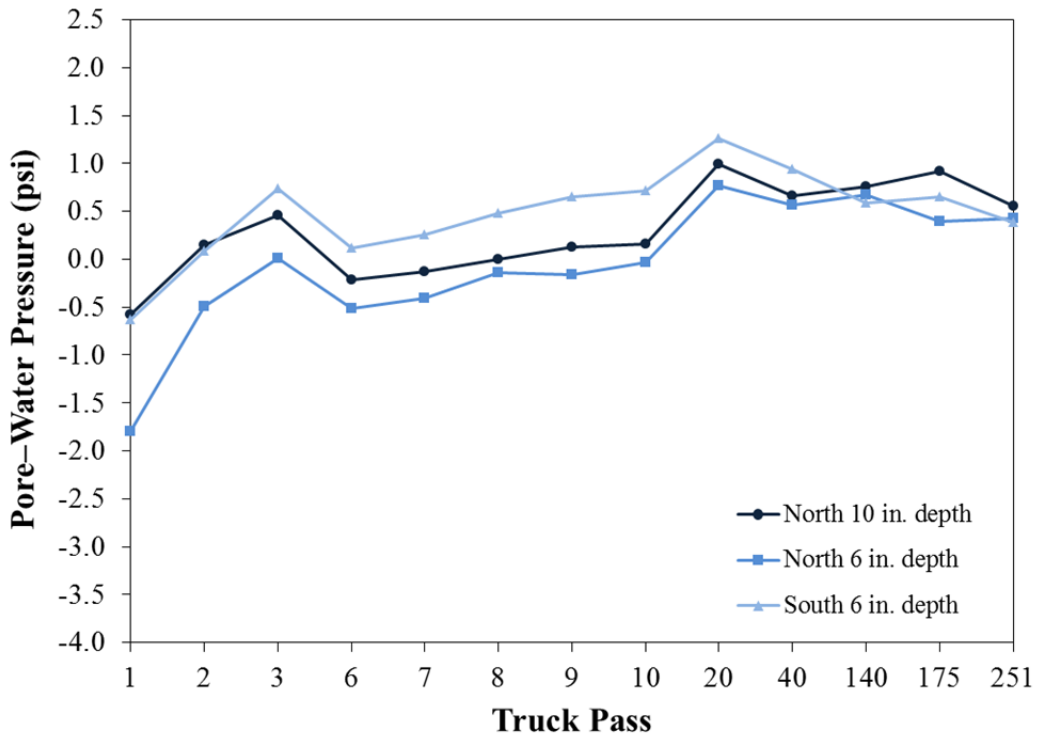
**Figure R-16: Dynamic pore-water pressure for Test Section Control 2.**
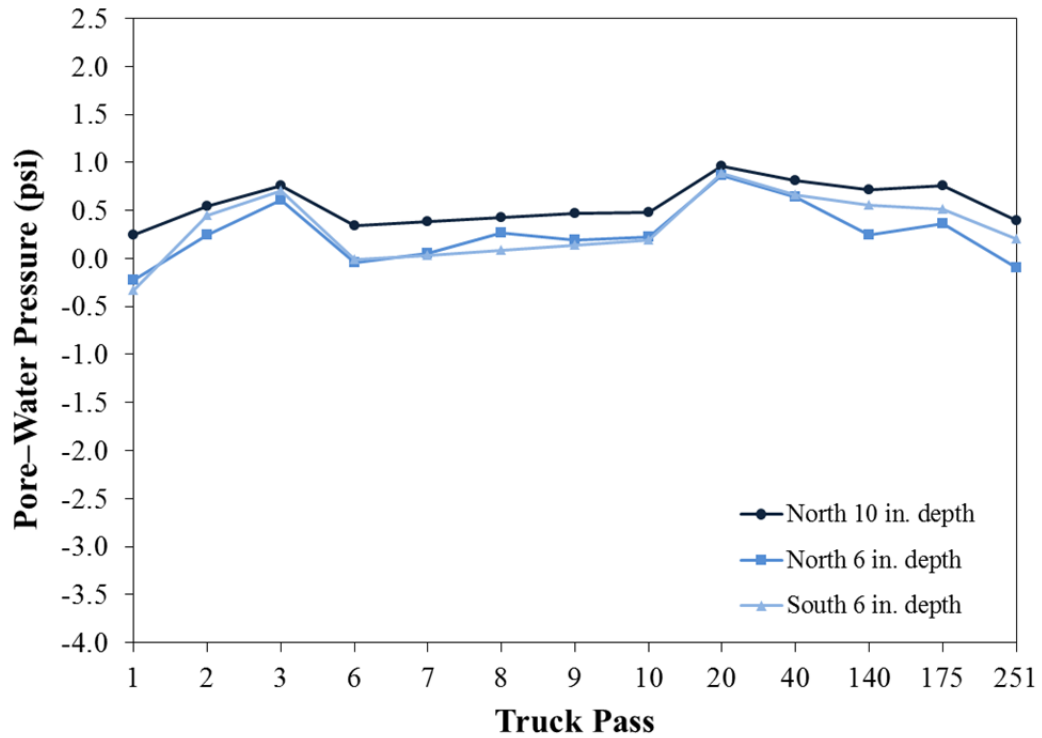
Figure R-17: Dynamic pore-water pressure for Test Section Control 3.